Application de l'assimilation de données à la mécanique des fluides numérique : de la turbulence isotrope aux écoulements urbains

Vincent Mons

To cite this version:

Vincent Mons. Application de l'assimilation de données à la mécanique des fluides numérique : de la turbulence isotrope aux écoulements urbains. Fluid Dynamics [physics.flu-dyn]. Université Pierre et Marie Curie - Paris VI, 2016. English. NNT : 2016PA066400 . tel-01927598v2

HAL Id: tel-01927598
https://theses.hal.science/tel-01927598v2

Submitted on 24 Sep 2019

THÈSE DE DOCTORAT DE L'UNIVERSITÉ PIERRE ET MARIE CURIE

Spécialité : Mécanique des Fluides

École Doctorale de Sciences Mécaniques, Acoustique, Électronique et Robotique de Paris (ED 391)

Présentée par

Vincent MONS

pour obtenir le grade de

DOCTEUR DE L'UNIVERSITÉ PIERRE ET MARIE CURIE

Application de l'assimilation de données à la mécanique des fluides numérique : de la turbulence isotrope aux écoulements urbains

---

dirigée par Jean-Camille CHASSAING, Pierre SAGAUT et Thomas GOMEZ

à l'Institut Jean le Rond d'Alembert

Soutenue à l'UPMC le 18 novembre 2016 devant le jury composé de

Claude CAMBON, Directeur de recherche, École Centrale de Lyon	Examinateur
Jean-Camille CHASSAING, Maître de conférence, UPMC	Directeur de thèse
Thomas GOMEZ, Professeur, Université de Lille 1	Directeur de thèse
Benoît-Joseph GRÉA, Ingénieur de recherche, CEA	Membre invité
Laurent JACQUIN, Professeur, ONERA	Rapporteur
Régis MARCHIANO, Professeur, UPMC	Examinateur
Marcello MELDI, Maître de conférence, Université de Poitiers	Membre invité
Pierre SAGAUT, Professeur, Aix-Marseille Université	Directeur de thèse
Olivier THUAL, Professeur, Institut National Polytechnique de Toulouse	Rapporteur
Christos VASSILICOS, Professeur, Imperial College London	Examinateur

Abstract

Computational fluid dynamics (CFD) is a valuable tool to investigate complex flows, and may provide detailed information about fluid phenomena that is not accessible through experimental or theoretical approaches. However, aside from possible errors arising during the physical modelling or discretization processes, uncertainties in the input quantities required by the CFD solver may prevent from an accurate estimation of the considered flow. For example, the numerical reproduction of the flow past an airfoil needs, among others, proper knowledge of the angle of attack and Mach number, which are rarely known with accuracy in real applications. Besides, the more complex the flow is, the harder is the prescription of appropriate initial and boundary conditions for numerical simulation.

In this thesis, we investigate the use of various data assimilation (DA) techniques in the context of CFD, with the ultimate goal of enhancing the prediction of real-world flows. DA consists in merging numerical predictions and experimental observations in order to improve the estimation of the CFD solver inputs. Both methodological aspects of DA and its potential application to physics investigations are explored for various flow configurations. First, DA is considered for the theoretical analysis of grid turbulence decay. Fundamental aspects of anisotropic homogeneous turbulence are also investigated through spectral modelling. Various DA methodologies are deployed in conjunction with a Navier-Stokes solver and are assessed for the reconstruction of unsteady compressible flows with large control vectors. Sensor placement strategies are developed to enhance the performances of the DA process. Finally, a first application of DA to Large Eddy Simulations of full-scale urban flows is proposed with the aim of identifying source and wind parameters from concentration measurements.

Résumé

La mécanique des fluides numérique (MFN) est devenue un outil indispensable dans les milieux académique et industriel dans la mesure où elle permet d'obtenir des informations sur des écoulements complexes qui sont difficilement accessibles par des approches expérimentales ou théoriques. Toutefois, mis à part d'éventuels défauts dans la modélisation physique ou dans le processus de discrétisation, la prescription de mauvais paramètres d'entrée peut être à l'origine d'erreurs significatives dans la prédiction numérique de l'écoulement étudié. A titre d'exemple, la simulation numérique d'un écoulement autour d'un profil d'aile nécessite, entre autres, une connaissance précise des valeurs de l'angle d'attaque et du nombre de Mach. En outre, l'identification de conditions initiale et aux limites appropriées est d'autant plus difficile que l'écoulement étudié est complexe.

Dans cette thèse, l'application de l'assimilation de données (AD) à la MFN est étudiée, avec comme objectif global de contribuer à l'amélioration de la prévision numérique d'écoulements complexes. L'AD consiste à fusionner les outils de prévision numérique avec des données expérimentales afin d'améliorer l'estimation des paramètres d'entrée du code MFN. Les aspects méthodologiques de l'AD et son application pour des études physiques sont tous deux examinés dans cette thèse. Dans un premier temps, l'AD est utilisée pour une étude théorique de la turbulence de grille. Un modèle spectral pour les écoulements turbulents homogènes et anisotropes est également proposé. Plusieurs méthodes d'AD sont ensuite implémentées pour un code MFN et appliquées à la reconstruction d'écoulements instationnaires et compressibles en présence d'incertitudes sur des paramètres d'entrée de grandes dimensions afin d'évaluer les forces et faiblesses respectives de ces techniques. Des stratégies pour le placement optimal de réseaux de capteurs sont élaborées afin d'améliorer les performances du processus d'AD. Enfin, l'AD est appliquée à l'identification de sources de polluants et à la reconstruction de conditions météorologiques pour des écoulements en milieu urbain prédits par Simulation des Grandes Échelles.

Remerciements

En premier lieu, je tiens à remercier mes directeurs. Je suis extrêmement reconnaissant envers Pierre Sagaut de m'avoir accepté pour travailler sur ce beau sujet ainsi que d'avoir su donner les grandes directives qui ont permis à ce travail d'aboutir. Je le remercie pour tout ce qu'il m'a apporté, et je ne peux que regretter la distance Paris-Marseille. Je remercie très chaleureusement Jean-Camille Chassaing pour son soutien et sa présence au quotidien qui ont été extrêmement précieux, voire indispensables, au cours de ces trois années, tant sur le plan scientifique que celui du moral. Je le remercie pour tout. Enfin, merci à Thomas Gomez d'avoir manifesté de l'intérêt pour ces travaux.

Je tiens à témoigner toute ma reconnaissance à Olivier Thual et Laurent Jacquin pour avoir accepté la charge de rapporteur pour cette thèse. Je tiens également à remercier les autres membres du jury. Je suis très reconnaissant envers Christos Vassilicos d'avoir accepté de se constituer examinateur pour cette thèse. Je tiens à remercier Régis Marchiano qui a suivi cette thèse dès la seconde année. Je souhaite exprimer ma gratitude envers Claude Cambon pour le rôle spécial que ce dernier a joué au cours de cette thèse et pour tout ce qu'il m'a transmis. J'adresse également un grand merci à Benoît-Joseph Gréa et Marcello Meldi pour avoir accepté de prendre part au jury.

Je souhaite exprimer ma gratitude envers ceux avec qui j'ai échangé au cours de cette thèse et qui ont permis d'enrichir cette dernière. Je remercie à nouveau Claude Cambon pour tout ce qu'il a apporté pour faire aboutir l'étude du chapitre 4. Je suis très reconnaissant envers Luca Margheri pour sa disponibilité et tout ce qu'il a pu me transmettre, et sans qui l'étude du chapitre 7 n'aurait pas pu être menée. Je remercie chaleureusement Antoine Briard pour le quotidien et qui a largement étendu les résultats du chapitre 4 dans ses propres travaux. Enfin, merci à Guillaume de Guyon-Crozier et Denis Kalamulla que j'ai eu le plaisir de côtoyer lors de leurs stages de master 1 et qui ont permis d'explorer certains aspects du problème du chapitre 6.

J'en profite pour remercier les personnes qui ont joué un rôle majeur dans mon parcours académique et sans qui je n'aurais probablement pas eu l'occasion de réaliser cette thèse. Je pense en premier lieu à Pierre Sagaut, ainsi qu'à Hélène Dumontet et Jean-Jacques Marigo qui m'ont permis de réaliser un léger détour avant de revenir étudier à l'UPMC. Je remercie à nouveau Marcello Meldi ainsi que Stéphane Gounand pour tout le temps consacré et pour ce qu'ils m'ont apporté lors de mes stages de master.

Je tiens à remercier les équipes de direction, administrative ainsi qu'informatique de d'Alembert pour m'avoir assisté dans un certain nombre de démarches au cours de cette thèse. Je pense en particulier à Stéphane Zaleski, Simona Otarasanu, Olivier Labbey et Evelyne Mignon. Je remercie également les membres de l'école doctorale SMAER, et en particulier Djimédo Kondo pour sa bienveillance.

Je remercie l'ensemble des doctorants et post-doctorants de d'Alembert qui ont égayé ces trois années. Je remercie spécialement Antoine, Maya, Kokou, Long et Alessio ainsi que l'ensemble de mes cobureaux. Je souhaite remercier également l'ensemble des permanents de l'institut. Je pense en particulier à Jean-Camille bien sûr, à Sophie dont la gentillesse a éclairé ces trois années, et à Jean-François.

Enfin, je tiens à remercier l'ensemble de mes proches pour m'avoir soutenu lors de ces trois années. Je remercie particulièrement Benjamin dont la proximité géographique pendant la thèse a été très heureuse. Je suis extrêmement reconnaissant envers mes parents qui m'ont toujours soutenu et m'ont transmis le goût de l'effort sans lequel rien de tout cela n'aurait été possible. Merci à ma soeur Cécile sans laquelle tout serait bien vide. Enfin, je remercie Juliette pour sa patience, son soutien et son accompagnement qui m'ont été indispensables lors de ces trois années.

Published content

Chapters 3 to 5 are based on the following publications:

- Vincent Mons, Jean-Camille Chassaing, Thomas Gomez and Pierre Sagaut (2014). Is isotropic turbulence decay governed by asymptotic behavior of large scales? An eddy-damped quasi-normal Markovian-based data assimilation study. Physics of Fluids, 26, 115105
- Vincent Mons, Claude Cambon and Pierre Sagaut (2016). A spectral model for homogeneous shear-driven anisotropic turbulence in terms of spherically averaged descriptors. Journal of Fluid Mechanics, 788, 147-182
- Vincent Mons, Jean-Camille Chassaing, Thomas Gomez and Pierre Sagaut (2016). Reconstruction of unsteady viscous flows using data assimilation schemes. Journal of Computational Physics, 316, 255-280

The following article has also been published partly based on the results of chapter 4:

- Antoine Briard, Thomas Gomez, Vincent Mons and Pierre Sagaut (2016). Decay and growth laws in homogeneous shear turbulence. Journal of Turbulence, 17, 699-726

Chapters 6 and 7 are based on the following submitted manuscripts:

- Vincent Mons, Jean-Camille Chassaing and Pierre Sagaut (2016). Optimal sensor placement for variational data assimilation of unsteady flows past a rotationally oscillating cylinder. Journal of Fluid Mechanics (under revision)
- Vincent Mons, Luca Margheri, Jean-Camille Chassaing and Pierre Sagaut (2016). Data assimilation-based reconstruction of urban flows. Journal of Wind Engineering and Industrial Aerodynamics (submitted)

Contents

Chapter 1

Global introduction

1.1 Motivations and objectives of the study

Computational fluid dynamics (CFD) is a valuable tool to investigate fluid mechanics problems, since it may provide detailed information about fluid phenomena that is not accessible through experimental or theoretical approaches. Accordingly, CFD has achieved widespread use in both fundamental studies and engineering applications. However, despite having reached a certain level of maturity, the reproduction of real-world flows through CFD remains challenging. The difficulties encountered in the numerical prediction of complex flows may originate from at least three main factors:

1. Physical modelling: the prediction of fluid phenomena requires the determination of appropriate mathematical models that capture the physics of the flow. These models are generally expressed in terms of partial differential equations that reflect conservation laws. For some complex flows, such as reacting or multiphase flows, deriving appropriate model equations is still an open issue.
2. Numerical methods: once the model equations of the flow are established, numerical schemes and discretization techniques are used to translate them into a numerical algorithm. Errors arising during the discretization process may originate from a variety of factors ranging from a lack of stability of the numerical schemes to an inadequate mesh given the geometry of the flow.
3. Inputs of the simulation: the numerical integration of the model equations generally requires the prescription of initial and boundary conditions, since partial differential equations are solved. The mathematical model may also involve adjustable parameters, whose values have to be specified. A wrong specification of the CFD solver inputs may induce significant errors in the prediction of the flow.

Issue 1 may not be the most serious problem in CFD, since conservation laws of fluid systems are well known, at least for single-phased flows, while issue 2 can be addressed through the improvement of numerical methods, even if accurate and robust schemes are already available. Accordingly, issue 3 appears to be prominent in CFD applications. For example, the numerical reproduction of the flow past an airfoil needs, among others, proper knowledge of the angle of attack and Mach number, which are rarely known with accuracy in real applications. Besides, the more complex the flow is, the harder is the prescription of appropriate initial and boundary conditions for numerical simulation. Therefore, there is a need for the development of methodologies providing appropriate estimations of the CFD solver inputs from external information.

Experimental fluid dynamics (EFD) is another way to study fluid mechanics problems, and is by essence appropriate to investigate real-world flows. However, EFD suffers from other limitations than those encountered in CFD. In particular, measurements are usually fragmentary in the sense that they are restricted in time and space, and thus can not provide a full description of the flow. Advanced interpolation techniques [34, 92] may be considered in order to complete sparse experimental data, but such methods usually do not allow to satisfy all the physical constraints on the flow.

A promising strategy to obtain detailed and accurate information about real-world flows may consist in combining the high resolution of CFD with observations from EFD [94]. This is precisely the principle of data assimilation (DA) [133], which consists in incorporating EFD information in CFD predictions through the determination of suitable inputs for the CFD solver. In other words, the aim of DA is to infer initial and boundary conditions and/or model parameters from limited experimental data. From the perspective of numericists, DA allows to drive CFD predictions towards real-world flows of interest. From the perspective of experimentalists, DA is an efficient methodology to complete sparse experimental data through CFD, thus allowing a proper enforcement of conservation laws. From a broader perspective, DA may be considered as an efficient tool to solve inverse problems.

In this thesis, we consider DA methodologies as used in earth sciences, which stem from the efforts of the meteorological community to determine appropriate initial conditions for climate prediction models from various sources of data [197]. These techniques have been developed in the context of large-scale and nonlinear systems, and therefore appear appropriate for fluid systems and CFD. Two main classes of DA methodologies may be distinguished. The first one relies on a deterministic formulation of the DA problem where the goal is to minimize the squared norm of the discrepancies between observations and numerical prediction [128]. The second class of techniques is derived in a stochastic framework from Bayes' theorem [224]. It is worth keeping in mind that the stochastic formulation of DA has been used in meteorological applications partly to take into account badly-known dynamics and imperfect models, since it remains difficult in earth sciences to derive model equations that reflect the full complexity of the physics of oceanographic and atmospheric systems. One might therefore wonder if the stochastic approach in DA, which requires more prior information than the deterministic one, is the most appropriate to CFD where governing equations are generally well known. However, both approaches are investigated in this thesis.

So far, two DA techniques have been applied to CFD, namely variational DA, which is based on optimal control [128, 137], and Kalman filtering, directly derived from the Bayesian formulation of DA [77, 111]. These two approaches have been investigated separately, while they vastly differ in their implementations and may produce distinct results. Moreover, recent hybrid DA approaches, which have not yet been considered in CFD, deserve attention due to their interesting combination of deterministic and stochastic techniques. Lastly, only a few studies have been dedicated to fully unsteady flows. Accordingly, further investigations are required to study methodological aspects of DA in the context of CFD, with the aim of identifying suitable approaches to determine initial condition, boundary conditions or model parameters for the numerical prediction of unsteady flows and characterizing their relative performances and advantages.

Along with the CFD solver used to estimate the flow and the assimilation methodology, observations are one of the primary components in DA. Since measurements represent the only available knowledge about the reference flow to be reconstructed, observation networks should be carefully designed in order to extract as much relevant information as possible. Despite the existence of several techniques for sensor placement in DA proposed in the meteorological community, the determination of efficient strategies for CFD applications is still an open question, while the choice of the observation locations may significantly deteriorate or enhance the results of the DA procedure.

As mentioned above, a required characteristic of the DA techniques considered here is their ability to solve inverse problems for large-scale and nonlinear systems. Accordingly, in addition to allow to enhance CFD and EFD results, DA may be considered as an appropriate tool to perform physical investigations of fluid mechanics problems. In particular, variational DA techniques provide the gradient of the flow solution with respect to all the components of a vector of interest such as the initial field, thus allowing to perform detailed sensitivity analyses of systems of large dimension. There is therefore significant potential to perform theoretical analyses through DA.

According to the above discussion, the aim of this thesis is threefold:

- Methodological aspects of DA are investigated in the context of unsteady fluid mechanics, with the aim of identifying appropriate techniques to infer large-dimensional inputs for CFD solvers from external information.
- Sensor placement strategies are developed for DA in order to maximize the efficiency of the assimilation process.
- The potential of DA to perform physical studies and sensitivity analyses is explored.

Flows of increasing complexity are considered in order to address the issues mentioned above. Homogeneous isotropic turbulence (HIT) and the use of the 1D eddy-damped quasi-normal Markovian (EDQNM) spectral model to compute HIT decay are first considered. The low computational cost of this model makes it appropriate for preliminary DA studies, while HIT decay remains a subject of great interest for turbulence theory. DA is here employed to identify the characteristics of the initial kinetic energy spectrum that lead grid turbulence decay. Next, various DA schemes are implemented in conjunction with a Navier-Stokes solver for bidimensional unsteady compressible flows, allowing to investigate inverse problems of higher dimensions. These DA techniques are here used to identify appropriate initial and boundary conditions from various types of observations of the flow past a cylinder in the presence of coherent gusts or performing rotary oscillations around its axis. As a final test case, the possibility of reconstructing complex turbulent urban flows through DA is investigated. Computations rely on a high-fidelity Large Eddy Simulation (LES) solver, and the issue of inferring characteristics of a pollutant source and meteorological conditions from measurements of concentration in an actual urban area is examined.

In addition to the study of DA in the context of fluid mechanics, spectral modelling of homogeneous turbulence is also considered in this thesis. The aim is to develop a model for anisotropic turbulence in the presence of mean velocity gradients that combines a spherically-averaged level of description with a rigorous description of anisotropy and EDQNM-based modelling for nonlinear terms. This approach allows to obtain a spectral model that can be used to calculate anisotropic turbulent flows at both very high and low Reynolds numbers, with good resolution of both large and small scales and over very long evolution times. This model is used to study both the interactions of turbulence with mean flows and its return to isotropy.

1.2 Thesis layout

The thesis is structured as follows:

- In chapter 2, a review of DA methods is provided.

Part I is dedicated to the study of homogeneous turbulence through spectral approaches and DA.

- In chapter 3, variational DA is used with the EDQNM model for the identification of the scales governing grid turbulence decay. The issue of anomalous decay regimes is examined.
- In chapter 4, a spectral model for homogeneous sheared turbulence is proposed and validated against grid turbulence experiments and Direct Numerical Simulations (DNS).

Part II is dedicated to the application of DA to CFD.

- In chapter 5, various DA techniques are implemented and assessed with a Navier-Stokes solver for bidimensional unsteady compressible flows. Different reconstruction scenarios for the flow past a cylinder in the presence of coherent gusts are investigated.

- In chapter 6, an adjoint-based sensor placement procedure is developed and assessed for the reconstruction of flows past a rotationally oscillating cylinder.
- In chapter 7, DA is applied to the identification of source characteristics and meteorological conditions in an urban environment with a LES solver. A sensor placement strategy based on global sensitivity methods is proposed.

Chapter 2

Review of data assimilation techniques

2.1 Introduction

This chapter is dedicated to a review of data assimilation (DA) techniques as developed in the atmospheric, oceanic and hydrologic communities. A more elaborate and exhaustive introduction to DA and discussions about its application to earth sciences may be found in textbooks such as [79, 112, 126, 133, 175, 199]. This chapter is organized as follows. The DA problem is defined in §2.2, in both deterministic and stochastic frameworks. Various DA techniques are then described in §2.3-§2.8, with an emphasis on the methods deployed in the present work.

2.2 Statement of the data assimilation problem

2.2.1 Deterministic formulation

DA basically aims at combining measured observations with a dynamical model in order to improve the estimation of the state of the system under consideration, such as the atmosphere or a newtonian fluid [197]. There are thus two primary components in DA: the dynamical model used to perform predictions about the state of the system, and observations of the system. In the present chapter, for the sake of clarity and to facilitate the use of an unified notation in the presentation of the different DA schemes, we adopt a discrete formulation of the DA problem, i.e. we consider state of the model, model operator (governing equations) and observations that are discretized in both space and time. The continuous formulation of the DA problem, which is possibly more appropriate for the derivation of variational schemes, is employed in chapters 3 and 6. In the discrete framework, it is assumed that the state of the system, such as a flow field, is described by the vector $\boldsymbol{x}_k \in \mathbb{R}^{N_s}$ at discrete time k, where N_s is the dimension of the state of the system after spatial discretization. The vector $\boldsymbol{x}_k$ is advanced in time according to

$$\boldsymbol{x}_{k+1} = \boldsymbol{m}_k(\boldsymbol{x}_k) \quad 0 \leq k \leq N-1, \tag{2.1}$$

where N is the number of time steps, the operator $\boldsymbol{m}_k$ denotes the fully discretized governing equations of the system, which are possibly non-autonomous and nonlinear. In a deterministic framework, given (2.1), the state $\boldsymbol{x}_k$ is uniquely specified by the initial condition $\boldsymbol{x}_0$. Again for the sake of conciseness, the case where the model operator $\boldsymbol{m}_k$ contains adjustable/badly-known parameters, such as boundary conditions or model parameters, is not considered in the present chapter. However, the extension of the DA schemes exposed in the following to the reconstruction of adjustable parameters in (2.1) is straightforward, and is performed in chapters 5-7. Aside from the dynamical model (2.1) that allows to predict the state of the system, it is assumed that observations of the system $\boldsymbol{y}_k \in \mathbb{R}^{N_o}$ are available, with N_o the dimension of the observations. These observations can be related to the state of the system according to

$$\boldsymbol{y}_k = \boldsymbol{h}(\boldsymbol{x}_k), \tag{2.2}$$

where $\boldsymbol{h}$ is the operator that maps the state space to the observation space. In a deterministic framework, available observations could be used to determine an accurate initial state in order to improve the prediction of the state of the system based on (2.1). This leads to the following least-square problem, where the initial state $\boldsymbol{x}_0$ is searched as a minimizer of a cost function defined as

$$J = \frac{1}{2} \sum_{k=0}^{N} \left\| \boldsymbol{y}_k - \boldsymbol{h}(\boldsymbol{x}_k) \right\|^2, \tag{2.3}$$

where $\|\cdot\|$ denotes the Euclidean norm. Observations are not necessarily available at all discrete times, but it is assumed so in the following for the sake of simplicity, without loss of generality. The cost function J in (2.3) is minimized under the dynamical constraint (2.1), and this deterministic formulation of the DA problem provides an appropriate framework for the variational methods exposed in §2.3.

2.2.2 Stochastic formulation

An implicit assumption in the deterministic formulation of the DA problem is that the model operator in (2.1) accurately reflects the dynamics of the system. However, in meteorological applications, where the considered systems are highly multi-scale and difficult to model faithfully, and whose dynamics are possibly noisy and chaotic, the assumption of perfect model in (2.1) is not necessarily adapted. Besides, observations may also be corrupted by noise or may contain errors. Equations (2.1) and (2.2) may be modified accordingly to take into account additive, possibly random, error terms

$$\boldsymbol{x}_{k+1} = \boldsymbol{m}_k(\boldsymbol{x}_k) + \boldsymbol{\epsilon}^m_{k+1}, \quad \boldsymbol{y}_k = \boldsymbol{h}(\boldsymbol{x}_k) + \boldsymbol{\epsilon}^o_k. \tag{2.4}$$

where $\boldsymbol{\epsilon}^m_k$ and $\boldsymbol{\epsilon}^o_k$ refer to model and observation errors respectively. In a stochastic framework, both state vector and observations are fully characterized by probability distributions. The problem of estimating the state of the system from available observations can be thus formulated via Bayes' theorem [216, 224]

$$p\left((\boldsymbol{x}_l)_{l=0}^N | (\boldsymbol{y}_l)_{l=0}^N\right) = \frac{p\left((\boldsymbol{y}_l)_{l=0}^N | (\boldsymbol{x}_l)_{l=0}^N\right) p\left((\boldsymbol{x}_l)_{l=0}^N\right)}{p\left((\boldsymbol{y}_l)_{l=0}^N\right)}, \tag{2.5}$$

with the notation $(\boldsymbol{x}_l)_{l=0}^N = (\boldsymbol{x}_0, \boldsymbol{x}_1, \cdots, \boldsymbol{x}_N)$. In (2.5), $p\left((\boldsymbol{y}_l)_{l=0}^N | (\boldsymbol{x}_l)_{l=0}^N\right)$ is the data distribution, i.e. the distribution of the measurements conditioned by the observed system. This probability distribution quantifies the errors and noise in the observation process. $p\left((\boldsymbol{x}_l)_{l=0}^N\right)$ is called the prior distribution, and reflects the knowledge about the state of the system before taking account observations. The probability $p\left((\boldsymbol{y}_l)_{l=0}^N\right)$ is the marginal distribution of the data, and can be thought of as a normalizing constant in (2.5) according to

$$p\left((\boldsymbol{y}_l)_{l=0}^N\right) = \int_{\mathbb{R}^{(N+1)N_s}} p\left((\boldsymbol{y}_l)_{l=0}^N | (\boldsymbol{x}_l)_{l=0}^N\right) p\left((\boldsymbol{x}_l)_{l=0}^N\right) \mathrm{d}\boldsymbol{x}_0 \mathrm{d}\boldsymbol{x}_1 \cdots \mathrm{d}\boldsymbol{x}_N. \tag{2.6}$$

The posterior distribution $p\left((\boldsymbol{x}_l)_{l=0}^N | (\boldsymbol{y}_l)_{l=0}^N\right)$ in (2.5) is the primary quantity of interest in the DA problem, since it quantifies the knowledge about the state of the system conditioned by the available data. The DA problem may thus be solved by identifying the state $(\boldsymbol{x}_l)_{l=0}^N$ that maximizes the posterior distribution. The Bayesian formulation of the DA problem (2.5) furnishes an appropriate framework for the unification of the different DA techniques, and is well adapted to the case of noisy observations and badly-known dynamics. However, compared to the deterministic framework, the Bayesian approach requires more information about the system and the observations since (2.5) needs the prescription of prior and observation statistics, which may be difficult to characterize.

2.3 Variational schemes

2.3.1 Deterministic formulation

Variational DA schemes, as proposed in [128], address DA as an optimal control problem [137]. Using a classical result of constrained optimization [3], the minimization of the cost function J in (2.3) under the dynamical constraint (2.1) is performed through the introduction of the following Lagrangian

$$\mathcal{L} = \frac{1}{2}\sum_{k=0}^{N}\left\|\boldsymbol{y}_k - \boldsymbol{h}(\boldsymbol{x}_k)\right\|^2 - \sum_{k=0}^{N-1}(\boldsymbol{x}_{k+1} - \boldsymbol{m}_k(\boldsymbol{x}_k))^{\mathrm{T}}\,\tilde{\boldsymbol{x}}_{k+1}, \tag{2.7}$$

where the superscript T indicates the transpose operator. Equation (2.7) involves the Lagrange multipliers, or adjoint variables, $\tilde{\boldsymbol{x}}_k$. The first-order optimality conditions

$$\frac{\partial \mathcal{L}}{\partial \tilde{\boldsymbol{x}}_k} = \boldsymbol{0} \quad 1 \le k \le N, \qquad \frac{\partial \mathcal{L}}{\partial \boldsymbol{x}_k} = \boldsymbol{0} \quad 0 \le k \le N \tag{2.8}$$

lead respectively to the direct model (2.1) and to the following adjoint problem:

$$\tilde{\boldsymbol{x}}_N = \left(\frac{\partial \boldsymbol{h}}{\partial \boldsymbol{x}_N}(\boldsymbol{x}_N)\right)^{\mathrm{T}}(\boldsymbol{h}(\boldsymbol{x}_N) - \boldsymbol{y}_N), \tag{2.9a}$$

$$\tilde{\boldsymbol{x}}_k = \left(\frac{\partial \boldsymbol{m}_k}{\partial \boldsymbol{x}_k}(\boldsymbol{x}_k)\right)^{\mathrm{T}}\tilde{\boldsymbol{x}}_{k+1} + \left(\frac{\partial \boldsymbol{h}}{\partial \boldsymbol{x}_k}(\boldsymbol{x}_k)\right)^{\mathrm{T}}(\boldsymbol{h}(\boldsymbol{x}_k) - \boldsymbol{y}_k) \quad 0 \le k \le N-1. \tag{2.9b}$$

Equation (2.9) involves the adjoint, here transpose, operators associated to the gradient matrices $\frac{\partial \boldsymbol{m}_k}{\partial \boldsymbol{x}_k}(\boldsymbol{x}_k)$ and $\frac{\partial \boldsymbol{h}}{\partial \boldsymbol{x}_k}(\boldsymbol{x}_k)$, which depend on the state $\boldsymbol{x}_k$ in the case of nonlinear model and observation operators. The gradient of the Lagrangian with respect to the initial condition $\boldsymbol{x}_0$, which forms the control vector in this optimization problem, is evaluated according to

$$\frac{\partial \mathcal{L}}{\partial \boldsymbol{x}_0} = \tilde{\boldsymbol{x}}_0. \tag{2.10}$$

Once computed through a backward evaluation of (2.9), the gradient (2.10) can be used in a gradient-based descent algorithm in order to obtain the minimizing initial state. It can be noticed that equation (2.8) only provides necessary optimality conditions, and second-order conditions should be considered to ensure the optimality of the retrieved initial condition. Second-order information can be obtained through the use of a second-order adjoint model [130, 221], which may also be employed in a Newton method, or to solve meta-optimization problems. An example of such a problem is given in chapter 6 [55]. However, the numerical implementation of the first-order adjoint model $\left(\frac{\partial \boldsymbol{m}_k}{\partial \boldsymbol{x}_k}(\boldsymbol{x}_k)\right)^{\mathrm{T}}$ in (2.9) may already be difficult, and the coding of the second-order adjoint model requires *a fortiori* significant efforts and computational resources. Accordingly, the second-order adjoint model is hardly ever used in practical applications, and, when employed, variational schemes rely on the first-order adjoint model only.

2.3.2 Stochastic formulation

The equations in §2.3.1 form the DA scheme known as 4DVar in the meteorology community, even if the standard formulation of the 4DVar scheme [65] includes a prior information term in the cost function in (7.2), which originates from the stochastic formulation of the DA problem exposed in §2.2.2. However, contrary to (2.4), the standard 4DVar formulation assumes a perfect dynamical model, so that (2.4) is rewritten as

$$\boldsymbol{x}_{k+1} = \boldsymbol{m}_k(\boldsymbol{x}_k), \quad \boldsymbol{y}_k = \boldsymbol{h}(\boldsymbol{x}_k) + \boldsymbol{\epsilon}_k^o. \tag{2.11}$$

Accordingly, the state of the system at a given time is completely determined by the initial state $\boldsymbol{x}_0$, but DA is performed with noisy observations, which may justify the need of adding prior information about the initial state during the assimilation and to rely on the use of the Bayesian formulation of the DA problem. In order to simplify the derivation of the 4DVar scheme, it is assumed that the initial state $\boldsymbol{x}_0$ is Gaussian distributed with mean $\boldsymbol{x}_0^b$ and covariance matrix $\mathbf{B}$. The observation error $\boldsymbol{\epsilon}_k^o$ in (2.11) is also assumed to be Gaussian distributed, uncorrelated in time, with zero mean and covariance matrix $\mathbf{R}$ (see also §2.4.1). The Gaussian assumption allows to consider the denominator in (2.5) as only a normalizing constant, and the posterior statistics of interest $p\left(\boldsymbol{x}_0|(\boldsymbol{y}_l)_{l=0}^N\right)$ can be computed through

$$p\left(\boldsymbol{x}_0|(\boldsymbol{y}_l)_{l=0}^N\right) \propto p\left(\boldsymbol{x}_0\right) p\left((\boldsymbol{y}_l)_{l=0}^N|(\boldsymbol{x}_l)_{l=0}^N\right) \propto e^{-J}, \quad J = \frac{1}{2}\left\|\boldsymbol{x}_0 - \boldsymbol{x}_0^b\right\|_{\mathbf{B}^{-1}}^2 + \frac{1}{2}\sum_{k=0}^{N}\left\|\boldsymbol{y}_k - \boldsymbol{h}(\boldsymbol{x}_k)\right\|_{\mathbf{R}^{-1}}^2, \tag{2.12}$$

with $\|\cdot\|_{\mathbf{B}^{-1}} = \cdot^{\mathrm{T}}\mathbf{B}^{-1}\cdot$ and $\|\cdot\|_{\mathbf{R}^{-1}} = \cdot^{\mathrm{T}}\mathbf{R}^{-1}\cdot$. According to (2.12), finding the initial state $\boldsymbol{x}_0$ that maximizes the posterior distribution is equivalent to the determination of a minimizing initial state of a cost function. As in §2.3.1, this minimization problem is solved using optimal control techniques, and the gradient of the cost function J in (2.12) is evaluated through

$$\mathcal{L} = \frac{1}{2}\left\|\boldsymbol{x}_0 - \boldsymbol{x}_0^b\right\|_{\mathbf{B}^{-1}}^2 + \frac{1}{2}\sum_{k=0}^{N}\left\|\boldsymbol{y}_k - \boldsymbol{h}(\boldsymbol{x}_k)\right\|_{\mathbf{R}^{-1}}^2 - \sum_{k=0}^{N-1}\left(\boldsymbol{x}_{k+1} - \boldsymbol{m}_k(\boldsymbol{x}_k)\right)^{\mathrm{T}}\tilde{\boldsymbol{x}}_{k+1}, \tag{2.13a}$$

$$\tilde{\boldsymbol{x}}_N = \left(\frac{\partial \boldsymbol{h}}{\partial \boldsymbol{x}_N}(\boldsymbol{x}_N)\right)^{\mathrm{T}} \mathbf{R}^{-1}\left(\boldsymbol{h}(\boldsymbol{x}_N) - \boldsymbol{y}_N\right), \tag{2.13b}$$

$$\tilde{\boldsymbol{x}}_k = \left(\frac{\partial \boldsymbol{m}_k}{\partial \boldsymbol{x}_k}(\boldsymbol{x}_k)\right)^{\mathrm{T}}\tilde{\boldsymbol{x}}_{k+1} + \left(\frac{\partial \boldsymbol{h}}{\partial \boldsymbol{x}_k}(\boldsymbol{x}_k)\right)^{\mathrm{T}} \mathbf{R}^{-1}\left(\boldsymbol{h}(\boldsymbol{x}_k) - \boldsymbol{y}_k\right) \quad 0 \le k \le N-1, \tag{2.13c}$$

$$\frac{\partial \mathcal{L}}{\partial \boldsymbol{x}_0} = \tilde{\boldsymbol{x}}_0 + \mathbf{B}^{-1}\left(\boldsymbol{x}_0 - \boldsymbol{x}_0^b\right). \tag{2.13d}$$

2.4 The Kalman filter

2.4.1 Linear model and observation operators

The Kalman filter [111] may be derived from the Bayesian formulation of the DA problem given in §2.2.2. In its original formulation, the Kalman filter relies on the assumption of linear model and observations. Accordingly, equation (2.4) is rewritten as

$$\boldsymbol{x}_{k+1} = \mathbf{M}_k\boldsymbol{x}_k + \boldsymbol{\epsilon}_{k+1}^m, \quad \boldsymbol{y}_k = \mathbf{H}\boldsymbol{x}_k + \boldsymbol{\epsilon}_k^o, \tag{2.14}$$

where $\mathbf{M}_k$ and $\mathbf{H}$ are the model and observation matrices respectively. The Kalman filter is a sequential DA scheme: observations are taken into account as soon as they are available to improve the estimation of the state of the system, allowing to perform 'real-time' DA. On the contrary, the 4DVar scheme exposed in §2.3 is referred to as a 'off-line', or retrospective method, since the observations over discrete times $0 \le k \le N$ are used all at once, and the retrieved estimation of the system (through the determination of an optimal initial state) at a given time benefits from the assimilation of both past and future observations. Before proceeding further, the following assumptions about the random terms $\boldsymbol{\epsilon}_k^m$ and $\boldsymbol{\epsilon}_k^o$ in (2.14) are made. It is assumed that these terms have zero mean, are uncorrelated in time, and that model and observation errors are independent random variables

$$\mathbb{E}\left[\boldsymbol{\epsilon}_k^m\right] = \mathbf{0}, \quad \mathbb{E}\left[\boldsymbol{\epsilon}_k^o\right] = \mathbf{0}, \quad \mathbb{E}\left[\boldsymbol{\epsilon}_k^m\boldsymbol{\epsilon}_l^{o\mathrm{T}}\right] = \mathbf{0}, \quad \mathbb{E}\left[\boldsymbol{\epsilon}_k^m\boldsymbol{\epsilon}_l^{m\mathrm{T}}\right] = \mathbf{Q}_k\delta_{kl}, \quad \mathbb{E}\left[\boldsymbol{\epsilon}_k^o\boldsymbol{\epsilon}_l^{o\mathrm{T}}\right] = \mathbf{R}\delta_{kl} \quad 0 \le k, l \le N, \tag{2.15}$$

with no summation over repeated indices (as in the whole chapter), $\mathbf{Q}_k$ and $\mathbf{R}$ refer to the covariance matrices associated to model and observation errors statistics respectively. It is also assumed that the predicted state of the system, both before and after assimilation, is an unbiased estimation of the 'true' state of the system $\boldsymbol{x}_k^t$. Besides, observations are also supposed to be unbiased, and we can write

$$\boldsymbol{x}_k^f = \boldsymbol{x}_k^t + \boldsymbol{\epsilon}_k^f, \quad \boldsymbol{x}_k^a = \boldsymbol{x}_k^t + \boldsymbol{\epsilon}_k^a, \quad \mathbb{E}\left[\boldsymbol{y}_k\right] = \mathbf{H}\boldsymbol{x}_k^t \quad 0 \leq k \leq N, \tag{2.16}$$

where $\boldsymbol{x}_k^f$ and $\boldsymbol{x}_k^a$ refer to the estimation of the state of the system before (forecast or prior information) and after assimilation respectively. The random error terms $\boldsymbol{\epsilon}_k^f$ and $\boldsymbol{\epsilon}_k^a$ are thus supposed to have zero mean, and the forecast and assimilated covariance matrices $\mathbf{P}_k^f$ and $\mathbf{P}_k^a$ are defined as

$$\mathbb{E}\left[\boldsymbol{\epsilon}_k^f\right] = \mathbf{0}, \quad \mathbb{E}\left[\boldsymbol{\epsilon}_k^a\right] = \mathbf{0}, \quad \mathbb{E}\left[\boldsymbol{\epsilon}_k^f \boldsymbol{\epsilon}_k^{f\mathrm{T}}\right] = \mathbf{P}_k^f, \quad \mathbb{E}\left[\boldsymbol{\epsilon}_k^a \boldsymbol{\epsilon}_k^{a\mathrm{T}}\right] = \mathbf{P}_k^a \quad 0 \leq k \leq N. \tag{2.17}$$

The Kalman filter consists of two steps: an assimilation step where available observations are used to improve the estimation of the state of the system, and a forecast step where the state vector and its statistics are propagated in time relying on (2.14). The assimilation step may be obtained from the Bayesian formulation of the DA problem (2.5), supplemented by the Gaussian assumption for both forecast (prior) and observation statistics. For this sequential filter, posterior statistics at discrete time k are quantified through the distribution $p\left(\boldsymbol{x}_k|\boldsymbol{y}_k\right)$, which is found as

$$p\left(\boldsymbol{x}_k|\boldsymbol{y}_k\right) \propto p\left(\boldsymbol{x}_k\right) p\left(\boldsymbol{y}_k|\boldsymbol{x}_k\right) \propto e^{-J}, \quad J = \frac{1}{2}\left\|\boldsymbol{x}_k - \boldsymbol{x}_k^f\right\|_{\mathbf{P}_k^{f\,-1}}^2 + \frac{1}{2}\left\|\boldsymbol{y}_k - \mathbf{H}\boldsymbol{x}_k\right\|_{\mathbf{R}^{-1}}^2. \tag{2.18}$$

Finding the assimilated state $\boldsymbol{x}_k^a$ that maximizes the posterior distribution is thus equivalent to the determination of the state that minimizes the cost function J in (2.18). Since this cost function is quadratic, the solution of the minimization problem is easily found as

$$\boldsymbol{x}_k^a = \boldsymbol{x}_k^f + \left(\mathbf{P}_k^{f\,-1} + \mathbf{H}^{\mathrm{T}}\mathbf{R}^{-1}\mathbf{H}\right)^{-1}\mathbf{H}^{\mathrm{T}}\mathbf{R}^{-1}\left(\boldsymbol{y}_k - \mathbf{H}\boldsymbol{x}_k^f\right). \tag{2.19}$$

Using

$$\left(\mathbf{P}_k^{f\,-1} + \mathbf{H}^{\mathrm{T}}\mathbf{R}^{-1}\mathbf{H}\right)^{-1}\mathbf{H}^{\mathrm{T}}\mathbf{R}^{-1} = \mathbf{P}_k^f\mathbf{H}^{\mathrm{T}}\left(\mathbf{R} + \mathbf{H}\mathbf{P}_k^f\mathbf{H}^{\mathrm{T}}\right)^{-1}, \tag{2.20}$$

equation (2.19) can be rewritten as

$$\boldsymbol{x}_k^a = \boldsymbol{x}_k^f + \mathbf{K}_k\left(\boldsymbol{y}_k - \mathbf{H}\boldsymbol{x}_k^f\right), \quad \mathbf{K}_k = \mathbf{P}_k^f\mathbf{H}^{\mathrm{T}}\left(\mathbf{R} + \mathbf{H}\mathbf{P}_k^f\mathbf{H}^{\mathrm{T}}\right)^{-1}. \tag{2.21}$$

The covariance matrix of the assimilated state $\boldsymbol{x}_k^a$ is derived using (2.15)

$$\mathbf{P}_k^a = \left(\mathbf{I} - \mathbf{K}_k\mathbf{H}\right)\mathbf{P}_k^f = \left(\frac{\partial^2 J}{\partial \boldsymbol{x}_k^2}\right)^{-1}. \tag{2.22}$$

Equations (2.18)-(2.22) illustrate the equivalence between the assimilation step of the Kalman filter and variational methods as depicted in §2.3.2 in the case of sequential DA, linear model and observation operators, Gaussian statistics for the additive random error terms, and unbiased observations and estimations of the state of the system [136, 142, 197]. The solution (2.21)-(2.22) of the DA problem with the above assumptions, which is here equivalent to a minimum variance solution, is also known as the best linear unbiased estimator (BLUE). The second step of the Kalman filter consists in propagating both the assimilated state and its covariance matrix until the next time of observation according to

$$\boldsymbol{x}_{k+1}^f = \mathbf{M}_k\boldsymbol{x}_k^a + \boldsymbol{\epsilon}_{k+1}^m, \quad \mathbf{P}_{k+1}^f = \mathbf{M}_k\mathbf{P}_k^a\mathbf{M}_k^{\mathrm{T}} + \mathbf{Q}_{k+1}. \tag{2.23}$$

If observations are available at discrete time $k+1$, they are assimilated by using (2.21)-(2.22), replacing k by $k+1$.

2.4.2 Nonlinear dynamics

In the context of nonlinear dynamics, the propagation equation (2.23) is not valid anymore, and one should consider the evolution of a full probability density function according to Kolmogorov's (or Fokker-Planck) equation [107]. To ease the computational burden associated to the propagation of a probability density, a common assumption is to consider the evolution of a few moments only, along with *ad hoc* approximations to solve the closure problem that arises in this case. A simple and well-known extension of the Kalman filter as described in §2.4.1 to nonlinear dynamics is the so-called extended Kalman filter, where only the mean and the covariance matrix of the state vector are propagated in time, and the closure approximation consists in neglecting all moments with higher orders than the covariances. Accordingly, considering nonlinear model and observation operators as in (2.4), the assimilation step of the extended Kalman filter is given by

$$\boldsymbol{x}_k^a = \boldsymbol{x}_k^f + \mathbf{K}_k \left(\boldsymbol{y}_k - \boldsymbol{h}(\boldsymbol{x}_k^f)\right), \quad \mathbf{P}_k^a = \left(\mathbf{I} - \mathbf{K}_k \frac{\partial \boldsymbol{h}}{\partial \boldsymbol{x}_k}(\boldsymbol{x}_k^f)\right)\mathbf{P}_k^f, \quad \mathbf{K}_k = \mathbf{P}_k^f \left(\frac{\partial \boldsymbol{h}}{\partial \boldsymbol{x}_k}(\boldsymbol{x}_k^f)\right)^{\mathrm{T}} \left(\mathbf{R} + \frac{\partial \boldsymbol{h}}{\partial \boldsymbol{x}_k}(\boldsymbol{x}_k^f)\mathbf{P}_k^f \left(\frac{\partial \boldsymbol{h}}{\partial \boldsymbol{x}_k}(\boldsymbol{x}_k^f)\right)^{\mathrm{T}}\right)^{-1}, \tag{2.24}$$

and the forecast step is performed according to

$$\boldsymbol{x}_{k+1}^f = \boldsymbol{m}_k(\boldsymbol{x}_k^a) + \boldsymbol{\epsilon}_{k+1}^m, \quad \mathbf{P}_{k+1}^f = \frac{\partial \boldsymbol{m}_k}{\partial \boldsymbol{x}_k}(\boldsymbol{x}_k^a)\mathbf{P}_k^a \left(\frac{\partial \boldsymbol{m}_k}{\partial \boldsymbol{x}_k}(\boldsymbol{x}_k^a)\right)^{\mathrm{T}} + \mathbf{Q}_{k+1}. \tag{2.25}$$

Further discussion about the extended Kalman filter and presentation of more elaborate extensions of the Kalman filter to nonlinear dynamics may be found in [59, 79, 133].

2.5 Ensemble Filtering

2.5.1 The ensemble Kalman filter

At least two problems may arise in the application of the Kalman filter to large-scale nonlinear systems such as those encountered in fluid mechanics applications. Firstly, the storing and the propagation in time of the covariance matrix associated to the statistics of the state vector according to (2.25) (or (2.23) for linear systems) become costly to perform if the dimension of the state vector is large. Secondly, the approximations to extend the Kalman filter to nonlinear dynamics do not ensure the stability of the filter in this case, as illustrated in [76]. To overcome these difficulties, it was proposed in [77] to describe and propagate the statistics of the state vector through the use of Monte Carlo techniques, instead of relying on approximate explicit evolution equations for the moments of the distribution. In this framework, prior, or forecast, statistics of $\boldsymbol{x}_k$ are evaluated via an ensemble of realizations that are gathered in the matrix $\mathbf{A}_k^f$ defined as

$$\mathbf{A}_k^f = \left(\boldsymbol{x}_k^{f(1)}, \boldsymbol{x}_k^{f(2)}, \cdots, \boldsymbol{x}_k^{f(N_{en})}\right), \tag{2.26}$$

where N_{en} is the number of members in the ensemble. The ensemble Kalman filter, as the Kalman filter, relies on the Gaussian assumption for the statistics of the state vector, allowing to consider only its mean and covariance matrix, which can be evaluated through the following Monte Carlo estimates

$$\mathbb{E}\left[\boldsymbol{x}_k^f\right] \simeq \frac{1}{N_{en}} \sum_{i=1}^{N_{en}} \boldsymbol{x}_k^{f(i)} = \overline{\boldsymbol{x}_k^f}, \quad \mathbf{P}_k^f \simeq \frac{1}{N_{en}-1}\mathbf{A}_k^{f\prime}\mathbf{A}_k^{f\prime\,\mathrm{T}}, \quad \mathbf{A}_k^{f\prime} = \left(\boldsymbol{x}_k^{f(1)} - \overline{\boldsymbol{x}_k^f}, \boldsymbol{x}_k^{f(2)} - \overline{\boldsymbol{x}_k^f}, \cdots, \boldsymbol{x}_k^{f(N_{en})} - \overline{\boldsymbol{x}_k^f}\right). \tag{2.27}$$

The assimilation step of the ensemble Kalman filter is derived similarly to that of the Kalman filter in §2.4.1, and if observations are available at discrete time k, the ensemble of realizations is updated according to

$$\mathbf{A}_k^a = \mathbf{A}_k^f + \mathbf{A}_k^{f\prime}\mathbf{H}_k^{f\prime\,\mathrm{T}}\left((N_{en}-1)\mathbf{R} + \mathbf{H}_k^{f\prime}\mathbf{H}_k^{f\prime\,\mathrm{T}}\right)^{-1}\left(\mathbf{Y}_k - \mathbf{H}_k^f\right), \tag{2.28}$$

with

$$\mathbf{H}_k^f = \left(\boldsymbol{h}(\boldsymbol{x}_k^{f(1)}), \boldsymbol{h}(\boldsymbol{x}_k^{f(2)}), \cdots, \boldsymbol{h}(\boldsymbol{x}_k^{f(N_{en})})\right), \quad \mathbf{H}_k^{f'} = \left(\boldsymbol{h}(\boldsymbol{x}_k^{f(1)}) - \boldsymbol{h}(\overline{\boldsymbol{x}_k^f}), \boldsymbol{h}(\boldsymbol{x}_k^{f(2)}) - \boldsymbol{h}(\overline{\boldsymbol{x}_k^f}), \cdots, \boldsymbol{h}(\boldsymbol{x}_k^{f(N_{en})}) - \boldsymbol{h}(\overline{\boldsymbol{x}_k^f})\right). \tag{2.29}$$

The ensemble of observations $\mathbf{Y}_k$ is obtained from perturbations with zero mean and covariance matrix $\mathbf{R}$ that are added to available data $\boldsymbol{y}_n$ [35]. An alternative to the update equation (2.28) that avoids the perturbation of the measurements, which may add a source of sampling error, was proposed with the ensemble square root filters [4, 25, 78, 141, 205, 223]. In these DA schemes, the assimilation step is performed separately for the ensemble mean $\overline{\boldsymbol{x}_k^f}$ and the ensemble perturbation matrix $\mathbf{A}_k^{f'}$ in (2.27). Following, e.g., [78], the ensemble mean is updated through a standard Kalman filter assimilation step

$$\overline{\boldsymbol{x}_k^a} = \overline{\boldsymbol{x}_k^f} + \mathbf{A}_k^{f'} \mathbf{H}_k^{f'\,\mathrm{T}} \left((N_{en} - 1)\mathbf{R} + \mathbf{H}_k^{f'} \mathbf{H}_k^{f'\,\mathrm{T}}\right)^{-1} \left(\mathbf{y}_k - \boldsymbol{h}(\overline{\boldsymbol{x}_k^f})\right). \tag{2.30}$$

Concerning the ensemble perturbation matrix, using

$$\mathbf{A}_k^{a'} \mathbf{A}_k^{a'\,\mathrm{T}} = \mathbf{A}_k^{f'} \left(\mathbf{I} - \mathbf{H}_k^{f'\,\mathrm{T}} \mathbf{C}_k^{-1} \mathbf{H}_k^{f'}\right) \mathbf{A}_k^{f'\,\mathrm{T}}, \quad \mathbf{C}_k = (N_{en} - 1)\mathbf{R} + \mathbf{H}_k^{f'} \mathbf{H}_k^{f'\,\mathrm{T}}, \tag{2.31}$$

and performing the eigenvalue decomposition

$$\mathbf{C}_k = \mathbf{Z}_k \boldsymbol{\Lambda}_k \mathbf{Z}_k^{\mathrm{T}}, \tag{2.32}$$

followed by the singular value decomposition

$$\boldsymbol{\Lambda}_k^{-\frac{1}{2}} \mathbf{Z}_k^{\mathrm{T}} \mathbf{H}_k^{f'} = \mathbf{U}_k \boldsymbol{\Sigma}_k \mathbf{V}_k^{\mathrm{T}}, \tag{2.33}$$

lead to the following update equation

$$\mathbf{A}_k^{a'} = \mathbf{A}_k^{f'} \mathbf{V}_k \left(\mathbf{I} - \boldsymbol{\Sigma}_k^{\mathrm{T}} \boldsymbol{\Sigma}_k\right)^{\frac{1}{2}} \mathbf{V}_k^{\mathrm{T}} \boldsymbol{\Theta}_k^{\mathrm{T}}, \tag{2.34}$$

with $\boldsymbol{\Theta}_k$ is a mean-preserving random orthogonal matrix, which may be chosen as the identity matrix. Variants of (2.34) are discussed in [141, 205]. The forecast step of the ensemble Kalman filter, both in its standard form and in its square-root version, is performed through the propagation in time of each member in the matrix $\mathbf{A}_k^a$ with the dynamical model in (2.4) (or (2.1) if model errors are not directly taken into account), allowing to form the matrix $\mathbf{A}_{k+1}^f$.

2.5.2 The ensemble smoother and ensemble Kalman smoother

The ensemble Kalman filter described in §2.5.1 is a sequential filter, as the Kalman filter of §2.4, in the sense that observations are taken into account as soon as they are available to improve the estimation of the state of the system at the same time. The extension of the ensemble Kalman filter to retrospective DA is performed by considering available observation at all times, the corresponding posterior statistics of interest are thus

$$p\left((\boldsymbol{x}_l)_{l=0}^N | (\boldsymbol{y}_l)_{l=0}^N\right) \propto \left((\boldsymbol{y}_l)_{l=0}^N | (\boldsymbol{x}_l)_{l=0}^N\right) p\left((\boldsymbol{x}_l)_{l=0}^N\right). \tag{2.35}$$

Again, the assumption of Gaussian statistics allows to consider the denominator in (2.5) as a normalizing constant. The ensemble smoother [216] directly solves the DA problem from (2.35). In a first step, an ensemble of realizations are propagated from discrete time 0 to time N in order to compute prior, or forecast, statistics. In a second step, the assimilation of observations is performed through an update equation of the same form as (2.28), except that time dimension is now taken into account. Accordingly, the assimilation step of the ensemble smoother is obtained by replacing in (2.28) the matrices $\mathbf{A}_k^f$ and $\mathbf{H}_k^f$ with

$$\mathbf{A}^f = \left(\left((\boldsymbol{x}_l^{f(1)\,\mathrm{T}})_{l=0}^N\right)^{\mathrm{T}}, \left((\boldsymbol{x}_l^{f(2)\,\mathrm{T}})_{l=0}^N\right)^{\mathrm{T}}, \cdots, \left((\boldsymbol{x}_l^{f(N_{en})\,\mathrm{T}})_{l=0}^N\right)^{\mathrm{T}}\right), \tag{2.36}$$

$$\mathbf{H}^f = \left(\left((\boldsymbol{h}(\boldsymbol{x}_l^{f(1)})^{\mathrm{T}})_{l=0}^{N} \right)^{\mathrm{T}}, \left((\boldsymbol{h}(\boldsymbol{x}_l^{f(2)})^{\mathrm{T}})_{l=0}^{N} \right)^{\mathrm{T}}, \cdots, \left((\boldsymbol{h}(\boldsymbol{x}_l^{f(N_{en})})^{\mathrm{T}})_{l=0}^{N} \right)^{\mathrm{T}} \right), \tag{2.37}$$

with a similar extension to time dimension of the matrices $\mathbf{A}_k^{f'}$, $\mathbf{H}_k^{f'}$, $\mathbf{Y}_k$ and $\mathbf{R}$ in (2.28). The so obtained assimilated ensemble stored in the matrix $\mathbf{A}^a$ thus corresponds to a minimum variance solution to the DA problem in both space and time. However, it was observed in [80] that the Gaussian assumption for the statistics of the state vector over the complete time interval from discrete time 0 to time N could be too crude for strongly nonlinear systems. This led to the introduction of the ensemble Kalman smoother in [80], where observations are assimilated sequentially, as in the ensemble Kalman filter. Nevertheless, measurements are used in order to improve the estimation of the state of the system at both present and past times, similarly to the ensemble smoother. The ensemble Kalman filter is derived from a sequential evaluation of the posterior statistics in (2.35). Assuming that the model evolution given in (2.4) is a first-order Markov process, and that the observations at different times are independent and conditional only on the state at the same time, (2.35) can be evaluated according to

$$p\left((\boldsymbol{x}_l)_{l=0}^{k} | (\boldsymbol{y}_l)_{l=0}^{k} \right) \propto p\left((\boldsymbol{x}_l)_{l=0}^{k-1} | (\boldsymbol{y}_l)_{l=0}^{k-1} \right) p(\boldsymbol{x}_k|\boldsymbol{x}_{k-1}) p(\boldsymbol{y}_k|\boldsymbol{x}_k) \quad 1 \le k \le N. \tag{2.38}$$

At discrete time k, (2.38) can be decomposed [64] into a forecast step

$$p\left((\boldsymbol{x}_l)_{l=0}^{k} | (\boldsymbol{y}_l)_{l=0}^{k-1} \right) = p\left((\boldsymbol{x}_l)_{l=0}^{k-1} | (\boldsymbol{y}_l)_{l=0}^{k-1} \right) p(\boldsymbol{x}_k|\boldsymbol{x}_{k-1}), \tag{2.39}$$

and an assimilation step

$$p\left((\boldsymbol{x}_l)_{l=0}^{k} | (\boldsymbol{y}_l)_{l=0}^{k} \right) \propto p\left((\boldsymbol{x}_l)_{l=0}^{k} | (\boldsymbol{y}_l)_{l=0}^{k-1} \right) p(\boldsymbol{y}_k|\boldsymbol{x}_k). \tag{2.40}$$

As in the ensemble Kalman filter, prior statistics $p\left((\boldsymbol{x}_l)_{l=0}^{k} | (\boldsymbol{y}_l)_{l=0}^{k-1} \right)$ are evaluated through ensemble forecasting from time $k-1$ to time k. The assimilation step of the ensemble Kalman smoother is derived from (2.40), relying again on the Gaussian assumption. The corresponding update equation is identical to (2.28), except that the ensemble matrix $\mathbf{A}_k^f$ has to be replaced with

$$\mathbf{A}_k^f = \left(\left((\boldsymbol{x}_l^{a(1)\,\mathrm{T}})_{l=0}^{k-1}, \boldsymbol{x}_k^{f(1)\,\mathrm{T}} \right)^{\mathrm{T}}, \left((\boldsymbol{x}_l^{a(2)\,\mathrm{T}})_{l=0}^{k-1}, \boldsymbol{x}_k^{f(2)\,\mathrm{T}} \right)^{\mathrm{T}}, \cdots, \left((\boldsymbol{x}_l^{a(N_{en})\,\mathrm{T}})_{l=0}^{k-1}, \boldsymbol{x}_k^{f(N_{en})\,\mathrm{T}} \right)^{\mathrm{T}} \right), \tag{2.41}$$

with a similar modification to the matrix $\mathbf{A}_k^{f'}$ in (2.28). The members of the ensemble are consequently updated from time 0 to time k using measurement at time k, and the resulting ensemble is gathered in a matrix $\mathbf{A}_k^a$. The different realizations are then propagated from time k to time $k+1$ using (2.4) to form the matrix $\mathbf{A}_{k+1}^f$. The ensemble Kalman smoother proved to achieve a better reconstruction of the state of the system than both the ensemble Kalman filter and the ensemble smoother in experiments with the Lorenz equations [80].

2.5.3 Localization and inflation

The use of a finite ensemble size to describe the statistics of the state vector may lie at the origin of spurious correlations between the components of the state vector, or between the state vector and the observations, due to sampling errors. These spurious correlations between variables known to be uncorrelated or separated by long spatial distances (and/or by a large time interval in the case of a smoother) entail unphysical updates of the state vector during the assimilation step, potentially leading to a drastic reduction of the variance of the ensemble and to filter divergence. Covariance inflation procedures [8] were first proposed to counteract the variance reduction associated to spurious correlations. Inflation may simply consist in pushing the members of the ensemble away from the mean according to

$$\boldsymbol{x}_k^{f(i)} \to \rho \left(\boldsymbol{x}_k^{f(i)} - \overline{\boldsymbol{x}_k^{f}} \right) + \overline{\boldsymbol{x}_k^{f}}, \tag{2.42}$$

where ρ is the inflation factor with $\rho > 1$. In (2.42), ρ is an arbitrarily fixed scalar, but Bayesian-based algorithms may be used in order to determine the value of the inflation factor adaptively [6], and further refinement may be achieved through assigning a different inflation factor to each component of the state vector [7].

A second way of reducing the effects of spurious correlations is localization [103], which amounts to replace the update equation (2.28) of the ensemble Kalman filter with

$$\mathbf{A}_k^a = \mathbf{A}_k^f + \mathbf{L}_1 \circ \left(\mathbf{A}_k^{f'} \mathbf{H}_k^{f'\,\mathrm{T}}\right)\left((N_{en} - 1)\mathbf{R} + \mathbf{L}_2 \circ \left(\mathbf{H}_k^{f'} \mathbf{H}_k^{f'\,\mathrm{T}}\right)\right)^{-1} \left(\mathbf{Y}_k - \mathbf{H}_k^f\right), \tag{2.43}$$

where $\circ$ denotes the element-wise (or Hadamard or Schur) product. $\mathbf{L}_1$ is a localization matrix acting on the correlations between the state vector and the observations, while $\mathbf{L}_2$ acts on the correlations between observations. These matrices may be used in order to impose a decay of correlation with distance, or to force a zero correlation between two independent variables. The extension of (2.43) to the ensemble smoother and ensemble Kalman smoother is straightforward, noticing that temporal localization may also be achieved by considering a lagged smoother [80, 167], where observations available at discrete time k are used to update the ensemble only from time $k - L$ to k, with L the lag parameter. However, the prescription of appropriate localization functions and parameters such as characteristic length and time scales may become very difficult in the case where complex multivariate models are considered [5].

2.6 Merging variational schemes and ensemble filtering

2.6.1 Hybrid schemes

The stochastic formulation of the DA problem exposed in §2.2.2, which is generally adopted in meteorological applications, requires the prescription of prior statistics, which reflect the knowledge about the discrepancies between the first-guess, or forecast, state and the true state of the system, as detailed in §2.3.2 and §2.4.1. Of course, in practical applications, the true state of the system is unknown, and prior statistics are generally difficult to characterize. However, it is clear from equations (2.13d), (2.21) or (2.28) that prior information directly influences the results of the assimilation through the matrices $\mathbf{B}$, $\mathbf{P}_k^f$ and $\mathbf{A}_k^f$ respectively. Accordingly, the determination of proper prior statistics is a major research area in the DA community [17, 18, 177]. This issue motivated the combined use of variational techniques (§2.3.2) and ensemble filtering (§2.5.1) in order to derive efficient composite methods with the advantages of both approaches. The ensemble Kalman filter allows to propagate in time the statistics of the state vector, naturally providing forecast (prior) statistics for the assimilation of next observations. However, the ensemble Kalman filter is subject to sampling errors, which may lead to significant adjustments and tuning in order to ensure the stability of the filter. On the other hand, variational techniques, as the 4DVar scheme, are more stable and adapted to large-scale systems thanks to the adjoint technique, but do not directly provide updated statistics of the state vector, and rely on a static covariance matrix for prior statistics (matrix $\mathbf{B}$ in §2.3.2). Hybrid approaches [57, 123, 143, 220, 233] propose to incorporate in a variational scheme information from an ensemble method. More precisely, a forecast covariance matrix $\mathbf{B}^f$ derived from the ensemble method is added to the static covariance matrix in the variational scheme, and the matrix $\mathbf{B}$ in (2.12) is replaced according to

$$\mathbf{B} \to \beta\mathbf{B} + (1-\beta)\mathbf{B}^f \quad \beta \in [0, 1]\,. \tag{2.44}$$

The variational scheme is used to update the mean of the ensemble while the latter is propagated in time with the ensemble method, and both schemes are thus run in parallel while feeding into each other. Comparisons with uncoupled variational and ensemble filtering schemes suggest the superiority of such hybrid approaches [233].

2.6.2 Ensemble-based variational schemes

Aside from the issue of the prescription of proper prior statistics in the stochastic formulation of the DA problem, a difficulty in the use of variational schemes is that they require the coding of the adjoint model involved in (2.9) or (2.13), which may be a tedious task, in particular in the case where the model operator is nonlinear and/or presents discontinuities. However, the variational framework has advantages compared to ensemble filtering, and has desirable properties such as scalability and robustness, as discussed in §2.6.1. This motivated the introduction of ensemble-based variational schemes [33, 140, 182, 203, 218, 219], which rely on a variational framework but use an ensemble of realizations to circumvent the need of an adjoint model. A closely related method to ensemble-based variational schemes, but derived from the ensemble Kalman smoother, can be found in [28]. In the ensemble-based variational schemes, starting from the stochastic formulation of the variational schemes exposed in §2.3.2, the initial state $\boldsymbol{x}_0$ is searched in a subspace spanned by an ensemble of realizations [140]. After choosing the first-guess initial state $\boldsymbol{x}_0^b$ and N_{en} samples around this vector, the initial state $\boldsymbol{x}_0$ is expressed as

$$\boldsymbol{x}_0 = \boldsymbol{x}_0^b + \mathbf{E}'\boldsymbol{\beta}, \quad \mathbf{E}' = \left(\boldsymbol{x}_0^{(1)} - \boldsymbol{x}_0^b, \boldsymbol{x}_0^{(2)} - \boldsymbol{x}_0^b, \cdots, \boldsymbol{x}_0^{(N_{en})} - \boldsymbol{x}_0^b\right). \tag{2.45}$$

The vector $\boldsymbol{\beta}$ in (2.45) forms the control vector in the ensemble-based variational schemes. From the linearizations

$$\boldsymbol{h}(\boldsymbol{x}_k) \simeq \boldsymbol{h}(\boldsymbol{x}_k^b) + \frac{\partial \boldsymbol{h}}{\partial \boldsymbol{x}_k^b}(\boldsymbol{x}_k^b)\frac{\partial \boldsymbol{x}_k^b}{\partial \boldsymbol{x}_0^b}(\boldsymbol{x}_0^b)\mathbf{E}'\boldsymbol{\beta}, \tag{2.46a}$$

$$\frac{\partial \boldsymbol{h}}{\partial \boldsymbol{x}_k^b}(\boldsymbol{x}_k^b)\frac{\partial \boldsymbol{x}_k^b}{\partial \boldsymbol{x}_0^b}(\boldsymbol{x}_0^b)\mathbf{E}' \simeq \left(\boldsymbol{h}(\boldsymbol{x}_k^{(1)}) - \boldsymbol{h}(\boldsymbol{x}_k^b), \boldsymbol{h}(\boldsymbol{x}_k^{(2)}) - \boldsymbol{h}(\boldsymbol{x}_k^b), \cdots, \boldsymbol{h}(\boldsymbol{x}_k^{(N_{en})}) - \boldsymbol{h}(\boldsymbol{x}_k^b)\right) = \mathbf{H}_k', \tag{2.46b}$$

where $\boldsymbol{x}_k^b$, $\boldsymbol{x}_k^{(1)}$, $\boldsymbol{x}_k^{(2)}$, $\cdots$, $\boldsymbol{x}_k^{(N_{en})}$ are the states of the system propagated at time k using the dynamical model (2.1) and the initial states $\boldsymbol{x}_0^b$, $\boldsymbol{x}_0^{(1)}$, $\boldsymbol{x}_0^{(2)}$, $\cdots$, $\boldsymbol{x}_0^{(N_{en})}$ respectively, the cost function in (2.12) can be rewritten as

$$J = \frac{1}{2}(N_{en} - 1)\boldsymbol{\beta}^{\mathrm{T}}\boldsymbol{\beta} + \frac{1}{2}\sum_{k=0}^{N}\left\|\boldsymbol{h}(\boldsymbol{x}_k^b) - \boldsymbol{y}_k + \mathbf{H}_k'\boldsymbol{\beta}\right\|_{\mathbf{R}^{-1}}^2, \tag{2.47}$$

using

$$\mathbf{B} \simeq \frac{1}{N_{en} - 1}\mathbf{E}'\mathbf{E}'^{\mathrm{T}}. \tag{2.48}$$

Since J in (2.47) is quadratic, the gradient and Hessian of J are easily found as

$$\frac{\partial J}{\partial \boldsymbol{\beta}} = (N_{en} - 1)\boldsymbol{\beta} + \sum_{k=0}^{N}\mathbf{H}_k'^{\mathrm{T}}\mathbf{R}^{-1}\left(\boldsymbol{h}(\boldsymbol{x}_k^b) - \boldsymbol{y}_k + \mathbf{H}_k'\boldsymbol{\beta}\right), \quad \frac{\partial^2 J}{\partial \boldsymbol{\beta}^2} = (N_{en} - 1)\mathbf{I} + \sum_{k=0}^{N}\mathbf{H}_k'^{\mathrm{T}}\mathbf{R}^{-1}\mathbf{H}_k', \tag{2.49}$$

allowing to readily compute the minimizing vector $\boldsymbol{\beta}$. Such scheme is degenerated to the deterministic case by considering the cost function

$$J = \frac{1}{2}\sum_{k=0}^{N}\left\|\boldsymbol{h}(\boldsymbol{x}_k^b) - \boldsymbol{y}_k + \mathbf{H}_k'\boldsymbol{\beta}\right\|^2. \tag{2.50}$$

Even if the use of finite-size ensembles inevitably implies a loss of precision compared to the adjoint technique, the variational framework ensures a greater stability with respect to the characteristics of the ensemble (size and statistics) than the ensemble filtering approach, as illustrated in chapter 5. Combined with the ease of implementation of such schemes, the ensemble-based variational technique is thus an appealing substitute to adjoint-based or ensemble-Kalman-based schemes. Variants of ensemble-based variational methods based on the singular value decomposition or on the proper orthogonal decomposition are discussed in [182, 203, 204] and considered in chapter 7. Similarly to the hybrid schemes discussed in §2.6.1, which are based on standard variational schemes relying on an adjoint model, hybrid ensemble-based variational schemes that use a combination of static and ensemble-based covariance matrices as in (2.44) have been proposed in the literature [72, 118, 138, 144]. In practice, adding a static covariance matrix in ensemble-based variational schemes might be useful to counteract the degeneracy of the ensemble-based covariance matrix.

2.7 Nudging

Nudging [101] consists in adding to the equations of the dynamical model a forcing term proportional to the difference between the actual estimation of the state of the system and available measurements in order to force the model toward the observations. Applying nudging to (2.1) leads to

$$\boldsymbol{x}_{k+1} = \boldsymbol{m}_k(\boldsymbol{x}_k) + \mathbf{N}_{k+1}\left(\boldsymbol{y}_{k+1} - \boldsymbol{h}(\boldsymbol{m}_k(\boldsymbol{x}_k))\right). \tag{2.51}$$

The nudging matrix $\mathbf{N}_k$ may be considered as constant [101], or be determined through optimal control [217, 236]. Nudging may be used in order to take into account model errors and to relax the strong constraint (perfect model) assumption in a variational scheme. Variants of the nudging technique and possible hybridization with variational methods are also proposed in [13, 14].

2.8 Particle filtering

All the DA schemes derived from the stochastic formulation of the DA problem that are discussed above in this chapter rely on the Gaussian assumption for the statistics of the state vector. This assumption greatly simplifies the derivation of DA methods, and allows to consider only the mean and the covariance matrix associated to the state vector of the system. However, for strongly nonlinear systems such as those encountered in geophysical applications, it may be argued that the full probability density function of the state vector should be considered instead of only a few moments [29]. In this case, Monte Carlo, or particle methods, may be used to propagate the distribution of the state vector in time [214]. In particle filtering, the expected value of any function f of the trajectory $(\boldsymbol{x}_l)_{l=0}^k$ until time k after taking into account available observations from time 0 to k is approximated by

$$\mathbb{E}\left[f((\boldsymbol{x}_l)_{l=0}^k)\right] = \int_{\mathbb{R}^{(k+1)N_s}} f((\boldsymbol{x}_l)_{l=0}^k)\, p\left((\boldsymbol{x}_l)_{l=0}^k | (\boldsymbol{y}_l)_{l=0}^k\right) \mathrm{d}\boldsymbol{x}_0 \mathrm{d}\boldsymbol{x}_1 \cdots \mathrm{d}\boldsymbol{x}_k \simeq \sum_{i=1}^{N_{en}} w_k^{(i)} f((\boldsymbol{x}_l^{(i)})_{l=0}^k), \tag{2.52}$$

or equivalently, the posterior distribution is expressed as a weighted sum of N_{en} Diracs centered on realizations of the trajectory $(\boldsymbol{x}_l)_{l=0}^k$

$$p\left((\boldsymbol{x}_l)_{l=0}^k | (\boldsymbol{y}_l)_{l=0}^k\right) \simeq \sum_{i=1}^{N_{en}} w_k^{(i)} \delta\left((\boldsymbol{x}_l^{(i)})_{l=0}^k - (\boldsymbol{x}_l)_{l=0}^k\right), \quad \sum_{i=1}^{N_{en}} w_k^{(i)} = 1, \tag{2.53}$$

where $\boldsymbol{x}_k^{(i)}$ refers to the ith particle a time k. Starting from a particle representation of the prior of the initial state $p(\boldsymbol{x}_0) = \frac{1}{N_{en}} \sum_{i=1}^{N_{en}} \delta\left(\boldsymbol{x}_0^{(i)} - \boldsymbol{x}_0\right)$, the weights $w_k^{(i)}$ are updated each time new observations are available from the sequential formulation of (2.52)

$$\mathbb{E}\left[f((\boldsymbol{x}_l)_{l=0}^k)\right] = \int_{\mathbb{R}^{(k+1)N_s}} f((\boldsymbol{x}_l)_{l=0}^k)\, p\left((\boldsymbol{x}_l)_{l=0}^{k-1} | (\boldsymbol{y}_l)_{l=0}^{k-1}\right) p\left(\boldsymbol{x}_k | \boldsymbol{x}_{k-1}\right) \frac{p\left(\boldsymbol{y}_k | \boldsymbol{x}_k\right)}{p\left(\boldsymbol{y}_k\right)} \mathrm{d}\boldsymbol{x}_0 \mathrm{d}\boldsymbol{x}_1 \cdots \mathrm{d}\boldsymbol{x}_k, \tag{2.54}$$

assuming first-order Markov dynamics and independent observations. A straightforward way to sequentially evaluate the weights $w_k^{(i)}$ from (2.54) consists in sampling the state vector at time k from the transition distribution $p\left(\boldsymbol{x}_k | \boldsymbol{x}_{k-1}\right)$. Accordingly, the weights are recursively found as

$$w_k^{(i)} \propto w_{k-1}^{(i)} p\left(\boldsymbol{y}_k | \boldsymbol{x}_k^{(i)}\right). \tag{2.55}$$

The proportionality coefficient in (2.55) takes into account the normalization to one of the sum of the weights. In proceeding in this way, only the weights $w_k^{(i)}$ are updated when new observations are available, while the particles $\boldsymbol{x}_k^{(i)}$ are left unchanged. Many particles may thus move away from the observations, their associated weights tend to zero, and a lot of statistical information is lost. This partly explains the huge number of realizations required by the particle filter, making its application to large-scale applications very challenging. In order to reduce the somewhat unaffordable computational cost in particle filtering, (2.54) may be modified through the introduction of a density that allows the incorporation of observation information during the propagation of the particles. This may be simply peformed as

$$\mathbb{E}\left[f((\boldsymbol{x}_l)_{l=0}^{k})\right] = \int_{\mathbb{R}^{(k+1)N_s}} f((\boldsymbol{x}_l)_{l=0}^{k}) p\left((\boldsymbol{x}_l)_{l=0}^{k-1} | (\boldsymbol{y}_l)_{l=0}^{k-1}\right) p\left(\boldsymbol{x}_k|\boldsymbol{x}_{k-1}\right) \frac{p\left(\boldsymbol{y}_k|\boldsymbol{x}_k\right)}{p\left(\boldsymbol{y}_k\right)} \frac{q\left(\boldsymbol{x}_k|\boldsymbol{x}_{k-1},\boldsymbol{y}_k\right)}{q\left(\boldsymbol{x}_k|\boldsymbol{x}_{k-1},\boldsymbol{y}_k\right)} \mathrm{d}\boldsymbol{x}_0 \mathrm{d}\boldsymbol{x}_1 \cdots \mathrm{d}\boldsymbol{x}_k, \quad (2.56)$$

where $q\left(\boldsymbol{x}_k|\boldsymbol{x}_{k-1},\boldsymbol{y}_k\right)$ is referred to as the proposal density. The only constraint on the choice of this distribution is that its support is equal or superior to that of the posterior distribution of the state vector to avoid division by zero. Sampling the state vector at time k from $q\left(\boldsymbol{x}_k|\boldsymbol{x}_{k-1},\boldsymbol{y}_k\right)$ instead of $p\left(\boldsymbol{x}_k|\boldsymbol{x}_{k-1}\right)$ allows to push the particles toward the observartions, leading to the following recursive estimation of the weights

$$w_k^{(i)} \propto w_{k-1}^{(i)} \frac{p\left(\boldsymbol{y}_k|\boldsymbol{x}_k^{(i)}\right) p\left(\boldsymbol{x}_k^{(i)}|\boldsymbol{x}_{k-1}^{(i)}\right)}{q\left(\boldsymbol{x}_k^{(i)}|\boldsymbol{x}_{k-1}^{(i)},\boldsymbol{y}_k\right)}. \quad (2.57)$$

The sampling of the state vector from the chosen proposal density may be performed either through the addition of a nudging term in the model equations [215], as in (2.51), or based on ensemble Kalman filtering [174]. Aside from the question of the choice of the proposal density, further adjustments and modifications to the particle filter based on (2.57) may be still required in the case of large-scale systems in order to avoid filter divergence [214].

Part I

Study of homogeneous turbulence through spectral modelling and data assimilation

Introduction

The free decay of homogeneous isotropic turbulence (HIT) is one of the most important test cases in turbulence studies due to its relevance in understanding the physical behaviour of turbulent flows and its implications in turbulence modelling. Freely decaying HIT has been therefore extensively investigated in the literature, and exhaustive reviews may be found in [19, 69, 132, 188]. In standard approaches, the decay of statistical quantities is represented by a power law, such as $\mathcal{K} \backsim t^{n_{\mathcal{K}}}$ for the turbulent kinetic energy $\mathcal{K}$. Theoretical analyses suggest an algebraic relation between the exponent $n_{\mathcal{K}}$ and the slope of the kinetic energy spectrum at large scales, which is in good agreement with numerical simulations performed with the eddy-damped quasi-normal Markovian (EDQNM) model [56, 62, 154]. However, an important point is that significant discrepancies between theoretical predictions about the value of the exponent $n_{\mathcal{K}}$ and results obtained in grid turbulence experiments remain, as illustrated in figure 1 of [154]. Therefore, bridging the gap between experimental data and analytical results dealing with freely decaying HIT is still a prominent issue in turbulence theory. Factors that may influence the decay of turbulence and possibly explain the above mentioned discrepancies are enumerated below:

- Initial condition effects: it has been confirmed by recent studies that there is no loss of memory of the initial or upstream conditions in turbulent flows [85, 155]. On the contrary, as previously mentioned, turbulence decay appears to be fixed by the initial shape of the energy spectrum at large scales. More precisely, dimensional analysis and EDQNM simulations performed in [154] indicate that HIT decay is governed by the features of the large scales close to the peak of the energy spectrum, and not by the largest scales of the flow, as generally stated in the literature. In addition to this study, a detailed, scale-by-scale sensitivity analysis of HIT decay with respect to the characteristics of the initial kinetic energy spectrum could provide a deeper insight and quantitative information about the influence of each scale of the flow on the intensity of the decay.

- Production mechanisms and time-lasting effects: turbulence production mechanisms in grid turbulence experiments are intimately related to the shape of the upstream kinetic energy spectrum, or initial spectrum according to Taylor's frozen turbulence hypothesis. These production effects are far from being universal in experimental studies, and a detailed investigation of the sensitivity of HIT decay as discussed above could help to correlate the way of generating turbulence in experiments and the observed value of the decay exponent. Moreover, the issue of the influence of production mechanisms on turbulence decay has been recently renewed by experimental studies dealing with fractal-generated turbulence [96, 104, 122, 151, 166, 202, 212], where possible exponential turbulence decay [86] and anomalous decay exponents that are not in the range predicted by classical approaches are observed. Recent theoretical and numerical studies [153, 156] suggest that anomalous decay exponents may originate from the unusual bumped shape of the energy spectrum produced by a multi-scale forcing, while exponential decay may be observed in the case of slowly vanishing production effects.

- Reynolds number effects: due to technological limitations, a huge number of experimental studies are conducted at moderate Reynolds numbers. In such intermediate regimes, decay exponents of statistical quantities exhibit a dependence on the Reynolds number, while the analytically predicted values of these exponents are constant for sufficiently low or high Reynolds numbers. Clearly, these effects, which are investigated in [74, 155], do not facilitate the comparisons between experimental and analytical studies.

- Influence of anisotropy: it is well known that grid-generated turbulence is not perfectly isotropic [62]. Instead, it may be considered as weakly axisymmetric with slightly more kinetic energy in the axial direction than in the transverse ones. Numerical investigations of axisymmetric turbulence [46, 70, 161] suggest that, after the return to isotropy of the small scales, the anisotropy of the flow has no influence on the value of the decay exponents. Nonetheless, anisotropy could still induce non-trivial transient effects that affect the decay.

- Breakdown of homogeneity: at last, a lack of homogeneity in experimental devices could corrupt comparisons with predictions concerning HIT decay. Indeed, it has been confirmed by Direct Numerical Simulations (DNS) [75] that turbulence remains inhomogeneous even far downstream of the grid.

All these observations may encourage the blending of numerical tools able to recover classical theoretical predictions with experimental data in order to take into account the various factors discussed above, with the ultimate goal of reconciling experimental and analytical results about freely decaying HIT. Data assimilation (DA) techniques seem particularly appropriate for operating this coupling and for the identification of the most important factors that affect HIT decay. In chapter 3, it is thus proposed to employ a variational DA scheme as discussed in §2.3.1 in order to perform a scale-by-scale sensitivity analysis of HIT decay with respect to the features of the initial kinetic energy spectrum. The results thus obtained may constitute valuable informations to address the first two points above and to identify the detailed characteristics of the energy spectrum that lead HIT decay. Employing a variational DA scheme instead of other DA methods discussed in chapter 2 is motivated by the fact that the variational technique, through the adjoint equations, furnishes the gradient of the flow solution with respect to all the components of the control vector in the DA problem, allowing to readily perform first-order sensitivity analyses. This study is based on the use of the EDQNM model for isotropic turbulence [172], which proved to be a valuable tool for the study of HIT [132, 188], but also of more complex homogeneous flows such as rotating turbulence [20, 37], and stably [87] and unstably [36] stratified turbulence. It is noteworthy that Reynolds effects can be easily taken into account with the EDQNM model due to its capacity to investigate turbulent flows from high to low Reynolds number regimes and over long evolution times. Moreover, the tractability of the EDQNM model makes it an appropriate numerical method for DA purposes. In addition to the analysis of §3.1 [160] for the identification of the scales governing grid turbulence decay, complementary DA experiments are performed in §3.2, which allow to confirm the relation between unusual shapes of the initial energy spectrum and anomalous decay regimes observed in, e.g., fractal-generated turbulence experiments. Appendix A furnishes details about the derivation of the adjoint EDQNM model.

In chapter 4 [162], a spectral model adapted to moderately anisotropic homogeneous flows, which seem more representative of grid-generated turbulence than strictly isotropic turbulence, is proposed. This model is based on anisotropic EDQNM modelling and involves spherical descriptors, which depend only on the modulus of the wavenumber, to describe directional and polarization anisotropies. Even if this description unavoidably entails a loss of information compared to a full 3D level of description in Fourier space, the associated reduction in computational complexity and cost is highly valuable to perform detailed parametric studies. As illustrated in chapter 4 and [32], the proposed model is appropriate for the study of moderately anisotropic turbulent flows in the presence of mean flow gradients inducing production effects and their return to isotropy. An extension to the passive scalar case is proposed in [31]. In addition to chapter 4, a more detailed derivation of the proposed model is provided in appendix B.

Chapter 3

Data assimilation-based analysis of grid turbulence decay

3.1 Is isotropic turbulence decay governed by asymptotic behavior of large scales? An eddy-damped quasi-normal Markovian-based data assimilation study

PHYSICS OF FLUIDS **26**, 115105 (2014)

Is isotropic turbulence decay governed by asymptotic behavior of large scales? An eddy-damped quasi-normal Markovian-based data assimilation study

V. Mons,[1] J.-C. Chassaing,[1] T. Gomez,[1] and P. Sagaut[2]
[1] *Institut Jean Le Rond d'Alembert, UPMC Univ Paris 06, UMR 7190, F-75005 Paris, France and CNRS, UMR 7190, Institut Jean Le Rond d'Alembert, F-75005 Paris, France*
[2] *Aix Marseille Universite, CNRS, Centrale Marseille, M2P2 UMR 7340, 13451 Marseille, France*

(Received 8 July 2014; accepted 29 October 2014; published online 17 November 2014)

The present paper deals with the identification of the scales and features of the initial kinetic energy spectrum that govern the decay regime of freely decaying homogeneous isotropic turbulence (HIT). To this end, a Data Assimilation (DA) study is performed, which is based on a variational optimal control problem with the eddy-damped quasi-normal Markovian (EDQNM) model whose adjoint equation is derived in the present work. The DA procedure consists in reconstructing the initial kinetic energy spectrum in order to minimize the error committed on some features of decaying turbulence with respect to a targeted EDQNM simulation. The present results show that the decay of HIT over finite time is governed by a finite range of large scales, i.e., the scales ranging from the initial to the final integral scales (or equivalently by wave numbers comprised between the initial and the final location of the peak of the energy spectrum). The important feature of the initial condition is the slope of the energy spectrum at these scales, if such a slope can be defined. This is coherent with previous findings dealing with decay of non-self-similar solutions, or with the key assumptions that underly the Comte-Bellot–Corrsin theory. A consequence is that the finite time decay of HIT is not driven by the asymptotic large-scale behavior of the energy spectrum $E(k \to 0, t = 0)$ or the velocity correlation function $f(r \to +\infty, t = 0)$, or even scales such as $kL \ll 1$ or $L/r \ll 1$. Governing scales are such that $kL(t) = O(1)$ for values of the integral scale $L(t)$ observed during the finite time decay under consideration. As a matter of fact, a null sensitivity of finite time decay of turbulence with respect to the asymptotic large scale features of the initial condition is observed. Therefore, the asymptotic features of the initial condition should not be investigated defining an inverse problem based of features of turbulence decay observed over a finite time. © *2014 AIP Publishing LLC*. [http://dx.doi.org/10.1063/1.4901448]

I. INTRODUCTION

Homogeneous isotropic turbulence (HIT) decay has been among the most important issue in turbulence theory, since isotropic turbulence is the framework in which the deepest investigations of nonlinear features of turbulence can be performed. As a consequence, HIT decay is a very active field of research since about one century, and many issues related to this phenomenon remain to be investigated and clarified. Among them, the question of identifying the features of the initial condition that govern the turbulent kinetic energy decay rate still deserves further investigations. More precisely, one should find which scales and which features associated to these scales control the decay of turbulence. These questions have received a continuous attention since the seminal works carried out in the early 20th century (see classical books, e.g., Refs. 1–4), and has been renewed by recent discussions[5,6] dealing with the possible occurrence of anomalous decay regimes if fractal/multiscale grid topologies are used in grid turbulence experiments. It is also important keeping in mind that this topic is also relevant for practical engineering purposes, since HIT decay is one of the cornerstone of statistical turbulence modeling for engineering applications.

The common wisdom, expressed in almost all textbooks, monographs, and research papers that address decaying HIT is that the turbulent kinetic energy $\mathcal{K}$ follows an algebraic decay law, i.e., $\mathcal{K}(t) \propto t^{n_{\mathcal{K}}}$, where the decay exponent $n_{\mathcal{K}}$ is assumed to be time-independent after a possible transient relaxation phase when an asymptotic decay regime is reached. The question of the dependence of $n_{\mathcal{K}}$ to some specific features of the initial condition has raised some controversies, but the most recent works[7] indicate that there is no universal decay regime (the solution $\mathcal{K}(t) \propto t^{-1}$ has been advocated in several papers and books, e.g., Refs. 8–10) and that the decay rate is definitely governed by the details of the initial conditions, showing, as advocated by George,[11,12] that "initial (and/or upstream) conditions do matter." An almost ubiquitous statement in devoted papers and book chapters is that the decay exponent $n_{\mathcal{K}}$ is related to the large-scale asymptotic behavior of the longitudinal velocity correlation function $f(r, t = 0)$ in the physical space, or equivalently, to the asymptotic behavior of the kinetic energy spectrum $E(k, t = 0)$. Assuming that $f(r \to +\infty, t = 0) \propto r^{-m}$ or equivalently that $E(k \to 0, t = 0) \propto k^{\sigma}$, several theories/approaches yielded the derivation of expressions of the form $n_{\mathcal{K}}(m)$ or $n_{\mathcal{K}}(\sigma)$ (since σ and m are tied by an exact non-trivial relation[13]). Several famous theories dealing with isotropic turbulence decay rely on this asymptotic behavior and related assumptions about the analyticity of $E(k)$ which lead to consider low-k expansions of the form $E(k \to 0) = \frac{\mathfrak{L}k^2}{4\pi^2} + \frac{\mathfrak{I}k^4}{24\pi^2} + \ldots$, where $\mathfrak{L}$ and $\mathfrak{I}$ refer to the Saffman and Loitsyansky integrals and are linked to linear and angular momentum conservations, respectively (see, e.g., Refs. 14–16).

But it is important noting that this common statement is not fully supported by existing data since:

- All physical systems are bounded in space and can be observed over finite times only. Therefore, real-life turbulent flows are driven by a limited range of finite-size scales, and they are observed over a finite time. Therefore, a direct link with asymptotic behavior at $k \to 0$ or $r \to +\infty$ cannot be established. Therefore, the asymptotic limit is usually understood in practice as defining very large scales such that $kL \ll 1$ or $L/r \ll 1$ where L refers to the longitudinal integral velocity scale of turbulence or the turbulent scale $\mathcal{K}^{3/2}/\varepsilon$.
- Due to technological limitations, it is very difficult to measure experimentally the energy spectrum and the correlation function for scales larger than a few integral scales. And it should be kept in mind that the measured spectrum is usually the 1D spectrum, not the 3D spectrum. In a similar way, Direct Numerical Simulation provides a pretty poor description of very large scales, due to limitations in the computational domain size, with some possible significant effects on the decay features.[17] Therefore, the exact behavior of the high Reynolds number 3D energy spectrum and the velocity correlation function at scales much larger than the integral scale escapes both experimental and numerical investigation at present time.
- Among the most useful and powerful existing predictive theory for decaying HIT, one should mention the Comte-Bellot–Corrsin theory (further extended by several researchers to account for different initial spectrum shapes,[18,19] saturation effect,[19] and Reynolds number regimes[7,20]), that relies on a single length scale, L, which is associated to the peak of the kinetic energy spectrum. Its recent extension[21,22] to non-self-similar initial energy spectra with two characteristic large scales seems to indicate that HIT decay is governed by the detailed features of the energy spectrum for scales that are close to the integral length scale, not by the asymptotic behavior at the largest scales. This result raises a consistency problem between the different approaches, since it seems to indicate that important scales are such that $kL \sim 1$, not $kL \ll 1$.

The goal of the present study is to further investigate the issue of identifying the scales that govern HIT decay of finite time. To this end, it is proposed to use advanced mathematical tools, namely, Data Assimilation methods (e.g., see Refs. 23 and 24). These methods have been developed in the fields of meteorology and oceanography to reconstruct optimal initial conditions using information dealing with the time evolution of the solution. In the present case, it is proposed to reconstruct the optimal initial 3D kinetic energy spectrum $E(k, t = 0)$ considering an arbitrarily fixed turbulence decay law which is determined numerically, and to look at the parts of the initial spectrum that are reconstructed by the optimization loop. More precisely, since an optimal-control-based Data Assimilation method is used, the gradient of the solution during its evolution with respect to the features of the initial condition can be computed, giving a deep insight into the sensitivity of the flow evolution with respect to the initial condition. This procedure will allow for a clear, mathematically grounded identification of the features and scales of the initial solution that govern the decay over an arbitrarily fixed finite time.

In order to investigate a wide range of initial conditions and flow regimes, it is chosen to use the eddy-damped quasi-normal Markovian[2,4,25] (EDQNM) model to compute time evolution of the kinetic energy spectrum in the Data Assimilation procedure. The EDQNM model is also used to calculate reference decay laws. This highly versatile model is known to yield very accurate results for isotropic turbulence decay with good resolution at both large and small scales, ensuring the reliability of the results. The adjoint EDQNM problem is derived in the present work for the purpose of the optimization procedure for the reconstruction of the initial energy spectrum. The development of the adjoint EDQNM model in the Data Assimilation procedure will allow to obtain the gradient of the EDQNM solution with respect to the characteristics of the initial energy spectrum. Using this gradient, the scale-by-scale sensitivity of the decay regime can be precisely quantified, allowing a detailed and rigorous identification of the characteristics of the energy spectrum that lead the decay. In addition, the present work will allow to determine which are the features of the energy spectrum that can be inferred from the knowledge of the temporal evolutions of different statistical quantities. To the knowledge of the authors, this is the first time that a optimal control theory based scale-by-scale sensitivity analysis of decay regime, including decay regime exponents, is provided.

It should be kept in mind that the role of very large scales in HIT decay has been intrinsically addressed in works dealing with time evolution of three-range initial energy spectra and possible existence of non-self-similar decay regimes over arbitrary time. The most recent work on that topic is Meldi and Sagaut,[22] in which dimensional analysis and EDQNM simulations were performed considering an arbitrary three-range initial energy spectrum. Results reported in this paper show that the governing scales are the ones comprised in the large scale range located near the spectrum peak, not the asymptotically large ones. The present work yields a much deeper insight into this topic, since it provides: (i) a mathematically grounded evaluation of the scale-by-scale gradient of decay exponents and (ii) a rigorous identification of scales that govern the HIT decay over a finite time. These two informations were not present in previous works, since they require the use of the optimal control theory.

The paper is organized as follows. The EDQNM model for solving Lin's equation is briefly recalled in Sec. II. The modeling of the initial energy spectrum $E(k, t = 0)$ is discussed in Sec. III. The Data Assimilation method used in the present paper is presented in Sec. IV, along with the derivation of the adjoint EDQNM problem. Results are displayed and analyzed in Sec. V.

II. EQUATIONS OF THE ISOTROPIC EDQNM MODEL

In this section, we briefly recall the underlying hypotheses and the equations of the EDQNM model for HIT. The reader may refer to Refs. 2,4, and 25 for an exhaustive description of the EDQNM model. The different moments of velocity fluctuations obey an infinite hierarchy of open equations where the partial time derivative of moments of order n is governed by moments of order $n + 1$. The Quasi-Normal (QN) approximation, which is based on the assumption that the fluctuating velocity probability distributions are normal distributions, can be used to close the evolution equations of second and third-order moments. This hypothesis implies that the fourth order cumulants of the velocity field, which represent the difference between the velocity distribution and the normal distribution, are identically zero. In the classical version of the EDQNM model for HIT, the fourth order cumulants are instead supposed to be linearly dependent on the third-order moments of the velocity field. This assumption is equivalent to the introduction of an eddy-damping term, as proposed by Orszag.[25] The evolution equation of third-order moments is further simplified by the Markovian assumption, which implies that the characteristic evolution time of the eddy-damping rate can be considered negligible with respect to the turbulence evolution time. Once the expression thus obtained for the third-order moments is included in the evolution equation of second-order moments, the latter is closed. After spherical integration, an evolution equation for the energy spectrum is finally obtained. The equations of the EDQNM model for HIT are

$$\frac{\partial E}{\partial t}(k) + 2\nu k^2 E(k) = T(E,k), \tag{1}$$

$$T(E,k) = \iint_{\Delta_k} \theta_{kpq} G_{kpq} E(q)\big(k^2 E(p) - p^2 E(k)\big) dp dq, \tag{2}$$

$$G_{kpq} = \frac{xy + z^3}{q}; \quad x = -\frac{\underline{p}.\underline{q}}{pq}; \quad y = -\frac{\underline{k}.\underline{q}}{kq}; \quad z = -\frac{\underline{k}.\underline{p}}{kp}, \tag{3}$$

$$\theta_{kpq} = \frac{1 - e^{-\mu_{kpq} t}}{\mu_{kpq}}; \quad \mu_{kpq} = \nu(k^2 + p^2 + q^2) + \eta_k + \eta_p + \eta_q; \quad \eta_k = A\sqrt{\int_0^k r^2 E(r) dr}, \tag{4}$$

where $E(k)$ is the spectral kinetic energy at wavenumber k (for the sake of readability, the time dependency is omitted in the above expressions), ν is the kinematic viscosity, Δ_k refers to the area in the plane (p, q) so that $\underline{k} + \underline{p} + \underline{q} = \underline{0}$. The expression here used for the damping factor $\eta(k)$ in (4) is the proposal by Pouquet *et al.*,[26] we take $A = 0.355$.[27]

III. FUNCTIONAL FORMS FOR THE INITIAL ENERGY SPECTRUM

In order to ensure the realizability condition for the energy spectrum ($E(k) \geq 0\,\forall k$) during the numerical data assimilation procedure, a functional form is prescribed for the initial energy spectrum. Two functional forms are considered in this paper. The first one is the proposal by Meyers and Meneveau.[28] This functional form accounts for all known features of the energy spectrum, and it is written as follows:

$$E(k) = Ck^{-5/3}(k/k_{L_2})^{-\beta} f_L(k/k_{L_2}) f_\eta(k/k_\eta), \tag{5}$$

$$f_L(x) = \left(\frac{x}{[x^p + \alpha_5]^{1/p}}\right)^{5/3+\beta+\sigma_2}; \quad f_\eta(x) = \exp(-\alpha_1 x)\left[1 + \frac{\alpha_2 (x/\alpha_4)^{\alpha_3}}{1 + (x/\alpha_4)^{\alpha_3}}\right]. \tag{6}$$

σ_2 refers to the slope of the energy spectrum at large scales. Both k_{L_2} and α_5 govern the position of the peak of the spectrum, and the parameter p prescribes its shape. β is the intermittency correction. k_η sets the position of the Kolmogorov scale, while the parameters α_1-α_4 govern the shape of the spectrum at small scales and the bottleneck correction. The constant C, which includes the dissipation rate and the Kolmogorov constant, is here used for normalization. To get a better insight into the influence of large scales on the decay, Eq. (5) is modified in the following way:

$$E^0(k) = \begin{cases} Bk^{\sigma_1} & k < k_{L_1} \\ Ck^{-5/3}(k/k_{L_2})^{-\beta} f_L(k/k_{L_2}) f_\eta(k/k_\eta) & k \geq k_{L_1} \end{cases} \tag{7}$$

with

$$Bk_{L_1}^{\sigma_1} = Ck_{L_1}^{-5/3}(k_{L_1}/k_{L_2})^{-\beta} f_L(k_{L_1}/k_{L_2}) f_\eta(k_{L_1}/k_\eta) \tag{8}$$

by the continuity of the energy spectrum at $k = k_{L_1}$. Equation (7) allows to distinguish the very large scales ($k < k_{L_1}$), which are characterized by the slope σ_1, from the large scales close to the peak of the initial energy spectrum $E^0(k)$, which are characterized by the slope σ_2. When the functional form (7) is used, the control vector (see Secs. IV A and IV B) is of dimension 11 and contains the parameters σ_1, σ_2, p, β, k_{L_2}, k_η, and α_1-α_5. The separation between large and very large scales is fixed at $k_{L_1}/k_{L_2} = 10^{-3}$. With this value, at least one decade between the wavenumber k_{L_1} and the final position of the peak of the energy spectrum is granted (see Sec. V A). The advantage of the functional form (7) is that a small number of parameters is used for the description of the initial energy spectrum, which may facilitate optimization in the same way as the use of non-uniform rational basis splines (NURBS) in classical aerodynamic shape optimization.[29,30] On the other hand, the non-local character of these parameters precludes a detailed scale-by-scale analysis of the sensitivity of the turbulence decay with respect to the characteristics of the initial energy spectrum. Because of this, we also consider a second functional form which is written as

$$E^0(k) = B(k)k^{s(k)}, \tag{9}$$

where $s(k)$ refers to the local slope of the initial energy spectrum and forms the control vector, while $B(k)$ ensures the continuity of the spectrum. The discrete form of (9) for the ith energy mode is given by

$$E_i^0 = B_i k_i^{s_i} \quad ; \quad B_i = B_{i-1} k_i^{s_{i-1}-s_i}. \tag{10}$$

In this way, the dimension of the control vector, which is formed by the slopes s_i, is equal to the number of resolved modes, which ranges from 150 to 200 in the present work. The functional form (9) therefore allows a scale-by-scale description of the initial energy spectrum while ensuring the realizability condition.

IV. DATA ASSIMILATION METHOD FOR OPTIMAL RECONSTRUCTION OF THE INITIAL SOLUTION

A. Variational formulation and gradient with respect to the initial condition

The variational formulation of the data assimilation problem for the EDQNM model is derived in the present section. The reader may refer to Refs. 23 and 31 for a detailed description of variational methods applied to data assimilation. Recent applications of variational data assimilation in the field of fluid mechanics may be found in Refs. 24, 32, and 33. Given a reference realization of decay of HIT, i.e., a reference EDQNM simulation in our case, and the observation y of this decay, we evaluate the discrepancies between this reference decay and another decay denoted by the energy spectrum (depending on time) E thanks to the functional, or cost function, defined by

$$J(E) = \frac{1}{2}\,\|y - H(E)\|_{\mathcal{O}}^2 . \tag{11}$$

Following the classical terminology used in the data assimilation community, the reference decay is referred to as the true state, and the solution associated to the energy spectrum E is referred to as the estimated state. H is the observation operator from the model space, denoted by $\mathcal{M}$, to the observation space, denoted by $\mathcal{O}$. This operator allows to compare E to the available information y on the true state. The inner product for the observation space $\mathcal{O}$ depends on the type of available observations. The inner product of two vectors a and b in the model space is defined by

$$\langle a, b\rangle_{\mathcal{M}} = \int_0^{T_f}\int_0^{\infty} a(k,t)b(k,t)dkdt, \tag{12}$$

where T_f is the finite duration of the decay under consideration. T_f also refers to the size of the assimilation window. Before proceeding further in the derivation, let us introduce a few notations. Given an operator Ψ from vector space $\mathcal{A}$ to vector space $\mathcal{B}$, the Gâteaux derivative of Ψ at E in the direction F, with both E and F in $\mathcal{A}$, is denoted by

$$\left\langle \frac{\partial \Psi}{\partial E}(E), F\right\rangle_{\mathcal{A}} = \frac{\partial \Psi}{\partial E}\Big|_E (F) = \lim_{\epsilon\to 0}\frac{d}{d\epsilon}\Psi(E+\epsilon F). \tag{13}$$

The adjoint operator of Ψ is denoted by Ψ^* and is defined by

$$\langle \Psi(E), G\rangle_{\mathcal{B}} = \langle E, \Psi^*(G)\rangle_{\mathcal{A}} \;\; \forall E \in \mathcal{A}, \forall G \in \mathcal{B}. \tag{14}$$

The aim of data assimilation is to minimize the cost function J defined by Eq. (11) in order to recover the true state starting from the estimated state using the observation y. In the variational framework, this problem is formulated as an optimal control problem. In this paper, we choose the initial energy spectrum as the control vector. In other words, we aim to recover the true initial energy spectrum, or more precisely the set of parameters of the functional form prescribed for the latter. This problem of optimal control of the initial condition is similar to those described in Refs. 34 and 35. The minimization of the cost function J is performed by the computation of its gradient with respect to the initial condition coupled with a descent method. This gradient may also be used to conduct a sensitivity analysis. When computing the gradient, we want the energy spectrum E to obey the EDQNM equations (1)–(4). This leads to the introduction of the Lagrangian $\mathcal{L}$ defined by

$$\begin{aligned}\mathcal{L}(E,\tilde{E}) = J(E) + \left\langle \tilde{E}, \frac{\partial E}{\partial t} + 2\nu k^2 E - T(E)\right\rangle_{\mathcal{M}} &= \frac{1}{2}\left\| y - H(E)\right\|^2_{\mathcal{O}} \\ &+ \left\langle \tilde{E}, \frac{\partial E}{\partial t} + 2\nu k^2 E - T(E)\right\rangle_{\mathcal{M}},\end{aligned} \tag{15}$$

where the Lagrange multiplier $\tilde{E}$ will be referred to as the adjoint spectrum in the following. Necessary conditions for $(E, \tilde{E})$ to be a minimizer of $\mathcal{L}$ are given by

$$\left\langle \frac{\partial \mathcal{L}}{\partial E}(E,\tilde{E}), F\right\rangle_{\mathcal{M}} = \left\langle \frac{\partial H}{\partial E}\Big|_E (F), H(E) - y\right\rangle_{\mathcal{O}} + \left\langle \tilde{E}, \frac{\partial F}{\partial t} + 2\nu k^2 F - \frac{\partial T}{\partial E}\Big|_E (F)\right\rangle_{\mathcal{M}} = 0 \ \ \forall F \in \mathcal{M}, \tag{16}$$

$$\left\langle \frac{\partial \mathcal{L}}{\partial \tilde{E}}(E,\tilde{E}), \tilde{F}\right\rangle_{\mathcal{M}} = \left\langle \frac{\partial E}{\partial t} + 2\nu k^2 E - T(E), \tilde{F}\right\rangle_{\mathcal{M}} = 0 \ \ \forall \tilde{F} \in \mathcal{M}. \tag{17}$$

After integration by parts, these conditions take the final form

$$\begin{aligned}\left\langle \frac{\partial \mathcal{L}}{\partial E}(E,\tilde{E}), F\right\rangle_{\mathcal{M}} = &\left\langle \left(\frac{\partial H}{\partial E}\Big|_E\right)^{*} (H(E) - y) - \frac{\partial \tilde{E}}{\partial t} + 2\nu k^2 \tilde{E} - \left(\frac{\partial T}{\partial E}\Big|_E\right)^{*} (\tilde{E}), F\right\rangle_{\mathcal{M}} \\ &+ \int_0^{\infty} \big(\tilde{E}(k,T_f)F(k,T_f) - \tilde{E}(k,0)F(k,0)\big) dk = 0 \ \ \forall F \in \mathcal{M},\end{aligned} \tag{18}$$

$$\left\langle \frac{\partial \mathcal{L}}{\partial \tilde{E}}(E,\tilde{E}), \tilde{F}\right\rangle_{\mathcal{M}} = \left\langle \frac{\partial E}{\partial t} + 2\nu k^2 E - T(E), \tilde{F}\right\rangle_{\mathcal{M}} = 0 \ \ \forall \tilde{F} \in \mathcal{M}. \tag{19}$$

Equation (18) involves the adjoint of the gradient of the observation operator and that of the gradient of the energy transfer term defined by Eq. (2), whose expressions will be precised later on. We introduce the following notations for these two adjoint operators:

$$\tilde{T}|_E(\tilde{E},k) = \left(\frac{\partial T}{\partial E}\Big|_E\right)^{*}(\tilde{E},k); \ \ \tilde{H}|_E(y,k) = \left(\frac{\partial H}{\partial E}\Big|_E\right)^{*}(y,k). \tag{20}$$

By setting

$$\frac{\partial E}{\partial t}(k) + 2\nu k^2 E(k) - T(E,k) = 0, \tag{21}$$

$$-\frac{\partial \tilde{E}}{\partial t}(k) + 2\nu k^2 \tilde{E}(k) - \tilde{T}|_E(\tilde{E},k) = \tilde{H}|_E\big(y - H(E), k\big) = \tilde{f}(E,y,k); \ \ \tilde{E}(k,T_f) = 0, \tag{22}$$

we deduce the gradient of $\mathcal{L}$ with respect to the initial condition $E^0(k) = E(k, 0)$ from (18)

$$\frac{\partial \mathcal{L}}{\partial E^0}(E,\tilde{E},k) = -\tilde{E}(k,0). \tag{23}$$

The term $\tilde{f}$ introduced in Eq. (22) is referred to as the adjoint forcing in the following. Equations (21)–(23) allow to design an optimization procedure which is described in Sec. IV B. The gradient (23) can also be used to quantify the sensitivity, or the variation $\Delta\mathcal{L}$, of the Lagrangian $\mathcal{L}$ with respect to a perturbation ΔE^0 of the initial energy spectrum, according to the following first-order approximation:

$$\Delta\mathcal{L}(E,\tilde{E}) \simeq \int_0^{\infty} \frac{\partial \mathcal{L}}{\partial E^0}(E,\tilde{E},k)\Delta E^0(k) dk. \tag{24}$$

In the case where the initial energy spectrum is perturbed only at the wavenumber $k = k_p$ ($\Delta E^0(k) = \delta(k - k_p)\Delta E_p$ in (24) where δ is the Dirac distribution), $\Delta\mathcal{L} = \frac{\partial\mathcal{L}}{\partial E^0}(k = k_p)\Delta E_p$, so the gradient $\frac{\partial\mathcal{L}}{\partial E^0}(k = k_p)$ gives directly the sensitivity of the Lagrangian $\mathcal{L}$ when only the energy mode $E^0(k_p)$ is perturbed. We now provide the expression of the gradient of the energy transfer term and that of its adjoint. The expression of the Gâteaux derivative of the transfer term at E in the direction F is given by

$$\frac{\partial T}{\partial E}\Big|_E(F,k) = \iint_{\Delta_k} \theta_{kpq}G_{kpq}\Big[F(q)\big(k^2E(p) - p^2E(k)\big) + F(p)k^2E(q) - F(k)p^2E(q)\Big]dpdq$$
$$+ \iint_{\Delta_k} \mathcal{D}_{kpq}\Big\{\frac{\int_0^k r^2F(r)dr}{\eta_k} + \frac{\int_0^p r^2F(r)dr}{\eta_p} + \frac{\int_0^q r^2F(r)dr}{\eta_q}\Big\}dpdq, \tag{25}$$

where the factor $\mathcal{D}_{kpq}$ is defined by

$$\mathcal{D}_{kpq} = \frac{A^2}{2}\frac{-1 + (\mu_{kpq}t + 1)e^{-\mu_{kpq}t}}{\mu_{kpq}^2}G_{kpq}E(q)\big(k^2E(p) - p^2E(k)\big). \tag{26}$$

The definition of the different terms involved in Eqs. (25) and (26) are given in Eqs. (3) and (4). By using the definition (14) of an adjoint operator, and by several applications of Fubini's theorem, we deduce the following expression for the adjoint transfer term $\tilde{T}|_E$ involved in Eq. (22):

$$\begin{aligned}\tilde{T}|_E(\tilde{E},k) = \iint_{\Delta_k} &\Big[\theta_{pkq}G_{pkq}\tilde{E}(p)p^2E(q) + \theta_{qpk}G_{qpk}\tilde{E}(q)\big(q^2E(p) - p^2E(q)\big)\\ &- \theta_{kpq}G_{kpq}\tilde{E}(k)p^2E(q)\Big]dpdq\\ &+ \int_k^\infty \iint_{\Delta_r} \tilde{E}(r)\frac{\mathcal{D}_{rpq}}{\eta_r}k^2dpdqdr + \int_k^\infty \iint_{\Delta_p} \tilde{E}(r)\frac{\mathcal{D}_{rpq}}{\eta_p}k^2drdqdp\\ &+ \int_k^\infty \iint_{\Delta_q} \tilde{E}(r)\frac{\mathcal{D}_{rpq}}{\eta_q}k^2dpdrdq.\end{aligned} \tag{27}$$

A remarkable feature of Eq. (27) is the presence of triple sums which make $\tilde{T}|_E$ costly to evaluate compared to the original transfer term. From a practical point of view, one has to implement the adjoint of the discrete version of the gradient of the transfer term given by Eq. (25), instead of the discrete version of Eq. (27). However, the expressions obtained by these two approaches are similar.

B. Optimization procedure

As noted above, Eqs. (21)–(23) allow the computation of the gradient of the Lagrangian $\mathcal{L}$ defined by (15) with respect to the initial condition E^0 of the estimated decay. Since we impose a functional form for the initial energy spectrum, we need the gradient of $\mathcal{L}$ with respect to the different parameters of the functional forms defined by Eq. (7) or Eq. (9). The gradient of $\mathcal{L}$ with respect to the control vector $\underline{a}$, which contains the parameters of Eq. (7) or Eq. (9), is formally given by

$$\frac{\partial\mathcal{L}}{\partial\underline{a}} = \frac{\partial\mathcal{L}}{\partial E^0}\frac{\partial E^0}{\partial\underline{a}}. \tag{28}$$

The gradient $\frac{\partial E^0}{\partial\underline{a}}$ is determined analytically using Eq. (7) or Eq. (9). In order to recover the true initial condition whose only observation y is available about the associated decay, we employ the following iterative optimization procedure to minimize $\mathcal{L}$:

1. Start with a first guess for the set of parameters $\underline{a}$ and compute the corresponding initial energy spectrum (i.e., the estimated initial energy spectrum) with Eq. (7) or Eq. (9).

2. At the ith iteration, solve the forward EDQNM problem defined by Eq. (21) from $t = 0$ to $t = T_f$.
3. Solve backward from $t = T_f$ to $t = 0$ the adjoint problem defined in (22) with the spectrum E calculated at the previous step. The adjoint spectrum at $t = 0$ gives the gradient of $\mathcal{L}$ with respect to the initial energy spectrum according to Eq. (23).
4. Compute the gradient of $\mathcal{L}$ with respect to the set of parameters of Eq. (7) or Eq. (9) thanks to Eq. (28). This allows for the determination of a descent direction $\underline{d}^{(i)}$. We choose the quasi-Newton Broyden-Fletcher-Goldfarb-Shanno (BFGS) method[31] to compute $\underline{d}^{(i)}$. Accordingly, the set of parameters is updated in the following way:

$$\underline{a}^{(i+1)} = \underline{a}^{(i)} + \gamma^{(i)}\underline{d}^{(i)}, \tag{29}$$

   where $\gamma^{(i)}$ is the step length which is determined by the use of bicomplex numbers. The use of bicomplex numbers with the BFGS method is detailed in the Appendix A.
5. Return to step 2 until convergence.

C. Types of observations

In this paper, we consider several types of observations of the true decay, which are denoted by y in the expression of the cost function given by (11). A first possibility is to observe the energy spectrum itself at different times during the decay. In this way, we get *a priori* as much information as possible about the decay. However, the complete energy spectrum is rarely accessible experimentally. So we also consider the observations of statistical integral quantities with physical meaning such as the kinetic energy $\mathcal{K}$, the integral scale L, and the dissipation rate ε, which are more easily measured in grid turbulence experiments. These quantities are defined as

$$\mathcal{K} = \int_0^\infty E(k)dk \;\; ; \;\; L = \frac{3\pi}{4}\frac{1}{\mathcal{K}}\int_0^\infty \frac{E(k)}{k}dk \;\; ; \;\; \varepsilon = \int_0^\infty 2\nu k^2 E(k)dk. \tag{30}$$

The issue of deriving exact values for these integral quantities from truncated solutions/measurements is not addressed in the present study (see Ref. 36), since the EDQNM approach enables a very good spectral resolution (9 decades in the present work).

In Sec. V C 4, we also use the observation of the power-law exponent $n_{\mathcal{K}}$ driving the decay of $\mathcal{K}$ according to the following relation:

$$\mathcal{K}(t) \sim t^{n_{\mathcal{K}}}. \tag{31}$$

Using the evolution equation of $\mathcal{K}$ in the case of freely decaying HIT

$$\frac{\partial \mathcal{K}}{\partial t} = -\varepsilon, \tag{32}$$

we deduce the following expression for $n_{\mathcal{K}}$:

$$n_{\mathcal{K}} = -\left(\frac{\partial}{\partial t}\left(\frac{\mathcal{K}}{\varepsilon}\right)\right)^{-1} = \left(1 + \frac{\mathcal{K}}{\varepsilon^2}\frac{\partial \varepsilon}{\partial t}\right)^{-1}. \tag{33}$$

Starting from the Lin equation, the exact expression of $\frac{\partial \varepsilon}{\partial t}$ in freely decaying isotropic turbulence is given by

$$\frac{\partial \varepsilon}{\partial t} = -\int_0^\infty 4\nu^2 k^4 E(k)dk + \int_0^\infty 2\nu k^2 T(E,k)dk, \tag{34}$$

where we use Eq. (2) for the transfer term $T(E, k)$. We do not expect the optimization procedure presented in Sec. IV B to recover all the features of the true initial energy spectrum when observing these statistical quantities. For example, we may reasonably suppose that it will be difficult to recover details of the shape of the initial spectrum in the dissipative range when observing the kinetic energy $\mathcal{K}$ since decay of turbulent kinetic energy is expected to be mainly driven by large scales. In contrast, we expect the optimization procedure to be very sensitive to large scales, whatever the type of observations. Indeed, the temporal evolutions of $\mathcal{K}$, L, and ε are expected to follow power laws, as

TABLE I. Analytical formulae for the prediction of the power-law exponents driving the decay of the flow statistical quantities, in the case of isotropic turbulence. The high Re_λ formulae are proposed by Comte-Bellot and Corrsin[37] and revisited by Meldi and Sagaut,[22] while the low Re_λ formulae are elaborated by Clark and Zemach.[20]

	$n_{\mathcal{K}}$	n_ε	n_L
High Re_λ	$-2\dfrac{\sigma-q+1}{\sigma-q+3}$	$-\dfrac{3(\sigma-q)+5}{\sigma-q+3}$	$\dfrac{2}{\sigma-q+3}$
Low Re_λ	$-\dfrac{\sigma+1}{2}$	$-\dfrac{\sigma+3}{2}$	$\dfrac{1}{2}$

the one given by (31), whose the theoretically predicted exponents are summarized in Table I. These exponents depend on the slope at large scales σ and on the coefficient q, which is a measure of the intensity of the non-local triadic interactions in the back-scatter energy transfer. The coefficient value is $q = 0$ for $\sigma = 1, 2, 3$ and $q \approx 0.52 - 0.55$ for $\sigma = 4$, see Ref. 22. In the formulae of Table I, it is implicitly assumed that large scales are described by a unique slope σ. The optimization procedure will allow to determine if the largest scales and the large scales close to the peak of the energy spectrum play a similar role in the decay or not. It is worth keeping in mind that the results of the data assimilation experiments of this paper are relative to the chosen types of observations. In particular, it would be possible to consider scalar quantities of the form $D = \int_0^\infty E(k)k^{-n}dk$ with $n \gg 1$, which give more weight to the largest scales than $\mathcal{K}$, L, and ε. However, we focused on the latter quantities in the present work, since they have a clear physical meaning.

We consider three ways of distributing observations in time. For the first one, the size of the assimilation window, i.e., the final time considered for the decay, is fixed at $T_f = 10^4\tau_0$, where τ_0 is the initial eddy turn-over time defined by $L(0)/\mathcal{K}(0)^{1/2}$. An observation of the true decay is performed every $10^3\tau_0$ from $t = 10^3\tau_0$ to $t = T_f = 10^4\tau_0$. Starting the observations from $t = 10^3\tau_0$ ensures that we witness a fully developed isotropic turbulence, and avoids the transient regime reported in EDQNM simulations.[2,7] This transient regime is related to the approximation represented by the use of a functional form which is not an exact solution of the EDQNM model to describe the initial energy spectrum. Accordingly, the expressions of the observation operator and of the inner product between two elements a and b in observation space, for example, in the case where the dissipation rate is observed, are

$$H(E,t) = \varepsilon(E,t) = \int_0^\infty 2\nu k^2 E(k,t)dk; \quad \langle a,b\rangle_{\mathcal{O}} = \int_0^{T_f} \sum_{n=1}^{10} \delta(t - n10^3\tau_0)a(t)b(t)dt. \tag{35}$$

The adjoint of the gradient of H as defined by Eq. (35) is

$$\tilde{H}|_E(y,k,t) = 2\nu k^2 \sum_{n=1}^{10} \delta(t - n10^3\tau_0)y(t). \tag{36}$$

Expressions similar to Eq. (36) are easily derived for the other types of scalar observations. However, we notice that $\tilde{H}|_E$ as defined by Eq. (36) does not depend on the spectrum E, since ε is a linear operator on the model space. This would not be the case if the integral scale L or the exponent $n_{\mathcal{K}}$ were observed. In the case where the energy spectrum is observed, i.e., $H(E, k, t) = E(k, t)$, the expression of the inner product in observation space and that of the adjoint of the gradient of H are

$$\langle a,b\rangle_{\mathcal{O}} = \int_0^{T_f} \sum_{n=1}^{10} \delta(t - n10^3\tau_0) \int_0^\infty a(k,t)b(k,t)dkdt; \quad \tilde{H}|_E(y,k,t) = \sum_{n=1}^{10} \delta(t - n10^3\tau_0)y(k,t). \tag{37}$$

Concerning the two other ways of distributing observations in time, they correspond to the two assimilation window sizes $T_f = 10^3\tau_0$ and $T_f = 10^4\tau_0$, with only a single observation of the true decay performed at $t = T_f$. In these two cases, the expressions of $\langle\cdot,\cdot\rangle_{\mathcal{O}}$ and $\tilde{H}|_E$ are deduced from Eqs. (35) to (37) by replacing $\sum_{n=1}^{10} \delta(t - n10^3\tau_0)$ with $\delta(t - T_f)$.

Since the statistical quantities defined by (30) evolve in time according to power-laws, the error $(y - H(E))$ might be several orders of magnitude larger or less at $t = 10^3\tau_0$ than at $t = T_f = 10^4\tau_0$. Large differences in the order of magnitude among the terms in the cost function defined in (11) may also be encountered when observing simultaneously several statistical quantities. Consequently, we define a slightly different cost function which involves relative errors instead of absolute errors. In this way, all terms in the sum are significant, even if we expect an amplification in time of the value of relative errors. The use of such cost function instead of that defined by Eq. (11) does not change the derivation in Sec. IV A, except for the expression of the adjoint forcing $\tilde{f}$ in (22). The expression of this new cost function and that of the corresponding adjoint forcing term are

$$J(E) = \frac{1}{2}\left\|\frac{y - H(E)}{y}\right\|_{\mathcal{O}}^2 \quad ; \quad \tilde{f}(E, y) = \tilde{H}|_E\left(\frac{y - H(E)}{y^2}\right). \tag{38}$$

The cost function defined by Eq. (38) is used when the kinetic energy $\mathcal{K}$, the integral scale L, the dissipation rate ε, or a combination of these are observed. When the exponent $n_{\mathcal{K}}$ is observed, the cost function defined by Eq. (11) may be used without modification since the value of $n_{\mathcal{K}}$ is supposed to be constant during the decay. In the case where the energy spectrum is observed, the error is normalized by the kinetic energy related to the true spectrum. The expression of the cost function and that of the adjoint forcing term are in this case

$$J(E) = \frac{1}{2}\left\|\frac{y - H(E)}{(\int_0^\infty y(k)dk)^{\frac{1}{2}}}\right\|_{\mathcal{O}}^2 ; \quad \tilde{f}(E, y) = \tilde{H}|_E\left(\frac{y - H(E)}{\int_0^\infty y(k)dk}\right). \tag{39}$$

V. DATA ASSIMILATION RESULTS

A. Setup of the data assimilation experiments

The principle of the data assimilation experiments presented in this paper is the following. After choosing the characteristics of a true initial energy spectrum and the type of the observations of the associated decay, we employ the optimization procedure described in Sec. IV B in order to recover the true initial energy spectrum, starting from an initial guess (i.e., an estimated initial energy spectrum). The setup of these different numerical data assimilation experiments is described in the present section.

The duration of the EDQNM simulations in this paper is equal or inferior to 10^4 initial eddy turn-over times τ_0. The smallest wavenumber of the mesh k_0 is chosen so that $k_0 = 10^{-5}k_L$, where k_L is the wavenumber associated to the initial position of the integral scale. This choice ensures that there is at least three decades of resolution between k_0 and the position of the integral scale at the end of the simulations. The largest resolved wavenumber k_M is chosen such that a resolution of at least one decade at the small scales, with respect to the initial position of the Kolmogorov scale, is granted. The total number of elements $M + 1$ is recovered so that $k_M = r^M k_0$, where r represents the constant aspect ratio between contiguous elements of the mesh. In the present work, $r = 1.122$, which means that each decade in the spectral space is discretized by 20 mesh elements. The temporal integration is made by a forward Euler scheme, which is self-adjoint, and the Courant-Friedrichs-Lewy (CFL) condition is based on the Kolmogorov scale.[2] The Lagrangian $\mathcal{L}$ defined by Eq. (15) is minimized in the way depicted in Sec. IV B and the Appendix A. The optimization procedure is stopped after achieving a substantial reduction by 6 orders of magnitude in the value of the cost function J in Eq. (11).

In Sec. V B, we consider the set 1 of numerical data assimilation experiments where the functional form defined by (7) is prescribed for the initial energy spectrum. The size of the assimilation window is fixed at $T_f = 10^4\tau_0$ and an observation of the true decay is performed every $10^3\tau_0$ from $t = 10^3\tau_0$ to $t = T_f$. The separation between large and very large scales is determined so that at least one decade between the wavenumber k_{L_1} and the position of the peak of the energy spectrum at the end of the assimilation window is granted. According to Comte-Bellot–Corrsin analysis, the maximum value of the exponent n_L in Table I is 0.5. So the maximum value of the integral scale at the end

TABLE II. Undimensional (if necessary) values of the different parameters of the functional form (7) for the true initial energy spectrum. The separation between large and very large scales is fixed at $k_{L_1}/k_{L_2} = 10^{-3}$.

σ_1	σ_2	β	p	k_{L_2}	α_1	α_2	α_3	α_4	α_5	k_η
2	2	0	1.5	1	4.2	1.8	3	0.2	1	3834

of the assimilation window is $L(t = T_f) \approx (T_f/\tau_0)^{0.5} L(t = 0) = 10^2 L(t = 0) \approx 10^2/k_{L_2}$, which leads to $k_{L_1}/k_{L_2} = 10^{-3}$. The true initial energy spectrum corresponds to a Saffman turbulence at high Reynolds number ($\sigma_1 = \sigma_2 = 2$ in Eq. (7)). The initial value of the Reynolds number based on the Taylor microscale $\lambda = \sqrt{10\mathcal{K}\nu/\varepsilon}$ is chosen so that $Re_\lambda(t = 0) = 800$. At $t = T_f = 10^4\tau_0$, $Re_\lambda \approx 400$, which ensures converged values of the power-law exponents in Table I in the high-Reynolds regime over the entire decay.[7] The estimated initial energy spectrum is obtained by perturbing by $\pm 10\%$ the values of the parameters of Eq. (7) chosen for the true spectrum. The latter are reported in Table II. The runs of the set are differentiated by the use of various types of observations: the energy spectrum $E(k)$, the kinetic energy $\mathcal{K}$, the integral scale L, the dissipation rate ε, $\mathcal{K}$ and L simultaneously, and $\mathcal{K}$, L, and ε simultaneously.

In Sec. V C, the functional form defined by (9) is prescribed for the initial energy spectrum. We consider three types of estimated initial energy spectra. The first one (type A) corresponds to a constant perturbation of -25% of the true value of the slope at large scales. The inertial and the dissipative ranges are, respectively, defined by a constant slope. For the second type of estimated initial energy spectra (type B), a random slope is assigned for the initial energy spectrum each half-decade. The slopes at large scales are uniformly picked between 1 and 4, so the corresponding mean is 2.5. The third type (type C) corresponds to the assignment of a random local slope for each of the energy modes. These three different initial energy spectra are illustrated in Figure 1. For the sets 2-8 of assimilation experiments, the true state represents a Saffman turbulence at high Reynolds number. The cases where the slope of the true initial energy spectrum verifies $\sigma = 1$ (exact self-similar decay) or $\sigma = 4$ (Batchelor turbulence) are investigated in the set 9. The initial value of the Reynolds is adjusted so that $Re_\lambda \approx 400$ at the end of the assimilation window. For the set 2 of assimilation experiments, the estimated initial energy spectrum of type A is employed and the

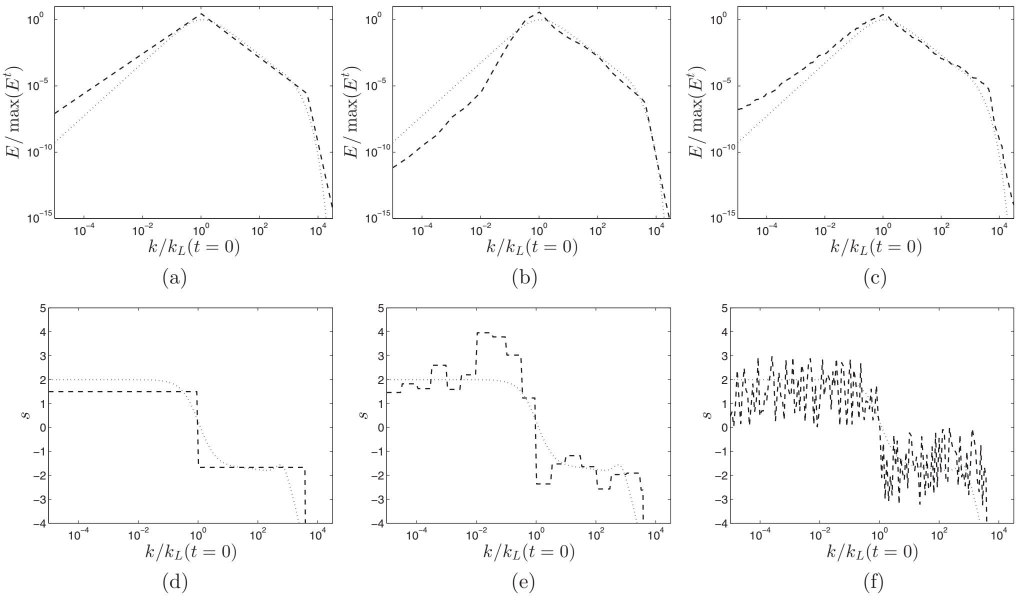

FIG. 1. First row: true (dotted line) and estimated (dashed line) initial spectra for the types A (a), B (b), and C (c). Second row: corresponding local slope in Eq. (9) for the types A (d), B (e), and C (f).

TABLE III. Characteristics of the different sets of numerical data assimilation experiments considered in this paper. N_s is the number of runs in a given set. The column F.F. indicates the functional form used for the different sets. T_f refers to the size of the assimilation window. N_o is the number of observations of the true decay. H refers to the type of the observations. $Re_\lambda(t = 0)$ is the initial Reynolds number based on the Taylor microscale. σ refers to the unique slope at large scales ($E(k \to 0) \sim k^\sigma$) of the true initial energy spectra. The column E.I.C indicates the type of the estimated initial energy spectrum (see Sec. V A and Figure 1).

Set	N_s	F.F.	T_f	N_o	H	$Re_\lambda(t=0)$	σ	E.I.C
1	6	Eq. (7)	$10^4\tau_0$	10	various	800	2	±10%
2	6	Eq. (9)	$10^4\tau_0$	10	various	800	2	A
3	3	Eq. (9)	$10^4\tau_0$	10	$\mathcal{K}$	800	2	A,B,C
4	3	Eq. (9)	$10^4\tau_0$	1	$\mathcal{K}$	800	2	A,B,C
5	3	Eq. (9)	$10^3\tau_0$	1	$\mathcal{K}$	800	2	A,B,C
6	3	Eq. (9)	$10^4\tau_0$	10	$n_\mathcal{K}$	800	2	A,B,C
7	3	Eq. (9)	$10^4\tau_0$	1	$n_\mathcal{K}$	800	2	A,B,C
8	3	Eq. (9)	$10^3\tau_0$	1	$n_\mathcal{K}$	800	2	A,B,C
9	2	Eq. (9)	$10^4\tau_0$	10	$\mathcal{K}$	400, 2000	1, 4	A

different runs of the set correspond to the use of different types of observations. The size of the assimilation window is fixed at $T_f = 10^4\tau_0$ with 10 observations of the true decay between $t = 10^3\tau_0$ and $t = T_f$. The sets 3-5 of assimilation experiments use only the observation of the kinetic energy $\mathcal{K}$, and for each of these sets the three types of initial energy spectra described above are employed. The size of the assimilation window and the frequency of the observations for the set 3 are the same as for the set 2, while only one observation is performed at the end of the assimilation window for the sets 4 and 5 where $T_f = 10^4\tau_0$ and $T_f = 10^3\tau_0$, respectively. Concerning the sets 6-8, the exponent $n_\mathcal{K}$ is observed and the three types of initial energy spectra are employed. These three different sets allow to investigate various window assimilations sizes and frequencies of observations. The kinetic energy is observed for the set 9 of simulations, where the assimilation window is fixed at $T_f = 10^4\tau_0$ with 10 observations of the true decay between $t = 10^3\tau_0$ and $t = T_f$. A summary of the characteristics of the different sets of assimilation experiments is reported in Table III.

For the sake of clarity, the results reported in the figures are sometimes scaled on the initial position of the integral scale $k_L(t = 0)$ or on its final position $k_L(t = T_f)$. We define the $\overline{\cdot}$ operator by

$$\overline{F(k)} = F(k)/\max_p(|F(p)|). \tag{40}$$

The energy spectrum may also be scaled by $\max_k E^t(k)$, where $E^t(k)$ is the true initial energy spectrum. In the tables and figures, the relative error $\epsilon_{a_j}^{(i)}$ on the parameter a_j of the functional form chosen for the initial energy spectrum at the ith iteration of the optimization procedure is defined by

$$\epsilon_{a_j}^{(i)} = \frac{|a_j^t - a_j^{(i)}|}{|a_j^t|}, \tag{41}$$

where a_j^t and $a_j^{(i)}$ are the true value of the parameter a_j and that obtained at the ith iteration of the optimization procedure, respectively. The partial derivatives of the Lagrangian $\mathcal{L}$ with respect to the different parameters a_j are reported in absolute value and are normalized by the norm of the gradient of the Lagrangian with respect to the set of parameters $\underline{a} = (a_1\ a_2\ \ldots)^T$ at the beginning of the optimization procedure (iteration (1)). For the sake of simplicity, we introduce the following notation:

$$\nabla_{a_j}\mathcal{L}^{(i)} = \left|\frac{\partial\mathcal{L}}{\partial a_j}^{(i)}\right| \Big/ \left\|\frac{\partial\mathcal{L}}{\partial \underline{a}}^{(1)}\right\|. \tag{42}$$

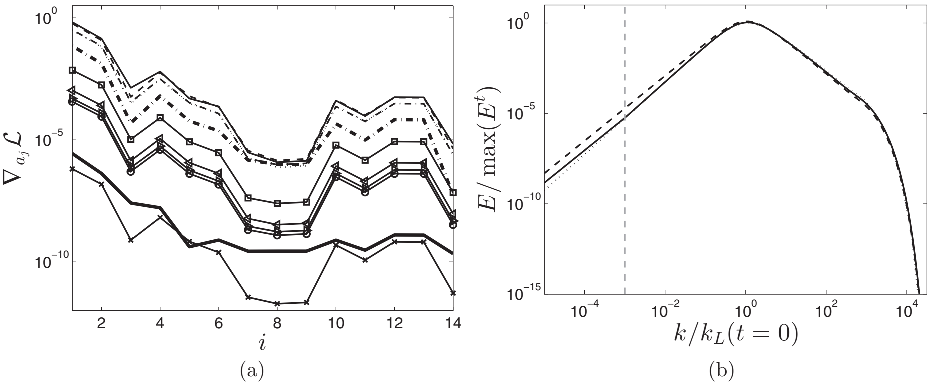

FIG. 2. (a) Derivatives of the Lagrangian $\mathcal{L}$ with respect to the different parameters in (7) (▬▬ σ_1, —— σ_2, - - - - β, - - - - p, ▬ ▬ ▬ k_{L_2}, -▶- α_1, -◀- α_2, -●- α_3, –■– α_4, ········ α_5, and -×- k_η) versus the number of iterations of the optimization procedure for the run of the set 1 (see Table III) where the kinetic energy $\mathcal{K}$ is observed. (b) True (dotted line), estimated (dashed line), and retrieved at the end of the optimization procedure (full line) initial energy spectra. The vertical dashed grey line marks the limit at $k = k_{L_1}$ in Eq. (7) between the largest scales and the large scales close to the peak of the energy spectrum.

B. Assimilation experiments based on the Meyers–Meneveau spectrum model

In this section, we consider the set 1 of numerical data assimilation experiments, in which the functional form defined by Eq. (7) is prescribed for the initial energy spectrum. The corresponding control vector contains 11 parameters. This set is illustrated by Figures 2, 3, 4(a), and 4(c). The true state corresponds to a Saffman turbulence at high Reynolds number, the estimated initial condition is obtained by perturbing by ±10% the true values of the parameters of (7), and various kinds of observations are used to perform the different data assimilation experiments of the set. We first consider the particular run where the kinetic energy $\mathcal{K}$ is observed. Results concerning this run are illustrated by Figure 2. The partial derivatives of the Lagrangian $\mathcal{L}$ defined by Eq. (15) with respect to the different parameters in (7) and their evolutions according to the iterations of the optimization procedure described in Sec. IV B are displayed in Figure 2(a). We notice that the derivative of the Lagrangian at the beginning of the minimization varies widely depending on the parameter considered. The four leading parameters are the slope at large scales close to the peak of the energy spectrum σ_2, k_{L_2}, and α_5, which both govern the initial position of the peak of the initial energy spectrum, and the intermittency correction β. The fact that σ_2 is the leading parameter is not

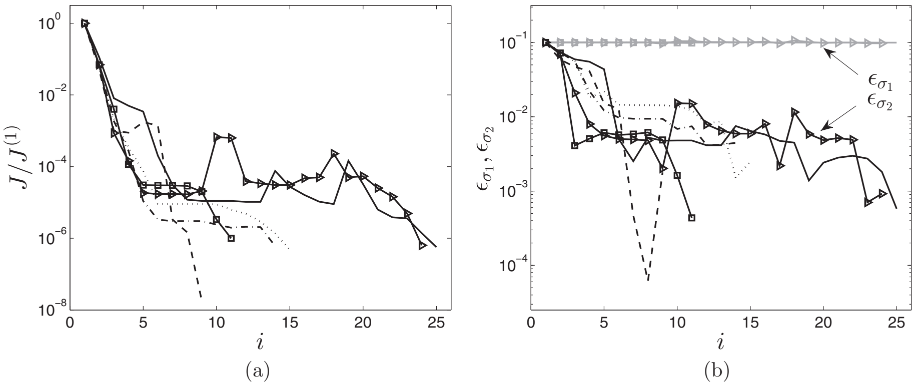

FIG. 3. Results from the different data assimilation experiments of the set 1 (see Table III). (a) Value of the cost function J normalized by its initial value and (b) relative errors on the slope at the largest scales σ_1 (grey lines) and on the slope at the large scales close to the peak of the initial energy spectrum σ_2 (black lines) versus the number of iterations of the optimization procedure. The six types of lines (besides color) correspond to different types of observations: —— $E(k)$, - - - - - - $\mathcal{K}$, - - - - L, ········ ε, –▶– $\mathcal{K}+L$, and –■– $\mathcal{K}+L+\varepsilon$.

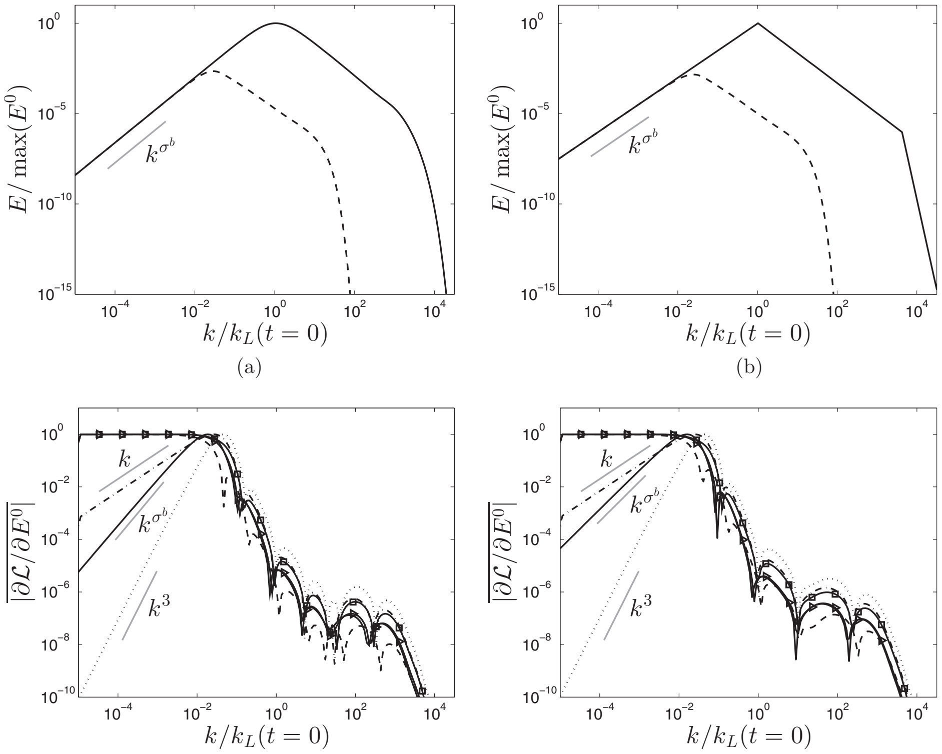

(a) (b)

(c) (d)

FIG. 4. First row: estimated energy spectra at $t = 0$ (full lines) and at $t = T_f = 10^4\tau_0$ (dashed lines) at the first iteration of the optimization procedure. Second row: gradient with respect to the initial energy spectrum E^0 of the Lagrangian $\mathcal{L}$ for different types of observations: —— $E(k)$, -·-· $\mathcal{K}$, - - - - L, ········ ε, -▶- $\mathcal{K} + L$, and -■- $\mathcal{K} + L + \varepsilon$. The first column corresponds to the use of the Meyers-Meneveau functional form defined in Eq. (7) (set 1 of data assimilation experiments, see Table III), while the functional form defined in Eq. (9) is employed for the results of the second column (set 2, see Table III). The predictions of Eqs. (44) and (46) (see the discussion in Sec. V B) are also reported in Figures (c) and (d) (small full grey lines). Notice that for the sets 1 and 2, the slope σ^b of the estimated energy spectrum at large scales is inferior to the slope σ^t of the true spectrum.

surprising when considering the formulae of the power-law exponents driving the decay of the flow statistical quantities reported in Table I. Figure 2(a) also indicates that the shape of the peak of the energy spectrum p plays an intermediate role, in agreement with results obtained in Refs. 19 and 38, and that the influence on the Lagrangian of $\alpha_1 - \alpha_4$, which parametrize the shape of the energy spectrum at small scales, is negligible with respect to the leading parameters. The same applies to the initial position of the Kolmogorov scale k_η. Small scales do not drive the decay and do not carry a significant amount of energy, so their influence is marginal. At the end of the assimilation window $k_L(t = T_F)/k_{L_1} \approx 10^{1.5}$, and it appears that the sensitivity of the Lagrangian with respect to the slope at very large scales σ_1 is also negligible. Contrary to the large scales close to the peak of the energy spectrum, the largest scales do not seem to play a significant role in the decay. This result is in accordance with the findings of Meldi and Sagaut,[22] and indicates that the asymptotic infrared behavior of the energy spectrum does not govern finite time HIT decay.

We now consider the performances of the different data assimilation experiments of set 1 with Figure 3(a), which displays the evolution of the cost function J in Eq. (11) observed when using various observations, i.e., direct observation of the full spectrum $E(k, t)$ or linear combinations of integral quantities (namely, kinetic energy $\mathcal{K}$, dissipation rate ε, and integral lengthscale L). The latter have all achieved a reduction by six orders of magnitude in the value of the cost function, corresponding to a fully converged solution. The reduction in the relative errors, which are defined by Eq. (41), on the slope at the largest scales σ_1 and on the slope at the large scales close to the peak

TABLE IV. Results for the different data assimilation experiments of the set 1 (see Table III) where different types of observations are used for the different runs. The partial derivatives of the Lagrangian $\mathcal{L}$ (defined in Eq. (42)) with respect to the slope at the largest scales σ_1, the slope at large scales close to the peak of the initial energy spectrum σ_2, the intermittency correction β, the shape p of the peak of the initial energy spectrum, and the parameter α_1 for small scales, are reported. The displayed values are those at the beginning, iteration (1), and at the end, iteration (M), of the optimization procedure. The relative errors (defined in Eq. (41)) at the end of the optimization procedure on those same parameters are also reported, starting from 10^{-1} at the beginning of the minimization for all parameters.

	$E(k)$	$\mathcal{K}$	L	ε	$\mathcal{K}+L$	$\mathcal{K}+L+\varepsilon$
$\nabla_{\sigma_1}\mathcal{L}^{(1)}$	1×10^{-6}	3×10^{-6}	7×10^{-4}	8×10^{-10}	2×10^{-4}	1×10^{-4}
$\nabla_{\sigma_2}\mathcal{L}^{(1)}$	7×10^{-1}	7×10^{-1}	8×10^{-1}	6×10^{-1}	7×10^{-1}	7×10^{-1}
$\nabla_{\beta}\ \mathcal{L}^{(1)}$	3×10^{-1}	3×10^{-1}	3×10^{-1}	3×10^{-1}	3×10^{-1}	3×10^{-1}
$\nabla_{p}\ \mathcal{L}^{(1)}$	7×10^{-2}	7×10^{-2}	6×10^{-2}	7×10^{-2}	7×10^{-2}	7×10^{-2}
$\nabla_{\alpha_1}\mathcal{L}^{(1)}$	1×10^{-3}	1×10^{-3}	9×10^{-4}	1×10^{-3}	1×10^{-3}	1×10^{-3}
$\nabla_{\sigma_1}\mathcal{L}^{(M)}$	1×10^{-8}	2×10^{-10}	1×10^{-8}	1×10^{-13}	6×10^{-8}	7×10^{-8}
$\nabla_{\sigma_2}\mathcal{L}^{(M)}$	3×10^{-4}	7×10^{-6}	4×10^{-5}	2×10^{-4}	2×10^{-5}	5×10^{-4}
$\nabla_{\beta}\ \mathcal{L}^{(M)}$	1×10^{-4}	3×10^{-6}	1×10^{-5}	2×10^{-4}	2×10^{-6}	3×10^{-4}
$\nabla_{p}\ \mathcal{L}^{(M)}$	4×10^{-5}	6×10^{-8}	3×10^{-6}	3×10^{-5}	5×10^{-7}	5×10^{-5}
$\nabla_{\alpha_1}\mathcal{L}^{(M)}$	5×10^{-7}	9×10^{-9}	4×10^{-8}	6×10^{-7}	7×10^{-9}	1×10^{-6}
$\epsilon_{\sigma_1}^{(M)}$	1×10^{-1}	1×10^{-1}	1×10^{-1}	1×10^{-1}	1×10^{-1}	1×10^{-1}
$\epsilon_{\sigma_2}^{(M)}$	6×10^{-4}	5×10^{-3}	2×10^{-3}	3×10^{-3}	9×10^{-4}	4×10^{-4}
$\epsilon_{\beta}^{(M)}$	8×10^{-2}	5×10^{-2}	1×10^{-1}	4×10^{-2}	3×10^{-2}	1×10^{-2}
$\epsilon_{p}^{(M)}$	5×10^{-3}	5×10^{-2}	1×10^{-1}	1×10^{-2}	2×10^{-2}	4×10^{-3}
$\epsilon_{\alpha_1}^{(M)}$	1×10^{-1}	1×10^{-1}	1×10^{-1}	1×10^{-1}	1×10^{-1}	1×10^{-1}

of the energy spectrum σ_2 during the optimization procedures are reported in Figure 3(b), in grey and black lines, respectively. Actually, no error reduction is achieved for σ_1, even when quantities which are *a priori* the most sensitive to large scales such as the energy spectrum itself or the integral scale are observed. In contrast, the true value of σ_2 is recovered with a good accuracy in all cases. The value of the relative errors on a few other parameters at the end of the optimization procedures are also reported in Table IV. In all cases, the Lagrangian $\mathcal{L}$ appears to be insensitive to the largest scales (slope σ_1) and to the small scales (parameter α_1), in comparison with the large scales close to the peak of the energy spectrum (slope σ_2). For parameters of secondary importance, as the initial shape of the energy peak p and the intermittency correction β, performances in terms of error reduction are intermediate. Observing the complete energy spectrum or several global quantities simultaneously leads to a better recovery of the true parameters than observing a single global quantity. This is not surprising given that the latter case provides less information than observing the complete spectrum or a combination of integral quantities. Results concerning the observation of the dissipation rate ε are interesting. Indeed, the "instantaneous" sensitivity of ε, i.e., the instantaneous change in $\varepsilon(t)$ resulting from a change in the spectrum $E(k, t)$ in (30), is maximum around the Taylor microscale, which corresponds to the typical scale at which viscous dissipation acts, and is negligible at large and very large scales. However, its temporal evolution is driven by large scales. Observing ε allows to uncouple the "instantaneous" sensitivity and the "dynamical" sensitivity (sensitivity with respect to the features of the initial energy spectrum in the sense of (24)) of the Lagrangian $\mathcal{L}$ with respect to large scales. Concerning the kinetic energy $\mathcal{K}$ and the integral scale L, they are mainly sensitive to large scales both "instantaneously" and "dynamically." Table IV indicates that the gradient (at the beginning of the optimization procedure) of the Lagrangian with respect to the slope at the largest scales σ_1 is much inferior when observing the dissipation rate ε than in the other cases. In contrast, the sensitivity of the Lagrangian with respect to the slope σ_2 is roughly the same for all the types of observations. This result is further evidence that only the large scales close to the peak of the energy spectrum lead the decay. Figure 2(b) reports the true initial energy spectrum, estimated initial spectrum, and initial spectrum obtained at the end of the optimization procedure for the run where the kinetic energy $\mathcal{K}$ is observed. The spectrum obtained at the end of the optimization procedure well coincides with the true spectrum, except at very large and very small scales. This result is similar for all the types of observations.

Figure 4(c) illustrates the gradient of the Lagrangian $\mathcal{L}$ with respect to the different modes of the initial energy spectrum for the different types of observations. These gradients vanish at small scales in roughly the same way, but exhibit different shapes at large scales. The latter may be recovered by considering the expressions of $\mathcal{K}$, L, and ε when taking into account the geometric series distribution of the mesh points in spectral space

$$\mathcal{K} \simeq \sum_i E_i k_i dr; \quad L \simeq \frac{3\pi}{4} \frac{\sum_i E_i dr}{\sum_i E_i k_i dr}; \quad \varepsilon \simeq \sum_i 2\nu E_i k_i^3 dr, \tag{43}$$

where the index i refers to the ith mode and dr is related to the quadrature method used. The gradient of these quantities at large scales is immediately deduced from (43)

$$\frac{\partial \mathcal{K}}{\partial E_i} \propto k_i; \quad \frac{\partial L}{\partial E_i} \propto \text{constant}; \quad \frac{\partial \varepsilon}{\partial E_i} \propto k_i^3. \tag{44}$$

In the case where the observation y of the true state is a scalar, the ith component of the adjoint forcing term in the adjoint problem defined in (22) is given by

$$\tilde{f}_i(E, y, k) \propto (y - H(E)) \frac{\partial H}{\partial E_i}, \tag{45}$$

where the coefficient of proportionality only depends on the normalization of the error $(y - H(E))$ in the cost function J (see Sec. IV C). Therefore, when $\mathcal{K}$, L, or ε is observed, the shape at large scales of the adjoint forcing term is given by (44). When the energy spectrum is observed, it is easy to derive that at large scales

$$\tilde{f}_i(E, y, k) \propto k_i^s; \quad s = \min(\sigma^t, \sigma^b), \tag{46}$$

where σ^t and σ^b are the slope at large scales for the true and estimated initial energy spectra, respectively (we have assumed a constant slope at large scales for the sake of simplicity). Moreover, it can be shown that, in the discrete case, performing an observation at the end of the assimilation window amounts to initialize the backward integration of the adjoint problem defined by Eq. (22) with the adjoint forcing term $\tilde{f}$ at $t = T_f$ (instead of 0 in the continuous case as stated in (22)). The reader may refer to Ref. 31 for the discrete formulation of variational data assimilation. So, at time $t = T_f$ the adjoint spectrum is initialized at large scales with a slope depending on the type of observations in the way depicted by (44) and (46). We now consider Figures 5(a) and 5(b) where are reported the temporal evolution of the energy spectrum during a forward integration and that of the adjoint spectrum during the corresponding backward integration. The kinetic energy $\mathcal{K}$ is observed. For these particular figures, only one measurement is performed at $t = T_f$. In this configuration, the adjoint forcing term in Eq. (22) is zero during the entire backward integration and only adjoint energy transfers and dissipation act. At $t = T_f$, the adjoint spectrum verifies $\tilde{E}(k, T_f) \propto k \ \forall k$, in accordance with Eq. (44) ($\frac{\partial \mathcal{K}}{\partial E_i} \propto k_i$ is actually verified $\forall k_i$). It appears from Figure 5(b) that adjoint energy transfers preserve the adjoint energy at large scales in a similar way as energy transfers for $E(k)$. Thus, only the adjoint forcing term might eventually affect large scales. Figures 5(c) and 5(d) illustrate the temporal evolution of $E(k)$ and $\tilde{E}(k)$ when the adjoint forcing term is not always zero, i.e., when several observations are performed before the end of the assimilation window. Performing observations before $t = T_f$ results in the addition of a term proportional to k to the adjoint spectrum at large scales due to the adjoint forcing during the backward integration. Therefore, the adjoint forcing affects the value of the adjoint spectrum at large scales but not his slope. It is worth noting that the slope at large scales of the gradients of the observation operators in Eq. (44) does not depend either on the characteristics of the true initial energy spectrum or on those of the estimated spectrum. All of this implies that, in the case where the observation of the true decay is a scalar such as $\mathcal{K}$, L, or ε, the gradient of the Lagrangian $\mathcal{L}$ defined in (15) with respect to the initial energy spectrum E^0 has a shape at large scales which depends only on the type of the observations. For example, when the kinetic energy $\mathcal{K}$ is observed, $\frac{\partial \mathcal{L}}{\partial E^0} \propto k$ at large scales whatever the features of the true

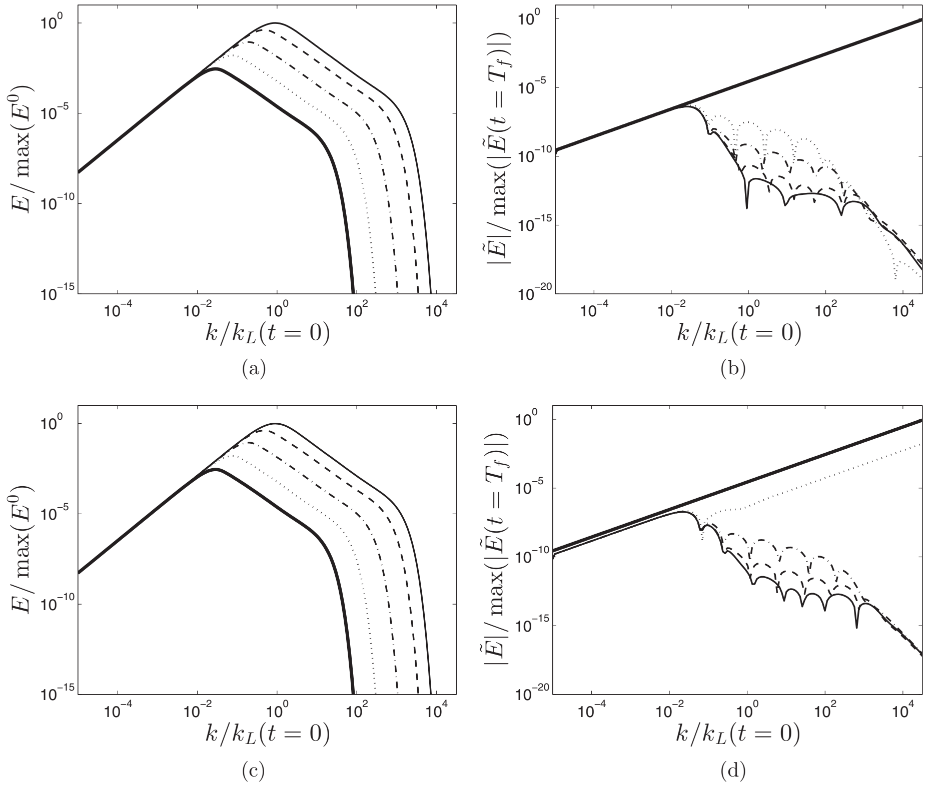

FIG. 5. Temporal evolutions of (a) the energy spectrum E and (b) the adjoint energy spectrum $\tilde{E}$ when the adjoint forcing term $\tilde{f}$ in Eq. (22) is zero during the backward integration (only one observation at the end of the assimilation window); and temporal evolutions of (c) the energy spectrum E and (d) the adjoint energy spectrum $\tilde{E}$ when the adjoint forcing term $\tilde{f}$ is non-identically zero (10 observations between $t = 10^3\tau_0$ and $t = T_f = 10^4\tau_0$). The curves have been sampled at the normalized times: —— $\frac{t}{\tau_0} = 1$; - - - $\frac{t}{\tau_0} = 10$; - · - · $\frac{t}{\tau_0} = 10^2$; ········ $\frac{t}{\tau_0} = 10^3$; ▬ $\frac{t}{\tau_0} = 10^4$. The kinetic energy $\mathcal{K}$ is observed.

energy spectrum, those of the estimated spectrum or the frequency of the observations. This result is subsequently confirmed in Secs. V C 1–V C 5.

Figure 4(c) also indicates that the maximum of the sensitivity of the Lagrangian is reached at the wavenumber k such that $k/k_L(t = 0) \approx 10^{-1.5}$ for the different types of observations, with $k_L(t = 0)$ the initial position of the integral scale. This value roughly coincides with the position of the peak of the energy spectrum at $t = T_f = 10^4\tau_0$, which is reported in Figure 4(a), and the theoretical value of the position of the integral scale at $t = T_f$ predicted by the formulae of Comte-Bellot and Corrsin[37] (see Table I with $\sigma = 2$ and $q = 0$)

$$\frac{k_L(T_f)}{k_L(0)} = \left(\frac{L(T_f)}{L(0)}\right)^{-1} \approx \left(\frac{T_f}{\tau_0}\right)^{-\frac{2}{5}} = 10^{-1.6}. \tag{47}$$

This observation is further discussed in Secs. V C 1–V C 5.

C. Assimilation experiments based on a scale-by-scale description of the energy spectrum

1. Experiments with various types of observations

From now on, we use the functional form defined in Eq. (9) which allows a local, scale-by-scale description of the initial energy spectrum. The control vector is formed by the local slopes associated to the resolved energy modes, and its dimension ranges from 150 to 200. We consider

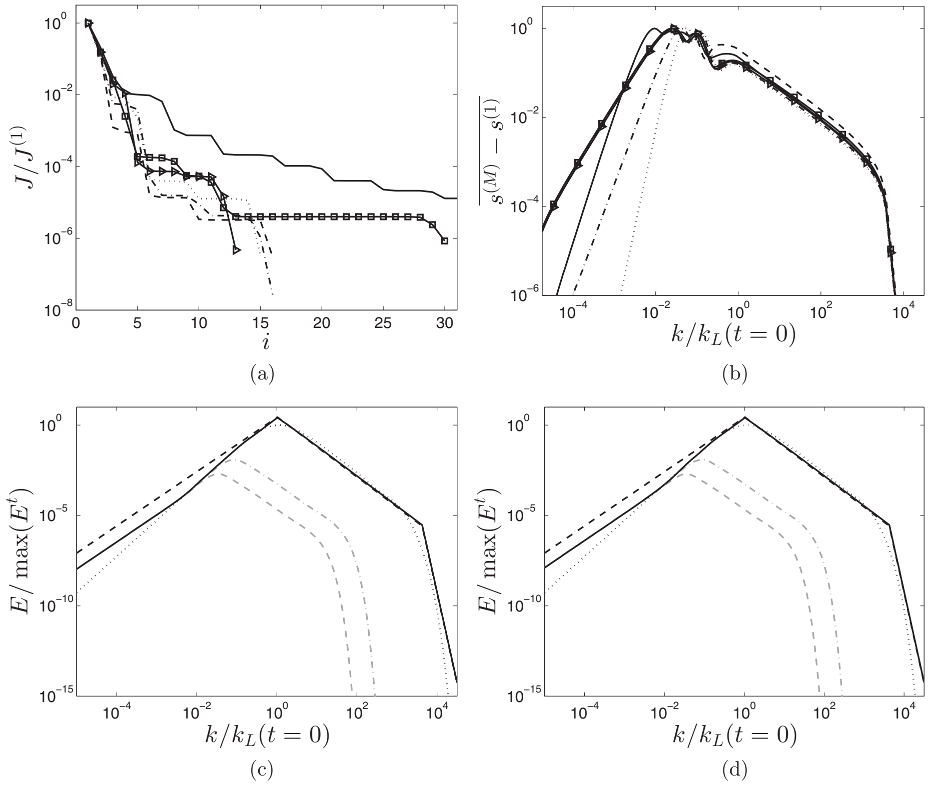

FIG. 6. Results from the different data assimilation experiments of the set 2 (see Table III). First row: (a) Value of the cost function J normalized by its initial value and (b) difference between the local slope of the initial energy spectrum obtained at the end of the optimization procedure (iteration (M)) and that of the spectrum at the first iteration (i.e., the estimated spectrum). The six types of lines correspond to different types of observations: —— $E(k)$, - - - - - - $\mathcal{K}$, - - - L, ········ ε, -▶- $\mathcal{K} + L$, and -■- $\mathcal{K} + L + \varepsilon$. Second row: true (black dotted line), estimated (black dashed line), and retrieved at the end of the optimization procedure (black full line) initial energy spectra when the energy spectrum $E(k)$ (c) and $\mathcal{K}$, L, and ε simultaneously (d) are observed. The energy spectra at $t = 10^3\tau_0$ (dashed-dotted grey lines) and at $t = T_f = 10^4\tau_0$ (dashed grey lines) are also reported in the figures.

the set 2 of numerical data assimilation experiments. The true state considered here without loss of generality is a Saffman turbulence at high Reynolds number, the estimated initial condition is of type A (see Figures 1(a) and 1(d) and Sec. V A), and various kinds of observations are used for the different assimilation experiments of the set. The results are illustrated in Figures 4(b), 4(d), and 6. The evolution of the cost function J during the different minimization procedures is reported in Figure 6(a). Except in the case where the energy spectrum is observed, the optimization procedure has achieved a reduction by 6 orders of magnitude in the value of the cost function in less than 30 iterations. This performance is largely identical to that when the functional form defined by Eq. (7) is used (see Figure 3(a)). So, when global quantities are observed, we do not notice a significant influence of the dimensionality of the control vector on the optimization procedure. Figures 6(c) and 6(d) report the true, estimated, and obtained at the end of the optimization procedure initial energy spectra when the energy spectrum or $\mathcal{K}$, L, and ε simultaneously are observed. In these two cases, we have access to a substantial information about the decay. A striking observation is that the optimization procedure has only recovered the true shape of the initial spectrum at scales located between the initial position of the peak of the energy spectrum and one decade before the position of the peak of the energy spectrum at the end of the assimilation window. This is also visible in Figure 6(b) which reports the difference between the local slope defined in Eq. (9) of the initial energy spectrum at the end and at the beginning of the optimization procedure. For all the runs, the maximum correction is made around the position of the peak of the energy spectrum at the end of the assimilation window. The slight differences among the different types of observations are explained by the fact that, for example, the integral scale is naturally more sensitive to large scales than the dissipation rate. But in all cases, the optimization procedure has not corrected the shape of the estimated initial energy spectrum at the largest scales even though this shape significantly differs from the true one. Furthermore, the shape of the initial energy spectrum at small scales does not appear to be of significant importance. The gradient of the Lagrangian $\mathcal{L}$ with respect to the initial energy spectrum is reported in Figure 4(d) for the different types observations. As in Figure 4(c), the shape at large scales of these gradients is given by relations (44) and (46) and the maximum of the sensitivity of the Lagrangian $\mathcal{L}$ is located around the position of the peak of the energy spectrum at the end of the assimilation window. The use of a different functional form for the initial energy spectrum has no effect on the shape of the gradient of the Lagrangian $\mathcal{L}$ with respect to the initial energy spectrum. These results, which are in line with those of Sec. V B, suggest that the measured quantities in grid turbulence experiments cannot allow to have access to the shape of the energy spectrum at the largest scales, since the latter do not seem to have a significative influence on the decay. The robustness of this finding is tested in Secs. V C 2–V C 5.

2. Experiments with various estimated initial energy spectra

We study the sensitivity of the previous results with respect to the shape of the estimated initial energy spectrum by considering the set 3 of assimilation experiments which is illustrated by Figure 7. The kinetic energy $\mathcal{K}$ is observed and three different estimated initial energy spectra are used for the runs of the set. The three estimated spectra are illustrated in Figure 1. Figure 7(a) indicates that the performances of the optimization procedure are not significatively affected by the characteristics of the estimated spectrum. The true, estimated, and retrieved at the end of the optimization procedure initial energy spectra are reported for each run of the set in Figures 7(d)–7(f). For the three runs, the optimization procedure recovers the same part of the true initial energy spectrum, which is also visible in Figure 7(b). The maximum correction of the local slope of the estimated energy spectrum is made at the scales close to the peak of the energy spectrum at the end of the assimilation window. The shape of the energy spectrum at small scales and at the large scales bigger than ten times the integral scale at the end of the assimilation window seems to have no impact on the value of the kinetic energy $\mathcal{K}$ during the considered decays. Figure 7(c) reports the gradient of the Lagrangian $\mathcal{L}$ with respect to the initial energy spectrum for the three runs of the set. In all cases, this gradient verifies $\frac{\partial \mathcal{L}}{\partial E^0} \propto k$ at large scales and the maximum of sensitivity is located at scales corresponding to the position of the peak of the energy spectrum at the end of the assimilation window. The results of the optimization procedure do not seem to depend on the choice of the estimated initial energy spectrum.

3. Experiments with various assimilation window sizes

In Secs. V B, V C 1, and V C 2, it was found that the maximum sensitivity of the Lagrangian $\mathcal{L}$ defined in (15) is located at the scales corresponding to the peak of the energy spectrum at the end of the assimilation window, which was fixed at $T_f = 10^4\tau_0$ with ten observations of the true decay between $t = 10^3\tau_0$ and $t = T_f$. In order to check the robustness of this result, we first consider the set 4 of assimilation experiments where only one observation of the true decay is performed at $t = T_f = 10^4\tau_0$. The three different types of estimated initial energy spectra illustrated in Figure 1 are used for the different runs of the set. The results are reported in Figures 8(a) and 8(c). The comparison between Figures 8(c) and 7(c) indicates that the frequency of the observations has no influence on the position of the maximum sensitivity of the Lagrangian $\mathcal{L}$. When only one observation of the true decay is performed, the optimization procedure reduces the value of the cost function J by 6 orders of magnitude in less than 5 iterations for all the runs of the set. By comparing Figures 8(a) and 7(b), it appears that the extent of the corrected part of the estimated initial energy spectrum does not significantly depend on the frequency of the observations. We now consider the set 5 where only one observation of the true decay is performed at the end of the assimilation window whose size is $T_f = 10^3\tau_0$. The results for this set are illustrated in Figures 8(b) and 8(d). In both Figures 8(a) and 8(b), the maximum correction is made around the final position of the integral scale. Besides, it

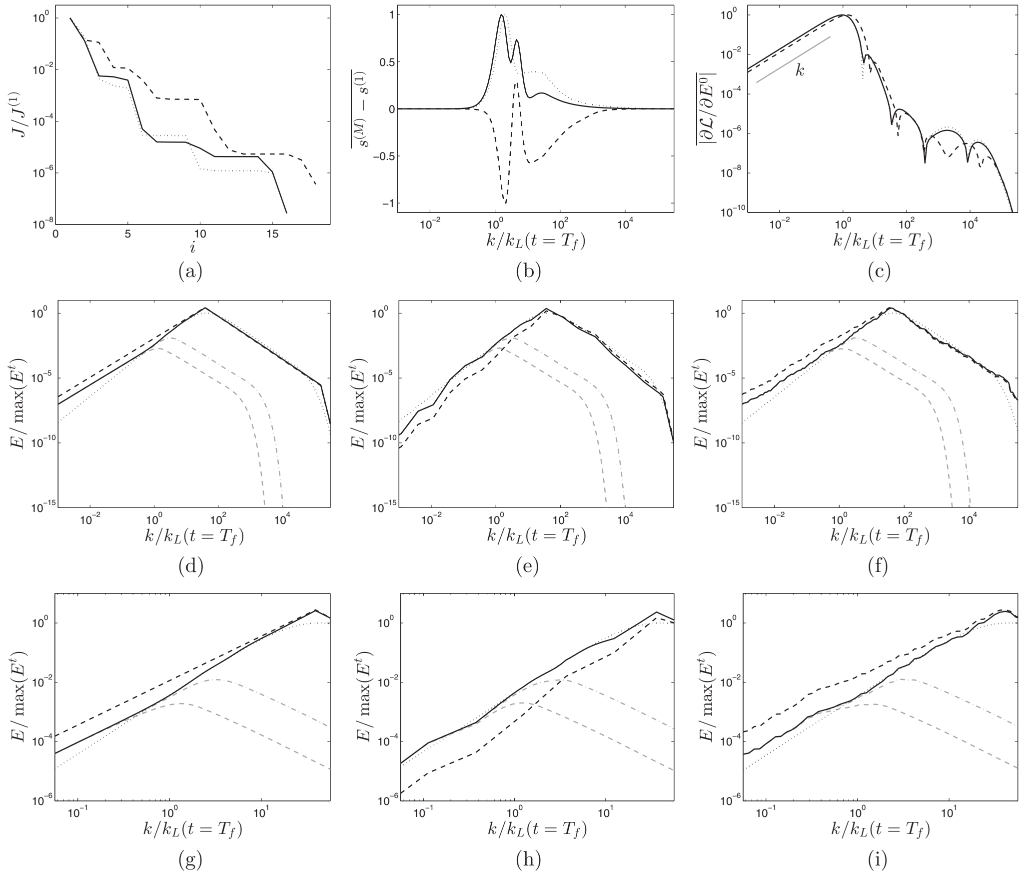

(a) (b) (c)

(d) (e) (f)

(g) (h) (i)

FIG. 7. Results from the different data assimilation experiments of the set 3 (the kinetic energy $\mathcal{K}$ is observed, see Table III). First row: (a) Value of the cost function J normalized by its initial value, (b) difference between the local slope of the initial energy spectrum obtained at the end of the optimization procedure (iteration (M)) and that of the spectrum at the first iteration (i.e., the estimated spectrum), and (c) gradient with respect to the initial energy spectrum E^0 of the Lagrangian $\mathcal{L}$ (at the first iteration of the optimization procedure). The three types of lines correspond to different estimated initial spectra: —— type A, - - - type B, ········ type C (see Figure 1). Second row: true (black dotted line), estimated (black dashed line), and retrieved at the end of the optimization procedure (black full line) initial energy spectra when the estimated initial energy spectrum is of type A (d), B (e), and C (f). The energy spectra at $t = 10^3\tau_0$ (dashed-dotted grey lines) and at $t = T_f = 10^4\tau_0$ (dashed grey lines) are also reported in the figures. A zoom of Figures (d)-(f) in the vicinity of the peak of the energy spectrum at $t = T_f$ is reported in Figures (g)-(i).

appears from Figures 8(c) and 8(d) that the maximum of sensitivity of the Lagrangian $\mathcal{L}$ is located around the position of the peak of the energy spectrum at the end of the assimilation window for both $T_f = 10^3\tau_0$ and $T_f = 10^4\tau_0$. This confirms that it is the size of the assimilation window T_f that determines the position of the maximum of sensitivity of the Lagrangian $\mathcal{L}$ at $k \approx k_L(T_f) = 1/L(T_f)$.

4. Observation of the exponent $n_{\mathcal{K}}$

The exponent $n_{\mathcal{K}}$ defined by Eq. (31), which characterizes the decay of the kinetic energy $\mathcal{K}$, is not directly accessible in grid turbulence experiments but is deduced from the measurements of the kinetic energy or other integral quantities. The interest of using the observation of the exponent $n_{\mathcal{K}}$ in the present work is that $n_{\mathcal{K}}$ furnishes a purely dynamical information about the decay that can be easily compared with most experimental results, unlike the observations used in Secs. V B and V C 1–V C 3. We consider the set 6 of assimilation experiments where the exponent $n_{\mathcal{K}}$ is observed, the true state corresponds to a Saffman turbulence at high Reynolds number, the different estimated initial energy spectra of Figure 1 are used for the different runs of the set and the size of

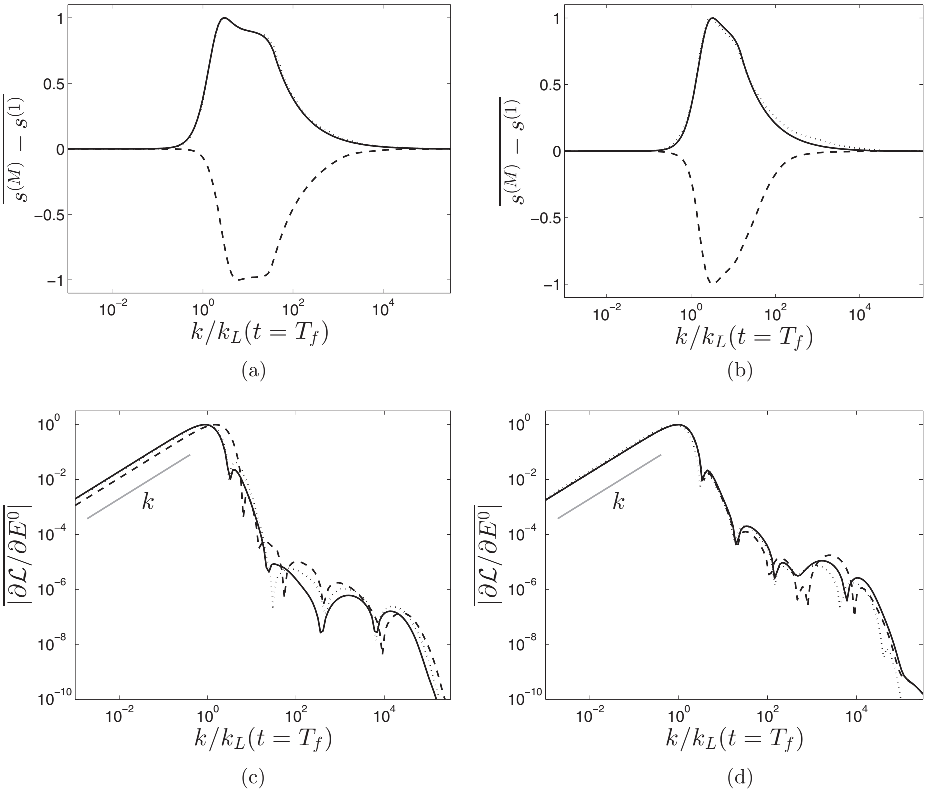

(a) (b)

(c) (d)

FIG. 8. Results from the different data assimilation experiments of the sets 4 and 5 (the kinetic energy $\mathcal{K}$ is observed, see Table III). First row: difference between the local slope of the initial energy spectrum obtained at the end of the optimization procedure (iteration (M)) and that of the spectrum at the first iteration (i.e., the estimated spectrum). Second row: gradient with respect to the initial energy spectrum E^0 of the Lagrangian $\mathcal{L}$ (at the first iteration of the optimization procedure). The first column corresponds to the window assimilation size $T_f = 10^4\tau_0$ (set 4) and the second column to $T_f = 10^3\tau_0$ (set 5). The three types of lines correspond to different estimated initial spectra: —— type A, - - - - type B, ········ type C (see Figure 1).

the assimilation window is fixed at $T_f = 10^4\tau_0$ with 10 observations of the true decay between $t = 10^3\tau_0$ and $t = T_f$. Results are reported in Figure 9 and are quite similar to those illustrated in Figure 7 where the kinetic energy $\mathcal{K}$ is observed. In particular, the maximum sensitivity of the Lagrangian $\mathcal{L}$ is still located at the scales corresponding to the position of the integral scale at the end of the assimilation window. It appears that the gradient of the Lagrangian with respect to the initial energy spectrum verifies $\frac{\partial\mathcal{L}}{\partial E^0} \propto k$ at large scales as in the case where the kinetic energy is observed. This result may be recovered by considering the expression of the Gâteaux derivative of $n_{\mathcal{K}}$ using relation (33) at the spectrum E in the direction F

$$\frac{\partial n_{\mathcal{K}}}{\partial E}\Big|_E(F) = -\frac{n_{\mathcal{K}}(E)^2}{\varepsilon(E)^2}\left[\left(\mathcal{K}(F) - 2\mathcal{K}(E)\frac{\varepsilon(F)}{\varepsilon(E)}\right)\frac{\partial\varepsilon}{\partial t}(E) + \mathcal{K}(E)\frac{\partial}{\partial E}\left(\frac{\partial\varepsilon}{\partial t}\right)\Big|_E(F)\right], \tag{48}$$

where the expression of the Gâteaux derivative of the operator $\frac{\partial\varepsilon}{\partial t}$ defined in (34) is given by

$$\frac{\partial}{\partial E}\left(\frac{\partial\varepsilon}{\partial t}\right)\Big|_E(F) = -\int_0^\infty 4\nu^2k^4F(k)dk + \int_0^\infty 2\nu k^2\frac{\partial T}{\partial E}\Big|_E(F,k)dk. \tag{49}$$

The expression of $\frac{\partial T}{\partial E}|_E(F,k)$ is given for the EDQNM model in Eqs. (25) and (26). When taking into account the geometric series distribution of the mesh points in spectral space, the gradient of $n_{\mathcal{K}}$ with respect to the ith energy mode at large scales ($k_i \to 0$) is then

$$\frac{\partial n_{\mathcal{K}}}{\partial E_i} \simeq -\frac{n_{\mathcal{K}}^2}{\varepsilon^2}\frac{\partial\varepsilon}{\partial t}k_i dr. \tag{50}$$

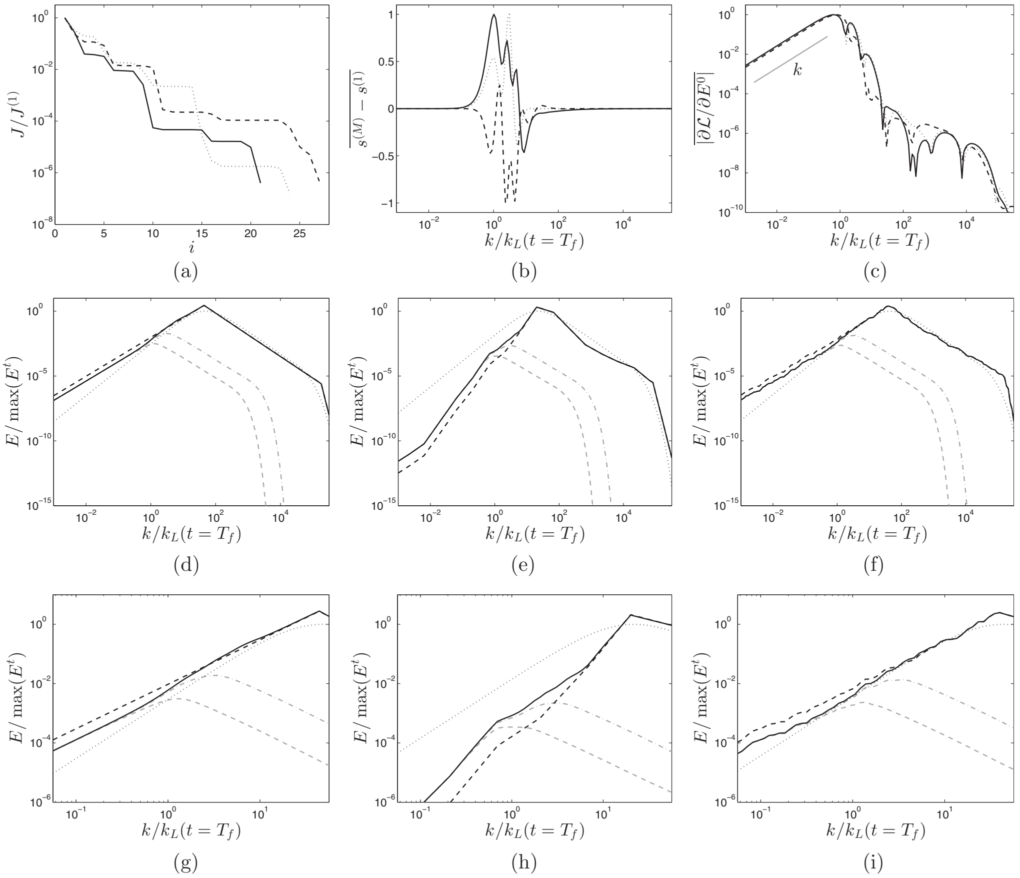

(a) (b) (c)

(d) (e) (f)

(g) (h) (i)

FIG. 9. Results from the different data assimilation experiments of the set 6 (the exponent $n_{\mathcal{K}}$ is observed, see Table III). First row: (a) Value of the cost function J normalized by its initial value, (b) difference between the local slope of the initial energy spectrum obtained at the end of the optimization procedure (iteration (M)) and that of the spectrum at the first iteration (i.e., the estimated spectrum), and (c) gradient with respect to the initial energy spectrum E^0 of the Lagrangian $\mathcal{L}$ (at the first iteration of the optimization procedure). The three types of lines correspond to different estimated initial spectra: —— type A, - - - type B, ········ type C (see Figure 1). Second row: true (black dotted line), estimated (black dashed line), and retrieved at the end of the optimization procedure (black full line) initial energy spectra when the estimated initial energy spectrum is of type A (d), B (e), and C (f). The energy spectra at $t = 10^3\tau_0$ (dashed-dotted grey lines) and at $t = T_f = 10^4\tau_0$ (dashed grey lines) are also reported in the figures. A zoom of Figures (d)-(f) in the vicinity of the peak of the energy spectrum at $t = T_f$ is reported in Figures (g)-(i).

We emphasize the fact that $\frac{\partial n_{\mathcal{K}}}{\partial E_i} \propto k_i$ at large scales is independent of the features of the considered energy spectrum. By a similar reasoning as in Sec. V B, we can deduce that the gradient of the Lagrangian $\mathcal{L}$ with respect to the initial energy spectrum has the same slope at large scales as in Eq. (50). So, whatever the characteristics of the true initial spectrum, those of the estimated spectrum, or the frequency of the observations, the sensitivity of the Lagrangian $\mathcal{L}$ defined in (15) vanishes like k as $k \to 0$ when the exponent $n_{\mathcal{K}}$ is observed. This confirms that only the energetic large scales close to the peak of the energy spectrum have a significant influence on the intensity of the decay measured by the exponent $n_{\mathcal{K}}$. This also confirms that the slope σ in the formulae of Table I refers only to the slope of the spectrum at the large scales close to the peak of the spectrum. It is interesting to compare the ways in which the optimization procedure has corrected the shape of the estimated initial energy spectrum in the cases where the kinetic energy $\mathcal{K}$ or the exponent $n_{\mathcal{K}}$ are observed. For example, we can compare Figures 7(e) and 7(h) with Figures 9(e) and 9(h). When the kinetic energy is observed, the true and retrieved at the end of the optimization procedure initial energy spectra well coincide at the large scales close to the peak of the spectrum at $t = T_f$, while only the slope of the estimated spectrum has been corrected in the same area when $n_{\mathcal{K}}$ is observed. This is consistent

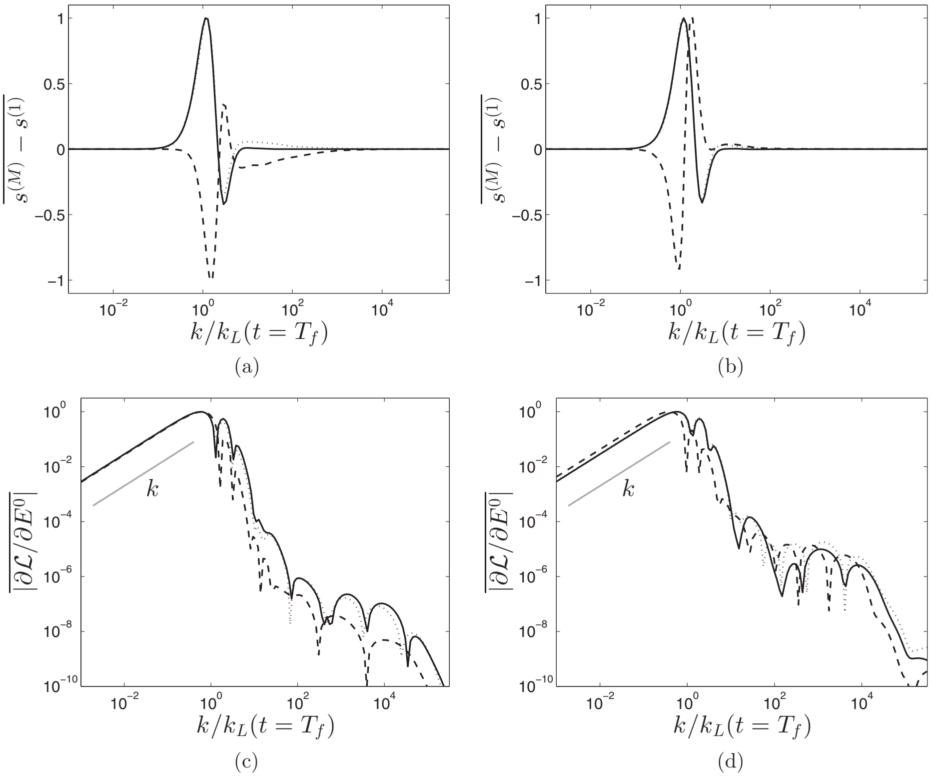

(a)

(b)

(c)

(d)

FIG. 10. Results from the different data assimilation experiments of the sets 7 and 8 (the exponent $n_{\mathcal{K}}$ is observed, see Table III). First row: difference between the local slope of the initial energy spectrum obtained at the end of the optimization procedure (iteration (M)) and that of the spectrum at the first iteration (i.e., the estimated spectrum). Second row: gradient with respect to the initial energy spectrum E^0 of the Lagrangian $\mathcal{L}$ (at the first iteration of the optimization procedure). The first column corresponds to the window assimilation size $T_f = 10^4\tau_0$ (set 7) and the second column to $T_f = 10^3\tau_0$ (set 8). The three types of lines correspond to different estimated initial spectra: ——— type A, - - - - type B, ········ type C (see Figure 1).

with the fact that observing the decay exponent only, one has no control of the absolute value of the kinetic energy. It also shows that, if the kinetic energy is high enough to sustain high-Reynolds number evolution without transition to low-Reynolds number regime (which exhibits different decay exponent values), only the shape of large scale energy spectrum matters.

Figures 10(a), 10(c), 10(b), and 10(d) report the results for the sets 7 and 8 of assimilation experiments, respectively. For these two sets, only one observation of the true decay is performed at the end of the assimilation window, the sizes of the assimilation window $T_f = 10^3\tau_0$ and $T_f = 10^4\tau_0$ are considered. Concerning the sensitivity of the Lagrangian with respect to the initial energy spectrum, the comparison between Figures 9 and 10 do not suggest a dependence of the results with respect to the size of the assimilation window or the frequency of the observations. It appears from Figures 10(a) and 10(b) that the value of the exponent $n_{\mathcal{K}}$ at a given time seems determined by a narrow area of the energy spectrum. The initial shape of the peak of the spectrum, that in the inertial and dissipative ranges, and the large scales ten times bigger than the integral scale seem to have no significative influence on the value of $n_{\mathcal{K}}$.

5. Experiments with various true initial energy spectra

In Secs. V B and V C 1–V C 4, the true initial energy spectrum corresponds to a Saffman turbulence (constant slope $\sigma = 2$ at large scales) at high Reynolds number. We investigate the robustness of the previous results with respect to the shape of the true initial energy spectrum by considering the set 9 of assimilation experiments. The kinetic energy $\mathcal{K}$ is observed, and 10 observations of the true decay are performed between $t = 10^3\tau_0$ and the end of the assimilation

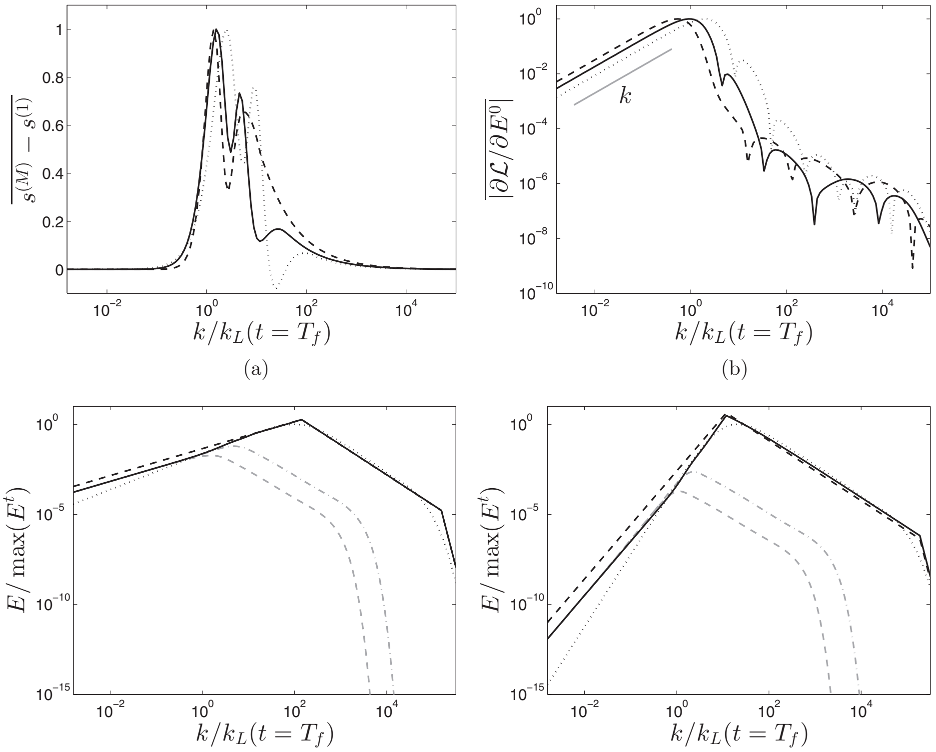

(c) (d)

FIG. 11. Results from the different data assimilation experiments of the set 9 (the kinetic energy $\mathcal{K}$ is observed, see Table III). First row: (a) difference between the local slope of the initial energy spectrum obtained at the end of the optimization procedure (iteration (M)) and that of the spectrum at the first iteration (i.e., the estimated spectrum), and (b) gradient with respect to the initial energy spectrum E^0 of the Lagrangian $\mathcal{L}$ (at the first iteration of the optimization procedure). The three types of lines correspond to different true initial spectra with a constant slope σ at large scales: ········ $\sigma = 1$, —— $\sigma = 2$, - - - $\sigma = 4$. Second row: true (black dotted line), estimated (black dashed line), and retrieved at the end of the optimization procedure (black full line) initial energy spectra when the true initial energy spectrum verifies $\sigma = 1$ (c) and $\sigma = 4$ (d). The energy spectra at $t = 10^3\tau_0$ (dashed-dotted grey lines) and at $t = T_f = 10^4\tau_0$ (dashed grey lines) are also reported in the figures.

window $t = T_f = 10^4\tau_0$. Two true initial energy spectrum are considered: the first one with a constant slope $\sigma = 1$ at large scales (exact self-similar decay), and the second one with $\sigma = 4$ which corresponds to Batchelor turbulence. The initial Reynolds number is adjusted so that $Re_\lambda \approx 400$ at $t = T_f$. The estimated initial spectra are of type A (see Figures 1(a) and 1(d)). The results are illustrated in Figure 11. To ease the comparison with previous findings, results concerning Saffman turbulence (specifically, the results concerning the run of the set 3 where the estimated initial spectrum is of type A) are also reported in Figures 11(a) and 11(b). It appears from Figure 11(b) that the gradient of the Lagrangian $\mathcal{L}$ in Eq. (15) with respect to the initial energy spectrum verifies $\frac{\partial \mathcal{L}}{\partial E^0} \propto k$ at large scales whatever the shape of the true initial energy spectrum as predicted in Sec. V B. The maximum of sensitivity of the Lagrangian is located at the scales close to the integral scale at the end of the assimilation window in all cases. The analysis of Figures 11(a), 11(c), and 11(d) indicates that, as in the case of Saffman turbulence, the shape of the spectrum at the largest scales does not affect the value of the kinetic energy during the considered decays. The fact that the permanence of large eddies ($E(k, t) = E(k, 0)$, $k/k_L(t) \ll 1$) holds true (i.e., when the slope at large scales σ verifies $1 \leq \sigma \leq 3$) or not does not seem to have an influence on the results. For the sake of brevity, the studies of the influences on the results of the shape of the estimated initial energy spectrum, the frequency of the observations and the size of the assimilation window when the true energy spectrum has a constant slope $\sigma = 1$ or $\sigma = 4$ at large scales are not exposed, since the conclusions are exactly the same than for Saffman turbulence. We have also checked that the results of Sec. V C 4 are valid whatever the shape of the true initial energy spectrum as predicted. In particular, it has been verified that the gradient of the Lagrangian $\mathcal{L}$ with respect to the initial energy spectrum verifies $\frac{\partial \mathcal{L}}{\partial E^0} \propto k$ at large scales when the exponent $n_{\mathcal{K}}$ is observed, irrespective of the characteristics of the true initial energy spectrum.

VI. CONCLUDING REMARKS

The present paper was devoted to the analysis of decaying HIT, with the purpose of identifying scales and related features that govern the decay regime. To this end, a Data Assimilation based approach was used, that relies on a variational approach for the optimal control of the shape of the initial energy spectrum. Following this approach, the elements on which the sensitivity of the Data Assimilation method is maximal are interpreted as the scales that govern turbulence decay.

The present results show that HIT decay is governed by scales ranging from the initial location of the peak of the energy spectrum (or the integral scale) to the final location of this peak. A significant sensitivity is observed for scales larger than up to one decade the final integral scales. Scales smaller than the integral scales play a negligible role. This can be understood by reminding that the dissipation amplitude, which mainly occurs at small scales, is modulated by the amount of energy transferred at small scales from the large ones by the nonlinear kinetic energy cascade process. The fact that the energy cascade amplitude is governed by large scales close to the peak of the energy spectrum can be understood looking at the expression of the nonlinear transfer term. Using asymptotic analysis, Brasseur and Wei[39] have shown that the rate of change of kinetic energy at a small scale k due to a distant triadic interaction with a large scale p is proportional to $\sqrt{pE(p)}$. Therefore, the amount of kinetic energy available to be dissipated at small scales is mostly driven by large scales such that $\sqrt{pE(p)}$ is maximum, i.e., scales located near the peak of the energy spectrum.

An important point is that this conclusion is robust, since it is observed in all cases considered in the present paper, that mix both full energy spectrum and integral observations and both Meyers-Meneveau parametric spectrum model and local scale by scale initial spectrum model. An open question is the dependency of present results with respect to the spectral closure used to solve the Lin equation, the EDQNM model in the present case. Since only EDQNM has been used in the present work, this question cannot be fully answered. But the accuracy, the robustness, and the versatility of EDQNM for isotropic turbulence has been demonstrated by many authors in a large number of works during the last 40 years, showing that present results can be considered in a positive way. It should also be reminded that it has been demonstrated that EDQNM represents the minimal closure level that is able to handle all features of decaying HIT,[40,41] since it is based on a closure of the evolution equation for the third-order velocity correlations, and therefore it does not assume any arbitrary shape of $T(k)$ or dissipation rate.

Therefore, looking at present results, it is reasonable to state that:

1. HIT decay is not governed by the asymptotic large scale behavior of the energy spectrum, $E(k \to 0, t = 0)$, or the velocity correlation function, $f(r \to \infty, t = 0)$. The decay regime over finite time is governed by large scales ranging approximately from the initial integral scale to the final integral scale, a vanishing sensitivity being observed for large scales located within one decade outside these bounds. The most important feature is the shape of the spectrum in this range. If a slope can be identified, then Comte-Bellot–Corrsin's formula yield an accurate prediction of the decay regime. This is coherent with previous results dealing with evolution of initially non-self-similar energy spectra[21,22] and also with the recent observation that initial spectra with a large flat plateau may lead to anomalous high decay exponents over a finite time.[42] It should also be emphasized that, according to present observations, large scales should be understood as scales slightly larger than $L(t)$ such that $kL(t) = O(1)$, for the range of values taken by $L(t)$ during the finite time evolution under consideration. How large are these scales can be illustrated considering the classical evolution law

$$L(t) = L_0 \left(1 + \frac{t}{t_0}\right)^{n_L}, \tag{51}$$

where L_0 and $t_0 = \mathcal{K}(t = 0)/\varepsilon(t = 0)$ denote the initial value of the integral scale and the characteristic turbulent time scale, respectively. The time needed to reach a given value of the ratio $\zeta = L(t)/L_0$ is

$$t \simeq t_0 \zeta^{1/n_L}. \tag{52}$$

We now consider the same example as Clark and Zemach,[20] i.e., a wind tunnel with mean bulk velocity $U = 20$ m s^{-1} generating an isotropic turbulence with a kinetic energy equal to one-tenth of the mean velocity kinetic energy, i.e., $\mathcal{K}_0 = 20$ m^2 s^{-2}, with a mesh of 1 cm generating an initial peak in the energy spectrum at wave number $k_0 = 100$ m^{-1}. Considering air at classical atmospheric conditions, one has $\nu = 1.5 \times 10^{-5}$ m^2 s^{-2} for viscosity. The initial Reynolds numbers are $Re_L = \sqrt{\mathcal{K}_0}/k_0\nu = \mathcal{K}_0^2/\varepsilon_0\nu = 3 \times 10^3$ and $Re_\lambda = \sqrt{20/3}\sqrt{Re_L} \simeq 141$, which is close to values reported in many experiments, corresponding to the lower bound of the range of validity of high-Reynolds Comte-Bellot–Corrsin analysis.[7] The associated values are $\varepsilon_0 = k_0\mathcal{K}_0^{3/2} \simeq 8944$ m^2 s^{-3} and $t_0 = k_0^{-1}\mathcal{K}_0^{-1/2} \simeq 2 \times 10^{-3}$ s. According to Comte-Bellot–Corrsin analysis, one has $0.3 \leq n_L \leq 0.5$, leading to a minimum value of $1/n_L$ equal to 2. Therefore, the minimum time needed to reach the ratio ζ is $t \simeq 2 \times 10^{-3}\zeta^2$ s. For a one decade variation, $\zeta = 10$ and $t = 0.2$ s, corresponding to a minimal duct length equal to $20 \times 0.2 = 4$ m, which is of the order of the duct available in most existing grid turbulence experiments. For $\zeta = 100$, one obtains $t = 20$ s and a duct length equal to 400 m, which is obviously not reachable in practice. Therefore, in many available experiments, the range of scales that governed turbulence decay are very close to the initial integral length scale, leading to $kL_0 = O(1)$, not to $kL(t) \ll 1$.

2. The asymptotic features of both $E(k)$ and $f(r)$ escape both experimental and numerical investigations, since asymptotically large scales cannot be directly measured or computed. And present results show that the decay regime is not sensitive to those scales over finite time (i.e., real-life) realizations. Therefore, they cannot be investigated by some "inverse problem" approach based on the observed features of the decay, especially if only evolution of integral quantities is reported.
3. Another point here is that in wind tunnel grid turbulence the largest scales are anisotropic and non-homogeneous due to wall effects, but this breakdown of homogeneity at very large scales is not observed to significantly corrupt the nearly isotropic behavior reported by many researchers. This is coherent with the present conclusions. The role of anisotropy could also be investigated using Data Assimilation via a procedure similar to the present one, if the isotropic EDQNM model is replaced by an anisotropic one. Some "direct mode" analyses were recently carried out[43] that show that global decay exponent are not very sensitive to a weak initial anisotropy, but no systematic analysis of existing wind tunnel data was possible due to the lack of reconstruction of anisotropic initial conditions starting from experimental data via an inverse problem. Future works will deal with Data Assimilation coupled to anisotropic EDQNM, enabling a re-analysis of existing experimental databases (but omitting inhomogeneous effects) to get a deeper insight into the role of initial anisotropy on turbulence decay.

APPENDIX: USING BICOMPLEX NUMBERS ALONG WITH THE BFGS METHOD FOR OPTIMIZATION

The step 4 of the optimization procedure described in Sec. IV B to minimize the Lagrangian in Eq. (15) consists in updating the set of estimated parameters $\underline{a}$ of the functional form chosen for the initial energy spectrum according to the following relation:

$$\underline{a}^{(i+1)} = \underline{a}^{(i)} + \gamma^{(i)}\underline{d}^{(i)}. \tag{A1}$$

First, the descent direction $\underline{d}^{(i)}$ is chosen to minimize $\mathcal{L}(\underline{a}^{(i)} + \underline{d}^{(i)})$. By using Newton's method, $\underline{d}^{(i)}$ can be determined with the following relation:

$$\underline{d}^{(i)} = -\left(\frac{\partial^2\mathcal{L}}{\partial\underline{a}^2}\right)^{-1}\frac{\partial\mathcal{L}}{\partial\underline{a}}(\underline{a}^{(i)}). \tag{A2}$$

The gradient $\frac{\partial \mathcal{L}}{\partial \underline{a}}$ is given by the steps 2 and 3 of the optimization procedure. However, the Hessian $\frac{\partial^2 \mathcal{L}}{\partial \underline{a}^2}$ is unknown. The BFGS method proposes an approximation of the Hessian which is updated at each iteration using the values of the Lagrangian and of its gradient. The reader may refer to Ref. 31 for a complete presentation of the BFGS method with those of other quasi-Newton methods. Once the approximate Hessian is obtained, the descent direction $\underline{d}^{(i)}$ can be determined from relation (A2). To make the method more robust, the step length parameter $\gamma^{(i)}$ is now introduced. The best choice for the value of $\gamma^{(i)}$ is that which minimizes the function F defined by

$$F(x) = \mathcal{L}(\underline{a}^{(i)} + x\underline{d}^{(i)}). \tag{A3}$$

By again using Newton's method with the first guess $x = 1$, which would be the optimal value if the Hessian was computed exactly, $\gamma^{(i)}$ is determined with the following relation:

$$\gamma^{(i)} = 1 - \frac{F'(1)}{F''(1)}. \tag{A4}$$

In this paper, we choose to use bicomplex variables for the computation of the first and second derivates of the function F in (A4). The use of multicomplex variables allows to extent the complex-step differentiation for the estimation of first-order derivatives of real functions[44] to the computation of higher-order derivatives. The reader may refer to Refs. 45 and 46 for an exhaustive description of multicomplex numbers and their use for the computation of derivatives. The set $\mathbb{C}^2$ of bicomplex numbers is defined as

$$\mathbb{C}^2 := \{Z = z_1 + z_2 i_2 / z_1, z_2 \in \mathbb{C}\} := \{Z = x_0 + x_1 i_1 + x_2 i_2 + x_{12} i_1 i_2 / x_0, x_1, x_2, x_{12} \in \mathbb{R}\} \tag{A5}$$

with $i_1^2 = i_2^2 = -1$. In this way, higher-order multicomplex scapes are defined recursively. We define the operators Im_1 and Im_{12} from $\mathbb{C}^2$ to $\mathbb{R}$ in the following manner:

$$Im_1(Z) = x_1; \quad Im_{12}(Z) = x_{12}, \tag{A6}$$

where $Z = x_0 + x_1 i_1 + x_2 i_2 + x_{12} i_1 i_2 \in \mathbb{C}^2$ with $x_0, x_1, x_2, x_{12} \in \mathbb{R}$. The following expansion in a Taylor series of the real function F is performed in order to compute its derivatives at the real x:

$$\begin{aligned} F(x + (i_1 + i_2)h) &= F(x) + (i_1 + i_2)hF'(x) + \frac{(i_1 + i_2)^2}{2} h^2 F''(x) + \frac{(i_1 + i_2)^3}{6} h^3 F^{(3)}(x) + O(h^4) \\ &= F(x) + (i_1 + i_2)hF'(x) + (-1 + i_1 i_2)h^2 F''(x) - \frac{2}{3}(i_1 + i_2)h^3 F^{(3)}(x) + O(h^4) \end{aligned} \tag{A7}$$

with h a small real parameter. We can get the following expressions of $F'(x)$ and $F''(x)$ from (A7):

$$F'(x) = \frac{Im_1(F(x + (i_1 + i_2)h))}{h} + O(h^2); \quad F''(x) = \frac{Im_{12}(F(x + (i_1 + i_2)h))}{h^2} + O(h^2). \tag{A8}$$

Thus, following on from a bicomplex forward integration of the problem defined in Eq. (21) with the set of parameters $\underline{a}^{(i)} + (1 + (i_1 + i_2)h)\underline{d}^{(i)}$, the step length $\gamma^{(i)}$ is obtained from relations (A3), (A4) and (A8) taking $x = 1$.

[1] G. K. Batchelor, *The Theory of Homogeneous Turbulence* (Cambridge University Press, 1953).

[2] M. Lesieur, *Turbulence in Fluids*, 4th ed. (Springer, 2008).

[3] P. A. Davidson, *Turbulence: An Introduction for Scientists and Engineers* (Oxford University Press, 2004).

[4] P. Sagaut and C. Cambon, *Homogeneous Turbulence Dynamics* (Cambridge University Press, 2008).

[5] P. C. Valente and J. C. Vassilicos, "The decay of turbulence generated by a class of multiscale grids," J. Fluid Mech. **687**, 300–340 (2011).

[6] P. C. Valente and J. C. Vassilicos, "Dependence of decaying homogeneous isotropic turbulence on inflow conditions," Phys. Lett. A **376**, 510–514 (2012).

[7] M. Meldi and P. Sagaut, "Further insights into self-similarity and self- preservation in freely decaying isotropic turbulence," J. Turbul. **14**(8), 24–53 (2013).

[8] C. G. Speziale and P. S. Bernard, "The energy decay in self-preserving isotropic turbulence revisited," J. Fluid Mech. **241**, 645–667 (1992).

[9] J. R. Ristorcelli, "The self-preserving decay of isotropic turbulence: Analytic solutions for energy and dissipation," Phys. Fluids **15**, 3248–3250 (2003).

[10] J. R. Ristorcelli and D. Livescu, "Decay of isotropic turbulence: Fixed points and solutions for nonconstant $G \sim Re_\lambda$ palinstrophy," Phys. Fluids **16**, 3487–3490 (2004).
[11] W. K. George, "The decay of homogeneous isotropic turbulence," Phys. Fluids A **4**, 1492–1509 (1992).
[12] W. K. George, "Asymptotic effect on initial upstream conditions on turbulence," J. Fluids Eng. **134**, 061203 (2012).
[13] A. Llor and O. Soulard, "Comment on "Energy spectra at low wavenumbers in homogeneous incompressible turbulence" [Phys. Lett. A **375**, 2850 (2011)]," Phys. Lett. A **377**, 1157–1159 (2013).
[14] P. A. Davidson, "The role of angular momentum conservation in homogeneous turbulence," J. Fluid Mech. **632**, 329–358 (2009).
[15] P. A. Davidson, "The minimum energy decay rate in quasi-isotropic grid turbulence," Phys. Fluids **23**, 085108 (2011).
[16] J. C. Vassilicos, "An infinity of possible invariants for decaying homogeneous turbulence," Phys. Lett. A **375**, 1010–1013 (2011).
[17] T. Ishida, P. A. Davidson, and Y. Kaneda, "On the decay of isotropic turbulence," J. Fluid Mech. **564**, 455–475 (2006).
[18] M. Lesieur and D. Schertzer, "Self-similar damping of turbulence at large Reynolds number," J. Mec. **17**, 609–646 (1978).
[19] L. Skrbek and S. R. Stalp, "On the decay of homogeneous isotropic turbulence," Phys. Fluids **12**, 1997–2019 (2000).
[20] T. T. Clark and C. Zemach, "Symmetries and the approach to statistical equilibrium in isotropic turbulence," Phys. Fluids **10**, 2846–2858 (1998).
[21] G. L. Eyink and D. J. Thomson, "Free decay of turbulence and breakdown of self-similarity," Phys. Fluids **12**, 477–479 (2000).
[22] M. Meldi and P. Sagaut, "On non-self-similar regimes in homogeneous isotropic turbulence decay," J. Fluid Mech. **711**, 364–393 (2012).
[23] F. X. Le Dimet and O. Talagrand, "Variational algorithms for analysis and assimilation of meteorological observations: Theoretical aspects," Tellus **38A**, 97–110 (1986).
[24] A. Gronskis, D. Heitz, and E. Mémin, "Inflow and initial conditions for direct numerical simulation based on adjoint data assimilation," J. Comput. Phys. **242**, 480–497 (2013).
[25] S. A. Orszag, "Analytical theories of turbulence," J. Fluid Mech. **41**, 363–386 (1970).
[26] A. Pouquet, M. Lesieur, J. C. André, and C. Basdevant, "Evolution of high Reynolds number two-dimensional turbulence," J. Fluid Mech. **72**, 305–319 (1975).
[27] O. Métais and M. Lesieur, "Spectral large-eddy simulation of isotropic and stably stratified turbulence," J. Fluid Mech. **239**, 157–194 (1992).
[28] J. Meyers and C. Meneveau, "A functional form of the energy spectrum parametrizing bottleneck and intermittency effects," Phys. Fluids **20**, 065109 (2008).
[29] A. Bentamy, J.-Y. Trépanier, and F. Guibault, "Wing shape optimization using a constrained NURBS surface geometrical representation," in *Proceedings of the 23rd International Congress of Aeronautical Sciences*, ICAS 2002 (ICAS, 2002), p. 123.
[30] I. Ivanović, Z. Petrović, and S. Stupar, "Helicopter rotor blade shape optimization using NURBS for airfoil shape parameterization," AIP Conf. Proc. **1168**, 131–134 (2009).
[31] J. M. Lewis, S. Lakshmivarahan, and S. K. Dhall, *Dynamic Data Assimilation: A Least Squares Approach*, Encyclopedia of Mathematics and its Applications Vol. 104 (Cambridge University Press, 2006).
[32] G. Artana, A. Cammilleri, J. Carlier, and E. Mémin, "Strong and weak constraint variational assimilations for reduced order fluid flow modeling," J. Comput. Phys. **231**, 3264–3288 (2012).
[33] F. Fang, C. C. Pain, I. M. Navon, D. G. Cacuci, and X. Chen, "The independent set perturbation method for efficient computation of sensitivities with applications to data assimilation and a finite element shallow water model," Comput. Fluids **76**, 33–49 (2013).
[34] A. Guégan, P. J. Schmid, and P. Huerre, "Optimal energy growth and optimal control in swept Hiemenz flow," J. Fluid Mech. **566**, 11–45 (2006).
[35] S. Delport, M. Baelmans, and J. Meyers, "Maximizing dissipation in a turbulent shear flow by optimal control of its initial state," Phys. Fluids **23**, 045105 (2011).
[36] H. Wang and W. K. George, "The integral scale in homogeneous isotropic turbulence," J. Fluid Mech. **459**, 429–443 (2002).
[37] G. Comte-Bellot and S. Corrsin, "The use of a contraction to improve the isotropy of grid-generated turbulence," J. Fluid Mech. **25**, 657–682 (1966).
[38] M. Meldi, P. Sagaut, and D. Lucor, "A stochastic view of isotropic turbulence decay," J. Fluid Mech. **668**, 351–362 (2011).
[39] J. G. Brasseur and C. H. Wei, "Interscale dynamics and local isotropy in high Reynolds number turbulence within triadic interactions," Phys. Fluids **6**, 842–870 (1986).
[40] S. L. Woodruff and R. Rubinstein, "Multiple-scale perturbation analysis of slowly evolving turbulence," J. Fluid Mech. **565**, 95–103 (2006).
[41] R. Rubinstein and T. T. Clark, "Self-similar turbulence evolution and the dissipation rate transport equation," Phys. Fluids **17**, 095104 (2005).
[42] M. Meldi, H. Lejemble, and P. Sagaut, "On the emergence of non-classical decay regimes in multi-scale/fractal generated isotropic turbulence," J. Fluid Mech. **756**, 816–843 (2014).
[43] V. Mons, M. Meldi, and P. Sagaut, "Numerical investigation on the partial return to isotropy of freely decaying homogeneous axisymmetric turbulence," Phys. Fluids **26**, 025110 (2014).
[44] W. Squire and G. Trapp, "Using complex variables to estimate derivatives of real functions," SIAM Rev. **40**, 110–112 (1998).
[45] G. B. Price, *An Introduction to Multicomplex Spaces and Functions* (Marcel Dekker, Inc., New York, 1991).
[46] G. Lantoine, R. P. Russell, and T. Dargent, "Using multicomplex variables for automatic computation of high-order derivatives," ACM Trans. Math. Softw. **38**, 16 (2012).

3.2 Anomalous decay exponents

The present section is devoted to DA experiments performed to supplement the cases of §3.1. Firstly, the possibility of reconstructing a Gaussian-like initial energy spectrum from observations of the turbulent kinetic energy $\mathcal{K}$ is studied. Contrary to the DA experiments of §3.1 where the reference energy spectrum exhibits a constant (or nearly constant) slope at large scales, a transient regime can be noticed with such an initial condition where the shape of the energy spectrum changes from a Gaussian shape to $E(k) \propto k^4$ at large scales due to backscatter effects [132]. Such a case may thus appear appropriate to further test the robustness of the results of §3.1. Secondly, anomalous decay regimes are studied. These regimes, which do not fall within the predictions of the Comte-Bellot–Corrsin theory (§3.1), have been identified in both experimental [96, 212, 213] and numerical [153, 156] studies dealing with fractal-generated turbulence. Here, we investigate the possibility of reproducing such regimes through the determination of appropriate initial conditions. In what follows, the value of the initial Reynolds number based on the Taylor microscale is similar to that in §3.1 ($Re_\lambda(t = 0) = 800$), which ensures converged values of the decay exponents in the high Reynolds number regime [155].

The results of figure 3.1 are first examined. The reference initial kinetic energy spectrum is here chosen with a Gaussian shape given by

$$E^0(k) = C \exp\left(-(\log(kL))^2\right), \tag{3.1}$$

with C a normalizing constant and L the initial integral scale. The turbulent kinetic energy $\mathcal{K}$ is observed between $t = 10^3\tau_0$ and $t = T_f = 10^4\tau_0$ every $10^3\tau_0$. The first-guess, or estimated, initial spectrum is chosen with a functional form as proposed in [157] with a slope $\sigma = 4$ at large scales (Batchelor turbulence). Despite the existence of a transient regime where the reference spectrum changes from a Gaussian shape to a slope $\sigma = 4$ at large scales [56], results illustrated in figure 3.1 are similar to those obtained in §3.1. Only the shape of the initial spectrum at the most energetic scales has been satisfactorily reconstructed (3.1(a)), and large scales of the first-guess spectrum beyond the integral scale $L(t = T_f)$ at the end of the assimilation window have been left unchanged (3.1(c)). As illustrated in figure 3.1(b), the position of the peak of sensitivity of the decay well coincides with $L(t = T_f)$. Accordingly, the robustness of the results discussed in §3.1 is once again confirmed by this experiment using a less conventional initial spectrum.

The principle of the DA experiments to investigate anomalous decay regimes, whose results are illustrated in figures 3.2 and 3.3, is slightly different from that of the experiments of §3.1 and figure 3.1. Instead of imposing a reference initial kinetic energy spectrum, performing observations of the corresponding evolution, and then identifying the parts of the initial spectrum that are reconstructed by the DA procedure, values of the decay exponent for the turbulent kinetic energy $n_{\mathcal{K}}$ are directly imposed at given times. Since decay exponent values that are not in the range predicted by the Comte-Bellot–Corrsin theory are prescribed, the solution of the corresponding inverse problem is actually unknown, and DA is expected to bring valuable information concerning the shape of the energy spectrum in the case where anomalous decay exponents are observed. The case where the value $n_{\mathcal{K}} = -1.5$ is imposed between $t = 10^3\tau_0$ and $t = T_f = 10^4\tau_0$ is investigated in figure 3.2. It can be noticed that the lower bound for the value of $n_{\mathcal{K}}$ in classical theories is $-10/7 \simeq -1.43$, and that the value -1.5 is imposed over a significant time interval. The first-guess initial spectrum for the optimization procedure corresponds to a Saffman turbulence (slope $\sigma = 2$ at large scales). The initial energy spectrum obtained through the DA procedure is reported in figure 3.2(a). As confirmed by figure 3.2(c), the optimization process has drastically altered the shape of the first-guess spectrum at large scales smaller than ten times $L(t = T_f)$. The emphasized shape of the peak of the energy spectrum engenders an enhanced loss of energy at large energetic scales, while energy transfers seem unchanged at small scales compared to the first-guess evolution (figure 3.2(d)). Figure 3.2(e) illustrates the fact that the DA procedure has successfully driven the turbulent solution from an asymptotic regime with $n_{\mathcal{K}} = -1.2$ to $n_{\mathcal{K}} = -1.5$ between $t = 10^3\tau_0$ and $t = T_f = 10^4\tau_0$. This test case suggests that initial condition effects, and thus production mechanisms in grid turbulence experiments, may explain alone departures from classical predictions, even over significant evolution times that are not accessible in experiments.

An additional DA investigation, which is possibly more representative of some grid turbulence experiments, is illustrated in figure 3.3. The value $n_{\mathcal{K}} = -3$ is imposed at $t = 10\tau_0$. Even if transitory effects are already present

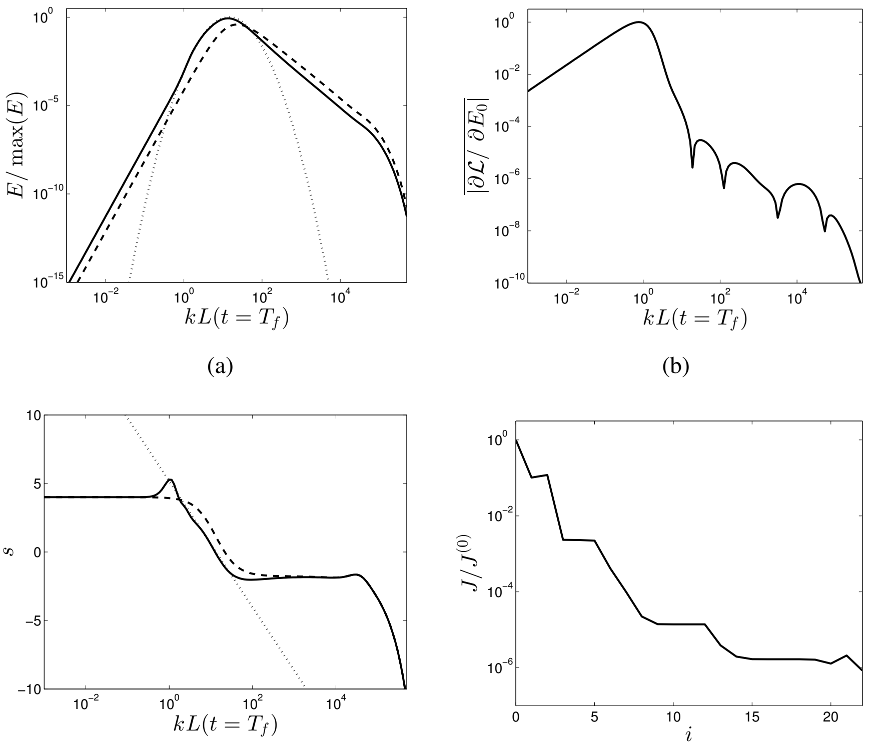

(a) (b)

(c) (d)

FIGURE 3.1: DA results when the turbulent kinetic energy $\mathcal{K}$ is observed with an initial Gaussian spectrum for the reference flow: (a) reference (dotted line), first-guess (dashed line) and assimilated (full line) initial spectra, (b) gradient of the Lagrangian involved in the optimization procedure with respect to the initial spectrum, (c) reference (dotted line), first-guess (dashed line) and assimilated (full line) local slopes of the corresponding initial spectra, (d) cost function versus the iteration of the optimization procedure.

in the first-guess evolution, which are due to the fact that the chosen initial energy spectrum is not a solution of the Lin equation combined with the neglect of a virtual origin (see dashed line in figure 3.3(e)), $n_{\mathcal{K}} = -3$ corresponds to a highly anomalous value of the decay exponent that is relatively close to the ones reported in [96, 212]. The initial energy spectrum retrieved from the DA process, starting from the same first-guess spectrum as in figure 3.2, exhibits a pronounced bump at the most energetic scales (figure 3.3(a)). This particular shape of the peak of the initial energy spectrum lies at the origin of a significant modification of energy transfers at large scales (figure 3.3(d)), inducing a drastic intensification of the decay at small times, as confirmed by figure 3.3(e). However, for longer evolution times, the assimilated solution converges towards a more conventional exponent decay value. Such a bumped shape of the initial energy spectrum inducing rapid turbulence decay is coherent with direct EDQNM analyses performed in [153, 156], and is also observed in the DNS of [89]. The present results thus confirm that initial condition effects alone can engender drastic deviations from classical values for the decay exponents.

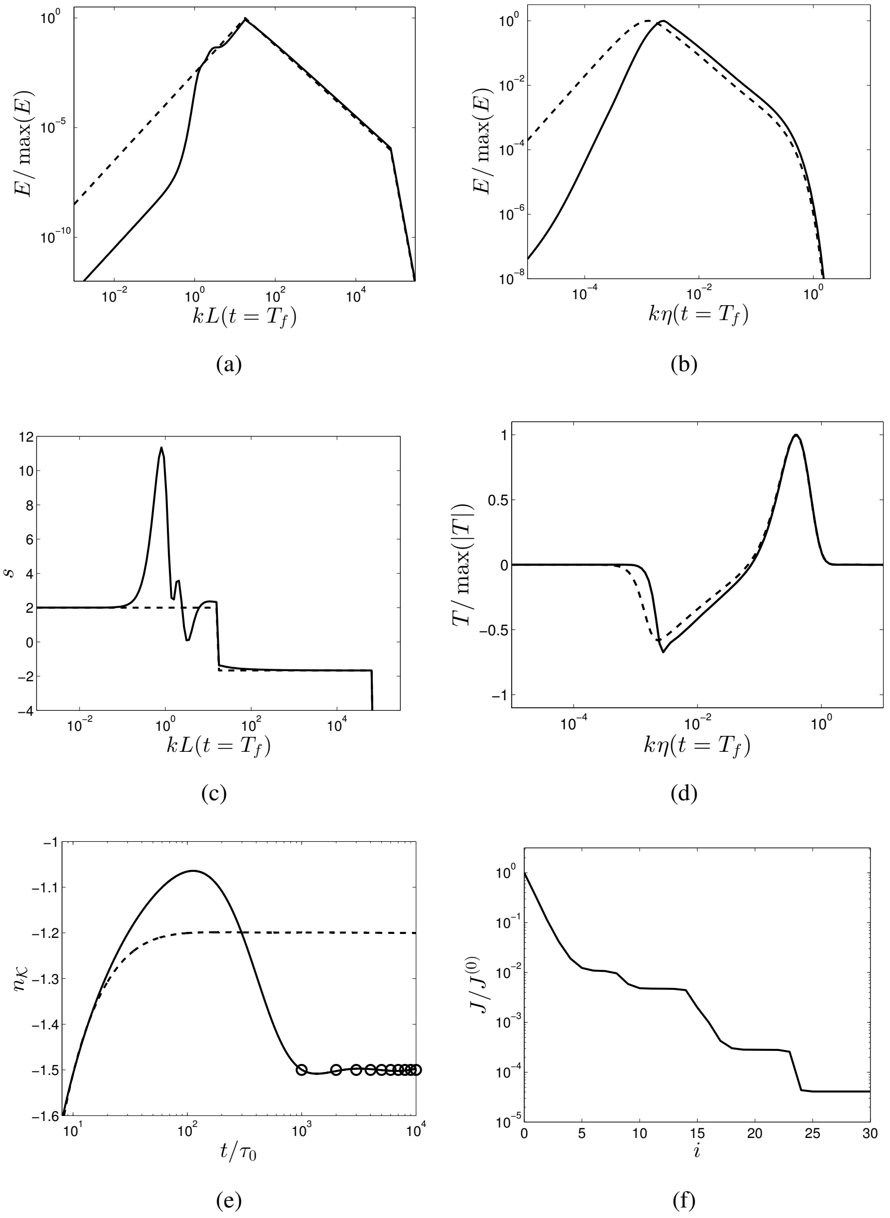

(a) (b)

(c) (d)

(e) (f)

FIGURE 3.2: DA results when we impose $n_{\mathcal{K}} = -1.5$ between $t = 10^3\tau_0$ and $t = T_f = 10^4\tau_0$: (a) initial energy spectrum, (b) energy spectrum at $t = T_f$, (c) local slope for the initial energy spectrum, (d) transfer term at $t = T_f$ and (e) power-law exponent for the first-guess (dashed line) and assimilated (full line) solutions, symbols in (e) correspond to the synthetic observations; (f) cost function versus the iteration of the optimization procedure.

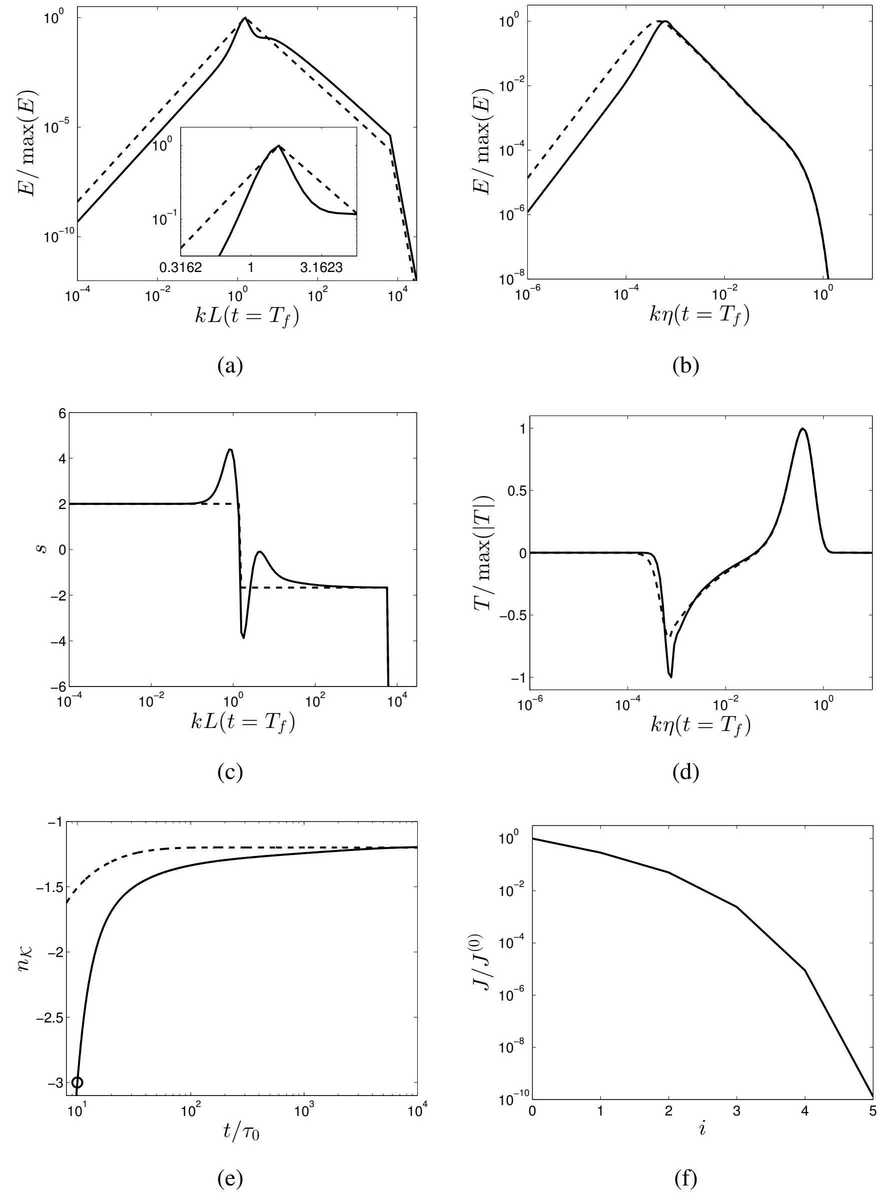

(a) (b)

(c) (d)

(e) (f)

FIGURE 3.3: DA results when we impose $n_{\mathcal{K}} = -3$ at $t = T_f = 10\tau_0$: (a) initial energy spectrum, (b) energy spectrum at $t = T_f$, (c) local slope for the initial energy spectrum, (d) transfer term at $t = T_f$ and (e) power-law exponent for the first-guess (dashed line) and assimilated (full line) solutions, symbols in (e) correspond to the synthetic observations; (f) cost function versus the iteration of the optimization procedure.

3.3 Conclusion

In this chapter, the decay of grid turbulence has been investigated through variational DA. In §3.1, the adjoint EDQNM model has been developed, and it has been shown through DA experiments that HIT decay over finite time is governed by large scales ranging approximately from the initial integral scale to the final integral scale, a vanishing sensitivity being observed for large scales located within one decade outside these bounds. This conclusion is robust, since it is observed in all cases considered, which use various types of observations, parameterizations of the initial kinetic energy spectrum and reference and first-guess spectra. This analysis that considers classical decay regimes predicted by the Comte-Bellot–Corrsin theory has been extended to the study of anomalous regimes in §3.2. The present results indicate that initial condition effects can engender alone significant departures from classical predictions of the value of the decay exponent. A characteristic bumped shape of the energy spectrum encountered in studies dealing with fractal-generated turbulence is recovered through DA.

In order to refine the present analysis of anomalous decay and to take into account time lasting production effects in future DA studies, one could consider the assimilation of not only the initial energy spectrum, but also of a spectral forcing term $F(k, t)$, parameterized or not, involved in the dynamics of the energy spectrum according to

$$\left(\frac{\partial}{\partial t} + 2\nu k^2\right) E(k, t) = T(k, t) + F(k, t). \tag{3.2}$$

A good first-guess for the shape of $F(k, t)$ to take into account fractal forcing could be found in [152, 153, 156]. Adding such a term in DA studies could allow to recover possible exponential decay as observed in [153, 156], while initial condition effects alone can engender only deviations of the value of the exponent in a decay power law.

In chapter 4, a spectral model adapted to moderately anisotropic homogeneous flows, which seem more representative of grid-generated turbulence than strictly isotropic turbulence, is proposed. The versatility of the present modelling, which is based on a spherically-averaged level of description and EDQNM, makes it a suitable candidate to incorporate anisotropy in future DA-based investigations of the decay of grid turbulence. Finally, taking into account inhomogeneity effects will require the use of other numerical techniques than those based on EDQNM approaches.

Chapter 4

A spectral model for homogeneous shear-driven anisotropic turbulence in terms of spherically averaged descriptors

J. Fluid Mech. (2016), *vol.* 788, *pp.* 147–182. © Cambridge University Press 2016
doi:10.1017/jfm.2015.705

A spectral model for homogeneous shear-driven anisotropic turbulence in terms of spherically averaged descriptors

Vincent Mons[1,2,†], **Claude Cambon**[3] and **Pierre Sagaut**[4]

[1]Sorbonne Univ, UPMC Univ Paris 06, UMR 7190, Inst Jean Le Rond d'Alembert,
F-75005, Paris, France

[2]CNRS, UMR 7190, Inst Jean Le Rond d'Alembert, F-75005, Paris, France

[3]Laboratoire de Mécanique des Fluides et d'Acoustique, Université de Lyon,
École Centrale de Lyon and CNRS, UMR 5509, Écully, France

[4]Aix Marseille Universite, CNRS, Centrale Marseille, M2P2 UMR 7340, 13451 Marseille, France

(Received 12 November 2014; revised 30 September 2015; accepted 27 November 2015;

A nonlinear spectral model in terms of spherically averaged descriptors is derived for the prediction of homogeneous turbulence dynamics in the presence of arbitrary mean-velocity gradients. The governing equations for the tensor $\hat{R}_{ij}(\boldsymbol{k}, t)$, the Fourier transform of the two-point second-order correlation tensor, are first closed by an anisotropic eddy-damped quasinormal Markovian procedure. This closure is restricted to turbulent flows where linear effects induced by mean-flow gradients have no essential qualitative effects on the dynamics of triple correlations compared with the induced production effects in the equations for second-order correlations. Truncation at the first relevant order of spectral angular dependence allows us to derive from these equations in vector $\boldsymbol{k}$ our final model equations in terms of the wavenumber modulus k only. Analytical spherical integration results in a significant decrease in computational cost. Besides, the model remains consistent with the decomposition in terms of directional anisotropy and polarization anisotropy, with a spherically averaged anisotropic spectral tensor for each contribution. Restriction of anisotropy to spherically averaged descriptors, however, entails a loss of information, and realizability conditions are considered to quantify the upper boundary of anisotropy that can be investigated with the proposed model. Several flow configurations are considered to assess the validity of the present model. Satisfactory agreement with experiments on grid-generated turbulence subjected to successive plane strains is observed, which confirms the capability of the model to account for production of anisotropy by mean-flow gradients. The nonlinear transfer terms of the model are further tested by considering the return to isotropy (RTI) of different turbulent flows. Different RTI rates for directional anisotropy and polarization anisotropy allow us to correctly predict the apparent delayed RTI shown after axisymmetric expansion. The last test case deals with homogeneous turbulence subjected to a constant pure plane shear. The interplay between linear and nonlinear effects is reproduced, yielding the eventual exponential growth of the turbulent kinetic energy.

Key words: homogeneous turbulence, turbulence modelling, turbulent flows

---

† Email address for correspondence: vincent.mons@sfr.fr

1. Introduction

Homogeneous anisotropic turbulence is a very important topic in turbulence theory, since it allows for a detailed analysis of linear and nonlinear effects of the mean-flow gradient on turbulence dynamics. A key point is the description of anisotropy, and the derivation of evolution equations that retain most of the structural and dynamical information on the flow evolution. The usual starting point for Fourier-space description is to consider the spectral tensor $\hat{R}_{ij}(\boldsymbol{k}, t)$, which is defined as the Fourier transform of the two-point second-order correlation tensor $R_{ij}(\boldsymbol{r}, t) = \langle u_i(\boldsymbol{x}, t) u_j(\boldsymbol{x} + \boldsymbol{r}, t)\rangle$. Evolution equations can be found for this tensor, which require some closures for nonlinear cubic terms and pressure–velocity correlation terms. A few closed forms have been proposed based on Heisenberg's transfer models, e.g. Canuto & Dubovikov (1996*a*,*b*,*c*). These models do not give a detailed insight into anisotropy, since they rely on a strictly isotropic transfer term as in homogeneous isotropic turbulence. A more general model can be obtained using higher-order closures in place of the quasilocal energy flux, as illustrated in Weinstock (2013), who used the eddy-damped quasinormal Markovian (EDQNM) closure for the isotropic turbulence of Orszag (1970) to derive expressions for the nonlinear transfer term and the nonlinear pressure–strain contribution. This work also relies on an exact treatment of the linear operators induced by mean-velocity gradients in the governing equation for the spectral tensor $\hat{R}_{ij}(\boldsymbol{k}, t)$, which is permitted by the $\boldsymbol{k}$-space level of description of the proposed model. The latter was used to perform an exhaustive analytical study of homogeneous turbulence subjected to a constant pure plane shear without limitations on time or wavenumber.

As in Weinstock (2013), this level of description in $\boldsymbol{k}$-space is the first step of the present model, which entirely includes the nonlinear closure for transfer terms. First, instead of considering the spectral tensor with all of its components, we use its decomposition in terms of directional anisotropy and polarization anisotropy (Cambon & Rubinstein 2006). A more general representation, say $(\mathscr{E}, Z, \mathscr{H})(\boldsymbol{k}, t)$, first introduced by Cambon & Jacquin (1989), also includes a helicity contribution generated by a helicity spectrum $\mathscr{H}(\boldsymbol{k}, t)$. The helicity spectrum, which is associated with the imaginary part of $\hat{R}_{ij}(\boldsymbol{k}, t)$, is not considered here because it remains zero in homogeneous turbulence if it is not initialized or forced, usually in an unphysical way (see also the trivial helicity equation in Cambon & Jacquin (1989) and Cambon *et al.* (2013)). In addition to their mathematical origin, the recourse to the two different terms $\mathscr{E}(\boldsymbol{k}, t)$ and $Z(\boldsymbol{k}, t)$ has physical meaning. For instance, the structure-based single-point modelling of Kassinos, Reynolds & Rogers (2001) can be related to these spectra, the dimensionality tensor being derived from the angular dependence of $\mathscr{E}(\boldsymbol{k}, t)$, and the stropholysis tensor from $Z(\boldsymbol{k}, t)$. This structure-based modelling is in contrast to other single-point models where anisotropy is characterized by the sole deviatoric tensor associated with the Reynolds stress tensor which is used to express the 'rapid' and 'slow' parts of the pressure–strain rate tensor. The linkage between our spectral approach based on the directional–polarization anisotropy decomposition and the structure-based single-point modelling of Kassinos *et al.* (2001) is detailed in appendix A of the present paper, along with discussions concerning other single-point models.

The compact decomposition of the spectral tensor discussed above simplifies, without any loss of generality, the derivation of dynamical equations, here Lin equations for $\mathscr{E}(\boldsymbol{k}, t)$ and $Z(\boldsymbol{k}, t)$, and that of closure relations. On the other hand, the numerical treatment of the angular dependence of $\mathscr{E}(\boldsymbol{k}, t)$ and $Z(\boldsymbol{k}, t)$

remains a challenge. As an example, the numerical cost of axisymmetric EDQNM models (Godeferd & Cambon 1994; Bellet *et al.* 2006; Favier *et al.* 2011) is much higher than that of the basic EDQNM for isotropic turbulence. These models were developed, from the first case of rotating turbulence (Cambon & Jacquin 1989), for flows dominated by interacting dispersive waves and without explicit linear effect in the governing equation for the energy density $\mathscr{E}(\boldsymbol{k}, t)$, requiring the use of the most complicated EDQNM version to handle the effects induced by the mean flow on triple correlations, such as the inhibition of the energy cascade in the case of rotating flows. This configuration is no longer considered here, and we focus in the present paper on turbulent flows interacting with mean-velocity gradients with a symmetric part, hence leading to energy production. At least for the flow configurations considered in this paper (turbulent flows in the presence of mean strain/shear), these production effects induced by the mean flow, which originate from the linear contributions in the equations for second-order correlations, prevail in the evolution of anisotropy compared with the ones that affect triple correlations (Sagaut & Cambon 2008). A self-consistent nonlinear model will be built accordingly, based on fully tensorial EDQNM closure for an arbitrary anisotropic second-order spectral tensor but with no explicit mean-gradient effect in the expression of the nonlinear transfer terms.

Our second step for deriving our final model equations does not include further closure assumptions, it is purely technical but essential to derive a tractable model, especially in terms of numerical treatment. The computational cost of the models in 3D Fourier space discussed above can be significantly reduced by deriving a 1D problem through integration over spheres with arbitrary radius in Fourier space, S_k. This yields expressions of governing equations for the spherically averaged tensor $\varphi_{ij}(k, t) = \int\int_{S_k} \hat{R}_{ij}(\boldsymbol{k}, t)\, \mathrm{d}^2\boldsymbol{k}$ that depend on the wavevector modulus, k, instead of $\boldsymbol{k}$. This was done by Clark & Zemach (1995) in their diffusion-approximation-based model, where the prescription of a scale-dependent relaxation rate leads to satisfactory comparisons with experimental data and to a good description of partial return to isotropy, which is confirmed in, e.g., Chasnov (1995). However, discussions in Choi & Lumley (2001), Kassinos *et al.* (2001) and Zusi & Perot (2013, 2014) about possible nonlinear return to isotropy can eventually motivate the use of anisotropic EDQMN closure and the distinction between directional anisotropy and polarization anisotropy. One can also mention the model of Cambon, Jeandel & Mathieu (1981), where a closure for nonlinear terms using anisotropic EDQNM was proposed, but without a separation of directional anisotropy and polarization anisotropy. Spherical integration requires a parametrization of the second-order spectral tensor to restore at least a part of its angular dependence, leading to a mathematically consistent model reduced to spherically averaged descriptors. This will be done in our final model by using truncated expansions in terms of angular harmonics of the second-order spectral tensor. A similar approach was considered by Herring (1974) in the context of the direct-interaction approximation (DIA) of Kraichnan (1959). In this work, the question of the number of spherical harmonics necessary to accurately describe the return to isotropy of axisymmetric turbulence is investigated numerically, and a scale-by-scale relaxation rate is identified. This truncation of spherical harmonic series lies at the origin of a loss of information that restricts the present model to moderate anisotropy. Realizability conditions will be considered in order to quantify the upper boundary of anisotropy intensity that can be investigated with the proposed model. A complementary approach to the models described above can be found in Kassinos & Akylas (2012), where explicit angular dependence is preserved, whereas scale information is lost after integration along rays of fixed orientation in Fourier space.

The key spherical descriptors of our spectral model are now introduced. Starting from a trace–deviator splitting of the real part of the spectral tensor $\hat{R}_{ij}(\boldsymbol{k}, t)$ restricted to the plane normal to the wavevector $\boldsymbol{k}$ by virtue of incompressibility,

$$\hat{R}_{ij}(\boldsymbol{k}, t) = \frac{1}{2}\hat{R}_{nn}(\boldsymbol{k}, t)P_{ij}(\boldsymbol{k}) + \mathrm{Re}\left(\hat{R}_{ij}(\boldsymbol{k}, t) - \frac{1}{2}\hat{R}_{nn}(\boldsymbol{k}, t)P_{ij}(\boldsymbol{k})\right), \quad P_{ij}(\boldsymbol{k}) = \delta_{ij} - \frac{k_i k_j}{k^2}, \tag{1.1a,b}$$

the following threefold decomposition in terms of isotropic, directional and polarization parts is obtained:

$$\hat{R}_{ij}(\boldsymbol{k}, t) = \underbrace{\frac{E(k, t)}{4\pi k^2}P_{ij}(\boldsymbol{k})}_{\hat{R}^{(iso)}_{ij}(\boldsymbol{k},t)} + \underbrace{\mathscr{E}^{(dir)}(\boldsymbol{k}, t)P_{ij}(\boldsymbol{k})}_{\hat{R}^{(dir)}_{ij}(\boldsymbol{k},t)} + \hat{R}^{(pol)}_{ij}(\boldsymbol{k}, t), \tag{1.2}$$

by separating the trace of $\hat{R}_{ij}(\boldsymbol{k}, t)$ into purely isotropic and directional anisotropy contributions, according to

$$\mathscr{E}(\boldsymbol{k}, t) = \frac{1}{2}\hat{R}_{nn}(\boldsymbol{k}, t), \quad \mathscr{E}^{(dir)}(\boldsymbol{k}, t) = \mathscr{E}(\boldsymbol{k}, t) - \frac{E(k, t)}{4\pi k^2}, \quad E(k, t) = \iint_{S_k} \mathscr{E}(\boldsymbol{k}, t)\,\mathrm{d}^2\boldsymbol{k}, \tag{1.3a,b}$$

where $E(k, t)$ corresponds to the kinetic energy spectrum. The polarization part $\hat{R}^{(pol)}_{ij}(\boldsymbol{k}, t)$ in (1.2) can be expressed in terms of a complex-valued scalar $Z(\boldsymbol{k}, t)$. This decomposition yields the following splitting of the spherically averaged tensor $\varphi_{ij}(k, t)$:

$$\varphi_{ij}(k, t) = \iint_{S_k} \hat{R}_{ij}(\boldsymbol{k}, t)\,\mathrm{d}^2\boldsymbol{k} = 2E(k, t)\left(\frac{1}{3}\delta_{ij} + H^{(dir)}_{ij}(k, t) + H^{(pol)}_{ij}(k, t)\right). \tag{1.4}$$

The dimensionless deviatoric part of the spherically averaged spectral tensor is therefore $H_{ij}(k, t) = H^{(dir)}_{ij}(k, t) + H^{(pol)}_{ij}(k, t)$, with

$$2E(k, t)H^{(dir)}_{ij}(k, t) = \iint_{S_k} \hat{R}^{(dir)}_{ij}(\boldsymbol{k}, t)\,\mathrm{d}^2\boldsymbol{k}, \quad 2E(k, t)H^{(pol)}_{ij}(k, t) = \iint_{S_k} \hat{R}^{(pol)}_{ij}(\boldsymbol{k}, t)\,\mathrm{d}^2\boldsymbol{k}. \tag{1.5a,b}$$

The aim of this paper is to propose a model based on the decomposition (1.4) of the averaged tensor $\varphi_{ij}(k, t)$, yielding a system of 11 equations for the global state vector $(E, EH^{(dir)}_{ij}, EH^{(pol)}_{ij})(k, t)$. This system is obtained in two steps. The first step is based on an anisotropic EDQNM closure for the equations that govern the whole spectral tensor $\hat{R}_{ij}(\boldsymbol{k}, t)$, or equivalently the scalar spectra $\mathscr{E}(\boldsymbol{k}, t)$ and $Z(\boldsymbol{k}, t)$ from the directional–polarization anisotropy decomposition. This closure is restricted to flows where linear effects induced by mean-velocity gradients lie at the origin of energy production which prevails in the evolution of anisotropy compared with the induced effects on the dynamics of triple correlations. The mean flow is taken into account through the linear operators, which reflect rapid distortion theory (RDT) if considered alone, in the governing equations for second-order moments, as done in Weinstock (2013). The second step consists in parametrizing the angular dependence of $\mathscr{E}(\boldsymbol{k}, t)$ and $Z(\boldsymbol{k}, t)$ in terms of the spherically averaged spectral descriptors $H_{ij}^{(dir)}(k, t)$ and $H_{ij}^{(pol)}(k, t)$ in order to derive a more tractable model in k-space. Even if spherical integration entails a loss of information that restricts the present model to moderate anisotropy and prevents a complete resolution of the flow in 3D Fourier space as in Weinstock (2013), the model developed in the present paper can be used to calculate homogeneous anisotropic flows in a wide range of configurations, without any restriction to a particular symmetry, including when non-stationary mean-velocity gradients are considered. This point will be illustrated by the different applications of the model considered in this paper.

The paper is organized as follows. In § 2, the governing equations for the spectral tensor $\hat{R}_{ij}(\boldsymbol{k}, t)$ are recalled along with those for the scalar spectra $\mathscr{E}(\boldsymbol{k}, t)$ and $Z(\boldsymbol{k}, t)$. The latter are then closed via an anisotropic EDQNM procedure. The spectral model in terms of spherically averaged descriptors is derived in § 3. Section 4 is devoted to the validation of the present model. To this end, several flow configurations are considered. First, multiple straining processes are addressed and comparisons with various experiments are performed. Several cases of return to isotropy (RTI) are then considered, to assess the capability of the model to account for slow pressure terms and possible lack of RTI with separate investigation of directional anisotropy and polarization anisotropy. The last test case deals with homogeneous turbulence subjected to a constant pure plane shear, to check the capability of the model to recover the asymptotic stage of exponential growth of kinetic energy predicted by, e.g., Weinstock (2013). The linkage between single-point models and the model of the present paper is discussed in appendix A.

2. Closed equations for the second-order spectral tensor in sheared turbulence

We consider incompressible homogeneous turbulence. In the presence of a mean-velocity gradient, the Navier–Stokes equation for the fluctuating velocity $u_i(\boldsymbol{x}, t)$ includes additional advection and deformation terms linked to the mean – or large-scale – velocity field $U_i(\boldsymbol{x}, t)$:

$$\left(\frac{\partial}{\partial t} + u_j \frac{\partial}{\partial x_j}\right) u_i + U_j \frac{\partial u_i}{\partial x_j} + \frac{\partial U_i}{\partial x_j} u_j = -\frac{\partial p}{\partial x_i} + \nu \nabla^2 u_i. \tag{2.1}$$

In (2.1), $p(\boldsymbol{x}, t)$ is the pressure divided by a reference density, and ν is the kinematic viscosity of the fluid. In § 2.1, we give the governing equation for the second-order spectral tensor $\hat{R}_{ij}(\boldsymbol{k}, t)$. The $(\mathscr{E}, Z)$ decomposition is applied to the latter tensor in § 2.2 and to its governing equation in § 2.3. Transfer terms appear from the latter decomposition, which are closed via the EDQNM procedure described in § 2.4.

2.1. *Craya's equations*

The mean flow $\boldsymbol{U}(\boldsymbol{x}, t)$ is characterized by a space-uniform gradient $\lambda_{ij}(t) = (\partial U_i/\partial x_j)(t)$ in accordance with homogeneity for the fluctuations. For the sake of readability, and without loss of generality, we will omit the time dependence of λ_{ij} in the following. In anisotropic homogeneous turbulence, all information about two-point second-order correlations is provided by the second-order spectral tensor

$\hat{R}_{ij}(\boldsymbol{k}, t)$, which is the Fourier transform of the two-point second-order correlation tensor $R_{ij}(\boldsymbol{r}, t) = \langle u_i(\boldsymbol{x}, t)u_j(\boldsymbol{x}+\boldsymbol{r}, t)\rangle$, with $\boldsymbol{r}$ the vector separating the two points in physical space. This tensor is defined as

$$\langle \hat{u}_i^*(\boldsymbol{p}, t)\hat{u}_j(\boldsymbol{k}, t)\rangle = \delta(\boldsymbol{k}-\boldsymbol{p})\hat{R}_{ij}(\boldsymbol{k}, t), \tag{2.2}$$

where $\hat{u}_i(\boldsymbol{k}, t)$ is the Fourier transform of the fluctuating velocity $u_i(\boldsymbol{x}, t)$, and the operators * and $\langle\,\rangle$ denote complex conjugate and ensemble average respectively. From the counterpart of (2.1) in Fourier space and using definition (2.2) one derives the governing equation for the tensor $\hat{R}_{ij}(\boldsymbol{k}, t)$ (see, e.g., Sagaut & Cambon (2008)),

$$\left(\frac{\partial}{\partial t} - \lambda_{ln}k_l\frac{\partial}{\partial k_n} + 2\nu k^2\right)\hat{R}_{ij}(\boldsymbol{k}, t) + M_{in}(\boldsymbol{k})\hat{R}_{nj}(\boldsymbol{k}, t) + M_{jn}(\boldsymbol{k})\hat{R}_{ni}(\boldsymbol{k}, t) = T_{ij}(\boldsymbol{k}, t), \tag{2.3}$$

with the linear operator induced by mean-velocity gradients

$$M_{ij}(\boldsymbol{k}) = \left(\delta_{in} - 2\frac{k_ik_n}{k^2}\right)\lambda_{nj}. \tag{2.4}$$

The transfer tensor $T_{ij}(\boldsymbol{k}, t)$ in (2.3) accounts for triadic interactions between vectors $\boldsymbol{k}$, $\boldsymbol{p}$ and $\boldsymbol{q}$ so that they form a triangle. It is possible to disentangle contributions from the tensorial transfer term, with zero integral over $\boldsymbol{k}$, and contributions from the fluctuating pressure $W_{ij}(\boldsymbol{k}, t)$ as follows:

$$T_{ij}(\boldsymbol{k}, t) = P_{in}(\boldsymbol{k})\tau_{nj}(\boldsymbol{k}, t) + P_{jn}(\boldsymbol{k})\tau^*_{ni}(\boldsymbol{k}, t) = \tau_{ij}(\boldsymbol{k}, t) + \tau^*_{ji}(\boldsymbol{k}, t) \underbrace{- \frac{k_ik_n}{k^2}\tau_{nj}(\boldsymbol{k}, t) - \frac{k_jk_n}{k^2}\tau^*_{ni}(\boldsymbol{k}, t)}_{W_{ij}(\boldsymbol{k}, t)}. \tag{2.5}$$

The tensor $W_{ij}(\boldsymbol{k}, t)$ contains a possible RTI mechanism, its integral over $\boldsymbol{k}$ gives the nonlinear – so-called slow – pressure–strain rate tensor, and both the $T_{ij}(\boldsymbol{k}, t)$ and $W_{ij}(\boldsymbol{k}, t)$ terms originate from the same tensor $\tau_{ij}(\boldsymbol{k}, t)$. In the same way, the tensor $\tau_{ij}(\boldsymbol{k}, t)$,

$$\tau_{ij}(\boldsymbol{k}, t) = k_n \iiint S_{ijn}(\boldsymbol{k}, \boldsymbol{p}, t)\,\mathrm{d}^3\boldsymbol{p}, \tag{2.6}$$

is given from the third-order three-point spectral tensor $S_{ijn}(\boldsymbol{k}, \boldsymbol{p}, t)$, defined by

$$\mathrm{i}\langle \hat{u}_i(\boldsymbol{q}, t)\hat{u}_j(\boldsymbol{k}, t)\hat{u}_n(\boldsymbol{p}, t)\rangle = \delta(\boldsymbol{k}+\boldsymbol{p}+\boldsymbol{q})S_{ijn}(\boldsymbol{k}, \boldsymbol{p}, t), \tag{2.7}$$

and the closure is applied to the equation that governs the latter tensor, as shown in § 2.4.

2.2. *The* $(\mathscr{E}, Z)$ *decomposition*

A general decomposition of the second-order spectral tensor $\hat{R}_{ij}(\boldsymbol{k}, t)$, for arbitrary anisotropy, results from a trace–deviator splitting, restricted to the plane normal to the wavevector $\boldsymbol{k}$ by virtue of incompressibility. It is consistent with the threefold decomposition in terms of the isotropic contribution, directional anisotropy and polarization anisotropy, from (1.2) (Cambon & Jacquin 1989; Cambon & Rubinstein 2006; Sagaut & Cambon 2008). The first term in the decomposition (1.2) of $\hat{R}_{ij}(\boldsymbol{k}, t)$ corresponds to its isotropic part. The second term characterizes 'directional anisotropy' via the scalar $\mathscr{E}^{(dir)}(\boldsymbol{k},t)=\mathscr{E}(\boldsymbol{k},t)-E(k,t)/(4\pi k^2)$, which corresponds to the difference between the energy density $\mathscr{E}(\boldsymbol{k},t)$ and its spherical average. The third term, which is generated by the scalar $Z(\boldsymbol{k},t)$, characterizes the 'polarization anisotropy', or tensorial anisotropy, at a given wavevector.

Following Cambon & Jacquin (1989), the contribution from the polarization anisotropy is generated by the single complex-valued pseudoscalar term $Z(\boldsymbol{k},t)$ as follows:

$$\hat{R}_{ij}^{(pol)}(\boldsymbol{k},t)=\mathrm{Re}(Z(\boldsymbol{k},t)N_i(\boldsymbol{k})N_j(\boldsymbol{k})), \tag{2.8}$$

with

$$Z(\boldsymbol{k},t)=\tfrac{1}{2}\hat{R}_{mn}(\boldsymbol{k},t)N_m(\boldsymbol{k})^*N_n(\boldsymbol{k})^*, \tag{2.9}$$

where the vector $\boldsymbol{N}(\boldsymbol{k})$, introduced by Cambon & Jacquin (1989) and recovered independently by Waleffe (1992) as the helical mode, is defined by

$$\boldsymbol{N}(\boldsymbol{k})=\boldsymbol{e}^{(2)}(\boldsymbol{k})-\mathrm{i}\boldsymbol{e}^{(1)}(\boldsymbol{k}),\quad \boldsymbol{e}^{(1)}(\boldsymbol{k})=\frac{\boldsymbol{k}\times\boldsymbol{n}}{|\boldsymbol{k}\times\boldsymbol{n}|},\quad \boldsymbol{e}^{(2)}(\boldsymbol{k})=\boldsymbol{e}^{(3)}(\boldsymbol{k})\times\boldsymbol{e}^{(1)}(\boldsymbol{k}),\quad \boldsymbol{e}^{(3)}(\boldsymbol{k})=\frac{\boldsymbol{k}}{k}. \tag{2.10a–d}$$

Here, $(\boldsymbol{e}^{(1)}(\boldsymbol{k}),\boldsymbol{e}^{(2)}(\boldsymbol{k}),\boldsymbol{e}^{(3)}(\boldsymbol{k}))$ is an orthonormal right-handed frame of reference associated with a privileged direction $\boldsymbol{n}$, which is often referred to as the Craya–Herring frame (Herring 1974; Sagaut & Cambon 2008). The realizability condition, or condition for the Hermitian covariance matrix $\hat{\boldsymbol{R}}(\boldsymbol{k},t)$ to be definite-positive, can be written as (Cambon, Mansour & Godeferd 1997)

$$|Z(\boldsymbol{k},t)|\leqslant\mathscr{E}(\boldsymbol{k},t)\quad\forall\boldsymbol{k},t. \tag{2.11}$$

2.3. *Lin equations for the* $(\mathscr{E},Z)$ *decomposition*

When taking into account the decomposition (1.2) of the second-order spectral tensor $\hat{R}_{ij}(\boldsymbol{k},t)$ with equation (2.8), (2.3) is equivalent to the following set of two equations in terms of $\mathscr{E}(\boldsymbol{k},t)$ and $Z(\boldsymbol{k},t)$:

$$\left(\frac{\partial}{\partial t}-\lambda_{ln}k_l\frac{\partial}{\partial k_n}+2\nu k^2\right)\mathscr{E}(\boldsymbol{k},t)-\mathscr{E}(\boldsymbol{k},t)S_{ij}\alpha_i\alpha_j+\mathrm{Re}(Z(\boldsymbol{k},t)S_{ij}N_i(\boldsymbol{k})N_j(\boldsymbol{k}))=T^{(\mathscr{E})}(\boldsymbol{k},t), \tag{2.12}$$

$$\begin{aligned}&\left(\frac{\partial}{\partial t}-\lambda_{ln}k_l\frac{\partial}{\partial k_n}+2\nu k^2\right)Z(\boldsymbol{k},t)-Z(\boldsymbol{k},t)S_{ij}\alpha_i\alpha_j\\&+\mathscr{E}(\boldsymbol{k},t)S_{ij}N_i^*(\boldsymbol{k})N_j^*(\boldsymbol{k})-2\mathrm{i}Z(\boldsymbol{k},t)\left(\frac{W_l}{2}\alpha_l-\Omega_E\right)=T^{(Z)}(\boldsymbol{k},t),\end{aligned} \tag{2.13}$$

where $\alpha_i=k_i/k$, $S_{ij}=(\lambda_{ij}+\lambda_{ji})/2$ is the symmetric part of the mean-velocity gradient and $W_i=\epsilon_{ijn}\lambda_{nj}$ refers to its antisymmetric part (mean vorticity). The rotation vector component Ω_E expresses the solid-body motion of the local Craya frame with respect to a fixed frame of reference, following characteristic lines. The expression of Ω_E is given by

$$\Omega_E=-\frac{k}{|\boldsymbol{k}\times\boldsymbol{n}|}\lambda_{ln}n_le_n^{(1)}-\lambda_{ln}e_l^{(2)}e_n^{(1)}. \tag{2.14}$$

The derivation of the above expressions may be found in Cambon *et al.* (2013), but with an error of sign in front of the rotation terms in (2.13). The nonlinear transfer terms on the right-hand sides of (2.12) and (2.13) are obtained by applying the $(\mathscr{E}, Z)$ decomposition to the transfer term $T_{ij}(\boldsymbol{k}, t)$ in (2.3):

$$T^{(\mathscr{E})}(\boldsymbol{k}, t) = \tfrac{1}{2}T_{ii}(\boldsymbol{k}, t) = \tfrac{1}{2}(\tau_{ii}(\boldsymbol{k}, t) + \tau_{ii}^{*}(\boldsymbol{k}, t)), \tag{2.15}$$

$$T^{(Z)}(\boldsymbol{k}, t) = \tfrac{1}{2}T_{ij}(\boldsymbol{k}, t)N_i^*(\boldsymbol{k})N_j^*(\boldsymbol{k}) = \tfrac{1}{2}(\tau_{ij}(\boldsymbol{k}, t) + \tau_{ji}^{*}(\boldsymbol{k}, t))N_i^*(\boldsymbol{k})N_j^*(\boldsymbol{k}), \tag{2.16}$$

where the tensor $\tau_{ij}(\boldsymbol{k}, t)$ is defined by equations (2.5) and (2.6). As mentioned earlier, $T_{ij}(\boldsymbol{k}, t)$ includes both the ‘true’ transfer tensor, with zero integral, and the contribution $W_{ij}(\boldsymbol{k}, t)$ involved in the RTI effect. The latter tensor can be generated from a scalar transfer term $T^{(RTI)}(\boldsymbol{k}, t)$ according to

$$W_{ij}(\boldsymbol{k}, t) = -\mathrm{Re}(T^{(RTI)}(\boldsymbol{k}, t)(\alpha_i N_j(\boldsymbol{k}) + \alpha_j N_i(\boldsymbol{k}))), \tag{2.17}$$

consistently with $\tau_{ij}(\boldsymbol{k}, t)k_j = 0$, $\tau_{ij}(\boldsymbol{k}, t)k_i \neq 0$ and

$$T^{(RTI)}(\boldsymbol{k}, t) = \alpha_i(\tau_{ij}(\boldsymbol{k}, t) + \tau_{ji}^{*}(\boldsymbol{k}, t))N_j^*(\boldsymbol{k}) = \alpha_i\tau_{ij}(\boldsymbol{k}, t)N_j^*(\boldsymbol{k}). \tag{2.18}$$

2.4. *The EDQNM closure for transfer terms*

In this section, a ‘triadic’ closure is applied to the equations governing the third-order spectral tensor $S_{ijn}(\boldsymbol{k}, \boldsymbol{p}, t)$ defined by (2.7), from which the term $\tau_{ij}(\boldsymbol{k}, t)$ in (2.6) is derived. From the counterpart of (2.1) in Fourier space and (2.7), its dynamics is obtained via

$$\begin{aligned}\left(\frac{\partial}{\partial t} + \nu(k^2 + p^2 + q^2) - \lambda_{lm}\left(k_l\frac{\partial}{\partial k_m} + p_l\frac{\partial}{\partial p_m}\right)\right) S_{ijn}(\boldsymbol{k}, \boldsymbol{p}, t) + M_{im}(\boldsymbol{q})S_{mjn}(\boldsymbol{k}, \boldsymbol{p}, t)&\\ + M_{jm}(\boldsymbol{k})S_{imn}(\boldsymbol{k}, \boldsymbol{p}, t) + M_{nm}(\boldsymbol{p})S_{ijm}(\boldsymbol{k}, \boldsymbol{p}, t) = T_{ijn}(\boldsymbol{k}, \boldsymbol{p}, t),&\end{aligned} \tag{2.19}$$

where $\boldsymbol{k} + \boldsymbol{p} + \boldsymbol{q} = \boldsymbol{0}$ and $T_{ijn}(\boldsymbol{k}, \boldsymbol{p}, t)$ is expressed in terms of a fourth-order spectral tensor

$$\begin{aligned}T_{ijn}(\boldsymbol{k}, \boldsymbol{p}, t) = P_{imp}(\boldsymbol{q}) \iiint S_{mpjn}(\boldsymbol{r}, \boldsymbol{k}, \boldsymbol{p}, t)\, \mathrm{d}^3\boldsymbol{r} + P_{jmp}(\boldsymbol{k}) \iiint S_{mpin}(\boldsymbol{r}, \boldsymbol{q}, \boldsymbol{p}, t)\, \mathrm{d}^3\boldsymbol{r}&\\ + P_{nmp}(\boldsymbol{p}) \iiint S_{mpij}(\boldsymbol{r}, \boldsymbol{q}, \boldsymbol{k}, t)\, \mathrm{d}^3\boldsymbol{r},&\end{aligned} \tag{2.20}$$

with

$$\langle \hat{u}_m(\boldsymbol{r})\hat{u}_p(\boldsymbol{r}')\hat{u}_j(\boldsymbol{k})\hat{u}_n(\boldsymbol{p})\rangle = S_{mpjn}(\boldsymbol{r}, \boldsymbol{k}, \boldsymbol{p})\delta(\boldsymbol{r} + \boldsymbol{r}' + \boldsymbol{k} + \boldsymbol{p}). \tag{2.21}$$

So far, the expressions that have been given for the governing equations for the second- and third-order spectral tensors are exact. They strictly reproduce the infinite hierarchy of moments up to $N = 3$, with equations for N-order moments having both linear closed terms and contributions from $N + 1$ moments being induced by basic nonlinearity. We now want to break this infinite hierarchy at the order $N = 3$. Equation (2.19) can be rewritten in the following form:

$$\left(\frac{\partial}{\partial t} + \nu(k^2 + p^2 + q^2)\right) S_{ijn}(\boldsymbol{k}, \boldsymbol{p}, t) = T_{ijn}(\boldsymbol{k}, \boldsymbol{p}, t) + L_{ijn}(\boldsymbol{k}, \boldsymbol{p}, t) = R_{ijn}(\boldsymbol{k}, \boldsymbol{p}, t), \tag{2.22}$$

where the tensor $R_{ijn}(\boldsymbol{k}, \boldsymbol{p}, t)$ gathers the linear operators induced by mean-velocity gradients through $L_{ijn}(\boldsymbol{k}, \boldsymbol{p}, t)$ and the fourth-order spectral tensor $T_{ijn}(\boldsymbol{k}, \boldsymbol{p}, t)$.

The problem then is to determine a closed expression for $R_{ijn}(\boldsymbol{k}, \boldsymbol{p}, t)$. The historical procedure, developed for homogeneous isotropic turbulence, starts from the quasinormal (QN) approximation (Millionschikov 1941; Proudman & Reid 1954), which states that the fluctuating velocity probability distributions are not too far from normal laws, in order to close the nonlinear contributions in $R_{ijn}(\boldsymbol{k}, \boldsymbol{p}, t)$. This assumption translates into vanishing fourth-order cumulants and can be written as

$$\begin{aligned}\langle \hat{u}_m(\boldsymbol{r})\hat{u}_p(\boldsymbol{r}')\hat{u}_j(\boldsymbol{k})\hat{u}_n(\boldsymbol{p})\rangle &= \langle \hat{u}_m(\boldsymbol{r})\hat{u}_p(\boldsymbol{r}')\rangle\langle \hat{u}_j(\boldsymbol{k})\hat{u}_n(\boldsymbol{p})\rangle + \langle \hat{u}_m(\boldsymbol{r})\hat{u}_j(\boldsymbol{k})\rangle\langle \hat{u}_p(\boldsymbol{r}')\hat{u}_n(\boldsymbol{p})\rangle \\ &\quad + \langle \hat{u}_m(\boldsymbol{r})\hat{u}_n(\boldsymbol{p})\rangle\langle \hat{u}_p(\boldsymbol{r}')\hat{u}_j(\boldsymbol{k})\rangle. \end{aligned} \tag{2.23}$$

Injecting (2.23) into (2.20) and using definitions (2.2) and (2.21) leads to the quasinormal contribution of the transfer term $T_{ijn}(\boldsymbol{k}, \boldsymbol{p}, t)$:

$$\begin{aligned}T^{(QN)}_{ijl}(\boldsymbol{k}, \boldsymbol{p}, t) &= 2\,(P_{imn}(\boldsymbol{q})\hat{R}_{mj}(\boldsymbol{k}, t)\hat{R}_{nl}(\boldsymbol{p}, t) + P_{jmn}(\boldsymbol{k})\hat{R}_{ml}(\boldsymbol{p}, t)\hat{R}_{ni}(\boldsymbol{q}, t) \\ &\quad + P_{lmn}(\boldsymbol{p})\hat{R}_{mi}(\boldsymbol{q}, t)\hat{R}_{nj}(\boldsymbol{k}, t)),\end{aligned} \tag{2.24}$$

with $P_{inm}(\boldsymbol{k}) = 1/2(k_m P_{in}(\boldsymbol{k}) + k_n P_{im}(\boldsymbol{k}))$; the projector $P_{ij}(\boldsymbol{k})$ is defined in (1.1). However, it was shown by O'Brien & Francis (1963) and Ogura (1963) that the purely quasinormal approximation fails in decaying isotropic turbulence for long elapsed times, yielding negative energy spectra at small k. Orszag (1970) showed that the improper treatment of relaxation effects in the purely quasinormal approximation lies at the origin of this lack of realizability. Consequently, he introduced an eddy viscosity, or eddy-damping (ED), term in the governing equation for third-order correlations. Without any additional assumption, $R_{ijn}(\boldsymbol{k}, \boldsymbol{p}, t)$ from (2.22) can be written as

$$R_{ijn}(\boldsymbol{k}, \boldsymbol{p}, t) = T^{(QN)}_{ijn}(\boldsymbol{k}, \boldsymbol{p}, t) + T^{(IV)}_{ijn}(\boldsymbol{k}, \boldsymbol{p}, t) + L_{ijn}(\boldsymbol{k}, \boldsymbol{p}, t). \tag{2.25}$$

In this equation, the only unknown, and unclosed, term is $T^{(IV)}_{ijn}(\boldsymbol{k}, \boldsymbol{p}, t)$, which represents the contribution from fourth-order cumulants. A natural extension of Orszag's introduction of eddy damping is to write

$$T^{(IV)}_{ijn}(\boldsymbol{k}, \boldsymbol{p}, t) = -(\eta(k, t) + \eta(p, t) + \eta(q, t))S_{ijn}(\boldsymbol{k}, \boldsymbol{p}, t), \tag{2.26}$$

while keeping in mind that fourth-order cumulants may act as a linear relaxation of triple correlations, which will reinforce the dissipative operator in (2.22) when added to the purely viscous terms on its left-hand side. The simple relationship (2.26), which is isotropic with a single eddy-damping scalar term, can be discussed with respect to two-time triadic theories as follows. In isotropic turbulence, the EDQNM is possibly derived from the basic DIA (Kraichnan 1959). However, such a derivation of $\eta(k, t)$ from the two-time response tensor is unsatisfactory and yields an inappropriate 'sweeping' time scale, so that more complicated Lagrangian theories must be called into play, such as Lagrangian-history DIA (LHDIA) (Kraichnan & Herring 1978) and Lagrangian renormalized approximation (LRA) (Kaneda 1981). The identification of a possible anisotropic shear-dependent alternative to (2.26) from these theories is a difficult task because they are essentially non-Markovian, and reduction to a single-time expression was only performed at very weak anisotropy (see, e.g., Yoshida, Ishihara & Kaneda (2003) for LRA). Finally, the test-field model (Kraichnan 1972), as an almost Markovian theory, is fully consistent with a linear relationship such as (2.26), but with a possibly more complex tensorial structure, too intricate here to be applied to a practical model. Concerning the choice of the relevant time scale to evaluate $\eta(k, t)$, many proposals exist, with 'sweeping', 'straining', linear and nonlinear time scales, see, e.g., Schiestel (1987), Kim & Chen (1989), Rubinstein (1996) and Zhou (2010). In the presence of mean shear, one can introduce a scalar mean straining time scale based on $\sqrt{\lambda_{ij}\lambda_{ij}}$, with λ_{ij} the mean-velocity gradient. However, the effects of mean shear/strain are explicit and closed (in terms of third-order correlations) in (2.22) via the operator $L_{ijn}(\boldsymbol{k}, \boldsymbol{p}, t)$. The contribution of the latter tensor was considered and analytically solved in previous EDQNM versions, which are mentioned in the introduction (such as, e.g., the model of Cambon & Jacquin (1989) for rotating flows). However, this approach will not be considered here for three reasons: (i) it was motivated and really needed for the study of anisotropic flows without energy production and in the presence of interacting dispersive waves leading the dynamics of triple correlations, which is not the general case here; (ii) it renders the tensorial structure of the EDQNM model much more complicated, via a threefold product of Green's functions, and explicitly dependent on the type of mean shear, preventing easy further projection on spherical harmonics; (iii) it is not correct when the direct (linear) effect of the mean shear/strain yields exponential growth, with a lack of convergence of the time integral (Cambon & Scott 1999). The eddy-damping coefficient $\eta(k, t)$ is finally chosen as

$$\eta(k, t) = A\sqrt{\int_0^k p^2 E(p, t)\, \mathrm{d}p}, \tag{2.27}$$

following Pouquet *et al.* (1975), which is an improved variant of Orszag (1970)'s proposal. The constant is fixed at $A = 0.36$ to recover a well-admitted value of the Kolmogorov constant (André & Lesieur 1977). The same equation is used in Weinstock (2013). Equation (2.22) can be now integrated using (2.25), (2.24) and (2.26), (2.27), and neglecting the contribution of $L_{ijn}(\boldsymbol{k}, \boldsymbol{p}, t)$. The solution thus obtained involves time integrals that are further simplified by a Markovianization procedure, which amounts to truncating the proper time memory of triple correlations. Even in the isotropic case, the eddy damping allows *a posteriori* Markovianization to be justified, arguing that the time variation is much more rapid in the exponential eddy-damping term than in the second-order moments present in the quasinormal term. Further details can be found in Cambon *et al.* (1981) and Sagaut & Cambon (2008). In the end, this anisotropic EDQNM closure for the tensor $\tau_{ij}(\boldsymbol{k}, t)$ defined by (2.6) amounts to

$$\tau_{ij}(\boldsymbol{k}, t) = k_l \iiint \theta_{kpq} T^{(QN)}_{ijl}(\boldsymbol{k}, \boldsymbol{p}, t)\, \mathrm{d}^3\boldsymbol{p}, \tag{2.28}$$

where

$$\theta_{kpq} = \frac{1 - \mathrm{e}^{-\mu_{kpq} t}}{\mu_{kpq}}, \quad \mu_{kpq} = \nu(k^2 + p^2 + q^2) + \eta(k, t) + \eta(p, t) + \eta(q, t). \tag{2.29a,b}$$

The expression (2.28) of $\tau_{ij}(\boldsymbol{k}, t)$ obtained from the EDQNM approximation is injected into (2.15) and (2.16) in order to obtain closed-form expressions of the transfer terms $T^{(\mathscr{E})}(\boldsymbol{k}, t)$ and $T^{(Z)}(\boldsymbol{k}, t)$:

$$\begin{aligned} T^{(\mathscr{E})}(\boldsymbol{k}, t) = \iiint & \theta_{kpq} 2kp\, [(\mathscr{E}'' + \mathrm{Re}\, X'')[(xy + z^3)(\mathscr{E}' - \mathscr{E}) - z(1 - z^2)(\mathrm{Re}\, X' - \mathrm{Re}\, X)] \\ & + \mathrm{Im}\, X''(1 - z^2)(x\, \mathrm{Im}\, X - y\, \mathrm{Im}\, X')]\, \mathrm{d}^3\boldsymbol{p}, \end{aligned} \tag{2.30}$$

$$T^{(Z)}(\boldsymbol{k},t)=\iiint \theta_{kpq}2kp\mathrm{e}^{-2\mathrm{i}\lambda}\left[(\mathscr{E}''+\operatorname{Re}X'')\left[(xy+z^3)(\operatorname{Re}X'-X)-z(1-z^2)(\mathscr{E}'-\mathscr{E})\right.\right.$$
$$\left.\left.+\mathrm{i}(y^2-z^2)\operatorname{Im}X'\right]+\mathrm{i}\operatorname{Im}X''(1-z^2)[x(\mathscr{E}+X)-\mathrm{i}y\operatorname{Im}X']\right]\mathrm{d}^3\boldsymbol{p}, \tag{2.31}$$

with $\mathscr{E}=\mathscr{E}(\boldsymbol{k},t)$, $\mathscr{E}'=\mathscr{E}(\boldsymbol{p},t)$, $\mathscr{E}''=\mathscr{E}(\boldsymbol{q},t)$, $X=Z(\boldsymbol{k},t)\mathrm{e}^{2\mathrm{i}\lambda}$, $X'=Z(\boldsymbol{p},t)\mathrm{e}^{2\mathrm{i}\lambda'}$, $X''=Z(\boldsymbol{q},t)\mathrm{e}^{2\mathrm{i}\lambda''}$, $x=-\boldsymbol{p}\cdot\boldsymbol{q}/(pq)$, $y=-\boldsymbol{k}\cdot\boldsymbol{q}/(kq)$ and $z=-\boldsymbol{k}\cdot\boldsymbol{p}/(kp)$. Here, λ, λ' and λ'' are angles that characterize the rotation of the plane of the triad around $\boldsymbol{k}$, $\boldsymbol{p}$ and $\boldsymbol{q}$ respectively; x, y and z refer to the cosines of the internal angles of the triangle formed by the triad. The above expressions for the transfer terms $T^{(\mathscr{E})}(\boldsymbol{k},t)$ and $T^{(Z)}(\boldsymbol{k},t)$ are also derived in Cambon *et al.* (1997) in a different way. Similarly, one can deduce a closed-form expression of the transfer term $T^{(RTI)}(\boldsymbol{k},t)$ defined by (2.18), which generates the 'slow' component of the pressure–strain rate tensor:

$$T^{(RTI)}(\boldsymbol{k},t)=\iiint \theta_{kpq}2\mathrm{e}^{-\mathrm{i}\lambda}p(xy+z)\sqrt{1-z^2}(\mathscr{E}''+\operatorname{Re}X'')$$
$$\times[(\mathscr{E}+X)(zk-qx)-k(z(\mathscr{E}'+\operatorname{Re}X')-\mathrm{i}\operatorname{Im}X')]\,\mathrm{d}^3\boldsymbol{p}. \tag{2.32}$$

3. Dynamical equations for spherically averaged descriptors

Strictly speaking, the Lin equations (2.12) and (2.13) with the closed-form expressions (2.30) and (2.31) of the transfer terms can be solved. However, important practical difficulties arise from the $\boldsymbol{k}$ dependence of the second-order spectral tensor $\hat{R}_{ij}(\boldsymbol{k},t)$, or equivalently from those of $\mathscr{E}(\boldsymbol{k},t)$ and $Z(\boldsymbol{k},t)$. In order to circumvent these difficulties, one solution is to integrate analytically the closed Lin equations over a sphere of radius k. This analytical integration requires a representation of the tensor $\hat{R}_{ij}(\boldsymbol{k},t)$, which is described in § 3.1. This representation involves spherically averaged descriptors whose governing equations, which are the main result of this paper, are derived in the remainder of this section. Limitations of the model in terms of anisotropy intensity are quantified in § 3.5.

3.1. *Representation of the second-order spectral tensor in terms of spherically averaged descriptors*

Here, we use for $\hat{R}_{ij}(\boldsymbol{k},t)$ the representation proposed by Cambon & Rubinstein (2006). This representation involves spherically averaged descriptors and is obtained by treating directionality and polarization anisotropy separately. It is written as

$$\hat{R}_{ij}(\boldsymbol{k},t)=\underbrace{\frac{E(k,t)}{4\pi k^2}P_{ij}(\boldsymbol{k})}_{\hat{R}^{(iso)}_{ij}(\boldsymbol{k},t)}\underbrace{-15\frac{E(k,t)}{4\pi k^2}P_{ij}(\boldsymbol{k})H^{(dir)}_{pq}(k,t)\alpha_p\alpha_q}_{\hat{R}^{(dir)}_{ij}(\boldsymbol{k},t)}$$
$$+\underbrace{5\frac{E(k,t)}{4\pi k^2}\left(P_{ip}(\boldsymbol{k})P_{jq}(\boldsymbol{k})+\frac{1}{2}P_{ij}(\boldsymbol{k})\alpha_p\alpha_q\right)H^{(pol)}_{pq}(k,t)}_{\hat{R}^{(pol)}_{ij}(\boldsymbol{k},t)}, \tag{3.1}$$

or equivalently

$$\mathscr{E}(\boldsymbol{k},t)=\frac{E(k,t)}{4\pi k^2}(1-15H^{(dir)}_{ij}(k,t)\alpha_i\alpha_j),\quad Z(\boldsymbol{k},t)=\frac{5}{2}\frac{E(k,t)}{4\pi k^2}H^{(pol)}_{ij}(k,t)N^*_i(\boldsymbol{k})N^*_j(\boldsymbol{k}), \tag{3.2a,b}$$

where the tensor $P_{ij}(\boldsymbol{k})$ is defined in (1.1) and $\alpha_i = k_i/k$. The tensors $\hat{R}^{(iso)}_{ij}(\boldsymbol{k}, t)$, $\hat{R}^{(dir)}_{ij}(\boldsymbol{k}, t)$ and $\hat{R}^{(pol)}_{ij}(\boldsymbol{k}, t)$ identify the isotropic, directional and polarization parts of $\hat{R}_{ij}(\boldsymbol{k}, t)$ respectively. The representation (3.1) is constructed so that the trace-free tensors $H^{(dir)}_{ij}(k, t)$ and $H^{(pol)}_{ij}(k, t)$, which depend only on k, measure the directional anisotropy and polarization anisotropy according to (1.5). Injecting the representation of $\mathscr{E}(\boldsymbol{k}, t)$ and $Z(\boldsymbol{k}, t)$ (3.2) into (2.12) and (2.13) and (2.30) and (2.31) allows us to integrate the latter analytically over a sphere of radius k and to derive a system of governing equations in terms of the spherically averaged descriptors $E(k, t)$, $H^{(dir)}_{ij}(k, t)$ and $H^{(pol)}_{ij}(k, t)$. In view of (3.1), (3.2) and (1.4), the latter completely determine the second-order spectral tensor $\hat{R}_{ij}(\boldsymbol{k}, t)$ and its spherically integrated counterpart $\varphi_{ij}(k, t)$, however restricted to moderate anisotropy. This point is discussed in § 3.5.

3.2. *Dynamics, final closure*

The system of governing equations for the spherically averaged descriptors $E(k, t)$, $H^{(dir)}_{ij}(k, t)$ and $H^{(pol)}_{ij}(k, t)$, which is the main result of this article, is written as follows:

$$\left(\frac{\partial}{\partial t} + 2\nu k^2\right) E(k, t) = S^L(k, t) + T(k, t), \tag{3.3}$$

$$\left(\frac{\partial}{\partial t} + 2\nu k^2\right) E(k, t) H^{(dir)}_{ij}(k, t) = S^{L(dir)}_{ij}(k, t) + S^{NL(dir)}_{ij}(k, t), \tag{3.4}$$

$$\left(\frac{\partial}{\partial t} + 2\nu k^2\right) E(k, t) H^{(pol)}_{ij}(k, t) = S^{L(pol)}_{ij}(k, t) + S^{NL(pol)}_{ij}(k, t), \tag{3.5}$$

with

$$2\left(\frac{\delta_{ij}}{3} T(k, t) + S^{NL(dir)}_{ij}(k, t) + S^{NL(pol)}_{ij}(k, t)\right) = S_{ij}(k, t) + P_{ij}(k, t). \tag{3.6}$$

The tensors $S^L(k, t)$, $S^{L(dir)}_{ij}(k, t)$ and $S^{L(pol)}_{ij}(k, t)$ account for the linear terms corresponding to the interactions with the mean flow, whereas $T(k, t)$, $S^{NL(dir)}_{ij}(k, t)$ and $S^{NL(pol)}_{ij}(k, t)$ correspond to nonlinear transfer terms. The tensor $P_{ij}(k, t)$ is the spherically integrated spectral counterpart of the slow pressure–strain rate tensor, to which an RTI is conventionally attributed. The tensor $S_{ij}(k, t)$ corresponds to a 'true' transfer tensor with $\int_0^\infty S_{ij}(k, t)\,\mathrm{d}k = 0\;\forall t$. Since the tensors $H^{(dir)}_{ij}(k, t)$ and $H^{(pol)}_{ij}(k, t)$ are symmetric and trace-free, the system (3.3)–(3.5) forms a set of 11 independent equations.

3.3. *Closure for the linear terms induced by mean-gradient effects*

These terms are exact and linear in the equation governing the full spectral tensor, or equivalently $\mathscr{E}(\boldsymbol{k}, t)$ and $Z(\boldsymbol{k}, t)$. Taken independently with zero contribution from third-order correlations, they reflect the RDT limit for the evolution of two-point second-order velocity correlations. In order to obtain the corresponding spherically averaged terms $S^L(k, t)$, $S^{L(dir)}_{ij}(k, t)$ and $S^{L(pol)}_{ij}(k, t)$, one has to analytically solve the spherical averaging of tensorial products of vectors $\boldsymbol{\alpha} = \boldsymbol{k}/k$. This is done following the procedure described in Cambon *et al.* (1981). Performing the spherical integration of the linear terms in (2.3) or that of the linear terms in (2.12), (2.13) with the representation (3.1) or (3.2) leads to

$$S^L(k,t) = -2\mathsf{S}_{lm}\frac{\partial}{\partial k}(kEH^{(dir)}_{lm}) - 2E\mathsf{S}_{lm}\left(H^{(dir)}_{lm} + H^{(pol)}_{lm}\right), \tag{3.7}$$

$$\begin{aligned} S^{L(dir)}_{ij}(k,t) = {} & \frac{2}{15}\mathsf{S}_{ij}E - \frac{2}{7}E\left(\mathsf{S}_{jl}H^{(pol)}_{il} + \mathsf{S}_{il}H^{(pol)}_{jl} - \frac{2}{3}\mathsf{S}_{lm}H^{(pol)}_{lm}\delta_{ij}\right) \\ & + \frac{2}{7}\left(\mathsf{S}_{il}\frac{\partial}{\partial k}(kEH^{(dir)}_{lj}) + \mathsf{S}_{lj}\frac{\partial}{\partial k}(kEH^{(dir)}_{li}) - \frac{2}{3}\mathsf{S}_{lm}\frac{\partial}{\partial k}(kEH^{(dir)}_{lm})\delta_{ij}\right) \\ & - \frac{1}{7}E\left(\mathsf{S}_{jl}H^{(dir)}_{li} + \mathsf{S}_{il}H^{(dir)}_{lj} - \frac{2}{3}\mathsf{S}_{lm}H^{(dir)}_{lm}\delta_{ij}\right) + E\left(\mathsf{A}_{jn}H^{(dir)}_{ni} + \mathsf{A}_{in}H^{(dir)}_{jn}\right) \\ & - \frac{1}{15}\mathsf{S}_{ij}\frac{\partial}{\partial k}(kE), \end{aligned} \tag{3.8}$$

$$\begin{aligned} S^{L(pol)}_{ij}(k,t) = {} & -\frac{2}{5}E\mathsf{S}_{ij} - \frac{12}{7}E\left(\mathsf{S}_{lj}H^{(dir)}_{li} + \mathsf{S}_{il}H^{(dir)}_{lj} - \frac{2}{3}\mathsf{S}_{lm}H^{(dir)}_{lm}\delta_{ij}\right) \\ & - \frac{2}{7}\left(\mathsf{S}_{jl}\frac{\partial}{\partial k}(kEH^{(pol)}_{il}) + \mathsf{S}_{il}\frac{\partial}{\partial k}(kEH^{(pol)}_{lj}) - \frac{2}{3}\mathsf{S}_{ln}\frac{\partial}{\partial k}(kEH^{(pol)}_{ln})\delta_{ij}\right) \\ & + \frac{1}{7}E\left(\mathsf{S}_{il}H^{(pol)}_{lj} + \mathsf{S}_{jl}H^{(pol)}_{li} - \frac{2}{3}\mathsf{S}_{lm}H^{(pol)}_{lm}\delta_{ij}\right) \\ & - \frac{1}{3}E\left(\mathsf{A}_{il}H^{(pol)}_{lj} + \mathsf{A}_{jl}H^{(pol)}_{li}\right), \end{aligned} \tag{3.9}$$

with $E = E(k,t)$, $H^{(dir)}_{ij} = H^{(dir)}_{ij}(k,t)$, $H^{(pol)}_{ij} = H^{(pol)}_{ij}(k,t)$, $\mathsf{S}_{ij} = (\lambda_{ij} + \lambda_{ji})/2$, $\mathsf{A}_{ij} = (\lambda_{ij} - \lambda_{ji})/2$; λ_{ij} refers to the mean-flow gradient as previously stated.

3.4. *Closure for the terms mediated by third-order correlations*

The transfer terms $T(k,t)$, $S^{NL(dir)}_{ij}(k,t)$ and $S^{NL(pol)}_{ij}(k,t)$ are obtained from the spherical integration of the expressions of the transfer terms $T^{(\mathscr{E})}(\boldsymbol{k},t)$ and $T^{(Z)}(\boldsymbol{k},t)$ closed by the EDQNM procedure (2.30) and (2.31) and using the representation (3.2) for $\mathscr{E}(\boldsymbol{k},t)$ and $Z(\boldsymbol{k},t)$. It is consistent to retain only linear contributions from the tensors $H^{(dir)}_{ij}(k,t)$ and $H^{(pol)}_{ij}(k,t)$ in the terms present on the right-hand sides of the system (3.3)–(3.5) in view of the discussion in § 3.5. Their low contribution is checked in § 4.7. In anisotropic triadic closure, the new difficulty is to solve the integral over the orientation of the plane of the triad (Cambon *et al.* 1997; Sagaut & Cambon 2008), which is performed analytically. The final results are

$$T(k,t) = \iint_{\Delta_k} \theta_{kpq} 16\pi^2 p^2 k^2 q (xy + z^3)\mathscr{E}''_0(\mathscr{E}'_0 - \mathscr{E}_0)\,\mathrm{d}p\,\mathrm{d}q, \tag{3.10}$$

$$\begin{aligned} S^{NL(dir)}_{ij}(k,t) = \iint_{\Delta_k} & \theta_{kpq} 4\pi^2 p^2 k^2 q \mathscr{E}''_0 \,[(y^2-1)(xy+z^3)(\mathscr{E}'_0 - \mathscr{E}_0)H^{(pol)''}_{ij} \\ & + z(1-z^2)^2\mathscr{E}'_0 H^{(pol)'}_{ij}]\,\mathrm{d}p\,\mathrm{d}q \end{aligned}$$

$$+\iint_{\varDelta_k}\theta_{kpq}8\pi^2p^2k^2q(xy+z^3)\mathscr{E}_0''\,[(3y^2-1)(\mathscr{E}_0'-\mathscr{E}_0)H_{ij}^{(dir)''}$$
$$+(3z^2-1)\mathscr{E}_0'H_{ij}^{(dir)'}-2\mathscr{E}_0H_{ij}^{(dir)}]\,\mathrm{d}p\,\mathrm{d}q, \tag{3.11}$$

$$\begin{aligned} S_{ij}^{NL(pol)}(k,t) \;=\; & \iint_{\varDelta_k}\theta_{kpq}4\pi^2p^2k^2q\mathscr{E}_0''\,[\,(xy+z^3)((1+z^2)\mathscr{E}_0'H_{ij}^{(pol)'}-4\mathscr{E}_0H_{ij}^{(pol)}) \\ & +z(z^2-1)(1+y^2)(\mathscr{E}_0'-\mathscr{E}_0)H_{ij}^{(pol)''}+2z(z^2-y^2)\mathscr{E}_0'H_{ij}^{(pol)'} \\ & +2yx(z^2-1)\mathscr{E}_0H_{ij}^{(pol)''}]\,\mathrm{d}p\,\mathrm{d}q \\ & +\iint_{\varDelta_k}\theta_{kpq}24\pi^2p^2k^2qz(z^2-1)\mathscr{E}_0''\,[\,(y^2-1)(\mathscr{E}_0'-\mathscr{E}_0)H_{ij}^{(dir)''} \\ & +(z^2-1)\mathscr{E}_0'H_{ij}^{(dir)'}]\,\mathrm{d}p\,\mathrm{d}q, \end{aligned} \tag{3.12}$$

$$\begin{aligned} P_{ij}(k,t) \;=\; & \iint_{\varDelta_k}\theta_{kpq}16\pi^2p^2k^2q(yz+x)\mathscr{E}_0''\,[\mathscr{E}_0'\,(y(z^2-y^2)(6H_{ij}^{(dir)''}+H_{ij}^{(pol)''}) \\ & -(xz+y)H_{ij}^{(pol)''})-y(z^2-x^2)\mathscr{E}_0(6H_{ij}^{(dir)''}+H_{ij}^{(pol)''})]\,\mathrm{d}p\,\mathrm{d}q, \end{aligned} \tag{3.13}$$

with $\mathscr{E}_0=(E(k,t))/(4\pi k^2)$, $\mathscr{E}_0'=(E(p,t))/(4\pi p^2)$, $\mathscr{E}_0''=(E(q,t))/(4\pi q^2)$, $H_{ij}^{()}=H_{ij}^{()}(k,t)$, $H_{ij}^{()'}=H_{ij}^{()}(p,t)$ and $H_{ij}^{()''}=H_{ij}^{()}(q,t)$, where $H_{ij}^{()}$ may refer to either $H_{ij}^{(dir)}$ or $H_{ij}^{(pol)}$. The integrals over p and q are performed over the domain $\varDelta_k$, so that k, p and q are the lengths of the sides of the triangle formed by $\boldsymbol{k}$, $\boldsymbol{p}$ and $\boldsymbol{q}$. The expression of the 'true' transfer $S_{ij}(k,t)$ can be deduced from (3.6) and (3.10)–(3.13).

3.5. *Properties of the model*

Spherical averaging of the Lin equations (2.12)–(2.13) allows us to obtain a model for anisotropic turbulence that can be used to calculate anisotropic turbulent flows at both very high and low Reynolds numbers, with good resolution of both large and small scales and over very long evolution times. Besides, (3.3)–(3.5) remain consistent with the decomposition of $\hat{\boldsymbol{R}}(\boldsymbol{k},t)$ in terms of directional anisotropy and polarization anisotropy. However, spherical integration also has a drawback since it implies a loss of information, which restricts the present model to moderately anisotropic flows. Looking at expansions of the scalars $\mathscr{E}(\boldsymbol{k},t)$ and $Z(\boldsymbol{k},t)$ in terms of powers of $\boldsymbol{\alpha}=\boldsymbol{k}/k$, the first approach by Cambon & Rubinstein (2006) can be translated into the following:

$$\mathscr{E}(\boldsymbol{k},t)=\frac{E(k,t)}{4\pi k^2}\left(1+U_{ij}^{(dir)2}(k,t)\alpha_i\alpha_j+U_{ijmn}^{(dir)4}(k,t)\alpha_i\alpha_j\alpha_m\alpha_n+\cdots\right), \tag{3.14}$$

$$Z(\boldsymbol{k},t)=\frac{1}{2}\frac{E(k,t)}{4\pi k^2}\left(U_{ij}^{(pol)2}(k,t)+U_{ijm}^{(pol)3}(k,t)\alpha_m+U_{ijmn}^{(pol)4}(k,t)\alpha_m\alpha_n+\cdots\right)N_i^*(\boldsymbol{k})N_j^*(\boldsymbol{k}). \tag{3.15}$$

The latter form is consistent with both scalar (for (3.14)) and tensor (for (3.15)) spherical harmonic expansion generated by the rotation group SO^3 decomposition, in agreement with Rubinstein, Kurien & Cambon (2015). With the identification

$$U_{ij}^{(dir)2}(k,t)=-15H_{ij}^{(dir)}(k,t),\qquad U_{ij}^{(pol)2}(k,t)=5H_{ij}^{(pol)}(k,t), \tag{3.16a,b}$$

the representation (3.2) is interpreted as the first-order truncation of expansions (3.14) and (3.15). The truncation of (3.14) and (3.15) lies at the origin of the loss of information, which limits the degree of anisotropy that can be investigated with the present model. The degree of anisotropy permitted by the representation (3.1) can be derived from realizability conditions. One may use condition (2.11). In order to derive a simple condition in terms of the tensors $H_{ij}^{(dir)}(k, t)$ and $H_{ij}^{(pol)}(k, t)$, one may also consider the weaker condition $\mathscr{E}(\boldsymbol{k}, t) \geqslant 0\, \forall \boldsymbol{k}, t$, which already proves to be very restrictive. In view of (3.2), this condition is equivalent to

$$\max_i \varLambda_i(H^{(dir)}(k, t)) \leqslant \tfrac{1}{15}\, \forall k, t, \tag{3.17}$$

where $\varLambda_i(H^{(dir)}(k, t))$ refers to the eigenvalues of $H_{ij}^{(dir)}(k, t)$. Condition (3.17) can help to quantify the upper boundary of anisotropy intensity to ensure that the present model represents correctly the corresponding turbulent flow. In § 4.7, criterion (3.17) is computed for the different flow configurations studied in this paper in order to check whether the representation (3.2) and the governing equations (3.3)–(3.5) can describe the corresponding turbulent flow. Since the representation (3.2) is restricted to the description of moderate anisotropy, we discard quadratic contributions from the tensors $H_{ij}^{(dir)}(k, t)$ and $H_{ij}^{(pol)}(k, t)$ which appear when the representation (3.2) is injected into (2.30)–(2.32). It is also important to keep in mind that the nonlinear transfer terms of the system (3.3)–(3.5) are not relevant when the mean flow acts only on triple correlations such as in the case for solid-body rotation, but are restricted to mean flows leading to linear production effects in the equations for second-order correlations. This is due to the specific EDQNM version used in § 2.4. In the end, the present model is suited for the study of turbulent flows where the anisotropy is moderate and where linear effects induced by mean-velocity gradients play a negligible role in the dynamics of triple correlations compared with those directly induced in the equations for second-order correlations. Since only flows dominated by production effects induced by a mean strain or shear are considered in § 4, we expect the EDQNM closure of § 2.4 to be valid in these configurations. Besides, the linear contributions in (3.4) and (3.5) originate from the exact linear terms of (2.12) and (2.13). Accordingly, it is inferred that the main source of possible discrepancies between the predictions obtained with (3.3)–(3.5) and experimental/direct numerical simulation (DNS) results is due to the loss of information following the first-order truncation of (3.14) and (3.15).

4. First applications and results: RTI and effect of mean shear

4.1. *Physical and numerical set-up*

The predictions of the model presented in § 3 are first compared with data from the experiments of Gence & Mathieu (1979, 1980). In these studies, two successive plane strains with different orientations are applied to grid-generated turbulence, and the RTI of the turbulence thus obtained is investigated in the latter experiment. We then consider the experiment of Chen, Meneveau & Katz (2006), where turbulence is subjected to a non-stationary straining–relaxation–destraining cycle. Both linear and nonlinear phenomena come into play in the response of turbulence to this particular straining. The case of turbulence subjected to an axisymmetric expansion or contraction is then investigated. The set-up of the numerical simulations performed with the present model is similar to that of the DNS of Zusi & Perot (2014). In particular, we want to check the ability of the present model to capture the initial increase of anisotropy when the strain is removed, only in the case of axisymmetric expansion, which is observed in the above-mentioned study. The next test case deals with an initially isotropic flow which is suddenly subjected to a mean shear and is then released. A comparison with the use of RDT to initialize the anisotropy of the flow will allow us to validate the linear part of the present model in the case of homogeneous shear turbulence. This case will also allow us to confirm the consistency between the present model and the permanence of large eddies (PLE). Finally, we consider the case where the mean shear is maintained during the evolution of the flow. Homogeneous shear turbulence has been studied experimentally (Tavoularis & Corrsin 1981; Tavoularis 1985; Rohr *et al.* 1988; Tavoularis & Karnik 1989; Shen & Warhaft 2000), numerically (Rogers, Moin & Reynolds 1986; Ishihara, Yoshida & Kaneda 2002; Brethouwer 2005; Isaza & Collins 2009) and theoretically (Lumley 1967; Leslie 1973; Yoshida *et al.* 2003; Weinstock 2013), and the results obtained with the system (3.3)–(3.5) will be compared with the predictions of these different studies. In the last subsection, it is checked that condition (3.17) is verified for all of the flow configurations discussed above.

As briefly mentioned above, concerning the study of the RTI of shear-released turbulence, the anisotropy of the flow can be initialized in two ways. A first possibility consists in deriving analytically an initial anisotropic condition thanks to RDT. The other option is to start with an isotropic field and to generate the anisotropy with the linear terms of (3.3)–(3.5) that account for the interactions with a mean flow. For $St \ll 1$, where S refers to the characteristic shear rate, these two ways of introducing anisotropy must be equivalent. This will help to validate the model developed in this paper. The complete RDT solution for homogeneous shear turbulence can be found in Townsend (1976), Piquet (2001) and Sagaut & Cambon (2008). The energy spectrum used for the RDT calculations, or directly to initialize the simulations, is written as

$$E(k) = C\varepsilon^{2/3}k^{-(5/3)}f(kL)g(k\eta), \tag{4.1}$$

with

$$f(x) = \left(\frac{x}{\left(x^{1.5} + 1.5 - \dfrac{\sigma}{4}\right)^{1/1.5}}\right)^{(5/3)+\sigma}, \quad g(x) = \exp(-5.2((x^4 + 0.4^4)^{1/4} - 0.4)). \tag{4.2a,b}$$

The functions defined by (4.2) have been proposed by Pope (2000) and Meyers & Meneveau (2008) respectively. Here, ε refers to the dissipation rate, L to the integral length scale, η to the Kolmogorov scale, and σ is the slope at large scales of the energy spectrum ($E(k \to 0) \propto k^{\sigma}$). In all simulations we set $\sigma = 2$, which corresponds to Saffman turbulence. The integral scale L and the Reynolds number are prescribed at the beginning of the simulation. As a consequence, η is initialized thanks to the relation $\eta = ((3/20)Re_\lambda^2)^{-(3/4)}L$, where Re_λ is the Reynolds number based on the Taylor microscale $\lambda = \sqrt{10\mathscr{K}\nu/\varepsilon}$. The constant C in (4.1) is adjusted in order to impose the initial value of the turbulent kinetic energy $\mathscr{K}$ so that $\mathscr{K}(t=0)/\tilde{\mathscr{K}_0} = 1$, where $\tilde{\mathscr{K}_0}$ is a reference energy. The spectral mesh used to perform the simulations covers a very broad wavenumber range in the spectral domain. The smallest wavenumber of the mesh k_0 (which roughly corresponds to the largest resolved scale) is chosen so that $k_0 = 10^{-8}k_L(t=0)$, where $k_L = 1/L$ is the wavenumber associated with the integral length scale L. The largest resolved wavenumber k_N is chosen such that a resolution of at least one decade at small scales, with respect to the initial value of the Kolmogorov scale $\eta(t=0)$, is granted. The relation $k_N = 10k_\eta(0)$ is thus imposed, where $k_\eta = 1/\eta$. The total number of elements $N+1$ is recovered so that $k_N = r^N k_0$, where r represents the constant aspect ratio between contiguous elements of the mesh. In the present work, $r = 1.122$, which means that each decade in the spectral space is discretized by 20 mesh elements. The temporal integration is made by a forward Euler scheme, and the Courant–Friedrichs–Lewy condition is based on the Kolmogorov scale (Lesieur 2008).

The anisotropy at the spectral level is evaluated with the deviatoric tensors $H_{ij}^{(dir)}(k, t)$ and $H_{ij}^{(pol)}(k, t)$ introduced in § 3.1, and $H_{ij}(k, t) = H_{ij}^{(dir)}(k, t) + H_{ij}^{(pol)}(k, t)$. The global anisotropy is quantified via the tensors $b_{ij}^{(dir)}(t)$, $b_{ij}^{(pol)}(t)$ and $b_{ij}(t) = b_{ij}^{(dir)}(t) + b_{ij}^{(pol)}(t)$, which originate from the $(\mathscr{E}, Z)$ decomposition of the Reynolds stress tensor:

$$\langle u_i u_j\rangle(t) = 2K_{ij}(t) = 2\mathscr{K}(t)\left(\frac{\delta_{ij}}{3} + b_{ij}^{(dir)}(t) + b_{ij}^{(pol)}(t)\right), \quad \mathscr{K}(t) = K_{ii}(t). \tag{4.3}$$

The tensors $b_{ij}^{(dir)}(t)$ and $b_{ij}^{(pol)}(t)$ are calculated from the tensors $H_{ij}^{(dir)}(k, t)$ and $H_{ij}^{(pol)}(k, t)$ according to

$$b_{ij}^{(dir)}(t) = \int_0^\infty E(k, t) H_{ij}^{(dir)}(k, t)\,\mathrm{d}k/\mathscr{K}(t), \quad b_{ij}^{(pol)}(t) = \int_0^\infty E(k, t) H_{ij}^{(pol)}(k, t)\,\mathrm{d}k/\mathscr{K}(t). \tag{4.4a,b}$$

We define the invariants $II(t)$ and $III(t)$ as

$$II(t) = b_{ij}(t) b_{ji}(t), \quad III(t) = b_{ik}(t) b_{kj}(t) b_{ij}(t). \tag{4.5a,b}$$

In order to quantitatively characterize the RTI process, we introduce the ratio $\rho(t)$ between a characteristic time of turbulence decay and a characteristic time of RTI, namely

$$\rho(t) = \frac{\mathscr{K}(t)\Big/\dfrac{\mathrm{d}\mathscr{K}}{\mathrm{d}t}(t)}{II(t)\Big/\dfrac{\mathrm{d}II}{\mathrm{d}t}(t)}. \tag{4.6}$$

For the comparison with the experiment of Chen *et al.* (2006), we use a two-component surrogate of the anisotropic tensor $b_{ij}(t)$, defined as

$$\tilde{b}_{ij}(t) = \frac{K_{ij}(t)/K_{ij}(t_0)}{K_{11}(t)/K_{11}(t_0) + K_{22}(t)/K_{22}(t_0)} - \frac{1}{2}\delta_{ij} \quad (i, j = 1, 2), \tag{4.7}$$

where t_0 refers to the time at which strain starts. The budget terms of the governing equation for the spherically integrated second-order spectral tensor $\varphi_{ij}(k, t)$ defined by (1.4),

$$\frac{\partial}{\partial t}\varphi_{ij}(k, t) = -2\nu k^2 \varphi_{ij}(k, t) + P_{ij}(k, t) + S_{ij}(k, t) + L_{ij}(k, t), \tag{4.8}$$

are also considered. The tensor $P_{ij}(k, t)$ is the spherically integrated spectral counterpart of the slow pressure–strain rate tensor and $S_{ij}(k, t)$ is a true transfer tensor with zero integral over k, the expressions of these two tensors are given in § 3. The term $L_{ij}(k, t)$, defined as

$$L_{ij}(k, t) = 2\left(\frac{\delta_{ij}}{3} S^L(k, t) + S_{ij}^{L(dir)}(k, t) + S_{ij}^{L(pol)}(k, t)\right), \tag{4.9}$$

includes all contributions of the linear terms of (3.3)–(3.5). The results reported in the figures are often scaled with an initial turbulent characteristic time τ_0, defined as $\tau_0 = \mathscr{K}(0)/\varepsilon(0)$. The kinetic energy spectrum $E(k, t)$ is scaled by k_{max} and E_{max}, defined by

$$\max_k E(k, t) = E_{max}(t) = E(k_{max}(t), t). \tag{4.10}$$

A similar scaling is used for the cross-correlation spectrum $\varphi_{13}(k, t)$.

4.2. *Comparison with the experiments of Gence and Mathieu*

In the experiments of Gence & Mathieu (1979, 1980), a plane strain is first applied to quasi-isotropic grid turbulence. A second strain is then applied, whose principal axes have been rotated by an angle α in the plane of the first strain. The mean-velocity gradients corresponding to the first and second strains are respectively

$$\lambda = \begin{pmatrix} 0 & 0 & 0 \\ 0 & S & 0 \\ 0 & 0 & -S \end{pmatrix}, \quad \lambda = \begin{pmatrix} 0 & 0 & 0 \\ 0 & S\cos(2\alpha) & -S\sin(2\alpha) \\ 0 & -S\sin(2\alpha) & -S\cos(2\alpha) \end{pmatrix}. \tag{4.11a,b}$$

In Gence & Mathieu (1980), the original experimental device is extended in such a way that the turbulence can develop downstream without a mean-velocity gradient. For these experiments, $S \simeq 2.9\tau_0^{-1}$ with $\tau_0 = \mathscr{K}(0)/\varepsilon(0)$, where the origin corresponds to the entrance of the distorting duct. The simulations are initialized with $Re_\lambda = 60$. No detailed spectral information is available in these works, and we assume that the turbulence is weakly axisymmetrically dilated at the entrance of the distorting duct. The initial condition is obtained from RDT and the degree of anisotropy is adjusted so that it coincides with the first measured values of the invariant II defined by (4.5). Experimental data for the downstream evolution of the invariant II are reported in figure 1 along with numerical results obtained with the system of governing equations (3.3)–(3.5). This figure shows a satisfactory agreement between experimental and numerical results, especially taking into account the uncertainty in the initial condition and a possible homogeneity fault in the experimental device. The first-order truncations in the description of anisotropy (§ 3.5) may also lie at the origin of discrepancies between experimental and numerical results. The system of governing equations (3.3)–(3.5) allows us to correctly capture the evolution of anisotropy, both in the straining regions and during the relaxation phases. Only the period of RTI for the angle $\alpha = \pi/4$ is not fully satisfactory, mainly because the boundary between the straining and relaxation regions in the experiments does not appear to be as clear as in the simulations. The case of straining without rotation in the second part of the distorting duct ($\alpha = 0$), followed by a relaxation phase, is further illustrated in figure 2. The present model properly captures the evolution of the anisotropy indicators b_{ij} and that of the turbulent kinetic energy, both in the region dominated by linear effects and in the purely nonlinear one.

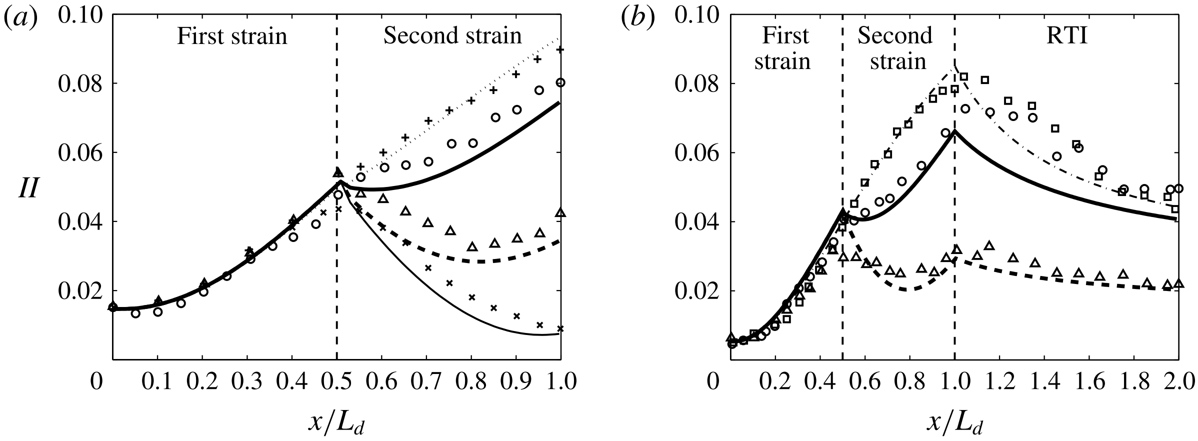

FIGURE 1. Evolution of the invariant II versus the position in the distorting duct of length L_d for the experiments of (*a*) Gence & Mathieu (1979) and (*b*) Gence & Mathieu (1980). Symbols correspond to experimental data and lines are obtained with the system of governing equations (3.3)–(3.5). Various values of the angle α between the principal axes of the two successive plane strains are investigated: $\alpha = 0$ (□, – – – – –), $\alpha = \pi/8$ (+, · · · · · ·), $\alpha = \pi/4$ (○, ▬▬), $\alpha = 3\pi/8$ (△, – – – –) and $\alpha = \pi/2$ (×, ——).

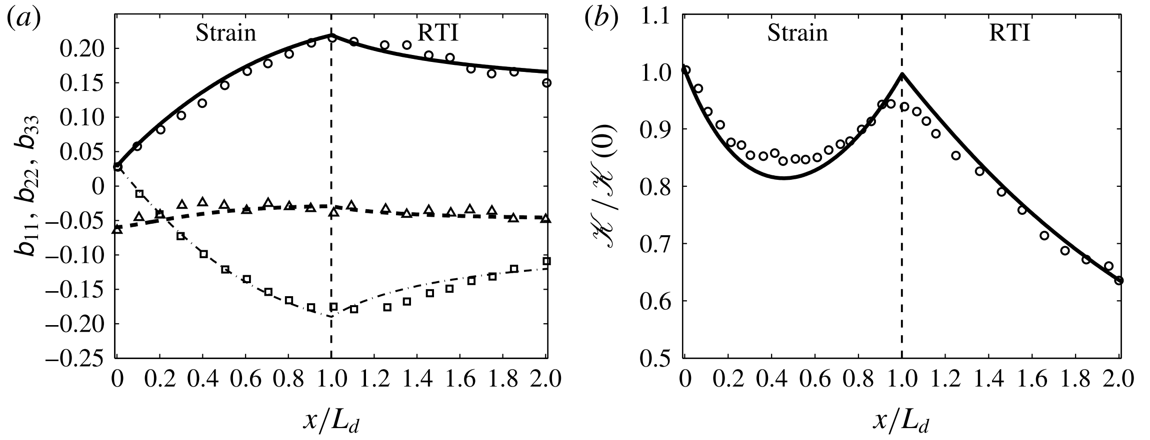

FIGURE 2. Evolution of (*a*) the anisotropy indicators b_{11} (△, – – – –), b_{22} (□, – – – – –) and b_{33} (○, ——) and (*b*) that of the turbulent kinetic energy $\mathscr{K}$ (○, ——) versus the position in the distorting duct of length L_d for the experiment in Gence & Mathieu (1980) without rotation in the second part of the distorting duct ($\alpha = 0$). Symbols correspond to experimental data and lines are obtained with the system of governing equations (3.3)–(3.5).

4.3. *Turbulence subjected to a straining–relaxation–destraining cycle*

The present model is further tested by comparing its predictions with the experiment of Chen *et al.* (2006), where a piston is used to apply plane straining and destraining on turbulence generated by active grids. The mean-velocity gradient in the experiment is of the form

$$\lambda(t) = \begin{pmatrix} S(t) & 0 & 0 \\ 0 & -S(t) & 0 \\ 0 & 0 & 0 \end{pmatrix}, \tag{4.12}$$

where the temporal evolution of $S(t)$ is given by figure 3(*a*). Initially, the mean flow corresponds to plane straining ($S(t) > 0$), until $t/\tau_0 \simeq 0.5$. After a relaxation

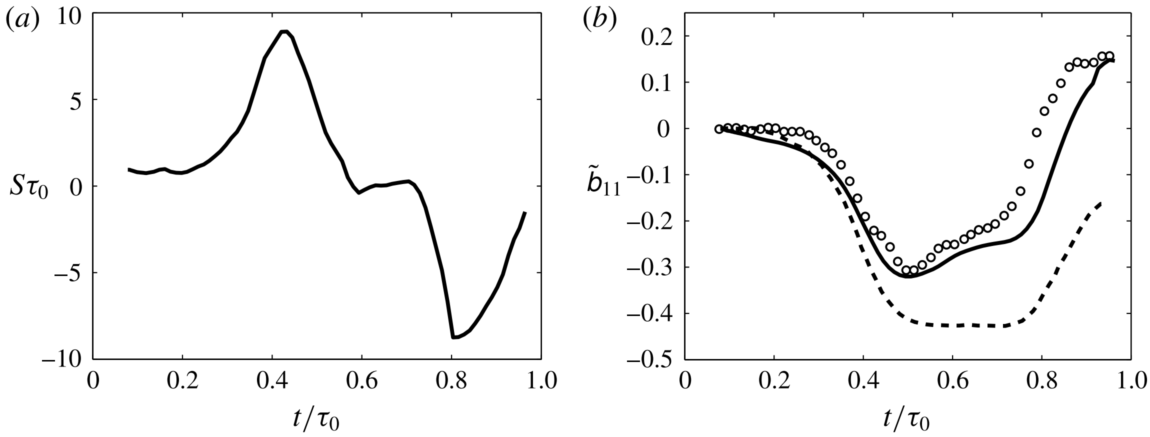

FIGURE 3. (*a*) Temporal evolution of the strain $S(t)$ applied to the turbulence; (*b*) experimental values (○), numerical values obtained with the present model (——) and RDT prediction (– – – –) for the temporal evolution of the anisotropy indicator $\tilde{b}_{11}(t)$ in the experiment of Chen *et al.* (2006).

phase ($0.5 \leqslant t/\tau_0 \leqslant 0.7$), destraining ($S(t) < 0$) is applied to the turbulence. In this experiment, the Taylor-microscale-based Reynolds number at the beginning of the straining cycle is $Re_\lambda \simeq 400$. The maximum value of the strain $S(t)$ reached in the experiment is $\simeq 9.5\tau_0^{-1}$. Figure 3(*b*) illustrates the temporal evolution of the anisotropy indicator $\tilde{b}_{11}(t)$ defined by (4.7). Experimental and numerical values obtained with the present model are reported, along with the RDT prediction, provided by Chen *et al.* (2006), corresponding to the mean flow defined by (4.12) and figure 3(*a*). The temporal evolution of $\tilde{b}_{11}(t)$ shows good agreement between the experiment and the present model. From the comparison with RDT results, it appears that nonlinear phenomena are significant on a quantitative level. This is partly due to the presence of a relaxation phase in the straining cycle. Thus, the validity of both linear and nonlinear contributions in the system of governing equations (3.3)–(3.5) can be confirmed by the comparison with this experiment.

4.4. *Turbulence subjected to axisymmetric expansion or contraction*

We now consider the case of turbulence subjected to an axisymmetric expansion or contraction. The corresponding mean-velocity gradients are respectively

$$\lambda = \begin{pmatrix} S/2 & 0 & 0 \\ 0 & S/2 & 0 \\ 0 & 0 & -S \end{pmatrix}, \quad \lambda = \begin{pmatrix} -S/2 & 0 & 0 \\ 0 & -S/2 & 0 \\ 0 & 0 & S \end{pmatrix}, \tag{4.13a,b}$$

with $S > 0$. These two configurations have been recently investigated in the DNS of Zusi & Perot (2014), where both effects of axisymmetric expansion and contraction on initially approximately isotropic turbulence and its subsequent relaxation have been studied. We want to check whether the present model is able to reproduce one of the main observation of this paper: the two-stage RTI of turbulence after an axisymmetric expansion. In this configuration, it has been observed that the anisotropy continues to increase after the release of the strain during a short period of time, before decreasing in a more conventional way. The reader has to keep in mind that the microscale-based Reynolds number in this work is moderate ($Re_\lambda \simeq 50$) and that two-stage RTI

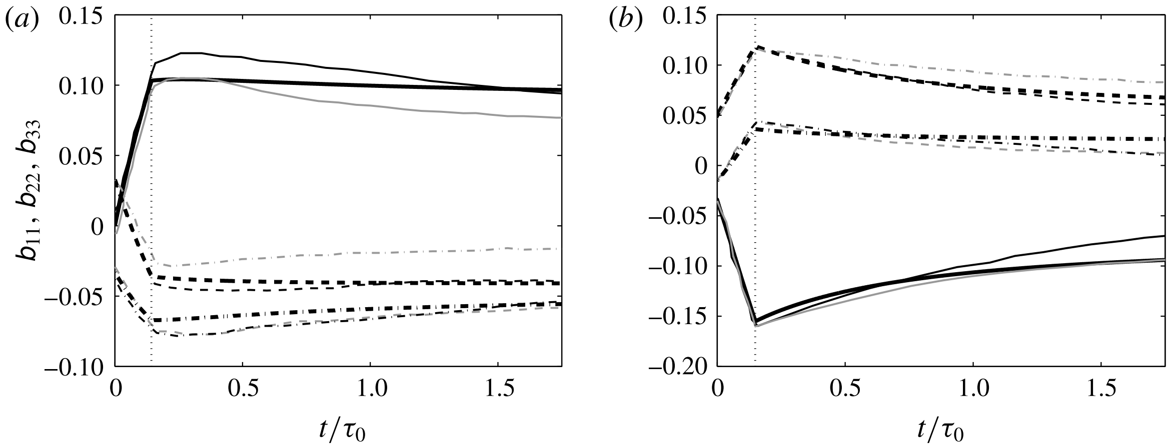

FIGURE 4. Time evolution of the different components of the global anisotropy tensor $b_{ij}(t)$ (– – – – b_{11}, - - - - - b_{22}, —— b_{33}) for (*a*) axisymmetric expansion and (*b*) contraction. The thick black lines correspond to numerical values obtained with the present model, while the thin black and grey lines refer to the DNS results of Zusi & Perot (2014) for two different initial conditions. The vertical dotted line marks the time at which strain is released.

is observed only after an expansion with sufficiently high strain rate ($S \geqslant 3\tau_0^{-1}$). A complete parametric study of this two-stage RTI should be performed, but this is beyond the scope of the present paper. Detailed numerical analyses of the RTI of axisymmetric turbulence can be found in Herring (1974), Chasnov (1995), Davidson, Okamoto & Kaneda (2012) and Mons, Meldi & Sagaut (2014).

First, a quantitative comparison between the predictions of the present model and the DNS results of Zusi & Perot (2014) is performed. Zusi & Perot (2014) use two different initial conditions in their work which are difficult to characterize. Besides, these initial fields are anisotropic and non-axisymmetric. Predictions concerning the time evolution of the different components of the tensor $b_{ij}(t)$ obtained with the present model and the DNS of Zusi & Perot (2014) are reported in figure 4. Both expansion and contraction cases are investigated with $S \simeq 3.4\tau_0^{-1}$, and simulations are initialized with $Re_\lambda = 50$. The production periods are well recovered by the model. In the RTI regions, significant discrepancies between the DNS results obtained with the two initial fields can be noticed, and the results obtained with the present model lie between these two predictions. Thus, given the uncertainties in the initial condition and a potential additional source of discrepancies originating from the limitation to moderate anisotropy of the present model (§ 3.5), these comparisons are relatively satisfactory. In particular, the major difference between the expansion and contraction cases is recovered: after the release of the strain, the anisotropy immediately decreases in the contraction case, whereas it slightly increases in the expansion case before decreasing. To further illustrate this observation, complementary runs are performed starting from initially isotropic turbulence, instead of an anisotropic and non-axisymmetric field, in order to get clearer results.

Figures 5 and 6 illustrate numerical results obtained with the present model for initially isotropic turbulence submitted to an axisymmetric expansion or contraction and then released. Simulations are initialized with $Re_\lambda = 50$ and we set $S = 5\tau_0^{-1}$. The axisymmetric expansion or contraction is maintained from $t = 0$ to $St = 1$. We first consider the results for axisymmetric expansion, which are reported in figures 5(*a*,*b*) and 6(*a*). The temporal evolution of the anisotropy indicator $b_{33}(t)$ is given in

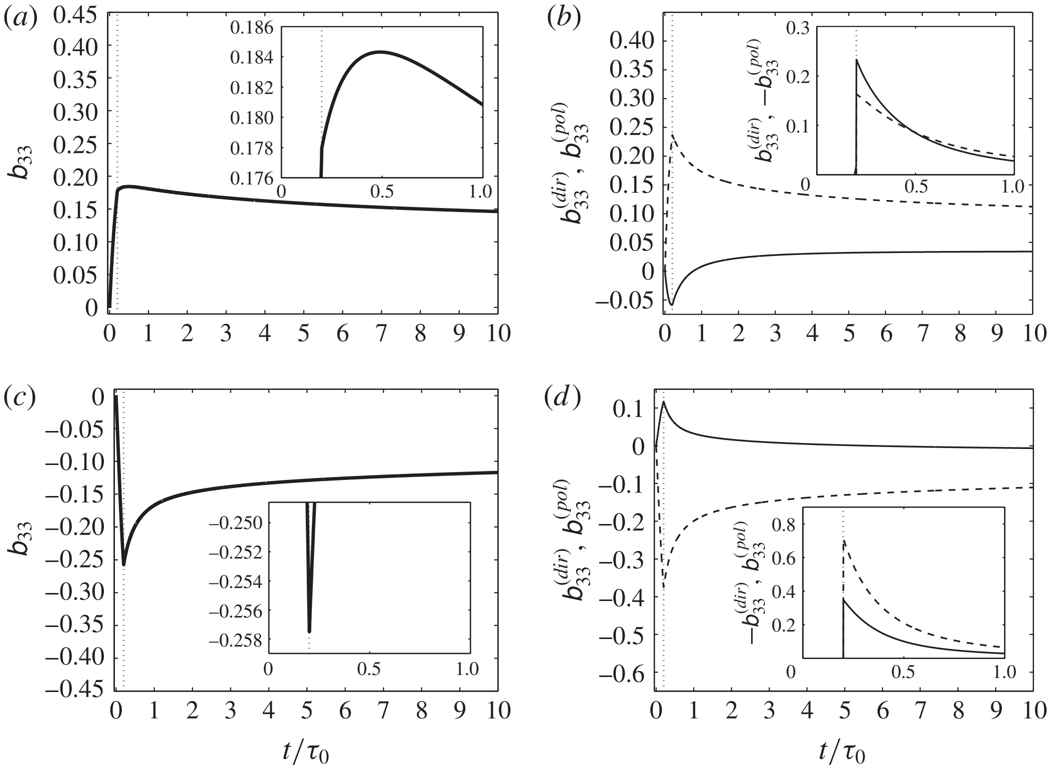

FIGURE 5. (*a*,*c*) Time evolution of the anisotropy indicator $b_{33}(t)$ (▬); (*b*,*d*) time evolution of $b_{33}^{(dir)}(k,\ t)$ (——) and $b_{33}^{(pol)}(k,\ t)$ (– – – –) with that of their time derivatives; (*a*,*b*) and (*c*,*d*) correspond to the axisymmetric expansion and contraction cases respectively. The vertical dotted line marks the time at which strain is released.

figure 5(*a*). Since we consider axisymmetric turbulence, the tensor $b_{ij}(t)$ is diagonal, with $b_{33}(t) = -b_{11}(t)/2 = -b_{22}(t)/2$. As observed above, $b_{33}(t)$ slightly increases after the release of the strain before decaying. Further insight into this two-stage RTI is given by figure 5(*b*), where the temporal evolution of the directivity and polarization components of $b_{33}(t) = b_{33}^{(dir)}(t) + b_{33}^{(pol)}(t)$ is reported, along with their time derivatives. Contrary to $b_{33}(t)$, both $b_{33}^{(dir)}(t)$ and $b_{33}^{(pol)}(t)$ immediately decay in magnitude after the release of the strain. However, since $b_{33}^{(dir)}(t)$ is negative, whereas both $b_{33}^{(pol)}(t)$ and $b_{33}(t)$ are positive, and it first decreases in magnitude at a faster rate than $b_{33}^{(pol)}(t)$, the total anisotropy indicator $b_{33}(t)$ increases. As soon as the polarization component decays at a faster rate than the directivity one, the global anisotropy decreases. The difference in the relaxation rates between directional anisotropy and polarization anisotropy in the present model, which lies at the origin of the increase of the total anisotropy, may be related to the difference in the relaxation rates between the dimensionality and circulicity tensors in Kassinos & Reynolds (1997) and Kassinos *et al.* (2001) (see appendix A for further details).

The case of RTI after an axisymmetric contraction is illustrated in figures 5(*c*,*d*) and 6(*b*). The anisotropy indicator $b_{33}(t)$ decays in magnitude immediately after the release of the strain, as $b_{33}^{(dir)}(t)$ and $b_{33}^{(pol)}(t)$ do. The polarization component, of the same sign as $b_{33}(t)$, decays in magnitude at a faster rate than the directivity one as soon as the strain is released. The qualitative difference in the RTI between expansion and contraction is even more striking by looking at figure 6(*a*,*b*), where the evolution of the invariant $II(t)$ is indicated for the expansion and contraction cases respectively. The temporal evolution of the invariant $III(t)$ and that of the ratio $\rho(t)$ between the

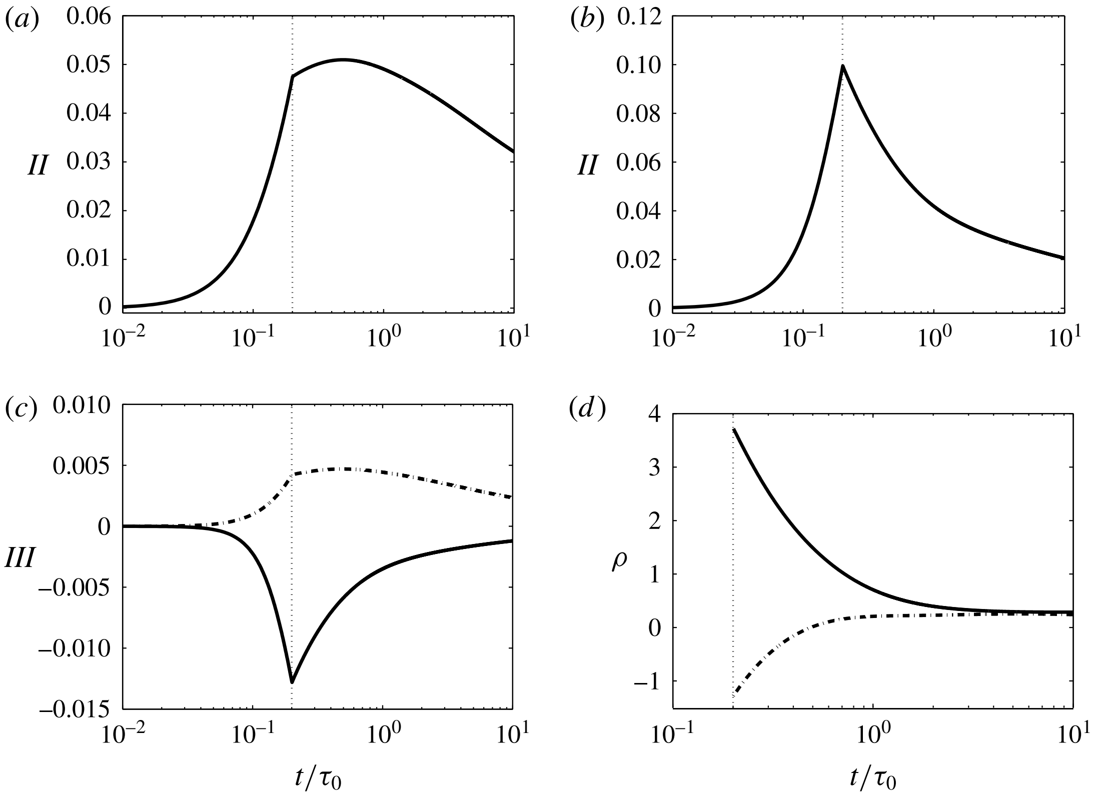

FIGURE 6. (*a*,*b*) Temporal evolution of the invariant $II(t)$ (——) for the axisymmetric (*a*) expansion and (*b*) contraction cases; (*c*,*d*) temporal evolution of (*c*) the invariant $III(t)$ and (*d*) the ratio $\rho(t)$ between characteristic times of decay and RTI for the expansion (– – – – –) and contraction (——) cases. The vertical dotted line marks the time at which strain is released.

characteristic times of decay and RTI defined by (4.6) are reported in figure 6(*c*,*d*). The expansion case is associated with a positive value for $III(t)$ (axial component $\langle u_3u_3\rangle(t)$ greater than the transverse ones), whereas $III(t)$ is negative in the contraction case. Figure 6(*d*) indicates that the RTI process is slower in the expansion case than in the contraction case ($\rho(t)$ takes a greater value if the RTI is faster and is negative during the slight increase of anisotropy in the expansion case). This result is consistent with the discussions in Gence (1983) and Choi & Lumley (2001).

4.5. *The RTI of shear-released turbulence*

The RTI of initially isotropic (Saffman) turbulence that is suddenly subjected to a mean shear and is then released is investigated. The mean-velocity gradient that corresponds to the application of a shear on the turbulent flow is

$$\lambda = \begin{pmatrix} 0 & 0 & S \\ 0 & 0 & 0 \\ 0 & 0 & 0 \end{pmatrix}. \tag{4.14}$$

The simulations are initialized with $Re_\lambda = 10^4$. The anisotropy of the flow is introduced by using either the RDT solution for homogeneous shear flow with $St = 0.42$ (this value allows us to observe a significant departure from isotropy of the diagonal components of the Reynolds stress tensor) or the linear terms of (3.3)–(3.5)

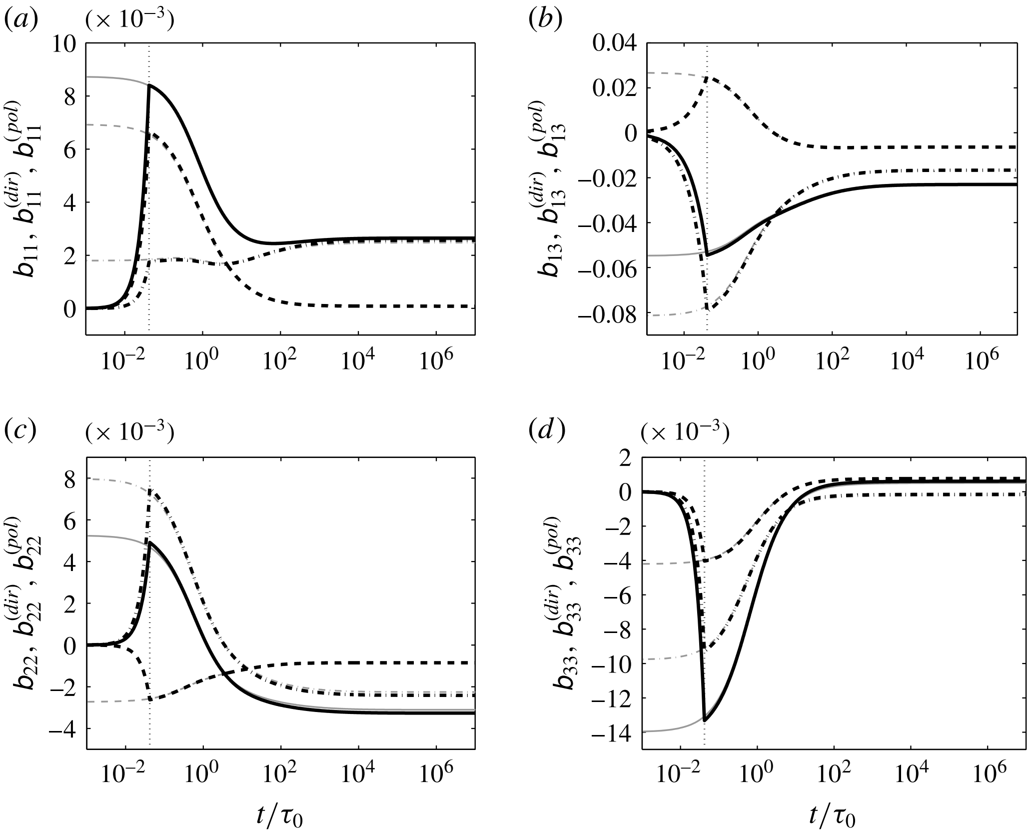

FIGURE 7. Global anisotropy indicators —— b_{ij}, - - - $b_{ij}^{(dir)}$ and -·-·- $b_{ij}^{(pol)}$ in the case of shear-released Saffman turbulence. The grey lines correspond to the use of RDT solutions for the initialization, whereas the black lines correspond to the use of the linear terms in (3.3)–(3.5) for the introduction of anisotropy. The vertical black dotted line marks the limit at $t = 0.042\tau_0$ after which the shear is released when the linear terms are used.

with $S = 10\tau_0^{-1}$ if $t < 0.042\tau_0$ and $S = 0$ if not, starting from an isotropic field. Results are illustrated in figures 7–9.

It appears from figure 7 that solutions initialized with RDT or with the linear terms (3.7)–(3.9) coincide, which confirms the validity of the linear terms of the present model in the case of homogeneous shear turbulence. The evolution of anisotropy is similar to that in the case of axisymmetric Saffman turbulence (Chasnov 1995; Davidson *et al.* 2012; Mons *et al.* 2014). After a transient regime which corresponds to the RTI of small scales, an asymptotic anisotropic state is reached due to the fulfilment of the PLE hypothesis ($E(k, t) = E(k, 0)$ for $k \ll k_{max}(t)$ if $1 \leqslant \sigma \leqslant 3$ with $E(k \to 0, t) \propto k^\sigma$). A similar behaviour was also observed with the model of Clark & Zemach (1995) for the relaxation of turbulence after the release of plane strain. Even the off-diagonal component $b_{13}(t)$ converges towards a non-zero value, which means that the cross-correlation $\langle u_1 u_3 \rangle(t)$ is maintained even though the mean shear is released.

The RTI of small scales during the transient regime is illustrated in figure 8 for the components of the spherically integrated second-order spectral tensor defined by (1.4), $\varphi_{13}(k, t)$ and $\varphi_{33}(k, t)$. Both the directional anisotropy and the polarization anisotropy become negligible in the inertial range for $t \geqslant 10\tau_0$. This result is also valid for the diagonal components $\varphi_{11}(k, t)$ and $\varphi_{22}(k, t)$ that are not illustrated here. Figure 8(*b*) indicates that the initial cross-correlation spectrum $\varphi_{13}(k, 0)$ given by RDT evolves like $k^{-5/3}$ in the inertial range. Then, due to purely nonlinear processes, this shape

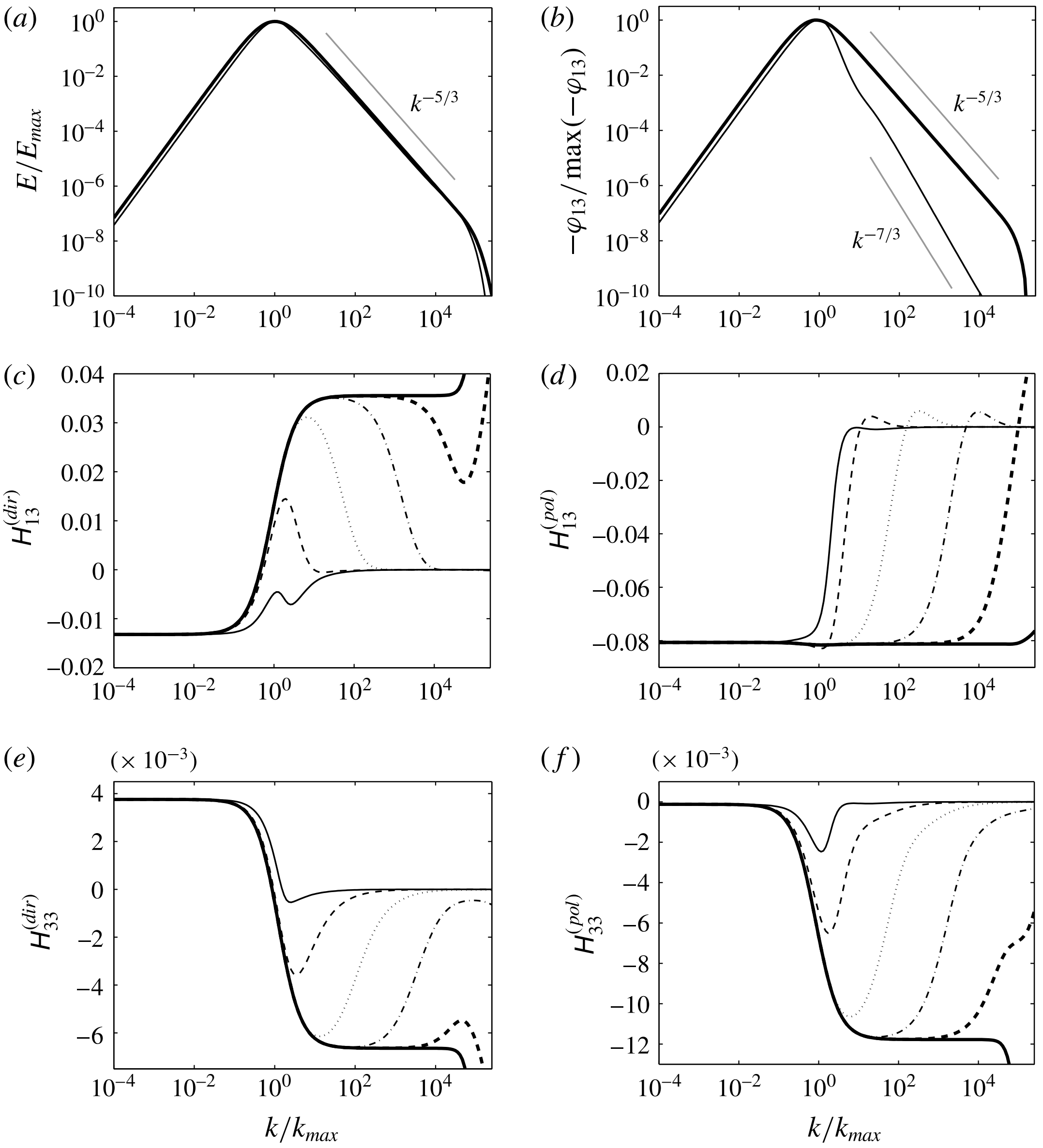

FIGURE 8. (*a*) Energy spectrum $E(k, t)$, (*b*) cross-correlation spectrum $\varphi_{13}(k, t)$ and spectra (*c*) $H_{13}^{(dir)}(k, t)$, (*d*) $H_{13}^{(pol)}(k, t)$, (*e*) $H_{33}^{(dir)}(k, t)$ and (*f*) $H_{33}^{(pol)}(k, t)$ for shear-released Saffman turbulence. The RDT is used for the initialization. The curves have been sampled at the normalized time: ▬▬ $t/\tau_0 = 0$; ▪ ▪ ▪ $t/\tau_0 = 10^{-3}$; - - - - - $t/\tau_0 = 10^{-2}$; · · · · · · $t/\tau_0 = 10^{-1}$; -·-·- $t/\tau_0 = 1$; —— $t/\tau_0 = 10$.

is modified and evolves like $k^{-7/3}$ at $t = 10\tau_0$. This result is consistent with the predictions of Lumley (1967), Leslie (1973), Yoshida *et al.* (2003) and Weinstock (2013).

The budget terms of the governing equation (4.8) are reported in figure 9 for the spectra $\varphi_{13}(k, t)$ and $\varphi_{33}(k, t)$ at $t = 0.1\tau_0$ and $t = 10\tau_0$. During the transient regime corresponding to the RTI of small scales ($t = 0.1\tau_0$), the nonlinear pressure–strain rate tensor $P_{ij}(k, t)$ has a significant influence in the inertial range. Its contribution is positive for the negative cross-correlation spectrum $\varphi_{13}(k, t)$, which would be identically zero in the isotropic case, and also positive for the spectrum $\varphi_{33}(k, t)$, since this component has been relatively damped by the mean shear via linear effects. Once small scales have returned to isotropy ($t = 10\tau_0$), the contribution of

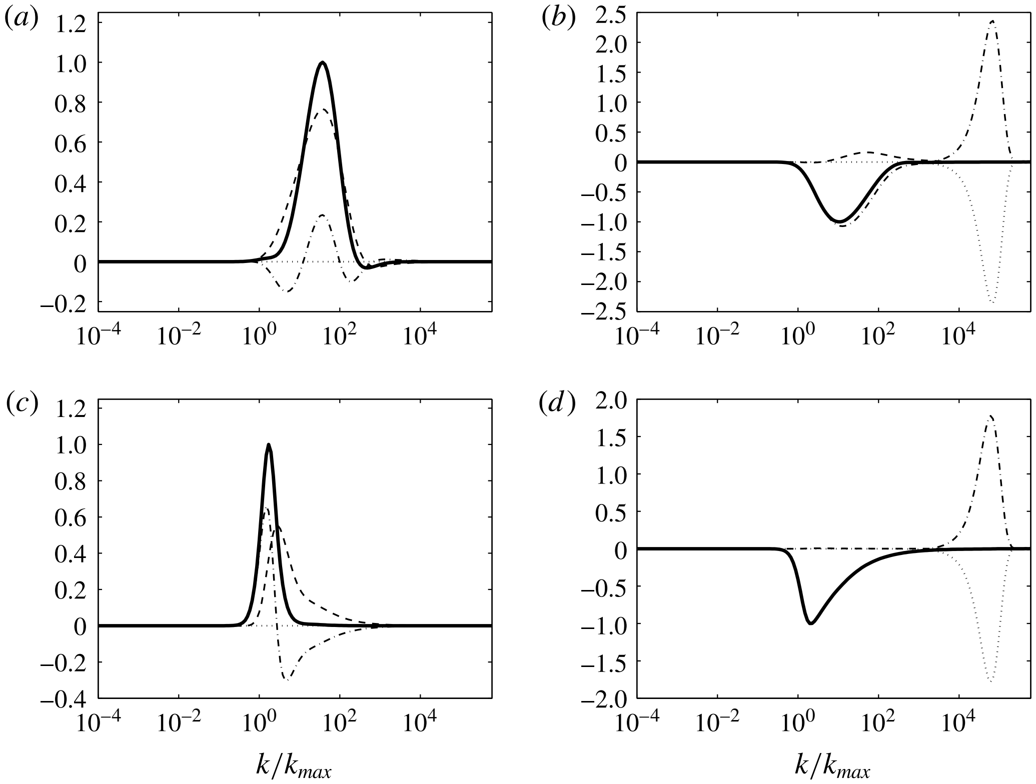

FIGURE 9. Budget terms of the equation $(\partial/\partial t)\varphi_{ij}(k,\,t) = -2\nu k^2\varphi_{ij}(k,\,t) + P_{ij}(k,\,t) + S_{ij}(k,\,t)$, premultiplied by k (–·–·– $kS_{ij}(k,\,t)$; ······ $-2\nu k^3\varphi_{ij}(k,\,t)$; – – – – $kP_{ij}(k,\,t)$; —— $k(\partial/\partial t)\varphi_{ij}(k,\,t)$), and normalized by $\max_k(|k(\partial/\partial t)\varphi_{ij}(k,\,t)|)$. Shear-released Saffman turbulence is considered and the RDT is used for the initialization; (*a*,*c*) refer to the component $\varphi_{13}(k,\,t)$, whereas (*b*,*d*) refer to the component $\varphi_{33}(k,\,t)$. The budget terms have been sampled at the normalized time $t/\tau_0 = 10^{-1}$ (*a*,*b*) and $t/\tau_0 = 10$ (*c*,*d*).

$P_{ij}(k, t)$ is negligible $\forall k$ for the component $\varphi_{33}(k, t)$ (as well as for the other diagonal components), even though large scales have not returned to isotropy. The shape of the transfer term $S_{33}(k,\,t)$ is then virtually identical to that in the isotropic case. Concerning the cross-correlation component, nonlinear terms act predominantly at scales close to the integral length scale. These results are consistent with previous studies dealing with the RTI of Saffman turbulence, where it is observed that small scales quickly return to isotropy after the release of the shear/strain, whereas large scales fully retain anisotropy due to the fulfilment of the PLE hypothesis.

4.6. *Homogeneous shear turbulence*

Finally, we address the case of homogeneous turbulence subjected to a constant maintained mean shear. The corresponding mean-velocity gradient is given by (4.14). Weinstock (2013) performed an exhaustive analytical study of this configuration in 3D Fourier space, without limitations on time or wavenumber. In this subsection, it is checked that the present model is able to recover results established in this prior work, among others. The corresponding simulation realized with the present model is initialized with $Re_\lambda = 50$, the shear rate is fixed at $S = 2\tau_0^{-1}$ and the turbulence is initially isotropic. The temporal evolutions of the components of the deviatoric tensor $b_{ij}(t)$ and that of the kinetic energy $\mathscr{K}(t)$ are reported in figure 10. The different components $b_{ij}(t)$ and the ratio $\varepsilon(t)/S\mathscr{K}(t)$ reach constant values after $St \approx 20$, as

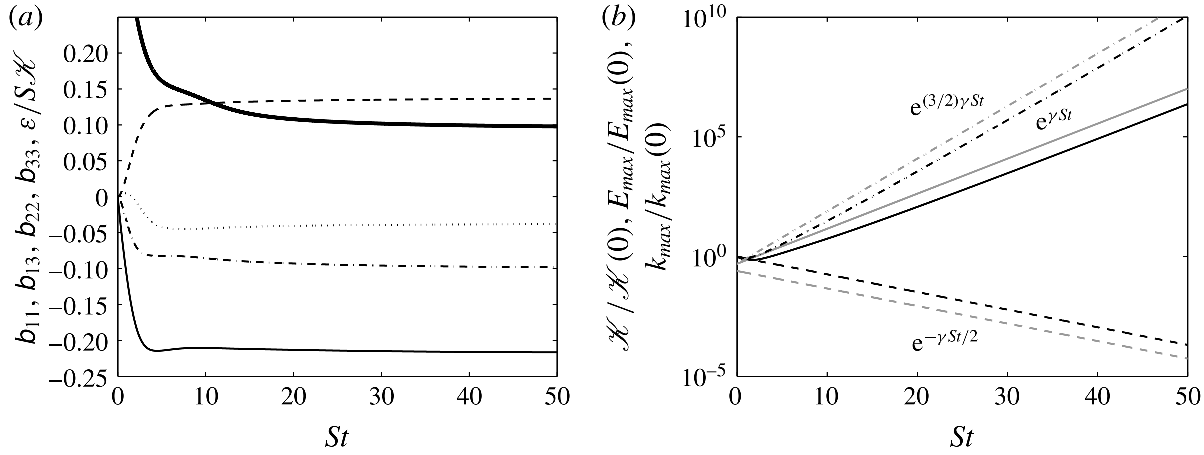

FIGURE 10. Temporal evolutions of (*a*) the different components of the global anisotropy tensor $b_{ij}(t)$ and the ratio $\varepsilon/S\mathscr{K}$ (– – – – b_{11}, —— b_{13}, · · · · · · b_{22}, – – – – – b_{33} and ▬▬ $\varepsilon/S\mathscr{K}$) and (*b*) those of the turbulent kinetic energy $\mathscr{K}(t)$ (——), k_{max} (– – – –) and E_{max} (– – – – –) defined in (4.10) and normalized by their initial values for homogeneous shear turbulence. The grey curves are plotted with $\gamma = 0.337$.

observed in, e.g., Weinstock (2013). Considering the governing equation for the turbulent kinetic energy $\mathscr{K}(t)$,

$$\frac{\mathrm{d}}{\mathrm{d}t}\mathscr{K}(t) = -2S\mathscr{K}(t)b_{13}(t) - \varepsilon(t), \tag{4.15}$$

one can deduce that for $St \geqslant 20$

$$\mathscr{K}(t) \sim \mathrm{e}^{\gamma St}, \quad \gamma = \text{const.} = -2b_{13} - \frac{\varepsilon}{\mathscr{K}S}. \tag{4.16}$$

As illustrated in figure 10(*b*), the results obtained with the present model are consistent with such an exponential growth of the kinetic energy. The model also predicts the temporal evolutions of the peak of the energy spectrum E_{max} and the corresponding wavenumber k_{max} defined in (4.10) as $E_{max}(t) \sim \mathrm{e}^{(3/2)\gamma St}$ and $k_{max}(t) \sim \mathrm{e}^{-\gamma St/2}$. All of these results are consistent with dimensional analysis and with the study performed in Weinstock (2013), in which $\gamma = 0.115$. The estimated value of the growth rate γ in a set of experiments (Tavoularis & Corrsin 1981; Tavoularis & Karnik 1989) ranges between 0.08 and 0.12, whereas values between 0.1 and 0.2 can be found in DNS studies (Rogers *et al.* 1986; Brethouwer 2005; Isaza & Collins 2009). Although a clear consensus about the value of the growth rate γ cannot be found in the literature, and its sensitivity with respect to initial conditions, Reynolds number and shear rate has to be further investigated, the present model overestimates γ ($\simeq 0.337$) in comparison with values found in the literature. This lack of quantitative agreement originates from the first-order truncations in the description of anisotropy (§ 3.5). Compared with previous test cases considered in the present paper, the cumulated shear reached in the simulation illustrated in figures 10 and 11 is much higher (see § 4.7), which provides asymptotic information at high Reynolds numbers. Concerning results in spectral space, the kinetic energy spectrum $E(k, t)$ at $St = 50$ (figure 11*a*) displays a $-5/3$ slope in the inertial range, as reported in experiments or DNS. Figure 11(*b*) reports the cross-correlation spectrum $\varphi_{13}(k, t)$

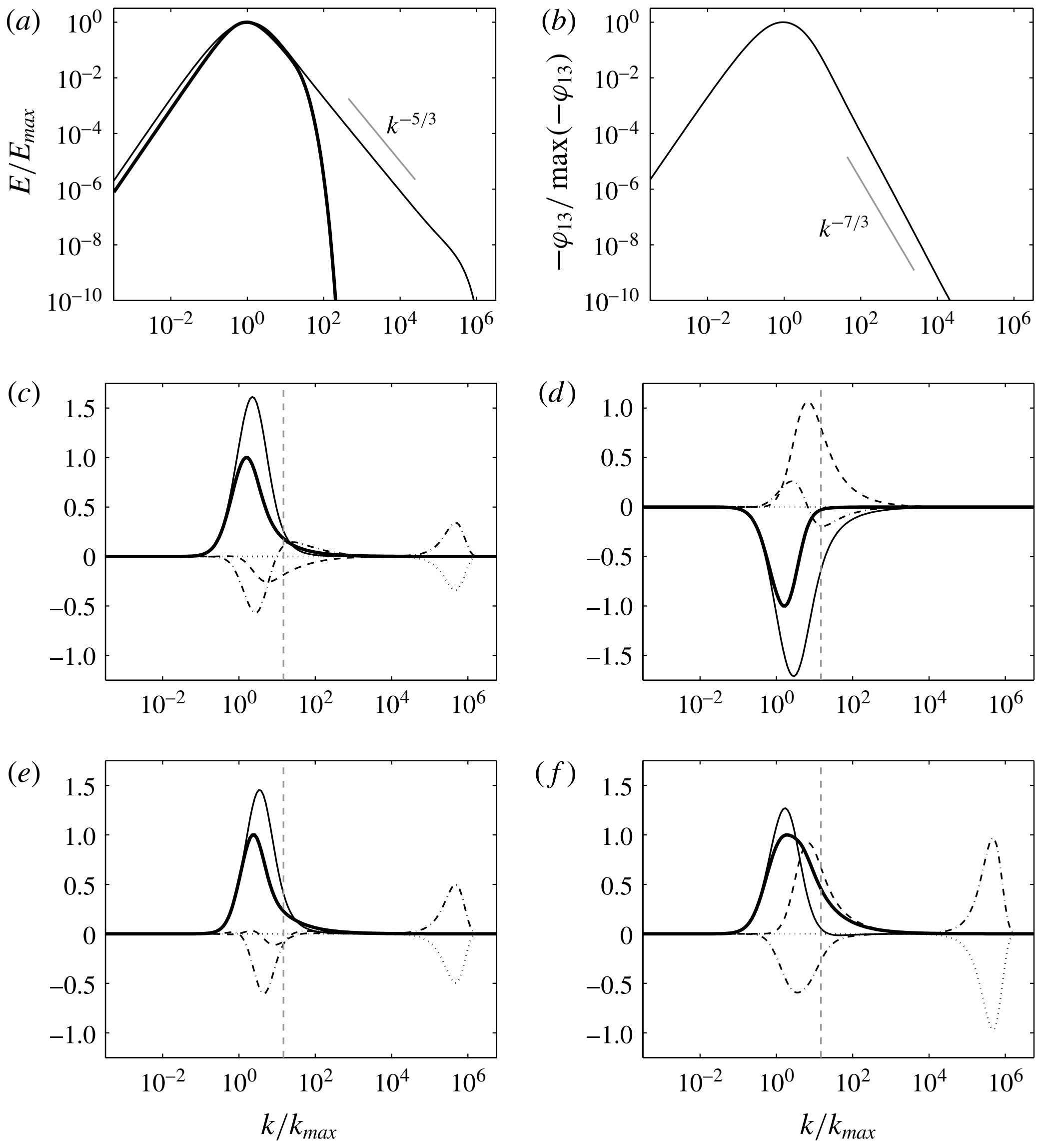

FIGURE 11. (*a*) Energy spectrum $E(k, t)$ and (*b*) cross-correlation spectrum $\varphi_{13}(k, t)$ at $St = 0$ (thick black line) and $St = 15$ (thin black lines). (*c*–*f*) Budget terms of the governing equation $(\partial/\partial t)\varphi_{ij}(k, t) = -2\nu k^2\varphi_{ij}(k, t) + P_{ij}(k, t) + S_{ij}(k, t) + L_{ij}(k, t)$, premultiplied by k (–·–·– $kS_{ij}(k, t)$; ······ $-2\nu k^3\varphi_{ij}(k, t)$; – – – – $kP_{ij}(k, t)$; —— $kL_{ij}(k, t)$; ▬▬ $k(\partial/\partial t)\varphi_{ij}(k, t)$), and normalized by $\max_k(|k(\partial/\partial t)\varphi_{ij}(k, t)|)$. The curves are sampled at $St = 50$ for homogeneous shear turbulence and refer to the components (*c*) $\varphi_{11}(k, t)$, (*d*) $\varphi_{13}(k, t)$, (*e*) $\varphi_{22}(k, t)$ and (*f*) $\varphi_{33}(k, t)$. The position of the shear scale L_s is also shown by vertical grey dashed lines.

at $St = 50$. The latter evolves like $k^{-7/3}$ in the inertial range, as predicted theoretically (Lumley 1967; Leslie 1973; Yoshida *et al.* 2003; Weinstock 2013) and observed in the experiments of Shen & Warhaft (2000) and the DNS of Ishihara *et al.* (2002). This result supports *a posteriori* the choice of eddy damping (2.26) and (2.27). The budget terms of the governing equation (4.8) are illustrated in figure 11(*c*–*f*). The position of the shear scale $L_s = \sqrt{\varepsilon/S^3}$ (Corrsin 1958) is also reported in the figures. For $1/L \leqslant k \leqslant 1/L_s$, the flow is expected to be dominated by production terms, whereas for $k \geqslant 1/L_s$, the contribution of nonlinear transfers should prevail. This interpretation is reasonably well supported by the present results. Figure 11(*c*–*f*) can help in visualizing the nonlinear process that lies at the origin of the exponential

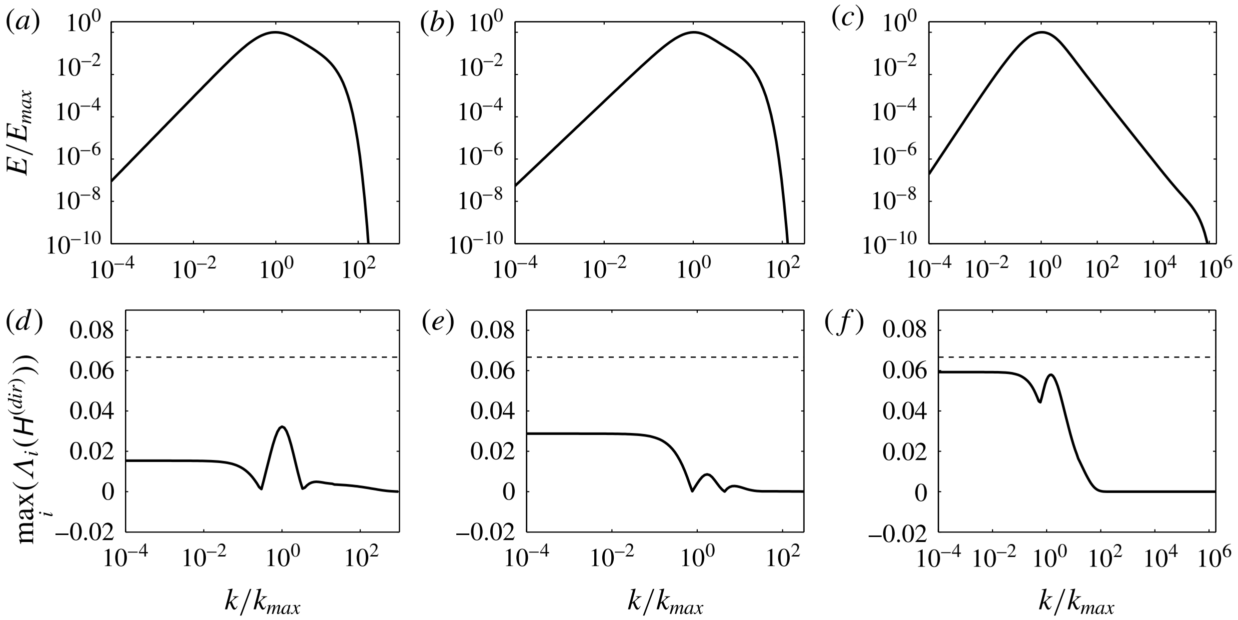

FIGURE 12. Energy spectrum (*a*–*c*) and maximal eigenvalue of the tensor $H_{ij}^{(dir)}(k, t)$ (*d*–*f*) for the different test cases investigated in this paper. The value $1/15$ from the criterion (3.17) is displayed as dashed lines. (*a*,*d*) The case of plane straining (case $\alpha = \pi/8$ of figure 1*a*); the curves are sampled at the end of the simulation ($St \simeq 1.4$). (*b*,*e*) The case of axisymmetric expansion of figure 4(*a*) ($St = 0.5$). (*c*,*f*) Results concerning homogeneous shear turbulence (figures 10 and 11); the curves are sampled at $St = 50$.

growth of the turbulent kinetic energy. Since the component $\varphi_{33}(k, t)$ is less fed than the other diagonal components by the mean shear, the nonlinear pressure–strain rate tensor $P_{33}(k, t)$ is strongly positive and redistributes energy from the components $\varphi_{11}(k, t)$ and $\varphi_{22}(k, t)$ to $\varphi_{33}(k, t)$ ($P_{ii}(k, t) = 0\ \forall k, t$). Since the cross-correlation component of the Reynolds stress tensor $2K_{13}(t)$ is fed by the mean shear via the term $-2SK_{33}(t)$, its production is enhanced, allowing an increase of the growth rate of the turbulent kinetic energy $\mathscr{K}(t)$ via the term $-2S\mathscr{K}(t)b_{13}(t) = -2SK_{13}(t)$.

4.7. *Realizability condition*

Due to spherical integration and truncation of expansions (3.14) and (3.15), the present model is limited to moderate anisotropy, and the criterion (3.17) is derived in § 3.5 in order to quantify the upper boundary of anisotropy intensity that can be investigated with the representation (3.2) and the corresponding system of governing equations (3.3)–(3.5). In this last subsection, it is checked that the different test cases considered in this paper can be described using the representation (3.2) and (3.3)–(3.5). Figure 12 reports the criterion (3.17) for typical flow configurations investigated in this paper: plane straining, axisymmetric expansion and pure plane shear. Rather than the absolute value of the typical strain or shear rate S, it is the accumulated strain/shear St that gives a good estimation of the anisotropy introduced in the flow. The interplay between linear and nonlinear contributions in (3.3)–(3.5) also affects the evolution of anisotropy in the flow, but this effect must be studied on a case-by-case basis in view of the significant differences that exist between, e.g., rotational and irrotational mean flows (Sagaut & Cambon 2008). It is worth keeping in mind that for the purpose of spherical integration, the same representation (3.2) is used for both linear contributions and transfer terms in (2.12) and (2.13), the latter being closed by the EDQNM. The different cases of plane straining/destraining investigated in this paper are associated with small values for the accumulated strain. Figure 12(*d*) illustrates the case $\alpha = \pi/8$ of figure 1(*a*) from the experiments of Gence and Mathieu. This configuration corresponds to the accumulated strain $St \simeq 1.4$, and the anisotropy of the flow at all scales is significantly lower than the upper bound of (3.17). This result is similar for the other cases of plane straining/destraining in this paper. The case of axisymmetric expansion of figure 4(*a*) is investigated in figure 12(*e*). The accumulated strain is $St = 0.5$ and the criterion (3.17) is respected at all scales. The same applies to the axisymmetric contraction case. Finally, the case of homogeneous shear turbulence is illustrated in figure 12(*f*) at $St = 50$, and criterion (3.17) is verified at all scales. Thus, all of the flow configurations considered in the present paper can be described by the representation (3.2) and the corresponding system of governing equations (3.3)–(3.5).

5. Conclusion and perspectives

Modelling of anisotropy in homogeneous flows has been considered at two different levels. The first one is the three-dimensional spectral level, in which a decomposition of the spectral tensor for arbitrary anisotropy lends support to a splitting of anisotropy at any subsequent level in terms of directional anisotropy and polarization anisotropy. In a second step, a model for spherically integrated quantities has been proposed, which is based on 11 coupled equations. It is dedicated to turbulent flows where the anisotropy is moderate and where linear effects induced by mean-velocity gradients play a negligible role in the dynamics of triple correlations compared with the induced production effects in the equations for the second-order correlations. This model is not restricted to a particular symmetry and can be used for a wide range of flow configurations, as illustrated by the different applications of the model considered in this paper. A satisfactory agreement with the experiments of Gence & Mathieu (1979, 1980) has been observed, which confirms the capability of the model to account for production of anisotropy by mean-flow gradients.

Concerning the RTI of initially deformed or sheared turbulence, the model is consistent with the PLE and ensures correct rapid RTI of the smallest scales. Different relaxation rates for directional anisotropy and polarization anisotropy allow us to correctly interpret the apparent delay in the RTI after axisymmetric expansion (Zusi & Perot 2014). In addition, our model fits well the recent experiment of Chen *et al.* (2006) with a non-stationary straining cycle. For turbulence continuously subjected to a pure plane shear, the model ensures a correct asymptotic regime with constant values for the components of the dimensionless deviatoric tensor $b_{ij}(t)$ associated with the Reynolds stress tensor. In addition, it can reproduce the exponential growth of the turbulent kinetic energy mediated by nonlinear pressure redistribution terms. However, first-order truncations in the description of anisotropy, which are the main sources of possible discrepancies between the present model and DNS/experimental results, prevent a good quantitative agreement with typical values of the growth rate found in the literature. For this configuration, an alternative approach, which is entirely formulated in 3D Fourier space and without limitation in time, can be found in Weinstock (2013).

Beyond moderate anisotropy, a more complex version of the model could possibly combine exact linear operators in $\boldsymbol{k}$-vectors, as in the left-hand side of (2.12)–(2.13), with transfer terms only generated by low-order angular harmonic expansions. Such a model could reproduce the dominant RDT dynamics for the largest scales, and the quasi-isotropic behaviour for scales smaller than a Corrsin scale.

Appendix A. Relationships between two-point spectral tensors and single-point tensors

The equations addressed in this paper involve several tensors: production by mean-velocity gradients, dissipation, transfer, pressure–strain rate. In the following, we give their expressions systematically in terms of $\boldsymbol{k}$, then in terms of k, obtained by spherically averaging the first one, and their final single-point contribution obtained by integrating on k, as in full Reynolds stress models (RSMs) with an additional structure-based tensor. Time dependence is implied (not explicitly written below).

A.1. *Production term by space-uniform mean-velocity gradient*

The production term by the space-uniform mean-velocity gradient in (2.3) is $\lambda_{il}\hat{R}_{lj}(\boldsymbol{k}) + \lambda_{jl}\hat{R}_{li}(\boldsymbol{k})$. By using the representation (3.1), its spherically integrated counterpart is

$$\iint_{S_k} \lambda_{il}\hat{R}_{lj}(\boldsymbol{k})+\lambda_{jl}\hat{R}_{il}(\boldsymbol{k})\,\mathrm{d}^2\boldsymbol{k}=\frac{4}{3}S_{ij}E+2E\left(\lambda_{il}H^{(dir)}_{lj}+\lambda_{jl}H^{(dir)}_{li}\right)+2E\left(\lambda_{il}H^{(pol)}_{lj}+\lambda_{jl}H^{(pol)}_{li}\right), \tag{A 1}$$

with $E=E(k)$, $H^{(dir)}_{ij}=H^{(dir)}_{ij}(k)$ and $H^{(pol)}_{ij}=H^{(pol)}_{ij}(k)$. The single-point counterpart of the production term is given by

$$\begin{aligned}\iiint \lambda_{il}\hat{R}_{lj}(\boldsymbol{k})+\lambda_{jl}\hat{R}_{il}(\boldsymbol{k})\,\mathrm{d}^3\boldsymbol{k} \;&=\; \frac{4}{3}S_{ij}\mathscr{K}+2\mathscr{K}\left(\lambda_{il}b^{(dir)}_{lj}+\lambda_{jl}b^{(dir)}_{li}\right)\\ &\quad +2\mathscr{K}\left(\lambda_{il}b^{(pol)}_{lj}+\lambda_{jl}b^{(pol)}_{li}\right),\end{aligned} \tag{A 2}$$

where the tensors $b^{(dir)}_{ij}$ and $b^{(pol)}_{ij}$ are defined by (4.4).

A.2. *Dissipation term*

The dissipation term in (2.3) is $2\nu k^2\hat{R}_{ij}(\boldsymbol{k})$. Its spherically integrated counterpart is

$$\iint_{S_k} 2\nu k^2\hat{R}_{ij}(\boldsymbol{k})\,\mathrm{d}^2\boldsymbol{k}=4\nu k^2E\left(\frac{\delta_{ij}}{3}+H^{(dir)}_{ij}+H^{(pol)}_{ij}\right). \tag{A 3}$$

The corresponding single-point contribution is

$$\iiint 2\nu k^2\hat{R}_{ij}(\boldsymbol{k})\,\mathrm{d}^3\boldsymbol{k}=\frac{2}{3}\delta_{ij}\varepsilon+\varepsilon^{(dir)}_{ij}+\varepsilon^{(pol)}_{ij}, \tag{A 4}$$

where $\varepsilon^{(dir)}_{ij}=\int_0^\infty 4\nu k^2E(k)H^{(dir)}_{ij}(k)\,\mathrm{d}k$, with a similar definition for $\varepsilon^{(pol)}_{ij}$.

A.3. *‘Rapid’ contribution of the pressure–strain rate tensor*

The rapid contribution of the pressure–strain rate tensor is given by $2\lambda_{ln}\alpha_l(\alpha_i\hat{R}_{nj}(\boldsymbol{k})+\alpha_j\hat{R}_{ni}(\boldsymbol{k}))$. Its spherically integrated counterpart is

$$\begin{aligned}&\iint_{S_k} 2\lambda_{ln}\alpha_l(\alpha_i\hat{R}_{nj}(\boldsymbol{k})+\alpha_j\hat{R}_{ni}(\boldsymbol{k}))\,\mathrm{d}^2\boldsymbol{k}\\ &\quad=\frac{4}{5}ES_{ij}-\frac{12}{7}E\left(S_{lj}H^{(dir)}_{li}+S_{li}H^{(dir)}_{lj}-\frac{2}{3}S_{lm}H^{(dir)}_{lm}\delta_{ij}\right)\end{aligned}$$

$$+4E\left(\mathsf{A}_{jl}\mathsf{H}_{il}^{(dir)}+\mathsf{A}_{il}\mathsf{H}_{jl}^{(dir)}\right)+\frac{12}{7}E\left(\mathsf{S}_{lj}\mathsf{H}_{li}^{(pol)}+\mathsf{S}_{li}\mathsf{H}_{lj}^{(pol)}-\frac{2}{3}\mathsf{S}_{lm}\mathsf{H}_{lm}^{(pol)}\delta_{ij}\right)$$
$$+\frac{4}{3}E\left(\mathsf{A}_{il}\mathsf{H}_{lj}^{(pol)}+\mathsf{A}_{jl}\mathsf{H}_{li}^{(pol)}\right). \tag{A 5}$$

Similarly to the transition from (A 1) to (A 2), the single-point contribution of the rapid component of the pressure–strain rate tensor is obtained from (A 5) by replacing $E(k)$, $\mathsf{H}_{ij}^{(dir)}(k)$ and $\mathsf{H}_{ij}^{(pol)}(k)$ with $\mathscr{K}$, $\mathsf{b}_{ij}^{(dir)}$ and $\mathsf{b}_{ij}^{(pol)}$ respectively. The closure of the rapid pressure–strain rate tensor in RSMs is generally applied to the tensor M_{ijpq}, defined by

$$\mathsf{M}_{ijpq}=\iiint \alpha_p\alpha_q\hat{\mathsf{R}}_{ij}(\boldsymbol{k})\,\mathrm{d}^3\boldsymbol{k}, \tag{A 6}$$

and made non-dimensional by the turbulent kinetic energy. The closure is usually in terms of the deviatoric tensor b_{ij}. Tensorial expansions range from linear (Launder, Reece & Rodi 1975; Lumley 1975) with a single tuned constant, to quadratic (Speziale, Sarkar & Gatski 1991) and even cubic (Craft, Ince & Launder 1996; Craft & Launder 2001) with increase in the number of tuned constants as the degree of nonlinearity increases.

A.4. *Transfer tensor from linear origin*

The spherically averaged version of the term $\lambda_{ln}k_l(\partial\hat{\mathsf{R}}_{ij}/\partial k_n)(\boldsymbol{k})$ is

$$\iint_{S_k}\lambda_{ln}k_l\frac{\partial\hat{\mathsf{R}}_{ij}}{\partial k_n}(\boldsymbol{k})\,\mathrm{d}^2\boldsymbol{k}=\frac{4}{7}\left(\mathsf{S}_{il}\frac{\partial}{\partial k}(kE\mathsf{H}_{lj}^{(dir)})+\mathsf{S}_{lj}\frac{\partial}{\partial k}(kE\mathsf{H}_{li}^{(dir)})-3\mathsf{S}_{lm}\frac{\partial}{\partial k}(kE\mathsf{H}_{lm}^{(dir)})\delta_{ij}\right)$$
$$-\frac{4}{7}\left(\mathsf{S}_{jl}\frac{\partial}{\partial k}(kE\mathsf{H}_{il}^{(pol)})+\mathsf{S}_{il}\frac{\partial}{\partial k}(kE\mathsf{H}_{lj}^{(pol)})-\frac{2}{3}\mathsf{S}_{ln}\frac{\partial}{\partial k}(kE\mathsf{H}_{ln}^{(pol)})\delta_{ij}\right)-\frac{2}{15}\mathsf{S}_{ij}\frac{\partial}{\partial k}(kE). \tag{A 7}$$

The k integral of the above expression is 0.

A.5. *Transfer tensor from nonlinear origin and 'slow' part of the pressure–strain rate tensor*

The expression of the 'true' nonlinear transfer tensor, with zero integral over $\boldsymbol{k}$, is $\tau_{ij}(\boldsymbol{k})+\tau_{ji}^{*}(\boldsymbol{k})$, and that of the slow part of the pressure–strain rate tensor is $-\alpha_i\alpha_n\tau_{nj}(\boldsymbol{k})-\alpha_j\alpha_n\tau_{ni}^{*}(\boldsymbol{k})$, with $\tau_{ij}(\boldsymbol{k})$ defined by (2.6). The spherically integrated counterparts of these tensors are given by (3.6) and (3.10), (3.13). Concerning RSMs, the slow pressure–strain rate tensor is generally closed as $-C\varepsilon\mathsf{b}_{ij}$ in order to relax the dimensionless deviatoric part of the Reynolds stress tensor b_{ij} weighted by the dissipation rate ε. More or less complicated expressions were proposed instead of the constant C.

A.6. *Kassinos et al. (2001) structure-based tensors*

The dimensionality tensor can be derived from a special index contraction of the tensor M_{ijpq} defined by (A 6), as $\mathsf{D}_{ij}=\mathsf{M}_{llij}$, whereas the two other contractions give 0 or the Reynolds stress tensor itself. Accordingly, it is found that

$$\mathsf{D}_{ij}=\iiint\alpha_i\alpha_j\hat{\mathsf{R}}_{mm}(\boldsymbol{k})\,\mathrm{d}^3\boldsymbol{k}=\int_0^{\infty}2E(k)\left(\frac{1}{3}\delta_{ij}-2\mathsf{H}_{ij}^{(dir)}(k)\right)\mathrm{d}k=2\mathscr{K}\left(\frac{1}{3}\delta_{ij}-2\mathsf{b}_{ij}^{(dir)}\right). \tag{A 8}$$

The circulicity tensor F_{ij} is not independent and is given by

$$F_{ij} = 2\mathscr{K}\left(\tfrac{1}{3}\delta_{ij} + b^{(dir)}_{ij} - b^{(pol)}_{ij}\right). \tag{A 9}$$

The last relevant tensor used by Kassinos *et al.* (2001) is the 'stropholysis' one, derived from $Q_{ijk} = \epsilon_{ipq} M_{jqpk}$, which can be expressed in the present formalism as

$$Q_{ijk} = \mathscr{K}\left(\tfrac{1}{3}\epsilon_{ikj} - 2\epsilon_{ipj} b^{(dir)}_{kp} + \tfrac{4}{3}\epsilon_{ikp} b^{(pol)}_{jp} + \tfrac{2}{3}\epsilon_{ipj} b^{(pol)}_{kp}\right). \tag{A 10}$$

In a fully symmetrized form, the spectral counterpart ($\boldsymbol{k}$-vector) of this third tensor is given by contributions from $\alpha_k \operatorname{Im}(Z(\boldsymbol{k})N_i(\boldsymbol{k})N_j(\boldsymbol{k}))$ (Sagaut & Cambon 2008). The latter expression is related to the term $U^{(pol)3}_{ijm}(k)$ in (3.15), and the contribution from our final model is zero, because of the truncation of the development of $Z(\boldsymbol{k})$ in terms of second-order angular harmonics. The true 'stropholysis' effect, which breaks mirror symmetry but is distinct from helicity, is given by the imaginary part of $Z(\boldsymbol{k})$: it is dynamically created by the last term on the left-hand side of (2.13) in the presence of rotational mean flows.

A.7. *Towards the ε-equation*

An equation for ε_{ij} can easily be found, in which $\mathrm{d}\varepsilon_{ij}/\mathrm{d}t$ results from the balance of different terms, obtained by integrating, over $\boldsymbol{k}$ then over k, nonlinear transfer terms, purely viscous contributions and linear mean-gradient terms. Only the scalar ε-equation is considered now, for comparison with RSMs. It reduces to

$$\frac{\mathrm{d}\varepsilon}{\mathrm{d}t} = 2\nu \int_0^\infty k^2 T(k)\,\mathrm{d}k - \int_0^\infty (2\nu k^2)^2 E(k)\,\mathrm{d}k + 2\nu \int_0^\infty k^2 S^L(k)\,\mathrm{d}k. \tag{A 11}$$

In single-point models, the two first terms on the right-hand side are globally closed as $-C_{\varepsilon 2}\varepsilon^2/\mathscr{K}$, whereas the last term is closed as $-C_{\varepsilon 1}\lambda_{mn}\langle u_m u_n\rangle \varepsilon/\mathscr{K}$. It should be noted that $\int_0^\infty T(k)\,\mathrm{d}k = 0$, but that its integral weighted by k^2 is positive, at least in isotropic turbulence, and corresponds to $\langle(\partial u_i/\partial x_j)\omega_i\omega_j\rangle$ or a nonlinear vortex stretching term in physical space, with ω_i the fluctuating vorticity.

REFERENCES

André, J. C. & Lesieur, M. 1977 Influence of helicity on the evolution of isotropic turbulence at high Reynolds number. *J. Fluid Mech.* **81**, 187–207.

Bellet, F., Godeferd, F. S., Scott, J. F. & Cambon, C. 2006 Wave turbulence in rapidly rotating flows. *J. Fluid Mech.* **562**, 83–121.

Brethouwer, G. 2005 The effect of rotation on rapidly sheared homogeneous turbulence and passive scalar transport. Linear theory and direct numerical simulation. *J. Fluid Mech.* **542**, 305–342.

Cambon, C., Danaila, L., Godeferd, F. S. & Scott, J. F. 2013 Third-order statistics and the dynamics of strongly anisotropic turbulent flows. *J. Turbul.* **14** (3), 121–160.

Cambon, C. & Jacquin, L. 1989 Spectral approach to non-isotropic turbulence subjected to rotation. *J. Fluid Mech.* **202**, 295–317.

Cambon, C., Jeandel, D. & Mathieu, J. 1981 Spectral modelling of homogeneous non-isotropic turbulence. *J. Fluid Mech.* **104**, 247–262.

CAMBON, C., MANSOUR, N. N. & GODEFERD, F. S. 1997 Energy transfer in rotating turbulence. *J. Fluid Mech.* **337**, 303–332.

CAMBON, C. & RUBINSTEIN, R. 2006 Anisotropic developments for homogeneous shear flows. *Phys. Fluids* **18**, 085106.

CAMBON, C. & SCOTT, J. F. 1999 Linear and nonlinear models of anisotropic turbulence. *Annu. Rev. Fluid Mech.* **31**, 1–53.

CANUTO, V. M. & DUBOVIKOV, M. S. 1996*a* A dynamical model for turbulence. I. General formalism. *Phys. Fluids* **8** (2), 571–586.

CANUTO, V. M. & DUBOVIKOV, M. S. 1996*b* A dynamical model for turbulence. II. Shear-driven flows. *Phys. Fluids* **8** (2), 587–598.

CANUTO, V. M. & DUBOVIKOV, M. S. 1996*c* A dynamical model for turbulence. III. Numerical results. *Phys. Fluids* **8** (2), 599–613.

CHASNOV, J. R. 1995 The decay of axisymmetric homogeneous turbulence. *Phys. Fluids* **7** (3), 600–605.

CHEN, J., MENEVEAU, C. & KATZ, J. 2006 Scale interactions of turbulence subjected to a straining–relaxation–destraining cycle. *J. Fluid Mech.* **562**, 123–150.

CHOI, K.-S. & LUMLEY, J. L. 2001 The return to isotropy of homogeneous turbulence. *J. Fluid Mech.* **436**, 59–84.

CLARK, T. T. & ZEMACH, C. 1995 A spectral model applied to homogeneous turbulence. *Phys. Fluids* **7** (7), 1674–1694.

CORRSIN, S. 1958 On local isotropy in turbulent shear flow. *NACA RM* 58B11.

CRAFT, T. J., INCE, N. Z. & LAUNDER, B. E. 1996 Recent developments in second-moment closure for buoyancy-affected flows. *Dyn. Atmos. Oceans* **23**, 99–114.

CRAFT, T. J. & LAUNDER, B. E. 2001 Principles and performance of TCL-based second-moment closures. *Flow Turbul. Combust.* **66**, 355–372.

DAVIDSON, P. A., OKAMOTO, N. & KANEDA, Y. 2012 On freely decaying, anisotropic, axisymmetric Saffman turbulence. *J. Fluid Mech.* **706**, 150–172.

FAVIER, B. F. N., GODEFERD, F. S., CAMBON, C., DELACHE, A. & BOS, W. J. T. 2011 Quasi-static magnetohydrodynamic turbulence at high Reynolds number. *J. Fluid Mech.* **681**, 434–461.

GENCE, J. N. 1983 Homogeneous turbulence. *Annu. Rev. Fluid Mech.* **15**, 201–222.

GENCE, J. N. & MATHIEU, J. 1979 On the application of successive plane strains to grid-generated turbulence. *J. Fluid Mech.* **93**, 501–513.

GENCE, J. N. & MATHIEU, J. 1980 The return to isotropy of an homogeneous turbulence having been submitted to two successive plane strains. *J. Fluid Mech.* **101**, 555–566.

GODEFERD, F. S. & CAMBON, C. 1994 Detailed investigation of energy transfers in homogeneous stratified turbulence. *Phys. Fluids* **6**, 2084–2100.

HERRING, J. R. 1974 Approach of axisymmetric turbulence to isotropy. *Phys. Fluids* **17** (5), 859–872.

ISAZA, J. C. & COLLINS, L. R. 2009 On the asymptotic behaviour of large-scale turbulence in homogeneous shear flow. *J. Fluid Mech.* **637**, 213–239.

ISHIHARA, T., YOSHIDA, K. & KANEDA, Y. 2002 Anisotropic velocity correlation spectrum at small scales in a homogeneous turbulent shear flow. *Phys. Rev. Lett.* **88**, 154501,1–4.

KANEDA, Y. 1981 Renormalized expansions in the theory of turbulence with the use of the Lagrangian position function. *J. Fluid Mech.* **107**, 131–145.

KASSINOS, S. C. & AKYLAS, E. 2012 Advances in particle representation modeling of homogeneous turbulence: from the linear PRM version to the interacting viscoelastic IPRM. In *ERCOFTAC Series*, vol. 18, pp. 81–101.

KASSINOS, S. C. & REYNOLDS, W. C. 1997 Advances in structure-based turbulence modeling. In *Annual Research Briefs – Center for Turbulence Research*, pp. 179–193.

KASSINOS, S. C., REYNOLDS, W. C. & ROGERS, M. M. 2001 One-point turbulence structure tensors. *J. Fluid Mech.* **428**, 231–248.

KIM, S.-W. & CHEN, C.-P. 1989 A multiple-time-scale turbulence model based on variable partitioning of the turbulent kinetic energy spectrum. *Numer. Heat Transfer* B **16**, 193–211.

KRAICHNAN, R. H. 1959 The structure of isotropic turbulence at very high Reynolds numbers. *J. Fluid Mech.* **5**, 497–543.

KRAICHNAN, R. H. 1972 Test-field model for inhomogeneous turbulence. *J. Fluid Mech.* **56**, 287–304.

KRAICHNAN, R. H. & HERRING, J. R. 1978 A strain-based Lagrangian-history turbulence theory. *J. Fluid Mech.* **88**, 355–367.

LAUNDER, B. E., REECE, G. J. & RODI, W. 1975 Progress in the development of a Reynolds-stress turbulent closure. *J. Fluid Mech.* **68**, 537–566.

LESIEUR, M. 2008 *Turbulence in Fluids*, 4th edn. Springer.

LESLIE, D. C. 1973 *Developments in the Theory of Turbulence*. Clarendon.

LUMLEY, J. L. 1967 Similarity and the turbulent energy spectrum. *Phys. Fluids* **10** (4), 855–858.

LUMLEY, J. L. 1975 *Lectures Series*, 76. Von Karman Institute.

MEYERS, J. & MENEVEAU, C. 2008 A functional form of the energy spectrum parametrizing bottleneck and intermittency effects. *Phys. Fluids* **20**, 065109.

MILLIONSCHIKOV, M. D. 1941 Theory of homogeneous isotropic turbulence. *Dokl. Akad. Nauk SSSR* **33**, 22–24.

MONS, V., MELDI, M. & SAGAUT, P. 2014 Numerical investigation on the partial return to isotropy of freely decaying homogeneous axisymmetric turbulence. *Phys. Fluids* **26**, 025110.

O'BRIEN, E. F. & FRANCIS, G. C. 1963 A consequence of the zero fourth cumulant approximation. *J. Fluid Mech.* **13**, 369–382.

OGURA, Y. 1963 A consequence of the zero fourth cumulant approximation in the decay of isotropic turbulence. *J. Fluid Mech.* **16**, 33–40.

ORSZAG, S. A. 1970 Analytical theories of turbulence. *J. Fluid Mech.* **41**, 363–386.

PIQUET, J. 2001 *Turbulent Flows – Models and Physics*, 2nd edn. Springer.

POPE, S. B. 2000 *Turbulent Flows*. Cambridge University Press.

POUQUET, A., LESIEUR, M., ANDRÉ, J. C. & BASDEVANT, C. 1975 Evolution of high Reynolds number two-dimensional turbulence. *J. Fluid Mech.* **72**, 305–319.

PROUDMAN, I. & REID, W. H. 1954 On the decay of a normally distributed and homogeneous turbulent velocity field. *Phil. Trans. R. Soc. Lond.* A **297**, 163–189.

ROGERS, M. M., MOIN, P. & REYNOLDS, W. C. 1986 The structure and modelling of the hydrodynamic and passive scalar fields in homogeneous shear turbulence. *Report No.* TF-25. Department of Mechanical Engineering, Stanford University, Stanford, CA.

ROHR, J. J., ITSWEIRE, E. C., HELLAND, K. N. & VAN ATTA, C. W. 1988 An investigation of the growth of turbulence in a uniform-mean-shear flow. *J. Fluid Mech.* **187**, 1–33.

RUBINSTEIN, R. 1996 A relaxation approximation for time-dependent second-order effects in shear turbulence. *Theor. Comput. Fluid Dyn.* **8**, 377–386.

RUBINSTEIN, R., KURIEN, S. & CAMBON, C. 2015 Scalar and tensor spherical harmonics expansion of the velocity correlation in homogeneous anisotropic turbulence. *J. Turbul.* **16** (11), 1058–1075.

SAGAUT, P. & CAMBON, C. 2008 *Homogeneous Turbulence Dynamics*. Cambridge University Press.

SCHIESTEL, R. 1987 Multiple-time-scale modeling of turbulent flows in one-point closures. *Phys. Fluids* **30** (3), 722–731.

SHEN, X. & WARHAFT, Z. 2000 The anisotropy of the small scale structure in high Reynolds number ($R_\lambda \sim 1000$) turbulent shear flow. *Phys. Fluids* **12**, 2976–2989.

SPEZIALE, C. G., SARKAR, S. & GATSKI, T. B. 1991 Modelling the pressure–strain correlation of turbulence: an invariant dynamical systems approach. *J. Fluid Mech.* **227**, 245–272.

TAVOULARIS, S. 1985 Asymptotic laws for transversely homogeneous turbulent shear flows. *Phys. Fluids* **28**, 999–1001.

TAVOULARIS, S. & CORRSIN, S. 1981 Experiments in nearly homogenous turbulent shear flow with a uniform mean temperature gradient. Part 1. *J. Fluid Mech.* **104**, 311–347.

TAVOULARIS, S. & KARNIK, U. 1989 Further experiments on the evolution of turbulent stresses and scales in uniformly sheared turbulence. *J. Fluid Mech.* **204**, 457–478.

TOWNSEND, A. A. 1976 *The Structure of Turbulent Shear Flow*, 2nd edn. Cambridge University Press.

WALEFFE, F. 1992 The nature of triad interactions in homogeneous turbulence. *Phys. Fluids* **4**, 350–363.

WEINSTOCK, J. 2013 Analytical theory of homogeneous mean shear turbulence. *J. Fluid Mech.* **727**, 256–281.

YOSHIDA, K., ISHIHARA, T. & KANEDA, Y. 2003 Anisotropic spectrum of homogeneous turbulent shear flow in a Lagrangian renormalized approximation. *Phys. Fluids* **15** (8), 2385–2397.

ZHOU, Y. 2010 Renormalization group theory for fluid and plasma turbulence. *Phys. Rep.* **488**, 1–49.

ZUSI, C. J. & PEROT, J. B. 2013 Simulation and modeling of turbulence subjected to a period of uniform plane strain. *Phys. Fluids* **25**, 110819.

ZUSI, C. J. & PEROT, J. B. 2014 Simulation and modeling of turbulence subjected to a period of axisymmetric contraction or expansion. *Phys. Fluids* **26**, 115103.

Part II

Data assimilation and computational fluid dynamics

Introduction

Data assimilation (DA) is being increasingly applied to computational fluid dynamics (CFD) due to its multiple possibilities of applications, as mentioned in chapter 1. DA can be used to determine initial condition, boundary conditions or model parameters for a CFD code from experimental fluid dynamics (EFD) observations of a given flow, thus improving the numerical prediction of complex realistic flows [94]. Among other possible uses, flow reconstruction through DA can be employed to complete experimental observations through the enforcement of dynamical constraints [97], to build robust reduced-order models [12, 117], or to perform detailed sensitivity analyses, with an example given in chapter 3 [160]. DA can be also considered in flow control problems to design efficient estimators [23]. Applications may range from aeronautics [115] to environmental fluid mechanics [93].

Two classes of DA methods as discussed in chapter 2 have been applied so far to fluid mechanics problems: variational DA (§2.3) [12, 23, 67, 83, 91, 173] and the Kalman filter in its standard (§2.4) [51, 100, 196] and ensemble formulations (§2.5) [60, 114, 115, 117]. These two DA schemes vastly differ in their implementations, and may produce distinct solutions in the case of nonlinear dynamics and/or observations. Kalman filter techniques are easy to implement due to their non-intrusive character, and provide not only an assimilated state of the flow but also the associated statistics. However, the assimilation process requires the prescription of prior statistics, which may be difficult to characterize while they may have dramatic impact on the results, as discussed in §2.6.1. An additional problem with ensemble filtering, which is however more suited to nonlinear large-scale systems than the standard Kalman filter, is that it is subject to finite ensemble size effects requiring *ad hoc* adjustments to ensure the stability of the filter (§2.5.3). On the other hand, the use of adjoint techniques in variational DA provides robustness and scalability to the assimilation procedure. However, the development of the adjoint model associated to the CFD code [176] is thus required, which may be a particularly tedious task in the case of complex flow solvers.

Only a few studies have been dedicated to the application of DA to Navier-Stokes solvers for fully unsteady flows [91, 196]. Moreover, despite the significant differences between variational DA and Kalman filtering mentioned above, these two techniques have always been investigated separately (see table 4.1). Accordingly, a comparative study between variational DA and Kalman filtering to fully delineate the pros and cons of these methods and quantify their relative performances in the context of CFD is still lacking.

Furthermore, other DA methodologies of chapter 2 than the two mentioned above could also be worthy of consideration in the context of CFD. In particular, hybrid techniques, ensemble-based variational schemes and particle filters are emerging methods in the meteorological community that have not yet been used in conjunction with Navier-Stokes solvers. Hybrid schemes (§2.6.1) aim at improving the estimation of prior statistics in variational DA through the incorporation of ensemble information, allowing to consider flow-dependent prior covariance matrix in the assimilation process. While the determination of better prior statistics may indeed enhance the results of variational DA, such approaches still require an adjoint model, and are therefore as demanding as standard variational schemes in terms of computational efforts. Particle filters (§2.8) allow to avoid the use of the Gaussian assumption and consider the propagation of the full probability density function of the system. However, one may wonder about the need of considering a fully stochastic formulation of DA in the context of CFD, especially given the number of adjustments required to ease the computational burden associated to the use of full probability density functions to characterize large scale systems. Recent applications of particle filtering to a shallow water model and to proper orthogonal decomposition-based reduced-order models can nevertheless be

study	DA scheme	characteristics of the flow			*Re*	assimilated quantities	observations
Bewley & Protas (2004) [23]	VDA	turbulent channel flow	incompressible 3D	unsteady (short assimilation window)	100	initial state	skin friction and pressure distributions
Papadakis & Mémin (2008) [173]	VDA	turbulent field	incompressible 2D	unsteady	–	initial state	velocity field
Colburn *et al.* (2011) [60]	EnKF	turbulent channel flow	incompressible 3D	statistically steady	100	flow field	skin friction and pressure distributions
Suzuki (2012) [196]	EKF	planar-jet flow	incompressible 2D	unsteady	2000	flow field	velocity field
Gronskis *et al.* (2013) [91]	VDA	cylinder wake flow	incompressible 2D	unsteady	170	initial state and boundary conditions	vorticity field
Foures *et al.* (2014) [83]	VDA	cylinder wake flow	incompressible 2D	steady (RANS solver)	150	Reynolds stress tensor term	velocity field
Kato *et al.* (2015) [115]	EnKF	flow past an airfoil	compressible 3D	statistically steady	$1.2 \cdot 10^7$	angle of attack, Mach number, turbulent viscosity	pressure distribution
chapter 5 [163]	EnKF, VDA, EnVar	cylinder wake flow in the presence of coherent gusts	compressible 2D	unsteady	100	initial state and boundary conditions	velocity field, pressure distribution, aerodynamic coefficients
chapter 6	VDA (OSP)	flow past a rotating cylinder	compressible 2D	unsteady	100	rotational speed of the cylinder and initial state	velocity field, aerodynamic coefficients
chapter 7	EnVar (OSP)	turbulent urban flow	compressible 3D	unsteady	$6.2 \cdot 10^7$	scalar source and wind parameters	gas concentration

TABLE 4.1: Summary of studies dealing with the use of data assimilation (DA) based on the solution of the Navier-Stokes equations, including the present ones. The different DA techniques investigated are: variational DA (VDA), the extended Kalman filter (EKF), the ensemble Kalman filter (EnKF) and ensemble-based variational schemes (EnVar). In chapters 6 and 7, the DA scheme is assisted by optimal sensor placement (OSP). In [23] and [60], the Reynolds number is based on the mean friction velocity and the half-channel height.

found in [61] and [117] respectively. Finally, ensemble-based variational schemes (§2.6.2) still use a variational framework, but rely on the propagation of an ensemble of realizations to avoid the need of an adjoint code. Such techniques may be the most interesting alternatives to variational DA and Kalman filtering among the methods discussed above, since they seem to combine the robustness of the former and the non-intrusive character of the latter. Ensemble-based variational DA, which has been recently applied to the shallow water model in [230], has not yet been considered in conjunction with Navier-Stokes solvers.

In compliance with the above discussion, a methodological study to determine appropriate DA techniques in the context of CFD is performed in chapter 5. Variational DA, ensemble Kalman filters, and ensemble-based variational schemes are deployed with a Navier-Stokes solver for unsteady bidimensional compressible flows, which is presented in appendix C along with the corresponding adjoint code. DA is used to infer initial and boundary conditions for flows past a cylinder in the presence of coherent gusts from observations ranging from the aerodynamic coefficients to the full velocity field. The influence of the DA setup on the performances of the three DA schemes is thoroughly addressed in various reconstruction scenarios with large control vectors, allowing a detailed assessment of the considered methodologies.

Aside from the question of the choice of the DA methodology, we also examine the issue of sensor network design for DA purposes. This problem is of crucial importance since measurements represent the only available information about the reference flow to be reconstructed, and observations should be thus required to provide as much information as possible about the reference flow. The determination of efficient strategies for sensor placement in the contexts of DA and CFD applications has not yet been investigated and is still an open question despite the existence of several techniques proposed in the meteorological community. An adjoint-based sensor placement procedure is proposed in chapter 6, which aims at identifying the regions of the flow that have the greatest sensitivity with respect to a change in the initial condition, boundary conditions or model parameters. The developed methodology is applied to the reconstruction of flows past a rotationally oscillating cylinder with the same direct and adjoint codes than in chapter 5. More precisely, the possibilities of identifying the rotational speed of the cylinder and the initial flow from observations of the velocity field at discrete locations are investigated through variational DA, with the expectation that optimal sensor placement will allow to improve the performances of the assimilation procedure.

As a final test case, we investigate the possibility of reconstructing urban flows through DA in chapter 7, allowing to consider much more complex flows than in previous chapters and to tend towards real-world applications. Computations rely on a Very Large Eddy Simulation (VLES)/Lattice Boltzmann Method (LBM) solver, which provides high-fidelity predictions of turbulent flows in an actual urban area that has already been considered in [148]. From the results of chapter 5, an ensemble-based variational DA scheme is implemented with this solver for the identification of the characteristics of a pollutant source and meteorological conditions from measurements of concentration. A sensor placement procedure is also developed to guide the design of observation networks. This methodology relies on uncertainty quantification techniques proposed in [150], see also appendix E, and is complementary to the strategy of chapter 6 in the sense that it is non-intrusive, while the methodology of chapter 6 requires an adjoint model. However, both approaches consist in placing sensors at locations in the flow with maximum sensitivity with respect to the control vector in the DA process, and they differ in the way in which sensitivity is evaluated.

Chapter 5

Reconstruction of unsteady viscous flows using data assimilation schemes

Journal of Computational Physics 316 (2016) 255–280

Contents lists available at ScienceDirect

Journal of Computational Physics

www.elsevier.com/locate/jcp

Reconstruction of unsteady viscous flows using data assimilation schemes

V. Mons [a,*], J.-C. Chassaing [a], T. Gomez [b,c], P. Sagaut [d]

[a] *Sorbonne Universités, UPMC Univ Paris 06, CNRS, UMR 7190, Institut Jean Le Rond d'Alembert, F-75005 Paris, France*
[b] *Université Lille Nord de France, F-59000 Lille, France*
[c] *USTL, LML, F-59650 Villeneuve d'Ascq, France*
[d] *Aix Marseille Université, CNRS, Centrale Marseille, M2P2 UMR 7340, 13451 Marseille, France*

ARTICLE INFO

Article history:
Received 20 October 2015
Received in revised form 5 April 2016
Accepted 9 April 2016
Available online 14 April 2016

Keywords:
Data assimilation
Variational assimilation
Kalman filter
Ensemble methods
Unsteady flows

ABSTRACT

This paper investigates the use of various data assimilation (DA) approaches for the reconstruction of the unsteady flow past a cylinder in the presence of incident coherent gusts. Variational, ensemble Kalman filter-based and ensemble-based variational DA techniques are deployed along with a 2D compressible Navier–Stokes flow solver, which is also used to generate synthetic observations of a reference flow. The performance of these DA schemes is thoroughly analyzed for various types of observations ranging from the global aerodynamic coefficients of the cylinder to the full 2D flow field. Moreover, different reconstruction scenarios are investigated in order to assess the robustness of these methods for large scale DA problems with up to 10^5 control variables. In particular, we show how an iterative procedure can be used within the framework of ensemble-based methods to deal with both non-uniform unsteady boundary conditions and initial field reconstruction. The different methodologies developed and assessed in this work give a review of what can be done with DA schemes in computational fluid dynamics (CFD) paradigm. In the same time, this work also provides useful information which can also turn out to be rational arguments in the DA scheme choice dedicated to a specific CFD application.

1. Introduction

Data assimilation (DA) techniques [1,2], which have been mainly developed in the fields of meteorology and oceanography, are increasingly considered in fluid mechanics. They provide a relevant mathematical framework to combine experimental observations with computational fluid dynamics (CFD) predictions in order to obtain a better description of the model inputs like initial condition, boundary conditions or model parameters [3,4]. DA can also be used to complete sparse observations [5] or to solve inverse problems [6]. Two different classes of DA techniques have been applied to fluid mechanics: variational methods [7], which are based on the use of the optimal control theory [8] to minimize the error between observations of a reference flow and a numerical estimation, and Kalman filter methods [9], which directly originate from the Bayesian formulation of the DA problem [10,11] and rely on the propagation in time of the statistics of the state vector. Variational-based DA techniques have been applied to proper orthogonal decomposition-based surrogate models [12,13], turbulence spectral models [6], and to the Navier–Stokes equations [3,14]. Foures et al. [14] performed DA experiments with

---

[*] Corresponding author.
E-mail address: vincent.mons@dalembert.upmc.fr (V. Mons).

http://dx.doi.org/10.1016/j.jcp.2016.04.022

the 2D steady Reynolds-averaged Navier–Stokes equations where the Reynolds stress tensor term forms the control vector, while Gronskis et al. [3] used experimental data to determine optimal initial and boundary conditions for 2D unsteady direct numerical simulations (DNS). Both studies considered the wake flow behind a circular cylinder at Reynolds numbers between 125 and 170. Kalman filter techniques have also been applied to Navier–Stokes solvers. Suzuki [5] implemented a reduced-order extended Kalman filter to complete particle image velocimetry data of a planar-jet flow at a Reynolds number of $Re = 2 \cdot 10^3$ using 2D unsteady DNS. As for the original Kalman filter, this DA scheme relies on an update formula for the covariance matrix associated to the statistics of the state vector that is costly to evaluate and not necessarily adapted to high-dimensional and nonlinear problems. Accordingly, ensemble Kalman filters (EnKF) [15], where statistics are propagated with an ensemble of realizations, have also been considered [16,17,4]. Colburn et al. [16] used the EnKF to estimate the statistical steady state of a 3D turbulent channel flow at $Re = 100$ with DNS. Kato et al. [4] estimated the angle of attack, Mach number and turbulent viscosity field for a CFD code with a variant of the EnKF to fit parietal pressure measurements for 2D and 3D steady transonic flows past airfoils at Reynolds numbers up to $1.2 \cdot 10^7$.

Variational and Kalman filter techniques vastly differ in their implementations, and, in particular in the case of nonlinear dynamics, may produce different solutions. Variational methods need the development of an adjoint code [18] to compute the gradient of a cost function that quantifies the discrepancies between observations and numerical estimation with respect to a control vector. On the other hand, Kalman filters are easy to implement due to their non-intrusive character, and can provide posterior statistics. However, the smoothness of the assimilated state and the stability of the DA algorithm are more difficult to ensure in Kalman filter applications. Besides, EnKF results are subject to finite-ensemble-size effects leading to spurious correlations, and supplementary adjustments may be needed if only small ensembles can be afforded [19,20]. To the authors' knowledge, only a few studies have been dedicated to unsteady flows [5,3], which do not involve solid boundaries inside the computational domain. In particular, a comparative study between variational and Kalman filters techniques for CFD based analysis of unsteady flows is still lacking. A third class of DA methods, namely ensemble-based variational (EnVar) schemes [21–23], also deserves attention. To the authors' knowledge, these techniques, recently applied to the shallow water model [24], have not yet been considered for CFD applications. EnVar schemes combine an optimization-based analysis step as in variational methods with the propagation of an ensemble of realizations, similarly to the EnKF, to evaluate the sensitivity of a cost function, avoiding the need for an adjoint code. The aim of the present work is to propose a first comparative study between variational methods, Kalman filter techniques, and EnVar schemes in the context of high-dimensional DA analysis for unsteady CFD. To this end, we consider 2D unsteady DNS computations of the flow around a cylinder at $Re = 100$ in the presence of incident coherent gusts [25]. Considering synthetic observations of a reference evolution, these three DA methods are used to reconstruct initial conditions and/or unsteady and potentially non-uniform boundary conditions. In other words, we are mainly interested in solving an inverse/parameter estimation problem and we focus in the present study on the use of retrospective/non-sequential DA techniques, not on purely sequential methods such as the EnKF. Various observations of the reference state are considered: the pressure distribution around the cylinder, lift and drag coefficients, or the entire velocity field. It must be kept in mind that global aerodynamic coefficients and discrete pressure measurements at cylinder surface are realistic from engineering point of view. The influence of the size and the type of the control vector on the performances of the three methods is examined in detail. The sensitivity of the results with respect to observation and prior statistics, and to the size of the ensemble for ensemble methods, is also thoroughly addressed.

The paper is structured as follows. The different DA methods used in this paper are presented in section 2, and their numerical implementation is detailed in section 3. The CFD code is described in section 4, along with the setup of the different DA experiments performed in this study. The corresponding results are reported in section 5. Section 6 is dedicated to conclusions and perspectives.

2. Data assimilation methods

2.1. The data assimilation problem

We consider the following dynamical model under the fully discrete form:

$$\boldsymbol{q}_{n+1} = \boldsymbol{m}_n(\boldsymbol{q}_n, \boldsymbol{\alpha}_n) \quad 0 \leqslant n \leqslant N-1 \tag{1}$$

where $\boldsymbol{q}_n$ is the state vector, $\boldsymbol{m}_n$ is an operator that maps the state vector from time t_n to t_{n+1}, and $\boldsymbol{\alpha}_n$ represents a set of parameters, such as boundary conditions or shape design parameters, that are potentially time-dependent. In the deterministic framework, given (1), the temporal evolution $(\boldsymbol{q}_n)_{n=1}^{N} = (\boldsymbol{q}_1, \boldsymbol{q}_2, \cdots, \boldsymbol{q}_N)$ would be uniquely specified by the vector $\boldsymbol{\gamma}$ defined by:

$$\boldsymbol{\gamma} = \left(\boldsymbol{q}_0^{\mathrm{T}}, (\boldsymbol{\alpha}_n^{\mathrm{T}})_{n=0}^{N-1}\right)^{\mathrm{T}} \tag{2}$$

This vector gathers the initial condition $\boldsymbol{q}_0$ and the nonstationary parameters of (1), where the superscript T indicates the transpose operator. In a stochastic context, one may consider an additive random error term in (1) so that the state vector $\boldsymbol{q}_n$ becomes a random variable. In addition, we suppose that observations $(\boldsymbol{y}_n)_{n=0}^{N}$ of a reference trajectory $(\boldsymbol{q}_n)_{n=0}^{N}$ are available according to:

$$\boldsymbol{y}_n = \boldsymbol{h}(\boldsymbol{q}_n) + \boldsymbol{\epsilon}_n \quad 0 \leqslant n \leqslant N \tag{3}$$

where $\boldsymbol{h}$ is the observation operator that maps the state space to the observation space and $\boldsymbol{\epsilon}_n$ is the possibly random measurement error. Even though these observations are not necessarily available at all times t_n, we will assume so in the following for the sake of simplicity, and without loss of generality. Here, the data assimilation (DA) procedure consists in estimating the temporal evolution $(\boldsymbol{q}_n)_{n=1}^N$ and the corresponding vector $\boldsymbol{\gamma}$ in (2) given the observations $(\boldsymbol{y}_n)_{n=0}^N$. In the probabilistic formulation of the DA problem [10,11], if $\boldsymbol{\gamma}$, $(\boldsymbol{q}_n)_{n=1}^N$ and $(\boldsymbol{y}_n)_{n=0}^N$ are considered as random variables, Bayes' theorem allows to combine a prior distribution $p(\boldsymbol{\gamma}, (\boldsymbol{q}_n)_{n=1}^N)$ (knowledge about the reference evolution before taking into account observations) and the data distribution $p((\boldsymbol{y}_n)_{n=0}^N | \boldsymbol{\gamma}, (\boldsymbol{q}_n)_{n=1}^N)$ (measurements conditioned by the observed reference evolution) to get a posterior distribution $p(\boldsymbol{\gamma}, (\boldsymbol{q}_n)_{n=1}^N | (\boldsymbol{y}_n)_{n=0}^N)$ (knowledge about the reference evolution conditioned by the data) according to:

$$p\left(\boldsymbol{\gamma}, (\boldsymbol{q}_n)_{n=1}^N | (\boldsymbol{y}_n)_{n=0}^N\right) \propto p\left(\boldsymbol{\gamma}, (\boldsymbol{q}_n)_{n=1}^N\right) p\left((\boldsymbol{y}_n)_{n=0}^N | \boldsymbol{\gamma}, (\boldsymbol{q}_n)_{n=1}^N\right) \tag{4}$$

The coefficient of proportionality for (4) is the marginal distribution of the data $p((\boldsymbol{y}_n)_{n=0}^N)$ and may be seen here as only a normalizing constant. Once the posterior distribution is obtained thanks to (4), the DA problem is solved by finding the trajectory $(\boldsymbol{q}_n)_{n=1}^N$ and the vector $\boldsymbol{\gamma}$ that maximize this probability (maximum likelihood analysis).

2.2. Variational data assimilation (4DVar)

The four-dimensional variational (4DVar) method [7] addresses DA as an optimal control problem [8]. The classical formulation of the 4DVar method [26,27] is first obtained by considering the dynamical model (1) without any random additional term. Accordingly, (4) may be rewritten as:

$$p\left(\boldsymbol{\gamma} | (\boldsymbol{y}_n)_{n=0}^N\right) \propto p\left(\boldsymbol{\gamma}\right) p\left((\boldsymbol{y}_n)_{n=0}^N | (\boldsymbol{q}_n)_{n=0}^N\right) \tag{5}$$

since in this case the relation between $(\boldsymbol{q}_n)_{n=1}^N$ and $\boldsymbol{\gamma}$ is deterministic. It is next assumed that the vector $\boldsymbol{\gamma}$ is Gaussian distributed with mean $\boldsymbol{\gamma}^{(e)}$ and covariance matrix $\mathbf{B}$. The error term $\boldsymbol{\epsilon}_n$ in (3) is also assumed to be Gaussian distributed with zero mean and covariance matrix $\mathbf{C}$. Accordingly, maximizing the posterior distribution in (5) is equivalent to minimize the following cost function:

$$J = \frac{1}{2} \|\boldsymbol{\gamma} - \boldsymbol{\gamma}^{(e)}\|^2_{\mathbf{B}^{-1}} + \sum_{n=0}^{N} \frac{1}{2} \|\boldsymbol{y}_n - \boldsymbol{h}(\boldsymbol{q}_n)\|^2_{\mathbf{C}^{-1}} \tag{6}$$

with $\|\cdot\|^2_{\mathbf{B}^{-1}} = \cdot^{\mathrm{T}}\mathbf{B}^{-1}\cdot$ and $\|\cdot\|^2_{\mathbf{C}^{-1}} = \cdot^{\mathrm{T}}\mathbf{C}^{-1}\cdot$. The cost function J in (6) is minimized under the equality constraint (1). This leads to the introduction of the Lagrangian $\mathcal{L}$ defined by:

$$\mathcal{L} = \frac{1}{2} \|\boldsymbol{\gamma} - \boldsymbol{\gamma}^{(e)}\|^2_{\mathbf{B}^{-1}} + \sum_{n=0}^{N} \frac{1}{2} \|\boldsymbol{y}_n - \boldsymbol{h}(\boldsymbol{q}_n)\|^2_{\mathbf{C}^{-1}} - \sum_{n=0}^{N-1} \left(\boldsymbol{q}_{n+1} - \boldsymbol{m}_n(\boldsymbol{q}_n, \boldsymbol{\alpha}_n)\right)^{\mathrm{T}} \tilde{\boldsymbol{q}}_{n+1} \tag{7}$$

The expression (7) involves the Lagrange multipliers, or adjoint variables, $\tilde{\boldsymbol{q}}_n$. First-order necessary conditions for the direct and adjoint evolutions $(\boldsymbol{q}_n)_{n=1}^N$ and $(\tilde{\boldsymbol{q}}_n)_{n=1}^N$ to minimize the Lagrangian $\mathcal{L}$ lead to the direct problem (1) and to the following adjoint problem:

$$\tilde{\boldsymbol{q}}_N = \left(\frac{\partial \boldsymbol{h}}{\partial \boldsymbol{q}_N}(\boldsymbol{q}_N)\right)^{\mathrm{T}} \mathbf{C}^{-1} \left(\boldsymbol{h}(\boldsymbol{q}_N) - \boldsymbol{y}_N\right) \tag{8}$$

$$\tilde{\boldsymbol{q}}_n = \left(\frac{\partial \boldsymbol{m}_n}{\partial \boldsymbol{q}_n}(\boldsymbol{q}_n, \boldsymbol{\alpha}_n)\right)^{\mathrm{T}} \tilde{\boldsymbol{q}}_{n+1} + \left(\frac{\partial \boldsymbol{h}}{\partial \boldsymbol{q}_n}(\boldsymbol{q}_n)\right)^{\mathrm{T}} \mathbf{C}^{-1} \left(\boldsymbol{h}(\boldsymbol{q}_n) - \boldsymbol{y}_n\right) \quad 0 \leq n \leq N-1 \tag{9}$$

Evaluating backward in time (9) with the terminal condition (8) allows to compute the gradient of the Lagrangian with respect to the control vector $\boldsymbol{\gamma}$ in (2) according to:

$$\frac{\partial \mathcal{L}}{\partial \boldsymbol{q}_0} = \tilde{\boldsymbol{q}}_0 + \mathbf{B}_{q_0}^{-1} \left(\boldsymbol{q}_0 - \boldsymbol{q}_0^{(e)}\right) \tag{10}$$

$$\frac{\partial \mathcal{L}}{\partial \boldsymbol{\alpha}_n} = \left(\frac{\partial \boldsymbol{m}_n}{\partial \boldsymbol{\alpha}_n}(\boldsymbol{q}_n, \boldsymbol{\alpha}_n)\right)^{\mathrm{T}} \tilde{\boldsymbol{q}}_{n+1} + \mathbf{B}_{\alpha_n}^{-1} \left(\boldsymbol{\alpha}_n - \boldsymbol{\alpha}_n^{(e)}\right) \quad 0 \leq n \leq N-1 \tag{11}$$

with $\mathbf{B}_{q_0}$ and $\mathbf{B}_{\alpha_n}$ the covariance matrices associated respectively to the initial condition and parameters $\boldsymbol{\alpha}_n$ if we assume they are uncorrelated. Once available, these gradients can be used in a descent algorithm to search the minimizing vector $\boldsymbol{\gamma}$, as described in section 3.1.

2.3. Ensemble Kalman smoother (EnKS)

The ensemble Kalman smoother (EnKS) [28] can be viewed as an extension of the ensemble Kalman filter (EnKF) [15] where the information from observations is propagated backward in time. Both for computational reasons and to better deal with nonlinear dynamics, the posterior distribution in (4) can be evaluated sequentially (each time observations are available) according to [28]:

$$\begin{aligned} &p\left((\boldsymbol{\alpha}_l)_{l=0}^{n-1},(\boldsymbol{q}_l)_{l=0}^{n}|(\boldsymbol{y}_l)_{l=0}^{n}\right)\propto \\ &p\left((\boldsymbol{\alpha}_l)_{l=0}^{n-2},(\boldsymbol{q}_l)_{l=0}^{n-1}|(\boldsymbol{y}_l)_{l=0}^{n-1}\right)p(\boldsymbol{\alpha}_{n-1})p(\boldsymbol{q}_n|\boldsymbol{q}_{n-1},\boldsymbol{\alpha}_{n-1})p(\boldsymbol{y}_n|\boldsymbol{q}_n) \quad 1\le n\le N \end{aligned} \tag{12}$$

The derivation of (12) requires that the stochastic counterpart of (1) is a first-order Markov process, and that the observations at different times are independent and conditional only on the state at the same time. At time $t=t_n$, equation (12) can be decomposed [29] into a forecast step

$$p\left((\boldsymbol{\alpha}_l)_{l=0}^{n-1},(\boldsymbol{q}_l)_{l=0}^{n}|(\boldsymbol{y}_l)_{l=0}^{n-1}\right)=p\left((\boldsymbol{\alpha}_l)_{l=0}^{n-2},(\boldsymbol{q}_l)_{l=0}^{n-1}|(\boldsymbol{y}_l)_{l=0}^{n-1}\right)p(\boldsymbol{\alpha}_{n-1})p(\boldsymbol{q}_n|\boldsymbol{q}_{n-1},\boldsymbol{\alpha}_{n-1}) \tag{13}$$

and an analysis step:

$$p\left((\boldsymbol{\alpha}_l)_{l=0}^{n-1},(\boldsymbol{q}_l)_{l=0}^{n}|(\boldsymbol{y}_l)_{l=0}^{n}\right)\propto p\left((\boldsymbol{\alpha}_l)_{l=0}^{n-1},(\boldsymbol{q}_l)_{l=0}^{n}|(\boldsymbol{y}_l)_{l=0}^{n-1}\right)p(\boldsymbol{y}_n|\boldsymbol{q}_n) \tag{14}$$

In the case where no model error is considered, as in the present study, the probability $p(\boldsymbol{q}_n|\boldsymbol{q}_{n-1},\boldsymbol{\alpha}_{n-1})$ in (12) and (13) is a delta function. All the probabilities in (14) are assumed to correspond to normal distributions, so that we only have to consider their associated means and covariance matrices. As in the EnKF, prior statistics $p\left((\boldsymbol{\alpha}_l)_{l=0}^{n-1},(\boldsymbol{q}_l)_{l=0}^{n}|(\boldsymbol{y}_l)_{l=0}^{n-1}\right)$ in (13) and (14) are obtained through Monte Carlo sampling and integration of the dynamical model in (1) from time t_{n-1} to t_n. Thus, prior statistics are evaluated from the matrix $\mathbf{A}_n^{(f)}$ defined by:

$$\mathbf{A}_n^{(f)}=\left(\boldsymbol{p}_n^{(1)},\boldsymbol{p}_n^{(2)},\cdots,\boldsymbol{p}_n^{(N_{en})}\right),\quad \boldsymbol{p}_n=\left((\boldsymbol{\alpha}_l^{\mathrm{T}})_{l=0}^{n-1},(\boldsymbol{q}_l^{\mathrm{T}})_{l=0}^{n}\right)^{\mathrm{T}} \tag{15}$$

where N_{en} is the number of members of the ensemble. Since we consider normal distributions in (14), finding the maximum likelihood analysis is equivalent to the determination of a variance minimizing analysis. Accordingly, if observations are available at time $t=t_n$, the matrix $\mathbf{A}_n^{(f)}$ is updated as [2]:

$$\mathbf{A}_n^{(a)}=\mathbf{A}_n^{(f)}+\mathbf{A}_n^{(f)'}\mathbf{H}_n'^{\mathrm{T}}\left((N_{en}-1)\mathbf{C}+\mathbf{H}_n'\mathbf{H}_n'^{\mathrm{T}}\right)^{-1}(\mathbf{Y}_n-\mathbf{H}_n) \tag{16}$$

with

$$\mathbf{A}_n^{(f)'}=\left(\boldsymbol{p}_n^{(1)}-\overline{\boldsymbol{p}_n},\cdots,\boldsymbol{p}_n^{(N_{en})}-\overline{\boldsymbol{p}_n}\right),\quad \mathbf{H}_n=\left(\boldsymbol{h}(\boldsymbol{q}_n^{(1)}),\cdots,\boldsymbol{h}(\boldsymbol{q}_n^{(N_{en})})\right) \tag{17}$$

$$\mathbf{H}_n'=\left(\boldsymbol{h}(\boldsymbol{q}_n^{(1)})-\boldsymbol{h}(\overline{\boldsymbol{q}_n}),\cdots,\boldsymbol{h}(\boldsymbol{q}_n^{(N_{en})})-\boldsymbol{h}(\overline{\boldsymbol{q}_n})\right),\quad \mathbf{Y}_n=\left(\boldsymbol{y}_n^{(1)},\cdots,\boldsymbol{y}_n^{(N_{en})}\right) \tag{18}$$

where the operator $\bar{\cdot}$ denotes ensemble average. The ensemble of observations $\mathbf{Y}_n$ is obtained from perturbations added to available data with zero mean and covariance matrix $\mathbf{C}$ [30]. The EnKS is initialized by prescribing statistics (mean and covariance matrix) to the control vector $\boldsymbol{\gamma}$ in (2). N_{en} realizations of this vector are sampled and propagated in time with (1). If observations are available at time $t=t_n$, all the trajectories of the ensemble are updated according to (16), including the realizations of $\boldsymbol{\gamma}$. The updated ensemble $\mathbf{A}_n^{(a)}$ is then propagated from time t_n to the next time of observation. The analysis step for the EnKF is recovered by replacing the definition of $\boldsymbol{p}_n$ in (15) by $\boldsymbol{p}_n=\left(\boldsymbol{\alpha}_{n-1}^{\mathrm{T}},\boldsymbol{q}_n^{\mathrm{T}}\right)^{\mathrm{T}}$.

2.4. Ensemble-based variational data assimilation (4DEnVar)

The four-dimensional ensemble-based variational (4DEnVar) scheme [21] combines the formulation of the 4DVar method with the use of a Monte Carlo ensemble to evaluate prior statistics as in the EnKF, avoiding the need of adjoint operators. In the 4DEnVar scheme, an optimal vector $\boldsymbol{\gamma}$ in (2) is searched in a subspace spanned by an ensemble of realizations [21,31,32,24]. After choosing a first-guess, or prior, vector $\boldsymbol{\gamma}^{(e)}$ and N_{en} samples around this first guess, the vector $\boldsymbol{\gamma}$ is expressed as:

$$\boldsymbol{\gamma}=\boldsymbol{\gamma}^{(e)}+\mathbf{E}'\boldsymbol{\beta},\quad \mathbf{E}'=\left(\boldsymbol{\gamma}^{(1)}-\boldsymbol{\gamma}^{(e)},\boldsymbol{\gamma}^{(2)}-\boldsymbol{\gamma}^{(e)},\cdots,\boldsymbol{\gamma}^{(N_{en})}-\boldsymbol{\gamma}^{(e)}\right) \tag{19}$$

Equation (19) involves the new control vector $\boldsymbol{\beta}$ with $\dim(\boldsymbol{\beta})=N_{en}$. After two successive linearizations:

$$\boldsymbol{h}(\boldsymbol{q}_n)\simeq\boldsymbol{h}(\boldsymbol{q}_n^{(e)})+\frac{\partial\boldsymbol{h}}{\partial\boldsymbol{q}_n^{(e)}}(\boldsymbol{q}_n^{(e)})\frac{\partial\boldsymbol{q}_n^{(e)}}{\partial\boldsymbol{\gamma}^{(e)}}(\boldsymbol{\gamma}^{(e)})\mathbf{E}'\boldsymbol{\beta} \tag{20}$$

Table 1
Schematic representation of the different DA algorithms considered in this paper.

4DVar	*EnKS*	*4DEnVar*
1. start with a first guess for the control vector $\boldsymbol{\gamma}$ (2) and prescribe prior and observation statistics	1. start with a first guess for the control vector $\boldsymbol{\gamma}$ (2) and prescribe prior and observation statistics	1. start with a first guess for the control vector $\boldsymbol{\gamma}$ (2) and prescribe prior and observation statistics
2. solve direct problem (1)	2. sample N_{en} realizations of $\boldsymbol{\gamma}$	2. sample N_{en} realizations of $\boldsymbol{\gamma}$
3. solve adjoint problem (8)–(9)	3. propagate the ensemble with (1) until the next time of observation	3. propagate the ensemble with (1)
4. use the gradients (10)–(11) to update $\boldsymbol{\gamma}$ according to (25)	4. update the ensemble trajectories with (16) (or with (27) if localization is used)	4. minimize cost function (22) using (24)
5. return to step 2 until stopping criterion reached	5. return to step 3 until the end of the assimilation window	5. update $\boldsymbol{\gamma}$ according to (19)
	6. return to step 2 until stopping criterion reached	6. return to step 2 until stopping criterion reached

$$\frac{\partial \boldsymbol{h}}{\partial \boldsymbol{q}_n^{(e)}}(\boldsymbol{q}_n^{(e)})\frac{\partial \boldsymbol{q}_n^{(e)}}{\partial \boldsymbol{\gamma}^{(e)}}(\boldsymbol{\gamma}^{(e)})\mathbf{E}' \simeq \left(\boldsymbol{h}(\boldsymbol{q}_n^{(1)})-\boldsymbol{h}(\boldsymbol{q}_n^{(e)}),\cdots,\boldsymbol{h}(\boldsymbol{q}_n^{(N_{en})})-\boldsymbol{h}(\boldsymbol{q}_n^{(e)})\right)=\mathbf{H}'_n \tag{21}$$

the cost function J in (6) can be rewritten as:

$$J=\frac{1}{2}(N_{en}-1)\boldsymbol{\beta}^{\mathrm{T}}\boldsymbol{\beta}+\sum_{n=0}^{N}\frac{1}{2}\|\boldsymbol{h}(\boldsymbol{q}_n^{(e)})-\boldsymbol{y}_n+\mathbf{H}'_n\boldsymbol{\beta}\|^2_{\mathbf{C}^{-1}} \tag{22}$$

using

$$\mathbf{B}\simeq\frac{1}{N_{en}-1}\mathbf{E}'\mathbf{E}'^{\mathrm{T}} \tag{23}$$

Since the cost function in (22) is quadratic in $\boldsymbol{\beta}$, explicit expressions of the gradient and Hessian of J are available:

$$\frac{\partial J}{\partial \boldsymbol{\beta}}=(N_{en}-1)\boldsymbol{\beta}+\sum_{n=0}^{N}\mathbf{H}'^{\mathrm{T}}_n\mathbf{C}^{-1}\left(\boldsymbol{h}(\boldsymbol{q}_n^{(e)})-\boldsymbol{y}_n+\mathbf{H}'_n\boldsymbol{\beta}\right),\quad \frac{\partial^2 J}{\partial \boldsymbol{\beta}^2}=(N_{en}-1)\mathbf{I}+\sum_{n=0}^{N}\mathbf{H}'^{\mathrm{T}}_n\mathbf{C}^{-1}\mathbf{H}'_n \tag{24}$$

where $\mathbf{I}$ is the identity matrix. Relations (24) are used to minimize the cost function in (22) with one iteration of the Newton method, and the so-obtained optimal vector $\boldsymbol{\beta}$ is used to update the prior vector $\boldsymbol{\gamma}^{(e)}$ according to (19). A new ensemble $\mathbf{E}'$ around the updated estimation of $\boldsymbol{\gamma}$ might then be sampled in order to further improve the analysis. This iterative form of the 4DEnVar algorithm, where the result of the assimilation is used as the first guess for the next iteration, is summarized in Table 1. The stopping criterion is a maximum number of iterations that is tuned to fix the total number of direct runs N_{rn} performed during the complete assimilation procedure. In this work, the EnKS is also tested in such an iterative form.

3. Practical implementation

3.1. Adjoint code and optimization procedure

For the purposes of the 4DVar scheme (section 2.2), the exact expressions of the different operators in equations (8)–(9) and (11) are hand-coded. This corresponds to the discrete adjoint approach [33,34,18]. In the present work, the operator $\boldsymbol{m}_n$ in (1) is nonlinear, and the operators in equations (8)–(9) and (11) depend on the direct solution $\boldsymbol{q}_n$, which has to be stored at all times for the backward integration of the adjoint problem. To minimize memory requirements, the direct solution is stored only at a few times t_n during the integration of the direct problem (1), and the missing $\boldsymbol{q}_n$ are recomputed during the backward integration of (8)–(9). In order to minimize the Lagrangian in (7), the gradients (10)–(11) obtained with the adjoint code are used in a descent algorithm. This iterative optimization procedure is initialized with a first guess for the control vector $\boldsymbol{\gamma}$. At the ith iteration, direct (1) and adjoint (8)–(9) problems are solved to compute the gradients (10)–(11). These gradients allow for the determination of a descent direction $\boldsymbol{d}^{(i)}$, and the control vector $\boldsymbol{\gamma}^{(i)}$ is updated according to:

$$\boldsymbol{\gamma}^{(i+1)}=\boldsymbol{\gamma}^{(i)}+\eta^{(i)}\boldsymbol{d}^{(i)} \tag{25}$$

The low-memory formulation of the quasi-newton BFGS method [35] is used to compute $\boldsymbol{d}^{(i)}$. The step length $\eta^{(i)}$ is evaluated with a backtracking-Armijo line search [36]. The optimization procedure is stopped after a given number of iterations that is tuned to fix the computational cost of the complete assimilation process. The 4DVar scheme is summarized in Table 1.

3.2. Observation and prior (or ensemble) statistics

Both the EnKS and 4DEnVar methods rely on the propagation of an ensemble of realizations, while the 4DVar scheme also requires the prescription of prior statistics. For the three schemes, the vector $\boldsymbol{\gamma}$ in (2) is assumed to be Gaussian distributed. The mean of this normal distribution corresponds to an estimated, or prior, vector $\boldsymbol{\gamma}^{(e)}$. In order to obtain smooth samples of the vector $\boldsymbol{\gamma}$, a non-diagonal covariance matrix is prescribed. For an estimated quantity with characteristic value b, such as the x-wise component u of the initial velocity field at all control volumes, the covariance matrix $\boldsymbol{\Sigma}$ is chosen of the form:

$$\Sigma_{ij} = \sigma^2 b^2 \exp\left(\frac{\|\boldsymbol{x}_i - \boldsymbol{x}_j\|}{l_c}\right) \tag{26}$$

where $\boldsymbol{x}_i = (x_i, y_j)^{\mathrm{T}}$ refers to the position of the ith control volume, l_c is a correlation length and σ^2 a relative (dimensionless) variance. Similarly to (26), a correlation time t_c is introduced to characterize the statistics of the unsteady boundary conditions. In this paper, the sensitivity of the results obtained with the different DA schemes with respect to the relative variances σ^2 related to the estimated quantities in $\boldsymbol{\gamma}$ will be studied. In the following, $\sigma^{(ic)}$ and $\sigma^{(ff)}$ refer to the relative standard deviations associated to initial and boundary (far-field) conditions, respectively. On the other hand, the correlation time t_c and length l_c are regarded as constants, since they are introduced only to smooth the samples of $\boldsymbol{\gamma}$. The characteristic length l_c is based on the diameter d_r of the cylinder (see section 4.2), the correlation time t_c and the characteristic values b for the different estimated physical quantities are based on l_c and on characteristic inflow conditions. For example, $b = u_r$ with u_r a reference inlet velocity if we consider the x-wise component u of the initial velocity field, and t_c is based on d_r/u_r. Concerning observation errors in (3), they are assumed to be Gaussian distributed with zero mean, uncorrelated, and are characterized by the relative standard deviation $\sigma^{(ob)}$.

3.3. Localization, inflation and smoother lag

The use of relatively small ensembles in EnKF techniques lies at the origin of spurious components (in particular off-diagonal ones) in the approximated correlation matrices involved in the update (16). To counteract these finite-ensemble-size effects, several techniques such as localization [19] and inflation [20] have been proposed in the literature. Localization may amount to replace the update equation (16) with

$$\mathbf{A}_n^{(a)} = \mathbf{A}_n^{(f)} + \mathbf{L_1} \circ (\mathbf{A}_n^{(f)'} \mathbf{H}_n'^{\mathrm{T}}) \left((N_{en} - 1)\mathbf{C} + \mathbf{L_2} \circ (\mathbf{H}_n' \mathbf{H}_n'^{\mathrm{T}})\right)^{-1} (\mathbf{Y}_n - \mathbf{H}_n) \tag{27}$$

where $\circ$ denotes the element-wise (or Hadamard or Schur product), $\mathbf{L_1}$ is a localization matrix acting on the correlations between the vector $\boldsymbol{p}_n$ defined in (15) and observations, while $\mathbf{L_2}$ acts on the correlations between observations. Since the vector $\boldsymbol{p}_n$ includes the parameters and the state vector in (1) from $t = t_0$ to $t = t_n$, the matrix $\mathbf{A}_n^{(f)'} \mathbf{H}_n'^{\mathrm{T}}$ accounts for spatio-temporal correlations between the components of $\boldsymbol{p}_n$ and the observations available at time $t = t_n$. Another way to enforce temporal localization is to consider a lagged smoother [28,37] where observations available at time $t = t_n$ are used to update the ensemble only from $t = t_{n-L}$ to $t = t_n$ with L the lag parameter. The determination of proper matrices $\mathbf{L_1}$ and $\mathbf{L_2}$ and/or lag L for state estimation may already be difficult, since it requires a good knowledge of the characteristic length and time scales of the problem to guarantee the optimality of the localization. Besides, for parameter estimation, the interpretation of localization is far from being straightforward in the general case.

In the present study, we are primarily interested in estimating an optimal vector $\boldsymbol{\gamma}$ defined in (2). The parameters $\boldsymbol{\alpha}_n$ correspond here to boundary conditions (see section 4.1). If observations are performed close to the center of the computational domain (which is the case here when the pressure distribution around the cylinder is observed, see section 4.2), introducing a correlation length for spatial localization has no real meaning since it should of the same order of magnitude as the size of the whole computational domain. Accordingly, only temporal localization is potentially considered here (this will not be the case for the following results unless otherwise stated). Using a lagged smoother is not the best choice for the present study because we have to take into account the time required for information to propagate from the boundaries of the computational domain to the observation locations. In the end, when localization is used, we take a all-ones matrix as matrix $\mathbf{L_2}$ (no localization for the correlations between observations). The components of $\mathbf{L_1}$ corresponding to correlations between the state vector are set to 1, while the components of $\mathbf{L_1}$ corresponding to correlations between parameters $\boldsymbol{\alpha}_l$ at time t_l with $0 \leqslant l \leqslant n-1$ and the observations performed at time t_n are set to $\exp\left(-(t_l + T_{bc} - t_n)^2/(\kappa T_{bc})^2\right)$. T_{bc} refers to the estimated time of propagation of information based on characteristic inlet conditions and the distance from the boundaries of the computational domain to the observation locations, and κ is a constant which is introduced to tune the temporal localization.

Multiplying inflation factors [20] between 1.01 and 1.05 were also considered in this study, but without significant improvement of the results. Therefore, the corresponding results are not shown here.

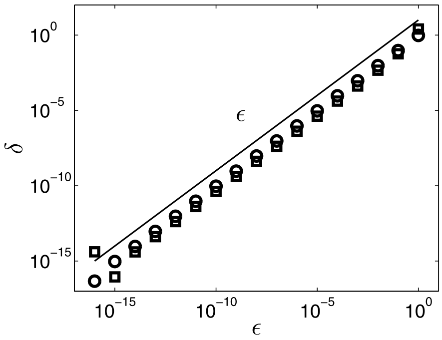

Fig. 1. Validation of the adjoint code: relative difference δ between the variations of the cost function J predicted by the adjoint code and finite differences versus the parameter ϵ in (32). The direction $\boldsymbol{\theta}$ corresponds to a perturbation of either the initial condition (◯) or the boundary conditions (☐).

4. Numerical setup

4.1. Governing equations and finite volume formulation

We consider the integral form of the two-dimensional compressible Navier–Stokes equations for perfect gas over a bounded domain of interest Ω:

$$\frac{\partial}{\partial t}\int_{\Omega} \boldsymbol{w} dV + \int_{\partial\Omega} (\mathbf{F}(\boldsymbol{w}) - \mathbf{G}(\boldsymbol{w})) \cdot \boldsymbol{n} dS = \mathbf{0} \tag{28}$$

with

$$\boldsymbol{w} = \begin{pmatrix} \rho \\ \rho u \\ \rho v \\ E \end{pmatrix}, \ \boldsymbol{F}(\boldsymbol{w}) = \begin{pmatrix} \rho u & \rho v \\ \rho u^2 + p & \rho u v \\ \rho u v & \rho v^2 + p \\ u(E+p) & v(E+p) \end{pmatrix}, \ \boldsymbol{G}(\boldsymbol{w}) = \begin{pmatrix} 0 & 0 \\ \tau_{xx} & \tau_{xy} \\ \tau_{xy} & \tau_{yy} \\ u\tau_{xx} + v\tau_{xy} - q_x & v\tau_{yy} + u\tau_{xy} - q_y \end{pmatrix} \tag{29}$$

$$\tau_{xx} = \mu \left(2\frac{\partial u}{\partial x} - \frac{2}{3}(\frac{\partial u}{\partial x} + \frac{\partial v}{\partial y}) \right), \ \tau_{yy} = \mu \left(2\frac{\partial v}{\partial y} - \frac{2}{3}(\frac{\partial u}{\partial x} + \frac{\partial v}{\partial y}) \right), \ \tau_{xy} = \mu(\frac{\partial u}{\partial y} + \frac{\partial v}{\partial x}) \tag{30}$$

$$q_x = -\kappa\frac{\partial T}{\partial x}, \ q_y = -\kappa\frac{\partial T}{\partial y}, \ p = \rho r T = (\gamma - 1)\rho e, \ E = \rho\left(e + \frac{1}{2}(u^2 + v^2)\right) \tag{31}$$

where $\boldsymbol{n}$, ρ, u, v, p, e, T, γ, μ, κ and r refer to the outer unit normal vector to the boundary $\partial\Omega$, density, x-wise and y-wise components of the velocity vector, pressure, specific internal energy, temperature, ratio of specific heats, dynamic viscosity, thermal conductivity and a constant in the ideal gas law, respectively. Equation (28) is discretized using a cell-centered finite-volume formulation on unstructured grids. Convective fluxes $\boldsymbol{F}(\boldsymbol{w})$ are evaluated using Roe's approximate Riemann solver [38]. Second-order spatial accuracy is achieved with the reconstruction procedure of Jawahar and Kamath [39]. Time integration is performed with a fully implicit second-order scheme that combines dual time stepping [40] and the LU-SGS method [41,42]. Thus, the state vector $\boldsymbol{q}_n$ in (1) is formed by the vector of conservative variables $\boldsymbol{w}$ at all control volumes, and the operator $\boldsymbol{m}_n$ refers to the fully discretized counterpart of (28). Inlet boundary conditions are considered as tunable parameters $\boldsymbol{\alpha}_n$. The correct implementation of the corresponding adjoint code is assessed in Fig. 1 where is reported the relative difference δ between the variations of the cost function $\Delta J^{(A)}$ and $\Delta J^{(F)}$ in various directions $\boldsymbol{\theta}$ obtained with the adjoint code and finite differences respectively. These quantities are defined by:

$$\Delta J^{(A)} = \left(\frac{\partial \mathcal{L}}{\partial \boldsymbol{\gamma}}\right)^{\mathrm{T}} \boldsymbol{\theta}, \quad \Delta J^{(F)} = \frac{J(\boldsymbol{\gamma} + \epsilon\boldsymbol{\theta}) - J(\boldsymbol{\gamma})}{\epsilon}, \quad \delta = \left| \frac{\Delta J^{(A)} - \Delta J^{(F)}}{\Delta J^{(A)}} \right| \tag{32}$$

where the gradient $\frac{\partial \mathcal{L}}{\partial \boldsymbol{\gamma}}$ is formed by the gradients in (10) and (11). For the two directions $\boldsymbol{\theta}$ investigated in Fig. 1, the difference δ converges like ϵ as $\epsilon \to 0$ until machine precision, which validates the adjoint code. The computational cost of the adjoint code is 4.5 times that of the direct code, including the recomputation of the direct solution (see section 3.1).

4.2. Flow configuration and data assimilation experiments setup

The principle of the DA experiments presented in this paper is the following. First, a reference numerical simulation with associated boundary and initial conditions is performed, and observations of this reference trajectory are performed. In a second step, the DA methods described in section 2 are used to recover the reference evolution and its associated boundary and initial conditions. These methods are initialized with a first-guess, or estimated run, and the state resulting from these procedures is referred to as the assimilated state.

We consider the flow around a circular cylinder at a Reynolds number of $Re = 100$ and a Mach number of $Ma = 0.2$, which are based on a reference inlet velocity u_r and the diameter of the cylinder d_r. The physical time step Δt for the simulations is chosen as $\Delta t = 1.3 \cdot 10^{-3} d_r/(S_t u_r)$, where $S_t = 0.165$ is the Strouhal number at $Re = 100$ [43]. The unstructured mesh is formed by $1.4 \cdot 10^4$ triangular elements, and the typical duration of a direct simulation is 500 seconds in CPU time with a 2.10 GHz Intel Xeon E5-2658 processor. In the following assimilation experiments, the reference runs correspond to an incoming gust of the form [44,45,25]:

$$u(t) = u_r + A\frac{t^2(t-T)^2}{(T/2)^4}\sin\left(\frac{2\pi}{T}(3t+T)\right), \quad t \in [0, T] \tag{33}$$

where $A = 0.2u_r$ and $T = 6.4d_r/u_r$ refer to the maximum gust amplitude and duration of the gust, respectively. Three types of DA experiments are performed in this study. In section 5.1, the initial condition and the direction of the gust for a reference state are assumed to be known. The direction of the gust is the same than that of the vortex shedding (in the x coordinate direction). However, the reference temporal evolution of the gust is considered to be unknown. Accordingly, the aim of the DA procedure consists in reconstructing an unsteady and uniform inlet velocity, and the dimension of the control vector $\boldsymbol{\gamma}$ in (2) is $\dim(\boldsymbol{\gamma}) = 2 \cdot 10^3$. In sections 5.2 and 5.3, we consider that both the reference temporal evolution of the incoming gust and the reference initial flow field are unknown, and $\dim(\boldsymbol{\gamma}) = 5.7 \cdot 10^4$. Finally, in section 5.4, the reference gust has an arbitrary direction, and DA is used to recover the non-uniform and unsteady boundary conditions and the initial flow field of the reference run. In this case, $\dim(\boldsymbol{\gamma}) = 4.4 \cdot 10^5$, the reference run is chosen so that the incoming gust has an incidence angle to the direction of the vortex shedding of 45°. For all these configurations, the estimated run is chosen without incoming gust (uniform and steady boundary conditions).

Various types of observations of the reference run are considered. In sections 5.1, 5.2 and 5.4, the pressure distribution around the cylinder $C_P(\theta)$ of the reference run is observed. This quantity is defined by:

$$C_P(\theta) = \frac{p(\theta) - p_r}{\frac{1}{2}\rho_r u_r^2} \tag{34}$$

where ρ_r and p_r are reference density and pressure respectively, $p(\theta)$ refers to the pressure on the periphery of the cylinder at angular coordinate θ (the origin is taken at the center of the cylinder). 30 measurement points are considered [46]. The observation of the aerodynamic coefficients C_L and C_D is performed in section 5.3. These coefficients are also used to evaluate the reconstruction of the reference state, and their expression is given by:

$$C_D = \frac{\boldsymbol{f}\cdot\boldsymbol{e_x}}{\frac{1}{2}\rho_r u_r^2 d_r}, \quad C_L = \frac{\boldsymbol{f}\cdot\boldsymbol{e_y}}{\frac{1}{2}\rho_r u_r^2 d_r}, \quad \boldsymbol{f} = \int_\Gamma (-p\mathbf{I} + \boldsymbol{\tau})\cdot\boldsymbol{n}dS \tag{35}$$

where $\boldsymbol{e}_x$ and $\boldsymbol{e}_y$ are the unit vectors in the x and y coordinate directions, Γ is the boundary of the cylinder, and the components of the symmetric matrix $\boldsymbol{\tau}$ are given in (30). Finally, the velocity field of the reference evolution at all control volumes of the computational domain is observed in sections 5.3 and 5.4. The time interval between two observations is always $0.2d_r/u_r$, except in one DA experiment of section 5.3 where the reference state is observed continuously in time. In all the figures that illustrate the temporal evolution of the inlet velocity or that of the coefficients C_L and C_D, the frequency of the symbols coincides with that of observations, except in the second row of Fig. 19. A summary of the DA experiments performed in this paper is given in Table 2.

In addition to the cost function J defined in (6), two other indicators are considered to evaluate the reconstruction of the reference flow obtained with the different DA procedures. The first one is the cost function J^{ob} defined by

$$J^{ob} = \sum_{n=0}^{N}\frac{1}{2}\|\boldsymbol{y}_n - \boldsymbol{h}(\boldsymbol{q}_n)\|^2 \tag{36}$$

where $\|\cdot\|$ denotes the Euclidean norm. The cost function J^{ob} measures only the discrepancies between the observations of the reference flow and the estimated one, without prior term, contrary to J. Another indicator, ϵ^{RMSE}, is used to quantify the discrepancies between the estimated and reference velocity fields over the whole computational domain, thus enabling a global evaluation of the reconstruction. It is defined by

$$\epsilon^{RMSE} = \left(\sum_{n=0}^{N}\|\boldsymbol{u}_n^{(r)} - \boldsymbol{u}_n^{(e)}\|^2 + \sum_{n=0}^{N}\|\boldsymbol{v}_n^{(r)} - \boldsymbol{v}_n^{(e)}\|^2\right)^{\frac{1}{2}} \tag{37}$$

where $\boldsymbol{u}_n$ and $\boldsymbol{v}_n$ refer to the x-wise and y-wise components of the velocity vector over the whole computational domain at time $t = t_n$, the superscripts (r) and (e) are introduced to distinguish between the reference and estimated flow fields respectively. The values of J, J^{ob} and ϵ^{RMSE} are generally compared to their values at the beginning of the assimilation procedure, J_0, J_0^{ob} and ϵ_0^{RMSE} respectively.

Table 2

Summary of the different DA experiments performed in this paper, which are characterized by the control vector $\boldsymbol{\gamma}$ (the corresponding section is also reported), observations of the reference state $\boldsymbol{y}_n$ (aerodynamic coefficients, pressure distribution around the cylinder or whole velocity field), the DA scheme, the relative standard deviations $\sigma^{(ob)}$, $\sigma^{(ff)}$ and $\sigma^{(ic)}$ associated to observation, boundary (far-field) and initial conditions statistics respectively, the number N_{en} of members in the ensemble, and the intensity κ of the localization.

$\boldsymbol{\gamma}$ (section)	$\boldsymbol{y}_n$	Scheme	$\sigma^{(ob)}$	$\sigma^{(ff)}$	$\sigma^{(ic)}$	N_{en}	κ
Uniform and unsteady boundary conditions (5.1)	$C_P(\theta)$	4DVar	$[10^{-3}, 10^{-1}]$	$[10^{-3}, 10^{-1}]$			
		EnKS	$[10^{-3}, 10^{-1}]$	$[10^{-3}, 10^{-1}]$		$[50, 100]$	$\emptyset$, $[1, 2]$
		4DEnVar	$[10^{-3}, 10^{-1}]$	$[10^{-3}, 10^{-1}]$		$[20, 100]$	
Initial condition + uniform and unsteady boundary conditions (5.2 and 5.3)	C_L, C_D	4DVar	10^{-2}	$10^{-1.5}$	10^{-2}		
		4DEnVar	10^{-2}	$10^{-1.5}$	10^{-2}	200	
	$C_P(\theta)$	4DVar	$[10^{-2}, 10^{-1}]$	$[10^{-2}, 10^{-1}]$	$[10^{-2.5}, 10^{-2}]$		
		EnKS	$[10^{-2}, 10^{-1}]$	$[10^{-2}, 10^{-1}]$	$[10^{-2.5}, 10^{-2}]$	$[100, 200]$	$\emptyset$, $[1, 2]$
		4DEnVar	$[10^{-2}, 10^{-1}]$	$[10^{-2}, 10^{-1}]$	$[10^{-2.5}, 10^{-2}]$	$[20, 200]$	
	u, v	4DVar	10^{-2}	$10^{-1.5}$	10^{-2}		
		4DEnVar	10^{-2}	$10^{-1.5}$	10^{-2}	200	
Initial condition + non-uniform and unsteady boundary conditions (5.4)	$C_P(\theta)$	4DVar	10^{-2}	$10^{-1.5}$	10^{-2}		
		4DEnVar	10^{-2}	$10^{-1.5}$	10^{-2}	200	
	u, v	4DVar	10^{-2}	$10^{-1.5}$	10^{-2}		
		4DEnVar	10^{-2}	$10^{-1.5}$	10^{-2}	200	

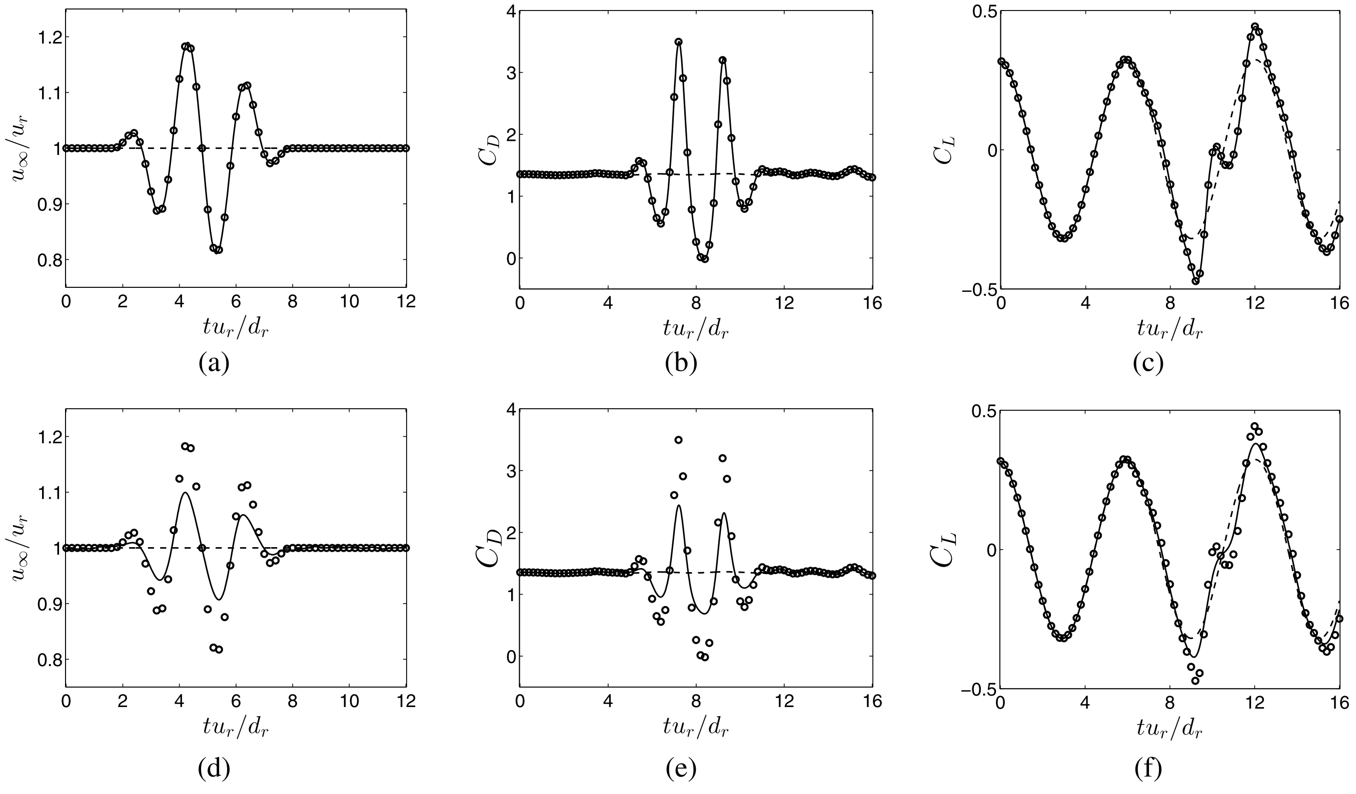

Fig. 2. Results obtained with the 4DVar method for gust reconstruction: temporal evolution of the inlet velocity (first column) and coefficients C_D (second column) and C_L (third column) for reference (◯), estimated (- - -) and assimilated (—) runs. Different observation and prior statistics are investigated: $\sigma^{(ob)} = 10^{-2}$ and $\sigma^{(ff)} = 10^{-1.5}$ (first row), and $\sigma^{(ob)} = 10^{-1}$ and $\sigma^{(ff)} = 10^{-2}$ (second row).

5. Results of data assimilation experiments

5.1. Uniform and unsteady gust reconstruction

In this section, the control vector $\boldsymbol{\gamma}$ is formed by the uniform and unsteady inlet boundary velocity $u_\infty(t)$, with $\dim(\boldsymbol{\gamma}) = 2 \cdot 10^3$. The reference and estimated runs are initialized with the same flow field. The pressure distribution around the cylinder is observed. First, we consider results obtained with the 4DVar method that are reported in Figures 2–4. The reconstruction of the reference flow is illustrated in Fig. 2 for two sets of relative variances $\sigma^{(ob)}$ and $\sigma^{(ff)}$ associated to observation and prior statistics (far-field conditions) respectively. When $\sigma^{(ob)} = 10^{-2}$ and $\sigma^{(ff)} = 10^{-1.5}$ (Figs. 2(a)–2(c)), starting from a steady inlet velocity for the estimated run, the 4DVar algorithm successfully reconstructs the unsteady profile (33) and fits well the reference temporal evolution of the aerodynamic coefficients C_L and C_D. In the case $\sigma^{(ob)} = 10^{-1}$

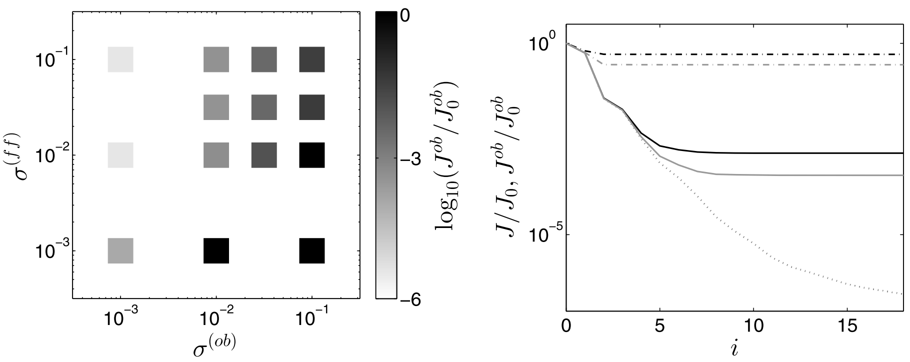

(a) (b)

Fig. 3. Results obtained with the 4DVar method for gust reconstruction: (a) reduction in the value of the cost function J^{ob}/J_0^{ob} at the end of the optimization procedure for different relative standard deviations $\sigma^{(ob)}$ and $\sigma^{(ff)}$ associated to observation and prior statistics respectively; (b) cost functions J (black lines) and J^{ob} (grey lines) versus the iteration of the optimization procedure for $\sigma^{(ob)} = 10^{-1}$ and $\sigma^{(ff)} = 10^{-2}$ (- · - ·), $\sigma^{(ob)} = 10^{-2}$ and $\sigma^{(ff)} = 10^{-1.5}$ (—), and in the case of perfect observations ($J = J^{ob}$, · · · · · ·).

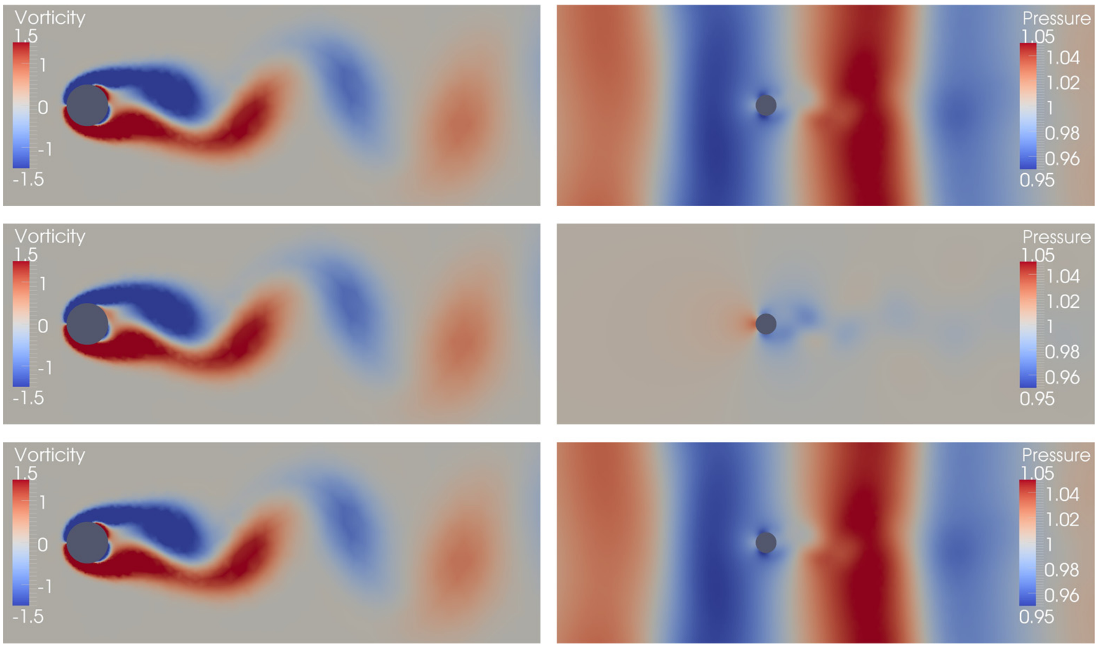

Fig. 4. Results obtained with the 4DVar method for gust reconstruction: dimensionless vorticity (left column) and pressure (right column) fields at $tu_r/d_r = 8$ for reference (first row), estimated (second row) and assimilated (third row) runs, $\sigma^{(ob)} = 10^{-2}$ and $\sigma^{(ff)} = 10^{-1.5}$.

and $\sigma^{(ff)} = 10^{-2}$ (Figs. 2(d)–2(f)), the weight of prior information in the cost function J in (6) is more important than that of observations, and the assimilated solution is still far from the reference one. Fig. 3(b) illustrates the evolution of the cost functions J and J^{ob} in (36) during the optimization procedure for both situations. In the case $\sigma^{(ob)} = 10^{-2}$ and $\sigma^{(ff)} = 10^{-1.5}$, the optimization procedure achieves a reduction by 3.5 orders of magnitude in the value of the cost function J^{ob} in 18 iterations. On the other hand, when $\sigma^{(ob)} = 10^{-1}$ and $\sigma^{(ff)} = 10^{-2}$, $J^{ob}/J_0^{ob} \simeq 0.28$ at the end of the optimization process. For the sake of comparison, the case where perfect observations are considered is also reported in Fig. 3(b), and a reduction by almost 7 orders of magnitude in the value of the cost function J^{ob} is then achieved in 18 iterations. The influence of observation and prior statistics on the results in terms of error reduction J^{ob}/J_0^{ob} is further investigated in Fig. 3(a). As expected, the reference solution can not be recovered when $\sigma^{(ob)}/\sigma^{(ff)} \gg 1$, i.e. with too noisy observations and high confidence in the prior estimate, and the reconstruction improves as $\sigma^{(ob)}$ decreases and $\sigma^{(ff)}$ increases. The good reconstruction of the gust in the case where $\sigma^{(ob)} = 10^{-2}$ and $\sigma^{(ff)} = 10^{-1.5}$, which will be considered as reference values in the rest of this section, can be also visualized in Fig. 4 where is reported the pressure field at $tu_r/d_r = 8$ for the reference, estimated and assimilated runs. The gust does not seem to significantly interact with the detached vortices, however, it slightly affects the repartition of vorticity around the cylinder.

We now address the use of the EnKS to perform the assimilation. First, the sensitivity of the results of the assimilation procedure, in terms of error reduction J^{ob}/J_0^{ob}, with respect to the size N_{en} of the ensemble and to the relative variances $\sigma^{(ob)}$ and $\sigma^{(ff)}$ is studied in Figs. 5(a)–5(b). As with the 4DVar method, it appears that the choice of statistics affects the quality of the reconstruction. However, the way the results depend on these statistics when the EnKS is used is not always

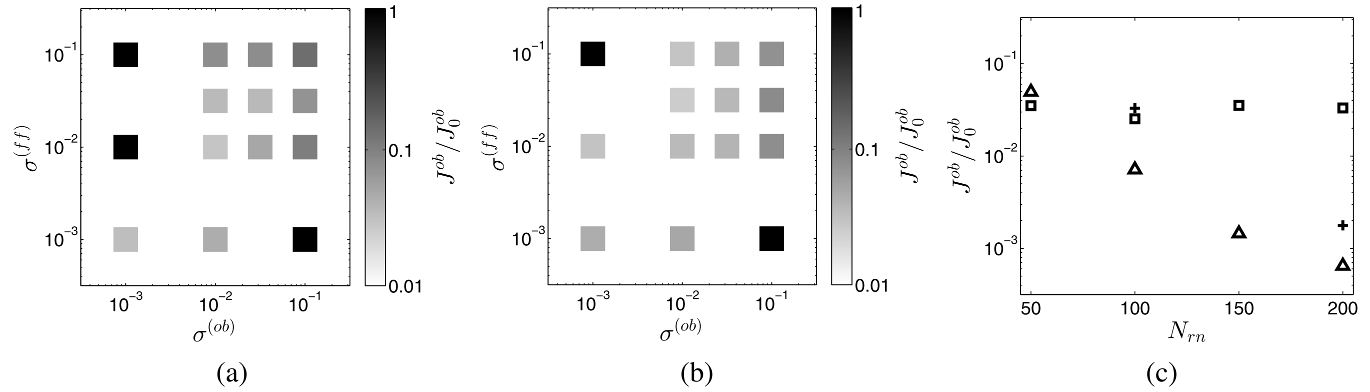

Fig. 5. Results obtained with the EnKS for gust reconstruction: (a)–(b) reduction in the value of the cost function J^{ob}/J_0^{ob} when the EnKS is used one time with (a) $N_{en} = 50$ or (b) $N_{en} = 100$ for different relative standard deviations $\sigma^{(ob)}$ and $\sigma^{(ff)}$ associated to observation and ensemble statistics respectively; (c) reduction in the value of the cost function J^{ob}/J_0^{ob} obtained with N_{rn} direct runs. The EnKS is used either one time with $N_{rn} = N_{en}$ (□) or iteratively with $N_{rn} = N_{en} \times i$, where i is the iteration number and $N_{en} = 50$ (△) or $N_{en} = 100$ (+), $\sigma^{(ob)} = 10^{-2}$ and $\sigma^{(ff)} = 10^{-1.5}$.

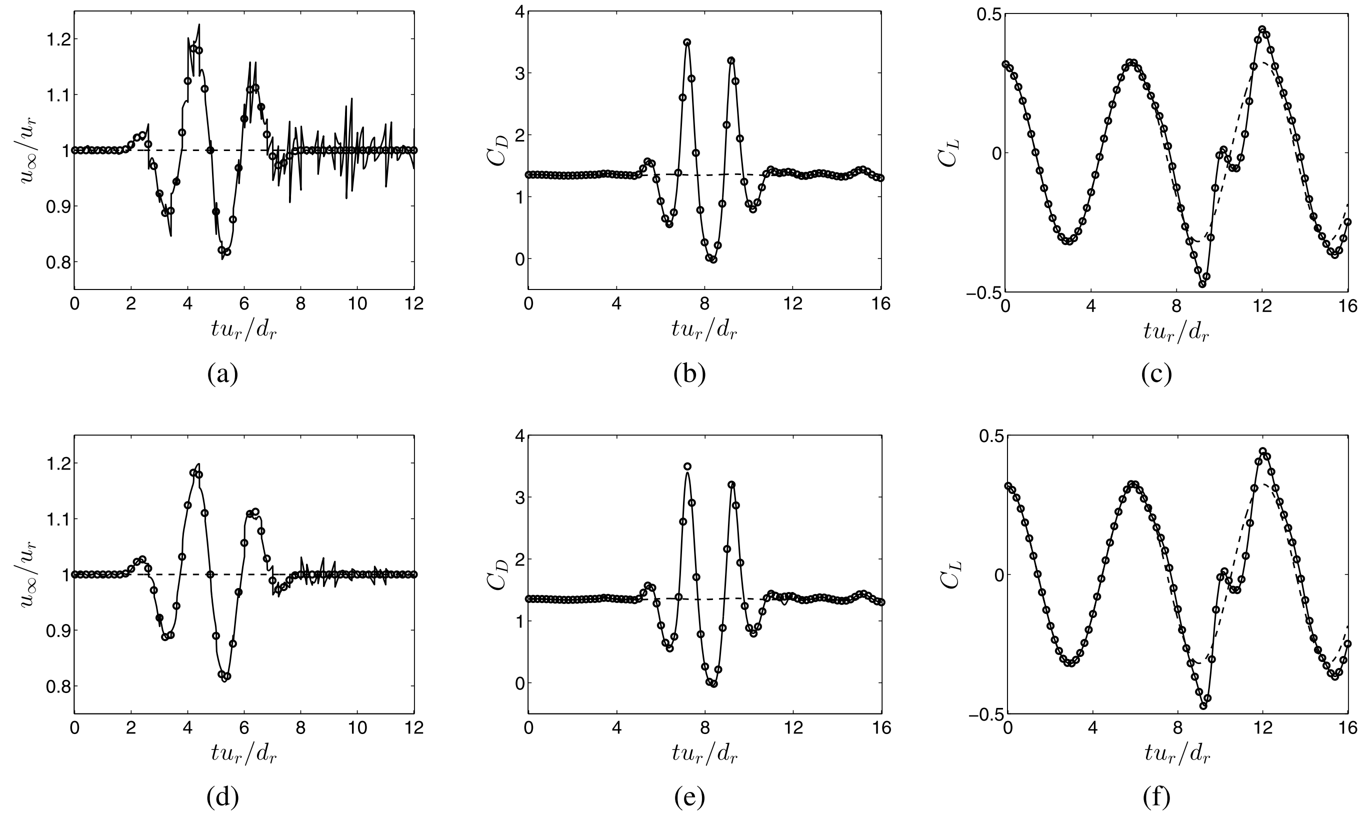

Fig. 6. Results obtained with the EnKS for gust reconstruction: temporal evolution of the inlet velocity (first column) and coefficients C_D (second column) and C_L (third column) for reference (○), estimated (- - -) and assimilated (–) runs. The EnKS is used iteratively with $N_{en} = 50$ (first row) or $N_{en} = 100$ (second row), in both cases the total number of direct runs for the assimilation is $N_{rn} = 200$, $\sigma^{(ob)} = 10^{-2}$ and $\sigma^{(ff)} = 10^{-1.5}$.

intuitive contrary to 4DVar. If the weight of observations is relatively too important ($\sigma^{(ob)}/\sigma^{(ff)} \ll 1$), the analysis step (16) entails spurious updates and a drastic reduction of the ensemble variance, potentially leading to filter divergence, and no satisfactory error reduction can be obtained. This phenomena may be amplified by finite-ensemble-size effects. Results improve when $\sigma^{(ob)}$ increases and $\sigma^{(ff)}$ decreases, i.e. when the weight of prior information in the assimilation process increases with respect to that of observations. However, though the ratio $\sigma^{(ob)}/\sigma^{(ff)}$ has to be sufficiently high to ensure the stability of the EnKS, the value of $\sigma^{(ff)}$ can not be too low either compared to that of $\sigma^{(ob)}$ if we want the observations to be taken into account in the assimilation process. In that respect, the EnKS appears to be more sensitive to observation and ensemble (or prior) statistics than the 4DVar scheme. This may be problematic since the determination of proper prior statistics is a challenging topic [47,48]. As expected, Figs. 5(a)–5(b) also illustrate that the stability of the EnKS and the results slightly improve when the size of the ensemble increases. In Fig. 5(c), the sensitivity of the results with respect to the size of the ensemble is further investigated. For ensemble size $N_{en} \geq 100$, there is no significant improvement in the results in terms of error reduction when the EnKS is used one time. On the other hand, for a same number N_{rn} of

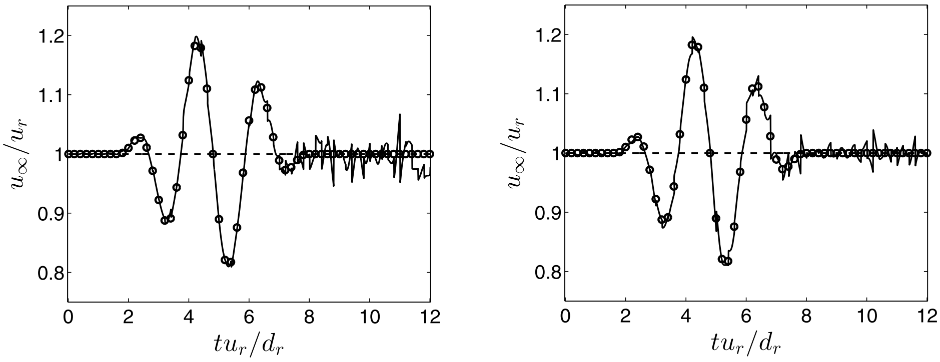

(a) (b)

Fig. 7. Results obtained with the EnKS for gust reconstruction: temporal evolution of the inlet velocity for reference (◯), estimated (- - -) and assimilated (—) runs. The EnKS is used iteratively with $N_{en} = 50$ and 4 iterations ($N_{rn} = 200$), $\sigma^{(ob)} = 10^{-2}$ and $\sigma^{(ff)} = 10^{-1.5}$. The localization procedure described in section 3.3 is used with either (a) $\kappa = 1$ or (b) $\kappa = 2$.

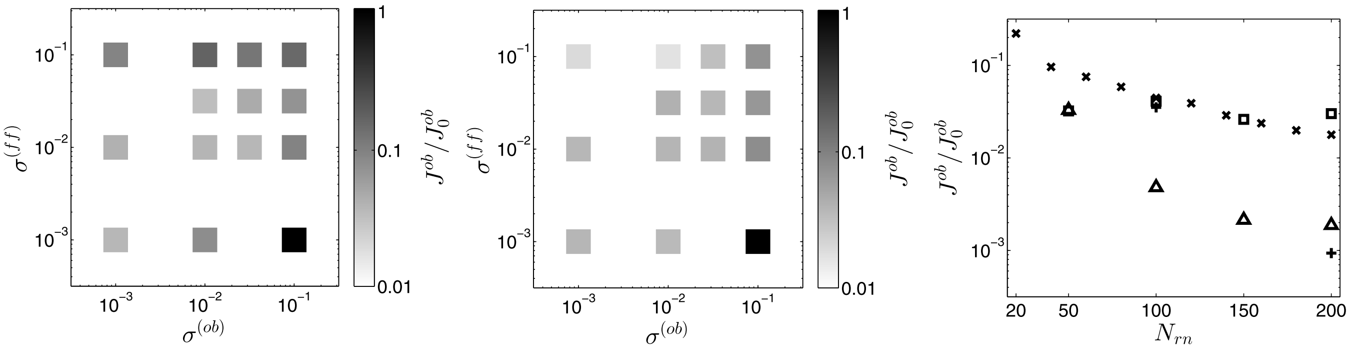

(a) (b) (c)

Fig. 8. Results obtained with the 4DEnVar method for gust reconstruction: (a)–(b) reduction in the value of the cost function J^{ob}/J^{ob}_0 when the 4DEnVar is used one time with (a) $N_{en} = 50$ or (b) $N_{en} = 100$ for different relative standard deviations $\sigma^{(ob)}$ and $\sigma^{(ff)}$ associated to observation and ensemble statistics respectively; (c) reduction in the value of the cost function J^{ob}/J^{ob}_0 obtained with N_{rn} direct runs. The 4DEnVar algorithm is used either one time with $N_{rn} = N_{en}$ (□) or iteratively with $N_{rn} = N_{en} \times i$, where i is the iteration number and $N_{en} = 20$ (×), $N_{en} = 50$ (△) or $N_{en} = 100$ (+), $\sigma^{(ob)} = 10^{-2}$ and $\sigma^{(ff)} = 10^{-1.5}$.

direct runs performed during the complete assimilation process, the value of the cost function J^{ob} continues to decrease when the EnKS is used iteratively (see Table 1). Here, for a total number of direct runs $N_{rn} = 200$, the reduction in the value of this cost function is at least 19 times greater when the EnKS is used iteratively with $N_{en} = 50$ or $N_{en} = 100$ than in the case where the EnKS is used one time with $N_{en} = 200$. As illustrated in Fig. 6, using iteratively the EnKS allows a reconstruction of the reference temporal evolution of the coefficients C_L and C_D that is comparable to that obtained with the 4DVar method. The gust is also satisfactorily recovered with $N_{en} = 100$. However, for $N_{en} = 50$, finite-ensemble-size effects are significant and lead to spurious oscillations in the reconstruction of the inlet velocity. In order to enhance the quality and the smoothness of the assimilated solution when $N_{en} = 50$, the localization procedure described in section 3.3 is used to obtain the results illustrated in Fig. 7. The smoothness of the reconstructed inlet velocity is improved compared to the results of Fig. 6(a). The best reconstruction seems to be obtained with $\kappa = 2$ (less severe localization).

Figs. 8–9 report results obtained with the 4DEnVar algorithm. The sensitivity of the results in terms of error reduction J^{ob}/J^{ob}_0 with respect to both observation and ensemble statistics is first studied in Figs. 8(a)–8(b). As with the 4DVar scheme, the reconstruction is better with lower values for $\sigma^{(ob)}$ and higher values for $\sigma^{(ff)}$, and contrary to the EnKS, the 4DEnVar method can be used with $\sigma^{(ob)}/\sigma^{(ff)} \ll 1$, i.e. with almost perfect observations. Thus, the 4DEnVar scheme seems more robust with respect to observation and ensemble statistics than the EnKS. The sensitivity of the 4DEnVar scheme with respect to the size of the ensemble is investigated in Fig. 8(c). It appears that the 4DEnVar algorithm can be used with $N_{en} = 20$, whereas it was checked in this study that the EnKS is not able to produce an assimilated state with $N_{en} < 50$ in this configuration. As the EnKS, the 4DEnVar algorithm is tested in an iterative form, which proves to be superior (at least with $N_{en} = 50$ or $N_{en} = 100$) than using the 4DEnVar scheme only one time with bigger ensembles. In particular, using 4DEnVar with $N_{en} = 50$ and 4 iterations of the algorithm allows to obtain a reduction in the value of the cost function J^{ob} that is 16 times greater than when using 4DEnVar one time with $N_{en} = 200$. The reconstruction of the reference temporal evolution of the inlet velocity and that of the coefficients C_L and C_D is illustrated in Fig. 9 for different ensemble sizes, the 4DEnVar algorithm is used iteratively. Even with $N_{en} = 20$, the reconstruction is correct, and results improve when the iterations are performed with larger ensembles. For $N_{en} = 50$ and $N_{en} = 100$, the results are comparable with those obtained

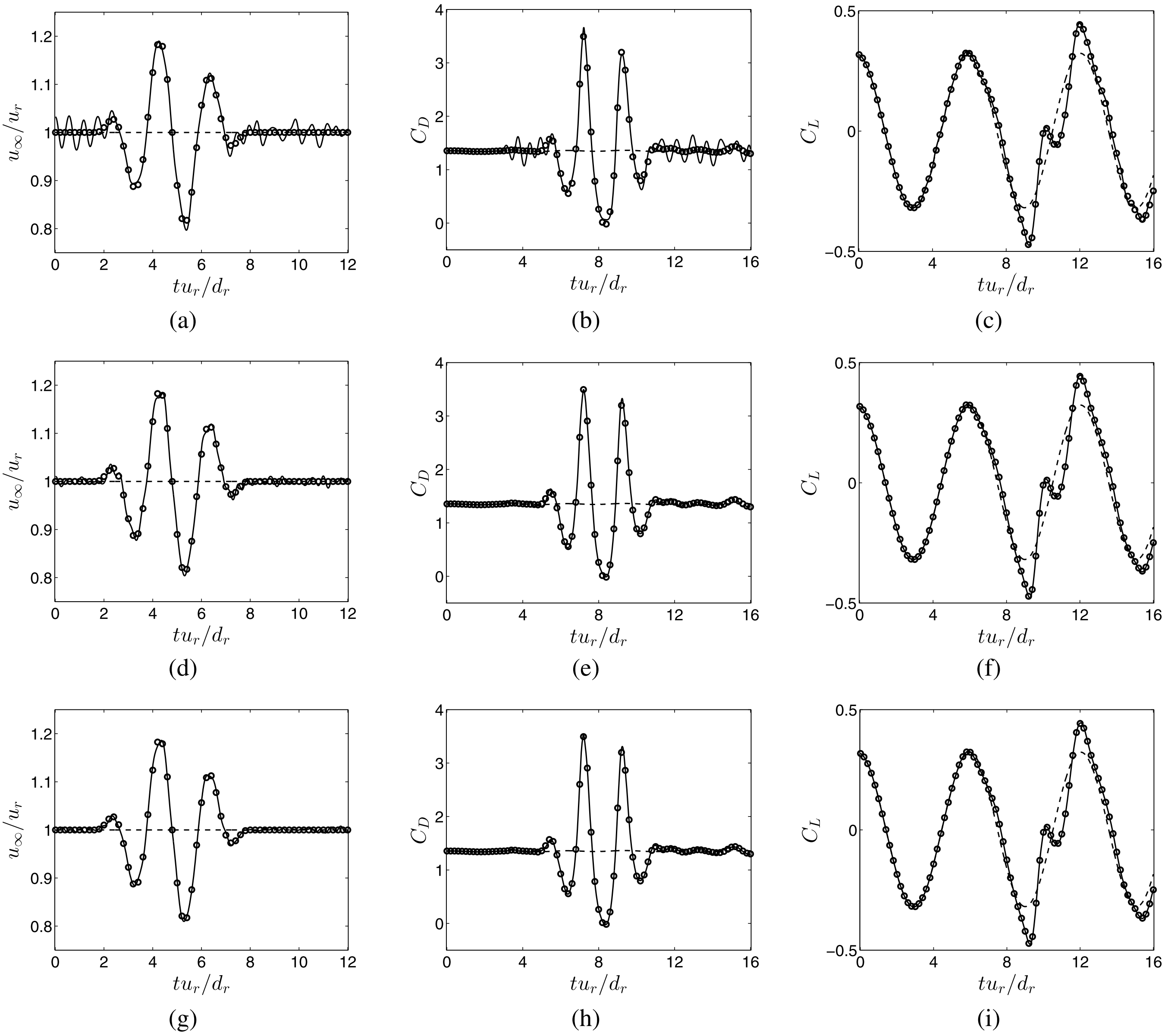

(a) (b) (c)

(d) (e) (f)

(g) (h) (i)

Fig. 9. Results obtained with the 4DEnVar method for gust reconstruction: temporal evolution of the inlet velocity (first column) and coefficients C_D (second column) and C_L (third column) for reference (◯), estimated (- - -) and assimilated (—) runs. The 4DEnVar algorithm is used iteratively with $N_{en} = 20$ (first row), $N_{en} = 50$ (second row) or $N_{en} = 100$ (third row), in all cases the total number of direct runs for the assimilation is $N_{rn} = 200$, $\sigma^{(ob)} = 10^{-2}$ and $\sigma^{(ff)} = 10^{-1.5}$.

with the 4DVar method. The robustness of the 4DEnVar scheme with respect to the size of the ensemble and to its statistics is confirmed in section 5.2.

However, as with the EnKS, the error reduction J^{ob}/J_0^{ob} achieved at the end of the assimilation procedure is not as large as for the 4DVar scheme for the same statistics and computational cost. The χ^2-test [49–51] can also be considered to assess and compare the assimilated solutions obtained with the different DA schemes. If the nonlinearities in the dynamics and the observations are moderate and the Gaussian assumption is valid, and if both prior and observation statistics are correctly modeled, the value of the quantity $\overline{\chi^2} = 2J^{(a)}/N_{ob}$ should be close to 1, where N_{ob} refers to the dimension of the observations multiplied by the number of observation times and $J^{(a)}$ is the value of the cost function in (6) for the assimilated state. Since the amplitude of the gust (33) corresponds to a perturbation of 20% of the reference velocity u_r, we choose to compare the DA schemes with $\sigma^{(ff)} = 10^{-1}$ in order to correctly reflect prior uncertainties, the value of $\sigma^{(ob)}$ is arbitrarily fixed to 10^{-2}. With this choice of parameters, we obtain $\overline{\chi^2} = 1.3$ with the 4DVar scheme and a computational cost equivalent to a total number of direct runs $N_{rn} = 100$. This result is satisfactory given the nonlinearity of the Navier–Stokes equations (28)–(31) and confirms both the validity of the hypotheses of the DA problem and the quality of the assimilated solution obtained by 4DVar. On the other hand, $\overline{\chi^2} = 77.9$ for the EnKS and $\overline{\chi^2} = 47.0$ for the 4DEnVar scheme with the same computational cost, which indicates that the assimilated states thus obtained are still relatively far from the optimal one with $N_{rn} = 100$. However, as illustrated in Figs. 5(c) and 8(c), using the EnKS and 4DEnVar schemes in

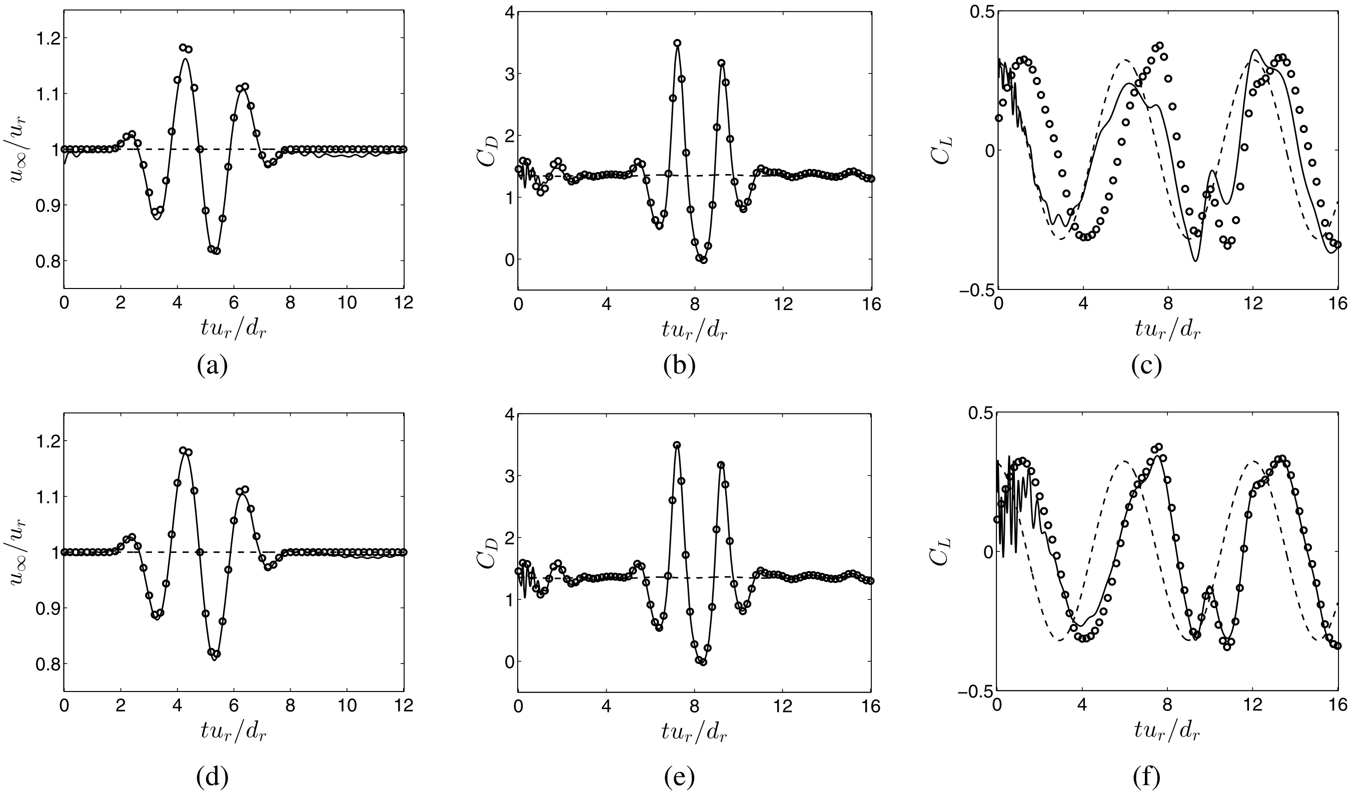

(a) (b) (c)
(d) (e) (f)

Fig. 10. Results obtained with the 4DVar method for gust and initial condition reconstruction: temporal evolution of the inlet velocity (first column) and coefficients C_D (second column) and C_L (third column) for reference (◯), estimated (- - -) and assimilated (—) runs. Different sets of observation and prior statistics are investigated: $\sigma^{(ob)} = 10^{-1.5}$, $\sigma^{(ff)} = 10^{-1.5}$ and $\sigma^{(ic)} = 10^{-2.5}$ (first row), and $\sigma^{(ob)} = 10^{-2}$, $\sigma^{(ff)} = 10^{-1.5}$ and $\sigma^{(ic)} = 10^{-2}$ (second row).

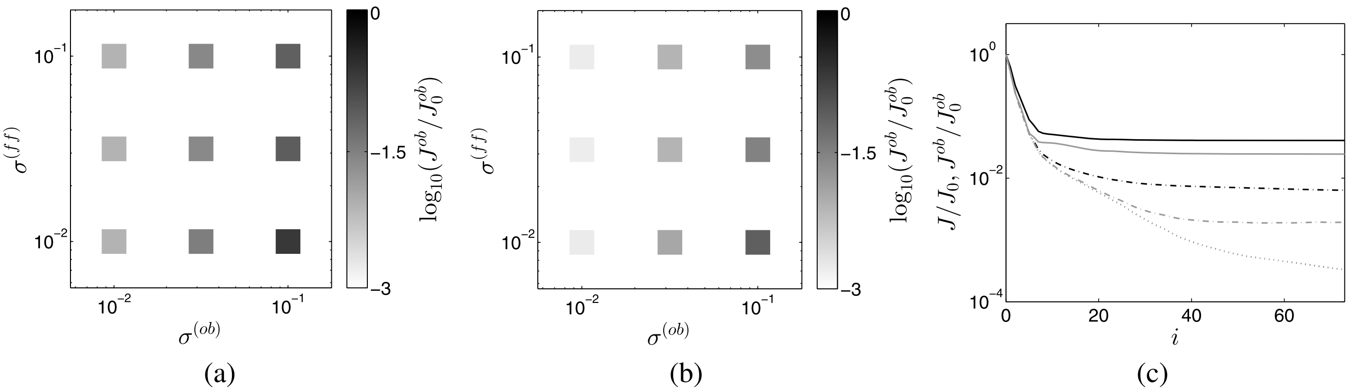

(a) (b) (c)

Fig. 11. Results obtained with the 4DVar method for gust and initial condition reconstruction: (a)–(b) reduction in the value of the cost function J^{ob}/J_0^{ob} at the end of the optimization procedure for different relative standard deviations $\sigma^{(ob)}$ and $\sigma^{(ff)}$ with (a) $\sigma^{(ic)} = 10^{-2.5}$ or (b) $\sigma^{(ic)} = 10^{-2}$; (c) cost functions J (black lines) and J^{ob} (grey lines) versus the iteration of the optimization procedure for $\sigma^{(ob)} = 10^{-2}$, $\sigma^{(ff)} = 10^{-1.5}$ and $\sigma^{(ic)} = 10^{-2}$ (-·-·), $\sigma^{(ob)} = 10^{-1.5}$, $\sigma^{(ff)} = 10^{-1.5}$ and $\sigma^{(ic)} = 10^{-2.5}$ (—), and in the case of perfect observations ($J = J^{ob}$, ······).

an iterative way allows to achieve a further error reduction (but it is more difficult to use the χ^2-test in this case since the prior estimate changes along the iterations, thus making comparisons between the different DA schemes less consistent).

5.2. *Gust and initial condition reconstruction*

In this section, we consider the case where both the inlet velocity and the initial condition of the reference run are poorly known. Thus, the control vector $\boldsymbol{\gamma}$ in the assimilation procedure is formed by the uniform and unsteady inlet velocity $u_\infty(t)$ and the complete initial field, its dimension is $\dim(\boldsymbol{\gamma}) = 5.7 \cdot 10^4$. The reference run corresponds to an inlet velocity given by (33), and the initial field contains a smaller gust (see Fig. 10(b) or 10(e)). The estimated run is chosen with a steady inlet velocity, the initial field contains no gust, and there is a shift in the vortex shedding compared to the reference evolution (see Fig. 10(c) or 10(f)). As in section 5.1, the pressure distribution around the cylinder $C_P(\theta)$ of the reference evolution is observed. Figs. 10–12 illustrate results obtained with the 4DVar method. It appears from the comparison between Figs. 3 and 11 that the dimension of the control vector strongly affects the rate of convergence of the optimization procedure.

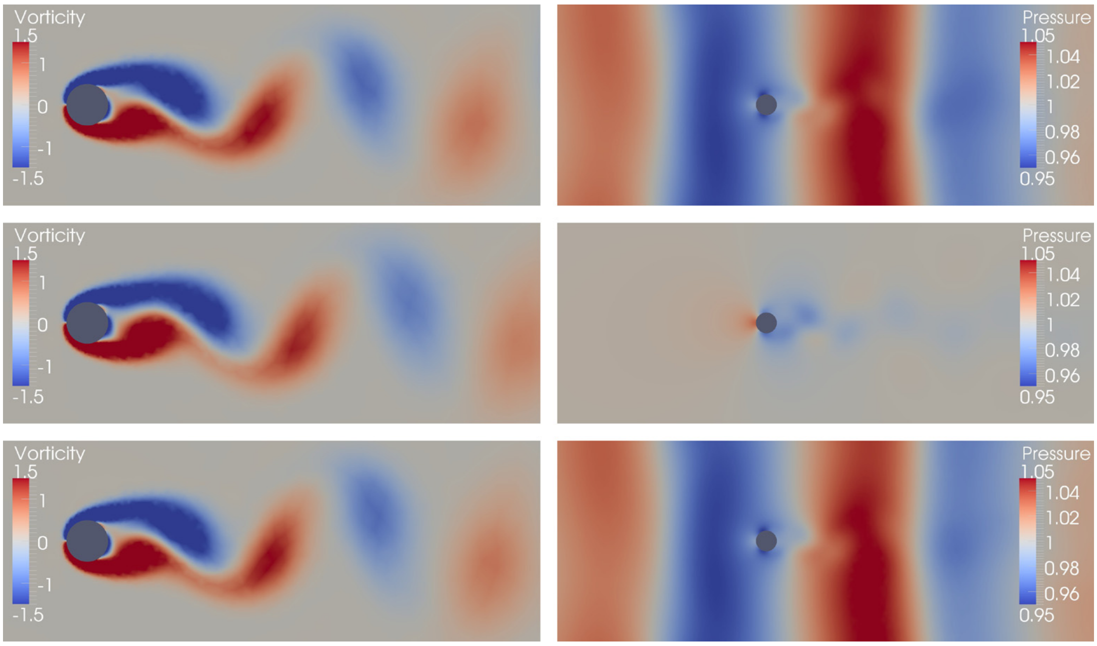

Fig. 12. Results obtained with the 4DVar method for gust and initial condition reconstruction: dimensionless vorticity field at $tu_r/d_r = 16$ (left column) and pressure field at $tu_r/d_r = 8$ (right column) for reference (first row), estimated (second row) and assimilated (third row) runs, $\sigma^{(ob)} = 10^{-2}$, $\sigma^{(ff)} = 10^{-1.5}$ and $\sigma^{(ic)} = 10^{-2}$.

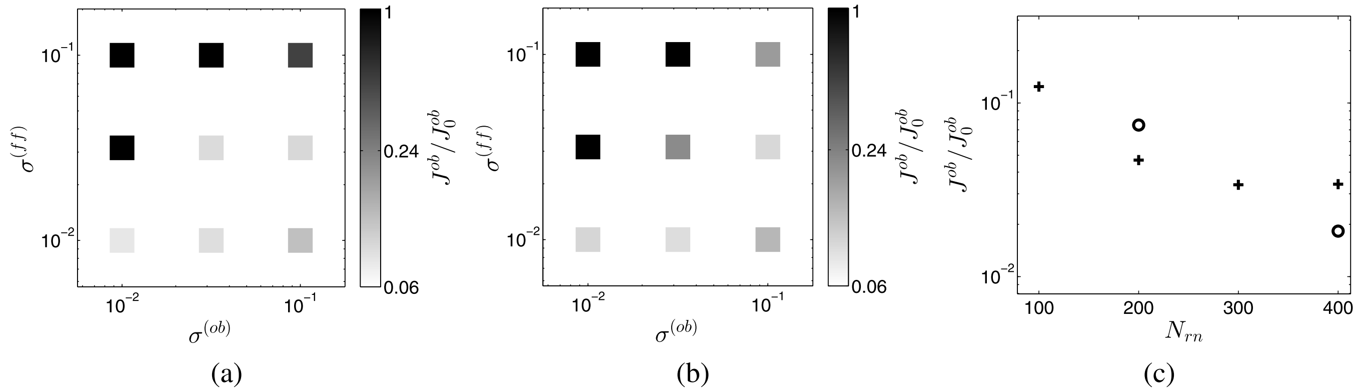

Fig. 13. Results obtained with the EnKS for gust and initial condition reconstruction: (a)–(b) reduction in the value of the cost function J^{ob}/J_0^{ob} when the EnKS is used one time with $N_{en} = 100$ for different relative standard deviations $\sigma^{(ob)}$ and $\sigma^{(ff)}$ with (a) $\sigma^{(ic)} = 10^{-2.5}$ or (b) $\sigma^{(ic)} = 10^{-2}$; (c) reduction in the value of the cost function J^{ob}/J_0^{ob} when the EnKS is used iteratively with $\sigma^{(ob)} = 10^{-1.5}$, $\sigma^{(ff)} = 10^{-1.5}$, $\sigma^{(ic)} = 10^{-2.5}$ and $N_{en} = 100$ (+) or $N_{en} = 200$ (◯).

Here, after 73 forward/backward integrations of the direct and adjoint problems, the optimization procedure achieves a reduction by 4 orders of magnitude in the value of the cost function J^{ob} in the case of perfect observations, while a reduction by 7 orders of magnitude in 18 iterations was obtained in section 5.1. The impact of observation and prior statistics on the results is examined in Figs. 10–11. Similarly to the results of section 5.1, the reconstruction of the reference evolution is satisfactory if the relative variances $\sigma^{(ff)}$ and $\sigma^{(ic)}$ associated to far-field and initial conditions respectively are sufficiently high and the relative variance $\sigma^{(ob)}$ associated to observation statistics sufficiently low. Using $\sigma^{(ob)} = 10^{-2}$, $\sigma^{(ff)} = 10^{-1.5}$ and $\sigma^{(ic)} = 10^{-2}$ (see Figs. 10(d)–10(f)), the reconstruction of the inlet velocity is very good and the reference temporal evolution of the coefficients C_L and C_D is almost perfectly recovered, excepted at the very beginning of the solution where spurious oscillations are present. This does not question the correct implementation of the adjoint code, since the assimilated solution passes through the reference values at observation times in the case of perfect observations. The influence of the frequency of observation on these oscillations is studied in section 5.3. Fig. 12 indicates that the 4DVar algorithm has successfully modified the shift in the vortex shedding and confirms the proper reconstruction of the gust.

Results obtained with the EnKS are illustrated in figures 13–15. The sensitivity of the results in terms of error reduction J^{ob}/J_0^{ob} with respect to the relative variances $\sigma^{(ob)}$, $\sigma^{(ic)}$ and $\sigma^{(ff)}$ is studied in Figs. 13(a)–13(b). As in section 5.1, the statistics of the ensemble and those of the observations have a strong influence on the stability of the EnKS, and for some values of these relative variances, the EnKS is not able to produce an assimilated state (no error reduction). Again, it appears that, for fixed observation-error statistics, the variances $\sigma^{(ic)}$ and $\sigma^{(ff)}$ have to be low enough in order to stabilize the EnKS algorithm, while these variances can not be too low either if we want the observations to be used to improve the estimated

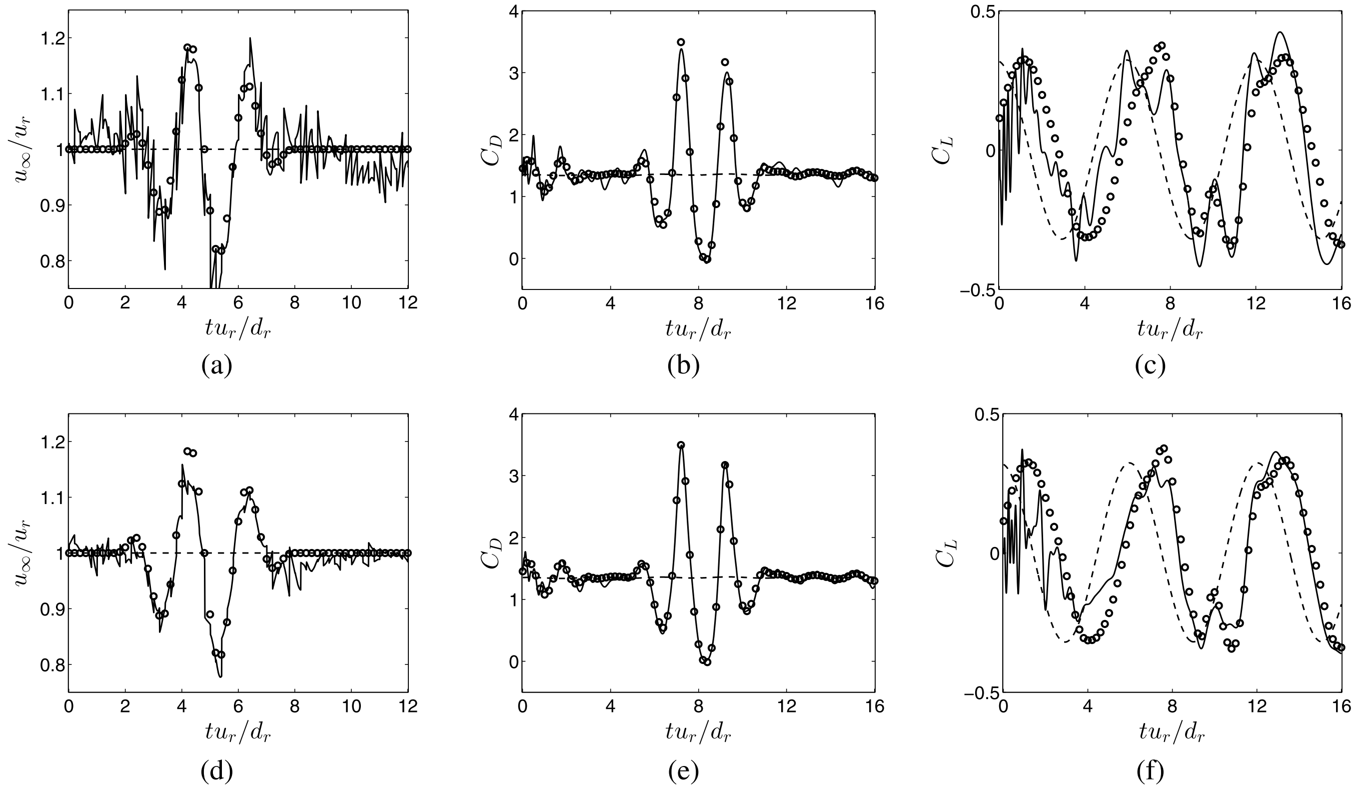

Fig. 14. Results obtained with the EnKS for gust and initial condition reconstruction: temporal evolution of the inlet velocity (first column) and coefficients C_D (second column) and C_L (third column) for reference (◯), estimated (- - -) and assimilated (—) runs. The EnKS is used iteratively with $N_{en} = 100$ (first row) or $N_{en} = 200$ (second row), in both cases the total number of direct runs for the assimilation is $N_{rn} = 400$, $\sigma^{(ob)} = 10^{-1.5}$, $\sigma^{(ff)} = 10^{-1.5}$ and $\sigma^{(ic)} = 10^{-2.5}$.

inlet or initial conditions. From this study, we set $\sigma^{(ob)} = 10^{-1.5}$, $\sigma^{(ff)} = 10^{-1.5}$, $\sigma^{(ic)} = 10^{-2.5}$ for the results illustrated in Figs. 13(c) and 14–15. The convergence of the EnKS, when used iteratively, is reported in Fig. 13(c) for $N_{en} = 100$ et $N_{en} = 200$. Assimilation experiments with $N_{en} < 75$ were also conducted, but failed. As for the 4DVar method, if we compare Figs. 5(c) and 13(c) for a same number of direct runs N_{rn}, it appears that the dimension of the control vector $\boldsymbol{\gamma}$ has a strong influence on the convergence of the EnKS. Beyond $N_{rn} = 400$, there is no real cost-effective improvement of the results. The assimilated trajectories obtained with $N_{rn} = 400$ are reported in Fig. 14. The reconstruction of the temporal evolution of the coefficients C_L and C_D is very good on the whole, even if it is not as good as with the 4DVar method. However, spurious oscillations due to finite-ensemble-size effects in the assimilated temporal evolution of the inlet velocity can be noticed, in particular for $N_{en} = 100$. As in section 5.1, the localization procedure of section 3.3 is tested to improve the quality of the reconstruction by the EnKS. Fig. 15 illustrates results for two ensemble sizes, and for $\kappa = 1$ and $\kappa = 2$. Here, contrary to section 5.1, the best results seem to be achieved with the most severe localization ($\kappa = 1$). This suggests a lack of robustness in the tuning of the localization procedure.

We now consider results obtained with the 4DEnVar algorithm that are reported in Figs. 16–17. The sensitivity of the results (in terms of error reduction J^{ob}/J_0^{ob}) with respect to ensemble and observation statistics is studied in Figs. 16(a)–16b when the 4DEnVar algorithm is used one time with $N_{en} = 100$. As in section 5.1, it appears that the 4DEnVar scheme is more robust with respect to these statistics compared to the EnKS and that it can be used in a context of perfect observations. It also appears that better results are obtained if the value of $\sigma^{(ic)}$ is not too important compared to that of $\sigma^{(ff)}$. This behavior is not observed in 4DVar results, and the facts that the assimilated solution is searched in a subspace spanned by an ensemble of realizations in the 4DEnVar scheme and that the estimated solution corresponds to greater perturbations of the far-field conditions of the reference flow than of its initial condition may explain this difference. Fig. 16(c) illustrates the convergence of the 4DEnVar algorithm, when used iteratively, with ensembles of size from $N_{en} = 20$ to $N_{en} = 200$. A strong result is that 4DEnVar is able to produce an assimilated state with only $N_{en} = 20$ while the dimension of the control vector is $\dim(\boldsymbol{\gamma}) = 5.7 \cdot 10^4$. Even if the 4DEnVar scheme converges faster when bigger ensembles are used, this suggests that DA can be performed while only very few direct runs are affordable, and that the quality of the assimilation is, to a certain extent, tunable, with the possibility to perform further iterations of the algorithm with very small ensembles. The difference in the robustness with respect to the ensemble size between the 4DEnVar scheme and the EnKS stems from the difference in the analysis step. The update (16) of the EnKS requires a reasonable estimate of the spatio-temporal covariance matrix of prior statistics, which is unrealistic to achieve with $N_{en} = 20$. On the other hand, the optimization-based analysis step of the 4DEnVar allows to extract an assimilated state even from limited information. As for the 4DVar method and the EnKS, the rate of convergence of the 4DEnVar algorithm in Fig. 16(c) is smaller than in Fig. 8(c). Fig. 17 confirms that it is

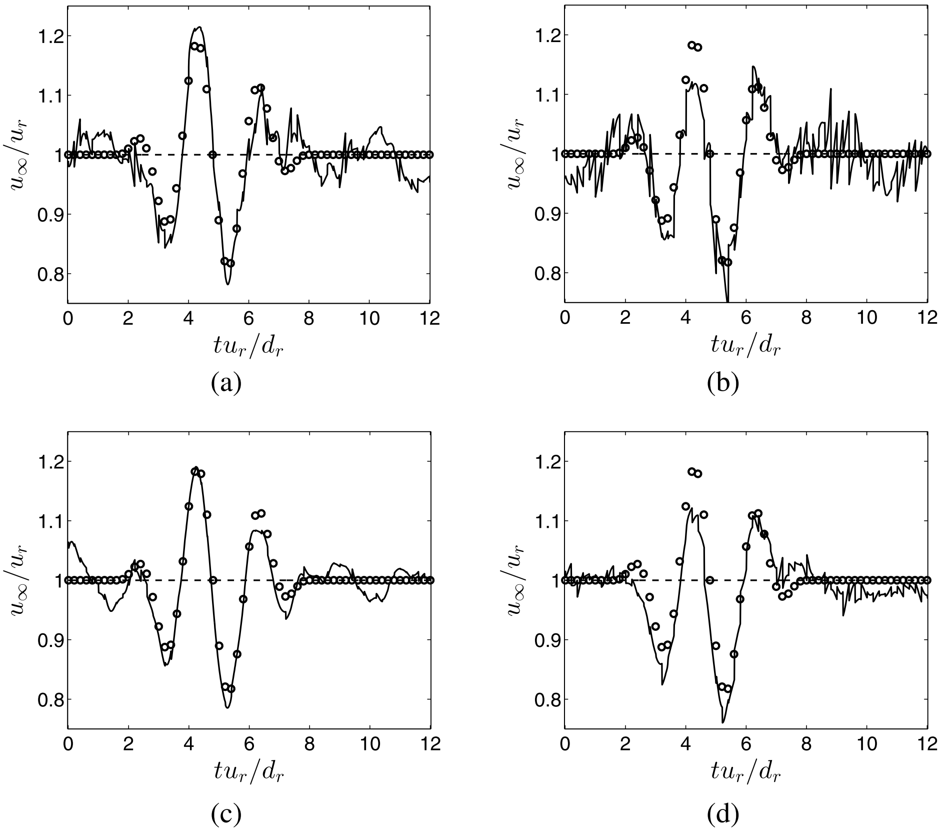

(a) (b)

(c) (d)

Fig. 15. Results obtained with the EnKS for gust and initial condition reconstruction: temporal evolution of the inlet velocity for reference (◯), estimated (- - -) and assimilated (—) runs. The EnKS is used iteratively with $N_{en} = 100$ (first row) or $N_{en} = 200$ (second row), in both cases the total number of direct runs for the assimilation is $N_{rn} = 400$, $\sigma^{(ob)} = 10^{-1.5}$, $\sigma^{(ff)} = 10^{-1.5}$ and $\sigma^{(ic)} = 10^{-2.5}$. The localization procedure described in section 3.3 is used with either $\kappa = 1$ (first column) or $\kappa = 2$ (second column).

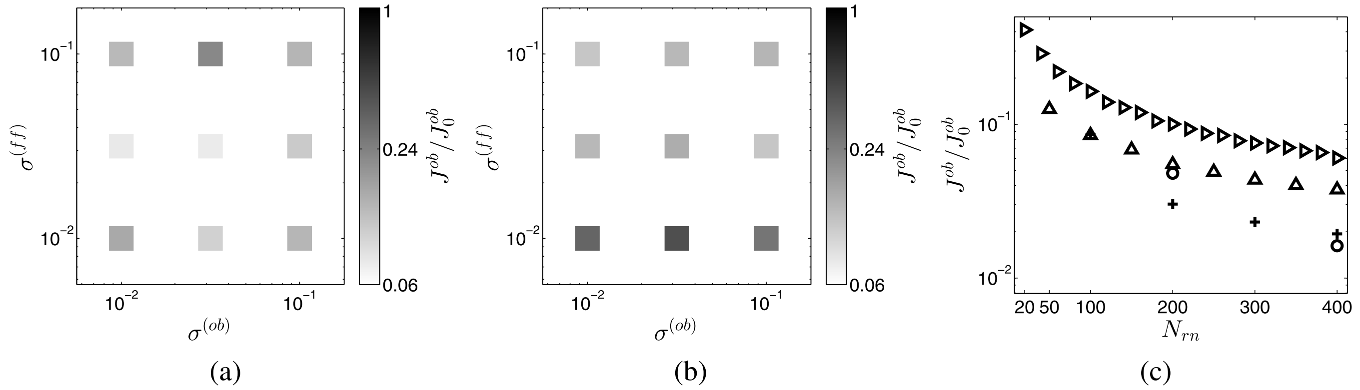

(a) (b) (c)

Fig. 16. Results obtained with the 4DEnVar method for gust and initial condition reconstruction: (a)–(b) reduction in the value of the cost function J^{ob}/J_0^{ob} when the 4DEnVar algorithm is used one time with $N_{en} = 100$ for different relative standard deviations $\sigma^{(ob)}$ and $\sigma^{(ff)}$ with (a) $\sigma^{(ic)} = 10^{-2.5}$ or (b) $\sigma^{(ic)} = 10^{-2}$; (c) reduction in the value of the cost function J^{ob}/J_0^{ob} when the 4DEnVar algorithm is used iteratively with $\sigma^{(ob)} = 10^{-1.5}$, $\sigma^{(ff)} = 10^{-1.5}$, $\sigma^{(ic)} = 10^{-2.5}$ and $N_{en} = 20$ (▷), $N_{en} = 50$ (△), $N_{en} = 100$ (+) or $N_{en} = 200$ (◯).

better to use the 4DEnVar scheme with large ensembles, however, as mentioned above, 4DEnVar is capable of dealing with very small ensembles and to provide significant improvement with respect to the estimated state in this case. The results obtained with $N_{en} = 200$ and two iterations of the algorithm are very good, however, they are still not as good as those obtained with the 4DVar method. As with the EnKS, there is no real cost-effective improvement of the reconstruction of the reference evolution beyond $N_{en} = 400$. The fact that the adjoint method furnishes the gradient of the Lagrangian in (7) with respect to all the components of the vector $\boldsymbol{\gamma}$ in (2), whereas the EnKS and 4DEnVar algorithms rely on the propagation of ensembles of size $N_{en} \ll \dim(\boldsymbol{\gamma})$, may explain that the 4DVar scheme can achieve a greater error reduction J^{ob}/J_0^{ob} than the EnKS and the 4DEnVar for similar computational cost. Nevertheless, the error reduction obtained with the 4DEnVar scheme, or with the EnKS after careful tuning of observation and prior statistics, is sufficiently large to produce satisfactory assimilated states.

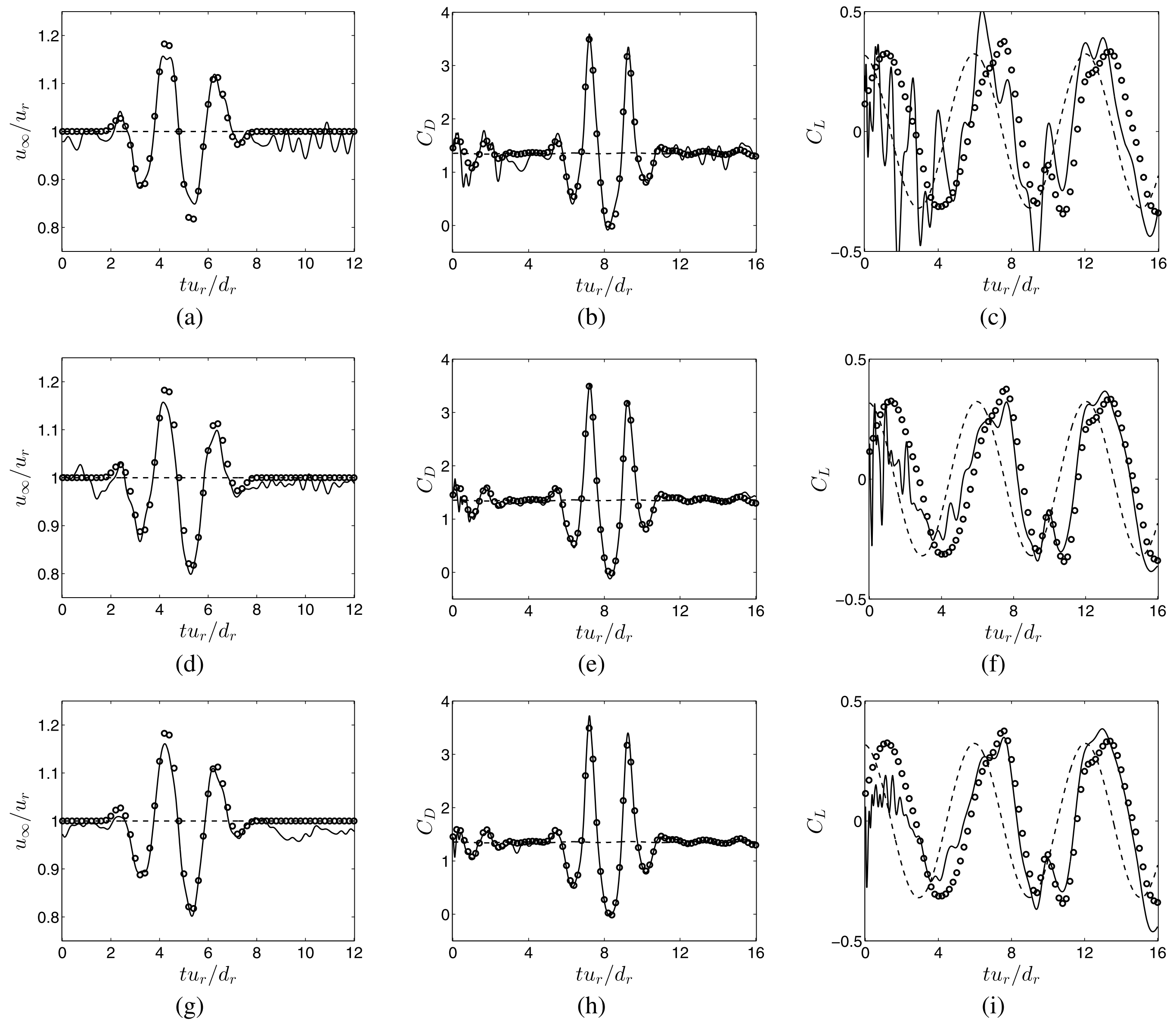

Fig. 17. Results obtained with the 4DEnVar method for gust and initial condition reconstruction: temporal evolution of the inlet velocity (first column) and coefficients C_D (second column) and C_L (third column) for reference (◯), estimated (- - -) and retrieved at the end of the DA procedure (—) runs. The 4DEnVar algorithm is used iteratively with $N_{en} = 20$ (first row), $N_{en} = 100$ (second row) or $N_{en} = 200$ (third row), in all cases the total number of direct runs for the assimilation is $N_{rn} = 400$, $\sigma^{(ob)} = 10^{-1.5}$, $\sigma^{(ff)} = 10^{-1.5}$ and $\sigma^{(ic)} = 10^{-2.5}$.

5.3. Data assimilation experiments with various types of observations

The setup of the DA experiments of this section is identical to that in section 5.2, and two other types of observations of the reference state are considered: the aerodynamic coefficients C_L and C_D, and the velocity field over the whole computational domain. Results obtained with the 4DVar scheme are reported in Figs. 18(a) and 19. The dimension of the observations has a strong influence on the rate of convergence of the optimization procedure (Fig. 18(a)), at least in the first iterations. When the coefficients C_L and C_D are considered, the dimension of the observations $\boldsymbol{y}_n$ is 2, and the optimization procedure converges at the fastest rate (in the first iterations), while $\dim(\boldsymbol{y}_n) = 2.8 \cdot 10^4$ when the complete flow field is observed, and the slowest convergence rate is observed in this case. However, it appears from Fig. 18(a) that the flaw in the observations due to stochastic perturbations tends to moderate the differences in the error reduction J^{ob}/J_0^{ob} between the different types of observations at the end of the optimization procedure, and a relatively similar final error reduction between 2 and 3 orders of magnitude is obtained for the different observations. It has been checked that in the case of perfect observations (results not shown here for the sake of brevity) the error reduction J^{ob}/J_0^{ob} reached at the end of the optimization procedure is much more important in the case where the coefficients C_L and C_D are observed (reduction by 6 orders of magnitude) than in the case where the whole velocity field is observed (reduction by 3 orders of magnitude), while results obtained with the pressure distribution are intermediate (reduction by 4 orders of magnitude). As illustrated in Fig. 19, a good convergence of the optimization procedure does not necessarily imply a good reconstruction.

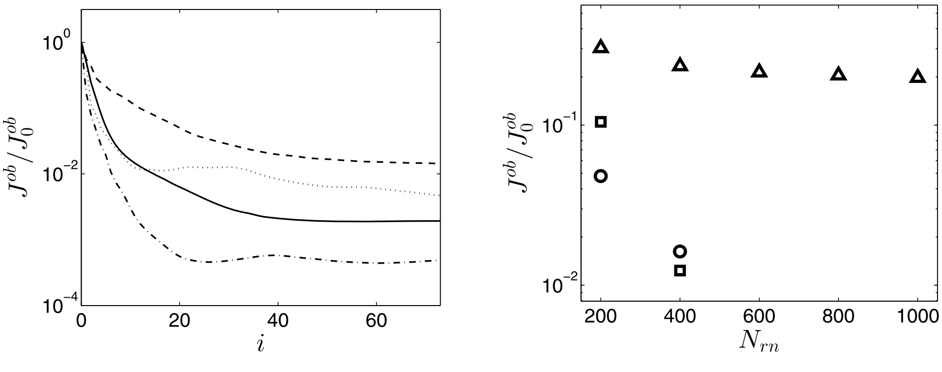

(a) (b)

Fig. 18. Results for gust and initial condition reconstruction: reduction in the value of the cost function J^{ob}/J_0^{ob} versus (a) the iteration of the optimization procedure in the 4DVar method or (b) the number N_{rn} of direct runs performed with the 4DEnVar scheme. Different types of observations of the reference evolution are considered: the aerodynamic coefficients C_L and C_D ($\cdots\cdots$, $\square$), the pressure distribution around the cylinder $C_P(\theta)$ (—, ○) and the complete velocity field (- - -, △). A complementary experiment is performed with the 4DVar method where the coefficients C_L and C_D are observed continuously in time (-·-·-). $\sigma^{(ob)} = 10^{-2}$, $\sigma^{(ff)} = 10^{-1.5}$ and $\sigma^{(ic)} = 10^{-2}$ for these experiments.

Table 3
Results obtained with the 4DVar and 4DEnVar schemes for gust and initial condition reconstruction: reduction in the error ϵ^{RMSE} defined in (37) obtained with different types of observations, the corresponding DA experiments are also illustrated in Figs. 18–20.

	Scheme					
	4DVar			4DEnVar		
$\mathbf{y}_n$	C_L, C_D	$C_P(\theta)$	u, v	C_L, C_D	$C_P(\theta)$	u, v
$\epsilon^{RMSE}/\epsilon_0^{RMSE}$	0.83	0.63	0.04	0.95	0.70	0.44

In Figs. 19(b)–19(c), the reference temporal evolution of the coefficients C_L and C_D, which are directly observed, is perfectly recovered, excepted at the very beginning of the assimilation window where spurious oscillations are noticed, this point is further investigated in the following. However, the optimization procedure has not recovered the reference temporal evolution of the inlet velocity, and the amplitude of the gust is still largely underestimated (Fig. 19(a)). This means that the observation of the integrated quantities C_L and C_D does not bring enough information to reconstruct an unsteady inlet velocity. The reconstruction of the gust is better when the pressure distribution around the cylinder is observed (Fig. 10), but the best results are obtained when the complete velocity field is observed (Figs. 19(g)–19(i)). The influence of the type of observations on the quality of the reconstruction is further illustrated in Table 3 where is reported the reduction in the value of the global error indicator ϵ^{RMSE} defined in (37) reached at the end of the different DA experiments discussed above. As expected, in terms of error on the whole velocity field, the best results are achieved when the latter is directly observed, while the poorest global reconstruction is obtained when the coefficients C_L and C_D are observed. A complementary DA experiment is performed where the coefficients C_L and C_D are observed continuously in time (Figs. 19(d)–19(f)). As expected, the spurious oscillations at the beginning of the assimilation window that were noticed in the present section and section 5.1 are no longer present. This confirms that these oscillations are only due to a finite frequency of observation. It also appears that increasing the frequency of observation allows to improve the reconstruction of the gust.

The sensitivity of the results obtained with the 4DEnVar scheme with respect to the type of observations is now investigated in Figs. 18(b) and 20. As for the 4DVar method, the rate of convergence is slower when the complete velocity field is observed than in the case where observations of smaller dimension are performed. In Figs. 20(b)-20(c), the temporal evolution of the coefficients C_L and C_D, which are directly observed, is very well reconstructed. In contrast, the evolution of the inlet velocity is poorly recovered (Fig. 20(a)), which confirms the conclusions drawn from the 4DVar results. Results obtained with the 4DEnVar scheme when the velocity field is observed over the whole computational domain are reported in Figs. 20(d)–20(f). The reconstruction of the reference temporal evolution of the drag coefficient C_D is correct, but that of the reference evolution of the lift coefficient C_L is less satisfactory, in particular at the beginning of the assimilation window. When interpreting this relatively poor performance, one has to keep mind that in this case the cost function J in (6) or (22) measures the discrepancies between the observations of the reference state and the estimated state over the whole computational domain, whereas the coefficient C_L represents a relatively local quantity. In that respect, the 4DVar scheme seems superior, since it achieves an excellent reconstruction of the evolution of the coefficient C_L even when the complete velocity field is observed. The better performances of 4DVar as compared to the 4DEnVar scheme in terms of global reconstruction are confirmed in Table 3. Nevertheless, the 4DEnVar scheme achieves a good reconstruction of the incoming gust, which is better than that obtained in the case where the coefficients C_L and C_D or the pressure distribution $C_P(\theta)$ (Fig. 17) are observed, as for the 4DVar scheme.

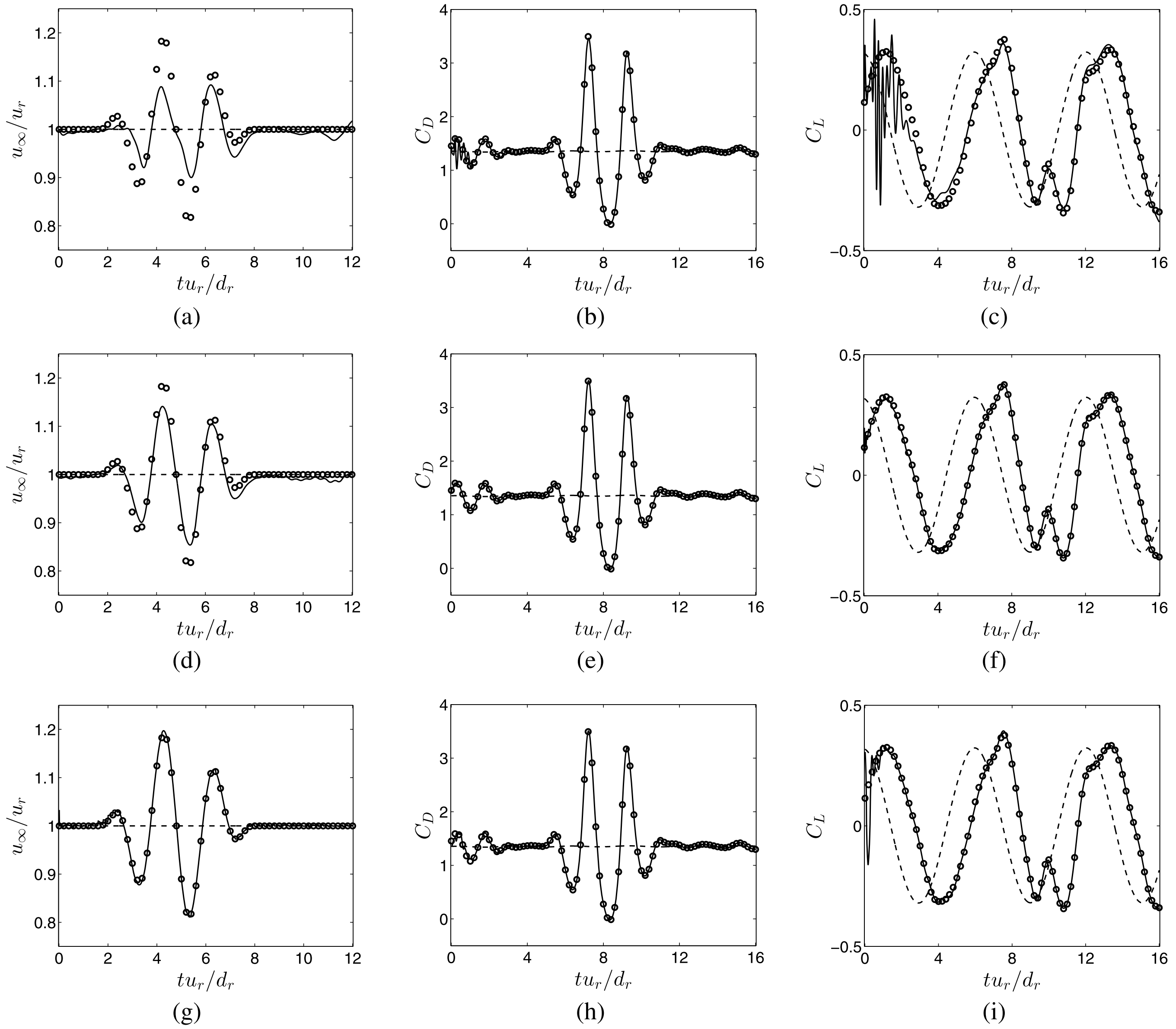

Fig. 19. Results obtained with the 4DVar method for gust and initial condition reconstruction: temporal evolution of the inlet velocity (first column) and coefficients C_D (second column) and C_L (third column) for reference (◯), estimated (- - -) and assimilated (—) runs. Different types of observations of the reference evolution are considered: the aerodynamic coefficients C_L and C_D (first and second rows) or the complete velocity field (third row). Observations are performed continuously in time for the results shown in the second row. $\sigma^{(ob)} = 10^{-2}$, $\sigma^{(ff)} = 10^{-1.5}$ and $\sigma^{(ic)} = 10^{-2}$ for these experiments.

5.4. Non-uniform and unsteady boundary conditions and initial field reconstruction

We now address the case where the gust has an arbitrary direction. Boundary conditions are thus unsteady and non-uniform, and, as in sections 5.2 and 5.3, we suppose that the reference initial field is also poorly known. Accordingly, the dimension of the control vector $\boldsymbol{\gamma}$ in (2) is $\dim(\boldsymbol{\gamma}) = 4.4 \cdot 10^5$. The reference run corresponds to an incoming gust with an incidence angle to the direction of the vortex shedding of 45°, and the pressure distribution $C_P(\theta)$ is observed. The 4DVar and 4DEnVar schemes are used to perform the assimilation (Figs. 21–23). Even if the 4DVar algorithm achieves a greater global error reduction, both methods satisfactorily reconstruct the reference temporal evolution of the coefficients C_L and C_D (Figs. 21–22). It is worth noting that in this configuration $\dim(\boldsymbol{\gamma})/N_{rn} \approx 10^3$, with N_{rn} the total number of direct runs performed with the 4DEnVar scheme. The reconstruction of the gust obtained with the two methods is evaluated in Fig. 23 where is reported the pressure field at two instants for reference, estimated and assimilated runs. Contrary to previous sections where boundary conditions are assumed to be uniform, the 4DVar and 4DEnVar schemes correctly recover the gust only in a region close to the cylinder and oriented in the direction of the reference gust (third and fourth rows of Fig. 23). This means that the 4DVar and 4DEnVar schemes can recover the reference boundary conditions only at locations that are aligned in the direction of the flow with the cylinder, i.e. where pressure is measured, since parietal pressure is not directly affected by the flow far from the cylinder. Complementary DA experiments are performed where the complete velocity field is observed. The corresponding results are reported in the fifth and sixth rows of Fig. 23. Since in this case

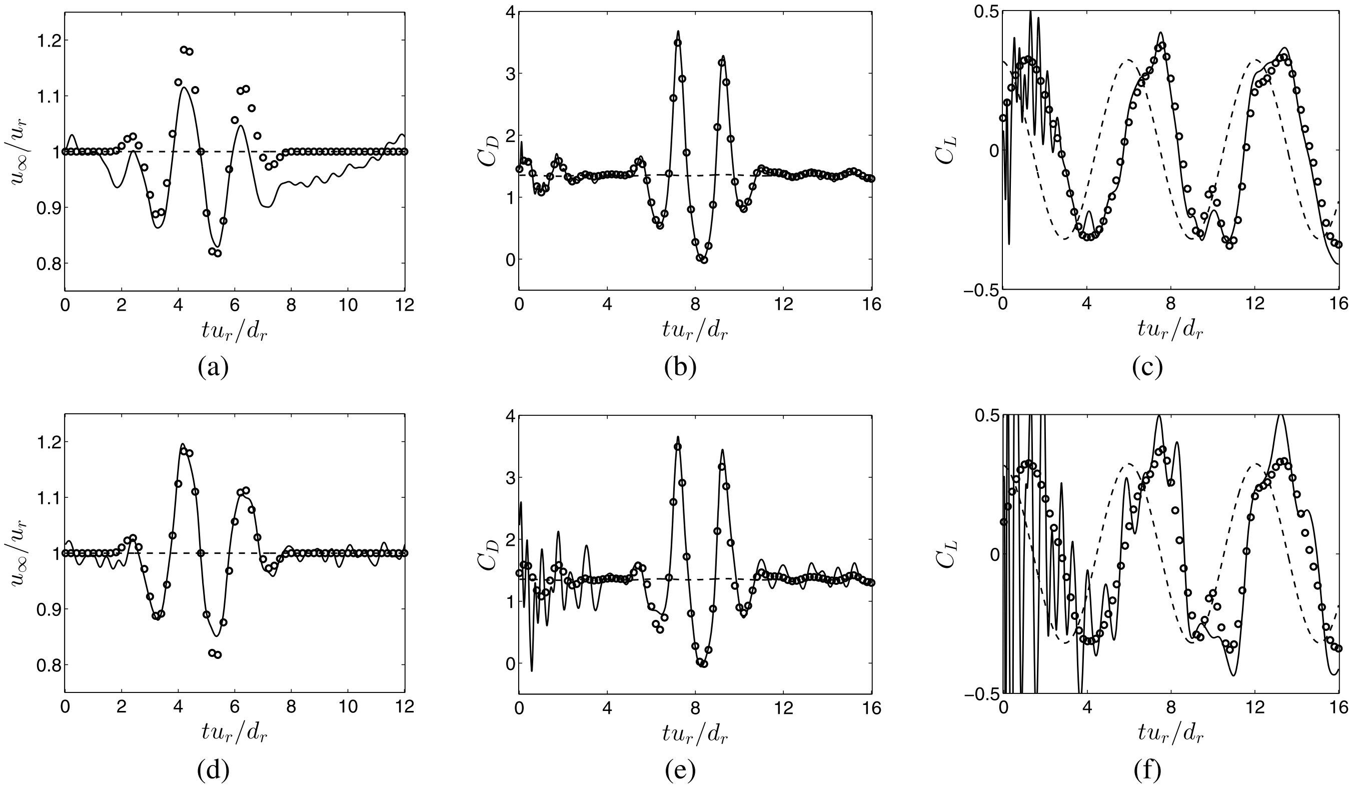

(a) (b) (c)

(d) (e) (f)

Fig. 20. Results obtained with the 4DEnVar method for gust and initial condition reconstruction: temporal evolution of the inlet velocity (first column) and coefficients C_D (second column) and C_L (third column) for reference (◯), estimated (- - -) and assimilated (—) runs. Different types of observations of the reference evolution are considered: the aerodynamic coefficients C_L and C_D (first row) or the complete flow field (second row). $\sigma^{(ob)} = 10^{-2}$, $\sigma^{(ff)} = 10^{-1.5}$ and $\sigma^{(ic)} = 10^{-2}$ for these experiments.

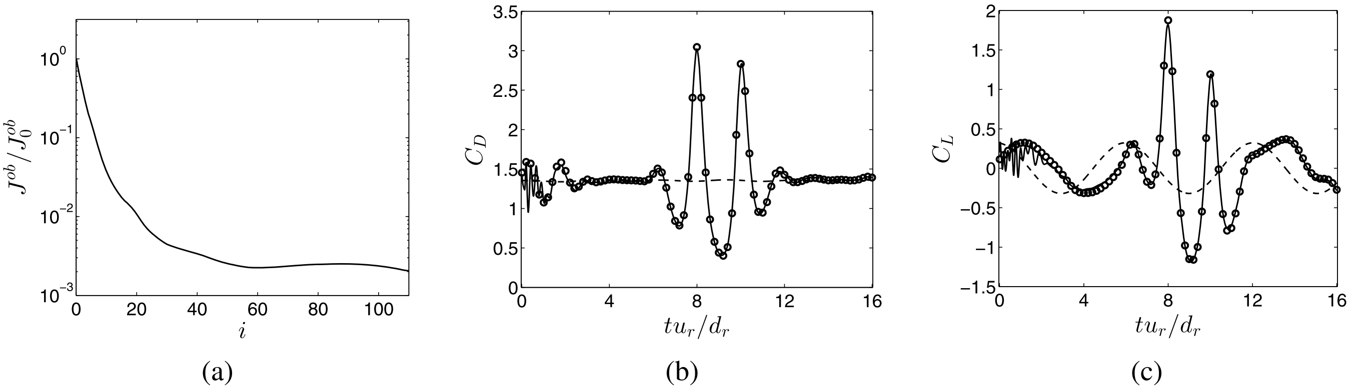

(a) (b) (c)

Fig. 21. Results obtained with the 4DVar method for non-uniform and unsteady boundary conditions and initial field reconstruction: (a) cost function J^{ob} versus the iteration of the optimization procedure; temporal evolution of the coefficients (b) C_D and (c) C_L for reference (◯), estimated (- - -) and assimilated (—) runs. $\sigma^{(ob)} = 10^{-2}$, $\sigma^{(ff)} = 10^{-1.5}$ and $\sigma^{(ic)} = 10^{-2}$ for this experiment.

information about the flow is available over the whole computational domain, the 4DVar and 4DEnVar schemes can recover the reference boundary conditions at all locations, leading to a better reconstruction of the gust. The results illustrated in the sixth row of Fig. 23 confirm the ability of the 4DEnVar scheme to deal with both control vectors and observations of high dimension.

5.5. Comparisons between data assimilation schemes

Table 4 summarizes results for different DA experiments of previous sections. Concerning the 4DVar scheme, the computational cost N_{rn} of the complete assimilation procedure in terms of direct runs is evaluated considering that the computational cost of solving the adjoint problem is equivalent to that of 4.5 direct runs. Ensemble methods are used with $N_{en} = 100$ when the pressure distribution $C_P(\theta)$ is observed in sections 5.1 and 5.2 and $N_{en} = 200$ in all other cases for the results reported in Table 4. The different DA schemes are compared with similar prior and observation statistics in Table 4. For the three DA schemes, the convergence rate of the assimilation procedure, in terms of error reduction J^{ob}/J_0^{ob},

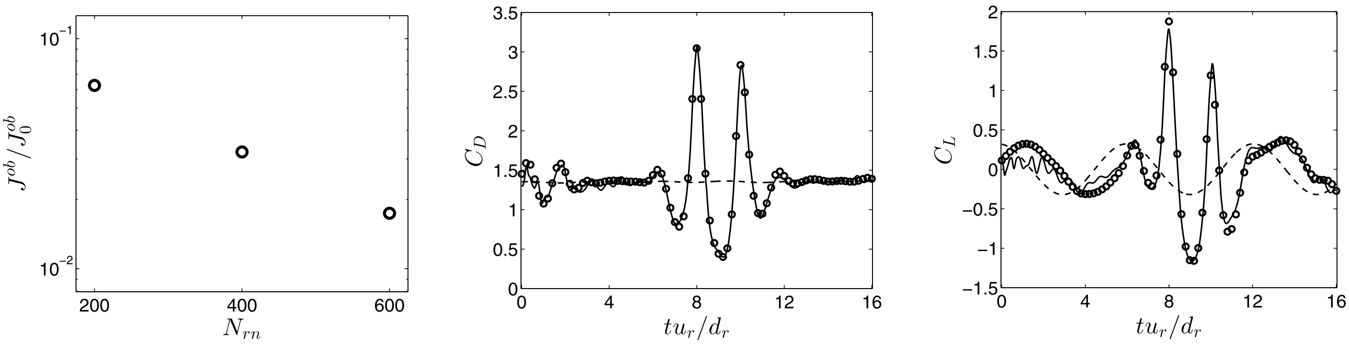

(a) (b) (c)

Fig. 22. Results obtained with the 4DEnVar method for non-uniform and unsteady boundary conditions and initial field reconstruction: (a) reduction in the value of the cost function J^{ob}/J_0^{ob} obtained with N_{rn} direct runs (the 4DEnVar scheme is used iteratively with $N_{en} = 200$); temporal evolution of the coefficients (b) C_D and (c) C_L for reference (◯), estimated (- - -) and assimilated (—) runs. $\sigma^{(ob)} = 10^{-2}$, $\sigma^{(ff)} = 10^{-1.5}$ and $\sigma^{(ic)} = 10^{-2}$ for this experiment.

Table 4
Error reduction J^{ob}/J_0^{ob} for different DA experiments in this paper that are characterized by the control vector $\boldsymbol{\gamma}$ (the corresponding section is also reported), observations of the reference state $\boldsymbol{y}_n$, the DA scheme and the computational cost N_{rn} of the complete assimilation procedure in terms of direct runs.

$\boldsymbol{\gamma}$ (section)	dim($\boldsymbol{\gamma}$)	$\boldsymbol{y}_n$	dim($\boldsymbol{y}_n$)	Scheme	N_{rn}	J^{ob}/J_0^{ob}
Uniform and unsteady boundary conditions (5.1)	$2.0 \cdot 10^3$	$C_P(\theta)$	30	4DVar	100	$3.6 \cdot 10^{-4}$
				EnKS	200	$1.8 \cdot 10^{-3}$
				4DEnVar	200	$9.4 \cdot 10^{-4}$
Initial condition + uniform and unsteady boundary conditions (5.2 and 5.3)	$5.7 \cdot 10^4$	C_L, C_D	2	4DVar	400	$4.7 \cdot 10^{-3}$
				4DEnVar	400	$1.2 \cdot 10^{-2}$
		$C_P(\theta)$	30	4DVar	400	$1.9 \cdot 10^{-3}$
				EnKS	400	$1.8 \cdot 10^{-2}$
				4DEnVar	400	$1.6 \cdot 10^{-2}$
		u, v	$2.8 \cdot 10^4$	4DVar	400	$1.4 \cdot 10^{-2}$
				4DEnVar	600	$2.0 \cdot 10^{-1}$
Initial condition + non-uniform and unsteady boundary conditions (5.4)	$4.4 \cdot 10^5$	$C_P(\theta)$	30	4DVar	600	$2.1 \cdot 10^{-3}$
				4DEnVar	600	$1.7 \cdot 10^{-2}$
		u, v	$2.8 \cdot 10^4$	4DVar	600	$1.6 \cdot 10^{-2}$
				4DEnVar	600	$3.5 \cdot 10^{-1}$

generally decreases when the dimension of the control vector or that of observations increases. This is particularly clear if we compare results of sections 5.1 and 5.4. In all configurations, for a similar computational cost, the 4DVar scheme achieves a greater error reduction than the EnKS or the 4DEnVar scheme. Nevertheless, this does not prevent from a satisfactory reconstruction of the reference trajectory with these methods (see, e.g., Figs. 6, 9 and 22). Even if the DA experiments have been conducted so that the required CPU time is similar for the three DA schemes for a given setup, it is worth noting that the parallelization of ensemble methods is much more straightforward than for 4DVar. Direct and adjoint solutions must be evaluated in a purely sequential way in the 4DVar scheme, while the solutions associated to the different members of the ensemble can be calculated simultaneously for the EnKS and the 4DEnVar scheme. In terms of error reduction, the performances of the EnKS and 4DEnVar schemes may seem similar, but one has to keep in mind that the statistics of the ensemble have to be carefully tuned (Figs. 5 and 13) for the EnKS before obtaining the results reported in Table 4. Moreover, the 4DEnVar scheme appears much more robust with respect to the size of the ensemble than the EnKS. However, an advantage of the EnKS compared to both 4DVar and 4DEnVar schemes is to provide the statistics of the assimilated solution. Fig. 24 illustrates the posterior statistics associated to far-field conditions obtained with the EnKS for one DA experiment of section 5.1 and one of section 5.2. The drastic reduction in the variance of the ensemble ($\sigma^{(ff)} = 10^{-1.5}$ for the estimated run while $\sigma^{(ff)} \approx 10^{-3}$ for the assimilated run in the two experiments illustrated in Fig. 24) confirms the convergence of the ensemble towards the assimilated solution. However, given the remaining discrepancies between the reconstructed and reference inlet velocities (see e.g. Fig. 24(c)), it appears that the EnKS largely underestimates the posterior statistics ($\sigma^{(ff)}$ should be closer to $10^{-1.5}$ at the end of the assimilation procedure to correctly reflect the errors between the reference and assimilated states). The benefits and drawbacks of the different DA schemes used in this paper are further discussed in the following section.

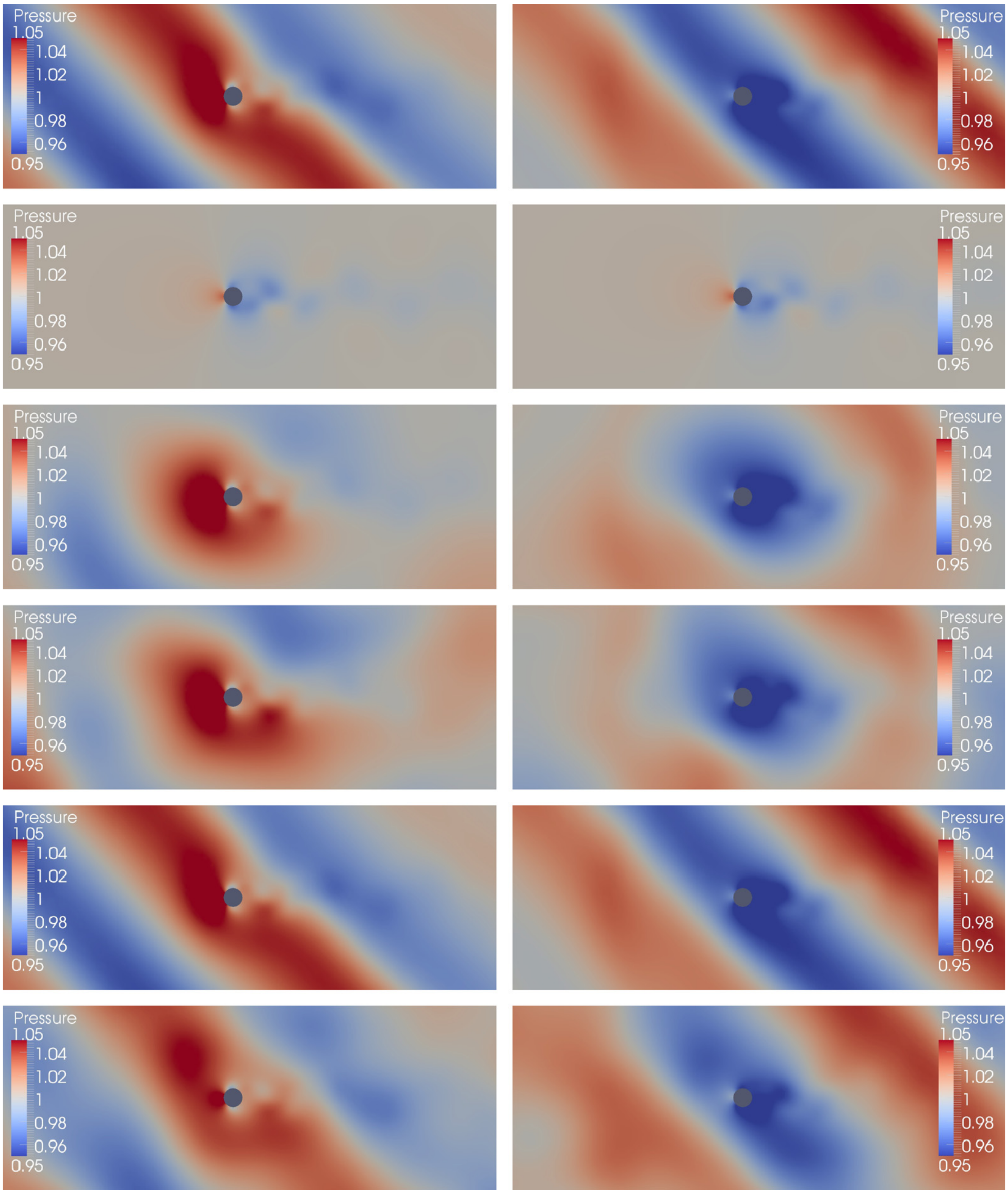

Fig. 23. Results obtained with the 4DVar and 4DEnVar methods for non-uniform and unsteady boundary conditions and initial field reconstruction: dimensionless pressure field at $tu_r/d_r = 8$ (left column) and $tu_r/d_r = 9.3$ (right column) for reference run (first row), estimated run (second row), assimilated run obtained with the 4DVar (third row) or 4DEnVar (fourth row) methods when $C_P(\theta)$ is observed, assimilated run obtained with the 4DVar (fifth row) or 4DEnVar (sixth row) methods when the complete velocity field is observed. $\sigma^{(ob)} = 10^{-2}$, $\sigma^{(ff)} = 10^{-1.5}$ and $\sigma^{(ic)} = 10^{-2}$ for these experiments.

6. Conclusion

In the present work, three different data assimilation (DA) schemes have been considered within the framework of the Navier–Stokes equations. It has been demonstrated that these techniques can be successfully used for the reconstruction of initial and boundary conditions for 2D unsteady flows around a cylinder in the presence of coherent gusts at $Re = 100$. Various reference states, control vectors, whose dimension ranges from $\approx 10^3$ to $\approx 10^5$, and types of observations have been considered. In all configurations, the variational scheme (4DVar) has achieved the largest error reduction between observations and estimation for a given computational cost and fixed observation and prior statistics. This may be explained by the fact that the adjoint method furnishes the gradient of the cost function that quantifies the discrepancies between observations and numerical estimation with respect to all the components of the control vector. On the contrary, the ensemble Kalman smoother (EnKS) and ensemble-based variational (4DEnVar) scheme rely on the propagation of ensembles of size that is largely inferior to the dimension of the control vector to evaluate the sensitivity of the flow solution. Another

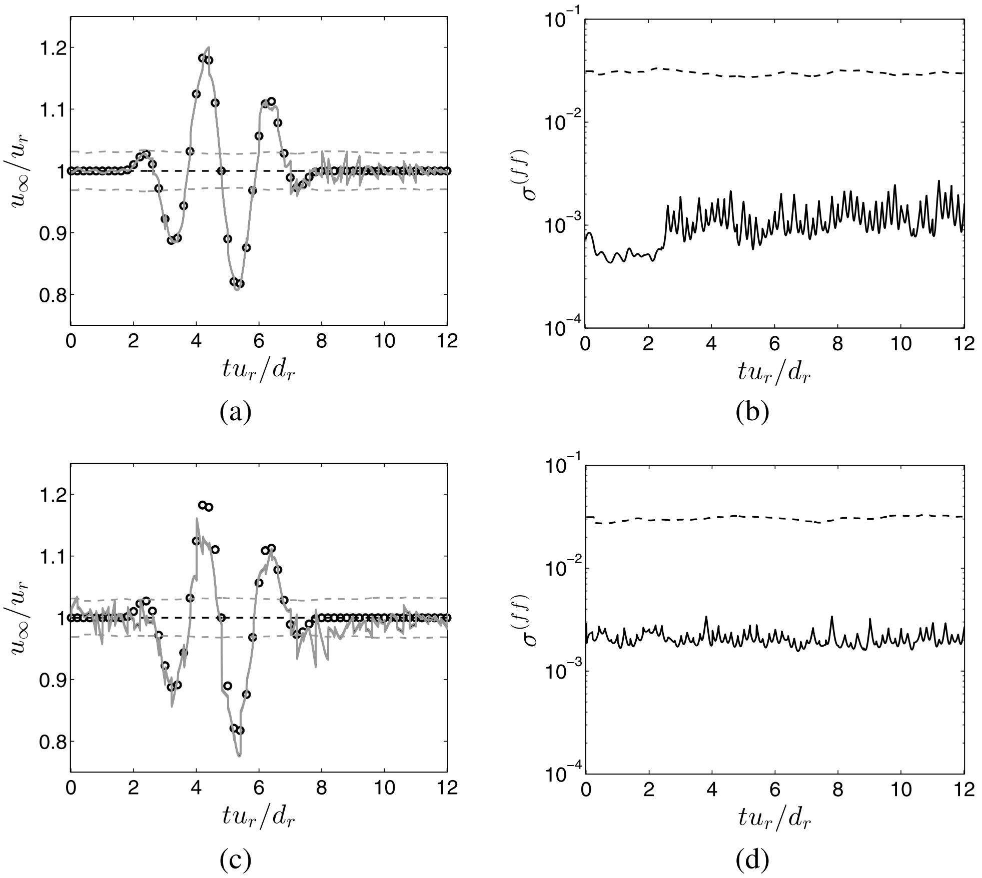

(a) (b)

(c) (d)

Fig. 24. Results obtained with the EnKS for gust reconstruction (first row, $N_{en} = 100$, $N_{rn} = 200$, $\sigma^{(ob)} = 10^{-2}$ and $\sigma^{(ff)} = 10^{-1.5}$) and gust and initial condition reconstruction (second row $N_{en} = 200$, $N_{rn} = 400$, $\sigma^{(ob)} = 10^{-1.5}$, $\sigma^{(ff)} = 10^{-1.5}$ and $\sigma^{(ic)} = 10^{-2.5}$): (a) and (c) temporal evolution of the inlet velocity for reference (◯), estimated (- - -) and retrieved at the end of the DA procedure (—) runs, black lines refer to the mean of the ensemble while grey line refer to the mean plus or minus the standard deviation; (b) and (d) relative standard deviation $\sigma^{(ff)}$ for estimated (- - -) and assimilated (—) runs.

advantage of the adjoint method is the physical interpretation of adjoint variables since the latter provide the first-order sensitivity of the cost function with respect to a change in the control variables. However, the implementation of the adjoint code may require significant efforts, in particular when the direct model is nonlinear or presents discontinuities. On the other hand, the EnKS and 4DEnVar schemes are non-intrusive DA methods that are easy to implement. Even if the EnKS and 4DEnVar schemes do not achieve an error reduction as significant as 4DVar for a similar computational cost, the reconstruction of the reference trajectory obtained with these methods can be very satisfactory. These two schemes have been tested in an iterative form, and it has been shown that the results thus obtained are better than in the case where only one loop on the main algorithm is performed with the same total number of direct runs performed during the assimilation procedure.

However, it has been observed that the EnKS may be more sensitive to prior and observation statistics, which are generally difficult to characterize, than the 4DVar and 4DEnVar schemes. Nevertheless, in the case where proper prior statistics are available, a benefit of the EnKS is to provide posterior statistics and not only an assimilated state. In contrast, the 4DEnVar scheme may be used in a deterministic framework and appears to be less sensitive to the statistics of the ensemble and to its size than the EnKS. The fact that the analysis step of the EnKS relies on a good estimation of the spatio-temporal covariance matrix of prior statistics, while 4DEnVar is primarily an optimization-based scheme, may explain the difference in the sensitivity to ensemble characteristics between the EnKS and 4DEnVar methods. Localization and inflation techniques may be considered to potentially enhance the robustness of the EnKS, but they introduce supplementary parameters that have to be tuned on a case-by-case basis. DA experiments with the 4DEnVar scheme have been successfully conducted with small ensembles down to 20 members, illustrating its robustness. Its ability to deal with control vectors and data with ensembles containing thousand times less members than the dimension of these quantities has been confirmed in the case where non-uniform and unsteady boundary conditions and the initial field are reconstructed from observations of the reference velocity field.

The robustness of the 4DEnVar scheme compared to the EnKS and its non-intrusiveness compared to 4DVar make it appealing for computational fluid dynamics (CFD) applications. Its use for 3D steady and unsteady flows could be considered in future work, possibly along the coupling with surface response-techniques to further decrease the number of direct runs performed during the assimilation procedure.

References

[1] J.M. Lewis, S. Lakshmivarahan, S.K. Dhall, Dynamic Data Assimilation: A Least Squares Approach, Encyclopedia of Mathematics and Its Applications, vol. 104, Cambridge University Press, 2006.

[2] G. Evensen, Data Assimilation: The Ensemble Kalman Filter, 2nd ed., Springer-Verlag, 2009.

[3] A. Gronskis, D. Heitz, E. Mémin, Inflow and initial conditions for direct numerical simulation based on adjoint data assimilation, J. Comput. Phys. 242 (2013) 480–497.

[4] H. Kato, A. Yoshizawa, G. Ueno, S. Obayashi, A data assimilation methodology for reconstructing turbulent flows around aircraft, J. Comput. Phys. 283 (2015) 559–581.

[5] T. Suzuki, Reduced-order Kalman-filtered hybrid simulation combining particle tracking velocimetry and direct numerical simulation, J. Fluid Mech. 709 (2012) 249–288.

[6] V. Mons, J.-C. Chassaing, T. Gomez, P. Sagaut, Is isotropic turbulence decay governed by asymptotic behavior of large scales? An eddy-damped quasi-normal Markovian-based data assimilation study, Phys. Fluids 26 (2014) 115105.

[7] F.X. Le Dimet, O. Talagrand, Variational algorithms for analysis and assimilation of meteorological observations: theoretical aspects, Tellus 38A (1986) 97–110.

[8] J.L. Lions, Optimal Control of Systems Governed by Partial Differential Equations, Springer-Verlag, 1971.

[9] R.E. Kalman, A new approach to linear filtering and prediction problems, J. Basic Eng. 82 (1960) 35–45.

[10] P.J. van Leeuwen, G. Evensen, Data assimilation and inverse methods in terms of a probabilistic formulation, Mon. Weather Rev. 124 (1996) 2898–2913.

[11] C.K. Wikle, L.M. Berliner, A Bayesian tutorial for data assimilation, Physica D 230 (2007) 1–16.

[12] J. D'Adamo, N. Papadakis, E. Mémin, G. Artana, Variational assimilation of POD low-order dynamical systems, J. Turbul. 8 (2007) 1–22.

[13] G. Artana, A. Cammilleri, J. Carlier, E. Mémin, Strong and weak constraint variational assimilations for reduced order fluid flow modeling, J. Comput. Phys. 231 (2012) 3264–3288.

[14] D.P.G. Foures, N. Dovetta, D. Sipp, P.J. Schmid, A data-assimilation method for Reynolds-averaged Navier–Stokes-driven mean flow reconstruction, J. Fluid Mech. 759 (2014) 404–431.

[15] G. Evensen, Sequential data assimilation with a nonlinear quasi-geostrophic model using Monte Carlo methods to forecast error statistics, J. Geophys. Res. 99 (1994) 10143–10162.

[16] C.H. Colburn, J.B. Cessna, T.R. Bewley, State estimation in wall-bounded flow systems. Part 3. The ensemble Kalman filter, J. Fluid Mech. 682 (2011) 289–303.

[17] H. Kato, S. Obayashi, Approach for uncertainty of turbulence modeling based on data assimilation technique, Comput. Fluids 85 (2013) 2–7.

[18] J.E.V. Peter, R.P. Dwight, Numerical sensitivity analysis for aerodynamic optimization: a survey of approaches, Comput. Fluids 39 (2010) 373–391.

[19] P.L. Houtekamer, H.L. Mitchell, A sequential ensemble Kalman filter for atmospheric data assimilation, Mon. Weather Rev. 129 (2001) 123–137.

[20] J.L. Anderson, S.L. Anderson, A Monte Carlo implementation of the nonlinear filtering problem to produce ensemble assimilations and forecasts, Mon. Weather Rev. 127 (1999) 2741–2758.

[21] C. Liu, Q. Xiao, B. Wang, An ensemble-based four-dimensional variational data assimilation scheme. Part I: technical formulation and preliminary test, Mon. Weather Rev. 136 (2008) 3363–3373.

[22] C. Liu, Q. Xiao, B. Wang, An ensemble-based four-dimensional variational data assimilation scheme. part II: observing system simulation experiments with Advanced Research WRF (ARW), Mon. Weather Rev. 137 (2009) 1687–1704.

[23] C. Liu, Q. Xiao, An ensemble-based four-dimensional variational data assimilation scheme. Part III: antarctic applications with advanced research WRF using real data, Mon. Weather Rev. 141 (2013) 2721–2739.

[24] Y. Yang, C. Robinson, D. Heitz, E. Mémin, Enhanced ensemble-based 4DVar scheme for data assimilation, Comput. Fluids 115 (2015) 201–210.

[25] I. Afgan, S. Benhamadouche, X. Han, P. Sagaut, D. Laurence, Flow over a flat plate with uniform inlet and incident coherent gusts, J. Fluid Mech. 720 (2013) 457–485.

[26] A.C. Lorenc, Analysis methods for numerical weather prediction, Q. J. R. Meteorol. Soc. 112 (1986) 1177–1194.

[27] P. Courtier, J.-N. Thépaut, A. Hollingsworth, A strategy for operational implementation of 4D-Var, using an incremental approach, Q. J. R. Meteorol. Soc. 120 (1994) 1367–1387.

[28] G. Evensen, P.J. van Leeuwen, An ensemble Kalman smoother for nonlinear dynamics, Mon. Weather Rev. 128 (2000) 1852–1867.

[29] E. Cosme, J. Verron, P. Brasseur, J. Blum, D. Auroux, Smoothing problems in a Bayesian framework and their linear Gaussian solutions, Mon. Weather Rev. 140 (2012) 683–695.

[30] G. Burgers, P.J. van Leeuwen, G. Evensen, Analysis scheme in the ensemble Kalman filter, Mon. Weather Rev. 126 (1998) 1719–1724.

[31] M. Buehner, P.L. Houtekamer, C. Charette, H.L. Mitchell, B. He, Intercomparison of variational data assimilation and the ensemble Kalman filter for global deterministic NWP. Part I: description and single-observation experiments, Mon. Weather Rev. 138 (2010) 1550–1566.

[32] M. Bocquet, P. Sakov, An iterative ensemble Kalman smoother, Q. J. R. Meteorol. Soc. 140 (2014) 1521–1535.

[33] S.K. Nadarajah, A. Jameson, Studies of continuous and discrete adjoint approaches to viscous automatic aerodynamic shape optimization, AIAA Paper No. 2001-2530, 2001.

[34] G. Carpentieri, B. Koren, M.J.L. van Tooren, Adjoint-based aerodynamic shape optimization on unstructured meshes, J. Comput. Phys. 224 (2007) 267–287.

[35] J. Nocedal, Updating quasi-Newton matrices with limited storage, Math. Comput. 35 (1980) 773–782.

[36] L. Armijo, Minimization of functions having Lipschitz continuous first partial derivatives, Pac. J. Math. 16 (1966) 1–3.

[37] L. Nerger, S. Schulte, A. Bunse-Gerstner, On the influence of model nonlinearity and localization on ensemble Kalman smoothing, Q. J. R. Meteorol. Soc. 140 (2014) 2249–2259.

[38] P.L. Roe, Approximate Riemann solvers, parameter vectors, and difference schemes, J. Comput. Phys. 43 (1981) 357–372.

[39] P. Jawahar, H. Kamath, A high-resolution procedure for Euler and Navier–Stokes computations on unstructured grids, J. Comput. Phys. 164 (2000) 165–203.

[40] A. Jameson, Time-dependent calculations using multigrid, with applications to unsteady flows past airfoils and wings, AIAA Paper No. 91-1596, 1991.

[41] D. Sharov, K. Nakahashi, Reordering of 3-D hybrid unstructured grids for vectorized LU-SGS Navier–Stokes computations, AIAA Paper No. 97-2102, 1997.

[42] H. Luo, J.D. Baum, R. Löhner, An accurate, fast, matrix-free implicit method for computing unsteady flows on unstructured grids, Comput. Fluids 30 (2001) 137–159.

[43] C. Liang, S. Premasuthan, A. Jameson, High-order accurate simulation of low-Mach laminar flow past two side-by-side cylinders using spectral difference method, Comput. Struct. 87 (2009) 812–827.

[44] W. Bierbooms, P.-W. Cheng, Stochastic gust model for design calculations of wind turbines, J. Wind Eng. Ind. Aerodyn. 90 (2002) 1237–1251.

[45] W. Bierbooms, A gust model for wind turbine design, JSME Int. J. Ser. B Fluids Therm. Eng. 47 (2004) 378–386.

[46] O. Cadot, A. Desai, S. Mittal, S. Saxena, B. Chandra, Statistics and dynamics of the boundary layer reattachments during the drag crisis transitions of a circular cylinder, Phys. Fluids 27 (2015) 014101.

[47] R.N. Bannister, A review of forecast error covariance statistics in atmospheric variational data assimilation. I: characteristics and measurements of forecast error covariances, Q. J. R. Meteorol. Soc. 134 (2008) 1951–1970.

[48] R.N. Bannister, A review of forecast error covariance statistics in atmospheric variational data assimilation. II: modelling the forecast error covariance statistics, Q. J. R. Meteorol. Soc. 134 (2008) 1971–1996.

[49] A.F. Bennett, L.M. Leslie, C.R. Hagelberg, P.E. Powers, Tropical cyclone prediction using a barotropic model initialized by a generalized inverse method, Mon. Weather Rev. 121 (1993) 1714–1729.

[50] R. Ménard, L.-P. Chang, Assimilation of stratospheric chemical tracer observations using a Kalman filter. Part II: χ^2-validated results and analysis of variance and correlation dynamics, Mon. Weather Rev. 128 (2000) 2672–2686.

[51] A. Tarantola, Inverse Problem Theory and Methods for Model Parameter Estimation, SIAM, 2005.

Chapter 6

Optimal sensor placement for variational data assimilation of unsteady flows past a rotationally oscillating cylinder

6.1 Introduction

In any data assimilation (DA) study, one may wonder which measurements of the reference flow to be reconstructed are the most appropriate to solve the DA problem. This question may arise in the design of an experimental sensor network, and is of crucial importance since these measurements represent the only available information about the reference flow. Of course, the issue of determining an 'optimal' observation network goes beyond the DA framework and may be relevant in any estimation problem. For example, efficient sensor placement has been considered in the context of flow reconstruction based on the proper orthogonal decomposition [58, 159, 225, 232]. This is also a topic of interest to the flow control community [2, 21, 48, 110] since the locations of sensors used to measure the flow are critical for the design of the estimator, and thus determines the success of the control strategy.

As regards DA applications, the impact of the observations on the DA process, or observation sensitivity, was often examined relying on the adjoint-based techniques developed in [16, 127] for '3D' (static) DA and in [68, 129] for '4D' (dynamic) DA. In these studies, observation sensitivity is understood as the gradient of the solution of the DA problem (the assimilated state), i.e. the flow solution that minimizes the discrepancies with the available measurements, with respect to the values or to the locations of the observations. In this framework, optimal measurements may be obtained through the minimization of a cost function that quantifies the discrepancies between the solution of the DA problem and a 'verification' state (reference assimilated state). Solving this optimization problem constrained by both the governing equations of the flow and the first-order optimality condition associated to the DA problem involves the use of a second-order adjoint model [130, 221], implying additional coding effort and computational burden. Such methodology was developed and applied to the optimization of observation locations with the two-dimensional shallow-water equations in [55]. Aside from the above techniques, one may wonder how it is possible to optimize observation locations *a priori*, i.e. before assimilating measurements. This question was examined by [113] where appropriate observation locations are derived from the optimization of an empirical observability Gramian matrix. The proposed methodology proved to be efficient with the Burgers equation in a low-dimensional test case (the dimension of the control vector in the DA problem is 13), but its extension to high-dimensional systems may be problematic, since evaluating observability for nonlinear large-scale systems remains difficult. On the other hand, an important advantage of the adjoint technique is to provide sensitivities at a computational cost similar to that of a forward integration of the dynamical model, regardless of the dimension of the problem.

In this chapter, an optimal sensor placement procedure for DA of viscous unsteady flows is investigated. The proposed approach can be performed before assimilating measurements and independently of the DA problem as in [113], i.e. is dedicated to the *a priori* design of an observation network. It relies on the use of adjoint-based techniques as in [55, 68, 129], but without the need of a second-order adjoint model. Indeed, the present methodology is designed to use the first-order adjoint model only, which is already involved in the variational scheme used to perform DA in this chapter. The proposed technique is applied to the reconstruction of flows in the presence of a cylinder performing rotary oscillations [15, 53, 125, 200, 201, 206]. This relatively simple configuration is of interest for, e.g., drag reduction purposes [52], and has been examined with adjoint-based optimal control in [22, 81, 95, 102, 180]. In this chapter, we investigate the possibility of reconstructing the forcing signal, i.e. the rotational speed of the cylinder, and the upstream flow, here included in the initial condition, from observations of the flow downstream or around the cylinder via variational DA. The proposed observation optimization procedure is used to identify optimal locations for velocity sensors, allowing a better reconstruction of the flow and/or a decrease in the computational cost in terms of calls to the adjoint code compared to a first-guess observation network.

This chapter is organized as follows. The observation optimization procedure is derived in §6.2. The physical setup of the DA experiments is presented in §6.3, along with the numerical method used. §6.4 is dedicated to the results of DA experiments, and the possibilities of reconstructing flows in the presence of a rotationally oscillating cylinder are delineated. The optimal sensor placement procedure is deployed and assessed by DA experiments in §6.5. §6.6 is dedicated to conclusions. Appendix D furnishes the discrete formulation of the observation optimization procedure, along with details about its numerical implementation.

6.2 Observation optimization, variational data assimilation and sensor selection procedures

The present optimal sensor placement procedure is derived as follows. First, a response function of the system under consideration, here flow obeying to the Navier-Stokes equations, is defined as the squared norm of observations of the system. The observation operator, which maps the state space to the observation space, is parameterized by a vector here formed by locations of sensors. The sensitivity (gradient) of this response function with respect to initial/boundary conditions and/or model parameters, which will form the control vector in the DA problem, is then computed using the adjoint technique. In a second step, the parameters of the observation operator are optimized through the maximization of the sensitivity of the response function, relying again on the adjoint technique. This method also provides a way to quantify the impact of each sensor in the sensitivity of the observations and to select the most important ones. Besides the derivation of the proposed methodology, the principle of variational DA is also recalled in this section, and optimization algorithms to solve the optimal sensor placement and DA problems are discussed.

6.2.1 Dynamical model

For the sake of generality in the derivation of the proposed observation optimization procedure, we consider a dynamical model under the generic form

$$\frac{\partial q}{\partial t} = f(q,\beta), \tag{6.1}$$

where q refers to the model variables, here a flow field, which are defined for a spatial domain Ω of any dimension (typically one to three) and a time interval $[0,T]$. q belongs to the model space denoted by $\mathcal{M}$ whose scalar product is defined by

$$\langle q, p\rangle_{\mathcal{M}} = \int_0^T \int_\Omega q(x,t)p(x,t)dxdt \quad \forall q,p \in \mathcal{M}. \tag{6.2}$$

The associated norm is given by $\|q\|_{\mathcal{M}} = \sqrt{\langle q, q\rangle_{\mathcal{M}}}\ \forall q \in \mathcal{M}$. Equation (6.1) also involves the nonlinear operator f, which corresponds here to the Navier-Stokes equations, and the vector β belonging to the parameter space denoted by $\mathcal{P}$. β may refer to parameters of the dynamical model, boundary conditions, or shape design parameters. Here, β refers to the rotational speed of the cylinder. Given (6.1), the solution q is uniquely specified by the initial condition q_0 ($q_0(x) = q(x, 0)\ \forall x \in \Omega$) and the parameters β. Before proceeding further, let us introduce a few notations. Given an operator g from vector space $\mathcal{A}$ to $\mathcal{B}$, the Gâteaux derivative of g at a in the direction c, with both a and c in $\mathcal{A}$, is denoted by

$$\left.\frac{\partial g}{\partial a}\right|_a (c) = \left\langle \frac{\partial g}{\partial a}(a), c \right\rangle_{\mathcal{A}} = \lim_{\epsilon \to 0} \frac{d}{d\epsilon} g(a + \epsilon c). \tag{6.3}$$

If g is a linear operator, one can define the adjoint operator g^* according to

$$\langle g(a), b\rangle_{\mathcal{B}} = \langle a, g^*(b)\rangle_{\mathcal{A}} \quad \forall a \in \mathcal{A},\ \forall b \in \mathcal{B}. \tag{6.4}$$

6.2.2 Sensitivity of observations

We now examine observations of the state q and their sensitivity with respect to a change in the initial condition q_0 or the parameters β. More precisely, we consider a response R of the model defined as the norm of the observations of the state vector q

$$R = \frac{1}{2}\|h(q, \lambda)\|^2_{\mathcal{O}}. \tag{6.5}$$

In (6.5), h is the observation operator that maps the model space $\mathcal{M}$ to the observation space $\mathcal{O}$. This operator will allow to compare the estimation of the state q with available measurements in the data assimilation (DA) procedure described in §6.2.4. It is assumed that the operator h is parameterized by the vector λ. This vector allows to tune the operator h, and thus to tune the observations performed on the system (6.1). In this chapter, λ will refer to the observation locations. To evaluate the change in the values of the observations resulting from a change in the state q, and more precisely to quantify the first-order sensitivity of the response R with respect to the initial condition q_0 and the parameters β, the adjoint technique [137] is employed to compute the gradient of R with respect to q_0 and β. The constraint (6.1) on the dynamics of q is taken into account through the introduction of the Lagrangian $\mathcal{L}_1$ defined by

$$\mathcal{L}_1 = \frac{1}{2}\|h(q, \lambda)\|^2_{\mathcal{O}} - \left\langle \tilde{q}, \frac{\partial q}{\partial t} - f(q, \beta) \right\rangle_{\mathcal{M}}, \tag{6.6}$$

where $\tilde{q}$ is referred to as the adjoint state. The variation of $\mathcal{L}_1$ in the direction $p \in \mathcal{M}$ is given by

$$\begin{aligned}
\left\langle \frac{\partial \mathcal{L}_1}{\partial q}, p \right\rangle_{\mathcal{M}} &= \left\langle h(q, \lambda), \left.\frac{\partial h}{\partial q}\right|_{q,\lambda}(p) \right\rangle_{\mathcal{O}} - \left\langle \tilde{q}, \frac{\partial p}{\partial t} - \left.\frac{\partial f}{\partial q}\right|_{q,\beta}(p) \right\rangle_{\mathcal{M}} \\
&= \left\langle \left(\left.\frac{\partial h}{\partial q}\right|_{q,\lambda} \right)^* (h(q, \lambda)), p \right\rangle_{\mathcal{M}} - \left\langle -\frac{\partial \tilde{q}}{\partial t} - \left(\left.\frac{\partial f}{\partial q}\right|_{q,\beta} \right)^* (\tilde{q}), p \right\rangle_{\mathcal{M}} \\
&\quad - \int_{\Omega} \left(\tilde{q}(x, T)p(x, T) - \tilde{q}(x, 0)p(x, 0) \right) dx.
\end{aligned} \tag{6.7}$$

The derivations in (6.7) involve the tangent linear model operator $\left.\frac{\partial f}{\partial q}\right|_{q,\beta}$ and its adjoint, which both depend on the state q if the model operator f is nonlinear, as is the case here. From (6.7), we can deduce the gradient of the Lagrangian $\mathcal{L}_1$ with respect to the initial condition q_0 and the parameters β of the model (6.1) according to the following system of equations

$$\tilde{q}(x,T) = 0 \quad \forall x \in \Omega, \tag{6.8a}$$

$$-\frac{\partial \tilde{q}}{\partial t} - \left(\frac{\partial f}{\partial q}\Big|_{q,\beta}\right)^{*}(\tilde{q}) = \tilde{h}(\lambda), \quad \tilde{h}(\lambda) = \left(\frac{\partial h}{\partial q}\Big|_{q,\lambda}\right)^{*}(h(q,\lambda)), \tag{6.8b}$$

$$\frac{\partial \mathcal{L}_1}{\partial q_0} = \tilde{q}_0, \quad \tilde{q}_0(x) = \tilde{q}(x,0) \quad \forall x \in \Omega, \tag{6.8c}$$

$$\frac{\partial \mathcal{L}_1}{\partial \beta} = \left(\frac{\partial f}{\partial \beta}\Big|_{q,\beta}\right)^{*}(\tilde{q}). \tag{6.8d}$$

The governing equation (6.8b) for the adjoint state has to be solved backward in time with the terminal condition (6.8a) in order to obtain the gradients (6.8c)-(6.8d). This backward integration requires the storing of the state q, as detailed in §6.3.2 and appendix D. The gradients (6.8c)-(6.8d) allow to quantify the first-order sensitivity of the response R defined in (6.5). For example, the change ΔR in the value of R resulting from a change $\Delta\beta$ in the parameters in (6.1) can be estimated through the first-order approximation

$$\Delta R \simeq \left\langle \frac{\partial \mathcal{L}_1}{\partial \beta}, \Delta\beta \right\rangle_{\mathcal{P}}. \tag{6.9}$$

6.2.3 Observation optimization problem

In any control or DA problem, it is crucial that the observation operator h, which represents the available information on the system (6.1), allows to effectively measure the state q. A desirable property of h is thus its sensitivity with respect to a change in the control variables, here the initial condition q_0 and the parameters β. Indeed, if a variation in the control vector entails no change in the values of the observations, i.e. changes in the system are not observable, the DA problem can not be solved satisfactorily. It is therefore preferable to design the operator h with maximum sensitivity with respect to the control vector. The first-order sensitivity of the observations with respect to the initial condition q_0 and the parameters β can be estimated through the gradients (6.8c)-(6.8d). Accordingly, we propose to formulate the observation optimization problem as the maximization of the norm of these gradients with respect to the vector λ that parameterizes the observation operator h. More precisely, this problem is expressed as

$$\max_{\lambda}\left\{ G = \frac{1}{2}\int_{\Omega}\left(\frac{\partial \mathcal{L}_1}{\partial q_0}\right)^2(x)dx + \frac{1}{2}\left\|\frac{\partial \mathcal{L}_1}{\partial \beta}\right\|^2_{\mathcal{P}} \right\}. \tag{6.10}$$

Once again, we use the adjoint technique to solve (6.10) and define the following Lagrangian $\mathcal{L}_2$ using (6.8)

$$\begin{aligned}\mathcal{L}_2 =& \frac{1}{2}\int_{\Omega}\tilde{q}_0^2(x)dx + \frac{1}{2}\left\|\left(\frac{\partial f}{\partial \beta}\Big|_{q,\beta}\right)^{*}(\tilde{q})\right\|^2_{\mathcal{P}} - \left\langle r, -\frac{\partial \tilde{q}}{\partial t} - \left(\frac{\partial f}{\partial q}\Big|_{q,\beta}\right)^{*}(\tilde{q}) - \tilde{h}(\lambda)\right\rangle_{\mathcal{M}} \\ &- \int_{\Omega} s(x)\tilde{q}(x,T)dx,\end{aligned} \tag{6.11}$$

where r and s are Lagrange multipliers that are introduced to take into account the constraints (6.8a) and (6.8b) on the dynamics of the adjoint variable $\tilde{q}$, the operator $\tilde{h}$ is defined in (6.8b). By setting

$$\begin{aligned}
\left\langle \frac{\partial \mathcal{L}_2}{\partial \tilde{q}}, \tilde{p} \right\rangle_{\mathcal{M}} =& \int_\Omega \tilde{q}_0(x)\tilde{p}(x,0)dx + \left\langle \left(\frac{\partial f}{\partial \beta}\Big|_{q,\beta} \right)^* (\tilde{q}), \left(\frac{\partial f}{\partial \beta}\Big|_{q,\beta} \right)^* (\tilde{p}) \right\rangle_{\mathcal{P}} \\
&+ \left\langle r, \frac{\partial \tilde{p}}{\partial t} + \left(\frac{\partial f}{\partial q}\Big|_{q,\beta} \right)^* (\tilde{p}) \right\rangle_{\mathcal{M}} - \int_\Omega s(x)\tilde{p}(x,T)dx \\
=& \left\langle \frac{\partial f}{\partial \beta}\Big|_{q,\beta} \left(\left(\frac{\partial f}{\partial \beta}\Big|_{q,\beta} \right)^* (\tilde{q}) \right), \tilde{p} \right\rangle_{\mathcal{M}} + \left\langle -\frac{\partial r}{\partial t} + \frac{\partial f}{\partial q}\Big|_{q,\beta}(r), \tilde{p} \right\rangle_{\mathcal{M}} \\
&+ \int_\Omega \left((\tilde{q}_0(x) - r(x,0))\, \tilde{p}(x,0) + (r(x,T) - s(x))\, \tilde{p}(x,T) \right) dx \\
=& 0 \quad \forall \tilde{p} \in \mathcal{M},
\end{aligned} \tag{6.12}$$

we obtain the system of equations that allows to compute the gradient of the Lagrangian $\mathcal{L}_2$ with respect to λ

$$r(x,0) = \tilde{q}_0(x) \quad \forall x \in \Omega, \tag{6.13a}$$

$$\frac{\partial r}{\partial t} - \frac{\partial f}{\partial q}\Big|_{q,\beta}(r) = \frac{\partial f}{\partial \beta}\Big|_{q,\beta} \left(\left(\frac{\partial f}{\partial \beta}\Big|_{q,\beta} \right)^* (\tilde{q}) \right), \tag{6.13b}$$

$$\frac{\partial \mathcal{L}_2}{\partial \lambda} = \left(\frac{\partial \tilde{h}}{\partial \lambda}\Big|_{\lambda} \right)^* (r). \tag{6.13c}$$

Once equation (6.13b) is integrated forward in time with the initial condition (6.13a), the gradient (6.13c) is available and can be used in a gradient-based optimization procedure to solve the maximization problem (6.10), as described in §6.2.5. Equation (6.13c) can be also employed to select the most important sensors in a observation network, as detailed in §6.2.6.

6.2.4 Data assimilation problem

In this subsection, the type of observations is fixed (operator h with fixed parameters λ), and it is assumed that observations y of a reference flow realization are available. To reconstruct the reference solution, the DA problem is formulated as the minimization of the discrepancies between the observations y and the estimation of the state q, as proposed by [128]. Accordingly, if both the initial condition q_0 and the parameters β for the reference evolution are unknown, the DA problem is expressed as (§2.2.1)

$$\min_{q_0,\beta} \left\{ J = \frac{1}{2} \|h(q,\lambda) - y\|_{\mathcal{O}}^2 \right\}. \tag{6.14}$$

As in §6.2.2 and §6.2.3, the problem (6.14) is solved with the adjoint technique, and the corresponding adjoint equations are similar to those in (6.8) but with a different forcing term in (6.8b). Following the derivations of §6.2.2, see also [128, 133] and §2.3.1, the gradient of the cost function J in (6.14) with respect to the initial condition q_0 and the parameters β is computed from the following system of equations

$$\hat{q}(x,T) = 0 \quad \forall x \in \Omega, \tag{6.15a}$$

$$-\frac{\partial \hat{q}}{\partial t} - \left(\frac{\partial f}{\partial q}\Big|_{q,\beta} \right)^* (\hat{q}) = \left(\frac{\partial h}{\partial q}\Big|_{q,\lambda} \right)^* (h(q,\lambda) - y), \tag{6.15b}$$

$$\frac{\partial \mathcal{L}_3}{\partial q_0} = \hat{q}_0, \quad \hat{q}_0(x) = \hat{q}(x,0) \quad \forall x \in \Omega, \tag{6.15c}$$

$$\frac{\partial \mathcal{L}_3}{\partial \beta} = \left(\frac{\partial f}{\partial \beta}\Big|_{q,\beta} \right)^* (\hat{q}), \tag{6.15d}$$

Observation optimization procedure (problem (6.10))

1. choose initial condition q_0 and parameters β and compute the corresponding solution q with a forward integration of the dynamical model (6.1);
2. choose the observation operator h and start the optimization procedure with a first guess for its parameters λ;
3. at the ith iteration, solve backward the adjoint equations (6.8a)-(6.8b) with the direct solution q evaluated in step 1;
4. solve forward equations (6.13a)-(6.13b) using the adjoint solution $\tilde{q}$ obtained at step 3;
5. compute the gradient (6.13c) in order to update the parameters λ according to (6.17);
6. return to step 3 until stopping criterion reached (minimum relative difference in the value of the cost function G in (6.10) between two successive iterations).

Table 6.1: Summary of the proposed observation optimization procedure.

with

$$\mathcal{L}_3 = J - \left\langle \hat{q}, \frac{\partial q}{\partial t} - f(q,\beta) \right\rangle_{\mathcal{M}} . \tag{6.16}$$

After the backward integration of (6.15b) with the terminal condition (6.15a), the gradients (6.15c)-(6.15d) can be used in a gradient-based optimization procedure to solve (6.14) in order to recover the initial condition q_0 and parameters β associated to the observations y.

6.2.5 Optimization algorithms

The gradients (6.13c) and (6.15c)-(6.15d) obtained with the adjoint method can be used in a generic gradient-based iterative procedure to solve the observation optimization and DA problems defined in (6.10) and (6.14) respectively. For these two optimization problems, the corresponding control vector γ is updated every iteration according to

$$\gamma^{(i+1)} = \gamma^{(i)} + \theta^{(i)} d^{(i)}. \tag{6.17}$$

$\gamma^{(i)}$ refers to the parameters λ of the observation operator h for the observation optimization problem, while it refers to the initial condition q_0 and the parameters β of the dynamical model (6.1) for the DA problem, evaluated at the ith iteration of the optimization procedure. $d^{(i)}$ is the ascent/descent direction which is obtained by the quasi-Newton Broyden-Fletcher-Goldfarb-Shanno (BFGS) method in its low-memory formulation [168]. The step length $\theta^{(i)}$ is evaluated with a backtracking-Armijo line search [11]. The iterative procedures to solve the observation optimization and DA problems are summarized in tables 6.1 and 6.2 respectively.

6.2.6 Sensor selection procedure

In the case where the vector λ in (6.5) refers to the locations where the observations are performed (sensors) as is the case here, the gradient (6.13c) can be also used to quantify the change in the sensitivity of the observations with respect to the initial condition q_0 and the parameters β that results from a change in the location of each sensor. In other words, equation (6.13c) provides the first-order sensitivity with respect to each sensor of the

---

Variational DA with synthetic observations (problem (6.14))

1. choose reference initial condition q_0 and parameters β, compute the corresponding solution q with a forward integration of the dynamical model (6.1), and generate the observations y;
2. start the optimization procedure with a first guess for the reference initial condition q_0 and parameters β;
3. at the ith iteration, solve forward the direct problem (6.1);
4. solve backward the adjoint equations (6.15a)-(6.15b) using the direct solution q obtained at step 3;
5. compute the gradients (6.15c)-(6.15d) in order to update the initial condition q_0 and the parameters β according to (6.17);
6. return to step 3 until stopping criterion reached (maximum decrease in the value of the cost funcion J in (6.14) or maximum number of iterations).

TABLE 6.2: Summary of the variational DA algorithm.

sensitivity of the observations, enabling to identify the sensors that contribute the most to the observability of changes in the state q. The importance of the ith sensor in the sensitivity of the observations can be thus estimated through the quantity ρ_i defined by

$$\rho_i = \left(\frac{\partial \mathcal{L}_2}{\partial x_i}\right)^2 + \left(\frac{\partial \mathcal{L}_2}{\partial y_i}\right)^2, \quad \rho_1 \geqslant \rho_2 \geqslant \cdots \geqslant \rho_{N_s}, \tag{6.18}$$

where $\frac{\partial \mathcal{L}_2}{\partial x_i}$ and $\frac{\partial \mathcal{L}_2}{\partial y_i}$ are the derivatives of the Lagrangian $\mathcal{L}_2$ defined in (6.11) with respect to the coordinates (x_i, y_i) of the ith sensor in the 2D case, these derivatives correspond to components of the gradient in (6.13c). The scalars $\rho_1, \rho_2, \cdots, \rho_{N_s}$ are sorted in decreasing order, and N_s refers to the total number of sensors. Accordingly, the number N_δ of the most important sensors that account for a ratio δ of the squared norm of the gradient in (6.13c) is given by

$$N_\delta = \min\left\{k \left| \frac{\sum_{i=1}^{k}\rho_i}{\sum_{i=1}^{N_s}\rho_i} \geqslant \delta \right.\right\}, \quad 0 < \delta \leqslant 1. \tag{6.19}$$

Equations (6.18)-(6.19) allow to define a sensor selection procedure that is parameterized by the scalar δ.

6.2.7 Comments on the present observation optimization procedure

We can make the following comments about the observation optimization procedure proposed in §6.2.3 and §6.2.5. Firstly, as for other sensor placement strategies [55, 113] applied to nonlinear systems, the results of this procedure depend on the chosen direct solution q in (6.5) that is fixed in the optimization process. Several solutions q will be thus considered in this chapter to test the present observation optimization procedure. Secondly, the choice of the cost function G in (6.10) is not unique. In particular, one may want to optimize the sensitivity of the observations with respect to only some components of the control vector for the DA problem. For example, if we are only interested in recovering parameters β of the dynamical model (6.1) for an observed reference solution, G may be defined as $G = \frac{1}{2}\left\|\frac{\partial \mathcal{L}_1}{\partial \beta}\right\|^2_{\mathcal{P}}$. This will be the case in the numerical experiments where the observation optimization procedure is used to increase the sensitivity of the observations with respect to only

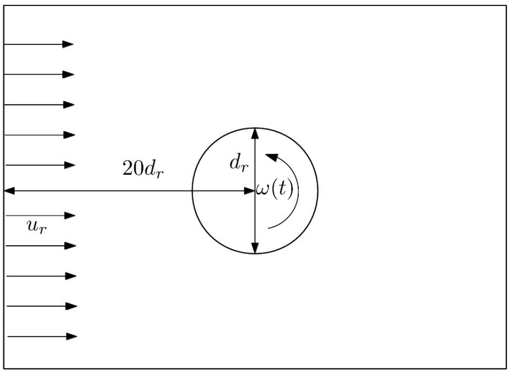

Figure 6.1: Schematic of the flow configuration and distance between inflow conditions and the cylinder in the computational domain.

the rotational speed of the cylinder. In terms of numerical implementation, if an adjoint code with the tangent linear model $\left.\frac{\partial f}{\partial q}\right|_{q,\beta}$ is already available, the system (6.13) only requires the development of the operator in the right-hand-side of (6.13c). The practical implementation of the present osbervation optimization procedure is further discussed in §6.3.2 and appendix D.

6.3 Physical and numerical setup of the numerical experiments

6.3.1 Flow configuration and numerical method

We consider the bidimensional flow around a cylinder of diameter d_r. The oncoming flow is assumed to be uniform at infinity and the corresponding velocity magnitude is u_r. The Reynolds number of the flow is defined as $Re = \frac{u_r d_r}{\nu}$ where ν is the kinematic viscosity of the fluid. The cylinder can rotate around its axis with the rotational speed $\omega(t)$. This flow configuration is illustrated in figure 6.1. We consider rotary oscillations of the form [15, 53, 125, 200, 201, 206]

$$\omega(t) = A\sin(2\pi f t + \varphi), \quad \alpha(t) = \frac{\omega(t) d_r}{2u_r}, \quad \mathcal{A} = \frac{A d_r}{2u_r}, \quad \mathcal{F} = \frac{f d_r}{u_r}. \tag{6.20}$$

These oscillations are characterized by their dimensionless amplitude $\mathcal{A}$ and frequency $\mathcal{F}$. We also introduce a phase term φ since flows with finite-time evolution are considered. It is assumed that the flow is solution of the two-dimensional unsteady compressible Navier-Stokes equations for perfect gas, their integral form over a bounded domain of interest Ω is given by

$$\frac{\partial}{\partial t}\int_\Omega \boldsymbol{w} dV + \int_{\partial\Omega} (\mathbf{F}(\boldsymbol{w}) - \mathbf{G}(\boldsymbol{w}))\cdot \boldsymbol{n} dS = \mathbf{0},\ \boldsymbol{w} = (\rho \ \ \rho u \ \ \rho v \ \ E)^{\mathrm{T}}, \tag{6.21a}$$

$$\mathbf{F}(\boldsymbol{w}) = \begin{pmatrix} \rho u & \rho v \\ \rho u^2 + p & \rho u v \\ \rho u v & \rho v^2 + p \\ u(E+p) & v(E+p) \end{pmatrix},\ \mathbf{G}(\boldsymbol{w}) = \begin{pmatrix} 0 & 0 \\ \tau_{xx} & \tau_{xy} \\ \tau_{xy} & \tau_{yy} \\ u\tau_{xx} + v\tau_{xy} - q_x & v\tau_{yy} + u\tau_{xy} - q_y \end{pmatrix}, \tag{6.21b}$$

$$\tau_{xx} = \mu\left(2\frac{\partial u}{\partial x} - \frac{2}{3}(\frac{\partial u}{\partial x} + \frac{\partial v}{\partial y})\right),\ \tau_{yy} = \mu\left(2\frac{\partial v}{\partial y} - \frac{2}{3}(\frac{\partial u}{\partial x} + \frac{\partial v}{\partial y})\right),\ \tau_{xy} = \mu(\frac{\partial u}{\partial y} + \frac{\partial v}{\partial x}), \tag{6.21c}$$

$$q_x = -\kappa\frac{\partial T}{\partial x},\ q_y = -\kappa\frac{\partial T}{\partial y},\ p = \rho r T = (\gamma - 1)\rho e,\ E = \rho\left(e + \frac{1}{2}(u^2 + v^2)\right), \tag{6.21d}$$

where $\boldsymbol{n}$, ρ, u, v, p, e, T, γ, μ, κ and r refer to the outer unit normal vector to the boundary $\partial\Omega$, density, x-wise and y-wise components of the velocity vector, pressure, specific internal energy, temperature, ratio of specific

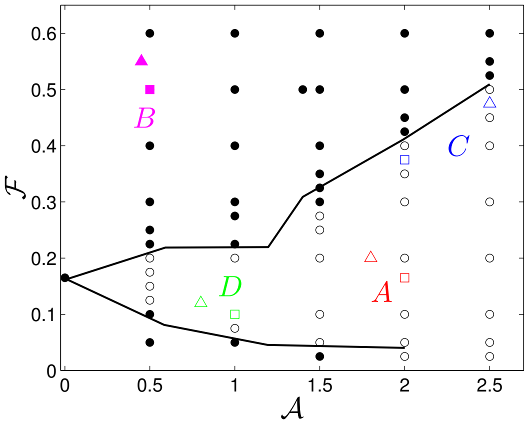

FIGURE 6.2: Lock-on (○) and non lock-on (●) regions in ($\mathcal{A}$,$\mathcal{F}$) space for the unsteady flow past a rotating cylinder at $Re = 100$. The configurations of the reference (triangles) and first-guess (squares) flows of table 6.4 are also reported. Solid lines approximately denote the boundary between the lock-on and non lock-on regions obtained by [53].

heats, dynamic viscosity, thermal conductivity and a constant in the ideal gas law, respectively. Equation (6.21) is discretized using a cell-centered finite-volume formulation on unstructured grids. Convective fluxes $\mathbf{F}(\boldsymbol{w})$ are evaluated using Roe's approximate Riemann solver [185]. Second-order spatial accuracy is achieved with the reconstruction procedure of [106]. Time integration is performed with a fully implicit second-order scheme that combines dual time stepping [105] and the LU-SGS method [145, 190]. The same Navier-Stokes solver is used in chapter 5 [163]. The unstructured mesh is formed by $1.4 \cdot 10^4$ elements with 96 nodes over the surface of the cylinder. The physical time step Δt of the simulations is chosen as $\Delta t = 1.33 \cdot 10^{-3} d_r/(0.165 u_r)$, where the value 0.165 refers to the dimensionless frequency of the oscillations in the vortex shedding at $Re = 100$ when the cylinder is stationary [226]. The simulations are performed with a Mach number of 0.2, corresponding to a nearly-incompressible flow dynamics in which acoustic waves are taken into account. In what follows, we define the drag coefficient C_D and the lift coefficient C_L as

$$C_D = \frac{\boldsymbol{f} \cdot \boldsymbol{e_x}}{\frac{1}{2}\rho_r u_r^2 d_r}, \quad C_L = \frac{\boldsymbol{f} \cdot \boldsymbol{e_y}}{\frac{1}{2}\rho_r u_r^2 d_r}, \quad \boldsymbol{f} = \int_\Gamma (-p\mathbf{I} + \boldsymbol{\tau}) \cdot \boldsymbol{n} dS, \tag{6.22}$$

where ρ_r and p_r are reference density and pressure respectively, $\boldsymbol{e}_x$ and $\boldsymbol{e}_y$ are the unit vectors in the x and y coordinate directions (the inflow is along the x-axis), Γ is the boundary of the cylinder, $\mathbf{I}$ is the identity matrix, and the components of the symmetric matrix $\boldsymbol{\tau}$ are given in (6.21).

Figure 6.2 and table 6.3 report results obtained with the present numerical method for flows past a cylinder under rotary oscillation according to (6.20) at $Re = 100$. These predictions are compared with those of [53] where the same flow configuration was investigated numerically. Two flow regimes can be identified. In the lock-on regime, the frequency of the vortex shedding is identical to that of the oscillations of the cylinder. On the other hand, for flows in the non lock-on regime, the vortex shedding is not synchronized with the rotary oscillation forcing. The regions of lock-on and non lock-on in ($\mathcal{A}$-$\mathcal{F}$) space are given in figure 6.2. The effect of rotary oscillation on characteristic flow quantities is further investigated in table 6.3. For the sake of comparison, the case where the cylinder is stationary ($\mathcal{A} = 0$) is also reported. With $\mathcal{A} = 2$ and $\mathcal{F} = 0.4$, the flow is in the lock-on regime and the decrease in the value of the drag coefficient compared with the stationary case is significant, there is also a decrease in the maximum amplitude of the lift coefficient. In the case where $\mathcal{A} = 1.4$ and $\mathcal{F} = 0.5$, the decrease in the value of the drag coefficient is less important and the maximum amplitude of the lift coefficient is increased. The flow is in the non lock-on region, and the frequency of the vortex shedding is close, but not identical, to the natural frequency.

$\mathcal{A}$	$\mathcal{F}$	regime	study	$\overline{C_D}$	C_L'	$\mathcal{F}_{vs}$
0			[139]	1.350	0.339	0.165
			[73]	1.356	0.287	0.166
			[178]	1.350	0.331	0.167
			[183]	1.326	0.310	0.166
			[53]	1.327	0.326	0.165
			present study	1.355	0.326	0.165
2	0.4	lock-on	[53]	1.231	0.299	0.4
			present study	1.266	0.313	0.4
1.4	0.5	non lock-on	[53]	1.253	0.340	0.154
			present study	1.289	0.374	0.156

Table 6.3: Time-averaged drag coefficient $\overline{C_D}$, maximum amplitude of the lift-coefficient fluctuations C_L', and dimensionless frequency of the vortex shedding $\mathcal{F}_{vs}$ for $Re = 100$ and various dimensionless amplitudes $\mathcal{A}$ and frequencies $\mathcal{F}$ obtained in several studies. When possible, the results of previous studies corresponding to the spatial and temporal resolutions that are the closest to the present ones are reported (run $L_{b|i}/D = 20$ in [178] and run D4 in [183]).

configuration	reference flow			first-guess flow		
	$\mathcal{A}$	$\mathcal{F}$	regime	$\mathcal{A}$	$\mathcal{F}$	regime
A	1.8	0.2	lock-on	2	0.165	lock-on
B	0.45	0.55	non lock-on	0.5	0.5	non lock-on
C	2.5	0.475	lock-on	2	0.375	lock-on
D	0.8	0.12	lock-on	1	0.1	lock-on

Table 6.4: Different configurations of reference and first-guess flows considered in the DA experiments of table 6.5. These flows correspond to a rotationally oscillating cylinder at $Re = 100$ with a rotational speed given by (6.20), the corresponding flow regime is reported.

6.3.2 Adjoint code

The observation optimization and DA procedures discussed in §6.2 require the development of the tangent linear operator associated to the Navier-Stokes equations (6.21) and that of its adjoint, respectively. In addition, due to the nonlinearity of (6.21) and due to the fact that equations (6.1) and (6.13b) are evaluated forward in time while (6.8b) and (6.15b) are evaluated backward, the storage of the direct solution q is required for the adjoint problems (6.8) and (6.15), while both q and the adjoint variable $\tilde{q}$ need to be stored for the adjoint problem (6.8) associated to the observation optimization procedure. In order to decrease memory requirements, the formulation of the observation optimization procedure proposed in appendix D is used. This formulation avoids the storage of the adjoint variable $\tilde{q}$ and involves the adjoint of the tangent linear operator of (6.21). Accordingly, the gradients (6.8c)-(6.8d), (6.13c) and (6.15c)-(6.15d) are all obtained with the adjoint operator $\left(\frac{\partial f}{\partial q}\Big|_{q,\beta}\right)^*$ associated to (6.21) and different forcing terms. To further limit memory requirements for the backward integrations with the adjoint operator, the direct solution q is stored only at a few times during the integration of the direct problem (6.21), and the missing snapshots are recomputed during the backward integrations. The adjoint operator for (6.21) is hand-coded following the discrete adjoint approach [44, 165, 176]. The same adjoint code is used and assessed in chapter 5.

6.3.3 Setup of the observation optimization and data assimilation experiments

The different methodologies presented in §6.2 are applied to the reconstruction of flows past a rotationally oscillating cylinder at $Re = 100$. More precisely, they are used for the determination of optimal initial flow field and/or rotational speed of the cylinder given observations of a reference flow. Unless otherwise stated, the size of the assimilation window T, i.e. the duration of observation of the reference flow, is fixed to $T = 16d_r/u_r$,

experiments	γ	dim(γ)	y	dim(y)	runs (configurations)	principle
1	$q_0 + (A, f, \varphi)$	$5.5 \cdot 10^4$	u, v (continuum)	$2.2 \cdot 10^3$	1A,B	DA
2	$q_0 + \omega(t)\ \forall t$	$5.7 \cdot 10^4$	u, v (continuum)	$2.2 \cdot 10^3$	2A,B	DA
3	$q_0 + (A, f, \varphi)$	$5.5 \cdot 10^4$	C_L, C_D	2	3A,B	DA
4	$\omega(t)\ \forall t$	$2 \cdot 10^3$	u, v (4 probes)	8	4A,C	OSP, DA
5	$q_0 + (A, f, \varphi)$	$5.5 \cdot 10^4$	u, v (4 probes)	8	5A,C,D	OSP, DA
6	$q_0 + (A, f, \varphi)$	$5.5 \cdot 10^4$	u, v (20 probes)	40	6A,C	OSP, DA

Table 6.5: Different types of numerical experiments performed in this chapter, which are characterized by the control vector γ in the optimization procedure for the DA problem (initial state q_0 and/or rotational speed of the cylinder, parameterized or not), the type of observations y (velocity field or aerodynamic coefficients), and the different configurations of reference and first-guess flows investigated (see table 6.4). Experiments of type 1-3 correspond to generic twin-experiment DA procedures, while experiments of type 4-6 also involve optimal sensor placement (OSP). Note that dim(λ) = dim(y) in the latter experiments, where λ refers to the parameters of the observation operator.

and the time interval between two observations is always $0.2d_r/u_r$. Since the distance between inflow conditions and the cylinder in the computational domain is $20d_r$ (see figure 6.1), the initial flow field here encompasses upstream conditions if observations are performed close to or downstream of the cylinder. Accordingly, there was here no need to consider boundary conditions in the control vector for the DA problem. Various reference flow realizations and first-guess flows (flow solutions used to initialize the optimization procedure in table 6.2), which are summarized in table 6.4, are considered in the numerical experiments. They may belong to either the lock-on or the non lock-on region. Three types of observations of the reference flow are considered: (i) the velocity field in a continuous region, (ii) the velocity field at discrete locations (probes), and (iii) the aerodynamic coefficients C_L and C_D. After spatial discretization, the qualifying term continuous refers to the case where the velocity field is observed at all the elements of the mesh in a given region. Various control vectors for the DA problem are considered. In the numerical experiments of type 4, the control vector is formed by the rotational speed $\omega(t)$ of the cylinder at all times, and the initial condition of the reference flow is assumed to be known. In the numerical experiments of type 1, 3 and 5-6, the control vector is formed by the initial condition of the flow and by the rotational speed of the cylinder parameterized by the amplitude A, the frequency f and the phase φ of the oscillations according to (6.20). Finally, in the experiments of type 2, the control vector is formed by the initial condition of the flow and by the rotational speed of the cylinder at all times. Given the present spatial and temporal discretizations, the initial flow field is a vector of dimension $5.5 \cdot 10^4$, while the unparameterized rotational speed of the cylinder is a vector of dimension $2 \cdot 10^3$.

Two categories of numerical experiments can be identified. The first one corresponds to experiments of type 1-3 where generic twin-experiment DA procedures, as described in table 6.2, are carried out. The corresponding results are reported in §6.4, which allow to delineate the possibilities of flow reconstruction in the presence of a rotationaly oscillating cylinder. For the second set of numerical experiments, the observation optimization procedure depicted in table 6.1 is used to find optimal locations for velocity sensors. It is combined with DA experiments, which are performed in order to assess its efficiency. This observation optimization/DA procedure is applied in experiments of type 4-6, whose results are discussed in §6.5. A summary of the numerical experiments performed in this chapter is given in table 6.5. In the following, the performances of the observation optimization and DA procedures can be estimated through the evolution of the cost functions G in (6.10) and J in (6.14), respectively, during the corresponding optimization processes. Since the observations of the reference flow are here generated synthetically, the quality of the reconstruction of the reference flow in the DA experiments may be evaluated using the L^2 norm of the discrepancies between the reference rotational speed of the cylinder denoted by $\omega^{(r)}$ and the assimilated one (i.e. obtained at the end of the DA procedure) $\omega^{(a)}$ according to

$$\epsilon^{\omega} = \left(\int_0^T \left(\omega^{(r)}(t) - \omega^{(a)}(t) \right)^2 dt \right)^{\frac{1}{2}} . \tag{6.23}$$

The values of G, J and ϵ^{ω} are generally compared to the ones at the beginning of the corresponding optimization process, G_0, J_0 and ϵ_0^{ω} respectively.

6.4 Analysis of data assimilation experiments

In this section, we consider the numerical experiments of type 1-3 (see table 6.5), which correspond to generic twin-experiment DA procedures. In a first step, a reference numerical simulation of the flow past a rotating cylinder is carried out, and observations of this reference flow are performed. In a second step, the minimization problem (6.14) is solved in order to recover the initial condition and/or the rotational speed of the cylinder for the reference flow, starting from a first-guess flow. This DA procedure is summarized in table 6.2. The ability of flow reconstruction past a rotationaly oscillating cylinder are investigated by varying the observations of the reference flow, the control vector in the DA optimization process, and the regime (lock-on/non lock-on) of the reference and first-guess flows.

6.4.1 Observation of the flow in a continuous region

6.4.1.1 Control on the initial condition and the parameterized rotational speed of the cylinder (type 1)

The results of the DA experiments of type 1 are first examined. For these simulations, the velocity field of the reference flow is observed in a continuous region which is located downstream of the cylinder (see, e.g., figure 6.3(a)). The control vector in the DA procedures is formed by the initial condition of the flow and the triplet of parameters (A, f, φ) characterizing the rotary oscillations of the cylinder according to (6.20). The corresponding results are reported in figure 6.3. The case where both the reference and first-guess flows in the DA procedure belong to the lock-on region (run 1A) is investigated in figures 6.3(a), 6.3(c), 6.3(e) and 6.3(g). It appears that the DA procedure successfully reconstructs the rotational speed of the reference flow starting from a first-guess flow corresponding to an error of 10% on the amplitude of the oscillations and an error of 17.5% on their frequency. The good reconstruction in the case where both the reference and first-guess flows are in the lock-on region was expected, since in this case the frequency of the vortex shedding is imposed by the frequency of the oscillations of the cylinder, which are actually the same. In addition, observing the velocity field in a continuous region downstream of the cylinder provides extensive information on the reference flow. Other reference and first-guess flows in the lock-on region are considered in §6.5.

The case where both the reference and first-guess flows lie in the non lock-on region (run 1B), i.e. when the frequency of the vortex shedding is not directly related to that of the oscillations of the cylinder, is addressed in figures 6.3(b), 6.3(d), 6.3(f) and 6.3(h). The first-guess run corresponds to an error of $\approx \pm 10\%$ on the amplitude and frequency of the oscillations of the cylinder for the reference flow. If we only consider figures 6.3(b) and 6.3(f), the reconstruction of the reference flow seems correct. In particular, the DA procedure has properly modified the slight shift in the vortex shedding between the reference and first-guess flows. However, it appears from figure 6.3(h) that the DA procedure has not recovered the reference rotational speed of the cylinder. It can be noticed that the optimization procedure has drastically damped the amplitude of the oscillations. Such behavior was expected because the frequency of the vortex shedding is close to the natural one (i.e. when the cylinder is stationary) in the non lock-on region. This means that the DA procedure has been able to fit the observations of the reference flow but has failed to solve the corresponding inverse problem, which may be ascribed to the physics of the flow in the non lock-on region. Note that additional DA experiments (results not shown here for the sake of brevity) were performed with a better first guess for the optimization process or with other reference flows in the non lock-on region. They confirmed the difficulty of correctly solving the DA inverse problem in the non lock-on regime.

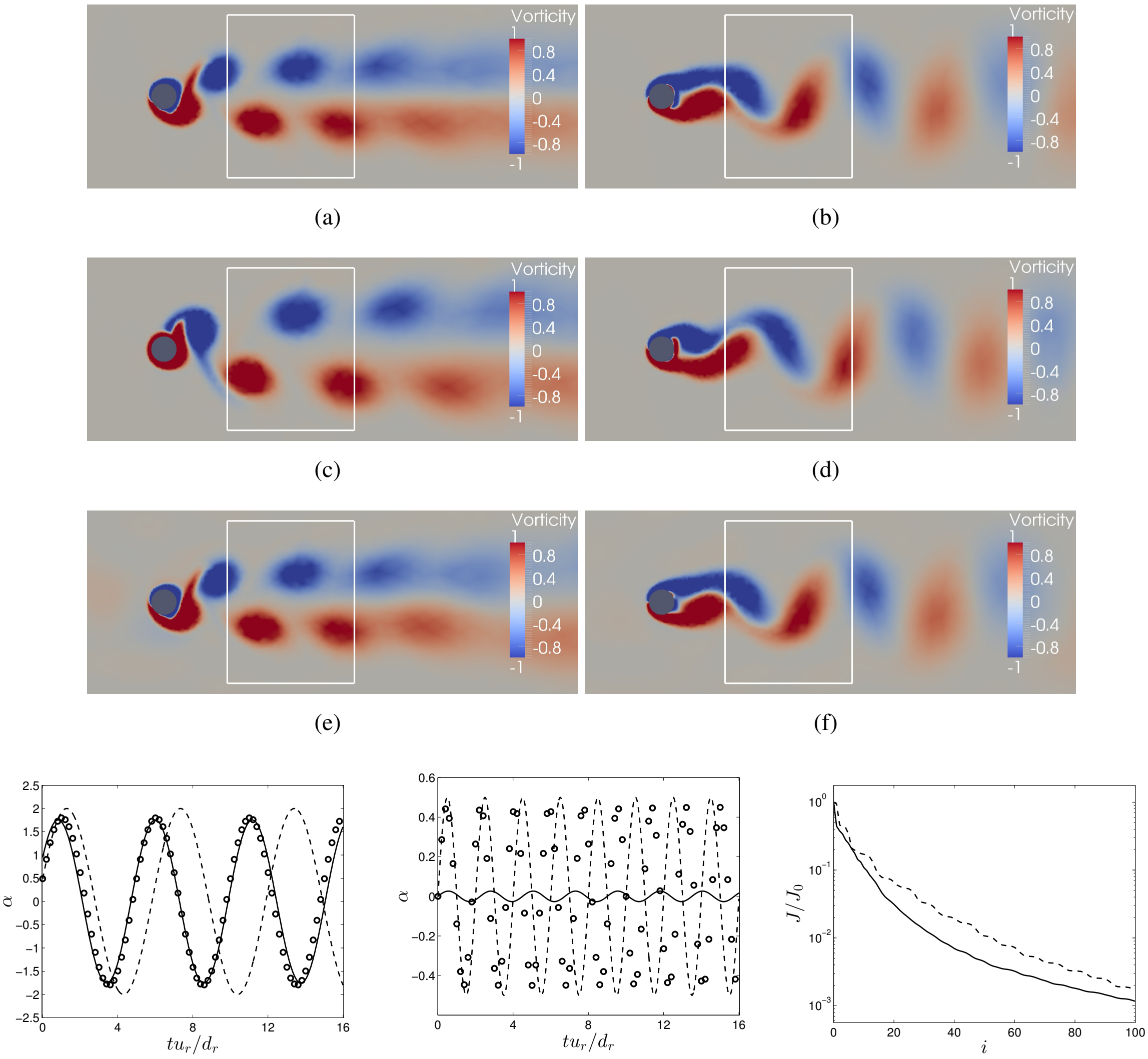

(a) (b)

(c) (d)

(e) (f)

(g) (h) (i)

Figure 6.3: Results for DA experiments of type 1: dimensionless vorticity field at $tu_r/d_r = 10$ for (a)-(b) reference, (c)-(d) first-guess and (e)-(f) assimilated flows, the observation domain is delineated in white lines; (g)-(h) dimensionless rotational speed α of the cylinder for reference (○), first-guess (- - - -) and assimilated (———) runs; (i) cost function J in (6.14) versus the iteration of the optimization process for runs 1A (———) and 1B (- - - -). Figures (a), (c), (e) and (g) (left column) refer to run 1A (lock-on), while figures (b), (d), (f) and (h) (right column) refer to run 1B (non lock-on).

6.4.1.2 Control on the initial condition and the rotational speed of the cylinder at all times (type 2)

We now consider the type 2 of numerical experiments where no particular form is prescribed to the rotary movement of the cylinder, and the control vector in the DA procedure is formed by the initial flow field and the rotational speed of the cylinder at all times (table 6.5). The velocity field of the reference flow is observed in a continuous region located downstream of the cylinder as in the experiments of type 1. Results for the configurations A and B of table 6.4 are reported in figure 6.4. It appears from the comparisons between figures 6.3(i) and 6.4(e) that increasing the size of the control vector and allowing more flexibility in the form of the rotational speed of the cylinder significantly slows down the convergence rate of the DA procedure. After 200 iterations of the optimization process, while experiments of type 1 were performed with 100 iterations, the assimilated solution is still far from the reference solution as illustrated in figure 6.4. Differences between the lock-on and non lock-on regimes are still visible in figures 6.4(c) and 6.4(d). The optimization procedure has significantly modified the first-guess rotational speed in the case where both the reference and first-guess flows are in the lock-on region (run 2A, figure 6.4(c)) and the assimilated rotational speed seems to get closer to the

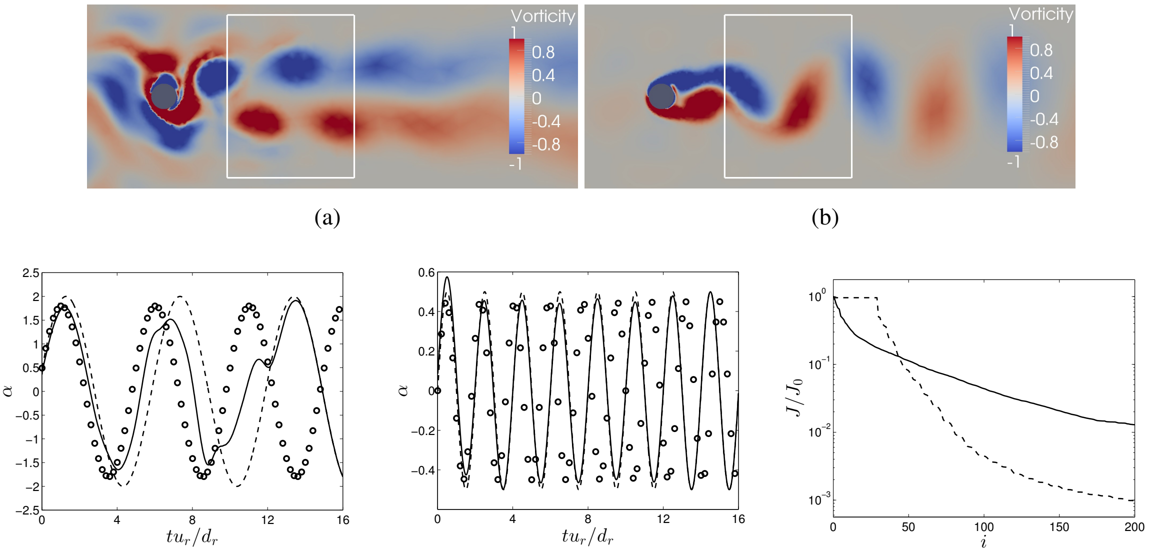

(a) (b)

(c) (d) (e)

Figure 6.4: Results for DA experiments of type 2: (a)-(b) dimensionless vorticity field at $tu_r/d_r = 10$ for assimilated flows, the observation domain is delineated in white lines; (c)-(d) dimensionless rotational speed α of the cylinder for reference (○), first-guess (- - -) and assimilated (——) runs; (e) cost function J in (6.14) versus the iteration of the optimization process for runs 2A (——) and 2B (- - -). Figures (a) and (c) refer to run 2A (lock-on), while figures (b) and (d) refer to run 2B (non lock-on).

reference one. On the other hand, when both the reference and first-guess flows are in the non lock-on region (run 2B, figure 6.4(d)), the optimization procedure has altered only slightly the amplitude of the signal without shifting its temporal evolution in order to correct its frequency. The fact that in both cases the DA procedure has not modified the rotational speed at the end of the assimilation window is due to the distance between the cylinder and the region where observations are performed (see figures 6.4(a)-6.4(b)). According to the present results, it seems difficult to satisfactorily reconstruct the reference flow in the case where the initial flow field is unknown and no functional form is prescribed to the rotational speed of the cylinder. Indeed, since the rotational speed of the cylinder at a given time has less weight in the DA procedure than one parameter of (6.20), the optimization procedure is more likely to modify the initial condition of the first-guess flow, which amounts here to adjust upstream conditions. As illustrated in figures 6.4(a)-6.4(b), the DA procedure has significantly altered the initial condition for both experiments 2A and 2B, which balances the limited reconstruction of the reference rotational speed and allows to fit the observations of the reference vorticity field (see reference vorticity fields in figures 6.3(a)-6.3(b)). This suggets a lack of unicity in the solution to the DA problem in this configuration, even in the case where both the reference and first-guess flows lie in the lock-on region. The case where the initial condition of the reference flow is assumed to be known and the control vector in the DA procedure is formed by the rotational speed of the cylinder at all times is investigated in §6.5.1.

6.4.2 Observation of the aerodynamic coefficients (type 3)

DA experiments of type 3 investigate the abality of reconstructing flows past a rotationally oscillating cylinder from the observation of integrated quantities such as the aerodynamic coefficients C_L and C_D. As in §6.4.1.1, the control vector in the DA procedures is formed by the initial flow field and the three parameters in (6.20). We can notice in figure 6.5 the qualitative difference in the evolution of the aerodynamic coefficients between the lock-on and non lock-on cases (runs 3A and 3B respectively). For example, concerning the lift coefficient C_L, its time evolution corresponds to a periodic signal with a single frequency identical to the forcing one in the lock-on case (figure 6.5(a)), whereas C_L oscillates in a compound manner in the non lock-on region (figure 6.5(d)). If we now consider the results of the DA procedures, it appears that, except at the very beginning of the assimilation window, the assimilated temporal evolution of the coefficients C_L and C_D almost perfectly match the reference

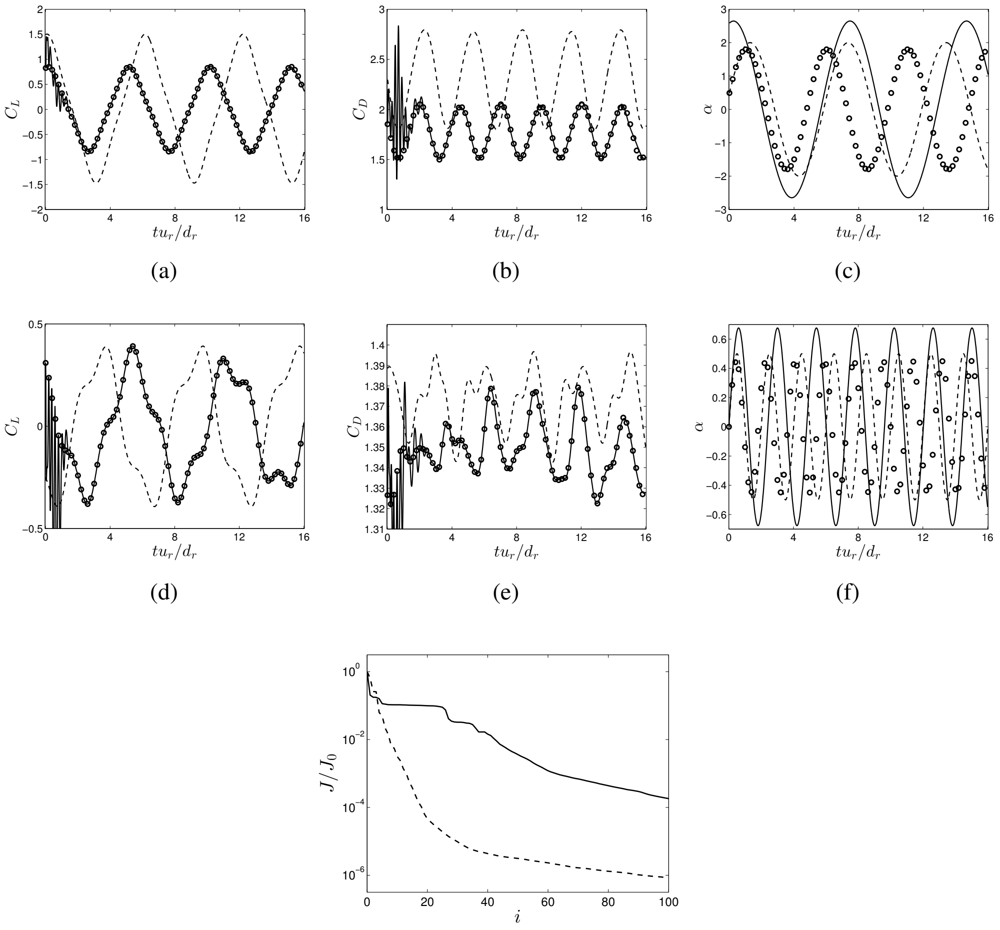

(a) (b) (c)

(d) (e) (f)

(g)

FIGURE 6.5: Results for DA experiments of type 3: temporal evolution of the lift coefficient ((a) and (d)), drag coefficient ((b) and (e)) and dimensionless rotational of the cylinder ((c) and (f)) for reference (○), first-guess (- - - -) and assimilated (——) runs; (g) cost function *J* in (6.14) versus the iteration of the optimization process for runs 3A (——) and 3B (- - - -). Figures (a)-(c) refer to run 3A (lock-on), while figures (d)-(f) refer to run 3B (non lock-on).

ones for both runs 3A and 3B. The spurious oscillations at the beginning of the assimilation window are due to the finite frequency of observation, as illustrated in chapter 5, and we can notice that the assimilated solution always passes through the reference values at observation times. However, for both runs, even in the case where both the reference and first-guess runs are in the lock-on region (run 3A), the optimization procedure fails to recover the rotational speed of the reference flow. Similarly to the results of §6.4.1.2, the optimization procedure has modified the initial condition of the first-guess flow in order to match the observations of the reference flow, which compensates for the lack of reconstruction of the reference rotational speed. The good fit to the observations is confirmed in figure 6.5(g), and it appears from the comparison between figures 6.3(i) and figure 6.5(g) that, for the present case, the low dimension of the observations allows to obtain a greater error reduction than in the experiments of type 1 with the same computational cost. The present results suggest that there is no unicity of the solution of the DA problem in the case where both the initial condition (encompassing upstream conditions) and the rotational speed of the cylinder (even parameterized) of the reference flow are unknown and the aerodynamic coefficients are observed. This may be due to the very low dimension of the observations compared to that of the control vector in this case.

6.5 Data assimilation experiments enhanced by optimal sensor placement

In this section, the observation optimization procedure introduced in §6.2.3 is employed to optimize locations of velocity sensors in order to improve the DA process applied to the reconstruction of flows past a rotationally oscillating cylinder. The principle of the numerical experiments of type 4-6 (see table 6.5) is the following. For all these experiments, the observations of the flow are performed using a finite number of velocity sensors. The corresponding observation operator h in (6.5) is parameterized by the locations of these velocity sensors, which form the control vector λ in the observation optimization problem (6.10). Firstly, an optimal observation network is determined, starting from a first guess for the locations of the sensors and using the observation optimization procedure summarized in table 6.1. In a second step, two DA experiments are carried out. The first one relies on the first-guess configuration of sensors, while the second one uses the optimized configuration. Comparisons between the results obtained with these two DA experiments allows to assess the improvement in the sensitivity of the sensors with respect to a change in the initial flow and/or in the rotational speed of the cylinder. The same reference and first-guess flows are used for the two DA experiments. Besides, the first-guess flow corresponds to the same flow solution than that used in the observation optimization procedure, i.e. the solutions used in step 1 of table 6.1 and in step 2 of table 6.2 are the same. From the results of §6.4.1.1, we only consider reference and first-guess flows that lie in the lock-on region to assess the performances of the optimal sensor placement procedure. Concerning the control vector in the DA experiments, two situations are considered. In the first one, the control vector is formed by the rotational speed $\omega(t)$ of the cylinder at all times, and, based on the results of §6.4.1.2, the initial field is assumed to be known. For the second configuration investigated, the control vector is formed by the initial condition of the flow and by the three parameters characterizing the rotational speed of the cylinder according to (6.20).

6.5.1 Control on the rotational speed at all times

6.5.1.1 Experiments with four sensors (type 4)

We first examine the results of the numerical experiments of type 4 where the control vector in the DA procedure is formed by the rotational speed of the cylinder at all times, the initial condition of the reference flow is assumed to be known. Accordingly, the observation optimization procedure is used to increase the sensitivity of the observations, here four velocity sensors, with respect to a change in the rotational speed of the cylinder. Results for the configuration A ($\mathcal{A} = 2$ and $\mathcal{F} = 0.165$ for the first-guess flow) of table 6.4 (run 4A) are reported in figure 6.6. The first step of this experiment, i.e. the observation optimization procedure, is illustrated in figures 6.6(a) and 6.6(b). The initial configuration of sensors, which is reported in white dots in figure 6.6(a), is chosen symmetrical and close to the centerline of the wake. Figure 6.6(b) illustrates the evolution of the cost function G defined in (6.10) during the corresponding optimization process, and its value is increased by a factor of almost five in three iterations. The corresponding optimized configuration of sensors is reported in black dots in figure 6.6(a). The sensors which were the closest to the cylinder have been placed further upstream by the optimization procedure, which automatically increases the sensitivity of the sensors with respect to the rotational speed of the cylinder at the end of the assimilation window. On the whole, it seems that the four sensors have been brought closer to the shedded vortices. It is noticeable that the optimized configuration of sensors is asymmetrical, contrary to the initial one. This may be explained by the finite size of the assimilation window, and it is expected that the optimized configuration tends to be symmetrical for longer assimilation windows. This statement is confirmed in §6.5.1.2.

We now consider the second step of this experiment. Two different DA experiments are performed in order to assess the efficiency of the observation optimization procedure, the results of which are illustrated in figures 6.6(c)-6.6(d). The DA experiment using the optimized configuration of sensors achieves a better reconstruction of the reference solution than the one using the first-guess configuration, in particular at the end of the assimilation window. This is due to the fact that sensors are placed further upstream in the optimized configuration

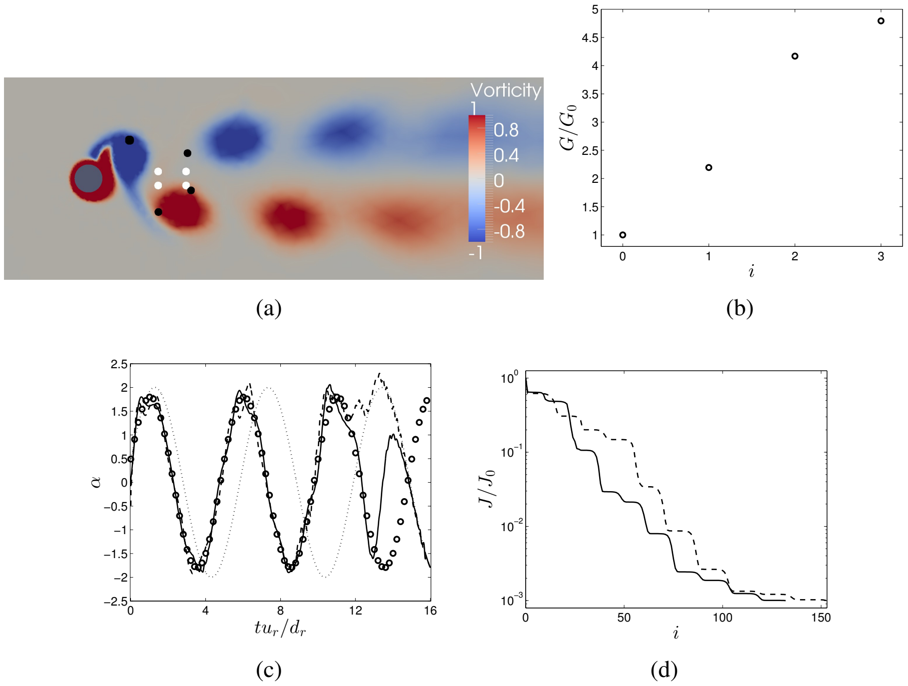

(a) (b)

(c) (d)

Figure 6.6: Results for experiment 4A ($\mathcal{A}$ = 2 and $\mathcal{F}$ = 0.165 for the first-guess flow). Results of the observation optimization procedure: (a) initial (white dots) and optimized (black dots) positions of velocity sensors in the vorticity field of the first-guess flow; (b) cost function G in (6.10) versus the iteration of the optimization process. Results of DA procedures: (c) dimensionless rotational speed α of the cylinder for reference (○), first-guess (··········) and assimilated runs obtained with the initial (- - - -) and optimized (———) configurations of velocity sensors; (d) cost function J in (6.14) versus the iteration of the optimization process with the initial (- - - -) and optimized (———) configurations of velocity sensors.

(figure 6.6(c)). This is confirmed in table 6.6 where is reported the reduction in the error on the reference rotational speed achieved by the two DA procedures. Besides, for the same final error reduction in the cost function J in (6.14) ($J/J_0 = 10^{-2}$), the DA procedure using the optimized configuration converges in less iterations than the one using the first-guess configuration. As indicated in table 6.6, even when taking into account the computational cost of the observation optimization procedure, the complete process of observation optimization followed by a DA procedure requires less calls to the adjoint code than directly performing a DA experiment with the initial configuration of sensors. Accordingly, the observation optimization procedure is efficient in terms of both computational cost and reconstruction of the reference flow in this case.

Now, the observation optimization procedure is further tested with the experiment 4C where reference and first-guess flows different from those in run 4A are used ($\mathcal{A}$ = 2 and $\mathcal{F}$ = 0.375 for the first-guess flow). The observation optimization procedure whose results are illustrated in figures 6.7(a)-6.7(b) is initialized with the same first-guess configuration of sensors than for run 4A. In this case, the observation optimization procedure has increased by two orders of magnitude the value of the cost function G in (6.10) in three iterations of the optimization process (figure 6.7(b)). The corresponding optimized configuration of sensors is indicated in figure 6.7(a). It could be expected that such an increase in the value of G implies significant differences between the results of the DA procedures performed with the initial and optimized configurations of sensors, as confirmed in figures 6.7(c)-6.7(d). The DA procedure using the first-guess configuration has great difficulties to retrieve the reference solution, and the time evolution of the assimilated rotational speed of the cylinder is very spiky. In fact, the error on the reference rotational speed has increased during the optimization procedure, and the value of the cost function J in (6.14) has decreased by less than an order of magnitude in 300 iterations, as indicated in table 6.6. In contrast, the DA procedure performed with the optimized configuration of sensors achieves a reduction in the value of the cost function J by three orders of magnitude in the same number of iterations. Moreover, even if the assimilated rotational speed still does not perfectly match the reference one, the reduction in the error ϵ^{ω} in

DA experiment	reference sensors			optimized sensors					
	N_{DA}	J/J_0	$\epsilon^{\omega}/\epsilon^{\omega}_0$	N_{DA}	J/J_0	$\epsilon^{\omega}/\epsilon^{\omega}_0$	N_{OO}	G/G_0	N_{tot}
4A	153	10^{-3}	0.68	132	10^{-3}	0.45	3	4.8	135
4C	300	0.34	1.32	300	10^{-3}	0.53	3	104.8	303
5A	54	10^{-2}	0.14	16	10^{-2}	0.11	11	16.0	27
5C	163	10^{-2}	0.54	29	10^{-2}	0.11	3	260.4	32
5D	27	10^{-2}	0.17	20	10^{-2}	0.04	3	1.9	23
6A	74	10^{-2}	0.23	50	10^{-2}	0.09	5	1.2	55
6C	70	10^{-2}	0.05	11	10^{-2}	0.04	8	1.4	19

TABLE 6.6: Number of iterations of the DA procedure N_{DA}, reduction in the value of the cost function in (6.14) J/J_0, and reduction in the error on the reference rotational speed defined in (6.23) $\epsilon^{\omega}/\epsilon^{\omega}_0$ achieved by DA experiments performed with the first-guess configuration of sensors and with the configuration obtained by the observation optimization procedure in experiments of type 4-6. For the DA experiments using the optimized configurations of sensors, the number of iterations of the observation optimization procedure N_{OO} and the increase in the cost function in (6.10) G/G_0 are also reported, along with the total number of calls to the adjoint code $N_{tot} = N_{DA} + N_{OO}$.

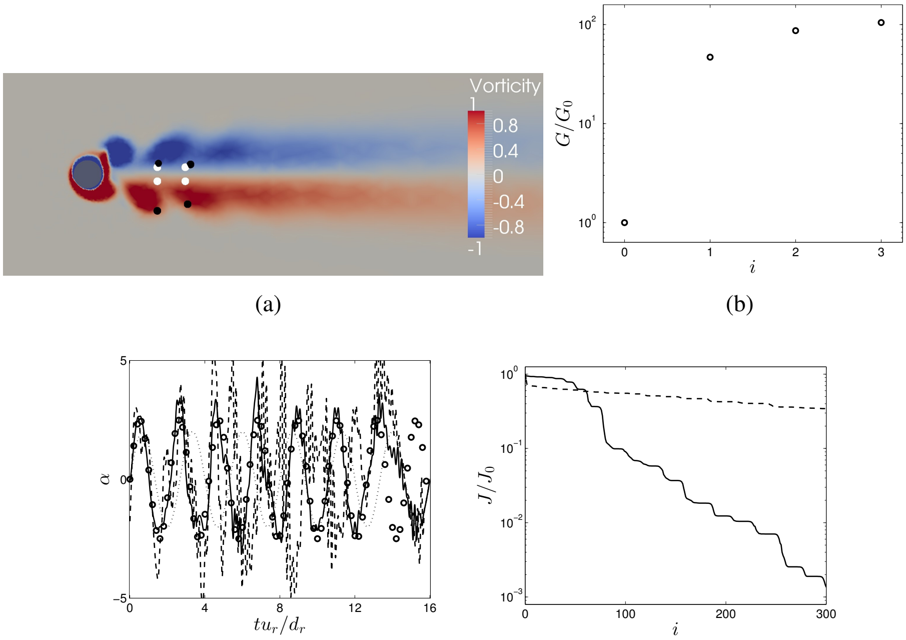

(a) (b)

(c) (d)

FIGURE 6.7: Results for experiment 4C ($\mathcal{A} = 2$ and $\mathcal{F} = 0.375$ for the first-guess flow). Results of the observation optimization procedure: (a) initial (white dots) and optimized (black dots) positions of velocity sensors in the vorticity field of the first-guess flow; (b) cost function G in (6.10) versus the iteration of the optimization process. Results of DA procedures: (c) dimensionless rotational speed α of the cylinder for reference (○), first-guess (⋯⋯⋯) and assimilated runs obtained with the initial (- - - -) and optimized (——) configurations of velocity sensors; (d) cost function J in (6.14) versus the iteration of the optimization process with the initial (- - - -) and optimized (——) configurations of velocity sensors.

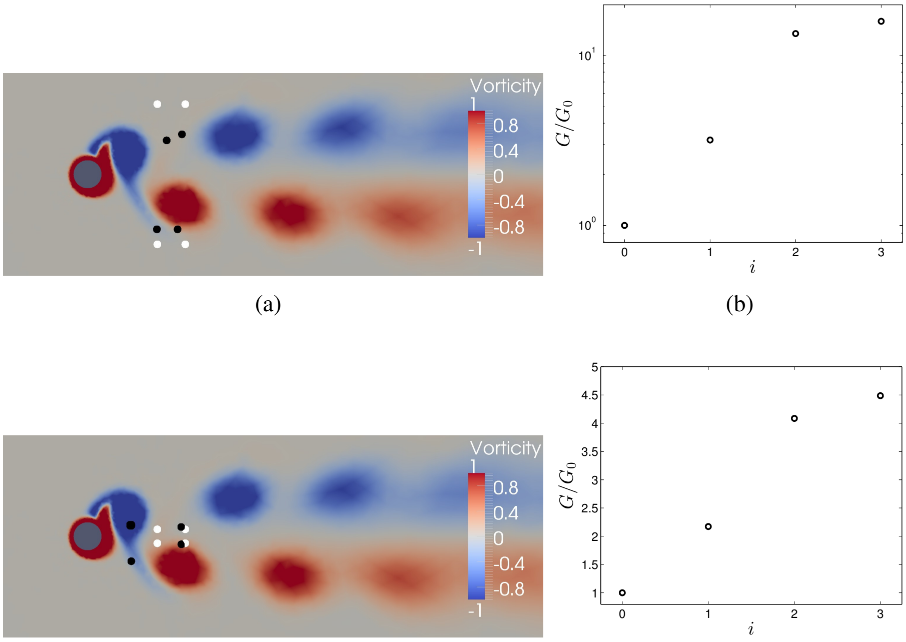

(a) (b)

(c) (d)

Figure 6.8: Results for complementary observation optimization procedures performed with a similar setup to that of experiment 4A (figure 6.6). (a)-(b): procedure with a different initial configuration of sensors; (c)-(d): procedure where the size of the assimilation size has been doubled. (a) and (c): initial (white dots) and optimized (black dots) positions of velocity sensors in the vorticity field of the first-guess flow; (b) and (d): cost function G in (6.10) versus the iteration of the optimization procedure.

(6.23) is significant. In the present case, the observation optimization procedure is thus particularly useful, since the optimized configuration of sensors allows to correctly solve the DA problem, whereas the DA experiment performed with the first-guess configuration failed to retrieve the reference flow realization.

6.5.1.2 Sensitivity to the data assimilation setup

Two complementary observation optimization procedures are performed to investigate the influence of the choice of the first-guess configuration of sensors and that of the size of the assimilation window on the optimized configuration. The setup of these computations is similar to that of experiment 4A, and the corresponding results are reported in figure 6.8. For the case illustrated in figures 6.8(a)-6.8(b), a different first-guess configuration of sensors is employed, and the sensors are initially placed outside of the wake of the cylinder. Similarly to figure 6.6(a), the observation optimization procedure tends to place the sensors closer to the shedded vortices. However, the optimized configurations in figures 6.6(a) and 6.8(a) are not identical while all the parameters of the corresponding experiments are the same. This suggests that the cost function G has multiple local maxima and that the solution of (6.10) is not unique. In figures 6.8(c)-6.8(d), the initial configuration of sensors is the same as in figure 6.6(a) but the size of the assimilation window has been doubled (simulations are performed until $t = T = 32d_r/u_r$ instead of $16d_r/u_r$). As anticipated, the optimized configuration of sensors appears less asymmetrical in this case than in figure 6.6(a).

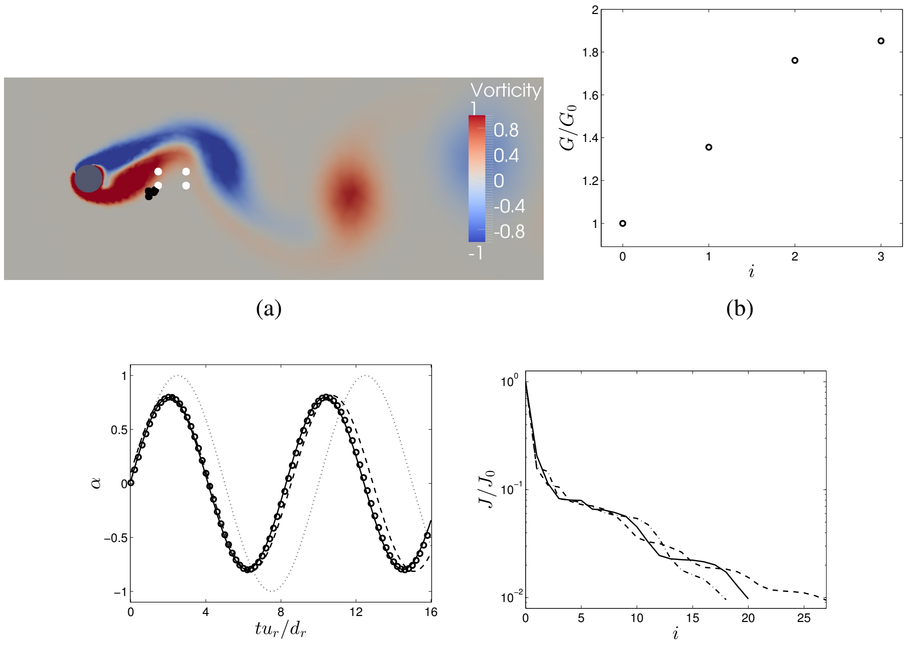

(a) (b)

(c) (d)

Figure 6.9: Results for experiment 5D ($\mathcal{A}$ = 1 and $\mathcal{F}$ = 0.1 for the first-guess flow). Results of the optimization procedure: (a) initial (white dots) and optimized (black dots) positions of velocity sensors in the vorticity field of the first-guess flow; (b) cost function G in (6.10) versus the iteration of the optimization process. Results of DA procedures: (c) dimensionless rotational speed α of the cylinder for reference (○), first-guess (··········) and assimilated runs obtained with the initial configuration of velocity sensors (- - - -) and optimized configuration with merged sensors (———); (d) cost function J in (6.14) versus the iteration of the optimization process with the initial configuration of sensors (- - - -), optimized configuration (-·-·) and optimized configuration with merged sensors (———).

6.5.2 Control on the initial condition and the parameterized rotational speed of the cylinder

6.5.2.1 Experiments with four sensors (type 5)

For the experiments of type 5-6 (see table 6.5) the control vector in the DA procedure is formed by the initial flow field and the three parameters characterizing the rotational speed of the cylinder according to (6.20). In these experiments, the optimization observation procedure of table 6.1 is thus used to increase the sensitivity of velocity sensors with respect to both the initial flow field and the rotational speed of the cylinder. The experiments of type 5 are first examined. Four velocity sensors are used to observe the flow, and various reference and first-guess solutions are considered. Results for configuration D ($\mathcal{A}$ = 1 and $\mathcal{F}$ = 0.1 for the first-guess flow) of table 6.4 (run 5D) are illustrated in figure 6.9. The initial configuration of sensors for the observation optimization procedure (see figures 6.9(a)-6.9(b)) seems to be a relatively good first guess since the cost function G has been increased by a factor of two by the optimization process, which is relatively low compared with the experiments of type 4. It is noticeable that the observation optimization procedure has clustered the sensors of the optimized configuration in a single location. In order to assess the previous results, three DA experiments are performed: the first one uses the first-guess configuration of sensors, the second one directly uses the optimized configuration with 4 sensors, and the third experiment employs the optimized configuration where the 4 sensors are merged into one single sensor. Even with a merged single sensor, the DA experiments performed with the optimized configuration achieve a better reconstruction of the reference rotational speed of the cylinder (see figure 6.9(c) and table 6.6) than the DA experiment using the first-guess configuration. Besides, the DA experiments performed with the optimized configuration reach the same error reduction J/J_0 in slightly less iterations than with the initial configuration.

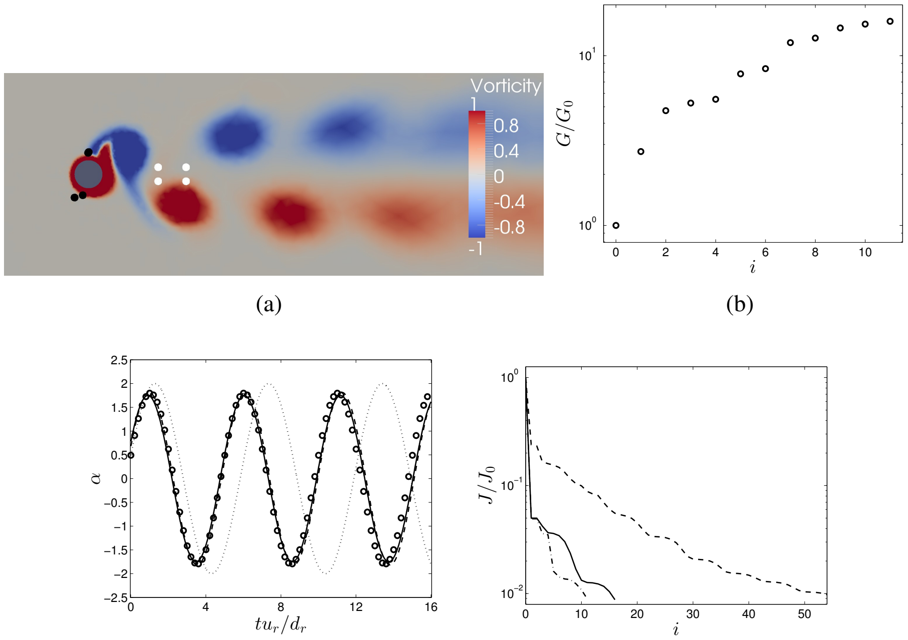

(a) (b)

(c) (d)

Figure 6.10: Results for experiment 5A ($\mathcal{A} = 2$ and $\mathcal{F} = 0.165$ for the first-guess flow). Results of the optimization procedure: (a) initial (white dots) and optimized (black dots) positions of velocity sensors in the vorticity field of the first-guess flow; (b) cost function G in (6.10) versus the iteration of the optimization process. Results of DA procedures: (c) dimensionless rotational speed α of the cylinder for reference (○), first-guess (·········) and assimilated runs obtained with the initial configuration of velocity sensors (- - - -) and optimized configuration with merged sensors (———); (d) cost function J in (6.14) versus the iteration of the optimization process with the initial configuration of sensors (- - - -), optimized configuration (- · - ·) and optimized configuration with merged sensors (———).

Results for experiment 5A are illustrated in figure 6.10. This experiment uses the same first-guess flow and first-guess configuration of sensors as experiment 4A, and it is interesting to note the differences between the obtained optimized configurations of sensors when the observation optimization procedure is used to increase the sensitivity of the sensors with respect to only the rotational speed of the cylinder (see figures 6.6(a)-6.6(b)) or with respect to both the initial flow field and the rotational speed of the cylinder (see figures 6.10(a)-6.10(b)). Compared to the former case, the observation optimization procedure has placed the velocity sensors further upstream in the latter case, which may be explained by the fact that the region of the initial flow in front of the cylinder can be here thought of as upstream conditions. The sensors of the optimized configuration are also much closer to the cylinder than those of the initial configuration. Two pairs of close sensors can be identified above and below the cylinder in the optimized configuration, and, similarly to experiment 5D, the optimized configuration is used in the DA experiments either directly or with two merged sensors. As indicated in table 6.6 and illustrated in figures 6.10(c)-6.10(d), the DA experiments using the optimized configuration of sensors achieve almost the same reduction in the error on the reference rotational speed as with the first-guess configuration, but three times less iterations of the optimization process are required in the former case. As for experiment 5D, merging the close sensors does not significantly degrade the optimality of the observation network.

The use of the configuration C of table 6.4 (run 5C) is examined in figure 6.11. Similarly to experiment 4C where the same first-guess flow is considered, the observation optimization procedure has increased the value of the cost function G by two orders of magnitude. The optimized configuration of sensors of figure 6.11(a) appears more symmetric than in figure 6.7(a). As illustrated in figure 6.11(d), the DA procedure performed with the optimized configuration of sensors converges at a much faster rate toward the reference flow than the one using the first-guess observation network. Indeed, 29 and 163 iterations of the optimization process are required in the former and latter cases respectively to achieve the error reduction $J/J_0 = 10^{-2}$. Besides, the error reduction on

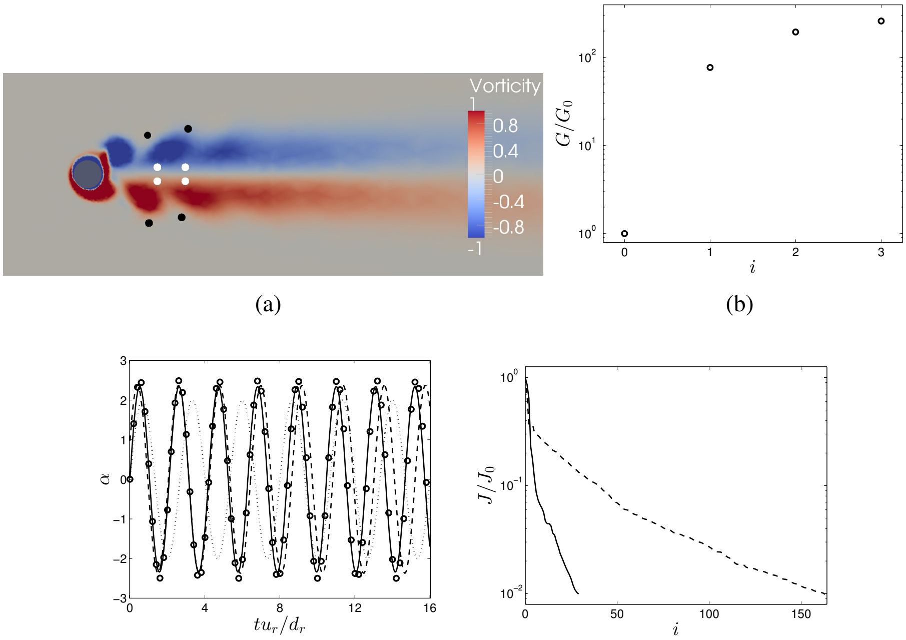

(a) (b)

(c) (d)

FIGURE 6.11: Results for experiment 5C ($\mathcal{A}$ = 2 and $\mathcal{F}$ = 0.375 for the first-guess flow). Results of the optimization procedure: (a) initial (white dots) and optimized (black dots) positions of velocity sensors in the vorticity field of the first-guess flow; (b) cost function G in (6.10) versus the iteration of the optimization process. Results of DA procedures: (c) dimensionless rotational speed α of the cylinder for reference (○), first-guess (··········) and assimilated runs obtained with the initial (- - - -) and optimized (——) configurations of velocity sensors; (d) cost function J in (6.14) versus the iteration of the optimization process with the initial (- - - -) and optimized (——) configurations of velocity sensors.

the reference rotational speed at the end of the optimization procedure is five times greater in the case where the optimized sensors are used than in the case where the first-guess configuration is employed. As summarized in table 6.6, the use of the observation optimization procedure is largely cost efficient in terms of both total number of calls to the adjoint code and reconstruction of the reference flow in this case.

6.5.2.2 Experiments with 20 sensors, sensor selection (type 6)

Finally, we consider experiments of type 6, whose setup is similar to that of the experiments of type 5, but now 20 velocity sensors are used to perform the observations of the flow. Generally speaking, when increasing the number of sensors to observe a given system, one could expect discrepancies in the sensitivity with respect to changes in the system between the different sensors. In this respect, it may be interesting to quantify the importance of each sensor and to indentify the most sensitive ones. The sensor selection procedure described in §6.2.6 is here used to select the most important sensors in the optimized observation networks. Results for experiment 6A are reported in figure 6.12. Starting from the first-guess configuration of sensors illustrated in figure 6.12(a), the configuration of figure 6.12(b) is obtained with the observation optimization procedure. The increase in the value of the cost function G achieved by the optimization procedure is moderate (by a factor 1.2) compared with the previous experiments using four sensors. Performing the observations with 20 sensors actually provides much more information about the flow than with four sensors, and it is expected that the gain in sensitivity obtained with observation optimization strategies becomes less drastic as the number of sensors increases. The most important sensors of the optimized configuration in the sense of equations (6.18)-(6.19) are selected with δ = 0.997 in figure 6.12(c). With this value, only 11 sensors remain, and we can notice that the removed sensors coincide with the ones of the first-guess configuration that have not been moved by the optimization process and were located the furthest from the shedded vortices. Three DA experiments are peformed to assess the results

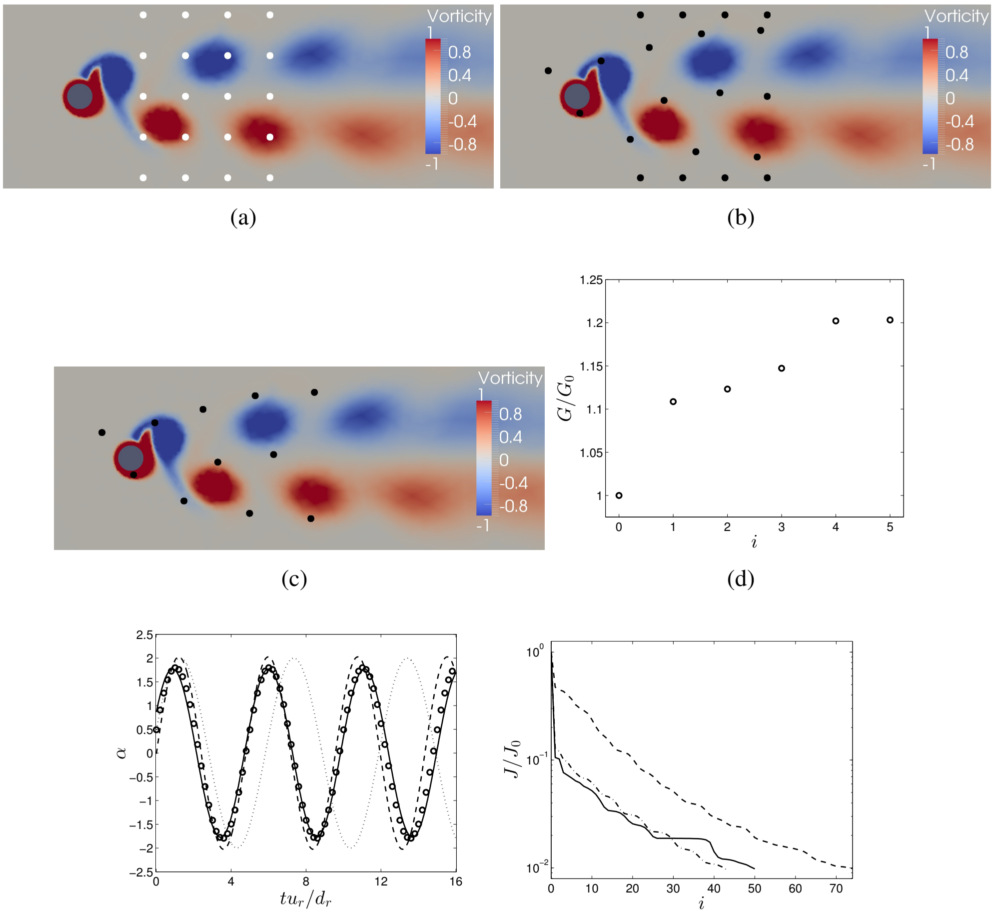

(a) (b)

(c) (d)

(e) (f)

FIGURE 6.12: Results for experiment 6A ($\mathcal{A} = 2$ and $\mathcal{F} = 0.165$ for the first-guess flow). Results of the observation optimization procedure: (a) initial configuration of velocity sensors (white dots), (b) optimized velocity sensors (black dots), and (c) optimized configuration with only the most important sensors; (d) cost function G in (6.10) versus the iteration of the optimization process. Results of DA procedures: (e) dimensionless rotational speed α of the cylinder for reference (○), first-guess (··········) and assimilated runs obtained with the initial configuration of velocity sensors (- - - -) and optimized configuration with only the most important sensors (———); (f) cost function J in (6.14) versus the iteration of the optimization process with the initial configuration of sensors (- - - -), optimized configuration (- · - ·) and optimized configuration with only the most important sensors (———).

of the observation optimization procedure, each using a sensor configuration among the three ones illustrated in figures 6.12(a)-6.12(c). The corresponding results are reported in figures 6.12(e)-6.12(f). The DA experiment performed with only the most important sensors of the optimized configuration achieves a better reconstruction of the reference rotational speed of the cylinder than the DA experiment using the first-guess configuration, and in less iterations, as summarized in table 6.6. Only retaining the most sensitive sensors does not appear to have significantly degrade the optimality of the observation network.

We finally consider the results of experiment 6C, which are illustrated in figure 6.13. The configuration of sensors obtained with the observation optimization procedure is illustrated in figure 6.13(b) starting from the same first-guess configuration as in experiment 6A. Some of the sensors have been placed far from the cylinder and upstream, and when considering this result we have to keep in mind that the observation optimization procedure is used here to increase the sensitivity of the sensors with respect to both the rotational speed of the cylinder and the initial flow field. Equations (6.18)-(6.19) with $\delta = 0.95$ are considered to select the most important sensors in the optimized configuration. The value of δ is adjusted in order to remove nearly half of the sensors, as in run 6A. The resulting configuration is illustrated in figure 6.13(c), where 10 sensors remain. Results for DA

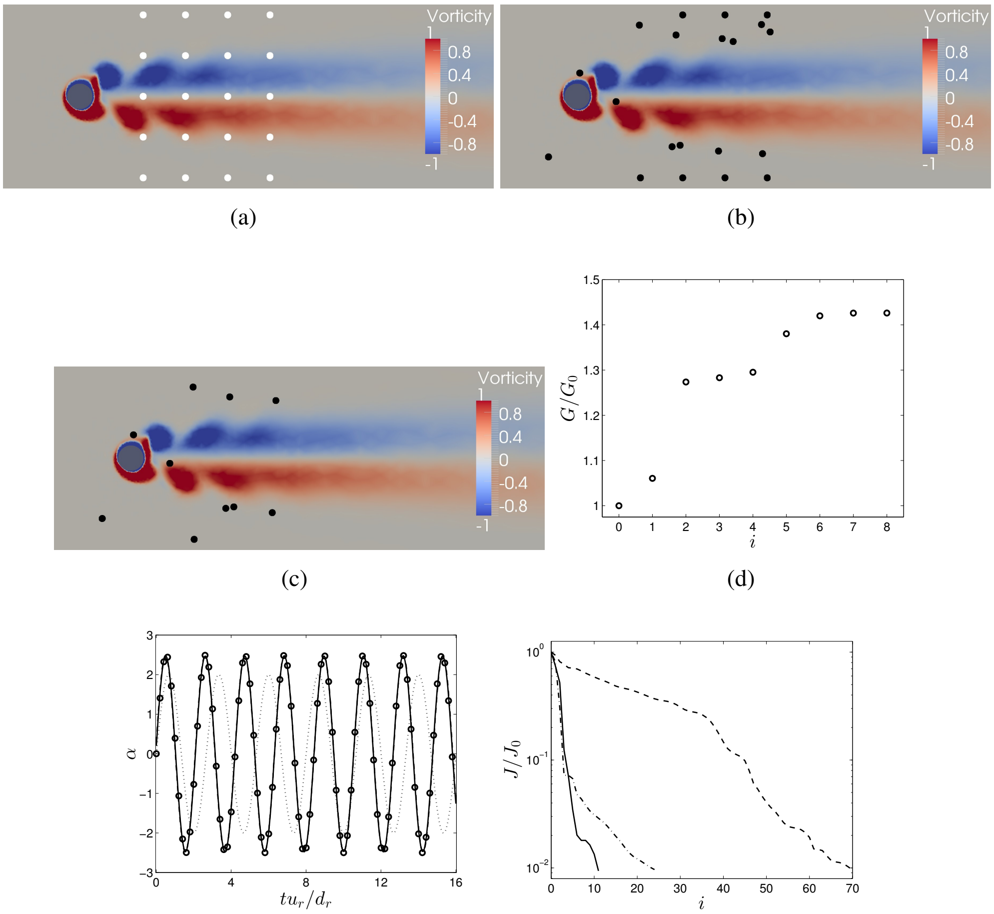

(a) (b)

(c) (d)

(e) (f)

FIGURE 6.13: Results for experiment 6C ($\mathscr{A} = 2$ and $\mathscr{F} = 0.375$ for the first-guess flow). Results of the observation optimization procedure: (a) initial configuration of velocity sensors (white dots), (b) optimized velocity sensors (black dots), and (c) optimized configuration with only the most important sensors; (d) cost function G in (6.10) versus the iteration of the optimization process. Results of DA procedures: (e) dimensionless rotational speed α of the cylinder for reference (○), first-guess (··········) and assimilated runs obtained with the initial configuration of velocity sensors (- - - -) and optimized configuration with only the most important sensors (———); (f) cost function J in (6.14) versus the iteration of the optimization process with the initial configuration of sensors (- - - -), optimized configuration (- · - ·) and optimized configuration with only the most important sensors (———).

procedures performed with the three configurations of sensors of figures 6.13(a)-6.13(c) are reported in figures 6.13(e)-6.13(f) and table 6.6. The DA experiments performed with the first-guess configuration and the optimized configurations of sensors have achieved a similar reduction in the error on the reference rotational speed of the cylinder. However, the DA experiment with only the most important sensors of the optimized configuration has reached this error reduction in almost seven times less iterations than the DA experiment performed with the first-guess configuration. Even with two times less sensors than the first-guess configuration of sensors, the optimized configuration proves to be superior for DA purposes.

6.6 Conclusion

In this chapter, an optimal sensor placement procedure for variational DA of unsteady flows has been proposed. This approach is dedicated to the *a priori* design of an observation network. It is based on the maximization of the norm of the gradient with respect to initial condition, boundary conditions or model parameters of a response function of the flow system. This response function is defined as the norm of observations of the flow. In other words, this procedure is aimed at identifying the regions of the flow that have the greatest sensitivity with respect to a change in control variables such as the initial condition, boundary conditions or model parameters in observation space. This methodology relies on the use of a first-order adjoint technique, and can be naturally coupled with variational DA. However, since observation optimization is performed before assimilating measurements, it is hoped that the proposed procedure will be of interest for a broader range of estimation problems, such as those encountered in flow control.

This method has been applied to the reconstruction of unsteady bidimensional flows past a rotationally oscillating cylinder at $Re = 100$. First, preliminary DA experiments have been conducted in order to delineate the possibilities of solving inverse problems in the context of forced wake flows. The present results suggest that, in the case where the flow lies in the non lock-on regime, it is difficult to retrieve the rotational speed of the cylinder and the initial flow field, which encompasses here upstream conditions, from observations of the velocity field downstream of the cylinder. More precisely, the DA procedure satisfactorily fits the available measurements, but does not correctly identify the associated initial condition and rotational speed. This result may be explained by the fact that the frequency of the wake flow is not directly related to the forcing one in this case, and actually tends to the natural frequency as the flow deviates from the lock-on region, possibly inducing a lack of unicity of the solution to the inverse problem. On the other hand, when the flow lies in the lock-on regime, the frequency of the wake flow is imposed by the forcing one, and the DA procedure is able to correctly retrieve both the rotation parameters and the initial field. The present study also suggests that the observation of global quantities such as the aerodynamic coefficients does not bring enough information to correctly solve the DA inverse problem.

In a second step, the proposed observation optimization procedure has been used for the design of optimal networks of velocity sensors downstream of the cylinder, allowing to improve the performances of the DA process. It has also been employed to identify and select the most important sensors in a given network. Compared to the corresponding first-guess configuration of sensors, in all the DA experiments considered, the use of the optimized network has allowed a significant decrease (up to five times less, run 5C) in the number of calls to the adjoint code (even when taking into account the supplementary cost associated to the observation optimization procedure) that are necessary to reach a given error reduction for the DA problem. Besides, the DA experiments performed with the optimal observation networks achieved a greater accuracy in the reconstructed flow. A case was indentified (run 4C) where the reconstructed rotational speed of the cylinder obtained with the first-guess network of sensors was worse than the first guess for the DA procedure, while the optimized sensors allowed to significantly improve the estimation of the rotational speed. Accordingly, the results obtained with the proposed methodology are encouraging, both in terms of quality of the reconstructed flow and computational cost-efficiency, making possible its application to the reconstruction of more complex flows. The use of an adjoint technique makes the present approach well adapted to high-dimensional problems, but other strategies for efficient sensor placement could be considered in the framework of other DA techniques such as ensemble Kalman filtering or ensemble-based variational DA, as illustrated in chapter 7.

Chapter 7

Data assimilation-based reconstruction of urban flows

7.1 Introduction

Reconstructing pollutant or contaminant source characteristics, such as location and intensity, from observations of the toxic gas concentration in urban areas is a problem of great interest for population protection and environmental preservation. Such an inverse problem is also a challenging one in several aspects. Firstly, in actual practice, only a limited number of measurements of the gas concentration is available, which may prevent from an accurate identification of the source, or, in the worst case, may render the problem severely ill-posed. Secondly, the dynamics of the flow and the dispersion of the gas in urban areas are complex due to the complex geometry of such environments. Achieving sufficiently high-fidelity predictions of urban flows may thus require significant computational ressources and the use of advanced computational fluid dynamics (CFD) solvers. Thirdly, in addition to the pollutant source characteristics, other types of uncertainties have to be considered for the resolution of the inverse problem. In particular, meteorological conditions such as the intensity and direction of the wind entering into the urban area, which have a dramatic impact on the velocity field and thus on the gas dispersion, are not accurately known in real applications. Consequently, the development of methodologies for source reconstruction in urban areas that are able to deal with the above difficulties is still an open issue, as discussed below.

Due to its importance in public safety, the identification of sources of pollutants dispersed in atmospheric environments has been largely investigated in the literature, and numerous techniques have been proposed and applied to this inverse problem. Among others, derivative-free optimization techniques such as pattern search methods [235], genetic algorithms [42], simulated annealing and hybrid variants [146] have been considered. Alternative optimization methods rely on the assumptions of known velocity field and linear relation between the concentration at measurement points and the parameters of the source [1, 191]. Stochastic techniques such as Bayesian inference and Markov chain Monte Carlo sampling have also been used for source reconstruction [231]. However, either because of the prohibitive computational cost when used in conjunction with CFD solvers, or because of the assumption of known velocity field, the above techniques do not appear well suited for realistic urban flow applications. As a matter of fact, these methods have been mainly applied to contaminant dissemination at a regional scale and Gaussian plume or puff dispersion models, but rarely to full-scale urban problems, with noticeable exceptions in [54, 121, 124, 231]. Moreover, all these studies still rely on the assumption of known velocity field, which is evaluated through Reynolds-averaged Navier-Stokes (RANS) approaches.

On the other hand, data assimilation (DA) techniques as developed in the meteorological community [43, 133] and discussed in chapter 2, can virtually deal with any type of uncertainty, and seem appropriate to solve large-scale inverse problems such as encountered in urban flows. Variational techniques [128], based on optimal control, and ensemble Kalman filters [77], which directly originate from the Bayesian formulation of the DA problem, are currently the most commonly used DA methods due to their high scalability and ease of implementation respectively. Recent applications of variational DA and ensemble Kalman filtering to source indentification may be found in [24] and [234] respectively, but these studies still consider simple Gaussian models for atmospheric gas dispersion.

In the present chapter, it is proposed to employ DA for urban flow reconstruction. More precisely, the use of an ensemble-based variational DA technique [140, 204] is considered, which combines the robustness of variational schemes with the ease of implementation of ensemble methods [163]. This DA scheme is deployed in conjunction with a Very Large Eddy Simulation (VLES)/Lattice Boltzmann Method (LBM) solver. This method, which appears more efficient in the prediction of urban flows than RANS models [90, 169, 207], provides high-fidelity estimations of the gas dispersion in an actual urban area. The proposed methodology is applied to the identification of both pollutant source characteristics and approaching wind conditions, and is assessed in terms of accuracy in the identified parameters and corresponding concentration field in various reconstruction scenarios.

In addition to the question of the inverse problem methodology when dealing with urban flows, the problem of identifying appropriate locations to perform observations of the concentration field is also examined in order to improve the performances of the DA process. In the contexts of pollutant release and DA, various sensor placement strategies have been proposed in the literature, which are based, among others, on specific risk-based criterions [50, 131], maximization of posterior statistics [1], observability concept [82, 113], variational tools, see [55] and chapter 6, or Kriging-based spatial interpolation [227]. In the present chapter, a sensor placement procedure is proposed, which is based on a global (in parameter space) sensitivity analysis of the concentration field with respect to source and wind parameters. This methodology is general in the sense that it may be applied to any inverse/DA problem, and appears robust thanks to the global character of the sensitivity analysis.

This chapter is structured as follows. The DA scheme used in this study is introduced in section 7.2. The considered urban area is described in section 7.3 along with the VLES/LBM solver for flow computation. The sensitivity analysis-based sensor placement procedure is developed in section 7.4. The setup of the DA experiments is presented in section 7.5, while results are reported in section 7.6. Section 7.7 is dedicated to conclusions and perspectives.

7.2 POD-ensemble-based variational (POD-EnVar) data assimilation scheme

A computational fluid dynamics (CFD) solver is represented by an operator $\boldsymbol{m}$ that maps an input vector $\boldsymbol{\gamma}$, which may be formed by initial and boundary conditions and by model parameters, to a flow field $\boldsymbol{q}$, discretized in both space and time, according to

$$\boldsymbol{q} = \boldsymbol{m}(\boldsymbol{\gamma}). \tag{7.1}$$

Aside from the numerical model (7.1), it is assumed that observations $\boldsymbol{y}$ of a reference flow are available. The observation operator denoted by $\boldsymbol{h}$ allows to compare the estimation of the flow $\boldsymbol{q}$ with available observations. In the standard variational formulation of data assimilation (DA) [133], the problem is to determine the input vector $\boldsymbol{\gamma}$ that minimizes the discrepancies between the estimation of the flow $\boldsymbol{q}$ and observations $\boldsymbol{y}$. The solution of this problem is referred to as the assimilated input vector in the following, with corresponding assimilated flow. The discrepancies between estimation and observations are evaluated through the cost function J defined by (§2.2)

$$J = \frac{1}{2} \|\boldsymbol{y} - \boldsymbol{h}(\boldsymbol{q})\|^2_{\mathbf{R}}, \tag{7.2}$$

where $\|\cdot\|^2_{\mathbf{R}} = \cdot^{\mathrm{T}}\mathbf{R}\cdot$, the superscript T indicates the transpose operator, and the matrix $\mathbf{R}$ is used to weight the different terms in J. In particular, in the case of noisy observations, $\mathbf{R}$ may be chosen as the inverse of the covariance matrix associated to the noise in the measurements. In order to enforce the dynamical constraint (7.1) on the flow realization $\boldsymbol{q}$ during the minimization of the cost function J, standard variational methods [128] rely on the use of an adjoint model [176] to evaluate the gradient of J with respect to the input vector $\boldsymbol{\gamma}$ (§2.3).

Here, we consider the use of ensemble-based variational schemes, see [140, 163, 204, 230] and §2.6.2, where the constraint (7.1) is taken into account implicitly through the propagation of an ensemble of realizations around a first-guess $\boldsymbol{\gamma}^f$. Such methodology thus allows to avoid the tedious coding of the adjoint model, while the optimization framework of these schemes ensures a greater stability with respect to the size of the ensemble compared to other ensemble DA methods such as the ensemble Kalman filter [77]. This robustness with respect to ensemble characteristics, which is illustrated in chapter 5, is particularly valuable in the case where expensive numerical models are used, as in the present study. In this framework, the minimizing input vector $\boldsymbol{\gamma}$ is searched in a subspace spanned by the ensemble of realizations, and is expressed as

$$\boldsymbol{\gamma} = \boldsymbol{\gamma}^f + \mathbf{A}\boldsymbol{w}, \tag{7.3}$$

where $\boldsymbol{w}$ is the new control vector in the minimization process, and the matrix $\mathbf{A}$ contains a set of suitable basis vectors built from the ensemble perturbation matrix $\mathbf{E}$ defined as

$$\mathbf{E} = \left(\boldsymbol{\gamma}^{(1)} - \boldsymbol{\gamma}^f, \boldsymbol{\gamma}^{(2)} - \boldsymbol{\gamma}^f, \cdots, \boldsymbol{\gamma}^{(N_{en})} - \boldsymbol{\gamma}^f\right), \tag{7.4}$$

where $\boldsymbol{\gamma}^{(1)}$, $\boldsymbol{\gamma}^{(2)}$, $\cdots$, $\boldsymbol{\gamma}^{(N_{en})}$ are N_{en} samples of the input vector that are centered around the first-guess $\boldsymbol{\gamma}^f$. A straightforward choice for the matrix $\mathbf{A}$ in (7.3) is $\mathbf{A} = \mathbf{E}$, see [140] and §2.6.2. However, following [204], further refinement may be achieved through the use of the proper orthogonal decomposition (POD) and the method of snapshots [192]. Employing POD allows to derive an optimal basis from the ensemble in the sense that the most energetic perturbations with respect to the first guess $\boldsymbol{\gamma}^f$ are kept, smoothes the resulting representation, and improves the condition number of the Hessian matrix associated to J that is inverted to solve the minimization problem. The POD step may be avoided in relatively simple and smooth problems, while it is useful to smooth noisy quantities of interest, here time-averaged scalar and velocity fields of a 3D turbulent flow, when solving the DA problem [150]. As in [204], the POD step is performed in the observation space in order to obtain orthogonal base vectors to fit the available measurements, instead of possibly linearly dependent vectors in the case where POD is not performed. The first-guess input vector and the N_{en} samples in (7.4) are propagated using the model (7.1), allowing to form the ensemble perturbation matrix in the observation space $\mathbf{H}$

$$\mathbf{H} = \left(\boldsymbol{h}(\boldsymbol{q}^{(1)}) - \boldsymbol{h}(\boldsymbol{q}^f), \boldsymbol{h}(\boldsymbol{q}^{(2)}) - \boldsymbol{h}(\boldsymbol{q}^f), \cdots, \boldsymbol{h}(\boldsymbol{q}^{(N_{en})}) - \boldsymbol{h}(\boldsymbol{q}^f)\right), \tag{7.5}$$

where $\boldsymbol{q}^{(i)} = \boldsymbol{m}(\boldsymbol{\gamma}^{(i)})$ $i \in \{1, 2, \cdots, N_{en}\}$ and $\boldsymbol{q}^f = \boldsymbol{m}(\boldsymbol{\gamma}^f)$. The POD representation of the ensemble is obtained by solving the eigenvalue problem

$$\mathbf{C}\boldsymbol{v}^{(i)} = \lambda^{(i)}\boldsymbol{v}^{(i)}, \quad \mathbf{C} = \frac{1}{N_{en}}\mathbf{H}^{\mathrm{T}}\mathbf{H}. \tag{7.6}$$

The N_{en} eigenvalues $\lambda^{(i)}$ are sorted by decreasing order, and a truncated basis of eigenvectors $\boldsymbol{v}^{(i)}$ is defined as

$$\mathbf{V} = \left(\boldsymbol{v}^{(1)}, \boldsymbol{v}^{(2)}, \cdots, \boldsymbol{v}^{(N_{\mathrm{POD}})}\right), \quad N_{\mathrm{POD}} = \min\left\{k \left| \frac{\sum_{i=1}^{k} \lambda^{(i)}}{\sum_{i=1}^{N_{en}} \lambda^{(i)}} \geqslant \epsilon_{\mathrm{POD}} \right.\right\}, \tag{7.7}$$

with $0 < \epsilon_{\mathrm{POD}} \leq 1$. Accordingly, the matrix

$$\mathbf{H}_{\mathrm{POD}} = \mathbf{H}\mathbf{V} \tag{7.8}$$

contains orthogonal ensemble perturbations in the observation space. Choosing the matrix $\mathbf{A}$ in (7.3) as

$$\mathbf{A} = \mathbf{E}\mathbf{V}, \tag{7.9}$$

allows to rely on the linear approximation

$$\boldsymbol{h}(\boldsymbol{q}) \simeq \boldsymbol{h}(\boldsymbol{q}^f) + \mathbf{H}_{\mathrm{POD}}\boldsymbol{w}, \tag{7.10}$$

and to rewrite the cost function J in (7.2) as

$$J = \frac{1}{2}\left\|\boldsymbol{h}(\boldsymbol{q}^f) - \boldsymbol{y} + \mathbf{H}_{\mathrm{POD}}\boldsymbol{w}\right\|^2_{\mathbf{R}}. \tag{7.11}$$

---

1. start with a first guess $\boldsymbol{\gamma}^f$ for the input vector
2. sample N_{en} realizations around $\boldsymbol{\gamma}^f$
3. propagate the realizations using the model (7.1)
4. construct the POD representation of the ensemble in observation space from (7.6)-(7.7)
5. compute the minimizing control vector $\boldsymbol{w}$ with (7.12)
6. update the estimation of the input vector $\boldsymbol{\gamma}$ using (7.3) with (7.9)
7. set the updated estimation as a new first-guess $\boldsymbol{\gamma}^f$ and return to step 2 until stopping criterion reached

---

Table 7.1: Schematic representation of the iterative POD-EnVar data assimilation algorithm.

Since the cost function in (7.11) is quadratic, the minimizing vector $\boldsymbol{w}$ is easily found as

$$\boldsymbol{w} = \left(\mathbf{H}_{\text{POD}}^{\text{T}}\mathbf{R}\mathbf{H}_{\text{POD}}\right)^{-1}\mathbf{H}_{\text{POD}}^{\text{T}}\mathbf{R}\left(\boldsymbol{y} - \boldsymbol{h}(\boldsymbol{q}^f)\right). \tag{7.12}$$

From (7.12), an assimilated input vector $\boldsymbol{\gamma}$ can be computed using (7.3) with (7.9). The latter may be then considered as the first guess for a new assimilation cycle in order to further improve the estimation of $\boldsymbol{\gamma}$. The corresponding iterative procedure is summarized in table 7.1.

7.3 Urban toxic gas dispersion

7.3.1 Urban flow CFD simulations

A general trend of last decades shows an increase of population living in urbanized areas. As a consequence, there is growing interest in the scientific communities to improve predictions in case of accidental or intentional releases of chemical, biological, radiological or nuclear (CBRN) products. The problem can be considered at different scales, and we will focus in the present study on medium range dispersions, i.e. we will consider an urban area of 1km^2. Recently, CFD has become the new standard for this kind of applications [27, 45, 99, 164]. However, urban flows are very complex in terms of numerical simulations: a real urban area is a complex array of bluff bodies invested by the atmospheric boundary layer, and the resulting flow is characterized by unsteadiness and separations. Consequently, researchers tried in the last decade to establish guidelines for such simulations. The most exhaustive guidelines for the application of CFD to flows in the urban environment are the ones proposed by the Architectural Institute of Japan (AIJ) [210] and by the COST action 743 [84]. Although LES proved to be more accurate, most of the CFD applications in the literature still rely on RANS turbulence models due to the associated reduced computational cost. However, the non-stationarity of LES has proved to be important to study CBRN releases and their dispersions, in particular in the span-wise direction [26, 90, 207, 208]. Aside from the quality of the turbulence model and the fidelity of the predictions, another important requirement for the CFD code is its ability to deal with the detailed geometry of urban environments. For these reasons, the Lattice Boltzmann Method (LBM) code PowerFLOW (Exa Corporation) was considered in the present study. The main advantages of the LBM methodology [47, 49, 120] are the massively parallelization capacity and the handling of complex geometries as required to simulate medium range CBRN dispersion in urban areas. The application of LBM is quite recent and there are few applications to urban flows [71, 169]. PowerFLOW employs a Very Large Eddy Simulation (VLES) turbulence model [194], where the large eddies are solved, thus preserving the unsteady nature of the solution and ensuring a high-fidelity prediction of the flow, while the smaller ones are modeled through a modified $k-\varepsilon$ RNG model [228]. This allows a decrease in

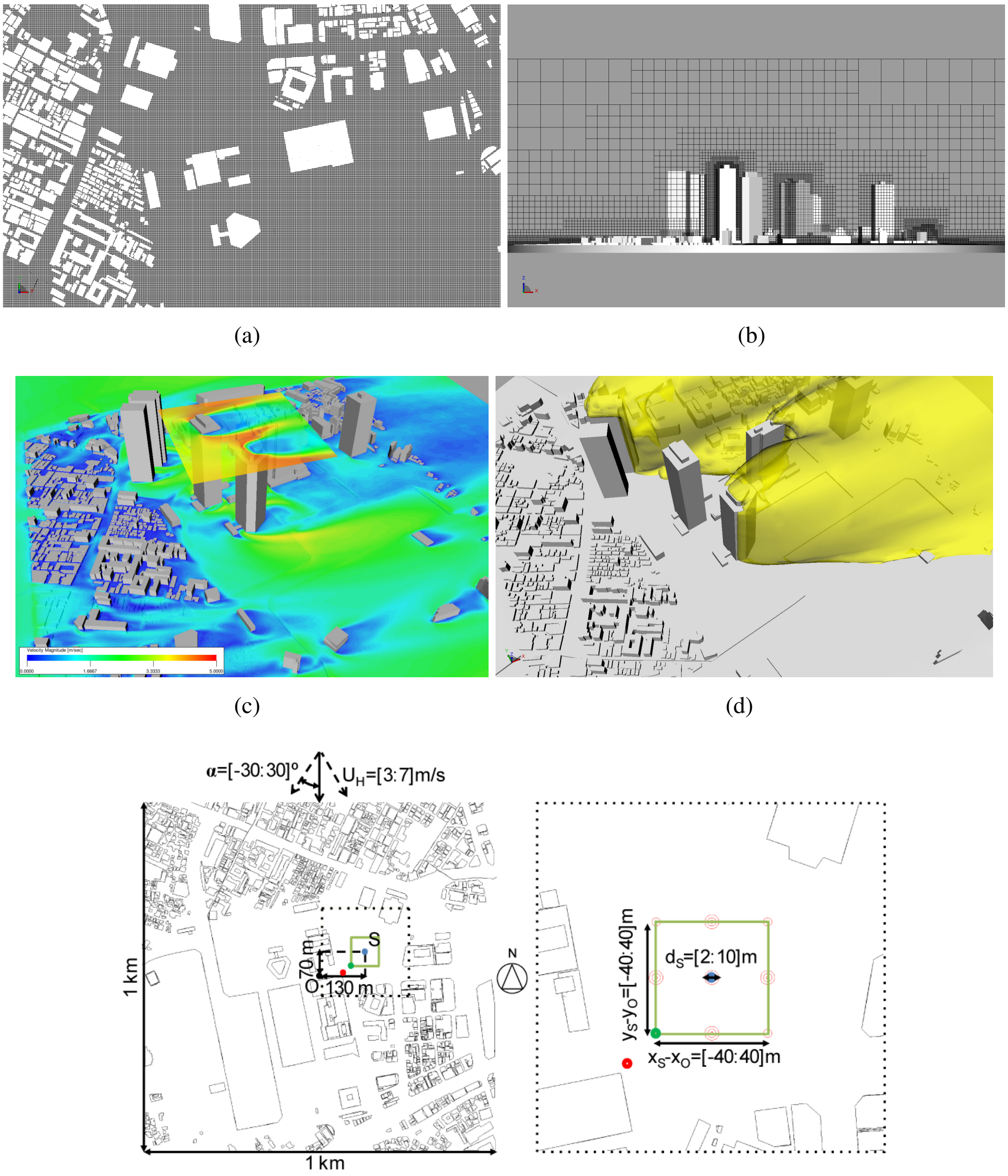

(a) (b)

(c) (d)

(e)

Figure 7.1: VLES/LBM prediction of gas dispersion in Shinjuku area [210]: (a)-(b) computational grid of the simulations ((a) top and (b) lateral views), (c) velocity magnitude field and (d) isosurface containing concentration levels higher than 1 ppm for a typical flow realization, and (e) wind and scalar source parameters along with ranges of variation considered in the sensitivity analysis of section 7.4.1. Blue dot refers to the reference position of the source, while green and red dots indicate the location of the source for the first and second first-guesses respectively, as reported in table 7.2.

computational cost compared to high-resolved LES, which is valuable in the case where many simulations have to be performed, as in the present study. Validations of the PowerFlow solver on urban flows may be found in [148, 149].

7.3.2 Gas dispersion in the Shinjuku area

In this study, we will focus on the dispersion of a non-reacting agent with density ρ comparable to air. The dynamics of the gas concentration C is modeled as a passive scalar according to

$$\frac{\partial \rho C}{\partial t} + \nabla \cdot (\rho \boldsymbol{U} C) = \nabla \cdot (\rho D \nabla C), \tag{7.13}$$

where $\boldsymbol{U}$ is the mean velocity vector and D is the diffusion coefficient, which is modeled in the case of VLES as

$$D = \frac{\nu_t}{Sc_t} + \nu, \tag{7.14}$$

where ν_t is the eddy viscosity, ν is the molecular viscosity and Sc_t is the turbulent Schmidt number. In the present application, we consider a continuous release from a pond-like source in a square-like area surrounded by high-rise buildings. The assumption of continuous release may be relevant for the study of pollutant releases [231, 235], and allows to consider time-averaged results if the physical duration of the simulation is long enough. Accordingly, all the velocity and concentration fields considered in this study are averaged in time. The reference geometry is the Shinjuku area of Tokyo, which is taken from the AIJ open source database [210]. The dimensions of the corresponding simulation domain are $2\,\text{km} \times 2\,\text{km} \times 0.6\,\text{km}$, and the computational grid counts $6 \cdot 10^6$ cells with a smallest cell size of $2\,\text{m}$ and 6 levels of variable resolution. Mesh refinement is set through embedded volumes. The characteristic time to obtain averaged results with a mean wind speed at the averaged building height $U_H = 5\,\text{m/s}$ is about 60 minutes of simulation in physical time, corresponding to about 10^5 time steps. The geometry of the urban environnement can be visualized in figures 7.1(a)-7.1(b), along with the mesh used in the present computations and examples of simulated velocity (figure 7.1(c)) and scalar (figure 7.1(d)) fields. About 8 hours on 96 2.4Ghz AMD Opteron 8431 cores are required for each simulation with no gas dispersion. Note that the computational cost can double in case of many passive scalar solutions. Regarding boundary conditions, the buildings and the floor are considered as smooth solid surfaces, while the lateral and top boundaries are set to be frictionless impermeable planes. Profiles for the inlet mean velocity and turbulent kinetic energy are obtained by interpolating experimental data conditions, while the inlet turbulent dissipation rate is recovered following the AIJ guidelines [210]. These inflow conditions are parameterized by the angle α which indicates the direction of the mean profile and by the characteristic mean flow intensity U_H. Outlet boundary conditions are set by imposing a static pressure. The gas is released from the floor with a zero injection speed, mimicking evaporation of a liquid pollutant reservoir, and the corresponding source is modeled as a solid wall with a Dirichlet condition $C = 10^6\,\text{ppm}$ applied on its surface at the source location. The release of the gas is therefore governed by the coordinates x_s and y_s of the source and by its diameter d_s which determines the quantity of gas that is injected in the flow. Accordingly, the input vector $\boldsymbol{\gamma}$ in (7.1) for the present simulations is

$$\boldsymbol{\gamma} = (\alpha, U_H, x_s, y_s, d_s)^{\mathrm{T}}, \tag{7.15}$$

where α and U_H allow to tune inlet boundary conditions (wind parameters), while x_s, y_s and d_s characterize the release of the gas (scalar source parameters). These input parameters are illustrated in figure 7.1(e).

The mean velocity magnitude and scalar fields for the input vector $\boldsymbol{\gamma}^{ref}$ whose components are reported in table 7.2 are illustrated in figure 7.2. This flow realization is referred to as the reference flow in the following, and the aim of the data assimilation experiments of section 7.6 will be to reconstruct this reference flow and the corresponding input parameters $\boldsymbol{\gamma}^{ref}$. In figure 7.2(a), instead of directly considering the concentration C of the gas, we use a modified concentration C^* which is defined as follows. In toxic gas dispersion problems, the main interest is on the map of concentration in logarithmic scale, from which one can obtained areas corresponding to a given toxic level threshold. In order to prevent the occurance of infinite values and to clip low levels of concentration, which are affected by errors from the finite averaging time, we apply an ad hoc transformation to the concentration C so that values < 1 ppm are kept on a linear scale while values > 1 ppm are in a log scale

$$C^* = \begin{cases} \log_{10}(10C) & C \geq 1\,\text{ppm} \\ C & C < 1\,\text{ppm} \end{cases}. \tag{7.16}$$

γ_i	γ_i^{min}	γ_i^{max}	γ_i^{ref}	γ_i^{f1}	γ_i^{f2}
$\alpha\,(^\circ)$	-30	30	0	0	-30
U_H (m/s)	3	7	5	5	7
x_s (m)	90	170	130	90	70
y_s (m)	30	110	70	30	10
d_s (m)	2	10	6	10	12

Table 7.2: Ranges of parameters $\left[\gamma_i^{min}, \gamma_i^{max}\right]$ considered in the sensitivity analysis of section 7.4.1, and input vectors $\boldsymbol{\gamma}^{ref}$, $\boldsymbol{\gamma}^{f1}$ and $\boldsymbol{\gamma}^{f2}$ for the reference and first-guess flows of the DA experiments of section 7.6.

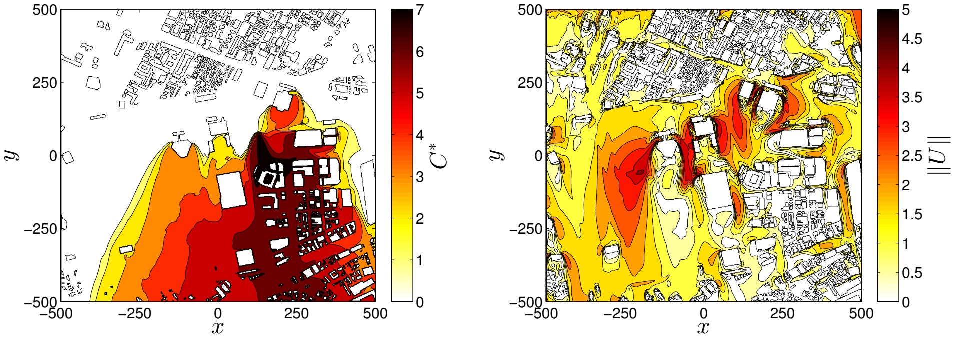

(a)

(b)

Figure 7.2: (a) Modified concentration C^* and (b) velocity magnitude (m/s) fields for the reference flow to be reconstructed in the DA experiments. The corresponding input vector $\boldsymbol{\gamma}^{ref}$ is reported in table 7.2.

In the following, all the reported results correspond to the plane $z = 10\,\mathrm{m}$. This altitude is relevant for pedestrian level applications, and is the same as that of measuring points used in field experiments conducted in the actual urban area of Shinjuku [209].

7.4 Sensitivity analysis-based placement of sensors

7.4.1 Sensitivity analysis of the gas concentration

In the present study, we consider measurements of the gas concentration for the reconstruction of the reference flow through data assimilation. Of course, in practical applications, the concentration field is not available over the full urban area, but only at a few measurement points. Accordingly, one may wonder how a small number of sensors could be appropriately placed to measure the flow. In any DA framework, the determination of an efficient observation network is a problem of crucial importance, since measurements represent the only available information about the reference flow to be reconstructed. A desirable property of the observations is their sensitivity with respect to a change in the input vector $\boldsymbol{\gamma}$. Indeed, if a variation in $\boldsymbol{\gamma}$ entails no change in the values of the observations, i.e. changes in the flow are not observable, the DA problem can not be solved satisfactorily. It is therefore preferable to design the observation network with maximum sensitivity with respect to $\boldsymbol{\gamma}$. Before specifying an appropriate criterion to design optimized measurements, we first need to evaluate the sensitivity of the flow solution in observation space with respect to the input vector. In the present study, this is performed through the computation of Sobol´ indices [193], which allow to estimate the global sensitivity of a quantity of interest $X(\boldsymbol{\gamma})$ that will be here the modified concentration field C^*, considering that the components of the input vector $\boldsymbol{\gamma}$ are random variables.

The main statistics that are required to compute the Sobol´ indices are obtained through quasi Monte Carlo (Sobol sequences) estimators [189]. As we rely on high-fidelity unsteady CFD simulations, the computational costs do not allow to directly compute the estimators, which require too many function calls (i.e. simulations). Therefore, a meta-modelling approach is preferred in this study: the c-APK method presented in [150], which is based on an efficient hybridization of c-ANOVA [147, 229] and POD/Kriging-based response surface methods [30]. The c-APK surrogate model relies on an adaptive strategy to achieve a conveniently desired global accuracy in complex realistic applications as the urban gas dispersion application. Once the meta-model is built, the mean estimate μ of $X(\boldsymbol{\gamma})$ is calculated as [150]

$$\mu = \frac{1}{q_{MC}} \sum_{i=1}^{q_{MC}} X_s(\boldsymbol{\gamma}^{(i)}), \tag{7.17}$$

where q_{MC} is the number of quasi Monte Carlo samples $\boldsymbol{\gamma}^{(i)}$ of the input vector, and $X_s(\boldsymbol{\gamma})$ refers to the c-APK surrogate model of $X(\boldsymbol{\gamma})$. The variance σ^2 is computed as

$$\sigma^2 = \frac{1}{q_{MC}-1} \sum_{i=1}^{q_{MC}} (X_s(\boldsymbol{\gamma}^{(i)}) - \mu)^2. \tag{7.18}$$

First-order sensitivity indices are derived from two independent sampling matrices $\mathbf{A}$ and $\mathbf{B}$ of dimensions $q_{MC} \times N$ with $N = \dim(\boldsymbol{\gamma})$. These sets are obtained from a quasi Monte Carlo sampling matrix of dimensions $q_{MC} \times 2N$, and they are used to estimate the partial variance σ_i^2 for the i-th component of $\boldsymbol{\gamma}$ according to [189]

$$\sigma_i^2 = \frac{1}{q_{MC}} \sum_{j=1}^{q_{MC}} X_s((\mathbf{B})^{(j)}) \left(X_s((\mathbf{A}_{\boldsymbol{B}}^i)^{(j)}) - X_s((\mathbf{A})^{(j)}) \right) \tag{7.19}$$

where $\mathbf{A}_{\boldsymbol{B}}^i$ is the matrix where all columns are from $\mathbf{A}$ except the i-th column which is from $\mathbf{B}$, and $(\mathbf{A})^{(j)}$ denotes the j-th row of matrix $\mathbf{A}$, i.e. the j-th sample in $\mathbf{A}$. Once computed, these partial variances allow to form the first-order Sobol´ indices S_i defined as

$$S_i = \frac{\sigma_i^2}{\sigma^2}, \quad S_i^* = \frac{S_i}{\sum_{j=1}^N S_j}. \tag{7.20}$$

The index S_i thus allows to quantify the first-order sensitivity of the quantity of interest $X(\boldsymbol{\gamma})$ with respect to the i-th parameter relatively to the total variance of $X(\boldsymbol{\gamma})$. In the following, we will also consider the indices S_i^* defined in (7.20) where the Sobol´ indices S_i are normalized by the sum of the first-order effects. This is done mainly to re-scale the Sobol' indices as if there were no higher order interactions and to smooth the estimators when their sum slightly exceeds 1. Thanks to this operation we will be able to directly use the normalized Sobol' indices in the sensor optimization framework.

Taking the modified concentration field C^* as the quantity of interest $X(\boldsymbol{\gamma})$, its mean μ, total variance σ^2 and normalized Sobol' indices S_i^* are evaluated according to the above procedure, and the resulting statistics are illustrated in figures 7.3 and 7.4. The input vectors $\boldsymbol{\gamma}^{(i)}$ needed in the estimators (7.17)-(7.19) are obtained assuming that the j-th component of $\boldsymbol{\gamma}$ follows the normal law with mean γ_j^{ref} and standard deviation $(1/4)(\gamma_j^{max} - \gamma_j^{min})$. The components of the vectors $\boldsymbol{\gamma}^{ref}$, $\boldsymbol{\gamma}^{min}$ and $\boldsymbol{\gamma}^{max}$ are reported in table 7.2. The investigated ranges of parameters correspond to typical ranges of uncertainties in field measurements, which are also used in other uncertainty quantification studies [10, 88]. Huge variations in the sensitivity of the concentration field can be identified from figures 7.3 and 7.4, both spatially and among the parameters in $\boldsymbol{\gamma}$. As illustrated in figure 7.3, the variability in the concentration is negligible in the north part of the city, while total variance reaches maximum values in the region close to the reference position of the scalar source and in the wake of the tallest buildings. Figure 7.4 shows that the most important parameter is the wind angle α (figure 7.4(a)), which determines the global direction of the dispersion. These results also highlight the importance of the coordinate x_s of the scalar source on the repartition of the gas (figure 7.4(c)), which may be explained by the fact that the $x-$direction corresponds, in average, to the direction orthogonal to that of the mean flow in the present study. The parameters y_s and d_s seem to play intermediate roles (figures 7.4(d) and 7.4(e)), even if the coordinate y_s appears to have

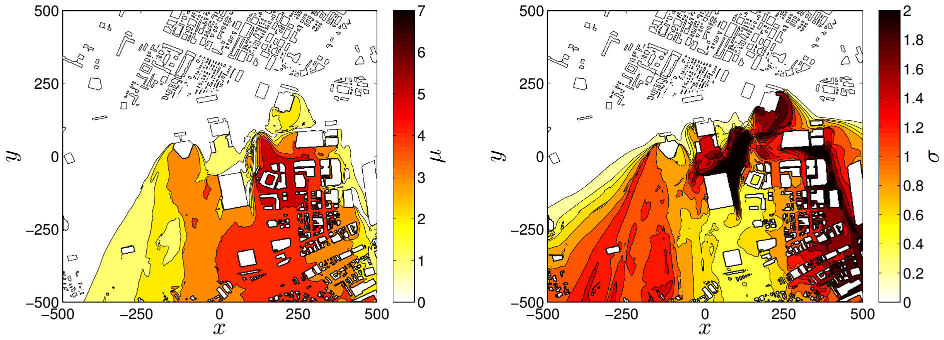

(a) (b)

FIGURE 7.3: (a) Mean and (b) standard deviation of the modified concentration field C^* with a normal law over the ranges $\left[\gamma_i^{min}, \gamma_i^{max}\right]$ in table 7.2 and obtained through the forward uncertainty quantification procedure of section 7.4.1.

more influence on the concentration in the region around the reference location of the scalar source. Finally, this sensitivity analysis indicates that the intensity of the wind U_H has little impact on the gas concentration (figure 7.4(b)), whatever the considered location in the urban area. These results will facilitate the interpretation of the assimilated solutions obtained in the DA experiments of section 7.6.

7.4.2 Standard and optimized sensor networks

From the above sensitivity analysis, it is possible to propose a criterion for the identification of optimized sensor networks before performing DA. A first requirement for efficient sensors may be that they are placed at locations where the gas concentration is not too low. In particular, in the case of toxic gas dispersion, we are indeed more interested in the good reconstruction of regions of high concentration than in the reconstruction of regions in which the gas is almost absent. A second requirement is that sensors are placed at locations with sufficiently high total variability. As mentioned above, if changes in the input parameters entail no variation in the values of the gas concentration at observation locations, measurements used in the DA process are worthless. Finally, it may be useful to favor locations where sensitivity is primarily determined by a particular parameter, thus allowing to improve the conditioning of the inverse problem and facilitating the reconstruction of chosen parameters. In the present case, the sensitivity of the concentration is mostly determined by the wind angle α in a large portion of the urban area, and, in a context of source identification, one could choose to privilege sensitivity with respect to the scalar source parameters. Accordingly, in the present study, we choose to define appropriate domains Ω for sensor placement as

$$\begin{aligned}\Omega = &\{(x,y) \in \mathcal{V} \,|\, \mu > a, \sigma/\mu > b\} \\ &\cap \left\{ \{(x,y) \in \mathcal{V} \,\middle|\, S^*(d_s) > c\} \cup \{(x,y) \in \mathcal{V} \,\middle|\, S^*(y_s) > d\} \cup \{(x,y) \in \mathcal{V} \,\middle|\, S^*(x_s) > e\} \right\},\end{aligned} \tag{7.21}$$

where $\mathcal{V}$ refers to the flow domain restricted to the plane $z = 10\,\text{m}$ (see section 7.3). The scalars a, b, c, d and e are adjustable parameters that allow to tune the domain Ω. Here, a is fixed to 1, which means that concentration levels < 1 ppm in average are not considered for sensor placement. We impose $b = 0.1$, thus ensuring that the relative standard deviation of the gas concentration at observation locations is at least 10%. The scalars c, d and e, which allow to specifically enhance the sensitivity of the sensors with respect to the scalar parameters, are chosen as $c = d = 0.33$ and $e = 0.4$. A slightly superior value is chosen for x_s, since the sensitivity of the gas concentration with respect to x_s is generally more important than with respect to y_s and d_s in the urban area. The domain Ω as defined in (7.21) is reported in figure 7.5. The locations of the sensors used in field experiments performed in the Shinjuku area [209] are also reported in blue crosses. The corresponding sensor network is referred to as the standard configuration of sensors in the following. This network contain 33 points of measurement, almost all of which are outside the domain Ω. Besides, a significant number of these sensors

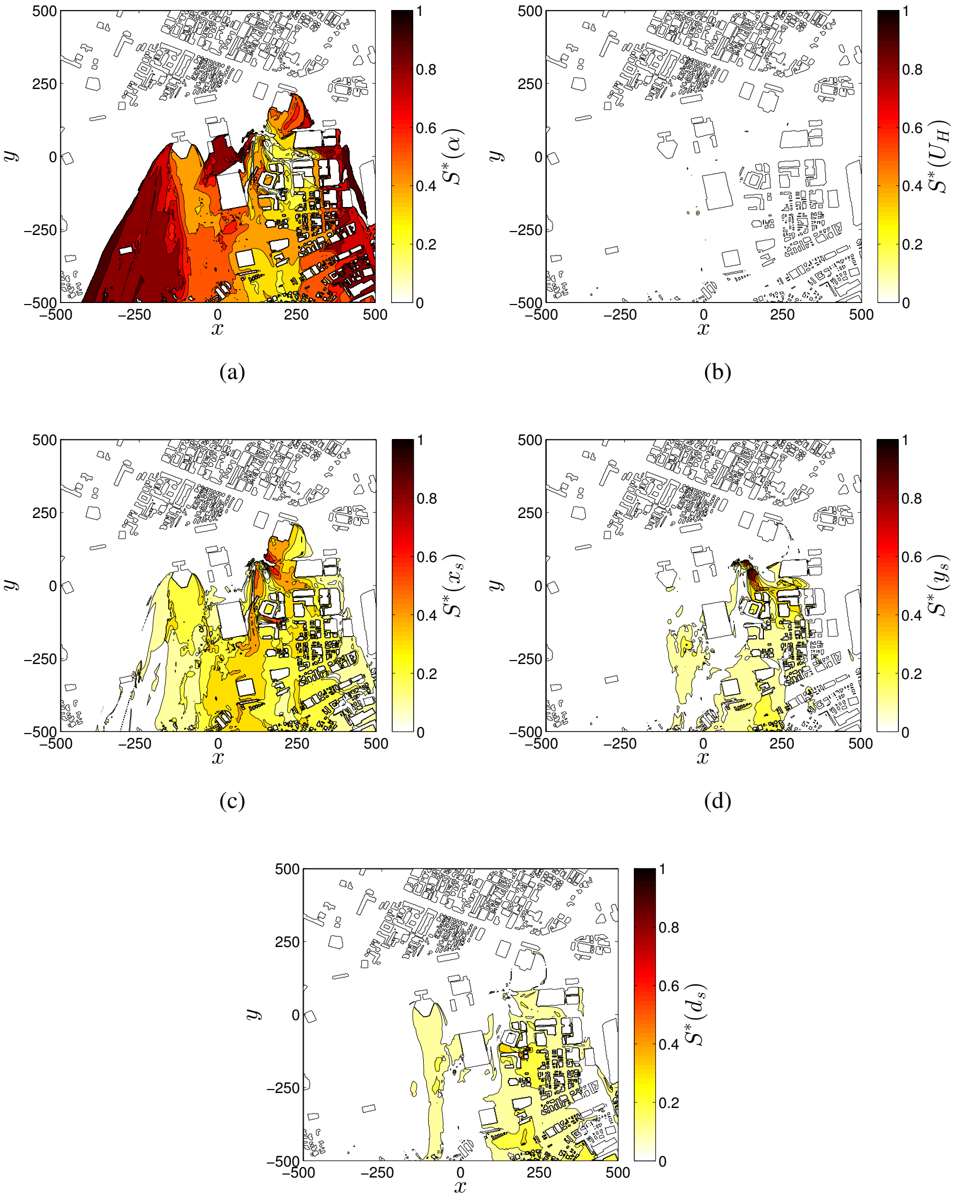

(a) (b)

(c) (d)

(e)

FIGURE 7.4: Normalized first-order Sobol´ indices of the modified concentration field C^* for the parameters (a) α, (b) U_H, (c) x_s, (d) y_s and (e) d_s with a normal law over the ranges $\left[\gamma_i^{min}, \gamma_i^{max}\right]$ in table 7.2 and obtained through the forward uncertainty quantification procedure of section 7.4.1.

are located in the north part of the urban area, where both the concentration of the gas and its sensitivity with respect to the input parameters are negligible. According to the present sensitivity analysis, these sensors used in field experiments do not therefore appear particularly appropriate for DA purposes. However, it may be noticed that these sensors were used to perform velocity measurements, and no gas dispersion was considered [209]. For a fair comparison with the use of the standard configuration of sensors, an optimized observation network is obtained by randomly picking 33 measurements points in the domain Ω while imposing a minimal distance of 40 m between these points. The thus obtained optimized observation network is reported in blue circles in figure 7.5. Both standard and sensitivity analysis-based optimized observation configurations are considered in the DA experiments of section 7.6, and it is expected that the proposed methodology for sensor placement will allow to improve the quality of the urban flow that is reconstructed through DA.

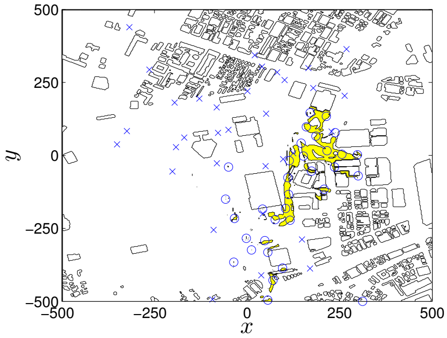

Figure 7.5: Domain Ω for appropriate sensor placement defined by (7.21) with $a = 1$, $b = 0.1$, $c = d = 0.33$ and $e = 0.4$ (yellow region). Standard (blue crosses) and optimized (blue circles) sensor configurations are also reported.

7.5 Setup of the data assimilation experiments

7.5.1 Observations and reconstruction scenarios

Various DA experiments, namely cases A-E, are performed in this study in order to assess the ability of the present POD-EnVar scheme to deal with the reconstruction of urban flows as described in section 7.3. For all these experiments, the aim is to recover the reference flow illustrated in figure 7.2, and whose corresponding input parameters $\boldsymbol{\gamma}^{ref}$ are reported in table 7.2, from observations of the modified concentration C^* defined in (7.16). Measurements are performed at discrete locations that are reported in figure 7.5. Experiments rely on either the standard configuration of sensors (cases A, C and E), or the optimized network derived in section 7.4 (cases B and D), allowing to assess the impact of sensitivity analysis-based sensor placement on the performances of the DA process. The observation of the velocity field $\boldsymbol{U}$ with the modified concentration C^* is also considered in experiment E.

In the experiments A and B, the wind parameters α and U_H of the reference flow are assumed to be known. Accordingly, the control vector $\boldsymbol{\gamma}$ in the DA process is formed by the three scalar parameters x_s, y_s and d_s. The first guess flow used to initialize the POD-EnVar scheme is obtained with the input vector $\boldsymbol{\gamma}^{f1}$ reported in table 7.2. It corresponds to a perturbation of a magnitude of 40 m of the reference position of the source in both $x-$ and $y-$directions, and to an error of 4 m on its diameter. The discrepancies between the reference and first guess flows are moderate, and cases A and B are performed primarily to validate the present methodology with relatively low computational cost, since the velocity field is fixed in these experiments, and only the scalar fields of the different flow realizations have to be computed. Concerning experiments C-E, both wind and scalar parameters are reconstructed via the DA procedure, and the first guess solution with input vector $\boldsymbol{\gamma}^{f2}$ is considered for the initialization. This first guess corresponds to an error of 60 m on the reference position of the source in both $x-$ and $y-$ directions, an error of 6 m on its size, of 30° on the wind angle and of 2 m/s on its intensity. These errors are more substantial than for the first guess of cases A and B, and it can be noticed that the position of the source in $\boldsymbol{\gamma}^{f2}$ is outside the range investigated in section 7.4. Accordingly, cases C-E are suitable experiments to further test the robustness of the DA procedure by complexifying the physics of the flow and adding variability due to badly known wind parameters. These experiments also allow to assess the robustness of the sensitivity analysis-based placement of sensors by considering a first guess realization slightly outside the range of parameters investigated in the sensitivity analysis. In all the experiments, the discrepancies between the reference and first guess flows correspond to typical uncertainties in the scalar and wind parameters [10, 88]. The setup of the different cases discussed above is summarized in table 7.3.

case	$\boldsymbol{\gamma}$	$\boldsymbol{y}$	sensors	first guess	N_{rn}
A	x_s, y_s, d_s	C^*	standard	$\boldsymbol{\gamma}^{f1}$	60
B	x_s, y_s, d_s	C^*	optimized	$\boldsymbol{\gamma}^{f1}$	40
C	$\alpha, U_H, x_s, y_s, d_s$	C^*	standard	$\boldsymbol{\gamma}^{f2}$	60
D	$\alpha, U_H, x_s, y_s, d_s$	C^*	optimized	$\boldsymbol{\gamma}^{f2}$	40
E	$\alpha, U_H, x_s, y_s, d_s$	$C^*, \boldsymbol{U}$	standard	$\boldsymbol{\gamma}^{f2}$	60

TABLE 7.3: Summary of the DA experiments performed in this study, which are characterized by the control vector $\boldsymbol{\gamma}$ in the assimilation process, the observations $\boldsymbol{y}$ of the reference flow and associated sensor network, and the first guess used to initialize the POD-EnVar scheme (see table 7.2). The total number N_{rn} of CFD computations performed in each experiment is also reported.

7.5.2 Choice of the POD-EnVar scheme parameters

All the DA experiments are performed using ensembles of size $N_{en} = 20$. Such a number of realizations remains affordable for intensive CFD simulations as the ones considered here, while results obtained in the DA experiments of chapter 5 relying on two-dimensional CFD computations suggest that $N_{en} = 20$ is a sufficiently high ensemble size to ensure the stability of ensemble-based variational schemes, even in the case of control vectors $\boldsymbol{\gamma}$ in the DA process of large dimension (up to $\approx 10^5$ variables). The N_{en} samples of the input vector in (7.4) are generated assuming that the realizations obey to a normal distribution $\mathcal{N}\left(\boldsymbol{\gamma}^f, \boldsymbol{\Lambda}\right)$ centered on a first guess $\boldsymbol{\gamma}^f$ and whose covariance matrix $\boldsymbol{\Lambda}$ is given by

$$\boldsymbol{\Lambda} = \mathrm{diag}\left(\Sigma_1^2, \Sigma_2^2, \cdots, \Sigma_N^2\right), \quad \Sigma_i = 0.33\frac{\gamma_i^{max} - \gamma_i^{min}}{2}, \tag{7.22}$$

with $N = \dim(\boldsymbol{\gamma})$, and the components of the vectors $\boldsymbol{\gamma}^{min}$ and $\boldsymbol{\gamma}^{max}$ are given in table 7.2. The choice of a normal distribution for the ensembles is standard in DA applications [133, 163]. It can be noticed that the reference input vector $\boldsymbol{\gamma}^{ref}$ verifies $|\gamma_i^{ref} - \gamma_i^f| > \Sigma_i$, with $\boldsymbol{\gamma}^f$ that refers to either $\boldsymbol{\gamma}^{f1}$ or $\boldsymbol{\gamma}^{f2}$, for each ith parameter to be reconstructed. Moreover, concerning the error on the position of the source in the $x-$ and $y-$directions for the first guess flow used in experiments C-E, the components of the corresponding input vector verify $|\gamma_i^{ref} - \gamma_i^{f2}| = 1.5(\gamma_i^{max} - \gamma_i^{min})/2$. In other words, the standard deviations associated to the ensembles of realizations are underestimated given the actual discrepancies between the parameters of the reference and first-guess flows. This situation may be representative of real-word applications where these discrepancies are generally unknown, since the reference input parameters to be reconstructed are, by definition, not available. Furthermore, experiments performed in chapter 5 indicate that the performances of the ensemble-based variational schemes may be relatively insensitive to the statistics of the ensemble.

When only the modified concentration C^* is observed, no particular weighting in the cost function in (7.2) is considered, and the matrix $\mathbf{R}$ is taken as the identity matrix. In the case where both C^* and the velocity field $\boldsymbol{u}$ are observed, the different terms in (7.2) are normalized, through $\mathbf{R}$, by characteristics values of C^* and of the components of $\boldsymbol{U}$, that are chosen as the maximum absolute values of these quantities among the observations of the reference flow. The parameter ϵ_{POD} of the POD representation (7.7) is fixed to $\epsilon_{\mathrm{POD}} = 0.999$ in the experiments. This value ensures the derivation of an appropriate basis in (7.3) while significant information about the ensemble is kept. The iterative procedure summarized in table 7.1 is stopped after two or three iterations in order to limit the number of runs realized during the complete assimilation procedure. Accordingly, with $N_{en} = 20$, between 40 and 60 CFD simulations are performed in each DA experiment.

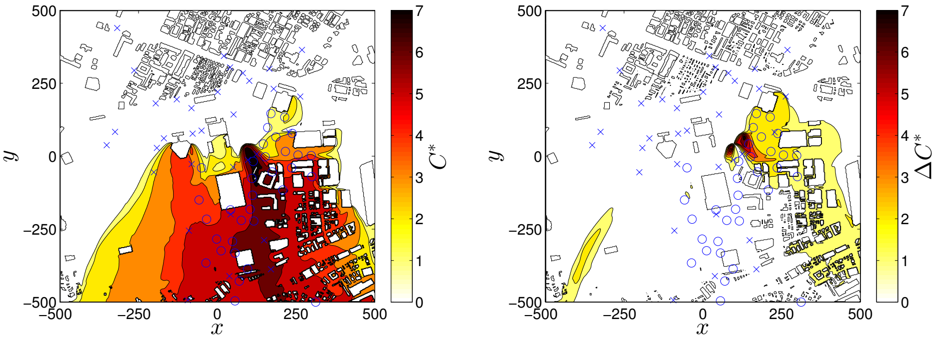

(a)

(b)

FIGURE 7.6: First guess flow used in cases A (figure 7.7) and B (figure 7.8): (a) modified concentration C^* and (b) error ΔC^* fields. The corresponding input vector $\boldsymbol{\gamma}^{f1}$ is described in table 7.2. Both standard (blue crosses) and optimized (blue circles) observation networks are reported.

7.6 Results of the data assimilation experiments

7.6.1 Reconstruction of scalar source parameters

In this subsection, the wind parameters α and U_H of the reference flow illustrated in figure 7.2 are assumed to be known, and the POD-EnVar methodology is employed to reconstruct the reference values of the scalar parameters x_s, y_s and d_s from observations of the modified concentration C^*. The first guess flow that is used to initialize the DA process for cases A and B is illustrated in figure 7.6, where both the modified concentration field C^* and error field ΔC^* are reported. The error ΔC^* is defined by

$$\Delta C^* = |C^* - C^{*\,ref}|, \tag{7.23}$$

where $C^{*\,ref}$ refers to the modified concentration of the reference flow (figure 7.2(a)). The discrepancies between the reference and first guess flows appear to be mainly concentrated in the vicinity of the reference position of the scalar source.

We first consider the use of the standard configuration of sensors for the assimilation, which corresponds to case A of table 7.3. The results of the corresponding DA procedure are illustrated in figure 7.7. In particular, the modified concentration field C^* that is obtained after three iterations of the POD-EnVar scheme is reported in figure 7.7(a). As confirmed by the comparison between figures 7.6(b) and 7.7(b), the discrepancies between the reference and estimated C^* fields have been significantly reduced by the assimilation process. However, it appears from figure 7.7(c) that the reconstructed scalar source does not well coincide with the reference one. While the reference position of the scalar source in the $x-$direction has been satisfactorily recovered, the DA procedure has not significantly improved the estimation of its position along the $y-$direction compared to the first guess flow. This is confirmed in figure 7.7(d) where is reported the evolution of the errors on the reference input parameters along the iterations of the POD-EnVar scheme. These errors are defined as

$$\epsilon(\gamma_i) = |\gamma_i - \gamma_i^{ref}|, \tag{7.24}$$

for the ith parameter, and are normalized by their values at the beginning of the assimilation process $\epsilon_0(\gamma_i)$. The evolution of the square root of the cost function J in (7.2) normalized by its initial value is also indicated. The fact that the DA procedure achieves a better reconstruction of the position of the source in the $x-$direction than in the $y-$direction is consistent with the results of the sensitivity analysis of section 7.4, which attributes a more important role to x_s than to y_s in the variability of the modified concentration field C^*, as shown in figures 7.4(c) and 7.4(d). Moreover, the results of figure 7.7 are satisfactory in the sense that the estimation of the field C^* is globally improved and that the errors on the three scalar source parameters have been reduced. A better precision

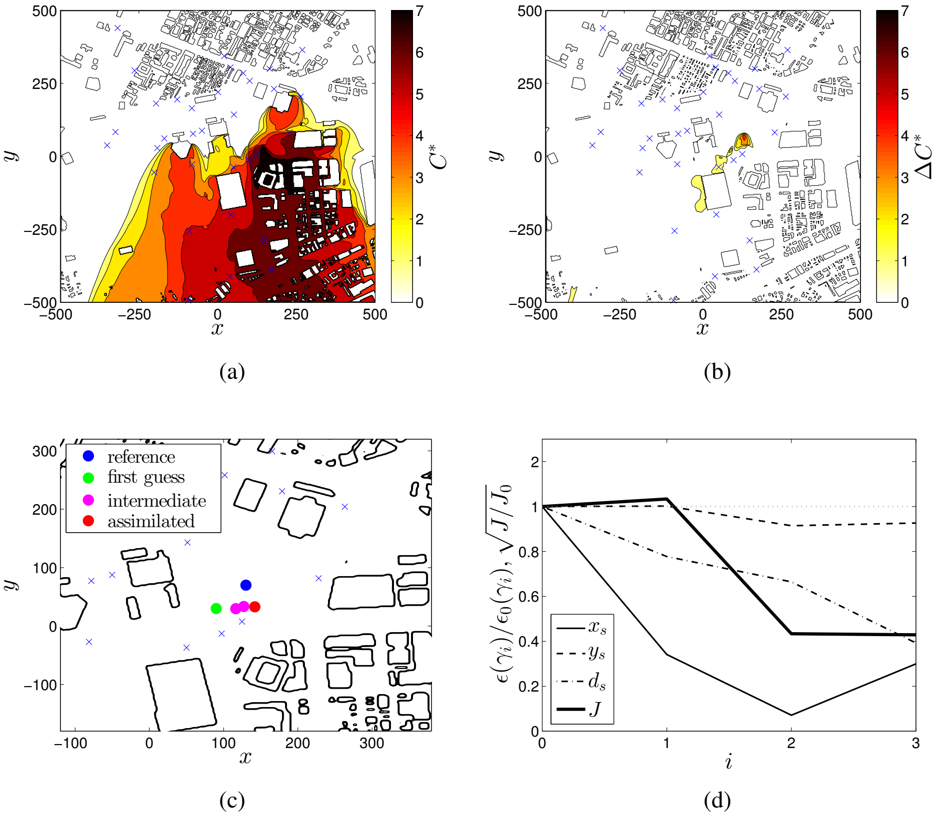

(a) (b)

(c) (d)

FIGURE 7.7: Results for case A in table 7.3 (reconstruction of the scalar source parameters, use of the first guess of figure 7.6, observations performed with the standard sensor network): (a) modified concentration C^* and (b) error ΔC^* fields of the assimilated flow obtained at the end of the assimilation procedure; (c) location of reference scalar source, first-guess source, intermediate assimilated sources, and assimilated source obtained at the end of the DA process. Blue crosses refer to the positions of the observations. (d) Errors on the input parameters and cost function J versus the iteration i of the POD-EnVar scheme.

in the location of the scalar source would be nevertheless appreciated. However, it seems unlikely to significantly improve the estimation of the input parameters by performing more computations with this DA setup given the relative stagnancy of the error indicators $\epsilon(\gamma_i)$ and J between the second and third iterations of the POD-EnVar scheme, as illustrated in figures 7.7(c)-7.7(d). Besides, figure 7.7(b) indicates that the discrepancies between the assimilated and reference C^* fields at observation locations are very low ($\Delta C^* < 1$), except for one sensor that is located at $x \simeq 50\,m$ and $y \simeq -37\,m$, near to the biggest building close to the center of the area (see figures 7.7(b)-7.7(c)). At this location, the Sobol´ indices associated to the scalar source parameters are negligible (figures 7.4(c)-7.4(e)). Accordingly, the standard observation network does not appear appropriate to further improve the estimation of x_s, y_s and d_s, since the corresponding sensors do not allow to identify significant discrepancies between the reference and assimilated flows and/or are placed at locations where C^* is not sensitive to a change in the scalar source parameters.

This leads to the consideration of case B where the optimized observation network obtained through the sensitivity analysis of section 7.4 is used. As illustrated in figure 7.6(b), much more sensors of the optimized configuration than of the standard network are located in regions of high discrepancies between the reference and the first guess flows. This confirms the good sensitivity-based placement of the sensors. Results of the assimilation procedure for case B are illustrated in figure 7.8. From the very first iteration of the POD-EnVar scheme, the reconstruction of the location of the scalar source is very good, both in $x-$ and $y-$ directions, as confirmed by figures 7.8(c)-7.8(d). The error on the estimation of the diameter d_s of the source has been slightly increased during the DA process, but d_s is the less imortant scalar parameter. Accordingly, the results obtained

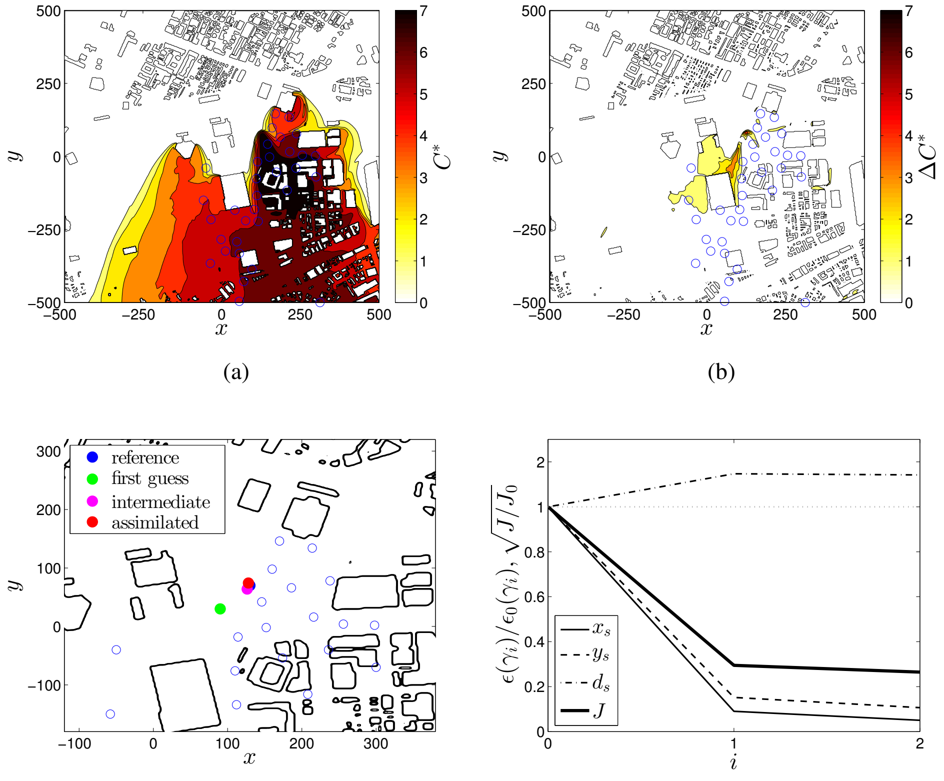

(a) (b)

(c) (d)

FIGURE 7.8: Results for case B in table 7.3 (reconstruction of the scalar source parameters, use of the first guess of figure 7.6, observations performed with the optimized sensor network): (a) modified concentration C^* and (b) error ΔC^* fields of the assimilated flow obtained at the end of the assimilation procedure; (c) location of reference scalar source, first-guess source, intermediate assimilated source, and assimilated source obtained at the end of the DA process. Blue circles refer to the positions of the observations. (d) Errors on the input parameters and cost function J versus the iteration i of the POD-EnVar scheme.

with the optimized configuration of sensors are very satisfactory in terms of reconstruction of the input parameters, and the POD-EnVar scheme is stopped after only two iterations given the moderate decrease in the cost function J between the first and second iterations. The corresponding assimilated C^* and ΔC^* fields are reported in figures 7.8(a) and 7.8(b) respectively. At all observation locations, it is observed that $\Delta C^* < 1$, which confirms the good reconstruction of the reference C^* field. The present results validate the present DA methodology and the choice of parameters for the POD-EnVar scheme, while they illustrate the impact of sensor placement on the performances of the DA procedure. The final errors on the reference values of x_s and y_s achieved at the end of the DA procedure, starting both from 40 m, are of 12.0 m and 37.1 m respectively for case A, where 60 CFD computations are performed, while these final errors are of 2.0 m and 4.3 m respectively for case B, which uses a total of 40 runs. These results thus support the efficacy of the proposed sensitivity analysis-based sensor placement procedure, which is further tested in the following.

7.6.2 Reconstruction of wind and scalar source parameters

We now consider the case where both wind and scalar source parameters are reconstructed with the POD-EnVar scheme. The first guess used in the following DA experiments (C-E) is illustrated in figure 7.9, and the corresponding input parameters γ^{f2} are reported in table 7.2. The latter correspond to a larger error on the position and diameter of the scalar source compared to the first guess used in section 7.6.1, and the errors on wind parameters are also relatively important. In particular, the error on the position of the source is of 60 m in both $x-$ and $y-$direction, and that on the wind angle α is of 30° with respect to the reference flow. The comparison

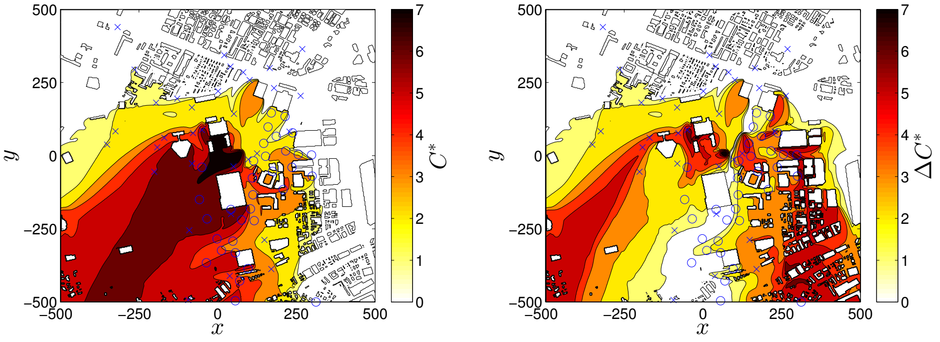

(a) (b)

FIGURE 7.9: First guess flow used in cases C (figure 7.10) , D (figure 7.11) and E (figure 7.12): (a) modified concentration C^* and (b) error ΔC^* fields. The corresponding input vector γ^{f2} is described in table 7.2. Both standard (blue crosses) and optimized (blue circles) observation networks are reported.

between figures 7.6(b) and 7.9(b) confirms that adding variability in the wind angle α has a drastic influence on the repartition of the modified concentration C^*, and huge discrepancies between the first guess and reference flows can be noticed over large parts of the city area.

The results of case C are first examined in figure 7.10, where the standard configuration of sensors is used for the assimilation. The comparison between figures 7.9(b) and 7.10(b) indicates that, in three iterations, the POD-EnVar scheme has effectively reduced the error on C^*. According to figures 7.10(c) and 7.10(d), the reference values of the wind angle α and of the coordinate x_s of the scalar source, which are the most influential parameters according to the sensitivity analysis of section 7.4, are satisfactorily recovered. The reconstruction of the diameter of the source d_s is also satisfactory, results concerning the wind intensity U_H are intermediate but surprisingly correct given the low sensitivity of C^* with respect to U_H, while the error on the coordinate y_s has been only slightly decreased during the assimilation procedure. Accordingly, the assimilated flow obtained with the POD-EnVar scheme is satisfactory on the whole, and the DA process has successfully dealt with this more complex inverse problem due to the consideration of the wind parameters. However, as in case A, a lack of precision in the identification of the position of the scalar source is noticed (figures 7.10(c)-7.10(d)), which originates from the insufficient improvement in the estimation of y_s. 60 CFD simulations have been performed to obtain these results, and it is not clear from figures 7.10(c) and 7.10(d) if significant further improvement in the quality of the assimilated flow could be obtained with more iterations of the POD-EnVar scheme.

The case where the optimized configuration of sensors is used in the DA process is investigated in figure 7.11, which corresponds to results of case D. As illustrated in figure 7.11(c) and 7.11(d), the reference input parameters are well recovered by the POD-EnVar scheme with this setup, and the identification of the location of the scalar source is very satisfactory. The errors on the wind angle α and on the coordinates x_s and y_s have been decreased by more than an order of magnitude in only two iterations of the assimilation procedure. The reconstruction of the diameter of the source d_s is not as good as for α, x_s and y_s, but remains correct. Only the estimation of the wind intensity U_H has not been improved by the POD-EnVar scheme, but U_H plays a negligible role in the sensitivity of the flow, as illustrated in figure 7.4. The discrepancies between the reference and assimilated C^* fields given in figure 7.11(b) have almost vanished compared to those between the reference and first guess flows reported in figure 7.9(b), except in a very narrow region that is not covered by the sensors. This confirms the excellent reconstruction of the flow and the fact that a bad estimation of U_H has no significant influence on the repartition of C^*. The observation of the velocity field $\boldsymbol{U}$ in addition to that of C^* could ensure a good estimation of U_H if needed, which is investigated in section 7.6.3. The comparison between the results of case C and D confirms the benefit of using sensitivity analysis-based placement of sensors. In particular, concerning the reconstruction of the three main input parameters, the final errors on α, x_s and y_s achieved at the end of the assimilation procedure are of 4.2°, 14.6 m and 44.0 m respectively for case C, while these errors are of 0.9°, 5.9 m and 0.2 m respectively for case D, starting from an error of 30° on α and of 60 m on both x_s and y_s. Besides,

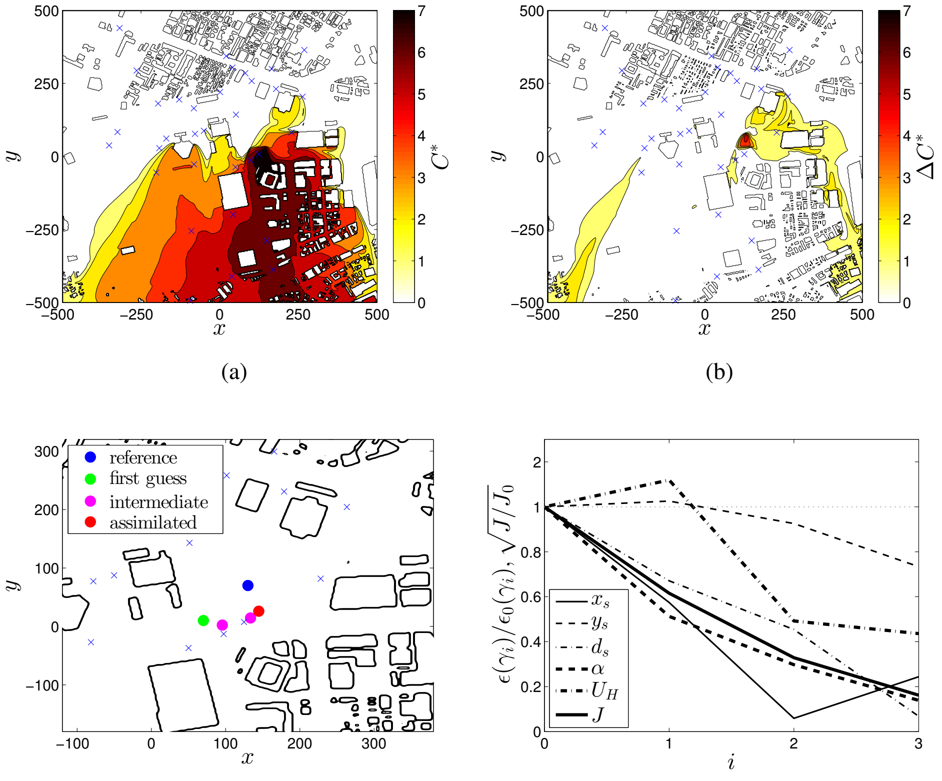

(a) (b)

(c) (d)

FIGURE 7.10: Results for case C in table 7.3 (reconstruction of wind and scalar source parameters, use of the first guess of figure 7.9, observations performed with the standard sensor network): (a) modified concentration C^* and (b) error ΔC^* fields of the assimilated flow obtained at the end of the assimilation procedure; (c) location of reference scalar source, first-guess source, intermediate assimilated sources, and assimilated source obtained at the end of the DA process. Blue crosses refer to the positions of the observations. (d) Errors on the input parameters and cost function J versus the iteration i of the POD-EnVar scheme.

60 CFD simulations are performed in case C, while 40 runs are required in case D. As in section 7.6.1, the proposed methodology for sensor placement appears efficient in terms of both accuracy of the reconstructed flow and computational cost of the DA procedure.

7.6.3 Observation of both concentration and velocity fields

Finally, the observation of the velocity field $\boldsymbol{U}$ in addition to the modified concentration field C^* is considered in case E whose corresponding results are reported in figure 7.12. The standard configuration of sensors is used, and the assimilation procedure is initialized with the same first guess than in cases C and D (see figure 7.9). As expected, the observation of the velocity field allows to achieve a better reconstruction of the wind parameters α and U_H than in cases C and D. In particular, if we compare with case C which relies on the same sensor configuration and number of realizations, the errors reached at the end of the DA process on α and U_H are of 4.2° and 0.9 m/s respectively in this case, while they are of 0.4° and 0.4 m/s respectively in case E, starting from errors of 30° and 2 m/s. Unavoidably, adding information about the velocity field in the cost function J in (7.2) reduces its sensitivity with respect to the scalar source parameters. This is illustrated in figures 7.12(c) and 7.12(d), which indicate that the DA process has left the estimation of x_s and y_s almost unchanged at the first iteration of the POD-EnVar scheme. However, after three iterations, the errors on x_s and y_s have been reduced nearly by half, with final errors of 32.5 m and 26.8 m respectively, compared to 14.6 m and 44.0 m respectively in case C, which roughly corresponds to the same distance between the reference and assimilated locations of the scalar source. Besides, the decrease in the error on the diameter d_s is quite satisfactory. According to the

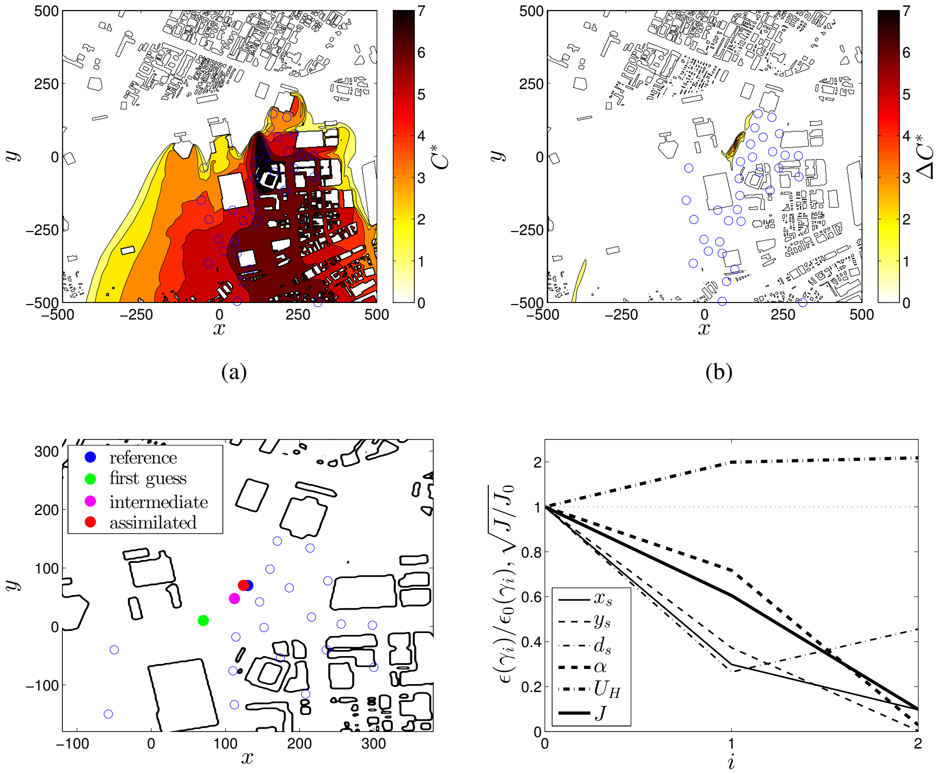

(a) (b)

(c) (d)

FIGURE 7.11: Results for case D in table 7.3 (reconstruction of wind and scalar source parameters, use of the first guess of figure 7.9, observations performed with the optimized sensor network): (a) modified concentration C^* and (b) error ΔC^* fields of the assimilated flow obtained at the end of the assimilation procedure; (c) location of reference scalar source, first-guess source, intermediate assimilated source, and assimilated source obtained at the end of the DA process. Blue circles refer to the positions of the observations. (d) Errors on the input parameters and cost function J versus the iteration i of the POD-EnVar scheme.

γ^f/case	$\epsilon(\alpha)$ (°)	$\epsilon(U_H)$ (m/s)	$\epsilon(x_s)$ (m)	$\epsilon(y_s)$ (m)	$\epsilon(d_s)$ (m)	sensors	N_{rn}
γ^{f1}	0	0	40.0	40.0	4.0	–	–
A	0	0	12.0	37.1	1.6	standard	60
B	0	0	2.0	4.3	6.8	optimized	40
γ^{f2}	30.0	2.0	60.0	60.0	6.0	–	–
C	4.2	0.9	14.6	44.0	0.4	standard	60
D	0.9	4.2	5.9	0.2	2.7	optimized	40
E	0.4	0.4	32.5	26.8	2.4	standard	60

TABLE 7.4: Errors $\epsilon(\gamma_i)$ defined in (7.24) on the input parameters reached at the end of experiments A-B using first guess γ^{f1} and experiments C-E using first guess γ^{f2}, the initial errors corresponding to the first guesses are also reported for the sake of comparison. The total number N_{rn} of CFD computations performed in each experiment and the configuration of sensors used are also indicated. Note that both velocity and concentration fields are observed in experiment E, while only the concentration field is measured in experiments A-D.

present results, after a few iterations of the POD-EnVar scheme, adding information about the velocity field in the cost function allows a relatively similar reconstruction of the scalar source parameters, while it significantly improves the estimation of the wind parameters.

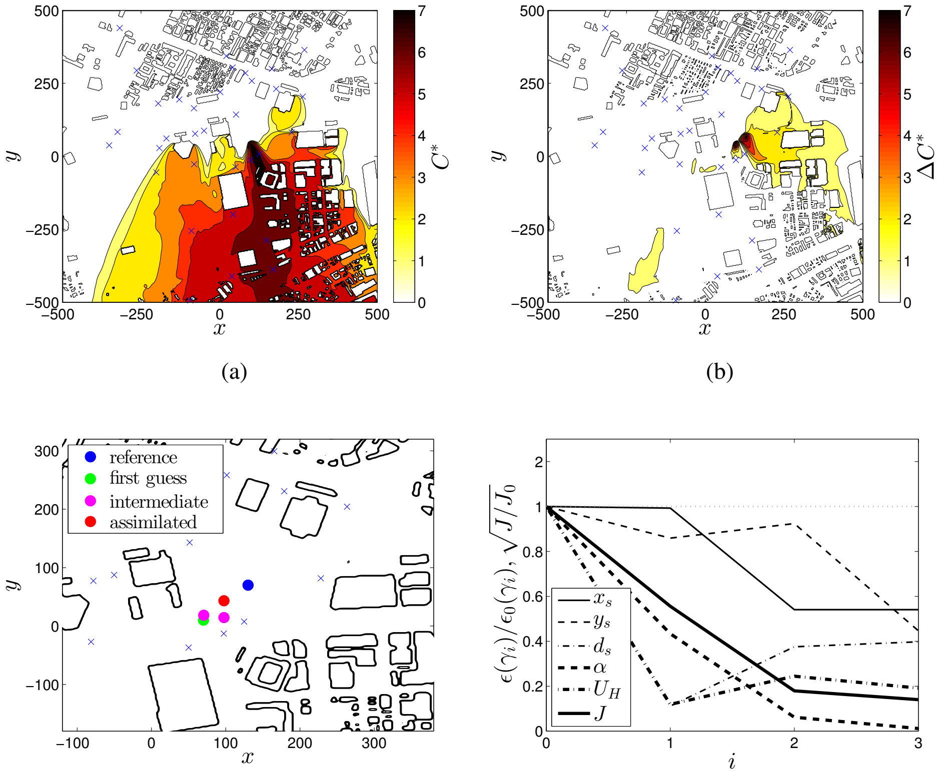

(a) (b)

(c) (d)

FIGURE 7.12: Results for case E in table 7.3 (reconstruction of wind and scalar source parameters, use of the first guess of figure 7.9, observations of both concentration and velocity fields performed with the standard sensor network): (a) modified concentration C^* and (b) error ΔC^* fields of the assimilated flow obtained at the end of the assimilation procedure; (c) location of reference scalar source, first-guess source, intermediate assimilated sources, and assimilated source obtained at the end of the DA process. Blue crosses refer to the positions of the observations. (d) Errors on the input parameters and cost function J versus the iteration i of the POD-EnVar scheme.

7.6.4 Measure of effectiveness

Table 7.4 summarizes the final errors $\epsilon(\gamma_i)$ defined in (7.24) reached at the end of the different DA experiments performed in this study, which may be compared with the initial errors for the corresponding first guesses. The use of the optimized sensor network allows to obtain a very satisfactory reduction in the error on the estimation of the coordinates x_s and y_s, and on that of the angle α in the case where wind parameters are considered. In addition to achieving a better reconstruction of these input parameters compared to the use of the standard sensors, less iterations of the POD-EnVar scheme are required in the former case. Results obtained with the optimized sensors concerning the diameter of the source d_s and the intensity of the wind U_H are less satisfactory, but these parameters are less important in the sensitivity of the gas concentration. One may wonder if even more precise results could be obtained concerning the estimations of α, x_s and y_s with more iterations of the DA procedure and using the optimized sensor configuration. However, given the results obtained so far, the improvement in the accuracy would be only marginal and hardly cost-effective. Besides, even if observations are generated synthetically, they can not be strictly perfect due to the finite duration of the simulations that is considered to perform time averaging (see section 7.3.2). Accordingly, keeping in mind that an expensive CFD solver is used, the present results obtained with the optimized sensors may be viewed as almost optimal. Moreover, the robustness of ensemble-based variational DA schemes with respect to noise in the observations is also confirmed in chapter 5.

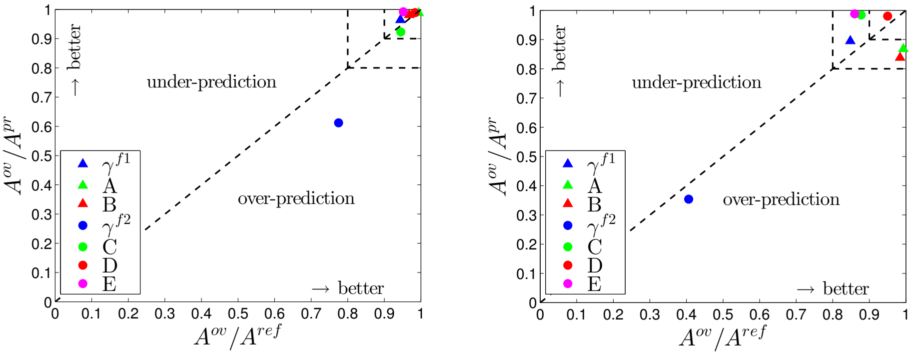

(a) (b)

FIGURE 7.13: Measure of effectiveness (MOE) for the thresholds (a) $C^{\text{MOE}} = 1$ ppm and (b) $C^{\text{MOE}} = 10^3$ ppm. Triangles refer to the DA experiments with the scalar source parameters only, dots to those with both scalar and wind parameters, while blue symbols correspond to the first guesses, green ones to the DA results obtained with the standard sensors, red ones to those obtained with the optimized configuration, and purple dots refer to the observation of both concentration and velocity fields.

Another way of assessing the performances of the DA process that is suitable for toxic gas dispersion applications is to consider the measure of effectiveness (MOE) discussed in [222], which allows a two-dimensional visualization of the global discrepancies between the assimilated and reference concentration fields. Given a predicted modified concentration field C^*, the reference field $C^{*\,ref}$, and a threshold of interest $C^{*\,MOE}$, we define the reference area A^{ref}, predicted area A^{pr} and overlap area A^{ov} as

$$A^{ref} = \iint_{\mathcal{V}^{ref}} dxdy, \quad \mathcal{V}^{ref} = \left\{(x,y) \in \mathcal{V} \middle| C^{*\,ref} \geq C^{*\,\text{MOE}}\right\}, \tag{7.25a}$$

$$A^{pr} = \iint_{\mathcal{V}^{pr}} dxdy, \quad \mathcal{V}^{pr} = \left\{(x,y) \in \mathcal{V} \middle| C^{*} \geq C^{*\,\text{MOE}}\right\}, \tag{7.25b}$$

$$A^{ov} = \iint_{\mathcal{V}^{ov}} dxdy, \quad \mathcal{V}^{ov} = \left\{(x,y) \in \mathcal{V} \middle| C^{*\,ref} \geq C^{*\,\text{MOE}}, C^{*} \geq C^{*\,\text{MOE}}\right\}, \tag{7.25c}$$

and the two-dimensional MOE in the plane with $x-$ and $y-$axes is evaluated according to

$$\text{MOE} = (x,y) = \left(\frac{A^{ov}}{A^{ref}}, \frac{A^{ov}}{A^{pr}}\right). \tag{7.26}$$

This representation provides relatively detailed information about the quality of the predicted concentration field as follows. According to the above definitions, we have $0 \leq x \leq 1$ and $0 \leq y \leq 1$. Point $(0,0)$ corresponds to the case where there is strictly no overlapping between the predicted and reference regions where the modified concentration is above the threshold $C^{*\,\text{MOE}}$, while point $(1,1)$ corresponds to a perfect agreement with $A^{ov} = A^{pr} = A^{ref}$. In the region defined by $x > y$, the area where the concentration is above $C^{*\,\text{MOE}}$ is overestimated compared to the reference one, while in the case $y > x$ there is underestimation of the size of the region where the gas lies. Along the line $x = 1$, the reference field is completely included in the predicted one, while for $y = 1$ the reference field completely envelops the predicted one.

The MOE for the two first guess flows considered in this study and for the assimilated flows obtained at the end of the DA process in experiments A-E are reported for the thresholds $C^{*\,\text{MOE}} = 1$ ($\Leftrightarrow$ $C^{\text{MOE}} = 1$ ppm) and $C^{*\,\text{MOE}} = 4$ ($\Leftrightarrow$ $C^{\text{MOE}} = 10^3$ ppm) in figures 7.13(a) and 7.13(b) respectively. Considering the threshold $C^{\text{MOE}} = 1$ ppm allows to assess the reconstruction of the whole area where gas is present (if concentrations < 1ppm are considered as negligible). It appears from figure 7.13(a) that the first guess with corresponding input vector $\boldsymbol{\gamma}^{f1}$, which is used in experiments A and B where only the scalar source parameters are reconstructed, already correctly predicts the area where the gas is present. The DA process still allows to further improve this estimation, and the MOE values for the assimilated flows obtained with the standard (experiment A) and optimized (experiment B) configurations of sensors are both very close to point $(1, 1)$. Experiments C-E where both wind and scalar parameters are reconstructed rely on the first guess with input vector $\boldsymbol{\gamma}^{f2}$, which corresponds to a significantly poorer estimation of the region of presence of the gas. This estimation is greatly improved by the DA process, and experiments C-E achieve relatively similar MOE values close to point $(1, 1)$, with slightly better results obtained with the optimized sensors. The reconstruction of regions with high concentration levels ($C^{\mathrm{MOE}} = 10^3$ ppm) is investigated in figure 7.13(b). It appears from the comparison between figures 7.13(a) and 7.13(b) that the error on the identification of the area of high concentration levels is higher than the error on the area of presence of the gas for the two first guesses. In particular, the first guess with input vector $\boldsymbol{\gamma}^{f2}$ corresponds to a very crude identification of the high concentration regions. Experiments A and B achieve similar enhancement in the estimation of the area of high concentration levels, and the reference high concentration regions are almost completely included in the assimilated ones. Concerning the results of experiments C-E, a drastic improvement in the prediction of the high concentration regions is obtained compared to the corresponding first guess. Experiments C and E give comparable predictions, which confirms that adding velocity information in the cost function in (7.2) does not degrade the quality of the reconstructed concentration field in favor of that of the velocity field. The best results are obtained in experiment D where the optimized sensor network is employed. This indicates that a lack of precision in the identification of the parameters d_s and U_H has no significant influence on the quality of the assimilated concentration field.

7.7 Conclusion

The application of data assimilation (DA) to the reconstruction of urban flows has been investigated in this chapter. An ensemble-based variational scheme has been implemented in conjunction with a Very Large Eddy Simulation (VLES)/Lattice Boltzmann Method (LBM) solver providing high-fidelity estimations of the flow in an actual urban area. The present results indicate that the proposed methodology is suitable for the identification of source characteristics and wind parameters from measurements of the gas concentration at discrete locations. In particular, with an appropriate DA setup, the position of the source and the direction of the wind are identified with an accuracy of only a few meters and better than one degree respectively, starting from uncertainties of almost a hundred meters in terms of distance from the reference source and of 30° on the wind angle. Besides, the computational cost associated to the DA process remains affordable since between 40 and 60 CFD simulations are performed to obtain the above results. Accordingly, this study demonstrates both the practicability and effectiveness of using DA in conjunction with high-fidelity CFD to solve inverse problems in full-scale urban environments (medium range dispersion in an area of 1km^2).

The present results also highlight the importance of the locations of the sensors to measure the flow in the performances of the DA process. A sensor placement methodology based on sensitivity analysis results has been proposed and assessed in this study. Both reduction in the computational cost and significant improvement in the quality of the reconstructed input parameters is achieved through appropriate sensor placement. Such results encourage the consideration of uncertainty quantification/sensitivity analysis methods in large-scale DA/inverse problem studies, both for the *a priori* design of the DA setup and as diagnostic tools of the assimilation results.

Even if the five parameters considered here are sufficient to obtain meaningful results, future studies could include more variables for the inverse problem in order to, among others, allow a more detailed parameterization of the wind profile, including time variability, or to take into account atmospheric stability. Such refinements could facilitate the use of real experimental data.

Chapter 8

Global conclusions and perspectives

8.1 Data assimilation and spectral modelling for the study of homogeneous turbulence

In part I, data assimilation (DA) and eddy-damped quasi-normal Markovian (EDQNM)-based modelling have been used to investigate the physics of homogeneous turbulence. Main results are:

- In chapter 3, detailed results about grid turbulence decay have been obtained through the combination of DA with the EDQNM model for homogeneous isotropic turbulence (HIT). The adjoint EDQNM model has been developed, and the scale-by-scale first-order sensitivity of HIT decay with respect to initial conditions has been quantified thanks to optimal control techniques. The results thus obtained confirm the major role of the peak of the energy spectrum in turbulence decay, and indicate that small scales and scales larger than ten times the integral scale have a negligible influence on turbulence dynamics. The present results also suggest that initial condition effects may possibly explain alone anomalous decay regimes encountered in, e.g., fractal-grid turbulence experiments.
- In chapter 4, a spectral model for homogeneous turbulence in the presence of mean velocity gradients has been developed. This model combines: i) a spherically-averaged level of description fully consistent with the irreducible anisotropic decomposition of the spectral tensor, ii) Rapid Distortion Theory-based linear term modelling and iii) EDQNM-based modelling for nonlinear terms. The proposed model is suited to the study of sheared turbulence and its return to isotropy, as confirmed by the various comparisons with experimental and Direct Numerical Simulation results.

DA has thus proved to be a valuable and efficient tool to identify the characteristics of the energy spectrum that lead HIT decay, encouraging the extension of such a study to more complex turbulent flows. The spectral model of chapter 4 seems a suitable candidate to incorporate anisotropy effects in future DA-based investigations of grid turbulence decay. Indeed, analytical spherical integration results in a significant decrease in computational cost compared to spectral models in 3D Fourier space, which is valuable in the case where the direct model, and possibly its adjoint, are called numerous times, as in DA algorithms. Other quantities than initial conditions could be considered in the assimilation process, such as the mean flow gradient or another external forcing term. More generally, DA could be used to perform detailed sensitivity analyses of the dynamics of other turbulent flows of theoretical or practical interest. EDQNM modelling would be still a numerical method of choice for more complex homogeneous turbulent flows such as rotating flows or with stable/unstable stratification due to their relatively low computational cost compared to DNS and their ability to investigate flows in the high Reynolds regime. Ensemble methods could be considered in the case of too complex direct solvers instead of variational DA.

8.2 Data assimilation in the context of computational fluid dynamics

In part II, the potentiality of applying DA to computational fluid dynamics (CFD) is explored along with methodological aspects. Main results are:

- In chapter 5, variational DA, ensemble Kalman filters and ensemble-based variational schemes have been implemented in conjunction with a Navier-Stokes solver for unsteady compressible flows. In particular, the corresponding adjoint code has been developed. These techniques have been used to infer initial and boundary conditions from various types of observations of the flow past a cylinder in the presence of coherent gusts. DA has been considered in both deterministic and stochastic frameworks. It is found from extensive investigations with large control vectors up to $\approx 10^5$ variables that, in a context of nearly perfect model and observations, variational techniques achieve the best identification of the observed flows. Ensemble Kalman filters allow to avoid the tedious coding of the adjoint code, but significant *ad hoc* adjustments have to be considered to ensure the stability of the filter. According to the present results, ensemble-based variational schemes appear less sensitive with respect to the characteristics of the ensemble, and their robustness compared to ensemble Kalman filters and non-intrusiveness compared to variational schemes make them appealing for complex CFD applications.
- In chapter 6, an adjoint-based sensor placement procedure has been proposed and applied to the reconstruction of flows past a rotationally oscillating cylinder. It is found that both reduction in the computational cost of the DA procedure and improvement in the accuracy of the identified rotational speed of the cylinder are achieved through optimal sensor placement. Gains may be as large as a reduction by a factor five in the number of calls to the direct and adjoint codes required in the assimilation process, while achieving a reconstruction that is five times better in terms of discrepancies with the reference flow.
- In chapter 7, ensemble-based variational DA has been successfully deployed in conjunction with a Large Eddy Simulation solver for the identification of pollutant source characteristics and meteorological conditions from concentration measurements in an actual full-scale urban environment. A non-intrusive sensor placement procedure, which relies on global sensitivity analysis methods, has been developed to guide the design of observation networks. In the present results, the location of the source is identified within a few meters through DA and appropriate sensor placement, and wind conditions are also reconstructed with high accuracy, with a total number of 40 CFD simulations in the assimilation process.

As illustrated through the various test cases considered here, DA appears as a valuable tool to infer appropriate inputs for CFD solvers from external information, thus allowing to enhance the prediction of flows of interest. However, despite encouraging results obtained in the present thesis, a remaining obstacle to the use of DA for the most intensive CFD applications may be computational cost. Concerning variational techniques, reduced order modelling approaches discussed in [66] that are based on the projection of both direct and adjoint models onto proper orthogonal decomposition (POD) bases could allow to speed up the assimilation process. Such methods may nonetheless still require the development of an adjoint code. In the framework of ensemble methods, non-intrusive meta-modelling techniques such as Kriging [109] could be considered in order to avoid too many calls to the CFD solver. An advantage of Kriging is that it provides an estimation of the error associated to the response surface, thus facilitating the simultaneous use of the direct code and surrogate model in ensemble-based DA.

However, the development of response surface methodologies that are appropriate for large-scale systems in the presence of high-dimensional uncertainties such as encountered in DA is still an open issue. Efficient strategies could be based on [116, 150, 198], where stochastic representations such as polynomial chaos expansion or analysis of variance representation, possibly allowing dimension reduction in the meta-modelling process, are combined with Kriging and/or POD techniques along with adaptive criteria for refinement in order to significantly decrease the computational cost for the construction of the surrogate model. In a purely probabilistic framework, fully coupled DA schemes and stochastic representations could be considered. An example is the probabilistic collocation-based Kalman filter (PCKF) [134, 135] where a polynomial chaos expansion is used instead of the direct model in an ensemble Kalman filter, allowing to avoid finite ensemble size effects during the assimilation process. This methodology could be extended to particle filtering, thus possibly facilitating its use in the context of CFD.

Generally speaking, DA could benefit from the coupling with sensitivity analysis and uncertainty quantification (UQ) techniques in order to, among others, perform meta-optimization of the DA setup. A first application is the design of efficient observation networks, which may significantly improve the performances of the DA process, as illustrated in chapter 7 with the methodologies developed in [148, 150]. A second application could be the determination of an ‘optimal’ form for the control vector in the DA problem through the *a priori* identification of the most important control variables. Sensitivity analysis techniques [63] could be considered in order to reduce the size of the control vector, thus possibly allowing to speed up the convergence of the assimilation procedure. Both DA and UQ with potential coupling are thus promising methodologies to go beyond direct analysis in CFD through the evaluation and reduction of the uncertainties in numerical prediction of complex flows due to badly known input parameters.

Appendix A

Derivation of the adjoint EDQNM model

Both continuous and discrete adjoint EDQNM models for isotropic turbulence are derived in this appendix. Validation aspects are also illustrated. More details may be found in chapter 3.

A.1 Continuous adjoint model

The continuous adjoint EDQNM model is derived in this section. First, notations of chapter 3 are recalled. Given an operator Ψ from vector space $\mathcal{A}$ to vector space $\mathcal{B}$, the Gâteaux derivative of Ψ at E in the direction F, with both E and F in $\mathcal{A}$, is denoted by

$$\left\langle \frac{\partial \Psi}{\partial E}(E), F \right\rangle_{\mathcal{A}} = \left.\frac{\partial \Psi}{\partial E}\right|_{E}(F) = \lim_{\epsilon \to 0} \frac{d}{d\epsilon}\Psi(E + \epsilon F). \tag{A.1}$$

If Ψ is a linear operator, its adjoint operator is denoted by Ψ^* and is defined by

$$\langle \Psi(E), G \rangle_{\mathcal{B}} = \langle E, \Psi^*(G) \rangle_{\mathcal{A}} \quad \forall E \in \mathcal{A}, \forall G \in \mathcal{B}. \tag{A.2}$$

In the following, $\mathcal{M}$ and $\mathcal{O}$ refer to model and observation spaces respectively, and the inner product of two vectors a and b in the model space is defined by

$$\langle a, b \rangle_{\mathcal{M}} = \int_0^{T_f} \int_0^{\infty} a(k,t) b(k,t) dk dt. \tag{A.3}$$

The EDQNM model for isotropic turbulence is

$$\frac{\partial E}{\partial t}(k) + 2\nu k^2 E(k) = T(E,k), \tag{A.4a}$$

$$T(E,k) = \iint_{\Delta_k} \theta_{kpq} G_{kpq} E(q)(k^2 E(p) - p^2 E(k)) dp dq, \tag{A.4b}$$

$$G_{kpq} = \frac{xy + z^3}{q}, \quad \theta_{kpq} = \frac{1 - e^{-\mu_{kpq} t}}{\mu_{kpq}}, \quad \mu_{kpq} = \nu(k^2 + p^2 + q^2) + \eta_k + \eta_p + \eta_q, \tag{A.4c}$$

$$\eta_k = A \sqrt{\int_0^k r^2 E(r) dr}. \tag{A.4d}$$

For the sake of readability, time dependency is omitted in the above expressions. We consider the Lagrangian $\mathcal{L}$ defined by

$$\mathcal{L}(E, \tilde{E}) = \frac{1}{2} \|y - H(E)\|_{\mathcal{O}}^2 + \left\langle \tilde{E}, \frac{\partial E}{\partial t} + 2\nu k^2 E - T(E) \right\rangle_{\mathcal{M}}, \tag{A.5}$$

where $\tilde{E}$ is the adjoint spectrum, y refers to observations of a reference decay and H is the observation operator that maps the model space to the observation space. Using (A.2) and after integration by parts, first-order optimality conditions are given by

$$\begin{aligned}\Big\langle \frac{\partial \mathcal{L}}{\partial E}(E,\tilde{E}),F\Big\rangle_{\mathcal{M}} =& \Big\langle \Big(\frac{\partial H}{\partial E}\Big|_E\Big)^*(H(E)-y) - \frac{\partial \tilde{E}}{\partial t} + 2\nu k^2\tilde{E} - \Big(\frac{\partial T}{\partial E}\Big|_E\Big)^*(\tilde{E}),F\Big\rangle_{\mathcal{M}} \\ &+ \int_0^\infty (\tilde{E}(k,T_f)F(k,T_f) - \tilde{E}(k,0)F(k,0))dk = 0 \ \ \forall F \in \mathcal{M},\end{aligned} \tag{A.6a}$$

$$\Big\langle \frac{\partial \mathcal{L}}{\partial \tilde{E}}(E,\tilde{E}),\tilde{F}\Big\rangle_{\mathcal{M}} = \Big\langle \frac{\partial E}{\partial t} + 2\nu k^2 E - T(E),\tilde{F}\Big\rangle_{\mathcal{M}} = 0 \ \ \forall \tilde{F} \in \mathcal{M}, \tag{A.6b}$$

which may be translated into

$$\frac{\partial E}{\partial t}(k) + 2\nu k^2 E(k) - T(E,k) = 0, \tag{A.7a}$$

$$-\frac{\partial \tilde{E}}{\partial t}(k) + 2\nu k^2 \tilde{E}(k) - \tilde{T}|_E(\tilde{E},k) = \tilde{H}|_E(y - H(E),k), \tag{A.7b}$$

$$\tilde{E}(k,T) = \tilde{E}(k,0) = 0, \tag{A.7c}$$

with

$$\tilde{T}|_E(\tilde{E},k) = \Big(\frac{\partial T}{\partial E}\Big|_E\Big)^*(\tilde{E},k),\ \tilde{H}|_E(\tilde{E},k) = \Big(\frac{\partial H}{\partial E}\Big|_E\Big)^*(\tilde{E},k). \tag{A.8}$$

The most difficult part in the derivation of the adjoint EDQNM model is the determination of the adjoint operator $\tilde{T}|_E(\tilde{E},k)$. We consider the following splitting

$$\Big\langle \tilde{E}, \frac{\partial T}{\partial E}\Big|_E(F)\Big\rangle_{\mathcal{M}} = I_1 + I_2, \tag{A.9a}$$

$$I_1 = \int_0^T\int_0^\infty \tilde{E}(k)\iint_{\Delta_k}\theta_{kpq}G_{kpq}\big[F(q)(k^2E(p) - p^2E(k)) + F(p)k^2E(q) - F(k)p^2E(q)\big]dpdqdkdt, \tag{A.9b}$$

$$I_2 = \int_0^T\int_0^\infty \tilde{E}(k)\iint_{\Delta_k}\frac{\partial\theta_{kpq}}{\partial E}\Big|_E(F)G_{kpq}E(q)(k^2E(p) - p^2E(k))dpdqdkdt. \tag{A.9c}$$

The contribution I_1 is first examined. Concerning the term in $F(p)$, the following simplications can be made through the use of Fubini's theorem

$$\begin{aligned}&\int_0^T\int_0^\infty \tilde{E}(k)\iint_{\Delta_k}\theta_{kpq}G_{kpq}F(p)k^2E(q)dpdqdkdt = \int_0^T\int_0^\infty\iint_{\Delta_k}\tilde{E}(k)\theta_{kpq}G_{kpq}F(p)k^2E(q)dpdqdkdt = \\ &\int_0^T\int_0^\infty\iint_{\Delta_p}\tilde{E}(k)\theta_{kpq}G_{kpq}F(p)k^2E(q)dkdqdpdt = \int_0^T\int_0^\infty F(p)\iint_{\Delta_p}\tilde{E}(k)\theta_{kpq}G_{kpq}k^2E(q)dkdqdpdt = \\ &\int_0^T\int_0^\infty F(k)\iint_{\Delta_k}\tilde{E}(p)\theta_{pkq}G_{pkq}p^2E(q)dpdqdkdt.\end{aligned} \tag{A.10}$$

Using similar results for the term in $F(q)$, I_1 can be rewritten as

$$\begin{aligned}I_1 = \int_0^T\int_0^\infty F(k)\Big\{&\iint_{\Delta_k}\theta_{pkq}G_{pkq}\tilde{E}(p)p^2E(q)dpdq + \iint_{\Delta_k}\theta_{qpk}G_{qpk}\tilde{E}(q)(q^2E(p) - p^2E(q))dpdq \\ &- \iint_{\Delta_k}\theta_{kpq}G_{kpq}\tilde{E}(k)p^2E(q)dpdq\Big\}dkdt.\end{aligned} \tag{A.11}$$

Concerning the contribution I_2, we first use

$$\frac{\partial\theta_{kpq}}{\partial E}\Big|_E(F) = \frac{-1+(\mu_{kpq}t+1)e^{-\mu_{kpq}t}}{\mu_{kpq}^2}\Big(\frac{\partial\eta_k}{\partial E}\Big|_E(F)+\frac{\partial\eta_p}{\partial E}\Big|_E(F)+\frac{\partial\eta_q}{\partial E}\Big|_E(F)\Big), \tag{A.12a}$$

$$\frac{\partial\eta_k}{\partial E}\Big|_E(F) = \frac{A^2}{2}\frac{\int_0^k r^2F(r)dr}{\eta_k}. \tag{A.12b}$$

I_2 can thus be rewritten as

$$I_2 = \int_0^T\int_0^\infty \tilde{E}(k)\iint_{\Delta_k}\mathcal{D}_{kpq}\left\{\frac{\int_0^k r^2F(r)dr}{\eta_k}+\frac{\int_0^p r^2F(r)dr}{\eta_p}+\frac{\int_0^q r^2F(r)dr}{\eta_q}\right\}dpdqdkdt, \tag{A.13a}$$

$$\mathcal{D}_{kpq} = \frac{A^2}{2}\frac{-1+(\mu_{kpq}t+1)e^{-\mu_{kpq}t}}{\mu_{kpq}^2}G_{kpq}E(q)(k^2E(p)-p^2E(k)). \tag{A.13b}$$

Similarly to the derivations in (A.10), the term in $\frac{1}{\eta_p}$ in (A.13a) is simplified as

$$\begin{aligned}&\int_0^T\int_0^\infty \tilde{E}(k)\iint_{\Delta_k}\frac{\mathcal{D}_{kpq}}{\eta_p}\int_0^p r^2F(r)drdpdqdkdt = \int_0^T\int_0^\infty\iint_{\Delta_k}\int_0^p \tilde{E}(k)\frac{\mathcal{D}_{kpq}}{\eta_p}r^2F(r)drdpdqdkdt =\\&\int_0^T\int_0^\infty\iint_{\Delta_p}\int_0^p \tilde{E}(k)\frac{\mathcal{D}_{kpq}}{\eta_p}r^2F(r)drdkdqdpdt = \int_0^T\int_0^\infty\int_0^p\iint_{\Delta_p}\tilde{E}(k)\frac{\mathcal{D}_{kpq}}{\eta_p}r^2F(r)dkdqdrdpdt =\\&\int_0^T\int_0^\infty\int_r^\infty\iint_{\Delta_p}\tilde{E}(k)\frac{\mathcal{D}_{kpq}}{\eta_p}r^2F(r)dkdqdpdrdt = \int_0^T\int_0^\infty F(r)\int_r^\infty\iint_{\Delta_p}\tilde{E}(k)\frac{\mathcal{D}_{kpq}}{\eta_p}r^2dkdqdpdrdt =\\&\int_0^T\int_0^\infty F(k)\int_k^\infty\iint_{\Delta_p}\tilde{E}(r)\frac{\mathcal{D}_{rpq}}{\eta_p}k^2drdqdpdkdt.\end{aligned} \tag{A.14}$$

Accordingly, using similar results for terms in $\frac{1}{\eta_k}$ and $\frac{1}{\eta_q}$, I_2 can be rewritten as

$$I_2 = \int_0^T\int_0^\infty F(k)\left\{\int_k^\infty\iint_{\Delta_r}\tilde{E}(r)\frac{\mathcal{D}_{rpq}}{\eta_r}k^2dpdqdr+\int_k^\infty\iint_{\Delta_p}\tilde{E}(r)\frac{\mathcal{D}_{rpq}}{\eta_p}k^2drdqdp+\int_k^\infty\iint_{\Delta_q}\tilde{E}(r)\frac{\mathcal{D}_{rpq}}{\eta_q}k^2dpdrdq\right\}dkdt, \tag{A.15}$$

and the final expression of $\tilde{T}|_E(\tilde{E},k)$ is

$$\begin{aligned}\tilde{T}|_E(\tilde{E},k) = &\iint_{\Delta_k}\left[\theta_{pkq}G_{pkq}\tilde{E}(p)p^2E(q)+\theta_{qpk}G_{qpk}\tilde{E}(q)(q^2E(p)-p^2E(q))-\theta_{kpq}G_{kpq}\tilde{E}(k)p^2E(q)\right]dpdq\\&+\int_k^\infty\iint_{\Delta_r}\tilde{E}(r)\frac{\mathcal{D}_{rpq}}{\eta_r}k^2dpdqdr+\int_k^\infty\iint_{\Delta_p}\tilde{E}(r)\frac{\mathcal{D}_{rpq}}{\eta_p}k^2drdqdp+\int_k^\infty\iint_{\Delta_q}\tilde{E}(r)\frac{\mathcal{D}_{rpq}}{\eta_q}k^2dpdrdq.\end{aligned} \tag{A.16}$$

A.2 Discrete adjoint model

We now consider the discrete adjoint approach. Given the spatio-temporal discretization

$$E_i^l = E(k_i,t^l),\quad k_i = k_0r^{i-1}\quad t^{l+1} = t^l+\Delta t^l,\quad i\in\{1;...;N\},\quad l\in\{0;...;M\}, \tag{A.17}$$

The discretized EDQNM model using an Euler scheme for time integration is

$$\boldsymbol{E}^{l+1} = \boldsymbol{m}^l(\boldsymbol{E}^l), \tag{A.18a}$$

$$m_i^l = E_i^l + \Delta t^l (T_i^l - 2\nu k_i^2 E_i^l), \tag{A.18b}$$

$$T_i^l = \sum_{p=1}^{N} \sum_{q=1}^{N} \theta_{ipq}^l C_{ipq} E_q^l (E_p^l k_p k_i^2 - E_i^l k_p^3) dS_{ipq}, \tag{A.18c}$$

$$C_{ipq} = x_{ipq} y_{ipq} + z_{ipq}^3, \tag{A.18d}$$

$$\theta_{ipq}^l = \frac{1 - e^{-\mu_{ipq}^l t^l}}{\mu_{ipq}^l}, \quad \mu_{ipq}^l = \nu(k^2 + p^2 + q^2) + N_{ipq}^l, \quad N_{ipq}^l = \eta_i^l + \eta_p^l + \eta_q^l, \tag{A.18e}$$

$$\eta_i^l = A \sqrt{\sum_{r=1}^{i} k_r^3 E_r^l dS'_{ri}}. \tag{A.18f}$$

The terms dS_{ipq} et dS'_{ri} refer to ponderation factors of quadrature rules taking into account the geometric discretization and the constraint on the vector triads. We consider the following Lagrangian

$$\mathcal{L} = \frac{1}{2} \sum_{l=0}^{M} \left(\boldsymbol{y}^l - \boldsymbol{h}(\boldsymbol{E}^l)\right)^{\mathrm{T}} (\boldsymbol{y}^l - \boldsymbol{h}(\boldsymbol{E}^l)) - \sum_{l=0}^{M-1} \left(\boldsymbol{E}^{l+1} - \boldsymbol{m}^l(\boldsymbol{E}^l)\right)^{\mathrm{T}} \tilde{\boldsymbol{E}}^{l+1}. \tag{A.19}$$

First-order optimality conditions are

$$\boldsymbol{E}^{l+1} = \boldsymbol{m}^l(\boldsymbol{E}^l) \quad 1 \le l \le M, \tag{A.20a}$$

$$\tilde{\boldsymbol{E}}^M = \boldsymbol{f}^M, \tag{A.20b}$$

$$\tilde{\boldsymbol{E}}^l = \tilde{\mathbf{M}}^l \tilde{\boldsymbol{E}}^{l+1} + \boldsymbol{f}^l \quad 0 \le l \le M-1, \tag{A.20c}$$

$$\tilde{\boldsymbol{E}}^0 = \mathbf{0}, \tag{A.20d}$$

with

$$\boldsymbol{f}^l = \left(\frac{\partial \boldsymbol{h}}{\partial \boldsymbol{E}^l}(\boldsymbol{E}^l)\right)^{\mathrm{T}} \left(\boldsymbol{h}(\boldsymbol{E}^l) - \boldsymbol{y}^l\right), \quad \tilde{\mathbf{M}}^l = \left(\frac{\partial \boldsymbol{m}^l}{\partial \boldsymbol{E}^l}(\boldsymbol{E}^l)\right)^{\mathrm{T}}. \tag{A.21}$$

The components of the adjoint operator $\tilde{\mathbf{M}}^l$ are given by

$$\tilde{M}_{ij}^l = \delta_{ij} + \Delta t^l \left(\frac{\partial T_j^l}{\partial E_i^l} - 2\nu k_j^2 \delta_{ij}\right), \tag{A.22}$$

with

$$\begin{aligned} \frac{\partial T_i^l}{\partial E_j^l} = & \sum_{p=1}^{N} \sum_{q=1}^{N} \frac{-1 + (\mu_{ipq}^l t^l + 1) e^{-\mu_{ipq}^l t^l}}{(\mu_{ipq}^l)^2} \frac{\partial N_{ipq}^l}{\partial E_j^l} C_{ipq} E_q^l (E_p^l k_p k_i^2 - E_i^l k_p^3) dS_{ipq} + \sum_{q=1}^{N} \theta_{ijq}^l C_{ijq} E_q^l k_j k_i^2 dS_{ijq} \\ & + \sum_{p=1}^{N} \theta_{ipj}^l C_{ipj} (E_p^l k_p k_i^2 - E_i^l k_p^3) dS_{ipj} - \delta_{ij} \sum_{p=1}^{N} \sum_{q=1}^{N} \theta_{ipq}^l C_{ipq} E_q^l k_p^3 dS_{ipq}, \end{aligned} \tag{A.23a}$$

$$\frac{\partial N_{ipq}^l}{\partial E_j^l} = \left\{ \begin{array}{cc|c} i < j & i \geqslant j & \\ \hline 0 & \frac{A^2}{2\eta_i^l} k_j^3 dS'_{ji} & p < j,\ q < j \\ \frac{A^2}{2\eta_p^l} k_j^3 dS'_{jp} & \frac{A^2}{2} k_j^3 \left(\frac{dS'_{ji}}{\eta_i^l} + \frac{dS'_{jp}}{\eta_p^l}\right) & p \geqslant j,\ q < j \\ \frac{A^2}{2\eta_q^l} k_j^3 dS'_{jq} & \frac{A^2}{2} k_j^3 \left(\frac{dS'_{ji}}{\eta_i^l} + \frac{dS'_{jq}}{\eta_q^l}\right) & p < j,\ q \geqslant j \\ \frac{A^2}{2} k_j^3 \left(\frac{dS'_{jp}}{\eta_p^l} + \frac{dS'_{jq}}{\eta_q^l}\right) & \frac{A^2}{2} k_j^3 \left(\frac{dS'_{ji}}{\eta_i^l} + \frac{dS'_{jp}}{\eta_p^l} + \frac{dS'_{jq}}{\eta_q^l}\right) & p \geqslant j,\ q \geqslant j \end{array} \right. \tag{A.23b}$$

Equation (A.20c) can be thus rewritten as

$$
\begin{aligned}
\tilde{E}_i^l = {} & \tilde{E}_i^{l+1} - 2\Delta t^l \nu k_i^2 \tilde{E}_i^{l+1} + \Delta t^l \Bigg\{ \sum_{j \geqslant i} \sum_{p=1}^{N} \sum_{q=1}^{N} \tilde{\theta}_{jpq}^l C_{jpq} \tilde{E}_j^{l+1} E_q^l (E_p^l k_p k_j^2 - E_j^l k_p^3) \frac{k_i^3}{\eta_j^l} dS'_{ij} dS_{jpq} \\
& + \sum_{p \geqslant i} \sum_{j=1}^{N} \sum_{q=1}^{N} \tilde{\theta}_{jpq}^l C_{jpq} \tilde{E}_j^{l+1} E_q^l (E_p^l k_p k_j^2 - E_j^l k_p^3) \frac{k_i^3}{\eta_p^l} dS'_{ip} dS_{jpq} + \sum_{q \geqslant i} \sum_{p=1}^{N} \sum_{j=1}^{N} \tilde{\theta}_{jpq}^l C_{jpq} \tilde{E}_j^{l+1} E_q^l (E_p^l k_p k_j^2 - E_j^l k_p^3) \frac{k_i^3}{\eta_q^l} dS'_{iq} dS_{jpq} \\
& + \sum_{j=1}^{N} \sum_{q=1}^{N} \theta_{jiq}^l C_{jiq} \tilde{E}_j^{l+1} E_q^l k_i k_j^2 dS_{jiq} + \sum_{j=1}^{N} \sum_{p=1}^{N} \theta_{jpi}^l C_{jpi} \tilde{E}_j^{l+1} (E_p^l k_p k_j^2 - E_j^l k_p^3) dS_{jpi} - \sum_{p=1}^{N} \sum_{q=1}^{N} \theta_{ipq}^l C_{ipq} \tilde{E}_i^{l+1} E_q^l k_p^3 dS_{ipq} \Bigg\} \\
& + f_i^l
\end{aligned}
\tag{A.24a}
$$

$$
\tilde{\theta}_{ipq}^l = \frac{-1 + (\mu_{ipq}^l t^l + 1) e^{-\mu_{ipq}^l t^l}}{(\mu_{ipq}^l)^2} \frac{A^2}{2}
\tag{A.24b}
$$

A.3 Validation of the adjoint code

In this section, we both illustrate the correct implementation of the adjoint code based on the discrete adjoint approach and the differences with the continuous adjoint approach. Given a cost function J, the prediction of its gradient with respect to the initial energy spectrum $\frac{\partial J}{\partial \boldsymbol{E}^0}$ that is obtained with the adjoint model (A.24), which corresponds to the discrete adjoint approach, is compared to first-order finite differences with step ϵ through the error δ defined as

$$
\delta(\epsilon) = \left| \frac{\frac{J(\boldsymbol{E}^0 + \epsilon \boldsymbol{F}^0) - J(\boldsymbol{E}^0)}{\epsilon} - \left(\frac{\partial J}{\partial \boldsymbol{E}^0}\right)^{\mathrm{T}} \boldsymbol{F}^0}{\left(\frac{\partial J}{\partial \boldsymbol{E}^0}\right)^{\mathrm{T}} \boldsymbol{F}^0} \right| .
\tag{A.25}
$$

Two cost functions are considered

$$
J_1(\boldsymbol{E}^0) = \frac{1}{2} (\boldsymbol{E}^M)^{\mathrm{T}} \boldsymbol{E}^M,
\tag{A.26a}
$$

$$
J_2(\boldsymbol{E}^0) = \frac{1}{2} \sum_{l=0}^{M} \left(\boldsymbol{E}^l\right)^T \boldsymbol{E}^l.
\tag{A.26b}
$$

The cost function J_1 only involves the adjoint operator $\tilde{\mathbf{M}}^l$ during the backward integration (A.20c), while an adjoint forcing term $\boldsymbol{f}^l$ has to be considered for J_2. Various perturbations $\boldsymbol{F}^0$ in (A.25) are used, which are illustrated in figure A.1. Type 1 is the initial energy spectrum used in the simulations itself, while types 2-6 correspond to perturbations of specific regions of the initial spectrum. The validation of the adjoint code is illustrated in figure A.2. Simulations are performed until ten initial eddy turn-over times. The error δ converges like ϵ as $\epsilon \to 0$ until machine precision in all the test cases considered, which confirms the correct implementation of the adjoint code. It is worth keeping in mind that the largest scales of the initial spectrum have no influence on the decay given the physical duration of the simulations.

In figure A.3(a), the continuous adjoint approach, where (A.7b) is discretized similarly to the direct model (A.18), is compared to the discrete adjoint approach. Perturbation of type 1 is used along with cost function J_1 and simulations are performed until one initial eddy turn-over time. Due to the geometrical spatial discretization, the continuous adjoint approach fails to accurately compute the gradient of the direct EDQNM code. In figure A.3(b), we investigate the case where both adjoint and direct models use a third-order Runge-Kutta scheme for temporal integration, which is not self-adjoint contrary to the Euler scheme, while the adjoint model is derived as (A.20c) concerning spatial discretization. Again, there is a loss of precision in the evaluation of the gradient with this hybrid discrete/continuous adjoint approach, but the effects of temporal discretization appear less significant

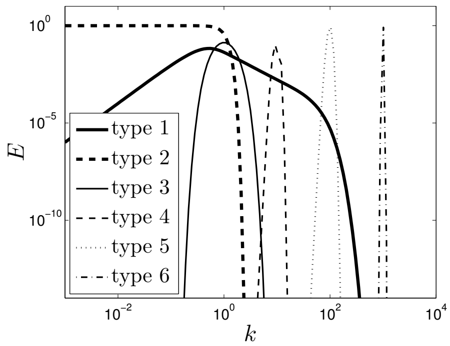

FIGURE A.1: Directions $\boldsymbol{F}^0$ considered for the validation of the adjoint code.

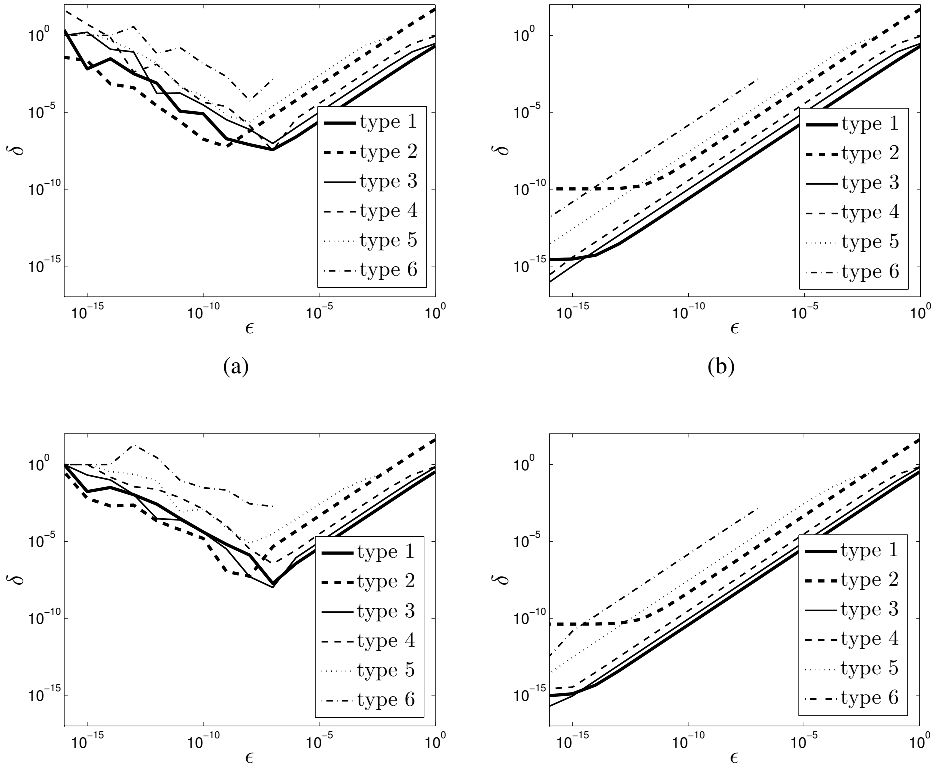

(a)

(b)

(c)

(d)

FIGURE A.2: Error $\delta(\epsilon)$ for various directions $\boldsymbol{F}^0$ and cost functions J_1 (first row) and J_2 (second row). Simulations are performed either in double (first column) or quadruple precision (second column).

than those of spatial discretization from the comparison of figures A.3(a) and A.3(b). Thanks to consistency, continuous and discrete approaches become equivalent as $\Delta t \to 0$. In this thesis, we only use the discrete adjoint approach for applications.

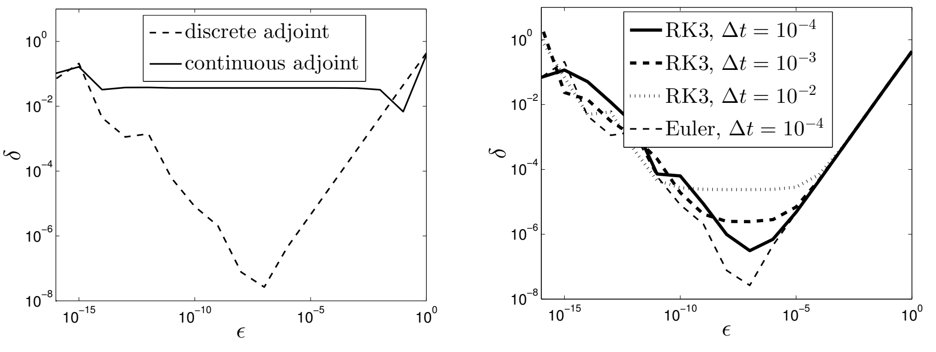

(a) (b)

FIGURE A.3: (a) Error $\delta(\epsilon)$ for continuous and discrete approaches with the Euler scheme, (b) error $\delta(\epsilon)$ in the case where both direct and adjoint models use a third-order Runge-Kutta scheme for time integration. Simulations are performed in double precision.

Appendix B

Anisotropic EDQNM modelling

In this appendix, a more detailed derivation of the spectral model discussed in chapter 4 [162] is provided. In particular, the derivation of the closed-form expressions for the generalized transfer terms is given, the spherical integration step is detailed, and the quadratic contributions of the anisotropic tensors in the spherically averaged transfer terms are evaluated. As shown in chapter 4, the present spectral model is derived in two steps. First, the governing equations for the second-order spectral tensor are closed via the EDQNM approximation, which is detailed in §B.1. In a second step, these closed equations are integrated analytically over spheres in Fourier space, and the final governing equations of the model are derived in §B.2.

B.1 Closed equations for the second-order spectral tensor in sheared turbulence

We consider incompressible, homogeneous turbulence. In the presence of a mean velocity gradient, the Navier-Stokes equation for the fluctuating velocity $u_i(\boldsymbol{x},t)$ includes additional advection and deformation terms linked to the mean — or large-scale — velocity field $U_i(\boldsymbol{x},t)$:

$$\left(\frac{\partial}{\partial t} + u_j \frac{\partial}{\partial x_j}\right) u_i + 2\epsilon_{inj}\Omega_n u_j + U_j \frac{\partial u_i}{\partial x_j} + \frac{\partial U_i}{\partial x_j} u_j = -\frac{\partial p}{\partial x_i} + \nu \nabla^2 u_i. \tag{B.1}$$

In view of the importance of rotating flows, we also consider an additional Coriolis force with angular velocity $\boldsymbol{\Omega}$. $p(\boldsymbol{x},t)$ is the pressure divided by a reference density, and can incorporate the centrifugal force in a rotating frame. ν is the kinematic viscosity of the fluid. In §B.1.1, we give the governing equation for the fluctuating velocity in Fourier space $\hat{u}_i(\boldsymbol{k},t)$ and that for the second-order spectral tensor $\hat{R}_{ij}(\boldsymbol{k},t)$. The ($\mathcal{E}$,$Z$) decomposition is applied to the latter tensor in §B.1.2 and to its governing equation in §B.1.3. Generalized transfer terms appear from the latter decomposition, which are closed via the EDQNM procedure described in §B.1.4. Final results are given in §B.1.5.

B.1.1 Craya's equations

The mean flow $\boldsymbol{U}(\boldsymbol{x},t)$ is characterized by a space-uniform gradient $\lambda_{ij}(t) = \partial U_i/\partial x_j$ in accordance with homogeneity for the fluctuations. For the sake of readability, and without loss of generality, we will omit the time dependence of λ_{ij} in the following. Accordingly, the counterpart of equation (B.1) in Fourier space is

$$\left(\frac{\partial}{\partial t} - \lambda_{ln} k_l \frac{\partial}{\partial k_n} + \nu k^2\right) \hat{u}_i(\boldsymbol{k},t) + M_{ij}(\boldsymbol{k}) \hat{u}_j(\boldsymbol{k},t) + \mathrm{i} P_{imn}(\boldsymbol{k}) \widehat{u_m u_n}(\boldsymbol{k},t) = 0, \tag{B.2}$$

with

$$M_{ij}(\boldsymbol{k}) = \left(\delta_{in} - 2\frac{k_i k_n}{k^2}\right)\lambda_{nj} + 2P_{in}\epsilon_{nmj}\Omega_m. \tag{B.3}$$

The following elementary properties of the Fourier transform are used to obtain (B.2)-(B.3):

$$\widehat{\frac{\partial u_i}{\partial x_j}}(\boldsymbol{k},t) = \mathrm{i}k_j\hat{u}_i(\boldsymbol{k},t), \quad \widehat{x_j u_i}(\boldsymbol{k},t) = \mathrm{i}\frac{\partial \hat{u}_i}{\partial k_j}(\boldsymbol{k},t) \tag{B.4}$$

Equation (B.3) involves the tensor $P_{ij}(\boldsymbol{k})$, which is the projection operator onto the plane perpendicular to the wave vector $\boldsymbol{k}$. The Kraichnan's projector $P_{imn}(\boldsymbol{k})$ in (B.2) may be expressed in terms of the projection operator $P_{ij}(\boldsymbol{k})$ as

$$P_{inm}(\boldsymbol{k}) = \frac{1}{2}\Big(k_m P_{in}(\boldsymbol{k}) + k_n P_{im}(\boldsymbol{k})\Big), \quad P_{ij}(\boldsymbol{k}) = \delta_{ij} - \frac{k_i k_j}{k^2}. \tag{B.5}$$

The convolution product in equation (B.2)

$$\widehat{u_i u_j}(\boldsymbol{k},t) = \iiint_{\boldsymbol{p}+\boldsymbol{q}=\boldsymbol{k}} \hat{u}_i(\boldsymbol{p},t)\hat{u}_j(\boldsymbol{q},t)\mathrm{d}^3\boldsymbol{p}, \tag{B.6}$$

lies at the origin of triadic interactions between wave vectors $\boldsymbol{k}$, $\boldsymbol{p}$ and $\boldsymbol{q}$ so that they form a triangle. In anisotropic homogeneous turbulence, all information about two-point second-order correlations is provided by the second-order spectral tensor $\hat{R}_{ij}(\boldsymbol{k},t)$, which is the Fourier transform of the two-point second-order correlation tensor $R_{ij}(\boldsymbol{r},t) = \langle u_i(\boldsymbol{x},t)u_j(\boldsymbol{x}+\boldsymbol{r},t)\rangle$, with $\boldsymbol{r}$ the vector separating the two points in physical space. By using

$$\Big\langle \hat{u}_i^*(\boldsymbol{p},t)\hat{u}_j(\boldsymbol{k},t)\Big\rangle = \delta(\boldsymbol{k}-\boldsymbol{p})\hat{R}_{ij}(\boldsymbol{k},t), \tag{B.7}$$

where the operators * and $\langle\rangle$ denote complex conjugate and ensemble average, respectively, one derives the governing equation for the tensor $\hat{R}_{ij}(\boldsymbol{k},t)$ from equation (B.2):

$$\left(\frac{\partial}{\partial t} - \lambda_{ln}k_l\frac{\partial}{\partial k_n} + 2\nu k^2\right)\hat{R}_{ij}(\boldsymbol{k},t) + M_{in}(\boldsymbol{k})\hat{R}_{nj}(\boldsymbol{k},t) + M_{jn}(\boldsymbol{k})\hat{R}_{ni}(\boldsymbol{k},t) = T_{ij}(\boldsymbol{k},t). \tag{B.8}$$

In the tensor $T_{ij}(\boldsymbol{k},t)$ in (B.8), it is possible to disentangle contributions from the exact tensorial transfer term, with zero integral over $\boldsymbol{k}$, and contributions from fluctuating pressure $W_{ij}(\boldsymbol{k},t)$ as follows:

$$T_{ij}(\boldsymbol{k},t) = P_{in}(\boldsymbol{k})\tau_{nj}(\boldsymbol{k},t) + P_{jn}(\boldsymbol{k})\tau^*_{ni}(\boldsymbol{k},t) = \tau_{ij}(\boldsymbol{k},t) + \tau^*_{ji}(\boldsymbol{k},t) \underbrace{-\frac{k_i k_n}{k^2}\tau_{nj}(\boldsymbol{k},t) - \frac{k_j k_n}{k^2}\tau^*_{ni}(\boldsymbol{k},t)}_{W_{ij}(\boldsymbol{k},t)} \tag{B.9}$$

The tensor $W_{ij}(\boldsymbol{k},t)$ underlies a possible return-to-isotropy mechanism, its integral on $\boldsymbol{k}$ gives the nonlinear — so-called slow — pressure-strain rate tensor, and both $T_{ij}(\boldsymbol{k},t)$ and $W_{ij}(\boldsymbol{k},t)$ terms originate from the same tensor $\tau_{ij}(\boldsymbol{k},t)$. In the same way, the tensor $\tau_{ij}(\boldsymbol{k},t)$

$$\tau_{ij}(\boldsymbol{k},t) = k_n \iiint S_{ijn}(\boldsymbol{k},\boldsymbol{p},t)\mathrm{d}^3\boldsymbol{p} \tag{B.10}$$

is exactly given from the third-order three-point spectral tensor $S_{ijn}(\boldsymbol{k},\boldsymbol{p},t)$, defined by

$$\mathrm{i}\langle\hat{u}_i(\boldsymbol{q},t)\hat{u}_j(\boldsymbol{k},t)\hat{u}_n(\boldsymbol{p},t)\rangle = \delta(\boldsymbol{k}+\boldsymbol{p}+\boldsymbol{q})S_{ijn}(\boldsymbol{k},\boldsymbol{p},t), \tag{B.11}$$

and the closure is applied to the equation which governs the latter tensor, as shown in §B.1.4.

B.1.2 The ($\mathcal{E}$,Z) decomposition

An optimal decomposition of the second-order spectral tensor $\hat{R}_{ij}(\boldsymbol{k},t)$, for arbitrary anisotropy, results from a trace-deviator splitting, restricted to the plane normal to the wave vector by virtue of incompressibility [37, 38, 188]. Here, the contribution of helicity is disregarded. This is equivalent to consider only the real part of $\hat{R}_{ij}(\boldsymbol{k},t)$. Accordingly, this decomposition is written as:

$$\hat{R}_{ij}(\boldsymbol{k},t) = \frac{1}{2}\hat{R}_{nn}(\boldsymbol{k},t)P_{ij}(\boldsymbol{k}) + \Re\left(\hat{R}_{ij}(\boldsymbol{k},t) - \frac{1}{2}\hat{R}_{nn}(\boldsymbol{k},t)P_{ij}(\boldsymbol{k})\right). \tag{B.12}$$

Equation (B.12) may be rewritten in terms of scalar quantities as follows:

$$\hat{R}_{ij}(\boldsymbol{k},t) = \frac{E(k,t)}{4\pi k^2}P_{ij}(\boldsymbol{k}) + \left(\mathcal{E}(\boldsymbol{k},t) - \frac{E(k,t)}{4\pi k^2}\right)P_{ij}(\boldsymbol{k}) + \Re\left(Z(\boldsymbol{k},t)N_i(\boldsymbol{k})N_j(\boldsymbol{k})\right), \tag{B.13}$$

where

$$\mathcal{E}(\boldsymbol{k},t) = \frac{1}{2}\hat{R}_{ii}(\boldsymbol{k},t), \quad Z(\boldsymbol{k},t) = \frac{1}{2}\hat{R}_{ij}(\boldsymbol{k},t)N_i^*(\boldsymbol{k})N_j^*(\boldsymbol{k}), \tag{B.14}$$

and the radial energy spectrum $E(k,t)$ is obtained from $\mathcal{E}(\boldsymbol{k},t)$ by

$$E(k,t) = \iint_{S_k} \mathcal{E}(\boldsymbol{k},t)\mathrm{d}^2\boldsymbol{k}, \tag{B.15}$$

where $\iint_{S_k} \mathrm{d}^2\boldsymbol{k}$ denotes integration over a spherical shell of radius k. The first term in the decomposition (B.13) of $\hat{R}_{ij}(\boldsymbol{k},t)$ corresponds to its isotropic part. The second term characterizes ‘directional anisotropy’ via the scalar $(\mathcal{E}(\boldsymbol{k},t) - E(k,t)/(4\pi k^2))$, which corresponds to the difference between the energy density $\mathcal{E}(\boldsymbol{k},t)$ and its spherical average. The third term, which is generated by the scalar $Z(\boldsymbol{k},t)$, characterizes ‘polarization anisotropy’, or tensorial anisotropy at a given wavevector. The decomposition (B.13) also involves the projection operator $P_{ij}(\boldsymbol{k})$ defined by (B.5) as well as the helical mode $\boldsymbol{N}(\boldsymbol{k})$, defined below. By virtue of incompressibility, a two-component decomposition of the fluctuating velocity can be written as

$$\hat{\boldsymbol{u}}(\boldsymbol{k},t) = u^{(1)}(\boldsymbol{k},t)\boldsymbol{e}^{(1)}(\boldsymbol{k}) + u^{(2)}(\boldsymbol{k},t)\boldsymbol{e}^{(2)}(\boldsymbol{k}), \tag{B.16}$$

or equivalently

$$\hat{\boldsymbol{u}}(\boldsymbol{k},t) = \xi_+(\boldsymbol{k},t)\boldsymbol{N}(\boldsymbol{k}) + \xi_-(\boldsymbol{k},t)\boldsymbol{N}^*(\boldsymbol{k}), \tag{B.17}$$

with

$$\boldsymbol{N}(\boldsymbol{k}) = \boldsymbol{e}^{(2)}(\boldsymbol{k}) - \mathrm{i}\boldsymbol{e}^{(1)}(\boldsymbol{k}), \quad \boldsymbol{e}^{(1)}(\boldsymbol{k}) = \frac{\boldsymbol{k}\times\boldsymbol{n}}{|\boldsymbol{k}\times\boldsymbol{n}|}, \quad \boldsymbol{e}^{(2)}(\boldsymbol{k}) = \boldsymbol{e}^{(3)}(\boldsymbol{k})\times\boldsymbol{e}^{(1)}(\boldsymbol{k}), \quad \boldsymbol{e}^{(3)}(\boldsymbol{k}) = \frac{\boldsymbol{k}}{k}, \tag{B.18}$$

where $(\boldsymbol{e}^{(1)}(\boldsymbol{k}), \boldsymbol{e}^{(2)}(\boldsymbol{k}), \boldsymbol{e}^{(3)}(\boldsymbol{k}))$ is an orthonormal right-handed frame of reference associated to a privileged direction $\boldsymbol{n}$, this frame is often referred to as Craya-Herring frame (see e.g. Herring [98], Sagaut and Cambon [188]). The realizability condition, or condition for the Hermitian covariance matrix $\hat{R}_{ij}(\boldsymbol{k},t)$ to be definite-positive, can be written as [40]:

$$|\, Z(\boldsymbol{k},t)\, | \leq \mathcal{E}(\boldsymbol{k},t) \quad \forall \boldsymbol{k}, t. \tag{B.19}$$

B.1.3 Generalized Lin equations

When taking into account the decomposition (B.13) of the second-order spectral tensor $\hat{R}_{ij}(\boldsymbol{k},t)$, equation (B.8) is equivalent to a set of two equations in terms of $\mathcal{E}(\boldsymbol{k},t)$ and $Z(\boldsymbol{k},t)$, so that Lin’s equation in isotropic turbulence is generalized as

$$\left(\frac{\partial}{\partial t} - \lambda_{ln}k_l\frac{\partial}{\partial k_n} + 2\nu k^2\right)\mathcal{E}(\boldsymbol{k},t) - \mathcal{E}(\boldsymbol{k},t)S_{ij}\alpha_i\alpha_j + \Re\left(Z(\boldsymbol{k},t)S_{ij}N_i(\boldsymbol{k})N_j(\boldsymbol{k})\right) = T^{(\mathcal{E})}(\boldsymbol{k},t), \tag{B.20}$$

$$\left(\frac{\partial}{\partial t} - \lambda_{ln} k_l \frac{\partial}{\partial k_n} + 2\nu k^2\right) Z(\boldsymbol{k},t) - Z(\boldsymbol{k},t) S_{ij}\alpha_i\alpha_j + \mathcal{E}(\boldsymbol{k},t) S_{ij} N_i^*(\boldsymbol{k}) N_j^*(\boldsymbol{k}) - 2\mathrm{i} Z(\boldsymbol{k},t)\left(2\Omega_l\alpha_l + \frac{W_l}{2}\alpha_l - \Omega_E\right) = T^{(Z)}(\boldsymbol{k},t), \tag{B.21}$$

where $\alpha_i = k_i/k$, $S_{ij} = (\lambda_{ij} + \lambda_{ji})/2$ is the symmetric part of the mean-velocity gradient, and $W_i = \epsilon_{ijn}\lambda_{nj}$ refers to its antisymmetric part. The rotation vector component Ω_E expresses the solid-body motion of the local Craya frame with respect to a fixed frame of references, following characteristic lines. The expression of Ω_E is given by:

$$\Omega_E = \frac{1}{2}\Im\left(N_j \frac{\partial N_j^*}{\partial k_n}\right)\lambda_{ln}k_l = -\lambda_{ln}k_l \frac{n_p\alpha_p}{|\boldsymbol{k}\times\boldsymbol{n}|} e_n^{(1)} = -\frac{k}{|\boldsymbol{k}\times\boldsymbol{n}|}\lambda_{ln}n_l e_n^{(1)} - \lambda_{ln} e_l^{(2)} e_n^{(1)}. \tag{B.22}$$

The derivation of the above expressions may be found in Cambon et al. [41], but with an error of sign in front of the rotation terms in (B.21). The nonlinear transfer terms in the right-hand-sides of equations (B.20) -(B.21) are obtained by applying the $(\mathcal{E}, Z)$ decomposition to the transfer term $T_{ij}(\boldsymbol{k},t)$ in equation (B.8):

$$T^{(\mathcal{E})}(\boldsymbol{k},t) = \frac{1}{2}T_{ii}(\boldsymbol{k},t) = \frac{1}{2}(\tau_{ii}(\boldsymbol{k},t) + \tau_{ii}^*(\boldsymbol{k},t)), \tag{B.23}$$

$$T^{(Z)}(\boldsymbol{k},t) = \frac{1}{2}T_{ij}(\boldsymbol{k},t)N_i^*(\boldsymbol{k})N_j^*(\boldsymbol{k}) = \frac{1}{2}(\tau_{ij}(\boldsymbol{k},t) + \tau_{ji}^*(\boldsymbol{k},t))N_i^*(\boldsymbol{k})N_j^*(\boldsymbol{k}), \tag{B.24}$$

where the tensor $\tau_{ij}(\boldsymbol{k},t)$ is defined by equations (B.9)-(B.10). As mentionned earlier, $T_{ij}(\boldsymbol{k},t)$ includes both the 'true' transfer tensor, with zero integral, and the contribution $W_{ij}(\boldsymbol{k},t)$ involved in the return-to-isotropy effect. The latter tensor can be generated from a scalar transfer term $T^{(RTI)}(\boldsymbol{k},t)$ according to

$$W_{ij}(\boldsymbol{k},t) = -\Re\left(T^{(RTI)}(\boldsymbol{k},t)(\alpha_i N_j(\boldsymbol{k}) + \alpha_j N_i(\boldsymbol{k}))\right), \tag{B.25}$$

consistently with $\tau_{ij}(\boldsymbol{k},t)k_j = 0$, $\tau_{ij}(\boldsymbol{k},t)k_i \neq 0$, and

$$T^{(RTI)}(\boldsymbol{k},t) = \alpha_i(\tau_{ij}(\boldsymbol{k},t) + \tau_{ji}^*(\boldsymbol{k},t))N_j^*(\boldsymbol{k}) = \alpha_i\tau_{ij}(\boldsymbol{k},t)N_j^*(\boldsymbol{k}) \tag{B.26}$$

B.1.4 EDQNM closure for transfer terms

In this section, a 'triadic' closure is applied to the equations governing the third-order spectral tensor $S_{ijn}(\boldsymbol{k},\boldsymbol{p},t)$ defined by equation (B.11), from which the term $\tau_{ij}(\boldsymbol{k},t)$ in equation (B.10) is derived. From the counterpart of (B.1) in Fourier space and (B.11), its dynamics is obtained via

$$\begin{aligned}&\left(\frac{\partial}{\partial t} + \nu(k^2+p^2+q^2) - \lambda_{lm}\left(k_l\frac{\partial}{\partial k_m} + p_l\frac{\partial}{\partial p_m}\right)\right)S_{ijn}(\boldsymbol{k},\boldsymbol{p},t) + M_{im}(\boldsymbol{q})S_{mjn}(\boldsymbol{k},\boldsymbol{p},t)\\ &+ M_{jm}(\boldsymbol{k})S_{imn}(\boldsymbol{k},\boldsymbol{p},t) + M_{nm}(\boldsymbol{p})S_{ijm}(\boldsymbol{k},\boldsymbol{p},t) = \mathcal{T}_{ijn}(\boldsymbol{k},\boldsymbol{p},t),\end{aligned} \tag{B.27}$$

where $\boldsymbol{k}+\boldsymbol{p}+\boldsymbol{q} = \boldsymbol{0}$ and $\mathcal{T}_{ijn}(\boldsymbol{k},\boldsymbol{p},t)$ is expressed in terms of a fourth-order spectral tensor

$$\mathcal{T}_{ijn}(\boldsymbol{k},\boldsymbol{p},t) = P_{imp}(\boldsymbol{q})\iiint S_{mpjn}(\boldsymbol{r},\boldsymbol{k},\boldsymbol{p},t)d^3\boldsymbol{r} + P_{jmp}(\boldsymbol{k})\iiint S_{mpin}(\boldsymbol{r},\boldsymbol{q},\boldsymbol{p},t)d^3\boldsymbol{r} + P_{nmp}(\boldsymbol{p})\iiint S_{mpij}(\boldsymbol{r},\boldsymbol{q},\boldsymbol{k},t)d^3\boldsymbol{r}, \tag{B.28}$$

with

$$\langle\hat{u}_m(\boldsymbol{r})\hat{u}_p(\boldsymbol{r}')\hat{u}_j(\boldsymbol{k})\hat{u}_n(\boldsymbol{p})\rangle = S_{mpjn}(\boldsymbol{r},\boldsymbol{k},\boldsymbol{p})\delta(\boldsymbol{r}+\boldsymbol{r}'+\boldsymbol{k}+\boldsymbol{p}). \tag{B.29}$$

So far, the expressions which have been given for the governing equations for the second- and third-order spectral tensors are exact. They strictly reproduce the infinite hierarchy of moments up to $N = 3$, with equations for N-order moments having both linear closed terms and contribution from $N+1$ moments being induced by basic nonlinearity. We now want to break this infinite hierarchy at the order $N = 3$. Equation (B.27) can be rewritten in the following form:

$$\left(\frac{\partial}{\partial t} + \nu(k^2+p^2+q^2)\right)S_{ijn}(\boldsymbol{k},\boldsymbol{p},t) = \mathcal{T}_{ijn}(\boldsymbol{k},\boldsymbol{p},t) + \mathcal{L}_{ijn}(\boldsymbol{k},\boldsymbol{p},t) = \mathcal{R}_{ijn}(\boldsymbol{k},\boldsymbol{p},t), \tag{B.30}$$

where the tensor $\mathcal{R}_{ijn}(\boldsymbol{k},\boldsymbol{p},t)$ gathers the linear operators induced by mean velocity gradients through $\mathcal{L}_{ijn}(\boldsymbol{k},\boldsymbol{p},t)$ and the fourth-order spectral tensor $\mathcal{T}_{ijn}(\boldsymbol{k},\boldsymbol{p},t)$. The problem then is to determine a closed expression for $\mathcal{R}_{ijn}(\boldsymbol{k},\boldsymbol{p},t)$. The historical procedure, developed for homogeneous isotropic turbulence, starts from the Quasi-Normal (QN) approximation [158, 181], which states that the fluctuating velocity probability distributions are not too far from normal laws, in order to close the nonlinear contributions in $\mathcal{R}_{ijn}(\boldsymbol{k},\boldsymbol{p},t)$. This assumption translates into vanishing fourth-order cumulants and can be written as:

$$\langle \hat{u}_m(\boldsymbol{r})\hat{u}_p(\boldsymbol{r}')\hat{u}_j(\boldsymbol{k})\hat{u}_n(\boldsymbol{p})\rangle = \langle \hat{u}_m(\boldsymbol{r})\hat{u}_p(\boldsymbol{r}')\rangle\langle \hat{u}_j(\boldsymbol{k})\hat{u}_n(\boldsymbol{p})\rangle + \langle \hat{u}_m(\boldsymbol{r})\hat{u}_j(\boldsymbol{k})\rangle\langle \hat{u}_p(\boldsymbol{r}')\hat{u}_n(\boldsymbol{p})\rangle + \langle \hat{u}_m(\boldsymbol{r})\hat{u}_n(\boldsymbol{p})\rangle\langle \hat{u}_p(\boldsymbol{r}')\hat{u}_j(\boldsymbol{k})\rangle. \tag{B.31}$$

Injecting (B.31) into (B.28) and using definitions (B.7) and (B.29) lead to the quasi-normal contribution of the transfer term $\mathcal{T}_{ijn}(\boldsymbol{k},\boldsymbol{p},t)$:

$$\mathcal{T}^{(QN)}_{ijl}(\boldsymbol{k},\boldsymbol{p},t) = 2\Big(P_{imn}(\boldsymbol{q})\hat{R}_{mj}(\boldsymbol{k},t)\hat{R}_{nl}(\boldsymbol{p},t) + P_{jmn}(\boldsymbol{k})\hat{R}_{ml}(\boldsymbol{p},t)\hat{R}_{ni}(\boldsymbol{q},t) + P_{lmn}(\boldsymbol{p})\hat{R}_{mi}(\boldsymbol{q},t)\hat{R}_{nj}(\boldsymbol{k},t)\Big), \tag{B.32}$$

with $P_{inm}(\boldsymbol{k}) = 1/2\,(k_m P_{in}(\boldsymbol{k}) + k_n P_{im}(\boldsymbol{k}))$, the projector $P_{ij}(\boldsymbol{k})$ is defined in (B.12). However, it was shown in [170, 171] that the purely quasi-normal approximation fails in decaying isotropic turbulence for long elapsed times, yielding negative energy spectra at small k. Orszag [172] showed that the improper treatment of relaxation effects in the purely quasi-normal approximation lies at the origin of this lack of realizability. Consequently, he introduced an eddy viscosity, or Eddy-Damping (ED) term, in the governing equation for third-order correlations. Without any additional assumption, $\mathcal{R}_{ijn}(\boldsymbol{k},\boldsymbol{p},t)$ from (B.30) can be written as

$$\mathcal{R}_{ijn}(\boldsymbol{k},\boldsymbol{p},t) = \mathcal{T}^{(QN)}_{ijn}(\boldsymbol{k},\boldsymbol{p},t) + \mathcal{T}^{(IV)}_{ijn}(\boldsymbol{k},\boldsymbol{p},t) + \mathcal{L}_{ijn}(\boldsymbol{k},\boldsymbol{p},t). \tag{B.33}$$

In this equation, the only unknown, and unclosed, term is $\mathcal{T}^{(IV)}_{ijn}(\boldsymbol{k},\boldsymbol{p},t)$ that represents the contribution from fourth-order cumulants. A natural extension of Orszag's introduction of eddy-damping is to write

$$\mathcal{T}^{(IV)}_{ijn}(\boldsymbol{k},\boldsymbol{p},t) = -\left(\eta(k,t) + \eta(p,t) + \eta(q,t)\right) S_{ijn}(\boldsymbol{k},\boldsymbol{p},t), \tag{B.34}$$

with keeping in mind that fourth-order cumulants may act as a linear relaxation of triple correlations, which will reinforce the dissipative operator in equation (B.30) when added to the purely viscous terms in its left-hand-side. The eddy-damping coefficient $\eta(k,t)$ is chosen as

$$\eta(k,t) = A\sqrt{\int_0^k p^2 E(p,t)\mathrm{d}p}, \tag{B.35}$$

following [179], which is an improved variant of [172]'s proposal. This choice restricts the present modelling to turbulent flows where linear effects induced by mean velocity gradients play a negligible role in the dynamics of triple correlations. The form of the eddy-damping contribution and its application to anisotropic flows is further discussed in chapter 4. The constant is fixed at $A = 0.36$ to recover a well admitted value of the Kolmogorov constant [9]. Equation (B.30) can be now integrated using (B.33), (B.32) and (B.34)-(B.35), and neglecting the contribution of $\mathcal{L}_{ijn}(\boldsymbol{k},\boldsymbol{p},t)$. The solution thus obtained involves time integrals that are further simplified by a Markovianization procedure, which amounts to truncate the proper time-memory of triple correlations. Further details can be found in [39, 188]. In the end, this anisotropic EDQNM closure for the tensor $\tau_{ij}(\boldsymbol{k},t)$ defined by (B.10) amounts to

$$\tau_{ij}(\boldsymbol{k},t) = k_l \iiint \theta_{kpq}\mathcal{T}^{(QN)}_{ijl}(\boldsymbol{k},\boldsymbol{p},t)\mathrm{d}^3\boldsymbol{p}, \tag{B.36}$$

where

$$\theta_{kpq} = \frac{1-\mathrm{e}^{-\mu_{kpq}t}}{\mu_{kpq}}, \quad \mu_{kpq} = \nu(k^2+p^2+q^2) + \eta(k,t) + \eta(p,t) + \eta(q,t). \tag{B.37}$$

The expression (B.36) of $\tau_{ij}(\boldsymbol{k},t)$ obtained from the EDQNM approximation is injected into (B.23)-(B.24) in order to obtain closed-form expressions of the transfer terms, as detailed in §B.1.5

B.1.5 Closed-form expressions of the generalized transfer terms

B.1.5.1 Geometrical relationships

In this section, the derivation of the closed-form expression of the transfer terms $T^{(\mathcal{E})}(\boldsymbol{k},t)$, $T^{(\mathcal{Z})}(\boldsymbol{k},t)$ and $T^{(RTI)}(\boldsymbol{k},t)$ is provided. First, various relationships about triadic geometry are given, which will be used in the derivation. In the following, the scalars x, y and z refer to the cosines of the internal angles of the triangle formed by the triad, and are defined as:

$$x = \cos(\alpha) = -\boldsymbol{p}\cdot\boldsymbol{q}/(pq), \quad y = \cos(\beta) = -\boldsymbol{k}\cdot\boldsymbol{q}/(kq), \quad z = \cos(\gamma) = -\boldsymbol{k}\cdot\boldsymbol{p}/(kp). \tag{B.38}$$

In addition to the Craya-Herring frame defined in (B.18), appropriate reference frames to derive geometrical coefficients may be defined with respect to the normal unit vector of the triad [188]. These frames are formed from the following vectors:

$$\boldsymbol{\gamma} = \frac{\boldsymbol{k}\times\boldsymbol{p}}{|\boldsymbol{k}\times\boldsymbol{p}|}, \quad \boldsymbol{\beta} = \boldsymbol{\alpha}\times\boldsymbol{\gamma}, \quad \boldsymbol{\beta}' = \boldsymbol{\alpha}'\times\boldsymbol{\gamma}, \quad \boldsymbol{\beta}'' = \boldsymbol{\alpha}''\times\boldsymbol{\gamma}, \tag{B.39}$$

which can be related to the Craya-Herring frame according to

$$\boldsymbol{N} = e^{\mathrm{i}\lambda}(\boldsymbol{\beta}+\mathrm{i}\boldsymbol{\gamma}) = e^{\mathrm{i}\lambda}\boldsymbol{W}, \quad \boldsymbol{N}' = e^{\mathrm{i}\lambda'}(\boldsymbol{\beta}'+\mathrm{i}\boldsymbol{\gamma}) = e^{\mathrm{i}\lambda'}\boldsymbol{W}', \quad \boldsymbol{N}'' = e^{\mathrm{i}\lambda''}(\boldsymbol{\beta}''+\mathrm{i}\boldsymbol{\gamma}) = e^{\mathrm{i}\lambda''}\boldsymbol{W}'', \tag{B.40}$$

with $\boldsymbol{N} = \boldsymbol{N}(\boldsymbol{k})$, $\boldsymbol{N}' = \boldsymbol{N}(\boldsymbol{p})$, $\boldsymbol{N}'' = \boldsymbol{N}(\boldsymbol{q})$, $\boldsymbol{\alpha} = \boldsymbol{k}/k$, $\boldsymbol{\alpha}' = \boldsymbol{p}/p$ and $\boldsymbol{\alpha}'' = \boldsymbol{q}/q$. λ, λ' and λ'' are angles that characterize the rotation of the plane of the triad around $\boldsymbol{k}$, $\boldsymbol{p}$ and $\boldsymbol{q}$, respectively. Useful relations are:

$$W_i^*W_j^* = e^{2\mathrm{i}\lambda}N_i^*N_j^*, \quad N_iN_j^* = P_{ij} - \mathrm{i}\epsilon_{ijl}\alpha_l, \tag{B.41}$$

$$\boldsymbol{\alpha}' = -z\boldsymbol{\alpha} - \sqrt{1-z^2}\boldsymbol{\beta}, \quad \boldsymbol{\alpha}'' = -y\boldsymbol{\alpha} + \sqrt{1-y^2}\boldsymbol{\beta}, \tag{B.42}$$

$$\boldsymbol{\beta}' = \sqrt{1-z^2}\boldsymbol{\alpha} - z\boldsymbol{\beta}, \quad \boldsymbol{\beta}'' = -\sqrt{1-y^2}\boldsymbol{\alpha} - y\boldsymbol{\beta}, \tag{B.43}$$

$$\boldsymbol{W}' = \sqrt{1-z^2}\boldsymbol{\alpha} + \frac{1-z}{2}\boldsymbol{N}e^{-\mathrm{i}\lambda} - \frac{1+z}{2}\boldsymbol{N}^*e^{\mathrm{i}\lambda}, \quad \boldsymbol{W}'' = -\sqrt{1-y^2}\boldsymbol{\alpha} + \frac{1-y}{2}\boldsymbol{N}e^{-\mathrm{i}\lambda} - \frac{1+y}{2}\boldsymbol{N}^*e^{\mathrm{i}\lambda}, \tag{B.44}$$

$$q\sin(\beta) = p\sin(\gamma), \quad k\sin(\beta) = p\sin(\alpha) \tag{B.45}$$

$$k(1-y^2) = p(xy+z), \quad k(1-z^2) = q(xz+y), \quad k(yz+x) = py(1-z^2) + qz(1-y^2) \tag{B.46}$$

$$k(1-2z^2y^2-xyz) = p(xy+z^3) + q(xz+y^3) \tag{B.47}$$

B.1.5.2 Splitting of the quasi-normal approximation

The expression of the tensor $\tau_{ij}(\boldsymbol{k},t)$ closed by the EDQNM procedure in (B.36) is decomposed according to:

$$\tau_{ij}(\boldsymbol{k},t) = 2\iiint \theta_{kpq}(\tau_{ij}^{+}+\tau_{ij}^{-})\mathrm{d}^3\boldsymbol{p}, \quad \tau_{ij}^{-} = \left(P'_{imn}\hat{R}_{mj}\hat{R}''_{nl} + P'_{lmn}\hat{R}''_{mi}\hat{R}_{nj}\right)k_l, \quad \tau_{ij}^{+} = \frac{1}{2}\left(P_{jmn}\hat{R}'_{ml}\hat{R}''_{ni} + P_{jmn}\hat{R}''_{ml}\hat{R}'_{ni}\right)k_l, \tag{B.48}$$

with $\hat{R}_{ij} = \hat{R}_{ij}(\boldsymbol{k},t)$, $\hat{R}'_{ij} = \hat{R}_{ij}(\boldsymbol{p},t)$, $\hat{R}''_{ij} = \hat{R}_{ij}(\boldsymbol{q},t)$, $P_{ijl} = P_{ijl}(\boldsymbol{k})$ and $P'_{ijl} = P_{ijl}(\boldsymbol{p})$. This decomposition facilitates the derivation of the closed-form expression of the generalized transfer terms, as detailed in the following. The contribution τ_{ij}^{-} originates from the first and third terms in the right-hand-side of (B.32), using

$$\iiint f(\boldsymbol{k},\boldsymbol{p},\boldsymbol{q})\mathrm{d}^3\boldsymbol{p} = \iiint f(\boldsymbol{k},\boldsymbol{q},\boldsymbol{p})\mathrm{d}^3\boldsymbol{p} \tag{B.49}$$

with $\boldsymbol{k}+\boldsymbol{p}+\boldsymbol{q}=\boldsymbol{0}$ and f an integrable function on $\mathbb{R}^9$. The contribution τ^+_{ij} comes from the second term in (B.32), and is written in a symmetrized form according to (B.49). Using

$$P'_{imn}\hat{R}''_{nl}k_l=\frac{1}{2}\left(-P'_{im}k_n\hat{R}''_{nl}k_l+p_m\left(\hat{R}''_{il}k_l+\frac{p_i}{p^2}k_n\hat{R}''_{nl}k_l\right)\right),\quad P'_{lmn}\hat{R}''_{ni}k_l=\frac{1}{2}k_l\hat{R}''_{li}\left(\left(1-\frac{2zk}{p}\right)p_m-k_m\right),\tag{B.50}$$

the contribution τ^-_{ij} can be rewritten as

$$\tau^-_{ij}=\frac{1}{2}k_l\hat{R}''_{ln}k_n\left(-\hat{R}_{ij}+2\alpha'_i\alpha'_m\hat{R}_{mj}\right)+\frac{1}{2}k_l\hat{R}''_{li}\left(2qx\alpha'_m-k_m\right)\hat{R}_{mj}.\tag{B.51}$$

From (B.51), useful simplifications are:

$$k_l\hat{R}''_{li}k_i=kp(xy+z)\left(\mathcal{E}''+\Re X''\right)\tag{B.52}$$

$$k_l\hat{R}''_{li}N_i=ke^{\mathrm{i}\lambda}\sin(\beta)\left(y\left(\mathcal{E}''+\Re X''\right)+\mathrm{i}\Im X''\right),\quad k_l\hat{R}''_{li}N^*_i=ke^{-\mathrm{i}\lambda}\sin(\beta)\left(y\left(\mathcal{E}''+\Re X''\right)-\mathrm{i}\Im X''\right)\tag{B.53}$$

$$p_m\hat{R}_{mj}N_j=-p\sin(\gamma)\left(\mathcal{E}e^{\mathrm{i}\lambda}+Z^*e^{-\mathrm{i}\lambda}\right),\quad p_m\hat{R}_{mj}N^*_j=-p\sin(\gamma)\left(\mathcal{E}e^{-\mathrm{i}\lambda}+Ze^{\mathrm{i}\lambda}\right),\tag{B.54}$$

with $\mathcal{E}=\mathcal{E}(\boldsymbol{k},t)$, $\mathcal{E}'=\mathcal{E}(\boldsymbol{p},t)$, $\mathcal{E}''=\mathcal{E}(\boldsymbol{q},t)$, $X=Z(\boldsymbol{k},t)e^{2\mathrm{i}\lambda}$, $X'=Z(\boldsymbol{p},t)e^{2\mathrm{i}\lambda'}$ and $X''=Z(\boldsymbol{q},t)e^{2\mathrm{i}\lambda''}$. Similarly, the contribution τ^+_{ij} can be simplified as:

$$\tau^+_{ij}=\frac{1}{2}k_l\hat{R}'_{ml}k_m\left(\hat{R}''_{ij}-2\alpha_n\alpha_j\hat{R}''_{ni}\right)+\frac{1}{2}k_n\hat{R}''_{ni}k_l\hat{R}'_{jl},\tag{B.55}$$

and the following relations can be used further in the derivation:

$$\alpha_l\hat{R}'_{lm}\alpha_m=(1-z^2)\left(\mathcal{E}'+\Re X'\right),\quad \hat{R}''_{ij}N^*_iN^*_j=e^{-2\mathrm{i}\lambda}\left[(1+y^2)\left(\mathcal{E}''+\Re X''\right)-2\mathcal{E}''-2\mathrm{i}y\Im X''\right]\tag{B.56}$$

$$k_n\hat{R}'_{ni}N^*_i=-k\sin(\gamma)e^{-\mathrm{i}\lambda}\left(z\left(\mathcal{E}'+\Re X'\right)-\mathrm{i}\Im X'\right),\quad k_n\hat{R}''_{ni}N^*_i=k\sin(\beta)e^{-\mathrm{i}\lambda}\left(y\left(\mathcal{E}''+\Re X''\right)-\mathrm{i}\Im X''\right)\tag{B.57}$$

$$\hat{R}''_{ij}N_iN^*_j=\mathcal{E}''(1+y^2)-\Re X''(1-y^2),\quad k_n\hat{R}'_{ni}N_i=-k\sin(\gamma)e^{\mathrm{i}\lambda}\left(z\left(\mathcal{E}'+\Re X'\right)+\mathrm{i}\Im X'\right).\tag{B.58}$$

B.1.5.3 Transfer term $T^{(Z)}(\boldsymbol{k},t)$

From (B.52)-(B.54) and (B.56)-(B.58), the contribution of τ^-_{ij} to the transfer term $T^{(Z)}(\boldsymbol{k},t)$ is found to be:

$$\tau^-_{ij}N^*_iN^*_j=kp\left(\mathcal{E}''+\Re X''\right)\left[-(xy+z^3)Z+z(1-z^2)\mathcal{E}e^{-2\mathrm{i}\lambda}\right]+\mathrm{i}\Im X''kp(1-z^2)x\left(\mathcal{E}e^{-2\mathrm{i}\lambda}+Z\right),\tag{B.59}$$

while the contribution of τ^+_{ij} is given by

$$\begin{aligned}\tau^+_{ij}N^*_iN^*_j=&\frac{1}{2}k^2e^{-2\mathrm{i}\lambda}(1-z^2)\left(\mathcal{E}'+\Re X'\right)\left[(1+y^2)\left(\mathcal{E}''+\Re X''\right)-2\mathcal{E}''-2\mathrm{i}y\Im X''\right]\\&-\frac{1}{2}k^2e^{-2\mathrm{i}\lambda}(x+yz)\left(y\left(\mathcal{E}''+\Re X''\right)-\mathrm{i}\Im X''\right)\left(z\left(\mathcal{E}'+\Re X'\right)-\mathrm{i}\Im X'\right),\end{aligned}\tag{B.60}$$

which can be replaced by the following expression, according to (B.49):

$$\begin{aligned}\tau^+_{ij}N^*_iN^*_j=&\frac{1}{4}k^2e^{-2\mathrm{i}\lambda}(1-z^2)\left(\mathcal{E}'+\Re X'\right)\left[(1+y^2)\left(\mathcal{E}''+\Re X''\right)-2\mathcal{E}''-2\mathrm{i}y\Im X''\right]\\&+\frac{1}{4}k^2e^{-2\mathrm{i}\lambda}(1-y^2)\left(\mathcal{E}''+\Re X''\right)\left[(1+z^2)\left(\mathcal{E}'+\Re X'\right)-2\mathcal{E}'-2\mathrm{i}z\Im X'\right]\\&-\frac{1}{2}k^2e^{-2\mathrm{i}\lambda}(x+yz)\left(y\left(\mathcal{E}''+\Re X''\right)-\mathrm{i}\Im X''\right)\left(z\left(\mathcal{E}'+\Re X'\right)-\mathrm{i}\Im X'\right).\end{aligned}\tag{B.61}$$

Using geometrical relations such as (B.46)-(B.47) allows to further simplify (B.61):

$$\begin{aligned}\tau^{+}_{ij}N^{*}_{i}N^{*}_{j} =& e^{-2\mathrm{i}\lambda}kp(xy+z^{3})\left(\mathcal{E}'+\Re X'\right)\left(\mathcal{E}''+\Re X''\right)-e^{-2\mathrm{i}\lambda}kp(xy+z)\left(\mathcal{E}''+\Re X''\right)\mathcal{E}'\\ &+\mathrm{i}e^{-2\mathrm{i}\lambda}kp(y^{2}-z^{2})\left(\mathcal{E}''+\Re X''\right)\Im X'+e^{-2\mathrm{i}\lambda}kpy(1-z^{2})\Im X'\Im X''.\end{aligned} \tag{B.62}$$

Combining (B.59) and (B.62) leads to the final closed-form expression of the transfer term $T^{(Z)}(\boldsymbol{k},t)$:

$$\begin{aligned}T^{(Z)}(\boldsymbol{k},t) = \iiint \theta_{kpq}2kpe^{-2\mathrm{i}\lambda}\Big[&(\mathcal{E}''+\Re X'')[(xy+z^{3})(\Re X'-X)-z(1-z^{2})(\mathcal{E}'-\mathcal{E})+\mathrm{i}(y^{2}-z^{2})\Im X']\\ &+\mathrm{i}\Im X''(1-z^{2})[x(\mathcal{E}+X)-\mathrm{i}y\Im X']\Big]\mathrm{d}^{3}\boldsymbol{p}.\end{aligned} \tag{B.63}$$

B.1.5.4 Transfer term $T^{(\mathcal{E})}(\boldsymbol{k},t)$

From the relations

$$T^{(\mathcal{E})}(\boldsymbol{k},t) = \frac{1}{4}\left(\tau_{ij}(\boldsymbol{k},t)+\tau^{*}_{ji}(\boldsymbol{k},t)\right)\left(N^{*}_{i}N_{j}+N_{i}N^{*}_{j}\right), \tag{B.64}$$

$$\tau^{-}_{ij}N_{i}N^{*}_{j} = kp(xy+z)\left(\mathcal{E}''+\Re X''\right)\left(-\mathcal{E}+(1-z^{2})\left(\mathcal{E}+Ze^{2\mathrm{i}\lambda}\right)\right)-kp(1-z^{2})x\left(y\left(\mathcal{E}''+\Re X''\right)+\mathrm{i}\Im X''\right)\left(\mathcal{E}+Ze^{2\mathrm{i}\lambda}\right), \tag{B.65}$$

$$\tau^{-}_{ij}N^{*}_{i}N_{j} = kp(xy+z)\left(\mathcal{E}''+\Re X''\right)\left(-\mathcal{E}+(1-z^{2})\left(\mathcal{E}+Z^{*}e^{-2\mathrm{i}\lambda}\right)\right)-kp(1-z^{2})x\left(y\left(\mathcal{E}''+\Re X''\right)-\mathrm{i}\Im X''\right)\left(\mathcal{E}+Z^{*}e^{-2\mathrm{i}\lambda}\right), \tag{B.66}$$

the contribution of τ^{-}_{ij} to the transfer term $T^{(\mathcal{E})}(\boldsymbol{k},t)$ is found to be:

$$\frac{1}{2}\tau^{-}_{ii} = \frac{1}{4}\tau^{-}_{ij}\left(N_{i}N^{*}_{j}+N^{*}_{i}N_{j}\right) = \frac{1}{2}kp\left(\mathcal{E}''+\Re X''\right)\left[-(xy+z^{3})\mathcal{E}+z(1-z^{2})\Re X\right]+\frac{1}{2}kp(1-z^{2})x\Im X\Im X''. \tag{B.67}$$

Similarly, using

$$\tau^{+}_{ij}N_{i}N^{*}_{j} = \frac{1}{2}(1-z^{2})\left(\mathcal{E}'+\Re X'\right)k^{2}\left[\mathcal{E}''(1+y^{2})-\Re X''(1-y^{2})\right]-\frac{1}{2}(x+yz)k^{2}\left(y\left(\mathcal{E}''+\Re X''\right)+\mathrm{i}\Im X''\right)\left(z\left(\mathcal{E}'+\Re X'\right)-\mathrm{i}\Im X'\right), \tag{B.68}$$

$$\tau^{+}_{ij}N^{*}_{i}N_{j} = \frac{1}{2}(1-z^{2})\left(\mathcal{E}'+\Re X'\right)k^{2}\left[\mathcal{E}''(1+y^{2})-\Re X''(1-y^{2})\right]-\frac{1}{2}(x+yz)k^{2}\left(y\left(\mathcal{E}''+\Re X''\right)-\mathrm{i}\Im X''\right)\left(z\left(\mathcal{E}'+\Re X'\right)+\mathrm{i}\Im X'\right), \tag{B.69}$$

one can find the contribution of τ^{+}_{ij} to $T^{(\mathcal{E})}(\boldsymbol{k},t)$:

$$\tau^{+}_{ij}\left(N^{*}_{i}N_{j}+N_{i}N^{*}_{j}\right) = k^{2}\left(\mathcal{E}'+\Re X'\right)\left(\mathcal{E}''+\Re X''\right)(y^{2}-2y^{2}z^{2}-xyz)+k^{2}(1-z^{2})\left(\mathcal{E}'+\Re X'\right)\left(\mathcal{E}''-\Re X''\right)-k^{2}(yz+x)\Im X'\Im X''. \tag{B.70}$$

After symmetrization using (B.49), (B.70) can be replaced by

$$\begin{aligned}\tau^{+}_{ij}\left(N^{*}_{i}N_{j}+N_{i}N^{*}_{j}\right) =& k^{2}\left(\mathcal{E}'+\Re X'\right)\left(\mathcal{E}''+\Re X''\right)(1-2y^{2}z^{2}-xyz)-k^{2}(1-y^{2})\left(\mathcal{E}''+\Re X''\right)\Re X'\\ &-k^{2}(1-z^{2})\left(\mathcal{E}'+\Re X'\right)\Re X''-k^{2}(yz+x)\Im X'\Im X'',\end{aligned} \tag{B.71}$$

which may be further simplified as

$$\tau^{+}_{ij}\left(N^{*}_{i}N_{j}+N_{i}N^{*}_{j}\right) = 2kp(xy+z^{3})\left(\mathcal{E}'+\Re X'\right)\left(\mathcal{E}''+\Re X''\right)-2kp(xy+z)\left(\mathcal{E}''+\Re X''\right)\Re X'-2kpy(1-z^{2})\Im X'\Im X''. \tag{B.72}$$

Using (B.67) and (B.72) allows to derive the closed-form expression of the transfer term $T^{(\mathcal{E})}(\boldsymbol{k},t)$:

$$T^{(\mathcal{E})}(\boldsymbol{k},t) = \iiint \theta_{kpq}2kp\Big[(\mathcal{E}''+\Re X'')[(xy+z^{3})(\mathcal{E}'-\mathcal{E})-z(1-z^{2})(\Re X'-\Re X)]+\Im X''(1-z^{2})(x\Im X-y\Im X')\Big]\mathrm{d}^{3}\boldsymbol{p}. \tag{B.73}$$

B.1.5.5 Transfer term $T^{(RTI)}(\boldsymbol{k}, t)$

The contributions of τ^-_{ij} and τ^+_{ij} to the transfer term $T^{(RTI)}(\boldsymbol{k}, t)$ are respectively given by:

$$\alpha_i \tau^-_{ij} N^*_j = e^{-\mathrm{i}\lambda} k(1 - y^2) \sqrt{1 - z^2} \left(\mathcal{E}'' + \Re X''\right) (\mathcal{E} + X) (zk - qx), \tag{B.74}$$

$$\begin{aligned} \alpha_i \tau^+_{ij} N^*_j = & \frac{1}{2} e^{-\mathrm{i}\lambda} k^2 (1 - z^2) \sqrt{1 - y^2} \left(\mathcal{E}' + \Re X'\right) \left(y(\mathcal{E}'' + \Re X'') - \mathrm{i}\Im X''\right) \\ & - \frac{1}{2} e^{-\mathrm{i}\lambda} k^2 (1 - y^2) \sqrt{1 - z^2} \left(\mathcal{E}'' + \Re X''\right) \left(z(\mathcal{E}' + \Re X') - \mathrm{i}\Im X'\right). \end{aligned} \tag{B.75}$$

Equation (B.75) may be replaced by the following expression, according to (B.49):

$$\alpha_i \tau^+_{ij} N^*_j = -e^{-\mathrm{i}\lambda} k^2 (1 - y^2) \sqrt{1 - z^2} \left(\mathcal{E}'' + \Re X''\right) \left(z(\mathcal{E}' + \Re X') - \mathrm{i}\Im X'\right). \tag{B.76}$$

From (B.74) and (B.76), one can deduces the final closed-form expression of $T^{(RTI)}(\boldsymbol{k}, t)$:

$$T^{(RTI)}(\boldsymbol{k}, t) = \iiint \theta_{kpq} 2 e^{-\mathrm{i}\lambda} p(xy + z) \sqrt{1 - z^2} (\mathcal{E}'' + \Re X'') \left[(\mathcal{E} + X)(zk - qx) - k \left(z(\mathcal{E}' + \Re X') - \mathrm{i}\Im X'\right)\right] \mathrm{d}^3 \boldsymbol{p}. \tag{B.77}$$

B.2 Dynamical equations for spherically-averaged descriptors

Strictly speaking, generalized Lin equations (B.20)-(B.21) with closed-form expressions (B.63) and (B.73) of the tranfer terms can be solved. However, important practical difficulties arise from the $\boldsymbol{k}$ dependence of the second-order spectral tensor $\hat{R}_{ij}(\boldsymbol{k}, t)$, or equivalently of that of $\mathcal{E}(\boldsymbol{k}, t)$ and $Z(\boldsymbol{k}, t)$. In order to circumvent these difficulties, one solution is to integrate analytically the closed Lin equations over a sphere of radius k. This analytical integration requires a representation of the tensor $\hat{R}_{ij}(\boldsymbol{k}, t)$, which is exposed in §B.2.1. This representation involves spherically-averaged descriptors whose governing equations are derived in the remainder of this section.

B.2.1 Representation of the second-order spectral tensor in terms of spherically-averaged descriptors

Here, we use for $\hat{R}_{ij}(\boldsymbol{k}, t)$ the representation proposed by Cambon and Rubinstein [38]. This representation involves spherically-averaged descriptors and is obtained by treating directionality and polarization anisotropy separately. It is written as:

$$\hat{R}_{ij}(\boldsymbol{k}, t) = \underbrace{\frac{E(k, t)}{4\pi k^2} P_{ij}(\boldsymbol{k})}_{\hat{R}^{(iso)}_{ij}(\boldsymbol{k},t)} \underbrace{- 15 \frac{E(k, t)}{4\pi k^2} P_{ij}(\boldsymbol{k}) H^{(dir)}_{pq}(k, t) \alpha_p \alpha_q}_{\hat{R}^{(dir)}_{ij}(\boldsymbol{k},t)} + \underbrace{5 \frac{E(k, t)}{4\pi k^2} \left(P_{ip}(\boldsymbol{k}) P_{jq}(\boldsymbol{k}) + \frac{1}{2} P_{ij}(\boldsymbol{k}) \alpha_p \alpha_q\right) H^{(pol)}_{pq}(k, t)}_{\hat{R}^{(pol)}_{ij}(\boldsymbol{k},t)}, \tag{B.78}$$

or equivalently

$$\mathcal{E}(\boldsymbol{k}, t) = \frac{E(k, t)}{4\pi k^2} \left(1 - 15 H^{(dir)}_{ij}(k, t) \alpha_i \alpha_j\right), \quad Z(\boldsymbol{k}, t) = \frac{5}{2} \frac{E(k, t)}{4\pi k^2} H^{(pol)}_{ij}(k, t) N^*_i(\boldsymbol{k}) N^*_j(\boldsymbol{k}), \tag{B.79}$$

where the tensor $P_{ij}(\boldsymbol{k})$ is defined by (B.5) and $\alpha_i = k_i/k$. The tensors $\hat{R}^{(iso)}_{ij}(\boldsymbol{k}, t)$, $\hat{R}^{(dir)}_{ij}(\boldsymbol{k}, t)$ and $\hat{R}^{(pol)}_{ij}(\boldsymbol{k}, t)$ identify the isotropic, directional and polarization parts of $\hat{R}_{ij}(\boldsymbol{k}, t)$, respectively. The representation (B.78) is constructed so that the trace-free tensors $H^{(dir)}_{ij}(k, t)$ and $H^{(pol)}_{ij}(k, t)$, which depend only on k, measure directional and polarization anisotropies according to

$$2E(k,t)H_{ij}^{(dir)}(k,t) = \iint_{S_k} \hat{R}_{ij}^{(dir)}(\boldsymbol{k},t)\mathrm{d}^2\boldsymbol{k}, \quad 2E(k,t)H_{ij}^{(pol)}(k,t) = \iint_{S_k} \hat{R}_{ij}^{(pol)}(\boldsymbol{k},t)\mathrm{d}^2\boldsymbol{k}, \tag{B.80}$$

These tensors generate directly the spherically integrated second-order spectral tensor $\varphi_{ij}(k,t)$:

$$\varphi_{ij}(k,t) = \iint_{S_k} \hat{R}_{ij}(\boldsymbol{k},t)\mathrm{d}^2\boldsymbol{k} = 2E(k,t)\left(\frac{\delta_{ij}}{3} + H_{ij}^{(dir)}(k,t) + H_{ij}^{(pol)}(k,t)\right). \tag{B.81}$$

Injecting the representation of $\mathcal{E}(\boldsymbol{k},t)$ and $Z(\boldsymbol{k},t)$ (B.79) into equations (B.20)-(B.21), (B.63) and (B.73) allows to integrate analytically the latter over a sphere of radius k and to derive a system of governing equations in terms of the spherically-averaged descriptors $E(k,t)$, $H_{ij}^{(dir)}(k,t)$ and $H_{ij}^{(pol)}(k,t)$. In view of (B.78)-(B.79) and (B.81), the latter completely determine the second-order spectral tensor $\hat{R}_{ij}(\boldsymbol{k},t)$ and its spherically integrated counterpart $\varphi_{ij}(k,t)$, however restricted to moderate anisotropy. This point is discussed in chapter 4.

B.2.2 Dynamics, final closure

The final system of governing equations is written as follows:

$$\left(\frac{\partial}{\partial t} + 2\nu k^2\right)E(k,t) = \mathcal{S}^L(k,t) + T(k,t), \tag{B.82}$$

$$\left(\frac{\partial}{\partial t} + 2\nu k^2\right)E(k,t)H_{ij}^{(dir)}(k,t) = \mathcal{S}_{ij}^{L(dir)}(k,t) + \mathcal{S}_{ij}^{NL(dir)}(k,t), \tag{B.83}$$

$$\left(\frac{\partial}{\partial t} + 2\nu k^2\right)E(k,t)H_{ij}^{(pol)}(k,t) = \mathcal{S}_{ij}^{L(pol)}(k,t) + \mathcal{S}_{ij}^{NL(pol)}(k,t), \tag{B.84}$$

with

$$2\left(\frac{\delta_{ij}}{3}T(k,t) + \mathcal{S}_{ij}^{NL(dir)}(k,t) + \mathcal{S}_{ij}^{NL(pol)}(k,t)\right) = \mathcal{S}_{ij}(k,t) + \mathcal{P}_{ij}(k,t). \tag{B.85}$$

The tensors $\mathcal{S}^L(k,t)$, $\mathcal{S}_{ij}^{L(dir)}(k,t)$ and $\mathcal{S}_{ij}^{L(pol)}(k,t)$, inherited from Rapid Distortion Theory (RDT), account for the linear terms corresponding to the interactions with the mean flow and the rotation of the frame, whereas $T(k,t)$, $\mathcal{S}_{ij}^{NL(dir)}(k,t)$ and $\mathcal{S}_{ij}^{NL(pol)}(k,t)$ correspond to nonlinear transfer terms. The tensor $\mathcal{P}_{ij}(k,t)$ is the spherically integrated spectral counterpart of the slow pressure-strain rate tensor, to which a return-to-isotropy is conventionally attributed. The tensor $\mathcal{S}_{ij}(k,t)$ corresponds to a 'true' transfer tensor with $\int_0^\infty \mathcal{S}_{ij}(k,t)dk = 0\ \forall t$. Since the tensors $H_{ij}^{(dir)}(k,t)$ and $H_{ij}^{(pol)}(k,t)$ are symmetric and trace-free, the system (B.82)-(B.84) forms a set of 11 different equations.

B.2.3 Closure for the terms inherited from RDT

In order to obtain the terms $\mathcal{S}^L(k,t)$, $\mathcal{S}_{ij}^{L(dir)}(k,t)$ and $\mathcal{S}_{ij}^{L(pol)}(k,t)$, one has to analytically solve the spherical averaging of tensorial products of vectors $\boldsymbol{\alpha} = \boldsymbol{k}/k$. This is done as [39]:

$$\iint_{S_k} \alpha_{i_1}\alpha_{i_2}\cdots\alpha_{i_{2N}}\mathrm{d}^2\boldsymbol{k} = \frac{4\pi k^2}{1\cdot 3\cdots(2N+1)}\delta^N_{i_1 i_2\cdots i_{2N}}, \tag{B.86}$$

where $\delta^N_{i_1 i_2\cdots i_{2N}}$ is defined by:

$$\delta^1_{ij} = \delta_{ij}, \quad \delta^N_{i_1 i_2\cdots i_{2N}} = \sum_{r=1}^{2N-1} \delta_{i_r i_{2N}}\delta^{N-1}_{i_1 i_2\cdots i_{r-1} i_{r+1}\cdots i_{2N-1}}. \tag{B.87}$$

A relatively efficient method to derive the expressions of $\mathcal{S}^L(k,t)$, $\mathcal{S}_{ij}^{L(dir)}(k,t)$ and $\mathcal{S}_{ij}^{L(pol)}(k,t)$ may consist, in a first step, in performing the spherical integration of the linear contributions of (B.8). In a second step, after taking half the trace of (B.8) and multiplying by the operator $P_{ij} = P_{ij}(\boldsymbol{k})$, spherical integration provides both isotropic and directional contributions. Polarization terms are obtained through the difference between the total contribution obtained in the first step and the isotropic and directional terms. Useful results are:

$$\iint_{S_k} H_{mn}^{()}\alpha_m\alpha_n P_{ij}\mathrm{d}^2\boldsymbol{k} = -\frac{8\pi k^2}{15}H_{ij}^{()}, \quad \iint_{S_k} H_{mn}^{()}N_m^* N_n^* N_i N_j\mathrm{d}^2\boldsymbol{k} = \frac{16\pi k^2}{5}H_{ij}^{()} \tag{B.88}$$

$$\iint_{S_k} H_{mn}^{()}\alpha_m N_n^*\alpha_i N_j\mathrm{d}^2\boldsymbol{k} = \frac{4\pi k^2}{5}H_{ij}^{()}, \quad \lambda_{ln}\iint_{S_k}\alpha_i\alpha_j\alpha_l\alpha_n\mathrm{d}^2\boldsymbol{k} = \frac{4\pi k^2}{15}\left(\lambda_{ij}+\lambda_{ji}\right), \tag{B.89}$$

$$\lambda_{ln}H_{pq}^{()}\iint_{S_k}\alpha_i\alpha_j\alpha_l\alpha_n\alpha_p\alpha_q\mathrm{d}^2\boldsymbol{k} = \frac{8\pi k^2}{105}\left[\left(\lambda_{li}+\lambda_{il}\right)H_{lj}^{()} + \left(\lambda_{lj}+\lambda_{jl}\right)H_{li}^{()} + \lambda_{ln}H_{ln}^{()}\delta_{ij}\right] \tag{B.90}$$

$$\iint_{S_k}\lambda_{ln}k_l\frac{\partial}{\partial k_n}(H_{pq}^{()}\alpha_p\alpha_q)\mathrm{d}^2\boldsymbol{k} = \frac{8\pi k^2}{15}\left(k\frac{\partial}{\partial k}(H_{ln}^{()}) + 3H_{ln}\right)\lambda_{ln}, \tag{B.91}$$

$$\begin{aligned}\iint_{S_k}\lambda_{ln}k_l\frac{\partial}{\partial k_n}(H_{pq}^{()}\alpha_p\alpha_q\alpha_i\alpha_j)\mathrm{d}^2\boldsymbol{k} =&\frac{8\pi k^2}{105}\Big[\left(\lambda_{li}+\lambda_{il}\right)\left(k\frac{\partial}{\partial k}(H_{lj}^{()}) + 3H_{lj}^{()}\right) + \left(\lambda_{lj}+\lambda_{jl}\right)\left(k\frac{\partial}{\partial k}(H_{li}^{()}) + 3H_{li}^{()}\right)\\ &+ \lambda_{ln}\left(k\frac{\partial}{\partial k}(H_{ln}^{()}) + 3H_{ln}\right)\delta_{ij}\Big],\end{aligned} \tag{B.92}$$

where $H_{ij}^{()}$ may refer to either $H_{ij}^{(dir)}(k,t)$, $H_{ij}^{(pol)}(k,t)$, $H_{ij}^{(dir)}(p,t)$, $H_{ij}^{(pol)}(p,t)$, $H_{ij}^{(dir)}(q,t)$ or $H_{ij}^{(pol)}(q,t)$. The final expressions of $\mathcal{S}^L(k,t)$, $\mathcal{S}_{ij}^{L(dir)}(k,t)$ and $\mathcal{S}_{ij}^{L(pol)}(k,t)$ can be written as:

$$\mathcal{S}^L(k,t) = -2S_{lm}\frac{\partial}{\partial k}(kEH_{lm}^{(dir)}) - 2ES_{lm}\left(H_{lm}^{(dir)} + H_{lm}^{(pol)}\right), \tag{B.93}$$

$$\begin{aligned}\mathcal{S}_{ij}^{L(dir)}(k,t) =&\frac{2}{15}S_{ij}E - \frac{2}{7}E\left(S_{jl}H_{il}^{(pol)} + S_{il}H_{jl}^{(pol)} - \frac{2}{3}S_{lm}H_{lm}^{(pol)}\delta_{ij}\right) - \frac{1}{15}S_{ij}\frac{\partial}{\partial k}(kE)\\ &+ \frac{2}{7}\left(S_{il}\frac{\partial}{\partial k}(kEH_{lj}^{(dir)}) + S_{lj}\frac{\partial}{\partial k}(kEH_{li}^{(dir)}) - \frac{2}{3}S_{lm}\frac{\partial}{\partial k}(kEH_{lm}^{(dir)})\delta_{ij}\right)\\ &- \frac{1}{7}E\left(S_{jl}H_{li}^{(dir)} + S_{il}H_{lj}^{(dir)} - \frac{2}{3}S_{lm}H_{lm}^{(dir)}\delta_{ij}\right) + E\left(A_{jn}H_{ni}^{(dir)} + A_{in}H_{jn}^{(dir)}\right),\end{aligned} \tag{B.94}$$

$$\begin{aligned}\mathcal{S}_{ij}^{L(pol)}(k,t) =& -\frac{2}{5}ES_{ij} - \frac{12}{7}E\left(S_{lj}H_{li}^{(dir)} + S_{il}H_{lj}^{(dir)} - \frac{2}{3}S_{lm}H_{lm}^{(dir)}\delta_{ij}\right) - \frac{1}{3}E\left(A_{il}H_{lj}^{(pol)} + A_{jl}H_{li}^{(pol)}\right)\\ &- \frac{2}{7}\left(S_{jl}\frac{\partial}{\partial k}(kEH_{il}^{(pol)}) + S_{il}\frac{\partial}{\partial k}(kEH_{lj}^{(pol)}) - \frac{2}{3}S_{ln}\frac{\partial}{\partial k}(kEH_{ln}^{(pol)})\delta_{ij}\right)\\ &+ \frac{1}{7}E\left(S_{il}H_{lj}^{(pol)} + S_{jl}H_{li}^{(pol)} - \frac{2}{3}S_{lm}H_{lm}^{(pol)}\delta_{ij}\right) - \frac{4}{3}E\left(\epsilon_{ilr}\Omega_l H_{rj}^{(pol)} + \epsilon_{jlr}\Omega_l H_{ri}^{(pol)}\right),\end{aligned} \tag{B.95}$$

with $E = E(k,t)$, $H_{ij}^{(dir)} = H_{ij}^{(dir)}(k,t)$, $H_{ij}^{(pol)} = H_{ij}^{(pol)}(k,t)$, $S_{ij} = (\lambda_{ij}+\lambda_{ji})/2$, $A_{ij} = (\lambda_{ij}-\lambda_{ji})/2$.

B.2.4 Closure from the terms mediated by third-order correlations

The transfer terms $T(k,t)$, $\mathcal{S}_{ij}^{NL(dir)}(k,t)$ and $\mathcal{S}_{ij}^{NL(pol)}(k,t)$ are obtained from the spherical integration of the expressions of the transfer terms $T^{(\mathcal{E})}(\boldsymbol{k},t)$ and $T^{(Z)}(\boldsymbol{k},t)$ closed by the EDQNM procedure (B.63) and (B.73) and using the representation (B.79) for $\mathcal{E}(\boldsymbol{k},t)$ and $Z(\boldsymbol{k},t)$. It is consistent to retain only linear contributions from the tensors $H_{ij}^{(dir)}(k,t)$ and $H_{ij}^{(pol)}(k,t)$ in the terms present in the right-hand-sides of the system (B.82)-(B.84) in view of the discussions in [38, 162]. Quadratic contributions of these tensors are nevertheless evaluated in §B.2.5. In anisotropic triadic closure, the new difficulty is to solve the integral over the orientation of the plane of the triad.

The integral $\iiint S(\boldsymbol{k},\boldsymbol{p},t)\mathrm{d}^3\boldsymbol{p}$ is simplified as

$$\iiint S(\boldsymbol{k},\boldsymbol{p},t)\mathrm{d}^3\boldsymbol{p} = \iint_{\Delta_k} \frac{pq}{k}\left(\int_0^{2\pi} \tilde{S}(\boldsymbol{k},p,q,\lambda)\mathrm{d}\lambda\right)\mathrm{d}p\mathrm{d}q, \tag{B.96}$$

using the new variables $(\boldsymbol{k},p_1,p_2,p_3) \to (\boldsymbol{k},p,q,\lambda)$. This system of bipolar variables is classical in isotropic turbulence, the integral over p and q is performed over the domain Δ_k so that k, p and q are the lengths of the sides of the triangle formed by $\boldsymbol{k}$, $\boldsymbol{p}$ and $\boldsymbol{q}$. At fixed $\boldsymbol{k}$, p and q give the geometry of the triad around $\boldsymbol{k}$, and the angle λ fixes the orientation of the plane of the triad around $\boldsymbol{k}$, and therefore the azimutal angle of $\boldsymbol{p}$ (or $\boldsymbol{q}$) around $\boldsymbol{k}$. In isotropic turbulence, the λ-integral amounts to a multiplication by 2π. Here, the anisotropic part of the closure needs integrals such as:

$$\int_0^{2\pi} \alpha'_i\alpha'_j\mathrm{d}\lambda = \pi\left[(1-z^2)\delta_{ij} + (3z^2-1)\alpha_i\alpha_j\right], \quad \int_0^{2\pi} W'_iW'_j\mathrm{d}\lambda = \pi(z^2-1)(\delta_{ij}-3\alpha_i\alpha_j), \tag{B.97}$$

$$\int_0^{2\pi} e^{-2\mathrm{i}\lambda}\alpha'_i\alpha'_jd\lambda = \pi\frac{1-z^2}{2}N^*_iN^*_j, \quad \int_0^{2\pi} e^{-2\mathrm{i}\lambda}W'_iW'_j\mathrm{d}\lambda = \pi\frac{(1+z)^2}{2}N^*_iN^*_j, \tag{B.98}$$

$$\int_0^{2\pi} e^{-2\mathrm{i}\lambda}W'^*_iW'^*_j\mathrm{d}\lambda = \pi\frac{(1-z)^2}{2}N^*_iN^*_j, \tag{B.99}$$

$$\int_0^{2\pi} e^{-\mathrm{i}\lambda}\alpha'_i\alpha'_j\mathrm{d}\lambda = \pi z\sqrt{1-z^2}(\alpha_iN^*_j+\alpha_jN^*_i), \quad \int_0^{2\pi} e^{-\mathrm{i}\lambda}W'_iW'_j\mathrm{d}\lambda = -\pi(1+z)\sqrt{1-z^2}(\alpha_iN^*_j+\alpha_jN^*_i), \tag{B.100}$$

$$\int_0^{2\pi} e^{-\mathrm{i}\lambda}W'^*_iW'^*_j\mathrm{d}\lambda = \pi(1-z)\sqrt{1-z^2}(\alpha_iN^*_j+\alpha_jN^*_i). \tag{B.101}$$

Similar results for $\alpha''_i\alpha''_j$ and $W''_iW''_j$ (or conjugate) are obtained by replacing z by y in equations (B.97)-(B.101) and by multiplying by -1 the right-hand-sides of (B.100)-(B.101). Since the above expressions depend only on $\boldsymbol{k}$ and the geometry of the triad, they allow to perform spherical integration using (B.88)-(B.89). Final results are:

$$T(k,t) = \iint_{\Delta_k} \theta_{kpq}16\pi^2p^2k^2q(xy+z^3)\mathcal{E}''_0(\mathcal{E}'_0-\mathcal{E}_0)\mathrm{d}p\mathrm{d}q, \tag{B.102}$$

$$\begin{aligned}\mathcal{S}^{NL(dir)}_{ij}(k,t) = &\iint_{\Delta_k} \theta_{kpq}4\pi^2p^2k^2q\mathcal{E}''_0\Big[(y^2-1)(xy+z^3)(\mathcal{E}'_0-\mathcal{E}_0)H^{(pol)''}_{ij} + z(1-z^2)^2\mathcal{E}'_0H^{(pol)'}_{ij}\Big]dpdq\\ &+ \iint_{\Delta_k} \theta_{kpq}8\pi^2p^2k^2q(xy+z^3)\mathcal{E}''_0\Big[(3y^2-1)(\mathcal{E}'_0-\mathcal{E}_0)H^{(dir)''}_{ij} + (3z^2-1)\mathcal{E}'_0H^{(dir)'}_{ij} - 2\mathcal{E}_0H^{(dir)}_{ij}\Big]\mathrm{d}p\mathrm{d}q,\end{aligned} \tag{B.103}$$

$$\begin{aligned}\mathcal{S}^{NL(pol)}_{ij}(k,t) = &\iint_{\Delta_k} \theta_{kpq}4\pi^2p^2k^2q\mathcal{E}''_0\Big[(xy+z^3)\Big((1+z^2)\mathcal{E}'_0H^{(pol)'}_{ij} - 4\mathcal{E}_0H^{(pol)}_{ij}\Big)\\ &+ z(z^2-1)(1+y^2)(\mathcal{E}'_0-\mathcal{E}_0)H^{(pol)''}_{ij} + 2z(z^2-y^2)\mathcal{E}'_0H^{(pol)'}_{ij} + 2yx(z^2-1)\mathcal{E}_0H^{(pol)''}_{ij}\Big]dpdq\\ &+ \iint_{\Delta_k} \theta_{kpq}24\pi^2p^2k^2qz(z^2-1)\mathcal{E}''_0\Big[(y^2-1)(\mathcal{E}'_0-\mathcal{E}_0)H^{(dir)''}_{ij} + (z^2-1)\mathcal{E}'_0H^{(dir)'}_{ij}\Big]\mathrm{d}p\mathrm{d}q,\end{aligned} \tag{B.104}$$

$$\begin{aligned}\mathcal{P}_{ij}(k,t) = &\iint_{\Delta_k} \theta_{kpq}16\pi^2p^2k^2q(yz+x)\mathcal{E}''_0\Big[\mathcal{E}'_0\Big(y(z^2-y^2)(6H^{(dir)''}_{ij} + H^{(pol)''}_{ij}) - (xz+y)H^{(pol)''}_{ij}\Big)\\ &- y(z^2-x^2)\mathcal{E}_0(6H^{(dir)''}_{ij} + H^{(pol)''}_{ij})\Big]\mathrm{d}p\mathrm{d}q,\end{aligned} \tag{B.105}$$

with $\mathcal{E}_0 = \frac{E(k,t)}{4\pi k^2}$, $\mathcal{E}_0' = \frac{E(p,t)}{4\pi p^2}$, $\mathcal{E}_0'' = \frac{E(q,t)}{4\pi q^2}$, $H_{ij}^{()} = H_{ij}^{()}(k,t)$, $H_{ij}^{()'} = H_{ij}^{()}(p,t)$ and $H_{ij}^{()''} = H_{ij}^{()}(q,t)$, where $H_{ij}^{()}$ may refer to either $H_{ij}^{(dir)}$ or $H_{ij}^{(pol)}$. The expression of the 'true' transfer $\mathcal{S}_{ij}(k,t)$ can be deduced from equations (B.85) and (B.102)-(B.105).

B.2.5 Quadratic contributions

In this last section, the quadratic contributions from the tensors $H_{ij}^{(dir)}(k,t)$ and $H_{ij}^{(pol)}(k,t)$ are derived. They should be needed only in the case of highly anisotropic turbulent flows and used in conjunction with a finer representation than (B.78), involving higher order terms [162, 186]. Intermediate results concerning the integration over the orientation of the plane of the triad for isotropic and directional contributions are:

$$\begin{aligned}
&\int_0^{2\pi} H_{ij}^{(dir)''} H_{lm}^{(dir)'} \alpha_i'' \alpha_j'' \alpha_l' \alpha_m' \mathrm{d}\lambda = 2\pi H_{ij}^{(dir)''} H_{lm}^{(dir)'} \Big\{ \\
&\alpha_i \alpha_j \alpha_l \alpha_m \Big[y^2 z^2 - \frac{1}{2} y^2 (1 - z^2) + 2yz(yz + x) - \frac{1}{2} z^2 (1 - y^2) + \frac{3}{8}(1 - y^2)(1 - z^2) \Big] \\
&- \frac{1}{2} yz(yz + x) \Big[\alpha_i \alpha_m \delta_{jl} + \alpha_i \alpha_l \delta_{jm} + \alpha_j \alpha_m \delta_{il} + \alpha_j \alpha_l \delta_{im} \Big] \\
&+ \frac{1}{8}(1 - y^2)(1 - z^2) \Big[\delta_{il}\delta_{jm} - \alpha_j \alpha_m \delta_{il} - \alpha_i \alpha_l \delta_{jm} + \delta_{im}\delta_{lj} - \alpha_j \alpha_l \delta_{im} - \alpha_i \alpha_m \delta_{lj} \Big] \Big\},
\end{aligned} \tag{B.106}$$

$$\begin{aligned}
&\int_0^{2\pi} H_{ij}^{(pol)''} H_{lm}^{(dir)'} \Re \left\{ W_i''^{*} W_j''^{*} \right\} \alpha_l' \alpha_m' \mathrm{d}\lambda = 2\pi H_{ij}^{(pol)''} H_{lm}^{(dir)'} \Big\{ \\
&\alpha_i \alpha_j \alpha_l \alpha_m \Big[z^2 (1 - y^2) - \frac{1}{2}(1 - y^2)(1 - z^2) - 2yz(yz + x) - \frac{1}{2} z^2 y^2 + \frac{3}{8} y^2 (1 - z^2) + \frac{1}{2} z^2 - \frac{1}{8}(1 - z^2) \Big] \\
&+ \frac{1}{2} yz(yz + x) \Big[\alpha_j \alpha_l \delta_{im} + \alpha_j \alpha_m \delta_{il} + \alpha_i \alpha_l \delta_{jm} + \alpha_i \alpha_m \delta_{jl} \Big] \\
&+ \frac{1}{8}(1 - z^2)(1 + y^2) \Big[\delta_{il}\delta_{jm} - \delta_{il} \alpha_j \alpha_m - \delta_{jm} \alpha_i \alpha_l + \delta_{im}\delta_{lj} - \delta_{im} \alpha_j \alpha_l - \delta_{lj} \alpha_i \alpha_m \Big] \Big\},
\end{aligned} \tag{B.107}$$

$$\begin{aligned}
&\int_0^{2\pi} H_{ij}^{(pol)''} H_{lm}^{(pol)'} \Re \left\{ W_i''^{*} W_j''^{*} \right\} \Re \left\{ W_l'^{*} W_m'^{*} \right\} \mathrm{d}\lambda = 2\pi H_{ij}^{(pol)''} H_{lm}^{(pol)'} \Big\{ \\
&\alpha_i \alpha_j \alpha_l \alpha_m \Big[2(1 - z^2)(1 - y^2) + 2yz(yz + x) + \frac{3}{8}(y^2 z^2 + 1) - \frac{1}{8}(y^2 + z^2) \Big] \\
&- \frac{1}{2} yz(yz + x) \Big[\alpha_j \alpha_l \delta_{im} + \alpha_j \alpha_m \delta_{il} + \alpha_i \alpha_l \delta_{jm} + \alpha_i \alpha_m \delta_{jl} \Big] \\
&+ \frac{1}{8}(y^2 z^2 + 1 + y^2 + z^2) \Big[\delta_{il}\delta_{jm} - \delta_{il} \alpha_j \alpha_m - \delta_{jm} \alpha_i \alpha_l + \delta_{im}\delta_{lj} - \delta_{im} \alpha_j \alpha_l - \delta_{lj} \alpha_i \alpha_m \Big] \Big\},
\end{aligned} \tag{B.108}$$

$$\begin{aligned}
&\int_0^{2\pi} H_{ij}^{(pol)''} H_{lm}^{(pol)'} \Im \left\{ W_i''^{*} W_j''^{*} \right\} \Im \left\{ W_l'^{*} W_m'^{*} \right\} \mathrm{d}\lambda = 2\pi H_{ij}^{(pol)''} H_{lm}^{(pol)'} \Big\{ \\
&\alpha_i \alpha_j \alpha_l \alpha_m \Big[2(yz + x) + \frac{1}{2} yz \Big] \\
&- \frac{1}{2}(yz + x) \Big[\alpha_j \alpha_l \delta_{im} + \alpha_j \alpha_m \delta_{il} + \alpha_i \alpha_l \delta_{jm} + \alpha_i \alpha_m \delta_{jl} \Big] \\
&+ \frac{1}{2} yz \Big[\delta_{il}\delta_{jm} - \delta_{il} \alpha_j \alpha_m - \delta_{jm} \alpha_i \alpha_l + \delta_{im}\delta_{lj} - \delta_{im} \alpha_j \alpha_l - \delta_{lj} \alpha_i \alpha_m \Big] \Big\},
\end{aligned} \tag{B.109}$$

while the polarization contributions can be derived from:

$$\begin{aligned}&\int_0^{2\pi} e^{-2\mathrm{i}\lambda} H_{ij}^{(dir)''} H_{lm}^{(dir)'} \alpha_i'' \alpha_j'' \alpha_l' \alpha_m' \mathrm{d}\lambda = 2\pi H_{ij}^{(dir)''} H_{lm}^{(dir)'} \Big\{ \\ &\frac{1}{4} y^2 (1-z^2) \alpha_i \alpha_j N_l^* N_m^* + \frac{1}{4} z^2 (1-y^2) \alpha_l \alpha_m N_i^* N_j^* - \frac{1}{8}(1-y^2)(1-z^2) \Big[N_i^* N_j^* \alpha_l \alpha_m + N_l^* N_m^* \alpha_i \alpha_j \Big] \\ &- \frac{1}{4} yz(yz+x) \Big[\alpha_i \alpha_m N_j^* N_l^* + \alpha_i \alpha_l N_j^* N_m^* + \alpha_j \alpha_m N_i^* N_l^* + \alpha_j \alpha_l N_i^* N_m^* \Big] \Big\},\end{aligned} \tag{B.110}$$

$$\begin{aligned}&\int_0^{2\pi} e^{-2\mathrm{i}\lambda} H_{ij}^{(pol)''} H_{lm}^{(dir)'} \Re\left\{ W_i''^{*} W_j''^{*} \right\} \alpha_l' \alpha_m' \mathrm{d}\lambda = 2\pi H_{ij}^{(pol)''} H_{lm}^{(dir)'} \Big\{ \\ &\frac{1}{4}(1-y^2)(1-z^2) \alpha_i \alpha_j N_l^* N_m^* + \frac{1}{4} z^2 (y^2+1) \alpha_m \alpha_l N_i^* N_j^* \\ &+ \frac{1}{4} yz(yz+x) \Big[\alpha_j \alpha_l N_i^* N_m^* + \alpha_j \alpha_m N_i^* N_l^* + \alpha_i \alpha_l N_j^* N_m^* + \alpha_i \alpha_m N_j^* N_l^* \Big] \\ &- \frac{1}{8} y^2 (1-z^2) \Big[\alpha_l \alpha_m N_i^* N_j^* + \alpha_i \alpha_j N_l^* N_m^* \Big] + \frac{1}{8}(1-z^2) \Big[\alpha_i \alpha_j N_l^* N_m^* - \alpha_l \alpha_m N_i^* N_j^* \Big] \Big\},\end{aligned} \tag{B.111}$$

$$\begin{aligned}&\int_0^{2\pi} e^{-2\mathrm{i}\lambda} H_{ij}^{(pol)''} H_{lm}^{(pol)'} \Re\left\{ W_i''^{*} W_j''^{*} \right\} \Re\left\{ W_l'^{*} W_m'^{*} \right\} \mathrm{d}\lambda = 2\pi H_{ij}^{(pol)''} H_{lm}^{(pol)'} \Big\{ \\ &\frac{1}{4}(z^2+1)(1-y^2) \alpha_i \alpha_j N_l^* N_m^* + \frac{1}{4}(y^2+1)(1-z^2) \alpha_l \alpha_m N_i^* N_j^* \\ &- \frac{1}{4} yz(yz+x) \Big[\alpha_j \alpha_l N_i^* N_m^* + \alpha_j \alpha_m N_i^* N_l^* + \alpha_i \alpha_l N_j^* N_m^* + \alpha_i \alpha_m N_j^* N_l^* \Big] \\ &- \frac{1}{8}(y^2 z^2 - 1) \Big[\alpha_l \alpha_m N_i^* N_j^* + \alpha_i \alpha_j N_l^* N_m^* \Big] + \frac{1}{8}(z^2 - y^2) \Big[\alpha_i \alpha_j N_l^* N_m^* - \alpha_l \alpha_m N_i^* N_j^* \Big] \Big\},\end{aligned} \tag{B.112}$$

$$\begin{aligned}&\int_0^{2\pi} e^{-2\mathrm{i}\lambda} H_{ij}^{(pol)''} H_{lm}^{(pol)'} \Im\left\{ W_i''^{*} W_j''^{*} \right\} \Im\left\{ W_l'^{*} W_m'^{*} \right\} \mathrm{d}\lambda = 2\pi H_{ij}^{(pol)''} H_{lm}^{(pol)'} \Big\{ \\ &\frac{1}{4}(yz+x) \Big[\alpha_j \alpha_m N_i^* N_l^* + \alpha_l \alpha_j N_i^* N_m^* + \alpha_i \alpha_m N_j^* N_l^* + \alpha_i \alpha_l N_j^* N_m^* \Big] \Big\},\end{aligned} \tag{B.113}$$

$$\begin{aligned}&\int_0^{2\pi} e^{-2\mathrm{i}\lambda} \mathrm{i} H_{ij}^{(dir)''} H_{lm}^{(pol)'} \alpha_i'' \alpha_j'' \Im\left\{ W_l'^{*} W_m'^{*} \right\} \mathrm{d}\lambda = 2\pi H_{ij}^{(dir)''} H_{lm}^{(pol)'} \Big\{ \\ &- \frac{1}{2} y^2 z \alpha_i \alpha_j N_l^* N_m^* + \frac{1}{4} z(1-y^2) \alpha_i \alpha_j N_l^* N_m^* \\ &- \frac{1}{4} y(yz+x) \Big[\alpha_i \alpha_m N_j^* N_l^* + \alpha_i \alpha_l N_j^* N_m^* + \alpha_j \alpha_m N_i^* N_l^* + \alpha_j \alpha_l N_i^* N_m^* \Big] \Big\},\end{aligned} \tag{B.114}$$

$$\begin{aligned}&\int_0^{2\pi} e^{-2\mathrm{i}\lambda} \mathrm{i} H_{ij}^{(pol)''} H_{lm}^{(pol)'} \Re\left\{ W_i''^{*} W_j''^{*} \right\} \Im\left\{ W_l'^{*} W_m'^{*} \right\} \mathrm{d}\lambda = 2\pi H_{ij}^{(pol)''} H_{lm}^{(pol)'} \Big\{ \\ &- \frac{1}{2} z(1-y^2) \alpha_i \alpha_j N_l^* N_m^* + \frac{1}{4} z(y^2-1) \alpha_i \alpha_j N_l^* N_m^* \\ &+ \frac{1}{4} y(yz+x) \Big[\alpha_i \alpha_m N_l^* N_j^* + \alpha_i \alpha_l N_j^* N_m^* + \alpha_j \alpha_m N_i^* N_l^* + \alpha_j \alpha_l N_i^* N_m^* \Big] \Big\}.\end{aligned} \tag{B.115}$$

Spherical integration is performed relying on the following relations:

$$\iint_{S_k} H_{ij}^{(dir)''} H_{lm}^{(dir)'} \delta_{il} \delta_{jm} P_{rs} \mathrm{d}^2 \boldsymbol{k} = \frac{8\pi k^2}{3} H_{lm}^{(dir)''} H_{lm}^{(dir)'} \delta_{rs}, \tag{B.116}$$

$$\iint_{S_k} H_{ij}^{(dir)''} H_{lm}^{(dir)'} \alpha_i \alpha_m \delta_{jl} P_{rs} \mathrm{d}^2 \boldsymbol{k} = \frac{4\pi k^2}{15} \Big[4 H_{lm}^{(dir)''} H_{lm}^{(dir)'} \delta_{rs} - H_{sl}^{(dir)''} H_{lr}^{(dir)'} - H_{rl}^{(dir)''} H_{ls}^{(dir)'} \Big], \tag{B.117}$$

$$\iint_{S_k} H_{ij}^{(dir)''} H_{lm}^{(dir)'} \alpha_i \alpha_j \alpha_l \alpha_m P_{rs} \mathrm{d}^2 \boldsymbol{k} = \frac{16\pi k^2}{105} \Big[3 H_{lm}^{(dir)''} H_{lm}^{(dir)'} \delta_{rs} - H_{sl}^{(dir)''} H_{lr}^{(dir)'} - H_{rl}^{(dir)''} H_{ls}^{(dir)'} \Big], \tag{B.118}$$

$$\iint_{S_k} H_{ij}^{(dir)''} H_{lm}^{(dir)'} N_i^* N_j^* \alpha_l \alpha_m N_r N_s \mathrm{d}^2\boldsymbol{k} = -\frac{32\pi k^2}{35}\Big[H_{rl}^{(dir)''} H_{ls}^{(dir)'} + H_{sl}^{(dir)''} H_{lr}^{(dir)'} - \frac{2}{3} H_{lm}^{(dir)''} H_{lm}^{(dir)'} \delta_{rs}\Big], \tag{B.119}$$

$$\iint_{S_k} H_{ij}^{(dir)''} H_{lm}^{(dir)'} \alpha_i \alpha_m N_j^* N_l^* N_r N_s \mathrm{d}^2\boldsymbol{k} = \frac{24\pi k^2}{35}\Big[H_{rl}^{(dir)''} H_{ls}^{(dir)'} + H_{sl}^{(dir)''} H_{lr}^{(dir)'} - \frac{2}{3} H_{lm}^{(dir)''} H_{lm}^{(dir)'} \delta_{rs}\Big]. \tag{B.120}$$

In the end, if quadratic contributions are taken into account, the system (B.82)-(B.84) may be rewritten as

$$\left(\frac{\partial}{\partial t} + 2\nu k^2\right) E(k,t) = \mathcal{S}^L(k,t) + T(k,t) + Q(k,t), \tag{B.121}$$

$$\left(\frac{\partial}{\partial t} + 2\nu k^2\right) E(k,t) H_{ij}^{(dir)}(k,t) = \mathcal{S}_{ij}^{L(dir)}(k,t) + \mathcal{S}_{ij}^{NL(dir)}(k,t) + Q_{ij}^{(dir)}(k,t), \tag{B.122}$$

$$\left(\frac{\partial}{\partial t} + 2\nu k^2\right) E(k,t) H_{ij}^{(pol)}(k,t) = \mathcal{S}_{ij}^{L(pol)}(k,t) + \mathcal{S}_{ij}^{NL(pol)}(k,t) + Q_{ij}^{(pol)}(k,t), \tag{B.123}$$

where $\mathcal{S}^L(k,t)$, $\mathcal{S}_{ij}^{L(dir)}(k,t)$, $\mathcal{S}_{ij}^{L(pol)}(k,t)$, $T(k,t)$, $\mathcal{S}_{ij}^{NL(dir)}(k,t)$ and $\mathcal{S}_{ij}^{NL(pol)}(k,t)$ are given in (B.93)-(B.95) and (B.102)-(B.104) respectively, and the quadratic contributions $Q(k,t)$, $Q_{ij}^{(dir)}(k,t)$ and $Q_{ij}^{(pol)}(k,t)$ are defined as:

$$\begin{aligned}
Q(k,t) = \iint_{\Delta_k} & \theta_{kpq} 20\pi^2 k^2 p^2 q \mathcal{E}_0'' \Big\{ 12(xy+z^3) H_{lm}^{(dir)''} \Big[\mathcal{E}_0' H_{lm}^{(dir)'}(3x^2-1) - \mathcal{E}_0 H_{lm}^{(dir)}(3y^2-1)\Big] \\
& - 6(xy+z^3) H_{lm}^{(pol)''} \Big[\mathcal{E}_0' H_{lm}^{(dir)'}(1-x^2) - \mathcal{E}_0 H_{lm}^{(dir)}(1-y^2)\Big] + 6z(1-z^2) H_{lm}^{(dir)''} \Big[\mathcal{E}_0' H_{lm}^{(pol)'}(1-x^2) - \mathcal{E}_0 H_{lm}^{(pol)}(1-y^2)\Big] \\
& - z(1-z^2) H_{lm}^{(pol)''} \Big[\mathcal{E}_0' H_{lm}^{(pol)'}(1+x^2) - \mathcal{E}_0 H_{lm}^{(pol)}(1+y^2)\Big] + 2xy(1-z^2) H_{lm}^{(pol)''} \Big[\mathcal{E}_0' H_{lm}^{(pol)'} - \mathcal{E}_0 H_{lm}^{(pol)}\Big]\Big\} \mathrm{d}p\mathrm{d}q,
\end{aligned} \tag{B.124}$$

$$\begin{aligned}
Q_{ij}^{(dir)}(k,t) = \iint_{\Delta_k} & \theta_{kpq} \frac{20}{7} \pi^2 k^2 p^2 q \mathcal{E}_0'' \Big\{ \\
& 12(xy+z^3)\Big[\mathcal{E}_0' \left\{\mathsf{H}^{(dir)''}, \mathsf{H}^{(dir)'}\right\}_{ij} (3xyz+1) - \mathcal{E}_0 \left\{\mathsf{H}^{(dir)''}, \mathsf{H}^{(dir)}\right\}_{ij} (1-3y^2)\Big] \\
& - 6(xy+z^3)\Big[\mathcal{E}_0' \left\{\mathsf{H}^{(pol)''}, \mathsf{H}^{(dir)'}\right\}_{ij} (1-2z^2-xyz) - \mathcal{E}_0 \left\{\mathsf{H}^{(pol)''}, \mathsf{H}^{(dir)}\right\}_{ij} (y^2-1)\Big] \\
& + 6z(1-z^2)\Big[\mathcal{E}_0' \left\{\mathsf{H}^{(dir)''}, \mathsf{H}^{(pol)'}\right\}_{ij} (1-2y^2-xyz) - \mathcal{E}_0 \left\{\mathsf{H}^{(dir)''}, \mathsf{H}^{(pol)}\right\}_{ij} (1-y^2)\Big] \\
& - z(1-z^2)\Big[\mathcal{E}_0' \left\{\mathsf{H}^{(pol)''}, \mathsf{H}^{(pol)'}\right\}_{ij} (1-2x^2-3xyz) - \mathcal{E}_0 \left\{\mathsf{H}^{(pol)''}, \mathsf{H}^{(pol)}\right\}_{ij} (1+y^2)\Big] \\
& - y(1-z^2)\Big[\mathcal{E}_0' \left\{\mathsf{H}^{(pol)''}, \mathsf{H}^{(pol)'}\right\}_{ij} (x+3yz) + \mathcal{E}_0 \left\{\mathsf{H}^{(pol)''}, \mathsf{H}^{(pol)}\right\}_{ij} 2x\Big]\Big\} \mathrm{d}p\mathrm{d}q,
\end{aligned} \tag{B.125}$$

$$\begin{aligned}
Q_{ij}^{(pol)}(k,t) = \iint_{\Delta_k} & \theta_{kpq} \frac{60}{7} \pi^2 k^2 p^2 q \mathcal{E}_0'' \Big\{ \\
& - 2(xy+z^3)\Big[\mathcal{E}_0' \left\{\mathsf{H}^{(dir)''}, \mathsf{H}^{(pol)'}\right\}_{ij} (3xyz+2z^2-1) - \mathcal{E}_0 \left\{\mathsf{H}^{(dir)''}, \mathsf{H}^{(pol)}\right\}_{ij} (2-6y^2)\Big] \\
& - (xy+z^3)\Big[\mathcal{E}_0' \left\{\mathsf{H}^{(pol)''}, \mathsf{H}^{(pol)'}\right\}_{ij} (1+xyz) - \mathcal{E}_0 \left\{\mathsf{H}^{(pol)''}, \mathsf{H}^{(pol)}\right\}_{ij} (2-2y^2)\Big] \\
& - 12z(1-z^2)\Big[\mathcal{E}_0' \left\{\mathsf{H}^{(dir)''}, \mathsf{H}^{(dir)'}\right\}_{ij} (xyz+2x^2-1) - \mathcal{E}_0 \left\{\mathsf{H}^{(dir)''}, \mathsf{H}^{(dir)}\right\}_{ij} (y^2-1)\Big] \\
& + 2z(1-z^2)\Big[\mathcal{E}_0' \left\{\mathsf{H}^{(pol)''}, \mathsf{H}^{(dir)'}\right\}_{ij} (3xyz+2y^2-1) + \mathcal{E}_0 \left\{\mathsf{H}^{(pol)''}, \mathsf{H}^{(dir)}\right\}_{ij} (1+y^2)\Big] \\
& + (y^2-z^2)\Big[\mathcal{E}_0' \left\{\mathsf{H}^{(pol)''}, \mathsf{H}^{(pol)'}\right\}_{ij} (z+yx) + \mathcal{E}_0' \left\{\mathsf{H}^{(dir)''}, \mathsf{H}^{(pol)'}\right\}_{ij} (6yx+2z)\Big] \\
& + y(1-z^2)\Big[\mathcal{E}_0' \left\{\mathsf{H}^{(pol)''}, \mathsf{H}^{(pol)'}\right\}_{ij} (yz+x) - \mathcal{E}_0 \left\{\mathsf{H}^{(pol)''}, \mathsf{H}^{(dir)}\right\}_{ij} 4x\Big]\Big\} \mathrm{d}p\mathrm{d}q,
\end{aligned} \tag{B.126}$$

with the notation

$$\left\{\mathsf{H}^{(dir)''},\mathsf{H}^{(pol)'}\right\}_{ij} = H^{(dir)''}_{il}H^{(pol)'}_{lj} + H^{(dir)''}_{jl}H^{(pol)'}_{li} - \frac{2}{3}H^{(dir)''}_{lm}H^{(pol)'}_{lm}\delta_{ij}. \tag{B.127}$$

Appendix C

A Navier-Stokes solver for compressible flows and its adjoint code

In this appendix, the Navier-Stokes solver used in chapters 5 and 6 is detailed, along with the methodology to derive the corresponding adjoint code.

C.1 A Navier-Stokes solver for compressible flows

C.1.1 Finite volume formulation

The integral form over a bounded domain of interest Ω of the two-dimensional unsteady compressible Navier-Stokes equations for perfect gas is given by

$$\frac{\partial}{\partial t}\int_{\Omega}\mathbf{Q}dV+\int_{\partial\Omega}(\mathbf{F}(\mathbf{Q})-\mathbf{G}(\mathbf{Q}))\cdot\boldsymbol{n}dS=\mathbf{0},\ \mathbf{Q}=(\rho\ \ \rho u\ \ \rho v\ \ E)^{\mathrm{T}}, \tag{C.1a}$$

$$\mathbf{F}(\mathbf{Q})=\begin{pmatrix}\rho u & \rho v\\ \rho u^2+p & \rho uv\\ \rho uv & \rho v^2+p\\ u(E+p) & v(E+p)\end{pmatrix},\ \mathbf{G}(\mathbf{Q})=\begin{pmatrix}0 & 0\\ \tau_{xx} & \tau_{xy}\\ \tau_{xy} & \tau_{yy}\\ u\tau_{xx}+v\tau_{xy}-q_x & v\tau_{yy}+u\tau_{xy}-q_y\end{pmatrix}, \tag{C.1b}$$

$$\tau_{xx}=\mu\left(2\frac{\partial u}{\partial x}-\frac{2}{3}(\frac{\partial u}{\partial x}+\frac{\partial v}{\partial y})\right),\ \tau_{yy}=\mu\left(2\frac{\partial v}{\partial y}-\frac{2}{3}(\frac{\partial u}{\partial x}+\frac{\partial v}{\partial y})\right),\ \tau_{xy}=\mu(\frac{\partial u}{\partial y}+\frac{\partial v}{\partial x}), \tag{C.1c}$$

$$q_x=-\kappa\frac{\partial T}{\partial x},\ q_y=-\kappa\frac{\partial T}{\partial y},\ p=\rho rT=(\gamma-1)\rho e,\ E=\rho\left(e+\frac{1}{2}(u^2+v^2)\right), \tag{C.1d}$$

where $\boldsymbol{n}$, ρ, u, v, p, e, T, γ, μ, κ and r refer to the outer unit normal vector to the boundary $\partial\Omega$, density, x-wise and y-wise components of the velocity vector, pressure, specific internal energy, temperature, ratio of specific heats, dynamic viscosity, thermal conductivity and a constant in the ideal gas law, respectively.

In the present solver, a cell-centered finite-volume formulation on an arbitrary unstructured triangular grid is used. We consider a triangular cell Ω_i whose boundary $\partial\Omega_i$ is defined by a finite number $N_f = 3$ of faces Γ_l according to

$$\partial\Omega_i=\bigcup_{l=1}^{N_f}\Gamma_l. \tag{C.2}$$

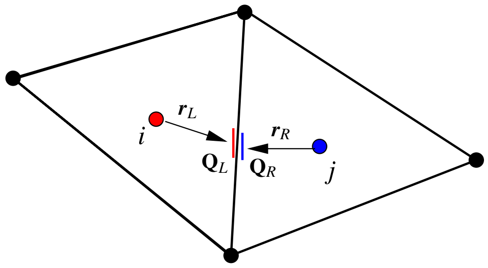

FIGURE C.1: Cell-centered linear reconstruction

For a second-order accurate spatial discretization, the line integral in (C.1a) is approximated according to

$$\int_{\Gamma_l} (\mathbf{F}(\mathbf{Q}) - \mathbf{G}(\mathbf{Q})) \cdot \boldsymbol{n} dS \simeq |\Gamma_l| \left(\mathbf{F}(\mathbf{Q}(\boldsymbol{x}_l, t)) - \mathbf{G}(\mathbf{Q}(\boldsymbol{x}_l, t))\right) \cdot \boldsymbol{n}_l, \tag{C.3}$$

where $\boldsymbol{x}_l$ is the midpoint of face Γ_l. Accordingly, the semi-discrete finite volume formulation of (C.1a) written for cell Ω_i is written as

$$\frac{d\bar{\mathbf{Q}}_i}{dt} = -\frac{1}{|\Omega_i|} \sum_{l=1}^{N_f} |\Gamma_l| \left(\mathbf{F}(\mathbf{Q}(\boldsymbol{x}_l, t)) - \mathbf{G}(\mathbf{Q}(\boldsymbol{x}_l, t))\right) \cdot \boldsymbol{n}_l = \mathbf{R}_i(\bar{\mathbf{Q}}), \tag{C.4}$$

with

$$\bar{\mathbf{Q}}(t) = \frac{1}{|\Omega_i|} \int_{\Omega_i} \mathbf{Q}(\boldsymbol{x}, t) dV. \tag{C.5}$$

Hereafter the bar symbol will be dropped for the sake of readability. Thus, $\mathbf{Q}$ refers to the flow solution at all control volumes while $\mathbf{Q}_i$ corresponds to the solution at the ith centroid.

C.1.2 Estimation of convective fluxes

Convective fluxes in (C.4) are replaced according to

$$[\mathbf{F}(\mathbf{Q}(\boldsymbol{x}_l, t)) \cdot \boldsymbol{n}_l]_{ij} \simeq \mathbf{F}^{\mathrm{num}}(\mathbf{Q}_L, \mathbf{Q}_R, \boldsymbol{n}_{ij}), \tag{C.6}$$

where subscripts L and R indicate the states of the flow properties at the right- and left-sides of the cell face between elements i and j as illustrated in figure C.1. The states $\mathbf{Q}_L$ and $\mathbf{Q}_R$ are estimated via

$$\mathbf{W}_L = \mathbf{W}_i + \left.\frac{\partial \mathbf{W}}{\partial \boldsymbol{x}}\right|_i \cdot \boldsymbol{r}_L, \tag{C.7a}$$

$$\mathbf{W}_R = \mathbf{W}_j + \left.\frac{\partial \mathbf{W}}{\partial \boldsymbol{x}}\right|_j \cdot \boldsymbol{r}_R, \tag{C.7b}$$

$$\mathbf{W}_i = \left(\rho_i \;\; u_i \;\; v_i \;\; p_i\right)^{\mathrm{T}}, \tag{C.7c}$$

where the gradient $\frac{\partial \mathbf{W}}{\partial \boldsymbol{x}}|_i$ is evaluated through the procedure described in §C.1.3. Roe's approximate Riemann solver [185, 211] is used to compute $\mathbf{F}^{\mathrm{num}}$, which is expressed as

$$\mathbf{F}^{\mathrm{num}}(\mathbf{Q}_L, \mathbf{Q}_R, \boldsymbol{n}) = \frac{1}{2}\left(\mathbf{F}^L + \mathbf{F}^R - \mathbf{A}\right), \tag{C.8a}$$

$$\mathbf{F}^L = \begin{pmatrix} \rho_L \hat{u}_L \\ \rho_L \hat{u}_L u_L + n_x p_L \\ \rho_L \hat{u}_L v_L + n_y p_L \\ \hat{u}_L \rho_L H_L \end{pmatrix}, \quad \mathbf{F}^R = \begin{pmatrix} \rho_R \hat{u}_R \\ \rho_R \hat{u}_R u_R + n_x p_R \\ \rho_R \hat{u}_R v_R + n_y p_R \\ \hat{u}_R \rho_R H_R \end{pmatrix}, \tag{C.8b}$$

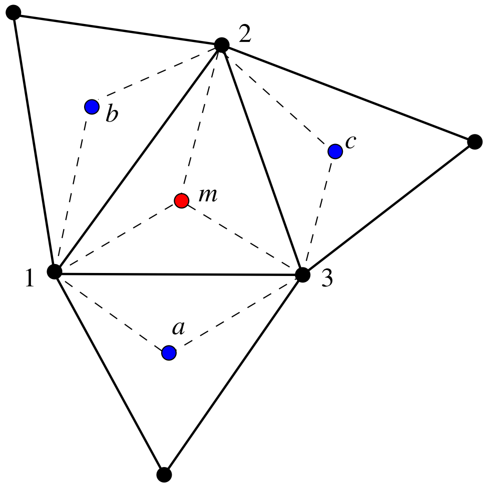

FIGURE C.2: Stencil used for the Jawahar-Kamath reconstruction [106].

$$\mathbf{A} = \begin{pmatrix} \tilde{\alpha}_1|\tilde{\lambda}_1| + \tilde{\alpha}_2|\tilde{\lambda}_2| + \tilde{\alpha}_3|\tilde{\lambda}_3| \\ |\tilde{\lambda}_1|\left[\tilde{\alpha}_1\bar{u} + \tilde{\rho}(\Delta u - n_x\Delta\hat{u})\right] + \tilde{\alpha}_2|\tilde{\lambda}_2|(\bar{u} + \tilde{a}n_x) + \tilde{\alpha}_3|\tilde{\lambda}_3|(\bar{u} - \tilde{a}n_x) \\ |\tilde{\lambda}_1|\left[\tilde{\alpha}_1\bar{v} + \tilde{\rho}(\Delta v - n_y\Delta\hat{u})\right] + \tilde{\alpha}_2|\tilde{\lambda}_2|(\bar{v} + \tilde{a}n_y) + \tilde{\alpha}_3|\tilde{\lambda}_3|(\bar{v} - \tilde{a}n_y) \\ |\tilde{\lambda}_1|\left[\tilde{\alpha}_1\frac{1}{2}\tilde{V}^2 + \tilde{\rho}(\bar{u}\Delta u + \bar{v}\Delta v - \tilde{u}\Delta\hat{u})\right] + \tilde{\alpha}_2|\tilde{\lambda}_2|(\tilde{H} + \tilde{u}\tilde{a}) + \tilde{\alpha}_3|\tilde{\lambda}_3|(\tilde{H} - \tilde{u}\tilde{a}) \end{pmatrix}, \tag{C.8c}$$

$$\boldsymbol{V} = \begin{pmatrix} u \\ v \end{pmatrix}, \quad V^2 = u^2 + v^2, \quad H = \frac{E+p}{\rho}, \quad \Delta u = u_R - u_L, \quad \hat{u}_R = u_R n_x + v_R n_y, \quad \hat{v}_R = -u_R n_y + v_R n_x, \tag{C.8d}$$

$$\tilde{\rho} = \sqrt{\rho_L \rho_R}, \quad \tilde{u} = \frac{\sqrt{\rho_L}\hat{u}_L + \sqrt{\rho_R}\hat{u}_R}{\sqrt{\rho_L} + \sqrt{\rho_R}}, \quad \tilde{v} = \frac{\sqrt{\rho_L}\hat{v}_L + \sqrt{\rho_R}\hat{v}_R}{\sqrt{\rho_L} + \sqrt{\rho_R}}, \quad \tilde{H} = \frac{\sqrt{\rho_L}\hat{H}_L + \sqrt{\rho_R}\hat{H}_R}{\sqrt{\rho_L} + \sqrt{\rho_R}}, \quad \tilde{a} = \left[(\gamma - 1)(\tilde{H} - \frac{1}{2}\tilde{V}^2)\right]^{\frac{1}{2}}, \tag{C.8e}$$

$$\bar{u} = \frac{\sqrt{\rho_L}u_L + \sqrt{\rho_R}u_R}{\sqrt{\rho_L} + \sqrt{\rho_R}}, \quad \bar{v} = \frac{\sqrt{\rho_L}v_L + \sqrt{\rho_R}v_R}{\sqrt{\rho_L} + \sqrt{\rho_R}}, \tag{C.8f}$$

$$\tilde{\lambda}_1 = \tilde{u}, \quad \tilde{\lambda}_2 = \tilde{u} + \tilde{a}, \quad \tilde{\lambda}_3 = \tilde{u} - \tilde{a}, \tag{C.8g}$$

$$\tilde{\alpha}_1 = \Delta\rho - \frac{\Delta p}{\tilde{a}^2}, \quad \tilde{\alpha}_2 = \frac{1}{2\tilde{a}^2}\left[\Delta p + \tilde{\rho}\tilde{a}\Delta\hat{u}\right], \quad \tilde{\alpha}_3 = \frac{1}{2\tilde{a}^2}\left[\Delta p - \tilde{\rho}\tilde{a}\Delta\hat{u}\right]. \tag{C.8h}$$

C.1.3 Linear reconstruction and viscous fluxes

The high-resolution Jawahar-Kamath procedure [106] is used to compute the gradient $\frac{\partial \mathbf{W}}{\partial x}|_i$ in (C.7). A typical stencil of this scheme is illustrated in figure (C.2). The gradient at the ith centroid is computed using the area-weighted average of the corresponding face gradients

$$\left.\frac{\partial \mathbf{W}}{\partial x}\right|_i = \frac{1}{S_{1a3c2b}}\left[(S_{13m} + S_{1a3})\left.\frac{\partial \mathbf{W}}{\partial x}\right|_{\Gamma_{13}} + (S_{3m2} + S_{3c2})\left.\frac{\partial \mathbf{W}}{\partial x}\right|_{\Gamma_{32}} + (S_{2m1} + S_{2b1})\left.\frac{\partial \mathbf{W}}{\partial x}\right|_{\Gamma_{21}}\right], \tag{C.9a}$$

$$\left.\frac{\partial \mathbf{W}}{\partial y}\right|_i = \frac{1}{S_{1a3c2b}}\left[(S_{13m} + S_{1a3})\left.\frac{\partial \mathbf{W}}{\partial y}\right|_{\Gamma_{13}} + (S_{3m2} + S_{3c2})\left.\frac{\partial \mathbf{W}}{\partial y}\right|_{\Gamma_{32}} + (S_{2m1} + S_{2b1})\left.\frac{\partial \mathbf{W}}{\partial y}\right|_{\Gamma_{21}}\right], \tag{C.9b}$$

where the area of the polygon S_{1a3c2b} is computed into elementary triangles according to $S_{1a3c2b} = S_{1a3} + S_{3c2} + S_{2b1} + S_{132}$. The face gradients are evaluated using an area-weighted average of gradients of a triangle formed by the two vertices of the cell face and a cell centroid. For instance, the gradient of face Γ_{13}, which involves triangles T_{13m} and T_{1a3} is expressed as

$$\left.\frac{\partial \mathbf{W}}{\partial x}\right|_{\Gamma_{13}} = \frac{1}{2(S_{13m}+S_{1a3})}\left[(\mathbf{W}_a-\mathbf{W}_m)(y_3-y_1)+(\mathbf{W}_1-\mathbf{W}_3)(y_a-y_m)\right], \tag{C.10a}$$

$$\left.\frac{\partial \mathbf{W}}{\partial y}\right|_{\Gamma_{13}} = -\frac{1}{2(S_{13m}+S_{1a3})}\left[(\mathbf{W}_a-\mathbf{W}_m)(x_3-x_1)+(\mathbf{W}_1-\mathbf{W}_3)(x_a-x_m)\right]. \tag{C.10b}$$

These face gradients are also directly used to compute viscous fluxes in (C.4). Equation (C.10) requires the flow solution at nodes, which is evaluated through pseudo Laplacian weighting [119, 184]. The value of $\mathbf{W}$ at node α is obtained from the N centroids i sharing this node according to

$$\mathbf{W}_\alpha = \frac{\sum_{i=1}^{N} w_i \mathbf{W}_i}{\sum_{i=1}^{N} w_i}, \tag{C.11a}$$

$$w_i = 1+\lambda_x(x_i-x_j)+\lambda_y(y_i-y_j), \quad \lambda_x = \frac{I_{xy}I_y - I_{yy}I_x}{I_{xx}I_{yy}-I_{xy}^2}, \quad \lambda_y = \frac{I_{xy}I_x - I_{xx}I_y}{I_{xx}I_{yy}-I_{xy}^2}, \tag{C.11b}$$

$$I_x = \sum_{i=1}^{N}(x_i-x_j), \quad I_y = \sum_{i=1}^{N}(y_i-y_j), \quad I_{xx} = \sum_{i=1}^{N}(x_i-x_j)^2, \quad I_{xy} = \sum_{i=1}^{N}(x_i-x_j)(y_i-y_j), \quad I_{yy} = \sum_{i=1}^{N}(y_i-y_j)^2. \tag{C.11c}$$

C.1.4 Time integration

Time integration of (C.4) is performed with a fully implicit second-order scheme that combines dual time stepping [105] and the LU-SGS method [145, 190]. First, discretization of (C.4) with physical time step Δt gives

$$\frac{3\mathbf{Q}^{n+1}-4\mathbf{Q}^{n}+\mathbf{Q}^{n-1}}{2\Delta t} = \mathbf{R}(\mathbf{Q}^{n+1}). \tag{C.12}$$

Equation (C.12) is solved through the introduction of a fictitious time τ

$$\frac{\partial \mathbf{Q}^n}{\partial \tau} = \hat{\mathbf{R}}^n, \quad \hat{\mathbf{R}}^n = \mathbf{R}(\mathbf{Q}^n) - \frac{3\mathbf{Q}^{n}-4\mathbf{Q}^{n-1}+\mathbf{Q}^{n-2}}{2\Delta t}, \tag{C.13}$$

and a stationary solution of (C.13) is searched using variable local time steps [105], which are represented through the scalar $\Delta\tau$ in (C.14)-(C.15) for the sake of simplicity. Discretization of (C.13) leads to

$$\frac{\Delta \mathbf{Q}^{n,m+1}}{\Delta\tau} = \hat{\mathbf{R}}^{n,m+1} \simeq \hat{\mathbf{R}}^{n,m} + \left(\frac{\partial \hat{\mathbf{R}}}{\partial \mathbf{Q}}\right)^{n,m}\Delta\mathbf{Q}^{n,m+1}, \quad \Delta\mathbf{Q}^{n,m+1} = \mathbf{Q}^{n,m+1}-\mathbf{Q}^{n,m}, \tag{C.14}$$

which is rearranged into

$$\left(\left(\frac{1}{\Delta\tau}+\frac{3}{2\Delta t}\right)\mathbf{I} - \left(\frac{\partial \mathbf{R}}{\partial \mathbf{Q}}\right)^{n,m}\right)\Delta\mathbf{Q}^{n,m+1} = \hat{\mathbf{R}}^{n,m}. \tag{C.15}$$

Equation (C.15) is solved with the LU-SGS method [145, 190]

$$\Delta\mathbf{Q}_i^* = D_i^{-1}\left[|\Omega_i|\hat{\mathbf{R}}_i^{n,m} - \sum_{j<i}\frac{1}{2}\left(\Delta\mathbf{F}_j^* - \lambda_{ji}\Delta\mathbf{Q}_j^*\right)|\Gamma_{ij}|\right], \tag{C.16a}$$

$$\Delta\mathbf{Q}_i^{n,m+1} = \Delta\mathbf{Q}_i^* - D_i^{-1}\sum_{j>i}\frac{1}{2}\left(\Delta\mathbf{F}_j - \lambda_{ji}\Delta\mathbf{Q}_j^{n,m+1}\right)|\Gamma_{ij}|, \tag{C.16b}$$

$$D_i = \frac{|\Omega_i|}{\Delta\tau_i} + \frac{3|\Omega_i|}{2\Delta t} + \frac{1}{2}\sum_{j}\lambda_{ij}|\Gamma_{ij}|, \tag{C.16c}$$

$$\Delta\mathbf{F}_i^* = \left(\mathbf{F}(\mathbf{Q}_i^{n,m} + \Delta\mathbf{Q}_i^*) - \mathbf{F}(\mathbf{Q}_i^{n,m})\right) \cdot \boldsymbol{n}_{ij}, \quad \Delta\mathbf{F}_i = \left(\mathbf{F}(\mathbf{Q}_i^{n,m} + \Delta\mathbf{Q}_i^{n,m+1}) - \mathbf{F}(\mathbf{Q}_i^{n,m})\right) \cdot \boldsymbol{n}_{ij}, \tag{C.16d}$$

$$\lambda_{ij} = |\boldsymbol{V}_i^{n,m} \cdot \boldsymbol{n}_{ij}| + a_i^{n,m} + \max\left\{\frac{4}{3\rho_i^{n,m}}, \frac{\gamma}{\rho_i^{n,m}}\right\} \frac{\mu}{Pr|\Gamma_{ij}|} C, \tag{C.16e}$$

$$\Delta\tau_i = \mathrm{CFL} \cdot \min\left\{\frac{L_i}{V_i^{n,m} + a_i^{n,m} + C_i \frac{4}{3} \frac{\mu}{\rho_i^{n,m} Pr}}, 0.5\Delta t\right\}. \tag{C.16f}$$

where C is an adjustable parameter, C_i and L_i refer to a geometrical factor and a characteristic length of element Ω_i respectively, and the CFL number is chosen as 500. The sums in (C.16) are performed over the elements j that are neighbours to element i. Pseudo-time integration is stopped after achieving a reduction by three orders of magnitude in the norm of the residual $\hat{\mathbf{R}}$.

C.1.5 Boundary conditions

Boundary conditions are elaborated using a ghost cell framework [211]. Wall boundary conditions still use Roe's solver [185] for convectives fluxes, while far-field conditions rely on the approach developed in [195].

C.2 Implementation of the adjoint code

C.2.1 Backward temporal integration

The adjoint code is obtained according to the discrete adjoint approach [44, 165, 176], i.e. the adjoint code is determined from the adjoint formulation of the fully discretized equations (C.16). The adjoint problem may be derived from the following optimization problem. Given a cost function $J(\mathbf{Q})$ that depends on the flow solution $\mathbf{Q}$ at all centroids and physical times, the following Lagragian $\mathcal{L}$ is defined in order to perform its optimization

$$\begin{aligned}\mathcal{L} =& J(\mathbf{Q}) \\ &- \sum_{n=0}^{N_t-1} \sum_{m=0}^{N_\tau-1} \sum_{j=1}^{N_\Omega} \left(\Delta\mathbf{Q}_j^* - D_j^{-1}\left[|\Omega_j|\hat{\mathbf{R}}_j^{n,m} - \sum_{k<j} \frac{1}{2}\left(\Delta\mathbf{F}_k^* - \lambda_{kj}\Delta\mathbf{Q}_k^*\right)|\Gamma_{jk}|\right]\right) \cdot \Delta\tilde{\mathbf{Q}}_j^* \\ &- \sum_{n=0}^{N_t-1} \sum_{m=0}^{N_\tau-1} \sum_{j=1}^{N_\Omega} \left(\Delta\mathbf{Q}_j^{n,m+1} - \Delta\mathbf{Q}_j^* + D_j^{-1} \sum_{k>j} \frac{1}{2}\left(\Delta\mathbf{F}_k - \lambda_{kj}\Delta\mathbf{Q}_k^{n,m+1}\right)|\Gamma_{jk}|\right) \cdot \Delta\tilde{\mathbf{Q}}_j^{n,m+1} \\ &- \sum_{n=0}^{N_t-1} \sum_{m=0}^{N_\tau-1} \sum_{j=1}^{N_\Omega} \left(\mathbf{Q}_j^{n,m+1} - \Delta\mathbf{Q}_j^{n,m+1} - \mathbf{Q}_j^{n,m}\right) \cdot \tilde{\mathbf{Q}}_j^{n,m+1},\end{aligned} \tag{C.17}$$

where $\Delta\tilde{\mathbf{Q}}_j^*$ and $\Delta\tilde{\mathbf{Q}}_j^{n,m}$ are referred to as adjoint increments in the following, and $\tilde{\mathbf{Q}}_j^{n,m}$ is the adjoint flow solution. These variables are introduced to take into account the dynamical constraint (C.16) on $\mathbf{Q}$ during the optimization process. The passage to next physical time step is performed according to

$$\mathbf{Q}^{n,N_\tau} = \mathbf{Q}^{n+1} = \mathbf{Q}^{n+1,0}, \tag{C.18}$$

where the number of dual iterations N_τ may possibly depend on n, even if this dependency is omitted in the following for the sake of simplicity. In (C.17), N_t and N_Ω refer to the number of physical time steps and the number of elements of the mesh respectively. From the first-order optimality conditions

$$\frac{\partial\mathcal{L}}{\partial\mathbf{Q}_j^{n,m}} = \mathbf{0}, \quad \frac{\partial\mathcal{L}}{\partial\Delta\mathbf{Q}_j^*} = \mathbf{0}, \quad \frac{\partial\mathcal{L}}{\partial\Delta\mathbf{Q}_j^{n,m+1}} = \mathbf{0}, \tag{C.19}$$

the following backward integration scheme for the adjoint variable is deduced

$$\Delta\tilde{\mathbf{Q}}_i^{n,m+1} = \tilde{\mathbf{Q}}_i^{n,m+1} - \sum_{j<i} \frac{1}{2} D_j^{-1} |\Gamma_{ji}| \left(\frac{\partial \Delta \mathbf{F}_i}{\partial \Delta \mathbf{Q}_i^{n,m+1}} - \lambda_{ij} \mathbf{I} \right)^{\mathrm{T}} \cdot \Delta\tilde{\mathbf{Q}}_j^{n,m+1}, \tag{C.20a}$$

$$\Delta\tilde{\mathbf{Q}}_i^{*} = \Delta\tilde{\mathbf{Q}}_i^{n,m+1} - \sum_{j>i} \frac{1}{2} D_j^{-1} |\Gamma_{ji}| \left(\frac{\partial \Delta \mathbf{F}_i^*}{\partial \Delta \mathbf{Q}_i^*} - \lambda_{ij} \mathbf{I} \right)^{\mathrm{T}} \cdot \Delta\tilde{\mathbf{Q}}_j^{*}, \tag{C.20b}$$

$$\begin{aligned}
\tilde{\mathbf{Q}}_i^{n,m} = &- \frac{\partial D_i^{-1}}{\partial \mathbf{Q}_i^{n,m}} \left(\sum_{j>i} \frac{1}{2} \left(\Delta \mathbf{F}_j - \lambda_{ji} \Delta \mathbf{Q}_j^{n,m+1} \right) |\Gamma_{ij}| \right) \cdot \Delta\tilde{\mathbf{Q}}_i^{n,m+1} - \sum_{j<i} \frac{1}{2} D_j^{-1} |\Gamma_{ji}| \left(\left(\frac{\partial \Delta \mathbf{F}_i}{\partial \mathbf{Q}_i^{n,m}} \right)^{\mathrm{T}} - \frac{\partial \lambda_{ij}}{\partial \mathbf{Q}_i^{n,m}} \Delta \mathbf{Q}_i^{n,m+1} \right) \cdot \Delta\tilde{\mathbf{Q}}_j^{n,m+1} \\
&- \frac{\partial D_i^{-1}}{\partial \mathbf{Q}_i^{n,m}} \left(\sum_{j<i} \frac{1}{2} \left(\Delta \mathbf{F}_j^* - \lambda_{ji} \Delta \mathbf{Q}_j^{*} \right) |\Gamma_{ij}| \right) \cdot \Delta\tilde{\mathbf{Q}}_i^{*} - \sum_{j>i} \frac{1}{2} D_j^{-1} |\Gamma_{ji}| \left(\left(\frac{\partial \Delta \mathbf{F}_i^*}{\partial \mathbf{Q}_i^{n,m}} \right)^{\mathrm{T}} - \frac{\partial \lambda_{ij}}{\partial \mathbf{Q}_i^{n,m}} \Delta \mathbf{Q}_i^{*} \right) \cdot \Delta\tilde{\mathbf{Q}}_j^{*} \\
&+ \tilde{\mathbf{Q}}_i^{n,m+1} + \frac{\partial D_i^{-1}}{\partial \mathbf{Q}_i^{n,m}} |\Omega_i| \hat{\mathbf{R}}_i^{n,m} \cdot \Delta\tilde{\mathbf{Q}}_i^{*} - \frac{3}{2\Delta t} D_i^{-1} |\Omega_i| \Delta\tilde{\mathbf{Q}}_i^{*} \\
&+ \sum_{j=1}^{N_\Omega} D_j^{-1} |\Omega_j| \left(\frac{\partial \mathbf{R}_j(\mathbf{Q}^{n,m})}{\partial \mathbf{Q}_i^{n,m}} \right)^{\mathrm{T}} \cdot \Delta\tilde{\mathbf{Q}}_j^{*} \\
&+ \left(\frac{\partial J}{\partial \mathbf{Q}_i^{n,m}} + \frac{2}{\Delta t} \sum_{p=0}^{N_\tau - 1} \left(D_i^{-1} |\Omega_i| \Delta\tilde{\mathbf{Q}}_i^{*} \right) \Big|^{n+1,p} - \frac{1}{2\Delta t} \sum_{p=0}^{N_\tau - 1} \left(D_i^{-1} |\Omega_i| \Delta\tilde{\mathbf{Q}}_i^{*} \right) \Big|^{n+2,p} \right) \delta_{mN_\tau}.
\end{aligned} \tag{C.20c}$$

The last contribution in (C.20c) allows to distinguish physical time steps. The majority of the gradients in (C.20) are simply obtained by deriving expressions in (C.16), while the most demanding part is the computation of the term $\sum_{j=1}^{N_\Omega} D_j^{-1} |\Omega_j| \left(\frac{\partial \mathbf{R}_j(\mathbf{Q}^{n,m})}{\partial \mathbf{Q}_i^{n,m}} \right)^{\mathrm{T}} \cdot \Delta\tilde{\mathbf{Q}}_j^{*}$ in (C.20c), i.e. the contribution from the numerical fluxes, which is detailed in §C.2.2. Since (C.20) is evaluated backward in time, the flow solution $\mathbf{Q}_i^{n,m}$, the increments $\Delta\mathbf{Q}_i^{n,m}$ and $\Delta\mathbf{Q}_i^{*}$ and the residuals $\hat{\mathbf{R}}_i^{n,m}$ have to be stored at all physical and dual times. In order to minimize memory requirements, the flow solution is stored only at a few times during the integration of the direct problem (C.16), and the missing snapshots are recomputed during the backward integration. Accordingly, after a forward integration of (C.16) where the direct solution has been stored every Δn physical steps, the following pseudo-algorithm is used to perform the backward integration for the adjoint flow field $\tilde{\mathbf{Q}}_i^{n,m}$:

1. Set $n_s = N_t - \Delta n$.
2. From physical time $n = n_s$ to $n = n_s + \Delta n$, recompute direct solution at all dual times according to (C.16). The quantities $\mathbf{Q}_i^{n,m}$, $\Delta\mathbf{Q}_i^{n,m}$, $\Delta\mathbf{Q}_i^{*}$ and $\hat{\mathbf{R}}_i^{n,m}$ have to be stored at all times.
3. From physical time $n = n_s + \Delta n$ to $n = n_s$, perform the following backward integration over dual time m:
   (a) compute adjoint residual $\Delta\tilde{\mathbf{Q}}_i^{n,m+1}$ with (C.20a);
   (b) compute adjoint residual $\Delta\tilde{\mathbf{Q}}_i^{*}$ with (C.20b);
   (c) evaluate the contribution $\sum_{j=1}^{N_\Omega} D_j^{-1} |\Omega_j| \left(\frac{\partial \mathbf{R}_j(\mathbf{Q}^{n,m})}{\partial \mathbf{Q}_i^{n,m}} \right)^{\mathrm{T}} \cdot \Delta\tilde{\mathbf{Q}}_j^{*}$ as detailed in §C.2.2;
   (d) compute adjoint flow field $\tilde{\mathbf{Q}}_i^{n,m}$ with (C.20c).
4. Replace n_s with $n_s - \Delta n$ and return to step 2 until $n_s = 0$.

C.2.2 Contributions from the numerical fluxes

In this subsection, time indices are omitted for the sake of readability. We consider contributions from convective fluxes in (C.20c), which are given by

$$\tilde{\mathbf{R}}_i^c = \sum_{j=1}^{N_\Omega} \left(\frac{\partial \bar{\mathbf{R}}_j^c}{\partial \mathbf{Q}_i} \right)^{\mathrm{T}} \cdot \Delta \bar{\mathbf{Q}}_j^*, \quad \bar{\mathbf{R}}_i^c = |\Omega_i| \mathbf{R}_i^c, \quad \mathbf{R}_i^c = -\frac{1}{|\Omega_i|} \sum_{l=1}^{N_f} |\Gamma_l| \mathbf{F}^{\mathrm{num}}(\mathbf{Q}_L, \mathbf{Q}_R, \boldsymbol{n}_l), \quad \Delta \bar{\mathbf{Q}}_i^* = D_i^{-1} \Delta \tilde{\mathbf{Q}}_i^*. \tag{C.21}$$

An efficient way to compute the residual $\tilde{\mathbf{R}}_i^c$ may consist in transforming the sum over the elements into a sum over the edges of the domain according to

$$\tilde{\mathbf{R}}_i^c = -\sum_{j=1}^{N_\Omega} \sum_{l=1}^{N_f} |\Gamma_l| \left(\frac{\partial \mathbf{F}^{\mathrm{num}}(\mathbf{Q}_L, \mathbf{Q}_R, \boldsymbol{n}_l)}{\partial \mathbf{Q}_i} \right)^{\mathrm{T}} \cdot \Delta \bar{\mathbf{Q}}_j^* = -\sum_{e=1}^{N_e} |\Gamma_e| \left(\frac{\partial \mathbf{F}^{\mathrm{num}}(\mathbf{Q}_{L(e)}, \mathbf{Q}_{R(e)}, \boldsymbol{n}_e)}{\partial \mathbf{Q}_i} \right)^{\mathrm{T}} \cdot \left(\Delta \bar{\mathbf{Q}}_{l(e)}^* - \Delta \bar{\mathbf{Q}}_{r(e)}^* \right), \tag{C.22}$$

with the convention that $\boldsymbol{n}_e$ is oriented from left to right element, N_e refers to the total number of edges in the mesh, $l(e)$ and $r(e)$ are the indices of the elements at the left and right sides of edge e, while $L(e)$ and $R(e)$ refer to the left and right states that are used in the evaluation of the convective fluxes, as illustrated in figure C.1. The gradient of the numerical fluxes is developed according to the chain rule

$$\frac{\partial \mathbf{F}^{\mathrm{num}}(\mathbf{Q}_{L(e)}, \mathbf{Q}_{R(e)}, \boldsymbol{n}_e)}{\partial \mathbf{Q}_i} = \frac{\partial \mathbf{F}^{\mathrm{num}}}{\partial \mathbf{W}_{L(e)}} \frac{\partial \mathbf{W}_{L(e)}}{\partial \mathbf{W}_i} \frac{\partial \mathbf{W}_i}{\partial \mathbf{Q}_i} + \frac{\partial \mathbf{F}^{\mathrm{num}}}{\partial \mathbf{W}_{R(e)}} \frac{\partial \mathbf{W}_{R(e)}}{\partial \mathbf{W}_i} \frac{\partial \mathbf{W}_i}{\partial \mathbf{Q}_i}. \tag{C.23}$$

The gradients $\frac{\partial \mathbf{F}^{\mathrm{num}}}{\partial \mathbf{W}_{L(e)}}$ and $\frac{\partial \mathbf{F}^{\mathrm{num}}}{\partial \mathbf{W}_{R(e)}}$ are obtained by deriving (C.8) with respect to the states $\mathbf{W}_{L(e)}$ and $\mathbf{W}_{R(e)}$. Deriving with respect to primitive variables appears easier than deriving with respect to conservative variables. An useful result, among others, is

$$\frac{\partial \mathbf{F}^L}{\partial \mathbf{W}_L} = \begin{pmatrix} \hat{u}_L & \rho_L n_x & \rho_L n_y & 0 \\ \hat{u}_L u_L & \rho_L(\hat{u}_L + u_L n_x) & \rho_L u_L n_y & n_x \\ \hat{u}_L v_L & \rho_L v_L n_x & \rho(\hat{u}_L + v_L n_y) & n_y \\ \frac{1}{2}\hat{u}_L V_L^2 & \rho_L(n_x H_L + \hat{u}_L u_L) & \rho(n_y H_L + \hat{u}_L v_L & \hat{u}_L \frac{\gamma}{\gamma-1} \end{pmatrix}. \tag{C.24}$$

This gradient is also used in (C.20). The other contributions in (C.8) are derived in a relatively similar and straightforward way. Concerning the gradients $\frac{\partial \mathbf{W}_{L(e)}}{\partial \mathbf{W}_i}$ and $\frac{\partial \mathbf{W}_{R(e)}}{\partial \mathbf{W}_i}$ in (C.23), they correspond to the gradient of the reconstruction procedure detailed in §C.1.3. Since both the Jawahar-Kamath and pseudo Laplacian weighting methodologies correspond to linear operators, the states $\mathbf{W}_{L(e)}$ and $\mathbf{W}_{R(e)}$ can be expressed as

$$\mathbf{W}_{L(e)} = \mathbf{W}_{l(e)} + \sum_{k=1}^{N_\Omega} L_{l(e)k}^{\mathrm{LR}} \mathbf{W}_k, \tag{C.25a}$$

$$\mathbf{W}_{R(e)} = \mathbf{W}_{r(e)} + \sum_{k=1}^{N_\Omega} L_{r(e)k}^{\mathrm{LR}} \mathbf{W}_k, \tag{C.25b}$$

where the factors $L_{r(e)k}^{\mathrm{LR}}$ are the components of the matrix associated to the linear reconstruction, which are only expressed in terms of geometrical factors corresponding to the Jawahar-Kamath and pseudo Laplacian weighting procedures. The gradients $\frac{\partial \mathbf{W}_{L(e)}}{\partial \mathbf{W}_i}$ and $\frac{\partial \mathbf{W}_{R(e)}}{\partial \mathbf{W}_i}$ are thus easily found as

$$\frac{\partial \mathbf{W}_{L(e)}}{\partial \mathbf{W}_i} = \left(\delta_{l(e)i} + L_{l(e)i}^{\mathrm{LR}} \right) \mathbf{I}, \tag{C.26a}$$

$$\frac{\partial \mathbf{W}_{R(e)}}{\partial \mathbf{W}_i} = \left(\delta_{r(e)i} + L_{r(e)i}^{\mathrm{LR}} \right) \mathbf{I}. \tag{C.26b}$$

The gradient $\frac{\partial \mathbf{W}_i}{\partial \mathbf{Q}_i}$ in (C.23) simply corresponds to the gradient matrix associated to the change from conservative variables to primitive variables, and is given by

$$\frac{\partial \mathbf{W}_i}{\partial \mathbf{Q}_i} = \begin{pmatrix} 1 & 0 & 0 & 0 \\ -\frac{u_i}{\rho_i} & \frac{1}{\rho_i} & 0 & 0 \\ -\frac{v_i}{\rho_i} & 0 & \frac{1}{\rho_i} & 0 \\ \frac{\gamma-1}{2}V_i^2 & -(\gamma-1)u & -(\gamma-1)v & \gamma-1 \end{pmatrix}. \tag{C.27}$$

Given the above results, equation (C.22) may be rearranged into

$$\tilde{\mathbf{R}}_i^c = -\sum_{e=1}^{N_e} |\Gamma_e| \left(\frac{\partial \mathbf{W}_i}{\partial \mathbf{Q}_i}\right)^{\mathrm{T}} \left[\left(\delta_{l(e)i} + L_{l(e)i}^{\mathrm{LR}}\right)\left(\frac{\partial \mathbf{F}^{\mathrm{num}}}{\partial \mathbf{W}_{L(e)}}\right)^{\mathrm{T}} + \left(\delta_{r(e)i} + L_{r(e)i}^{\mathrm{LR}}\right)\left(\frac{\partial \mathbf{F}^{\mathrm{num}}}{\partial \mathbf{W}_{R(e)}}\right)^{\mathrm{T}}\right] \cdot \left(\Delta\bar{\mathbf{Q}}_{l(e)}^* - \Delta\bar{\mathbf{Q}}_{r(e)}^*\right). \tag{C.28}$$

From a practical point of view, instead of performing a sum over all the edges of the domain for each element i as suggested by (C.28), only one loop over the edges of the mesh is performed in order to compute the adjoint residuals $\tilde{\mathbf{R}}_i^c$ according to the following pseudo-algorithm:

From edge $e = 1$ to $e = N_e$:

1. Evaluate the gradients $\frac{\partial \mathbf{F}^{\mathrm{num}}}{\partial \mathbf{W}_{L(e)}}$ and $\frac{\partial \mathbf{F}^{\mathrm{num}}}{\partial \mathbf{W}_{R(e)}}$, and compute $\Delta\tilde{\mathbf{F}}_{L(e)} = |\Gamma_e|\left(\frac{\partial \mathbf{F}^{\mathrm{num}}}{\partial \mathbf{W}_{L(e)}}\right)^{\mathrm{T}} \cdot \left(\Delta\bar{\mathbf{Q}}_{l(e)}^* - \Delta\bar{\mathbf{Q}}_{r(e)}^*\right)$ and $\Delta\tilde{\mathbf{F}}_{R(e)} = |\Gamma_e|\left(\frac{\partial \mathbf{F}^{\mathrm{num}}}{\partial \mathbf{W}_{R(e)}}\right)^{\mathrm{T}} \cdot \left(\Delta\bar{\mathbf{Q}}_{l(e)}^* - \Delta\bar{\mathbf{Q}}_{r(e)}^*\right)$
2. Add contributions $-\left(\frac{\partial \mathbf{W}_{l(e)}}{\partial \mathbf{Q}_{l(e)}}\right)^{\mathrm{T}} \cdot \Delta\tilde{\mathbf{F}}_{L(e)}$ and $-\left(\frac{\partial \mathbf{W}_{r(e)}}{\partial \mathbf{Q}_{r(e)}}\right)^{\mathrm{T}} \cdot \Delta\tilde{\mathbf{F}}_{R(e)}$ to adjoint residuals $\tilde{\mathbf{R}}_{l(e)}^c$ and $\tilde{\mathbf{R}}_{r(e)}^c$ respectively.
3. Identify elements i such that $L_{l(e)i}^{\mathrm{LR}} \neq 0$ or $L_{r(e)i}^{\mathrm{LR}} \neq 0$, and add contributions $-L_{l(e)i}^{\mathrm{LR}}\left(\frac{\partial \mathbf{W}_i}{\partial \mathbf{Q}_i}\right)^{\mathrm{T}} \cdot \Delta\tilde{\mathbf{F}}_{L(e)}$ and $-L_{r(e)i}^{\mathrm{LR}}\left(\frac{\partial \mathbf{W}_i}{\partial \mathbf{Q}_i}\right)^{\mathrm{T}} \cdot \Delta\tilde{\mathbf{F}}_{R(e)}$ to the corresponding residuals $\tilde{\mathbf{R}}_i^c$.

Taking into account boundary conditions is performed by replacing (C.22) with

$$\tilde{\mathbf{R}}_i^c = -\sum_{e|_{\mathrm{int}}} |\Gamma_e| \left(\frac{\partial \mathbf{F}^{\mathrm{num}}(\mathbf{Q}_{L(e)}, \mathbf{Q}_{R(e)}, \boldsymbol{n}_e)}{\partial \mathbf{Q}_i}\right)^{\mathrm{T}} \cdot \left(\Delta\bar{\mathbf{Q}}_{l(e)}^* - \Delta\bar{\mathbf{Q}}_{r(e)}^*\right) - \sum_{e|_{\mathrm{BC}}} |\Gamma_e| \left(\frac{\partial \mathbf{F}^{\mathrm{num,BC}}(\mathbf{Q}, \boldsymbol{n}_e)}{\partial \mathbf{Q}_i}\right)^{\mathrm{T}} \cdot \Delta\bar{\mathbf{Q}}_{l(e)}^*, \tag{C.29}$$

where sums are restricted either to interior edges or to edges corresponding to boundary conditions. The contributions of viscous fluxes are derived similarly to those of convectives fluxes, and the corresponding gradients are easily obtained using the following change of variables

$$\mathbf{V}_i = \begin{pmatrix} u_i \\ v_i \\ T_i \end{pmatrix}, \quad \frac{\partial \mathbf{V}_i}{\partial \mathbf{W}_i} = \begin{bmatrix} 0 & 1 & 0 & 0 \\ 0 & 0 & 1 & 0 \\ -\frac{p_i}{r\rho_i^2} & 0 & 0 & \frac{1}{r\rho_i} \end{bmatrix}. \tag{C.30}$$

C.2.3 Gradients with respect to the control variables

The adjoint model discussed in this section allows to obtain the gradient of the Lagrangian $\mathcal{L}$ in (C.17) with respect to the control variables of the considered optimization problem. In the context of data assimilation, we are often interested in the gradient of $\mathcal{L}$ with respect to the initial condition $\mathbf{Q}^0 = \mathbf{Q}^{0,0}$, which is given by

$$\frac{\partial \mathcal{L}}{\partial \mathbf{Q}^0} = \tilde{\mathbf{Q}}^0. \tag{C.31}$$

In the case where the numerical fluxes depend on adjustable parameters $\boldsymbol{\beta}^n$, such as unstationary boundary conditions, the gradient of $\mathcal{L}$ with respect to $\boldsymbol{\beta}^n$ is given by

$$\frac{\partial \mathcal{L}}{\partial \boldsymbol{\beta}^n} = \sum_{m=0}^{N_\tau - 1} \sum_{j=1}^{N_\Omega} D_j^{-1} |\Omega_j| \left(\frac{\partial \mathbf{R}_j(\mathbf{Q}^{n,m}, \boldsymbol{\beta}^n)}{\partial \boldsymbol{\beta}^n} \right)^{\mathrm{T}} \cdot \Delta \tilde{\mathbf{Q}}_j^*. \tag{C.32}$$

The procedure to validate the adjoint code is identical to that described in appendix A, and the correct implementation of the adjoint model is illustrated in chapter 5.

Appendix D

Discrete formulation of the observation optimization problem

The discrete version of the observation optimization procedure described in chapter 6 is given in this appendix, along with an alternative formulation for the computation of the gradient in (6.13c). The fully discretized counterpart of the dynamical model in (6.1) can be written as

$$\boldsymbol{q}_{n+1} = \boldsymbol{m}_n(\boldsymbol{q}_n, \boldsymbol{\beta}_n) \quad 0 \leqslant n \leqslant N-1, \tag{D.1}$$

where $\boldsymbol{m}_n$ is a nonlinear operator that maps the spatially discretized state vector $\boldsymbol{q}_n$ from discrete time n to $n+1$ and is parameterized by the vector $\boldsymbol{\beta}_n$. The time interval $[0, T]$ is discretized by $N+1$ time steps. The discrete Lagrangian used to evaluate the sensitivity of the observations, with associated operator $\boldsymbol{h}$ parameterized by $\boldsymbol{\lambda}$, is given by

$$\mathcal{L}_1 = \frac{1}{2}\sum_{n=0}^{N} \|\boldsymbol{h}(\boldsymbol{q}_n, \boldsymbol{\lambda})\|^2 - \sum_{n=0}^{N-1} \left(\boldsymbol{q}_{n+1} - \boldsymbol{m}_n(\boldsymbol{q}_n, \boldsymbol{\beta}_n)\right)^{\mathrm{T}} \tilde{\boldsymbol{q}}_{n+1}, \tag{D.2}$$

where $\|\cdot\|$ and $\cdot^{\mathrm{T}}$ denote the Euclidean norm and the transpose operator respectively. Similarly to the derivations in §6.2.2, the following system of equations can be deduced to compute the first-order sensitivity of the observations

$$\tilde{\boldsymbol{q}}_N = \left(\frac{\partial \boldsymbol{h}}{\partial \boldsymbol{q}_N}(\boldsymbol{q}_N, \boldsymbol{\lambda})\right)^{\mathrm{T}} \boldsymbol{h}(\boldsymbol{q}_N, \boldsymbol{\lambda}), \tag{D.3a}$$

$$\tilde{\boldsymbol{q}}_n = \left(\frac{\partial \boldsymbol{m}_n}{\partial \boldsymbol{q}_n}(\boldsymbol{q}_n, \boldsymbol{\beta}_n)\right)^{\mathrm{T}} \tilde{\boldsymbol{q}}_{n+1} + \left(\frac{\partial \boldsymbol{h}}{\partial \boldsymbol{q}_n}(\boldsymbol{q}_n, \boldsymbol{\lambda})\right)^{\mathrm{T}} \boldsymbol{h}(\boldsymbol{q}_n, \boldsymbol{\lambda}) \quad 0 \leq n \leq N-1, \tag{D.3b}$$

$$\frac{\partial \mathcal{L}_1}{\partial \boldsymbol{q}_0} = \tilde{\boldsymbol{q}}_0, \tag{D.3c}$$

$$\frac{\partial \mathcal{L}_1}{\partial \boldsymbol{\beta}_n} = \left(\frac{\partial \boldsymbol{m}_n}{\partial \boldsymbol{\beta}_n}(\boldsymbol{q}_n, \boldsymbol{\beta}_n)\right)^{\mathrm{T}} \tilde{\boldsymbol{q}}_{n+1} \quad 0 \leq n \leq N-1. \tag{D.3d}$$

The system (D.3) involves the transpose of gradient matrices associated to the model and observation operators. The system of adjoint equations for the discrete version of the DA problem exposed in §6.2.4 is obtained by replacing $\boldsymbol{h}(\boldsymbol{q}_n, \boldsymbol{\lambda})$ with $(\boldsymbol{h}(\boldsymbol{q}_n, \boldsymbol{\lambda}) - \boldsymbol{y}_n)$ in (D.2) and (D.3), where $\boldsymbol{y}_n$ is the observation of a reference state at time n. As in §6.2.3, the observation optimization problem is formulated as the maximization of the norm of the gradients (D.3c)-(D.3d) with respect to the vector $\boldsymbol{\lambda}$ that parameterizes the observation operator $\boldsymbol{h}$. The expression of the discretized counterpart of the Lagrangian $\mathcal{L}_2$ in (6.11) is given by

$$\begin{aligned}\mathcal{L}_2 =& \frac{1}{2}\|\tilde{\boldsymbol{q}}_0\|^2 + \frac{1}{2}\sum_{n=0}^{N-1}\left\|\left(\frac{\partial \boldsymbol{m}_n}{\partial \boldsymbol{\beta}_n}(\boldsymbol{q}_n,\boldsymbol{\beta}_n)\right)^{\mathrm{T}}\tilde{\boldsymbol{q}}_{n+1}\right\|^2 \\ & - \sum_{n=0}^{N-1}\left(\tilde{\boldsymbol{q}}_n - \left(\frac{\partial \boldsymbol{m}_n}{\partial \boldsymbol{q}_n}(\boldsymbol{q}_n,\boldsymbol{\beta}_n)\right)^{\mathrm{T}}\tilde{\boldsymbol{q}}_{n+1} - \tilde{\boldsymbol{h}}_n(\boldsymbol{\lambda})\right)^{\mathrm{T}}\boldsymbol{r}_n - (\tilde{\boldsymbol{q}}_N - \tilde{\boldsymbol{h}}_N(\boldsymbol{\lambda}))^{\mathrm{T}}\boldsymbol{s}\end{aligned}, \tag{D.4a}$$

$$\tilde{\boldsymbol{h}}_n(\boldsymbol{\lambda}) = \left(\frac{\partial \boldsymbol{h}}{\partial \boldsymbol{q}_n}(\boldsymbol{q}_n,\boldsymbol{\lambda})\right)^{\mathrm{T}}\boldsymbol{h}(\boldsymbol{q}_n,\boldsymbol{\lambda}) \quad 0 \le n \le N, \tag{D.4b}$$

while its gradient with respect to the parameters $\boldsymbol{\lambda}$ is obtained with

$$\boldsymbol{r}_0 = \tilde{\boldsymbol{q}}_0, \tag{D.5a}$$

$$\boldsymbol{r}_{n+1} = \frac{\partial \boldsymbol{m}_n}{\partial \boldsymbol{q}_n}(\boldsymbol{q}_n,\boldsymbol{\beta}_n)\boldsymbol{r}_n + \frac{\partial \boldsymbol{m}_n}{\partial \boldsymbol{\beta}_n}(\boldsymbol{q}_n,\boldsymbol{\beta}_n)\left(\frac{\partial \boldsymbol{m}_n}{\partial \boldsymbol{\beta}_n}(\boldsymbol{q}_n,\boldsymbol{\beta}_n)\right)^{\mathrm{T}}\tilde{\boldsymbol{q}}_{n+1} \quad 0 \leqslant n \leqslant N-1, \tag{D.5b}$$

$$\frac{\partial \mathcal{L}_2}{\partial \boldsymbol{\lambda}} = \sum_{n=0}^{N}\left(\frac{\partial \tilde{\boldsymbol{h}}_n}{\partial \boldsymbol{\lambda}}(\boldsymbol{\lambda})\right)^{\mathrm{T}}\boldsymbol{r}_n. \tag{D.5c}$$

The systems of equations (D.3) and (D.5) are the discrete counterparts of (6.8) and (6.13) respectively. Equation (D.5b) is evaluated forward and involves the tangent linear operator $\frac{\partial \boldsymbol{m}_n}{\partial \boldsymbol{q}_n}$, while equation (D.3b) is evaluated backward and involves the adjoint of this operator. Accordingly, the computation of the adjoint variables $\tilde{\boldsymbol{q}}_n$ in (D.3) and $\boldsymbol{r}_n$ in (D.5) needs to be performed in a sequential way, and the vector $\tilde{\boldsymbol{q}}_n$ at all discrete times t_n has to be stored for the integration of (D.5b), as the direct solution $\boldsymbol{q}_n$ at all discrete times has to be stored for the computation of $\tilde{\boldsymbol{q}}_n$ in (D.3). However, it appears from the inspection of (D.3) that the gradient of $\mathcal{L}_2$ with respect to $\boldsymbol{\lambda}$ may also be obtained through the following system of equations

$$\frac{\partial \tilde{\boldsymbol{q}}_N}{\partial \boldsymbol{\lambda}} = \frac{\partial \tilde{\boldsymbol{h}}_N}{\partial \boldsymbol{\lambda}}(\boldsymbol{\lambda}), \tag{D.6a}$$

$$\frac{\partial \tilde{\boldsymbol{q}}_n}{\partial \boldsymbol{\lambda}} = \left(\frac{\partial \boldsymbol{m}_n}{\partial \boldsymbol{q}_n}(\boldsymbol{q}_n,\boldsymbol{\beta}_n)\right)^{\mathrm{T}}\frac{\partial \tilde{\boldsymbol{q}}_{n+1}}{\partial \boldsymbol{\lambda}} + \frac{\partial \tilde{\boldsymbol{h}}_n}{\partial \boldsymbol{\lambda}}(\boldsymbol{\lambda}) \quad 0 \le n \le N-1, \tag{D.6b}$$

$$\frac{\partial \mathcal{L}_2}{\partial \boldsymbol{\lambda}} = \tilde{\boldsymbol{q}}_0^{\mathrm{T}}\frac{\partial \tilde{\boldsymbol{q}}_0}{\partial \boldsymbol{\lambda}} + \sum_{n=0}^{N-1}\left(\left(\frac{\partial \boldsymbol{m}_n}{\partial \boldsymbol{\beta}_n}(\boldsymbol{q}_n,\boldsymbol{\beta}_n)\right)^{\mathrm{T}}\tilde{\boldsymbol{q}}_{n+1}\right)^{\mathrm{T}}\left(\frac{\partial \boldsymbol{m}_n}{\partial \boldsymbol{\beta}_n}(\boldsymbol{q}_n,\boldsymbol{\beta}_n)\right)^{\mathrm{T}}\frac{\partial \tilde{\boldsymbol{q}}_{n+1}}{\partial \boldsymbol{\lambda}}. \tag{D.6c}$$

From the computational point of view, solving (D.6b) may require more memory than solving (D.5b) since a gradient matrix $\frac{\partial \tilde{\boldsymbol{q}}_n}{\partial \boldsymbol{\lambda}}$ is propagated in time in the former case instead of a vector. On the other hand, since (D.6b) is evaluated backward, the adjoint variable $\tilde{\boldsymbol{q}}_n$ in (D.3) and the gradient in (D.6c) can be computed simultaneously, which may save computational time, and avoids to store $\tilde{\boldsymbol{q}}_n$ at all times. If $\dim(\boldsymbol{\lambda}) < N + 1$, which is the case in the present study, the formulation (D.6) is therefore more economical in terms of memory requirements than (D.5) in the end. The system of equations (D.6) will be used instead of (D.5) in the present work to solve the observation optimization problem. Accordingly, computing gradients for the evaluation of the sensitivity of the observations and for the observation optimization problem amounts to propogate backward in time the variables $\tilde{\boldsymbol{q}}_n$ and $\frac{\partial \tilde{\boldsymbol{q}}_n}{\partial \boldsymbol{\lambda}}$ simultaneously with the adjoint operator $\left(\frac{\partial \boldsymbol{m}_n}{\partial \boldsymbol{q}_n}\right)^{\mathrm{T}}$ and different forcing terms.

Appendix E

The c-APK method for uncertainty quantification and sensitivity analysis

The anchored-ANOVA/POD/Kriging (c-APK) method for meta-modelling proposed in [148, 150] and used in chapter 7 to determine appropriate sensor locations is summarized in this appendix. This approach is based on a hybridization between the anchored-ANOVA representation and POD/Kriging methods along with the determination of efficient sampling and refinement strategies to limit computational cost.

E.1 The anchored-ANOVA decomposition

We consider a vectorial quantity of interest $\boldsymbol{X}(\boldsymbol{\gamma})$ that depends on the vector $\boldsymbol{\gamma}$ of dimension N whose components are here considered as random variables with associated measure $\mu(\boldsymbol{\gamma})$. The analysis of variance (ANOVA) [193] decomposition of $\boldsymbol{X}(\boldsymbol{\gamma})$ is defined as

$$\boldsymbol{X}(\boldsymbol{\gamma}) = \boldsymbol{X}_0 + \sum_{i_1} \boldsymbol{X}_{i_1}(\gamma_{i_1}) + \sum_{1\le i_1<i_2\le N} \boldsymbol{X}_{i_1,i_2}(\gamma_{i_1},\gamma_{i_2}) + \cdots + \boldsymbol{X}_{1,2,\cdots,N}(\gamma_1,\gamma_2,\cdots,\gamma_N), \tag{E.1}$$

with

$$\boldsymbol{X}_0 = \int \boldsymbol{X}(\boldsymbol{\gamma})d\mu(\boldsymbol{\gamma}), \tag{E.2a}$$

$$\int \boldsymbol{X}_{i_1,i_2,\cdots,i_s}(\gamma_{i_1},\gamma_{i_2},\cdots,\gamma_{i_s})d\mu(\gamma_{i_r}) = \boldsymbol{0} \quad 1 \le r \le s. \tag{E.2b}$$

Equation (E.2) thus ensures the orthogonality of the decomposition, and total and partial variances of $\boldsymbol{X}(\boldsymbol{\gamma})$ are obtained from the integral of the squared terms in (E.1)

$$\boldsymbol{\sigma}^2(\boldsymbol{X}) = \int \boldsymbol{X}^2(\boldsymbol{\gamma})d\mu(\boldsymbol{\gamma}) - \boldsymbol{X}_0^2, \tag{E.3a}$$

$$\boldsymbol{\sigma}^2(\boldsymbol{X}_{i_1,i_2,\cdots,i_s}) = \int \boldsymbol{X}^2_{i_1,i_2,\cdots,i_s}(\gamma_{i_1},\gamma_{i_2},\cdots,\gamma_{i_s})d\mu(\gamma_{i_1},\gamma_{i_2},\cdots,\gamma_{i_N}), \tag{E.3b}$$

$$\boldsymbol{\sigma}^2(\boldsymbol{X}) = \sum_{i_1}\boldsymbol{\sigma}^2(\boldsymbol{X}_{i_1}) + \sum_{1\le i_1<i_2\le N}\boldsymbol{\sigma}^2(\boldsymbol{X}_{i_1,i_2}) + \cdots + \boldsymbol{\sigma}^2(\boldsymbol{X}_{1,2,\cdots,N}), \tag{E.3c}$$

where the ith component of the vector $\boldsymbol{X}^2(\boldsymbol{\gamma})$ is given by $(X_i(\boldsymbol{\gamma}))^2$, with similar notations for $\boldsymbol{\sigma}^2(\boldsymbol{X})$, $\boldsymbol{X}_0^2$ and the contributions $\boldsymbol{X}^2_{i_1,i_2,\cdots,i_s}(\gamma_{i_1},\gamma_{i_2},\cdots,\gamma_{i_s})$ and $\boldsymbol{\sigma}^2(\boldsymbol{X}_{i_1,i_2,\cdots,i_s})$. In practice, it may be reasonable to assume that the low-order interactions between the components of the input vector $\boldsymbol{\gamma}$ have the main impact upon $\boldsymbol{X}(\boldsymbol{\gamma})$ [193, 229].

Accordingly, (E.1) is truncated up to second order and is approximated by

$$\boldsymbol{X}(\boldsymbol{\gamma}) \simeq \boldsymbol{X}_0 + \sum_{i_1} \boldsymbol{X}_{i_1}(\gamma_{i_1}) + \sum_{1\leq i_1<i_2\leq N} \boldsymbol{X}_{i_1,i_2}(\gamma_{i_1},\gamma_{i_2}). \tag{E.4}$$

In order to further decrease computational complexity, and in particular to avoid the evaluation of multidimensional integrals such as in (E.2), the measure $\mu(\boldsymbol{\gamma})$ is chosen as the Dirac measure located at a reference, or anchor, point $\boldsymbol{c}$ [147, 229]

$$d\mu(\boldsymbol{\gamma}) = \delta(\boldsymbol{\gamma} - \boldsymbol{c})d\boldsymbol{\gamma}. \tag{E.5}$$

The anchor point may be chosen as the centroid of the uncertain space. Using (E.2) and (E.5) allows to estimate recursively the terms in (E.4) according to

$$\boldsymbol{X}_0 = \boldsymbol{X}(c_1, c_2, \cdots, c_N), \tag{E.6a}$$

$$\boldsymbol{X}_{i_1}(\gamma_{i_1}) = \boldsymbol{X}(c_1, c_2, \cdots, \gamma_{i_1}, \cdots, c_N) - \boldsymbol{X}_0, \tag{E.6b}$$

$$\boldsymbol{X}_{i_1,i_2}(\gamma_{i_1},\gamma_{i_2}) = \boldsymbol{X}(c_1, c_2, \cdots, i_1, \cdots, i_2, \cdots, c_N) - \boldsymbol{X}_0 - \boldsymbol{X}_{i_1}(\gamma_{i_1}) - \boldsymbol{X}_{i_2}(\gamma_{i_2}). \tag{E.6c}$$

The anchored-ANOVA representation truncated to second order thus allows to decompose the original N-dimensional problem in mono- and bi-dimensional contributions that are evaluated by exploring hyper-lines and hyper-planes only, which greatly facilitates the handling of high-dimensional uncertain spaces.

E.2 The POD/Kriging sub-meta-models

E.2.1 POD representation of the anchored-ANOVA decomposition terms

Each term of the decomposition (E.4) is interpolated relying on the proper orthogonal decomposition (POD)/Kriging approach [30]. Considering the first-order term $\boldsymbol{X}_{i_1}(\gamma_{i_1})$, its POD representation is given by

$$\boldsymbol{X}_{i_1}(\gamma_{i_1}) = \overline{\boldsymbol{X}_{i_1}} + \sum_{n=1}^{N_{\mathrm{POD}}} \beta_n(\gamma_{i_1})\boldsymbol{\psi}^{(n)}, \tag{E.7}$$

where the vectors $\boldsymbol{\psi}^{(n)}$ form the POD basis, and $\overline{\boldsymbol{X}_{i_1}}$ is the mean value of $\boldsymbol{X}_{i_1}(\gamma_{i_1})$, which should be zero according to (E.2). The POD basis is obtained with the snapshot method [192] where the vectors $\boldsymbol{\psi}^{(n)}$ are found as linear combinations of N_{en} available samples of $\boldsymbol{X}_{i_1}(\gamma_{i_1})$. These samples are stored in the matrix $\mathbf{S}$ defined as

$$\mathbf{S} = \left(\boldsymbol{X}'_{i_1}(\gamma^{(1)}_{i_1}), \boldsymbol{X}'_{i_1}(\gamma^{(2)}_{i_1}), \cdots, \boldsymbol{X}'_{i_1}(\gamma^{(N_{en})}_{i_1})\right), \quad \boldsymbol{X}'_{i_1}(\gamma^{(j)}_{i_1}) = \boldsymbol{X}_{i_1}(\gamma^{(j)}_{i_1}) - \overline{\boldsymbol{X}_{i_1}}, \quad \overline{\boldsymbol{X}_{i_1}} = \frac{1}{N_{en}}\sum_{j=1}^{N_{en}} \boldsymbol{X}_{i_1}(\gamma^{(j)}_{i_1}). \tag{E.8}$$

The POD modes are found by maximizing the quantity $\frac{1}{N_{en}}\sum_{j=1}^{N_{en}}\left(\boldsymbol{\psi}^{(n)\mathrm{T}}\boldsymbol{X}'_{i_1}(\gamma^{(j)}_{i_1})\right)^2$ where $\boldsymbol{\psi}^{(n)}$ is searched as $\boldsymbol{\psi}^{(n)} \propto \sum_{j=1}^{N_{en}} v^{(n)}_j \boldsymbol{X}'_{i_1}(\gamma^{(j)}_{i_1})$ with the constraint $\|\boldsymbol{\psi}^{(n)}\|^2 = 1$. This leads to solve the following eigenvalue problem for the determination of the vectors $\boldsymbol{v}^{(n)}$

$$\mathbf{C}\boldsymbol{v}^{(n)} = \lambda^{(n)}\boldsymbol{v}^{(n)}, \quad \mathbf{C} = \frac{1}{N_{en}}\mathbf{S}^{\mathrm{T}}\mathbf{S}, \tag{E.9}$$

and the N_{POD} vectors $\boldsymbol{\psi}^{(n)}$ are found as

$$\boldsymbol{\psi}^{(n)} = \frac{1}{\sqrt{N_{en}\lambda^{(n)}}}\sum_{j=1}^{N_{en}} v^{(n)}_j \boldsymbol{X}'_{i_1}(\gamma^{(j)}_{i_1}), \tag{E.10a}$$

$$N_{\mathrm{POD}} = \min\left\{ k \left| \frac{\sum_{n=1}^{k}\lambda^{(n)}}{\sum_{n=1}^{N_{en}}\lambda^{(n)}} \geqslant \epsilon_{\mathrm{POD}} \right.\right\}, \tag{E.10b}$$

where both $\left(\boldsymbol{\psi}^{(1)}, \boldsymbol{\psi}^{(2)}, \cdots, \boldsymbol{\psi}^{(N_{\mathrm{POD}})}\right)$ and $\left(\boldsymbol{v}^{(1)}, \boldsymbol{v}^{(2)}, \cdots, \boldsymbol{v}^{(N_{\mathrm{POD}})}\right)$ are sets of orthonormal vectors. The parameter ϵ_{POD} allows to adjust the smoothness and the quantity of information kept in the POD basis.

E.2.2 Kriging-based interpolation of the coefficients

If the coefficients $\beta_n(\gamma_{i_1})$ in the POD representation (E.7) are known for the samples and are given by

$$\beta_n(\gamma_{i_1}^{(j)}) = \sqrt{N_{en}\lambda^{(n)}}\, v_j^{(n)}, \tag{E.11}$$

they are unknown at unsampled input parameters. Ordinary Kriging [108, 187] is used to obtain the coefficients $\beta_n(\gamma_{i_1})$ through interpolation. In this framework, $\beta_n(\gamma_{i_1})$ is modeled as a mean value ρ plus a stochastic deviation $Z(\gamma_{i_1})$ whose statistics are given by

$$\beta_n(\gamma_{i_1}) = \rho + Z(\gamma_{i_1}), \tag{E.12a}$$

$$\mathbb{E}\left[Z(\gamma_{i_1})\right] = 0, \quad \mathbb{E}\left[Z(\gamma_{i_1})^2\right] = \sigma^2, \quad \mathbb{E}\left[Z(x)Z(y)\right] = \sigma^2 C(x,y). \tag{E.12b}$$

If the correlation function $C(x,y)$ is assumed to be known, the values of the mean ρ and the variance σ^2 are obtained through the maximization of the likelihood of the samples

$$\rho = \frac{\mathbf{1}^{\mathrm{T}}\mathbf{R}^{-1}\boldsymbol{\beta}^s}{\mathbf{1}^{\mathrm{T}}\mathbf{R}^{-1}\mathbf{1}}, \quad \sigma^2 = \frac{\left(\boldsymbol{\beta}^s - \mathbf{1}\rho\right)^{\mathrm{T}}\mathbf{R}^{-1}\left(\boldsymbol{\beta}^s - \mathbf{1}\rho\right)}{N_{en}}, \tag{E.13a}$$

$$\mathbf{1} = (1, 1, \cdots, 1)^{\mathrm{T}}, \quad \dim(\mathbf{1}) = N_{en}, \quad \boldsymbol{\beta}^s = \left(\beta_n(\gamma_{i_1}^{(1)}), \beta_n(\gamma_{i_1}^{(2)}), \cdots, \beta_n(\gamma_{i_1}^{(N_{en})})\right)^{\mathrm{T}}, \quad R_{lm} = C(\gamma_{i_1}^{(l)}, \gamma_{i_1}^{(m)}). \tag{E.13b}$$

A linear predictor $\hat{\beta}_n(\gamma_{i_1})$ of $\beta_n(\gamma_{i_1})$ as modeled in (E.12) is searched as

$$\hat{\beta}_n(\gamma_{i_1}) = \boldsymbol{c}(\gamma_{i_1})^{\mathrm{T}}\boldsymbol{\beta}^s. \tag{E.14}$$

The determination of the vector $\boldsymbol{c}(\gamma_{i_1})$ that minimizes the esperance $\mathbb{E}\left[(\hat{\beta}_n(\gamma_{i_1}) - \beta_n(\gamma_{i_1}))^2\right]$ with the constraint $\mathbb{E}\left[(\hat{\beta}_n(\gamma_{i_1})\right] = \mathbb{E}\left[(\beta_n(\gamma_{i_1})\right]$ (unbiased estimator) leads to

$$\hat{\beta}_n(\gamma_{i_1}) = \rho + \boldsymbol{r}(\gamma_{i_1})^{\mathrm{T}}\mathbf{R}^{-1}\left(\boldsymbol{\beta}^s - \mathbf{1}\rho\right), \tag{E.15a}$$

$$\mathbb{E}\left[(\hat{\beta}_n(\gamma_{i_1}) - \beta_n(\gamma_{i_1}))^2\right] = \sigma^2\left(1 - \boldsymbol{r}(\gamma_{i_1})^{\mathrm{T}}\mathbf{R}^{-1}\boldsymbol{r}(\gamma_{i_1}) + \frac{\left(\boldsymbol{r}(\gamma_{i_1})^{\mathrm{T}}\mathbf{R}^{-1}\mathbf{1} - 1\right)^2}{\mathbf{1}^{\mathrm{T}}\mathbf{R}^{-1}\mathbf{1}}\right), \tag{E.15b}$$

$$\boldsymbol{r}(\gamma_{i_1}) = \left(C(\gamma_{i_1}, \gamma_{i_1}^{(1)}), C(\gamma_{i_1}, \gamma_{i_1}^{(2)}), \cdots, C(\gamma_{i_1}, \gamma_{i_1}^{(N_{en})})\right)^{\mathrm{T}}. \tag{E.15c}$$

E.3 Refinement and validation strategies

The convergence of the sub-meta-models is checked with the leave-one-out method, and a quad-tree-like re-sampling strategy is used for refinement, similarly to [30]. Keeping in mind that the c-APK method is applied to high-fidelity expensive simulations, in the case where $\boldsymbol{X}(\boldsymbol{\gamma})$ corresponds to a physical field discretized in space, the convergence is only checked in regions of interest where partial and/or global variances are sufficiently high. Besides, second-order terms are kept and refined only if the associated estimated partial variance is sufficiently high, following [147, 229]. More details are found in [148, 150].

Bibliography

[1] R. Abida and M. Bocquet. Targeting of observations for accidental atmospheric release monitoring. *Atmospheric Environment*, 43:6312–6327, 2009.

[2] I. Akhtar, J. Borggaard, J. A. Burns, H. Imtiaz, and L. Zietsman. Using functional gains for effective sensor location in flow control: a reduced-order modelling approach. *Journal of Fluid Mechanics*, 781: 622–656, 2015.

[3] G. Allaire. *Analyse numérique et optimisation*. Les Éditions de l'École polytechnique, 2012.

[4] J. L. Anderson. An Ensemble Adjustment Kalman Filter for Data Assimilation. *Monthly Weather Review*, 129:2884–2903, 2001.

[5] J. L. Anderson. Exploring the need for localization in ensemble data assimilation using a hierarchical ensemble filter. *Physica D*, 230:99–111, 2007.

[6] J. L. Anderson. An adaptive covariance inflation error correction algorithm for ensemble filters. *Tellus A*, 59:210–224, 2007.

[7] J. L. Anderson. Spatially and temporally varying adaptive covariance inflation for ensemble filters. *Tellus A*, 61:72–83, 2009.

[8] J. L. Anderson and S. L. Anderson. A Monte Carlo Implementation of the Nonlinear Filtering Problem to Produce Ensemble Assimilations and Forecasts. *Monthly Weather Review*, 127:2741–2758, 1999.

[9] J. C. André and M. Lesieur. Influence of helicity on the evolution of isotropic turbulence at high Reynolds number . *Journal of Fluid Mechanics*, 81:187–207, 1977.

[10] P. Armand, F. Brocheton, D. Poulet, F. Vendel, V. Dubourg, and T. Yalamas. Probabilistic safety analysis for urgent situations following the accidental release of a pollutant in the atmosphere. *Atmospheric Environment*, 96:1–10, 2014.

[11] L. Armijo. Minimization of functions having Lipschitz continuous first partial derivatives. *Pacific Journal of Mathematics*, 16:1–3, 1966.

[12] G. Artana, A. Cammilleri, J. Carlier, and E. Mémin. Strong and weak constraint variational assimilations for reduced order fluid flow modeling. *Journal of Computational Physics*, 231:3264–3288, 2012.

[13] D. Auroux. The back and forth nudging algorithm applied to a shallow water model, comparison and hybridization with the 4D-VAR. *International Journal for Numerical Methods in Fluids*, 61:911–929, 2009.

[14] D. Auroux and J. Blum. A nudging-based data assimilation method: the Back and Forth Nudging (BFN) algorithm. *Nonlinear Processes in Geophysics*, 15:305–319, 2008.

[15] S.-J. Baek and H. J. Sung. Quasi-periodicity in the wake of a rotationally oscillating cylinder. *Journal of Fluid Mechanics*, 408:275–300, 2000.

[16] N. L. Baker and R. Daley. Observation and background adjoint sensitivity in the adaptive observation-targeting problem. *Quarterly Journal of the Royal Meteorological Society*, 126:1431–1454, 2000.

[17] R. N. Bannister. A review of forecast error covariance statistics in atmospheric variational data assimilation. I: Characteristics and measurements of forecast error covariances. *Quarterly Journal of the Royal Meteorological Society*, 134:1951–1970, 2008.

[18] R. N. Bannister. A review of forecast error covariance statistics in atmospheric variational data assimilation. II: Modelling the forecast error covariance statistics. *Quarterly Journal of the Royal Meteorological Society*, 134:1971–1996, 2008.

[19] G. K. Batchelor. *The theory of homogeneous turbulence*. Cambridge University Press, 1953.

[20] F. Bellet, F. S. Godeferd, J. F. Scott, and C. Cambon. Wave turbulence in rapidly rotating flows. *Journal of Fluid Mechanics*, 562:83–121, 2006.

[21] B. A. Belson, O. Semeraro, C. W. Rowley, and D. S. Henningson. Feedback control of instabilities in the two-dimensional Blasius boundary layer: The role of sensors and actuators. *Physics of Fluids*, 25:054106, 2013.

[22] M. Bergmann, L. Cordier, and J.-P. Brancher. Optimal rotary control of the cylinder wake using proper orthogonal decomposition reduced-order model. *Physics of Fluids*, 17:097101, 2005.

[23] T. R. Bewley and B. Protas. Skin friction and pressure: the "footprints" of turbulence. *Physica D*, 196: 28–44, 2004.

[24] P. E. Bieringer, L. M. Rodriguez, F. Vandenberghe, J. G. Hurst, G. Bieberbach Jr., I. Sykes, J. R. Hannan, J. Zaragoza, and R. N. Fry Jr. Automated source term and wind parameter estimation for atmospheric transport and dispersion applications. *Atmospheric Environment*, 122:206–215, 2015.

[25] C. H. Bishop, B. J. Etherton, and S. J. Majumdar. Adaptive Sampling with the Ensemble Transform Kalman Filter. Part I: Theoretical Aspects. *Monthly Weather Review*, 129:420–436, 2001.

[26] B. Blocken, T. Stathopoulos, P. Saathoff, and X. Wang. Numerical evaluation of pollutant dispersion in the built environment: Comparisons between models and experiments. *Journal of Wind Engineering and Industrial Aerodynamics*, 96:1817–1831, 2008.

[27] B. Blocken, T. Stathopoulos, and J. P. A. J. van Beeck. Pedestrian-level wind conditions around buildings: Review of wind-tunnel and CFD techniques and their accuracy for wind comfort assessment. *Building and Environment*, 100:50–81, 2016.

[28] M. Bocquet and P. Sakov. An iterative ensemble Kalman smoother. *Quarterly Journal of the Royal Meteorological Society*, 140:1521–1535, 2014.

[29] M. Bocquet, C. A. Pires, and L. Wu. Beyond Gaussian Statistical Modeling in Geophysical Data Assimilation. *Monthly Weather Review*, 138:2997–3023, 2010.

[30] T. Braconnier, M. Ferrier, J.-C. Jouhaud, M. Montagnac, and P. Sagaut. Towards an adaptive POD/SVD surrogate model for aeronautic design. *Computers & Fluids*, 40:195–209, 2011.

[31] A. Briard, T. Gomez, and C. Cambon. Spectral modelling for passive scalar dynamics in homogeneous anisotropic turbulence. *Journal of Fluid Mechanics*, 799:159–199, 2016.

[32] A. Briard, T. Gomez, V. Mons, and P. Sagaut. Decay and growth laws in homogeneous shear turbulence. *Journal of Turbulence*, 17:699–726, 2016.

[33] M. Buehner, P. L. Houtekamer, C. Charette, H. L. Mitchell, and B. He. Intercomparison of Variational Data Assimilation and the Ensemble Kalman Filter for Global Deterministic NWP. Part I: Description and Single-Observation Experiments. *Monthly Weather Review*, 138:1550–1566, 2010.

[34] T. Bui-Thanh, M. Damodaran, and K. Willcox. Aerodynamic Data Reconstruction and Inverse Design Using Proper Orthogonal Decomposition. *AIAA Journal*, 42:1505–1516, 2004.

[35] G. Burgers, P. J. van Leeuwen, and G. Evensen. Analysis Scheme in the Ensemble Kalman Filter. *Monthly Weather Review*, 126:1719–1724, 1998.

[36] A. Burlot, B.-J. Gréa, F. S. Godeferd, C. Cambon, and J. Griffond. Spectral modelling of high Reynolds number unstably stratified homogeneous turbulence . *Journal of Fluid Mechanics*, 765:17–44, 2015.

[37] C. Cambon and L. Jacquin. Spectral approach to non-isotropic turbulence subjected to rotation. *Journal of Fluid Mechanics*, 202:295–317, 1989.

[38] C. Cambon and R. Rubinstein. Anisotropic developments for homogeneous shear flows. *Physics of Fluids*, 18:085106, 2006.

[39] C. Cambon, D. Jeandel, and J. Mathieu. Spectral modelling of homogeneous non-isotropic turbulence. *Journal of Fluid Mechanics*, 104:247–262, 1981.

[40] C. Cambon, N. N. Mansour, and F. S. Godeferd. Energy transfer in rotating turbulence. *Journal of Fluid Mechanics*, 337:303–332, 1997.

[41] C. Cambon, L. Danaila, F. S. Godeferd, and J. F. Scott. Third-order statistics and the dynamics of strongly anisotropic turbulent flows. *Journal of Turbulence*, 14:121–160, 2013.

[42] A. Cantelli, F. D'Orta, A. Cattini, F. Sebastianelli, and L. Cedola. Application of genetic algorithm for the simultaneous identification of atmospheric pollution sources. *Atmospheric Environment*, 115:36–46, 2015.

[43] G. R. Carmichael, A. Sandu, T. Chai, D. N. Daescu, E. M. Constantinescu, and Y. Tang. Predicting air quality: Improvements through advanced methods to integrate models and measurements. *Journal of Computational Physics*, 227:3540–3571, 2008.

[44] G. Carpentieri, B. Koren, and M. J. L. van Tooren. Adjoint-based aerodynamic shape optimization on unstructured meshes. *Journal of Computational Physics*, 224:267–287, 2007.

[45] I. P. Castro, Z.-T. Xie, V. Fuka, A. G. Robins, M. Carpentieri, D. Hertwig, and O. Coceal. Measurements and Computations of Flow in an Urban Street System. *Boundary-Layer Meteorology*, page , 2016. doi: 10.1007/s10546-016-0200-7.

[46] J. R. Chasnov. The decay of axisymmetric homogeneous turbulence. *Physics of Fluids*, 7:600–605, 1995.

[47] H. Chen, S. A. Orszag, I. Staroselsky, and S. Succi. Expanded analogy between Boltzmann kinetic theory of fluids and turbulence. *Journal of Fluid Mechanics*, 30:329–364, 2004.

[48] K. K. Chen and C. W. Rowley. H_2 optimal actuator and sensor placement in the linearised complex Ginzburg-Landau system. *Journal of Fluid Mechanics*, 681:241–260, 2011.

[49] S. Chen and G. D. Doolen. Lattice Boltzmann method for fluid flows. *Annual Review of Fluid Mechanics*, 30:329–364, 1998.

[50] Y. L. Chen and J. Wen. Sensor system design for building indoor air protection. *Building and Environment*, 43:1278–1285, 2008.

[51] M. Chevalier, J. Hoepffner, T. R. Bewley, and D. Henningson. State estimation in wall-bounded flow systems. Part 2. Turbulent flows. *Journal of Fluid Mechanics*, 552:167–187, 2006.

[52] H. Choi, W.-P. Jeon, and J. Kim. Control of Flow Over a Bluff Body. *Annual Review of Fluid Mechanics*, 40:113–139, 2008.

[53] S. Choi, H. Choi, and S. Kang. Characteristics of flow over a rotationally oscillating cylinder at low Reynolds number. *Physics of Fluids*, 14:2767–2777, 2002.

[54] F. K. Chow, B. Kosović, and S Chan. Source Inversion for Contaminant Plume Dispersion in Urban Environments Using Building-Resolving Simulations. *Journal of Applied Meteorology and Climatology*, 47:1553–1572, 2008.

[55] A. Cioaca and A. Sandu. An optimization framework to improve 4D-Var data assimilation system performance. *Journal of Computational Physics*, 275:377–389, 2014.

[56] T. T. Clark and C. Zemach. Symmetries and the approach to statistical equilibrium in isotropic turbulence. *Physics of Fluids*, 10:2846 – 2858, 1998.

[57] A. M. Clayton, A. C. Lorenc, and D. M. Barker. Operational implementation of a hybrid ensemble/4D-Var global data assimilation system at the Met Office. *Quarterly Journal of the Royal Meteorological Society*, 139:1445–1461, 2013.

[58] K. Cohen, S. Siegel, and T. McLaughlin. A heuristic approach to effective sensor placement for modeling of a cylinder wake. *Computers & Fluids*, 35:103–120, 2006.

[59] S. E. Cohn. An introduction to estimation theory. *Journal of the Meteorological Society of Japan*, 75: 257–288, 1997.

[60] C. H. Colburn, J. B. Cessna, and T. R. Bewley. State estimation in wall-bounded flow systems. Part 3. The ensemble Kalman filter. *Journal of Fluid Mechanics*, 682:289–303, 2011.

[61] B. Combés, D. Heitz, A. Guibert, and E. Mémin. A particle filter to reconstruct a free-surface flow from a depth camera. *Fluid Dynamics Research*, 47:051404, 2015.

[62] G. Comte-Bellot and S. Corrsin. The use of a contraction to improve the isotropy of grid-generated turbulence. *Journal of Fluid Mechanics*, 25:657 – 682, 1966.

[63] P. G. Constantine, M. Emory, J. Larsson, and G. Iaccarino. Exploiting active subspaces to quantify uncertainty in the numerical simulation of the HyShot II scramjet. *Journal of Computational Physics*, 302: 1–20, 2015.

[64] E. Cosme, J. Verron, P. Brasseur, J. Blum, and D. Auroux. Smoothing Problems in a Bayesian Framework and Their Linear Gaussian Solutions. *Monthly Weather Review*, 140:683–695, 2012.

[65] P. Courtier, J.-N. Thépaut, and A. Hollingsworth. A strategy for operational implementation of 4D-Var, using an incremental approach. *Quarterly Journal of the Royal Meteorological Society*, 120:1367–1387, 1994.

[66] R. Ştefănescu, A. Sandu, and I. M. Navon. POD/DEIM reduced-order strategies for efficient four dimensional variational data assimilation. *Journal of Computational Physics*, 295:569–595, 2015.

[67] J. D'Adamo, N. Papadakis, E. Mémin, and G. Artana. Variational assimilation of POD low-order dynamical systems. *Journal of Turbulence*, 8:1–22, 2007.

[68] D. N. Daescu. On the Sensitivity Equations of Four-Dimensional Variational (4D-Var) Data Assimilation. *Monthly Weather Review*, 136:3050–3065, 2008.

[69] P. A. Davidson. *Turbulence. An introduction for scientists and engineers*. Oxford University Press, 2004.

[70] P. A. Davidson, N. Okamoto, and Y. Kaneda. On freely decaying, anisotropic, axisymmetric Saffman turbulence. *Journal of Fluid Mechanics*, 706:150–172, 2012.

[71] L. S. F. de la Fuente. *Simulation of atmospheric tracer dispersion over urban geometries using a Lattice Boltzman method*. PhD thesis, Manchester Metropolitan University, 2003.

[72] G. Desroziers, J.-T. Camino, and L. Berre. 4DEnVar: link with 4D state formulation of variational assimilation and different possible implementations. *Quarterly Journal of the Royal Meteorological Society*, 140:2097–2110, 2014.

[73] H. Ding, C. Shu, K. S. Yeo, and D. Xu. Numerical simulation of flows around two circular cylinders by mesh-free least square-based finite difference methods. *International Journal of Numerical Methods in Fluids*, 53:305–332, 2007.

[74] L. Djenidi, Md. Kamruzzaman, and R. A. Antonia. Power-law exponent in the transition period of decay in grid turbulence. *Journal of Fluid Mechanics*, 779:544–555, 2015.

[75] O. Ertunç, N. Ozyilmaz, H. Lienhart, F. Durst, and K. Beronov. Homogeneity of turbulence generated by static-grid structures. *Journal of Fluid Mechanics*, 654:473 – 500, 2010.

[76] G. Evensen. Using the extended Kalman filter with a multilayer quasi-geostrophic ocean model. *Journal of Geophysical Research*, 97:17905–17924, 1992.

[77] G. Evensen. Sequential data assimilation with a nonlinear quasi-geostrophic model using Monte Carlo methods to forecast error statistics. *Journal of Geophysical Research*, 99:10143–10162, 1994.

[78] G. Evensen. Sampling strategies and square root analysis schemes for the EnKF. *Ocean Dynamics*, 54: 539–560, 2004.

[79] G. Evensen. *Data Assimilation: The Ensemble Kalman Filter (2nd edition)*. Springer-Verlag, 2009.

[80] G. Evensen and P. J. van Leeuwen. An Ensemble Kalman Smoother for Nonlinear Dynamics. *Monthly Weather Review*, 128:1852–1867, 2000.

[81] T. L. B. Flinois and T. Colonius. Optimal control of circular cylinder wakes using long control horizons. *Physics of Fluids*, 27:087105, 2015.

[82] A. D. Fontanini, U. Vaidya, and B. Ganapathysubramanian. A methodology for optimal placement of sensors in enclosed environments: A dynamical systems approach. *Building and Environment*, 100:145–161, 2016.

[83] D. P. G. Foures, N. Dovetta, D. Sipp, and P. J. Schmid. A data-assimilation method for Reynolds-averaged Navier-Stokes-driven mean flow reconstruction. *Journal of Fluid Mechanics*, 759:404–431, 2014.

[84] J. Franke, A. Hellsten, K. H. Schlünzen, and B. Carissimo. The COST 732 Best Practice Guideline for CFD simulation of flows in the urban environment: a summary. *International Journal of Environment and Pollution*, 44:419–427, 2011.

[85] W. K. George. Asymptotic Effect of Initial and Upstream Conditions on Turbulence. *Journal of Fluids Engineering*, 134:061203, 2012.

[86] W. K. George and H. Wang. The exponential decay of homogeneous turbulence. *Physics of Fluids*, 21: 025108, 2009.

[87] F. S. Godeferd and C. Cambon. Detailed investigation of energy transfers in homogeneous stratified turbulence. *Physics of Fluids*, 6:2084–2100, 1994.

[88] C. Gorlé, C. Garcia-Sanchez, and G. Iaccarino. Quantifying inflow and RANS turbulence model form uncertainties for wind engineering flows. *Journal of Wind Engineering and Industrial Aerodynamics*, 144:202–212, 2015.

[89] S. Goto and J. C. Vassilicos. Energy dissipation and flux laws for unsteady turbulence. *Physics Letters A*, 379:1144–1148, 2015.

[90] P. Gousseau, B. Blocken, T. Stathopoulos, and G. J. F. van Heijst. CFD simulation of near-field pollutant dispersion on a high-resolution grid: A case study by LES and RANS for a building group in downtown Montreal. *Atmospheric Environment*, 45:428–438, 2011.

[91] A. Gronskis, D. Heitz, and E. Mémin. Inflow and initial conditions for direct numerical simulation based on adjoint data assimilation. *Journal of Computational Physics*, 242:480–497, 2013.

[92] H. Gunes, S. Sirisup, and G. E. Karniadakis. Gappy data: To Krig or not to Krig? *Journal of Computational Physics*, 212:358–382, 2006.

[93] J. Habert, S. Ricci, E. Le Pape, O. Thual, A. Piacentini, N. Goutal, G. Jonville, and M. Rochoux. Reduction of the uncertainties in the water level-discharge relation of a 1D hydraulic model in the context of operational flood forecasting. *Journal of Hydrology*, 532:52–64, 2016.

[94] T. Hayase. Numerical simulation of real-world flows. *Fluid Dynamics Research*, 47:051201, 2015.

[95] J.-W. He, R. Glowinski, R. Metcalfe, A. Nordlander, and J. Periaux. Active Control and Drag Optimization for Flow Past a Circular Cylinder: I. Oscillatory Cylinder Rotation. *Journal of Computational Physics*, 163:83–117, 2000.

[96] R. J. Hearst and P. Lavoie. Decay of turbulence generated by a square-fractal-element grid. *Journal of Fluid Mechanics*, 741:567–584, 2014.

[97] D. Heitz, E. Mémin, and C. Schnörr. Variational fluid flow measurements from image sequences: synopsis and perspectives. *Experiments in Fluids*, 48:369–393, 2010.

[98] J. R. Herring. Approach of axisymmetric turbulence to isotropy. *Physics of Fluids*, 17:859–872, 1974.

[99] D. Hertwig, G. C. Efthimiou, J. G. Bartzis, and B. Leitl. CFD-RANS model validation of turbulent flow in a semi-idealized urban canopy. *Journal of Wind Engineering and Industrial Aerodynamics*, 111:61–72, 2012.

[100] J. Hoepffner, M. Chevalier, T. R. Bewley, and D. Henningson. State estimation in wall-bounded flow systems. Part 1. Perturbed laminar flows. *Journal of Fluid Mechanics*, 534:263–294, 2005.

[101] J. E. Hoke and R. A. Anthes. The Initialization of Numerical Models by a Dynamic-Initialization Technique. *Monthly Weather Review*, 104:1551–1556, 1976.

[102] C. Homescu, I. M. Navon, and Z. Li. Suppression of vortex shedding for flow around a circular cylinder using optimal control. *International Journal of Numerical Methods in Fluids*, 38:43–69, 2002.

[103] P. L. Houtekamer and H. L. Mitchell. A Sequential Ensemble Kalman Filter for Atmospheric Data Assimilation. *Monthly Weather Review*, 129:123–137, 2001.

[104] D. Hurst and J. C. Vassilicos. Scalings and decay of fractal-generated turbulence. *Physics of Fluids*, 19: 035103, 2007.

[105] A. Jameson. Time-Dependent Calculations using Multigrid, with Applications to Unsteady Flows past Airfoils and Wings, AIAA Paper No. 91-1596. 1991.

[106] P. Jawahar and H. Kamath. A High-Resolution Procedure for Euler and Navier–Stokes Computations on Unstructured Grids. *Journal of Computational Physics*, 164:165–203, 2000.

[107] A. H. Jazwinski. *Stochastic Processes and Filtering Theory*. Dover Publications, Inc., 2007.

[108] D. R. Jones, M. Schonlau, and W. J. Welch. Efficient Global Optimization of Expensive Black-Box Functions. *Journal of Global Optimization*, 13:455–492, 1998.

[109] J.-C. Jouhaud, P. Sagaut, and B. Labeyrie. A Kriging Approach for CFD/Wind-Tunnel Data Comparison. *ASME Journal of Fluids Engineering*, 128:847–855, 2006.

[110] F. Juillet, P. J. Schmid, and P. Huerre. Control of amplifier flows using subspace identification techniques. *Journal of Fluid Mechanics*, 725:522–565, 2013.

[111] R. E. Kalman. A New Approach to Linear Filtering and Prediction Problems. *Journal of Basic Engineering*, 82:35–45, 1960.

[112] E. Kalnay. *Atmospheric modeling, data assimilation and predictability*. Cambridge University Press, 2003.

[113] W. Kang and L. Xu. Optimal placement of mobile sensors for data assimilations. *Tellus A*, 64:17133, 2012.

[114] H. Kato and S. Obayashi. Approach for uncertainty of turbulence modeling based on data assimilation technique. *Computers & Fluids*, 85:2–7, 2013.

[115] H. Kato, A. Yoshizawa, G. Ueno, and S. Obayashi. A data assimilation methodology for reconstructing turbulent flows around aircraft. *Journal of Computational Physics*, 283:559–581, 2015.

[116] P. Kersaudy, B. Sudret, N. Varsier, O. Picon, and J. Wiart. A new surrogate modeling technique combining Kriging and polynomial chaos expansions - Application to uncertainty analysis in computational dosimetry. *Journal of Computational Physics*, 286:103–117, 2015.

[117] R. Kikuchi, T. Misaka, and S. Obayashi. Assessment of probability density function based on POD reduced-order model for ensemble-based data assimilation. *Fluid Dynamics Research*, 47:051403, 2015.

[118] D. T. Kleist and K. Ide. An OSSE-Based Evaluation of Hybrid Variational–Ensemble Data Assimilation for the NCEP GFS. Part II: 4DEnVar and Hybrid Variants. *Monthly Weather Review*, 143:452–470, 2015.

[119] D. D. Knight. A fully implicit Navier-Stokes algorithm using an unstructured grid and flux difference splitting . *Applied Numerical Mathematics*, 16:101–128, 1994.

[120] R. Kotapati, A. Keating, S. Kandasamy, B. Duncan, R. Shock, and H. Chen. The Lattice-Boltzmann-VLES Method for Automotive Fluid Dynamics Simulation, a Review, SAE Technical Paper 2009-26-0057. 2009.

[121] I. V. Kovalets, S. Andronopoulos, A. G. Venetsanos, and J. G. Bartzis. Identification of strength and location of stationary point source of atmospheric pollutant in urban conditions using computational fluid dynamics model. *Mathematics and Computers in Simulation*, 82:244–257, 2011.

[122] P.-A. Krogstad and P. A. Davidson. Freely-decaying, homogeneous turbulence generated by multi-scale grids. *Journal of Fluid Mechanics*, 680:417 – 434, 2011.

[123] D. D. Kuhl, T. E. Rosmond, C. H. Bishop, J. McLay, and N. L. Baker. Comparison of Hybrid Ensemble/4DVar and 4DVar within the NAVDAS-AR Data Assimilation Framework. *Monthly Weather Review*, 141:2740–2758, 2013.

[124] P. Kumar, A.-A. Feiz, S. K. Sing, P. Ngae, and G. Turbelin. Reconstruction of an atmospheric tracer source in an urban-like environment. *Journal of Geophysical Research: Atmospheres*, 120:12589–12604, 2015.

[125] S. Kumar, C. Lopez, O. Probst, G. Francisco, D. Askari, and Y. Yang. Flow past a rotationally oscillating cylinder. *Journal of Fluid Mechanics*, 735:307–346, 2013.

[126] W. Lahoz, B. Khattatov, and R. Ménard (Eds.). *Data Assimilation: Making Sense of Observations*. Springer-Verlag, 2010.

[127] R. H. Langland and N. L. Baker. Estimation of observation impact using the NRL atmospheric variational data assimilation adjoint system. *Tellus A*, 56:189–201, 2004.

[128] F.-X. Le Dimet and O. Talagrand. Variational algorithms for analysis and assimilation of meteorological observations: theoretical aspects. *Tellus A*, 38A:97–110, 1986.

[129] F.-X. Le Dimet, H.-E. Ngodock, B. Luong, and J. Verron. Sensitivity Analysis in Variational Data Assimilation. *Journal of the Meteorological Society of Japan*, 75:245–255, 1997.

[130] F.-X. Le Dimet, I. M. Navon, and D. N. Daescu. Second-Order Information in Data Assimilation. *Monthly Weather Review*, 130:629–648, 2002.

[131] R. W. Lee and J. J. Kulesz. A risk-based sensor placement methodology. *Journal of Hazardous Materials*, 158:417–429, 2008.

[132] M. Lesieur. *Turbulence in Fluids (4th edition).* Springer, 2008.

[133] J. M. Lewis, S. Lakshmivarahan, and S. K. Dhall. *Dynamic data assimilation: a least squares approach*, volume 104 of *Encyclopedia of Mathematics and its Applications*. Cambridge University Press, 2006.

[134] J. Li and D. Xiu. A generalized polynomial chaos based ensemble Kalman filter with high accuracy. *Journal of Computational Physics*, 228:5454–5469, 2009.

[135] W. Li, G. Lin, and D. Zhang. An adaptive ANOVA-based PCKF for high-dimensional nonlinear inverse modeling. *Journal of Computational Physics*, 258:752–772, 2014.

[136] Z. Li and I. M. Navon. Optimality of variational data assimilation and its relationship with the Kalman filter and smoother. *Quarterly Journal of the Royal Meteorological Society*, 127:661–683, 2001.

[137] J.-L. Lions. *Optimal control of systems governed by partial differential equations*. Springer-Verlag, 1971.

[138] C. Liu and M. Xue. Relationships among Four-Dimensional Hybrid Ensemble–Variational Data Assimilation Algorithms with Full and Approximate Ensemble Covariance Localization. *Monthly Weather Review*, 144:591–606, 2016.

[139] C. Liu, X. Zheng, and C. H. Sung. Preconditioned Multigrid Methods for Unsteady Incompressible Flows. *Journal of Computational Physics*, 139:35–57, 1998.

[140] C. Liu, Q. Xiao, and B. Wang. An Ensemble-Based Four-Dimensional Variational Data Assimilation Scheme. Part I: Technical Formulation and Preliminary Test. *Monthly Weather Review*, 136:3363–3373, 2008.

[141] D. M. Livings, S. L. Dance, and N. K. Nichols. Unbiased ensemble square root filters. *Physica D*, 237: 1021–1028, 2008.

[142] A. C. Lorenc. Analysis methods for numerical weather prediction. *Quarterly Journal of the Royal Meteorological Society*, 112:1177–1194, 1986.

[143] A. C. Lorenc. The potential of the ensemble Kalman filter for NWP-a comparison with 4D-Var. *Quarterly Journal of the Royal Meteorological Society*, 129:3183–3203, 2003.

[144] A. C. Lorenc, N. E. Bowler, A. M. Clayton, S. R. Pring, and D. Fairbairn. Comparison of Hybrid-4DEnVar and Hybrid-4DVar Data Assimilation Methods for Global NWP. *Monthly Weather Review*, 143:212–229, 2015.

[145] H. Luo, J. D. Baum, and R. Löhner. An accurate, fast, matrix-free implicit method for computing unsteady flows on unstructured grids. *Computers & Fluids*, 30:137–159, 2001.

[146] D. Ma, J. Deng, and Z. Zhang. Comparison and improvements of optimization methods for gas emission source identification. *Atmospheric Environment*, 81:188–198, 2013.

[147] X. Ma and N. Zabaras. An adaptive high-dimensional stochastic model representation technique for the solution of stochastic partial differential equations. *Journal of Computational Physics*, 229:3884–3915, 2010.

[148] L. Margheri. *Étude de l'impact des incertitudes dans l'évaluation du risque NRBC provoqué en zone urbaine*. PhD thesis, Université Pierre et Marie Curie, 2015.

[149] L. Margheri and P. Sagaut. An uncertainty quantification analysis in a simplified problem of urban pollutant dispersion by means of ANOVA-POD/Kriging-based response surfaces, ASME Fluids Engineering Division Summer Meeting, No. V01DT28A004. 2014.

[150] L. Margheri and P. Sagaut. A hybrid anchored-ANOVA-POD/Kriging method for response surface building based on unsteady high-fidelity CFD. *Journal of Computational Physics*, 324:137–173, 2016.

[151] N. Mazellier and J. C. Vassilicos. Turbulence without Richardson-like cascade. *Physics of Fluids*, 22: 075101, 2010.

[152] B. Mazzi and J. C. Vassilicos. Fractal-generated turbulence. *Journal of Fluid Mechanics*, 502:65 – 87, 2004.

[153] M. Meldi. The signature of initial production mechanisms in isotropic turbulence decay. *Physics of Fluids*, 28:035105, 2016.

[154] M. Meldi and P. Sagaut. On non-self-similar regimes in homogeneous isotropic turbulence decay. *Journal of Fluid Mechanics*, 711:364–393, 2012.

[155] M. Meldi and P. Sagaut. Further insights into self-similarity and self- preservation in freely decaying isotropic turbulence. *Journal of Turbulence*, 14:24–53, 2013.

[156] M. Meldi, H. Lejemble, and P. Sagaut. On the emergence of non-classical decay regimes in multi-scale/ fractal generated isotropic turbulence. *Journal of Fluid Mechanics*, 756:816–843, 2014.

[157] J. Meyers and C. Meneveau. A functional form of the energy spectrum parametrizing bottleneck and intermittency effects. *Physics of Fluids*, 20:065109, 2008.

[158] M. D. Millionschikov. Theory of homogeneous isotropic turbulence. *Doklady Akademii nauk SSSR*, 33: 22–24, 1941.

[159] P. Mokhasi and D. Rempfer. Optimized sensor placement for urban flow measurement. *Physics of Fluids*, 16:1758–1764, 2004.

[160] V. Mons, J.-C. Chassaing, T. Gomez, and P. Sagaut. Is isotropic turbulence decay governed by asymptotic behavior of large scales? An eddy-damped quasi-normal Markovian-based data assimilation study. *Physics of Fluids*, 26:115105, 2014.

[161] V. Mons, M. Meldi, and P. Sagaut. Numerical investigation on the partial return to isotropy of freely decaying homogeneous axisymmetric turbulence . *Physics of Fluids*, 26:025110, 2014.

[162] V. Mons, C. Cambon, and P. Sagaut. A spectral model for homogeneous shear-driven anisotropic turbulence in terms of spherically averaged descriptors. *Journal of Fluid Mechanics*, 788:147–182, 2016.

[163] V. Mons, J.-C. Chassaing, T. Gomez, and P. Sagaut. Reconstruction of unsteady viscous flows using data assimilation schemes. *Journal of Computational Physics*, 316:255–280, 2016.

[164] P. Moonen, T Defraeye, V. Dorer, B. Blocken, and J. Carmeliet. Urban physics: Effects of the microclimate on comfort, health and energy-demand. *Frontier of Architectural Research*, 1:197–228, 2012.

[165] S. K. Nadarajah and A. Jameson. Studies of continuous and discrete adjoint approaches to viscous automatic aerodynamic shape optimization, AIAA Paper No. 2001-2530. 2001.

[166] K. Nagata, Y. Sakai, T. Inaba, H. Suzuki, O. Terashima, and H. Suzuki. Turbulence structure and turbulence kinetic energy transport in multiscale/fractal-generated turbulence. *Physics of Fluids*, 25:065102, 2013.

[167] L. Nerger, S. Schulte, and A. Bunse-Gerstner. On the influence of model nonlinearity and localization on ensemble Kalman smoothing. *Quarterly Journal of the Royal Meteorological Society*, 140:2249–2259, 2014.

[168] J. Nocedal. Updating Quasi-Newton Matrices With Limited Storage. *Mathematics of Computation*, 35: 773–782, 1980.

[169] C. Obrecht, F. Kuznik, L. Merlier, J.-J. Roux, and B. Tourancheau. Towards aeraulic simulations at urban scale using the lattice Boltzmann method. *Environmental Fluid Mechanics*, 15:753–770, 2015.

[170] E. F. O'Brien and G. C. Francis. A consequence of the zero fourth cumulant approximation. *Journal of Fluid Mechanics*, 13:369–382, 1963.

[171] Y. Ogura. A consequence of the zero fourth cumulant approximation in the decay of isotropic turbulence. *Journal of Fluid Mechanics*, 16:33–40, 1963.

[172] S. A. Orszag. Analytical theories of turbulence. *Journal of Fluid Mechanics*, 41:363 – 386, 1970.

[173] N. Papadakis and E. Mémin. Variational Assimilation of Fluid Motion from Image Sequence. *SIAM Journal on Imaging Sciences*, 1:343–363, 2008.

[174] N. Papadakis, E. Mémin, A. Cuzol, and N. Gengembre. Data assimilation with the weighted ensemble Kalman filter. *Tellus A*, 62:673–697, 2010.

[175] S. K. Park and L. Xu (Eds.). *Data Assimilation for Atmospheric, Oceanic and Hydrologic Applications*. Springer-Verlag, 2009.

[176] J. E. V. Peter and R. P. Dwight. Numerical sensitivity analysis for aerodynamic optimization: A survey of approaches. *Computers & Fluids*, 39:373–391, 2010.

[177] A. Ponçot, J.-P. Argaud, B. Bouriquet, P. Erhard, S. Gratton, and O. Thual. Variational assimilation for xenon dynamical forecasts in neutronic using advanced background error covariance matrix modelling. *Annals of Nuclear Energy*, 60:39–50, 2013.

[178] O. Posdziech and R. Grudmann. A systematic approach to the numerical calculation of fundamental quantities of the two-dimensional flow over a circular cylinder. *Journal of Fluids and Structures*, 23: 479–499, 2007.

[179] A. Pouquet, M. Lesieur, J. C. André, and C. Basdevant. Evolution of high Reynolds number two-dimensional turbulence. *Journal of Fluid Mechanics*, 72:305 – 319, 1975.

[180] B. Protas and A. Styczek. Optimal rotary control of the cylinder wake in the laminar regime. *Physics of Fluids*, 14:2073–2087, 2002.

[181] I. Proudman and W. H. Reid. On the decay of a normally distributed and homogeneous turbulent velocity field. *Philosophical Transactions of the Royal Society A*, 297:163–189, 1954.

[182] C. Qiu and J. Chou. Four-dimensional data assimilation method based on SVD: Theoretical aspect. *Theoretical and Applied Climatology*, 83:51–57, 2006.

[183] L. Qu, C. Norberg, L. Davidson, S.-H. Peng, and F. Wang. Quantitative numerical analysis of flow past a circular cylinder at Reynolds number between 50 and 200. *Journal of Fluids and Structures*, 39:347–370, 2013.

[184] R. D. Rausch, J. T. Batina, and H. T. Y. Yang. Spatial adaptation of unstructured meshes for unsteady aerodynamic flow computations. *AIAA Journal*, 30:1243–1251, 1992.

[185] P. L. Roe. Approximate Riemann solvers, parameter vectors, and difference schemes. *Journal of Computational Physics*, 43:357–372, 1981.

[186] R. Rubinstein, S. Kurien, and C. Cambon. Scalar and tensor spherical harmonics expansion of the velocity correlation in homogeneous anisotropic turbulence . *Journal of Turbulence*, 16:1058–1075, 2015.

[187] J. Sacks, W. J. Welch, T. J. Mitchell, and H. P. Wynn. Design and Analysis of Computer Experiments. *Statistical Science*, 4:409–423, 1989.

[188] P. Sagaut and C. Cambon. *Homogeneous Turbulence Dynamics*. Cambridge University Press, 2008.

[189] A. Saltelli, P. Annoni, I. Azzini, F. Campolongo, M. Ratto, and S. Tarantola. Variance based sensitivity analysis of model output. Design and estimator for the total sensitivity index. *Computer Physics Communications*, 181:259–270, 2010.

[190] D. Sharov and K. Nakahashi. Reordering of 3-D Hybrid Unstructured Grids for Vectorized LU-SGS Navier-Stokes Computations, AIAA Paper No. 97-2102. 1997.

[191] S. K. Singh and R. Rani. A least-squares inversion technique for identification of a point release: Application to Fusion Field Trials 2007 . *Atmospheric Environment*, 92:104–117, 2014.

[192] L. Sirovich. Turbulence and the Dynamics of Coherent Structures Part I: Coherent Structures. *Quaterly of Applied Mathematics*, 45:561–571, 1987.

[193] I. M. Sobol'. Global sensitivity indices for nonlinear mathematical models and their Monte Carlo estimates. *Mathematics and Computers in Simulation*, 55:271–280, 2001.

[194] C. G. Speziale. Turbulence Modeling for Time-Dependent RANS and VLES: A Review. *AIAA Journal*, 36:173–184, 1998.

[195] J. L. Steger and R. F. Warming. Flux vector splitting of the inviscid gasdynamic equations with application to finite-difference methods. *Journal of Computational Physics*, 40:263–293, 1981.

[196] T. Suzuki. Reduced-order Kalman-filtered hybrid simulation combining particle tracking velocimetry and direct numerical simulation. *Journal of Fluid Mechanics*, 709:249–288, 2012.

[197] O. Talagrand. Assimilation of observations, an introduction. *Journal of the Meteorological Society of Japan*, 75:191–209, 1997.

[198] K. Tang, P. M. Congedo, and R. Abgrall. Adaptive surrogate modeling by ANOVA and sparse polynomial dimensional decomposition for global sensitivity analysis in fluid simulation. *Journal of Computational Physics*, 314:557–589, 2016.

[199] A. Tarantola. *Inverse Problem Theory and Methods for Model Parameter Estimation*. Society for Industrial and Applied Mathematics, 2005.

[200] B. Thiria and J. E. Wesfreid. Stability properties of forced wakes. *Journal of Fluid Mechanics*, 579: 137–161, 2007.

[201] B. Thiria, S. Goujon-Durand, and J. E. Wesfreid. The wake of a cylinder performing rotary oscillations. *Journal of Fluid Mechanics*, 560:123–147, 2006.

[202] A. Thormann and C. Meneveau. Decay of homogeneous, nearly isotropic turbulence behind active fractal grids. *Physics of Fluids*, 26:025112, 2014.

[203] X. Tian, Z. Xie, and A. Dai. An ensemble-based explicit four-dimensional variational assimilation method. *Journal of Geophysical Research*, 113:D21124, 2008.

[204] X. Tian, Z. Xie, and Q. Sun. A POD-based ensemble four-dimensional variational assimilation method. *Tellus A*, 63:805–816, 2011.

[205] M. K. Tippett, J. L. Anderson, C. H. Bishop, T. M. Hamill, and J. S. Whitaker. Ensemble Square Root Filters. *Monthly Weather Review*, 131:1485–1490, 2003.

[206] P. Tokumaru and P. E. Dimotakis. Rotary oscillation control of cylinder wake. *Journal of Fluid Mechanics*, 224:77–90, 1991.

[207] Y. Tominaga and T. Stathopoulos. Numerical simulation of dispersion around an isolated cubic building: Model evaluation of RANS and LES. *Building and Environment*, 45:2231–2239, 2010.

[208] Y. Tominaga and T. Stathopoulos. CFD simulation of near-field pollutant dispersion in the urban environment: A review of current modeling techniques. *Atmospheric Environment*, 79:716–730, 2013.

[209] Y. Tominaga, R. Yoshie, A. Mochida, H. Kataoka, K. Harimoto, and T. Nozu. Cross Comparisons of CFD Prediction for Wind Environment at Pedestrian Level around Buildings. Part 2 : Comparison of Results for Flowfield around Building Complex in Actual Urban Area. Proceedings of the Sixth Asia-Pacific Conference on Wind Engineering, pages 2661–2670, 2005.

[210] Y. Tominaga, A. Mochida, R. Yoshie, H. Katoaka, T. Nozu, M. Yoshikawa, and T. Shirasawa. AIJ guidelines for practical applications of CFD to pedestrian wind environment around buildings. *Journal of Wind Engineering and Industrial Aerodynamics*, 96:1749–1761, 2008.

[211] E. F. Toro. *Riemann Solvers and Numerical Methods for Fluid Dynamics (3rd edition)*. Springer-Verlag, 2010.

[212] P. C. Valente and J. C. Vassilicos. The decay of turbulence generated by a class of multiscale grids. *Journal of Fluid Mechanics*, 687:300 – 340, 2011.

[213] P. C. Valente and J. C. Vassilicos. Universal Dissipation Scaling for Nonequilibrium Turbulence. *Physical Review Letters*, 108:214503, 2012.

[214] P. J. van Leeuwen. Particle Filtering in Geophysical Systems. *Monthly Weather Review*, 137:4089–4114, 2009.

[215] P. J. van Leeuwen. Efficient nonlinear data-assimilation in geophysical fluid dynamics. *Computers & Fluids*, 46:52–58, 2011.

[216] P. J. van Leeuwen and G. Evensen. Data Assimilation and Inverse Methods in Terms of a Probabilistic Formulation. *Monthly Weather Review*, 124:2898–2913, 1996.

[217] P. A. Vidard, F.-X. Le Dimet, and A. Piacentini. Determination of optimal nudging coefficients. *Tellus A*, 55:1–15, 2003.

[218] B. Wang, J. Liu, S. Wang, W. Cheng, J. Liu, C. Liu, Q. Xiao, and Y.-H. Kuo. An Economical Approach to Four-dimensional Variational Data Assimilation. *Advances in Atmospheric Sciences*, 27:715–727, 2010.

[219] X. Wang and T. Lei. GSI-Based Four-Dimensional Ensemble–Variational (4DEnsVar) Data Assimilation: Formulation and Single-Resolution Experiments with Real Data for NCEP Global Forecast System. *Monthly Weather Review*, 142:3303–3325, 2014.

[220] X. Wang, D. M. Barker, C. Snyder, and T. M. Hamill. A Hybrid ETKF–3DVAR Data Assimilation Scheme for the WRF Model. Part I: Observing System Simulation Experiment. *Monthly Weather Review*, 136: 5116–5131, 2008.

[221] Z. Wang, I. M. Navon, F.-X. Le Dimet, and X. Zou. The Second Order Adjoint Analysis: Theory and Applications. *Meteorology and Atmospheric Physics*, 50:3–20, 1992.

[222] S. Warner, N. Platt, and J. F. Heagy. User-Oriented Two-Dimensional Measure of Effectiveness for the Evaluation of Transport and Dispersion Models. *Journal of Applied Meteorology*, 43:58–73, 2004.

[223] J. S. Whitaker and T. M. Hamill. Ensemble Data Assimilation without Perturbed Observations. *Monthly Weather Review*, 130:1913–1924, 2002.

[224] C. K. Wikle and L. M. Berliner. A Bayesian tutorial for data assimilation. *Physica D*, 230:1–16, 2007.

[225] K. Willcox. Unsteady flow sensing and estimation via the gappy proper orthogonal decomposition. *Computers & Fluids*, 35:208–226, 2006.

[226] C. H. K. Williamson. Vortex dynamics in the cylinder wake. *Annual Review of Fluid Mechanics*, 28: 477–539, 1996.

[227] L. Wu, M. Bocquet, and M. Chevallier. Optimal reduction of the ozone monitoring network over France. *Atmospheric Environment*, 44:3071–3083, 2010.

[228] V. Yakhot, S. A. Orszag, S. Thangam, T. B. Gatski, and C. G. Speziale. Development of turbulence models for shear flows by a double expansion technique. *Physics of Fluids A*, 36:1510–1520, 1992.

[229] X. Yang, M. Choi, G. Lin, and G. E. Karniadakis. Adaptive ANOVA decomposition of stochastic incompressible and compressible flows. *Journal of Computational Physics*, 231:1587–1614, 2012.

[230] Y. Yang, C. Robinson, D. Heitz, and E. Mémin. Enhanced ensemble-based 4DVar scheme for data assimilation. *Computers & Fluids*, 115:201–210, 2015.

[231] E. Yee, F.-S. Lien, A. Keats, and R. D'Amours. Bayesian inversion of concentration data: Source reconstruction in the adjoint representation of atmospheric diffusion. *Journal of Wind Engineering and Industrial Aerodynamics*, 96:1805–1816, 2008.

[232] B. Yildirim, C. Chryssostomidis, and G. E. Karniadakis. Efficient sensor placement for ocean measurements using low-dimensional concepts. *Ocean Modelling*, 27:160–173, 2009.

[233] M. Zhang and F. Zhang. E4DVar: Coupling an Ensemble Kalman Filter with Four-Dimensional Variational Data Assimilation in a Limited-Area Weather Prediction Model. *Monthly Weather Review*, 140: 587–600, 2012.

[234] X. L. Zhang, G. F. Su, H. Y. Yuan, J. G. Chen, and Q. Y. Huang. Modified ensemble Kalman filter for nuclear accident atmospheric dispersion: Prediction improved and source estimated. *Journal of Hazardous Materials*, 280:143–115, 2014.

[235] X. Zheng and Z. Chen. Back-calculation of the strength and location of hazardous materials releases using the pattern search method. *Journal of Hazardous Materials*, 183:474–481, 2010.

[236] X. Zou, I. M. Navon, and F.-X. Le Dimet. An optimal nudging data assimilation scheme using parameter estimation. *Quarterly Journal of the Royal Meteorological Society*, 118:1163–1186, 1992.